ISBN: 978-605-83575-0-1

2016 BOOK OF PROCEEDINGS

Chapter 7

ICENS

INTERNATIONAL CONFERENCE ON ENGINEERING AND NATURAL SCIENCES

24-28 May 2016 / Sarajevo

Organized by

EUROPE CONGRESS
www.europecongress.org

Supported by

ZENITH GROUP

CNR GROUP
where innovation starts

TURKISH AIRLINES

ICENS
INTERNATIONAL CONFERENCE ON ENGINEERING AND NATURAL SCIENCES
24-28 May 2016 /Sarajevo

Multi Token Circulation in a Common Channel for Location Information Sharing in Multi-UAV Systems

Eyup Emre Ulku[1], Ilker Bekmezci[2]

Abstract

By the help of the miniaturization and cost reduction in UAV technologies, instead of utilizing only one big UAV, the systems consists of multiple small UAVs can be realized. Although multi-UAV system can perform more efficiently in many application areas, it also have some limitations. Communication is one of the most important limitations of these systems, and Flying Ad hoc Network (FANET) is an effective solution when there is no preinstalled infrastructure. In FANET, UAVs need to know the position information of each other also to ensure collision free coordination. For this reason, sharing of location information between UAVs is an important role in FANET. Token based approach is one of the significant methods used for location information sharing. In this approach, a token which includes coordinates of the UAVs circulates between UAVs. Thus, UAVs know each other's position due to the circulating token. However, especially in UAV swarms, the circulation of the token takes longer time and it may result in higher error rates. Using more than one token can reduce average circulation time and location information error rates in multi-UAV systems. In the existing multi-token studies, it is assumed that each token uses separate communication channels to solve the token collision problem. In this paper, a new multi-token based location information sharing system is proposed for multi-UAV systems. In this system, while only one common channel is used for the circulation of tokens, another channel is utilized for control packets to minimize the token collisions. **Keywords: Flying Ad Hoc Network, Location Information Sharing, Multi Token Circulation, Unmanned Aerial Vehicles.**

1. INTRODUCTION

In recent years, unmanned aerial vehicles (UAVs) are becoming more popular in both civilian and military applications ([1], [2]). Mapping, search and rescue, regional surveillance, border monitoring, target searching and discovery operations are various application areas of UAVs ([2]-[5]). UAVs can fly autonomously [6]. With the help of this feature, several challenging missions can be accomplished without risking human lives by UAVs. In addition to this feature, UAVs are inexpensive and can be easily deployment vehicles [2]. These advantages are the reasons for the use of UAVs in many different area [7].

By the help of the miniaturization and cost reduction in UAV technologies, instead of utilizing only one big UAV, the systems consists of multiple small UAVs can be realized [8]. Instead of a single UAV, using multi UAV systems challenging and complex tasks can be performed more successfully in less time. Besides the important benefits of Multi-UAV systems, they also have some limitations. Communication is the most important problem in these limitations [8]. Communication is one of the most important factor to performed safe and coordinated flight in multi UAV systems. For this reason, communication problem should be solved firstly. Infrastructure based approach is the method that commonly used in the solution of communication problem in multi UAV systems [9]. In this method, communication range is restricted by the ground station coverage area. Also, because of the environmental obstacles, interruptions can be occurred in signal transduction. Infrastructure based approach is not always available in all circumstances. Therefore, there is need for an alternative method of communication.

Flying Ad hoc Network (FANET) is an effective solution when there is no preinstalled infrastructure [2]. Figure 1 shows the structure of FANET. In FANET, UAVs need to know the location information of each other also to ensure collision free coordination. With the help of location information sharing, UAVs can performed seamless and coordinated flight. Location sharing of information is the most important factor in success of FANET structure.

[1] *Corresponding author: Marmara University, Faculty of Technology, Department of Computer Engineering, 34722, Kadıköy/İstanbul, Turkey.* emre.ulku@marmara.edu.tr

[2] *Turkish Air Force Academy, Department of Computer Engineering, 34149, Yeşilköy/İstanbul, Turkey.* i.bekmezci@hho.edu.tr

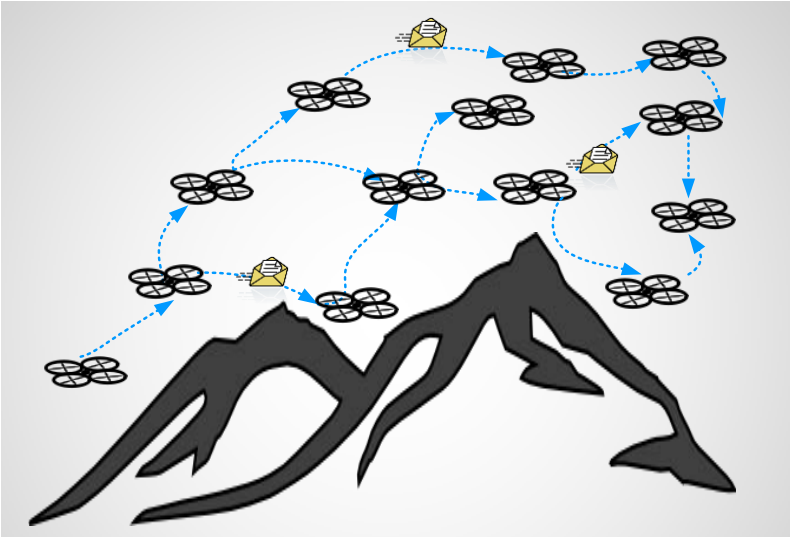

Figure 1. Flying Ad Hoc Network (FANET)

Token based approach is one of the significant methods used for location information sharing. In this approach, a token which includes coordinates of the UAVs circulates between UAVs. Thus, UAVs know each other‘s position due to the circulating token. However, especially in UAV swarms, the circulation of the token takes longer time and it may result in higher error rates. Using more than one token can reduce average circulation time and location information error rates in multi-UAV systems ([10], [11]).In the existing multi-token studies, it is assumed that each token uses separate communication channels and UAVs‘ hardware supports such a structure to solve the token collision problem ([10], [11]).

In this paper, a new multi-token based location information sharing system is proposed for multi-UAV systems. In this system, while only one common channel is used for the circulation of tokens, another channel is utilized for control packets to minimize the token collisions. The second channel provides minimum collision to direct the token transmission. This two channel structure ensures to obtain more realistic results for location information sharing in multi UAV systems.

The organization of this paper is as follows. In the second section of this paper, multiple token structure and two channel structure for location information sharing are explained. In the third part, conclusion of the study is presented and in the final part, what will be done in the future is discussed.

2. MULTI TOKEN STRUCTURE

All UAVs in FANET need to know location information of each other in order to accomplish seamless and coordinated flight. In this study, location information sharing between UAVs is performed by multi token structure. UAVs‘ location information is changing constantly because of high degree mobility of UAVs. With the widespread use of multiple UAVs, UAVs have been used in groups and even swarms. Especially UAV swarms consist of many UAVs. The number of UAV increases, the size of the location information that stored in the token is also increasing. In addition, the number of UAV should be visited by the token is increasing. For this reason, single token will not be sufficient after a certain number of UAV. In this case, UAVs learn position information of each other with delay. This delay will disrupt safety and coordination of the flight. In multi token structure, number of token is increased to avoid delays.

In this study, two communication channels are used regardless of the number of tokens. One channel is used for token circulation. In this channel, tokens that contains location information of all UAVs are circulated. The other channel is used for routing tokens. UAVs are communicated through this channel to avoid from collisions. In this channel UAVs are communicated by three different packets. These packets are CTS (Clear to Send), RTS (Request to Send) and NCTS (Not Clear to Send). The UAV which holds the token will send the token to one of its neighbors.

Example process of two channel model is shown in figure 2. Token holders UAVs are A and F at the beginning of the scenario. A sends its token to the D. RTS packet also goes to the D through other channel. D sends CTS packet to the A because it is available to receive token. CTS packet is also overheard from the E and G. Meanwhile, F wants to send the token to the E. Although E is available for receiving the token, it sends NCTS packet to the F. As E overhears the CTS packet, it knows that it will get the token in the next token sending. E sends NCTS packet to provide collision in the next token sending. After F gets the NCTS, it selects another available neighbor to send the token.

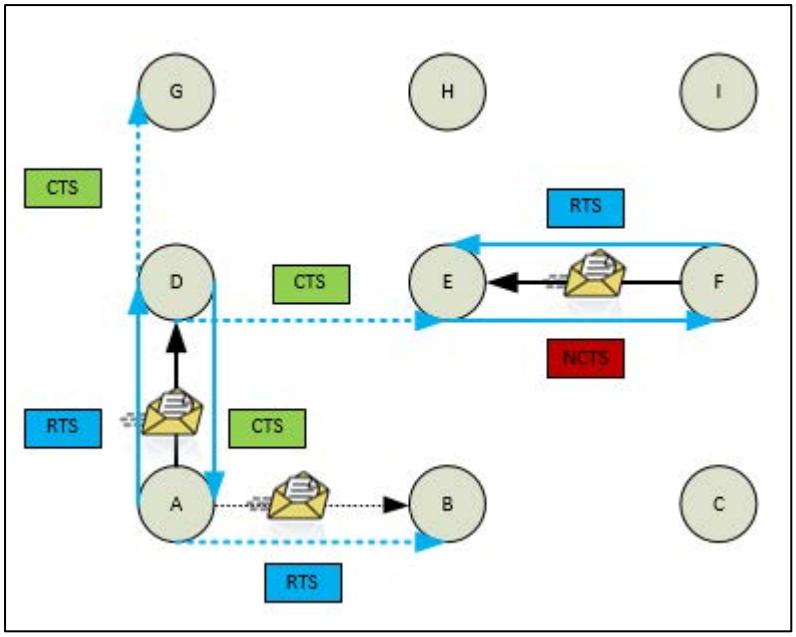

Figure 2. Example process of two channel model

Figure 3 shows the process of the token sending. The UAV which holds the token is called as TokenHolder. Firstly, TokenHolder determine its neighbors with the help of adjacency matrix. We want to select destination UAV which provide to avoid collisions. We are looking for the most appropriate UAV. If the TokenHolder gets or overhears CTS, RTS or NCTS packet from its neighbors then it eliminates these neighbors. The reason for this, TokenHolder knows that these UAVs will get or overhear the token in the next token sending. If the TokenHolder have more than one UAV then it selects one of the neighbor except the source UAV. After the elimination process of neighbors, if the TokenHolder has no neighbor, then it waits two token sending time.

3. CONCLUSION

In the previous studies, the circulation of UAVs‘ position information can be provided by multi token based approach is shown. After a certain number of UAV, the use of multiple tokens has been shown to give better results than a single token based approach ([10], [11]). In these studies, it is assumed that each token is transmitted from a separate channel. In this study, a 2 channel model is proposed in order to achieve more realistic results. A model is presented that can be avoid from collisions using only 2 channel for communication regardless of the number of tokens. All tokens are sent and received over a single communication channel. With the help of the second channel, UAVs send the tokens avoiding collisions. If necessary UAVs are waiting to avoid causing a collision.

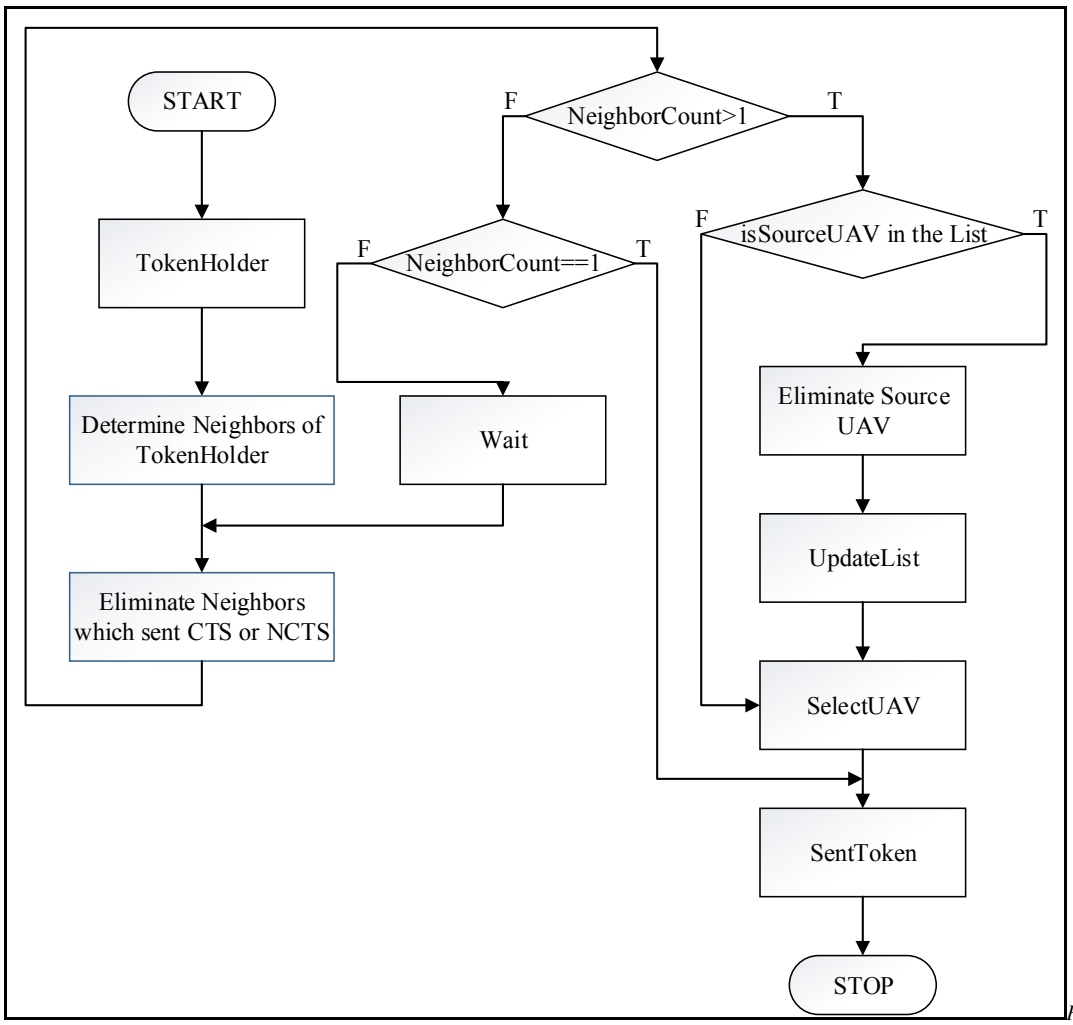

Figure 3. Flowchart of the TokenSent Process

4. FUTURE WORK

In subsequent studies, the model that is proposed in this paper is implemented to view the results of the system. Thus, we can obtain more accurate and realistic results. Then a comparison of results can be done. According to the number of UAVs, optimal number of tokens can be determined to provide circulation of UAVs‘ location information with minimal error.

REFERENCES

[1]. M. M. Nasir and Q. Shi-Yin, ―Investigation of Human Factors in UAV Accidents Based on Analysis of Statistical Data”, International Conference on Instrumentation, Measurement, Computer, Communication and Control, 2011, p. 1011-1015.
[2]. I. Bekmezci, O. K. Sahingoz and S. Temel, ―Flying Ad-Hoc Networks (FANETs): A Survey”; Ad Hoc Networks 11; 1254–1270, 2013.
[3]. H. Chen and K. He, ―U-Turn Optimization for Three-Dimensional Area Coverage of UAV”, Proceedings of 2015 IEEE International Conference on Mechatronics and Automation, 2015, p. 98-103.
[4]. A. Vega, C. Lin, K. Swaminathan, A. Buyuktosunoglu, S. Pankanti and P. Bose, ―Resilient, UAV-Embedded Real-Time Computing”, 33rd IEEE International Conference on Computer Design (ICCD), 2015, p. 736-739.
[5]. I. Jawhar, N. Mohamed and J. Al-Jaroodi, ―Data Communication in Linear Wireless Sensor Networks Using Unmanned Aerial Vehicles”, International Conference on Unmanned Aircraft Systems (ICUAS), Orlando, FL, USA, May 27-30 2014, p. 492-499.
[6]. X. Li and L. Yang, ―Design and Implementation of UAV Intelligent Aerial Photography System”, 2012 4th International Conference on Intelligent Human-Machine Systems and Cybernetics, p. 200-203.
[7]. D. Ho1, E. I. Grøtli1, P. B. Sujit, T. A. Johansen and J. B. Sousa, ―Cluster-based Communication Topology Selection and UAV Path Planning in Wireless Sensor Networks”, International Conference on Unmanned Aircraft Systems (ICUAS), Grand Hyatt Atlanta, Atlanta, GA, May 28-31, 2013, p. 59-68.
[8]. H. Tareque, S. Hossain and M. Atiquzzaman, ―On the Routing in Flying Ad hoc Networks”, Computer Science and Information Systems (FedCSIS), Lodz, Poland, 13-16 Sept. 2015, p. 1-9.
[9]. J. Li, Z. Wei, Y. Zhou, M. Deziel, L. Lamont and F. R. Yu, ―A Token-Based Connectivity Update Scheme for Unmanned Aerial Vehicle Ad Hoc Networks”, Ad-hoc and Sensor Networking Symposium, 2012, p. 713-718.
[10]. I. Bekmezci, E. E. Ulku, ―Location Information Sharing with Multi Token Circulation in Flying Ad Hoc Networks”, 7th International Conference on Recent Advances in Space Technologies (RAST), Istanbul, Turkey, June 16-19 2015, p. 669-673.

[11]. E. E. Ulku, I. Bekmezci, ―Multi Token Circulation For Multi-UAV Systems", 23th Signal Processing and Communications Applications Conference (SIU), Malatya, Turkey, May 16-19 2015, p. 1042-1045.

Eyup Emre Ulku received a B.S. and M.Sc. degrees in Teacher Training in Computer and Control from Marmara University in 2009 and 2012, respectively. In 2009, he joined as a Research Assistant in Marmara University. He has begun his Ph.D. studies in Computer Engineering program at Turkish Air Force Academy, Istanbul, Turkey in 2012. He is currently a Research Assistant in Marmara University, Faculty of Technology, Computer Engineering Department. His current research interests are in wireless communications, ad hoc networks, and image processing.

İlker Bekmezci received B.Sc., M.Sc., and Ph.D. degrees in computer engineering from Bogazici University, Istanbul, Turkey, in 1994, 1998, 2008, respectively. He is currently an associate professor with the Department of Computer Engineering, Turkish Air Force Academy, Istanbul, Turkey. His current research interests are in wireless communications and ad hoc networks

Investigation of Weak Motion Station's Soil-Engıneerıng Bedrock Conditions by Using Geophysical Methods

Özkan Cevdet Özdağ[3], Atilla Uluğ[2]

Abstract

In earthquake resistant building design; effects from nature must be determined for the structure location. This value is peak ground acceleration (PGA) which defined horizontal maximum value in time domain. If the Structures is built on bedrock, recorded on the bedrock PGA value is used directly. If the structure is on the ground, the bedrock of earthquake data must be moved to the ground surface. In practice, the PGA values are assumed to be known in the bedrock. It is found the effect of enlarging the ground transfer function. The two values are multiplied by each other and PGA values on the ground surface are reached. The most important event in this stage is defined to value of the bedrock PGA at the working area. When bedrock is on the surface, not showed bedrock effect. For this reason, the stations must be checked. If the station is on the bedrock, it must be made preliminary work as described above. In this study, It aimed to define the soil-bedrock models with the environment in which the broadband weak ground motion stations at İzmir/Balçova (BLCB)

.**Keywords:** Weak Motion, QTS.

5. INTRODUCTION

For a potential earthquake , earthquake force pre-determination should be make for identify earthquake-soil-structure behaviour on the soil surface. This equivalent static earthquake force value is called PGA. PGA value is known as the amplitude value of the earthquake at the time occasion and it is the horizontal trend amplitude value. For designing earthquake resistant building, if the building is constructing on bedrock and if the recorded PGA value on the bedrock exists then this value uses directly. Conversely if the building is constructing on soil then PGA value should be transferred on soil surface. Therefore linear system theorem to be use for this operation. In the Linear system theorem input data is the PGA value of the bedrock. Transfer spectrum is obtained from microtremor datas with Nakamura 1989 approach.

In application , either Quasi Transfer Spectrums obtained from microtremor datas to be used directly or theoretical soil transfer functions calculated from Vp, Vs and density values obtained with in situ geophysical measurements to be used.

PGA is defined in time-domain, and amplification AMP(f) is obtained in frequency-domain, we can invoke the Parseval's theorem from which it follows that root-meansquare (rms) spectral amplitude is proportional to the rms amplitude of the corresponding time series, (Herak, 2008)

Earthquake spectrum of bedrock multiply with soil transfer function and the earthquake spectrum on soil can be obtained. Then PGA value can be calculate with inverse Fourier transform in time domain

[3] *Corresponding author: Dokuz Eylül University, Aegean Implementation and Research Center, 35430, İnciraltı/İzmir Turkey.* cevdet.ozdag@deu.edu.tr

Additionally , PGA value of the bedrock is obtained from past seismological datas and scenerio earthquake studies. Then, the amplification effect of the soil transfer function can be obtained and both two values (PGA_b- DAF) multiply with each other and gives PGA value on the soil surface.

The most important concept of the study is the determination of the PGA value of the study area uniquely. The best method is the using of the earthquake stations on board of the bedrock

However as the bedrock overlaying on the soil surface it looses the features of the bedrock (seismic velocity values V_p , V_s and density ρ) As a result of this studiesconsidering obtained soil-bedrock models excavation is done till reaching bedrock and the station can be board (positioned)

If this condition is not satisfied then soil effect can be calculate from the earthquake records of the station boarded on the surface and extraction of the soil effect can be done. Earth crust is not uniform so seismic phases observed on the earthquake records carry lots of phenomenon features.

That means, propogating elastic wave from an earthquake source , includes a lot of events effect until it arrives to the recording station.

As a result of this, the features of the data recorded at the station is different from the features of the earthquake source data. Recorded data of the earthquake station includes the effects of earhtquake source, wave progressive medium (sesimic bedrock, engineering bedrock, soil), located position of earthquake station and effect of the recording device.

$$u(t) = s(t) * r(t) * e(t) * i(t) * z(t) + n(t) \quad (1)$$

u(t)= seismogram, s(t)= source function, r(t)= radiation pattern, e(t)= geometric propagation, earth transfer (transformation) function including absorption and dispersion effects, i(t)= device effect, z(t)= recording area soil effect, n(t)= noise, *= convolution operator

Nakamura hadn‘t make determination of bedrock interest with S wave velocity values in the studies 1998 and 2008.

Despite that, Nath (2000) determined the soil-bedrock model with soil (Vs <700 m/s), engineering bedrock (3000m/s>Vs>700m/s) and seismic bedrock (Vs>3000m/s) in terms of earthquake engineering (Figure 3).

Considering these concepts, Komazawa et al. 2002 investigated the soil-bedrock model with microgravity, microtremor H/V and modified spatial autocorrelation (SPAC) methods in Adapazarı plain and determined this model.

The soil-bedrock model, approval of the bedrock boundary done with Vs >3000 m/s.

Based on this concept, while earthquake-soil-structure common behaviour occurs earthquake force on the soil surface and wanted to be determined then seismic bedrock boundary should be taken principal for constructing point.

Moreover, earthquake force of the engineering bedrock level should be determine for making soil dynamic analyse.

According to İzmir Bay soil studies, Bornova flysches had been determined as engineering bedrock(Akgün vd. 2013).

In this study, the aim was the investigation of the weak motion stations BLCB and KNKB whether it is positioning on the engineering bedrock or not.

In the application, for the investigation of the engineering bedrock features determined according to the wave velocity value (Vs>760 m/s), MASW (Multichanel analysis of the surface waves), resistivity vertical electic sondage and microtremor studies were made at the stations area. Geology map of study area is shown at figure 1.

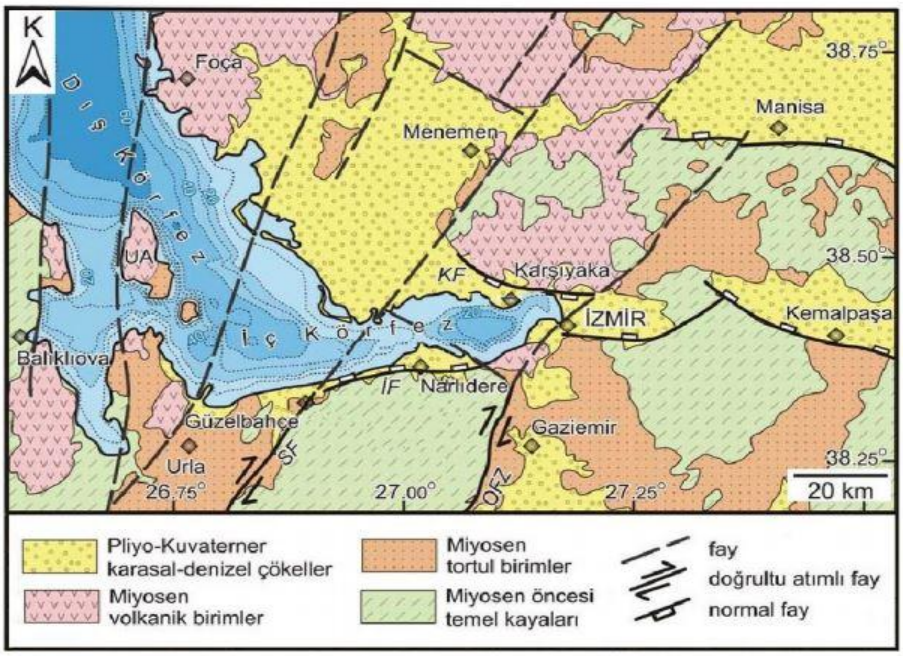

Figure 1. Geology Map Of Study Area (Uzel et. al. 2012)

6. APPLICATIONS AND RESULTS

KNKB from Seismometer station point of surface average 6 m deep. BLCB station is positioned at the point 1.5 deep surface.

KNKB station of the S wave velocity values but 10 m. After engineering the main rock depth property. Sismometrenin where the value of the S wave velocity average 1000 m/s.. But the environment is lateral and vertical directions in terms of seismic velocity values, horizontal infinite and homogenous. In addition, where the station, İzmir Gulf geologically Contour is defined as the main rock soil engineering located on Miocene aged limestone unit, punch unit Bornova, on the need to take into consideration.

BLBC station located on the Geological unit of Bornova as Complex. However, the S wave velocity values floor property (Vs < 760m/s.). Also at this point, the lateral and vertical directions in terms of seismic velocity values, horizontal infinite and uniform property don‘t observed.

BLCB and KNKB stations featured the long periods (Guralp CMG-3ESP) Quasi Seismometer micro-tremor records obtained from Transfer Spectra (QTS). When the media window size 81.92 seconds by selecting the low frequency (high period) the amplitude changes in value were taken into consideration (fig. 2.3, 4 and 5).

KNKB 0.4 Hz peak frequency value at the point of the station. has been identified as. This means that To > 1s. the effect of ground border for engineering anakayası – H/V spectrum of high amplitude values shift from inhumation.

Frequency control on a 1.5-point BLCB station 4 Hz we identified between. To < 1s. It is located on the ground near the surface of layers will impact the earthquake waves. This station recorded data in order to be considered the main rock engineering of soil near the surface of the Elimination of the effects of earthquake records.

Vertical Electric Sounding (VES) on the basis of the method of horizontal underground, composed of half infinite homogeneous layer is assumed. In practice, the two-point applied to the Earth electric current is measured between two points as the potential difference response. According to Ohm's law later resistivity values are calculated. Is not suitable for the operation of the station point BLCB VES at that point could not be made to work. However, KNKB made a point at the

station VES work vertical directions resistivity variations. KNKB in accordance with the average results for the station point MASW 10 m depth also increases observed after resistivity (Figure 2 and 3).

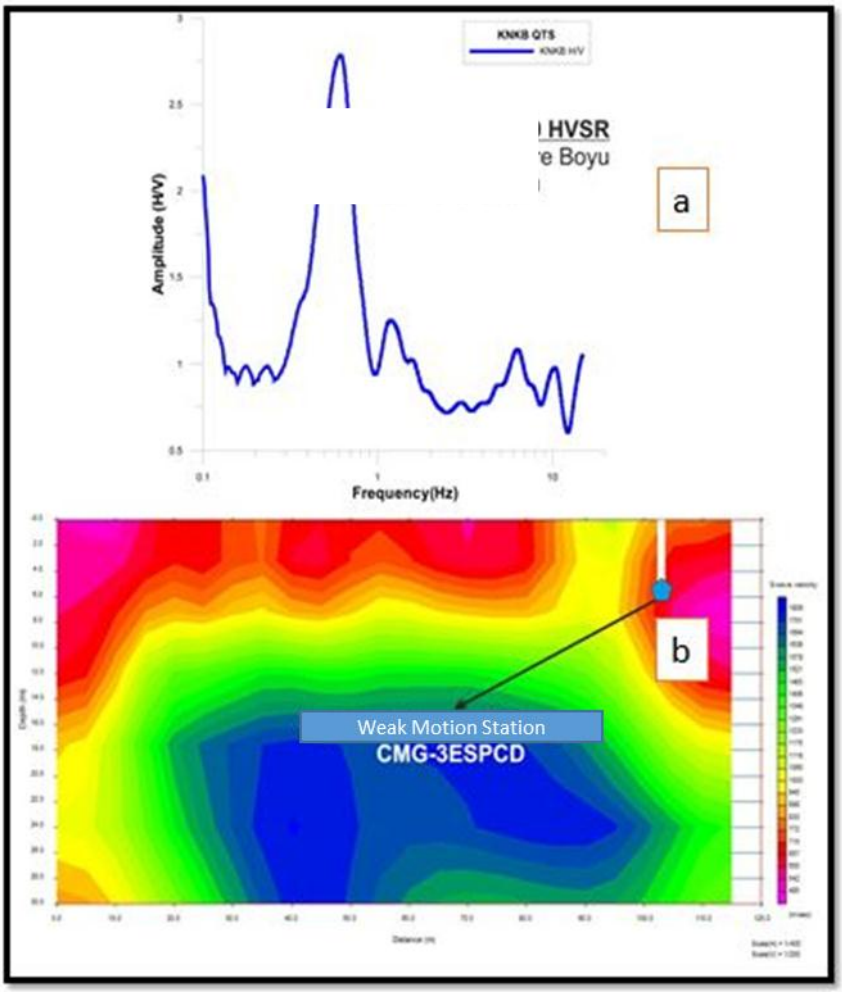

Figure 2.KNKB belongs to the point a) station HVSR analysis of the resulting spectrum b) 2B S-wave velocity depth distribution and position of the Seismometer.

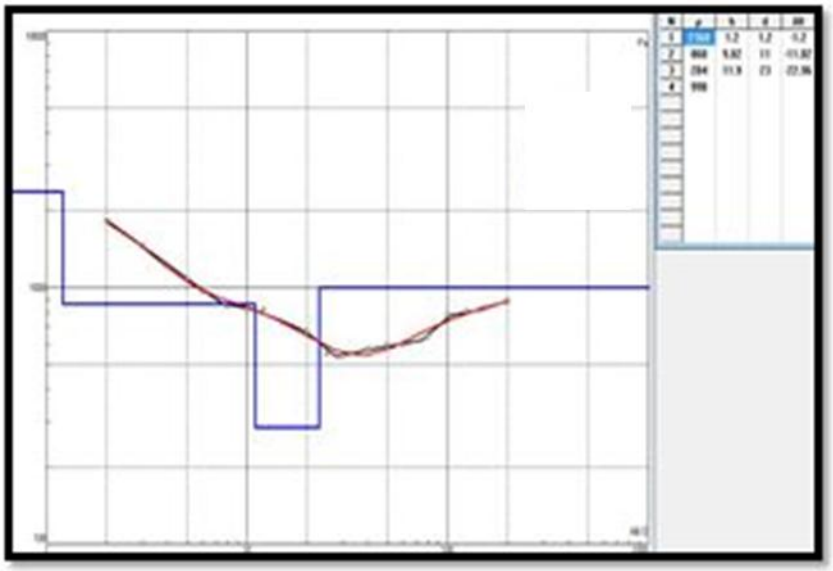

Figure 3. VES Results.

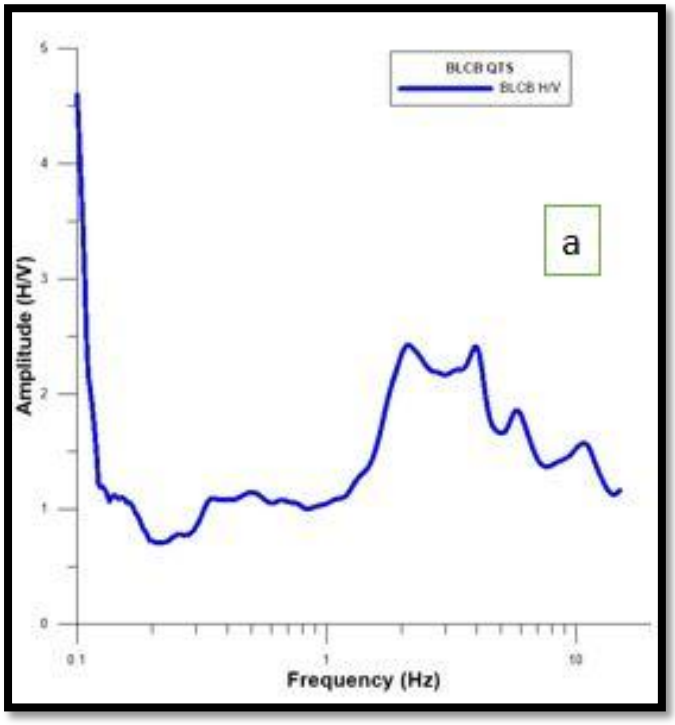

Figure 4. HVSR Spectrum from BLCB.

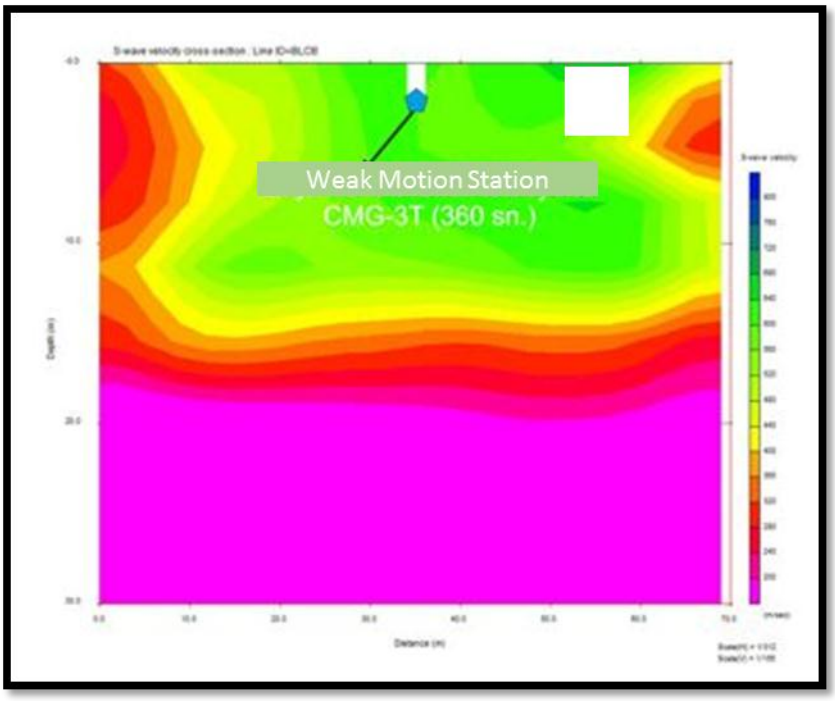

Figure 7. 2D Vs Section from BLCB.

7. CONCLUSION

The scope of this study, located in Buca in İzmir province and townships of Balçova and KNKB and defined as broadband weak ground motion station BLCB points in floor engineering anakayası Propertie is derived from the results of this study and the work area as a result of the common interpretation of the work before the following conclusions.

• KNKB weak ground motion station is located on old Limestone unit of geological environment in Miocene and according to the results of a CT scan station engineering MASW main rock (Vs > 760 m/s) were positioned in the vertical direction of this unit and continuity of supply has been found with the results that the DES. However, the circumference of the Gulf of İzmir as a ground of engineering geology master rock Bornova, punch, this station as a reference point in evaluating the station only, it is not recommended to be taken based on the S wave velocity values. This station is point this study with these characteristics are taken into consideration, the circumference of the Gulf floor can serve as the bedrock for the reference station is not appropriate.

• BLCB weak ground motion station geologically Gulf of İzmir Bornova main rock soil engineering of the circumference of the timetable. However this station recorded the earthquake records near the floor surface will have the effect of layers. This station is the main rock engineering Gulf circumference ground reference station to be used as ground for elimination of these effects near the surface of spectrum.

REFERENCES

[12]. Akgün, M., Gönenç, T., Pamukçu, O., Özyalın, Ş., Özdağ, Ö.C., (2013), Mühendislik Ana Kayasının Belirlenmesine Yönelik Jeofizik Yöntemlerin Bütünleşik Yorumu: İzmir Yeni Kent Merkezi Uygulamaları, Jeofizik Dergisi, doi 13.b02 jeofizik-1304-12

[13]. Aksarı, D., Karabulut, H. ve Özalaybey, S. (2010). Stress interactions of three moderate size earthquakes in Afyon, southwestern Turkey. Tectonophysics, 485, 141-153.

[14]. Cuenot, N., Charlery, J., Dorbath, L. ve Haessler, H. (2006). Faulting mechnasims and stres regime at the European HDR (Hot Dry Rock) site of Soultz - souts - Forests – France, Geothermics, 35, 561-575.

[15]. Giammanco, S., Palano, M., Scaltrito, A., Scarfi, L. ve Sortino, F. (2008). Possible role of fluid overpressure in the generation of earthquake swarms in active tectonic areas: The case of the Peloritani Mts. Sicily, Italy. Journal of Volconlogy and Geothermal Research, 178, 795-806.

[16]. Komozawa M., Morikawa, H., Nakamura, K., Akamatsu, J., N_shimura, K., Sawada, S., Erken, A., Önalp, A., (2002)., Bedrock structure in Adapazari, Turkey a possible cause of severe damage by the 1999 Kocaeli earthquake, Soil Dynamics and Earthquake Engineering, 22, 829-836
[17]. Nakamura, Y. (1989). A method for dynamic characteristics estimation of sub-surface using microtremor on the ground surface, QR of RTRI, 30,1, 25-33.
[18]. Nakamura, Y. (2008). On the H/V Spectrum The 14 th World Conference on Earthquake Engineering October 12-17, 2008, Beijing, China.
[19]. Nath K. (2000). Seismic Microzonation Framework – Principles & Applications. Workshop on Microzonation©Interline Publishing, Bangalore.
[20]. Park, C., B., Miller R., D., Xia J. (1999). Multichannel analysis of Surface Waves, Geophysics, 64, No.3, 800-808.

The Impact of Seasonal Changes on Quasi Transfer Spectrums

Özkan Cevdet Özdağ[4], Aykut Tunçel[2]

Abstract

Parameters, showing changes in earthquake spectrum, must be investigate where structure will build for earthquake resistant building design. This changes defined as Quasi transfer spectrums (QTS) and because of soil layers between surface and bedrock. Changes in physical parameter's of soil layers effect QTS directly. Because of that reason, S-Wave Velocity which is the most important parameter in soil parameters should be monitored as seasonal changes. The static ground-water level should be noted that the effect on S-Wave Velocity. It is recommended to ensure that the examination of amplitude-frequency changes of QTS depends on time. This study aimed to investigate the effect of seasonal changes on QTS. Microtremor data's were used for calculate seasonal changes (between 2012-2014) on QTS where recorded BLCB (İzmir/Balçova) broadband weak motion station.

Keywords: Ground-water level, QTS, Monitoring.

8. INTRODUCTION

The design of earthquake-resistant structures; the building will include the establishment of the relationship of the building with the ground and the most important one of the devastating impact the calculation of horizontal earthquake forces the necessity of an accurate way is inevitable. Many researchers by history about earthquake damage as a result of the studies in the design of earthquake-resistant structures depending on the properties of the ground floor surface lateral force and according to the terms of the ground examination of the spectrum were found to be significant (Akgün et al. 2013).

Gulf of Izmir situated at floors online engineering has been described as the main rock Bornova filişi (Akgün et al. 2013). Balcova BLCB weak ground motion station Bornova filişi. This station, which will be recorded and direct engineering of earthquake data as regards the main rock data should be investigated. Because it is a complex structure of Bornova filişi especially prone to lose their physical out onto the floor surface is special.

In this study, the BLCB weak ground motion records all the time in 2012 and 2014 mikrotremor data obtained on a monthly base Nakamura (1989) Quasi Transfer spectra were calculated with the approach. General Directorate of meteorology recorded station number İzmir/host 17220 2012 and 2014 years rainfall data have been obtained from the monthly average values of column charts.

[4] *Corresponding author: Dokuz Eylül University, Aegean Implementation and Research Center, 35430, İnciraltı/İzmir Turkey.*
cevdet.ozdag@deu.edu.tr

THEORY

8.1. QTS Spectrums

Soil types, number of layers, fundamental period and empirical transfer function was defined by using microtremor measurements (Nakamura 1989; Lermo and Chavez-Garcia 1994; Ansal et al 1997; Akgün et al 2013a; Akgün et al 2013b; Paudyal Y.R. et al 2012; Paudyal Y.R. et al 2013). The first implementation about the microtremor analysis based method was studied by Kanai (1957) and then this method was improved by Nakamura (1989). In recent, it has become widespread as a low-cost and effective tool to estimate the fundamental resonant frequency of sediments by measuring the microtremors at a single station (Figure 3). In the last two decades, the Horizontal-to-Vertical spectral (H/V) ratio method has been applied widely for the study of site effects in different regions of the world.

Using this method show that the microtremor H/V spectral ratios provide a reliable estimate of the resonance frequencies of soft soil deposits. The detailed information (discussion, applications, validations and limitations) about the H/V method have presented by many researchers, e.g. Bonnefoy-Claudet et al. (2006a, 2006b), Delgado et al. (2000), Field and Jacob (1993), Field et al. (1995), Gosar (2007), Gosar and Martinec (2009), Guo et al. (2002), Hardesty et al. (2010), Huang and Teng (1999), Lachet et al. (1996), Langston et al.(2009). Furthermore, studies of the other researchers have been concluded that there is a strong correlation between S velocity, resonance frequency and thickness of the sediments (D'Amcio et al. 2004; Delgardo et al. 2000; Dinesh et al. 2010; Gosar and Lenart 2010; Ibs-von Seht and Wohlenberg 1999; Özalaybey et al. 2011; Parolai et al. 2002; Sukumaran et al. 2011).

9. APPLICATIONS AND RESULTS

The station is located south of İzmir Balçova district of 35S 503674.00 D and 35S 424865.00 K coordinates BLCB built on Weak ground motion station.

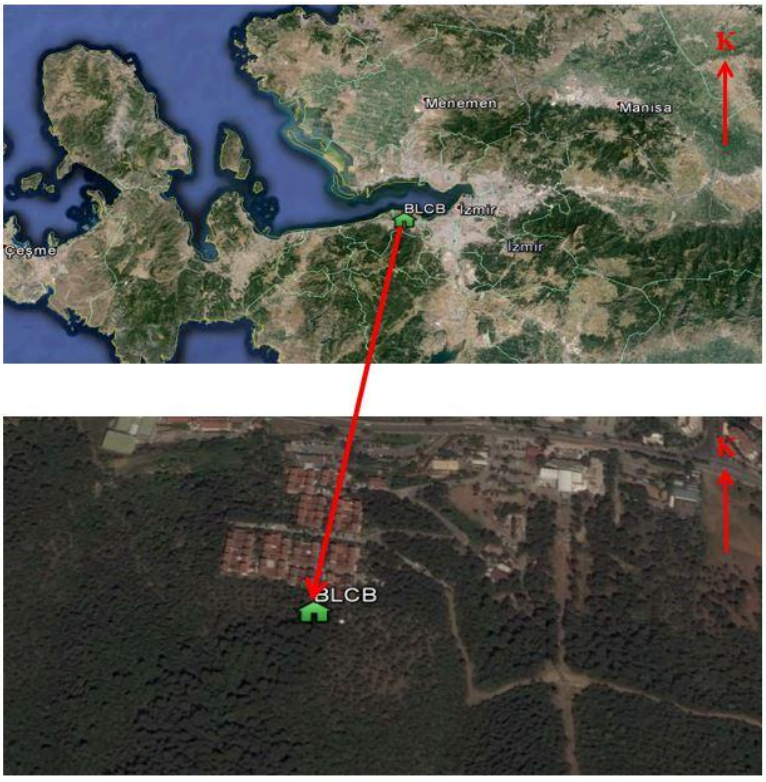

Figure 1. Study Area.

BLCB Station Long periods (T = 360 sec.) broadband-enabled Guralp Systems CMG-3ESPCD 360 sec sismometresi. The Seismometer 0.0083 – 50 hz frequency range is sensitive to noise. Is broadband and deep

effects and the effects of the recording surface. The station actively since 2004 noise and seismic records. Gulf of Izmir situated at floors online engineering has been described as the main rock Bornova filişi (Akgün et al. 2013). Filişini is built of Bornova BLCB station. Bedrock data directly of the recordings made at the station.

Scope of the study at the station recorded noise data obtained from the effect of seasonal change on the spectra of Quasi Transfer whether to investigate; It belongs to the General Directorate of meteorology was established in Central İzmir station number 17220 rain data are used.

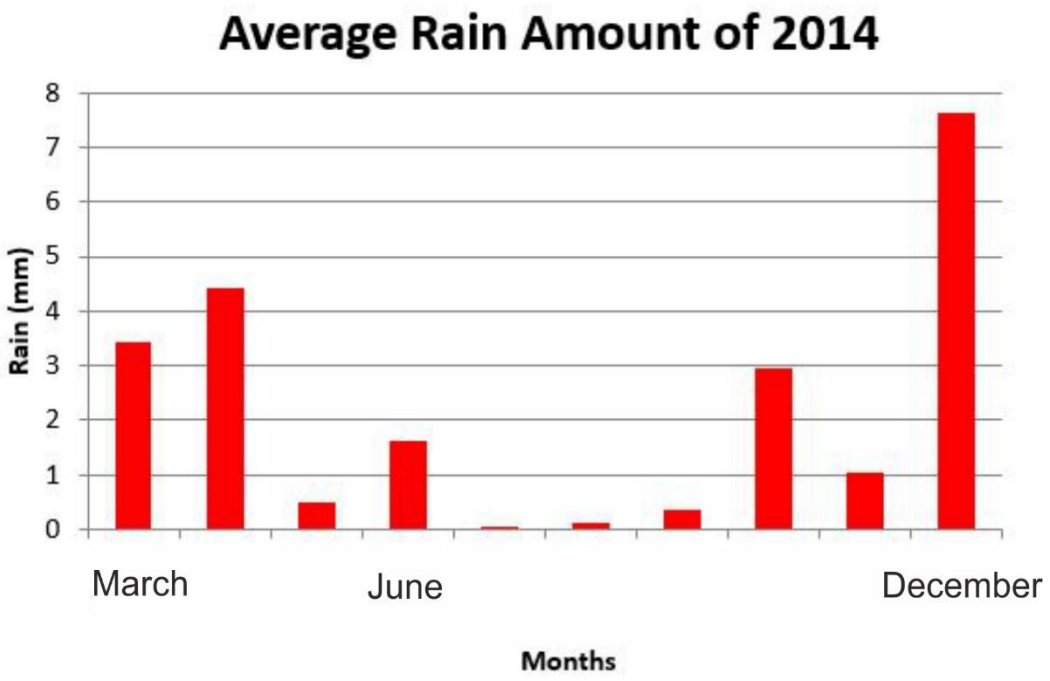

Figure 2. Average Rain Amounts.

10. CONCLUSION

Structural design, relocation is defined for periods of peak amplitude sensitivity region by month distribution were defined based on the amount of rainfall change and regions as a result of the common assessment 1. And 3. the range of change in the region is low 2. were found to be too broad a range of change in the region.

Structural design for the peak amplitude of the Velocity sensitivity region defined by month distribution were defined based on the amount of rainfall change and regions as a result of the common assessment 1. And 3. the range of change in the region is low 2. the range of change in the region were found to be too broad

Structural design for the peak amplitude of the acceleration sensitivity region defined by month distribution were defined based on the amount of rainfall change and regions as a result of the common assessment 1. 2 and 3. the range of change in the region was formed at low levels.

Overall results based on peak periods sensitivity zones as amplitude values change can occur. Should be examined in detail.

Evaluation of the resulting noise records BLCB station Quasi Transfer as a result of Spektrumlarının an increase in peak amplitude value at high frequencies are near the surface shows the existence of the effect. This affects engineering main rock near the surface that is as close to the surface areas of Bornova filişi physical and chemical effects are lost as a result of bedrock feature. The station, which will be held in the area where geophysical studies considering the depth of the bedrock Vs speed detected healthier results can be achieved.

REFERENCES

[21]. Akgün, M., Gönenç, T., Pamukçu,O., Özyalın, Ş., Özdağ, Ö.C., (2013a), Integrated Geophysical Methods For The Determination Of Engineering Bedrock: İzmir New City CenterMühendislik Ana Kayasının Belirlenmesine Yönelik Jeofizik Yöntemlerin Bütünleşik Yorumu: İzmir Yeni Kent Merkezi Uygulamaları, Turkish Journal of Geophysics(in Turkish), doi 13.b02 jeofizik-1304-12

[22]. Bonnefoy-Claudet S, Cotton F and Bard PY (2006a), –The Nature of Noise Wavefi eld and Its Applicationsfor Site Effects Studies: A Literature Review," Earth-Science Reviews, 79: 205–227.
[23]. Bonnefoy-Claudet S, Cornou C, Bard PY, Cotton F, Moczo P, Kristek J and Fäh D (2006b), –H/V Ratio: aTool for Site Effects Evaluation Results from 1-D noise Simulations," Geophysical Journal International, 167: 827–837.
[24]. D'Amico V, Picozzi M, Albarello D, Naso G and Tropenscovino S (2004), –Quick Estimates of Soft Sediment Thicknesses from Ambient Noise Horizontal to Vertical Spectral Ratios: a Case Study in Southern Italy," Journal of Earthquake Engineering, 8(6): 895–908.
[25]. Delgado J, Casado CL, Lopez Giner J, Estevez A, Cuenca A and Molina S (2000), –Microtremors as a Geophysical Exploration Tool: Applications and Limitations," Journal of Pure and Applied Geophysics,157:1445–1462.
[26]. Field E and Jacob K (1993), –The Theoretical Response of Sedimentary Layers to Ambient Seismic Noise," Geophysical Research Letters, 20(24): 2925–2928.
[27]. Field EH, Clement AC, Jacob KH, Aharonian V, Hough SE, Friberg PA, Babaian TO, Karapetian SS,Hovanessian SM and Abramian HA (1995), –Earthquake Site-response Study in Giuari (Formerly Leninakan) Armenia Using Ambient Noise Observations," Bulletin of the Seismological Society of America, 85(1): 349–353.
[28]. Gosar A (2007), –Microtremor HVSR Study for Assessing Site Effects in the Bovec Basin (NW Slovenia)Related to 1998 Mw 56 and 2004 Mw 52 Earthquakes," Engineering Geology, 91: 178–193.
[29]. Gosar A and Martinec M (2009), –Microtremor HVSR Study of Site Effects in the Ilirska Bistrica Town Area (S Slovenia)," Journal of Earthquake Engineering, 13:50–67.
[30]. Gosar A and Lenart A (2010), –Mapping the Thickness of Sediments in the Ljubljana Moor Basin (Slovenia) Using Microtremors," Bulletin of Earthquake Engineering, 8: 501–518.
[31]. Guo X, Wong YL and Yuan YF (2002), –Estimation of Damping Ratio of Soil Sites Using Microtremor,"Earthquake Engineering and Engineering Vibration, 1(1): 45-49.
[32]. Hardesty K, Wolf LW and Bodin P (2010), –Case History, Noise to Signal: A Microtremor Study a Liquefaction Sites in the New Madrid Seismic Zone," Geophysics, 75(3): 83–90.
[33]. Huang HC and Teng TL (1999), –An Evaluation on H/V Ratio vs Spectral Ratio for Site Response Estimation Using the 1994 Northridge Earthquake Sequence," Pure and Applied Geophysics, 156: 631– 649.
[34]. Ibs-von Seth, M., and Wohlenberg, J., (1999), Microtremor measurements used to map thickness of soft sediments, Bull. Seismol. Soc. Am., **89**:250-259.
[35]. Lachet C, Bard PY, Hatzfeld D, Theodulidis N, Papaioannou C and Savvaidis A (1996), –Site Effectsand Microzonation in the City of Thessaloniki (Greece) Comparison of Different Approaches," Bulletin of the Seismological Society of America, 67: 713–724.
[36]. Langston CA, Chiu Shu-Chioung C, Lawrence Z, Bodin P and Horton S (2009), –Array Observations of Microseismic Noise and the Nature of H/V in the Mississippi Embayment," Bulletin of the SeismologicalSociety of America, 99(5): 2893-2911.
[37]. Nakamura, Y., 1989. A method for dynamic characteristics estimation of subsurface using microtremor on the ground surface. Quarterly Report of Railway Technical Research Institute 30, 25te
[38]. Nakamura, Y. (2000). Clear Identification of Fundamental Idea of Nakamura's Technique and Its Applications, Proc. 12th World Conf. on Earthquake Engineering, 2656.
[39]. Özalaybey.,S, Zor,E., Ergintav, S. and Tapırdamaz, M.C (2011), Investigation of 3-D basin structures in the İzmitBay area (Turkey) by single-station microtremor and gravimetric methods. Geophysical Journal International. **186**, 883–894 doi:10.1111/j.1365-246X.2011.05085.x
[40]. Parolai S, Bormann P and Milkereit C (2002), –New Relationship between Vs Thickness of Sediments andResonance Frequency Calculated by the H/V Ratio of Seismic Noise for the Cologne Area (Germany),"Bulletin of the Seismological Society of America, 92(6):2521–2527.
[41]. Sukumaran P, Parvez IA, Sant DA, Rangarajan G and Krishnan K (2011), –Profi ling of Late Tertiary–Early Quaternary Surface in the Lower Reaches of Narmada Valley Using Microtremors," Journal of Asian Earth Sciences, 41: 325–334.

The Determination of Biogas Production Potential from Banana Waste in Turkey

***Hidayet Oğuz*[5], *Kerim Martin* [6]**

Abstract

Approximately 90% of world's energy has been supplied from fossil resources. Since the fossil sources are limited and harmful to environment, there is a significant requirement to renewable energy. By considering this situation while the governments are making their energy plan, they research for rising way of renewable energy rate in energy production.

According to TÜİK 2014 data, Turkey supplies 47.9% of its energy from naturel gas, 30.2% from coil, 16.1% from hydraulic energy, 4.9% from renewable energy and 0.9% from liquid fuels. Turkey supplying 75% of its energy from importation should use its own renewable energy sources to reduce energy dependence. The using rate of renewable energy has risen to 4.9% in 2014 while it was 0.6% in 2008. Sustaining of this rising and reaching to 16-20% line of using rate of renewable energy about 8-10 years are one of the energy plan of related ministry.

Turkey has so wide renewable energy sources. One of the most important sources is biomass. Energy production from biogas has been increasing among the biomass energy sources. Various materials are used for biogas production. One of resources is banana waste. In this study, banana waste potential of Turkey was investigated.

Banana is an annual plant that can be produced in greenhouses or open air fields. The amount of agricultural waste is twice of production. Banana is growing approximately in a 200 km line in the middle of Mediterranean region in Turkey. According to TÜİK data, banana production area was about 25000 decare in 2003 and 58380 decare in 2015. In these years, banana productions were 110000, 270500 tons, respectively. This increase in production causes an increase in waste too. At the end of study in response to this 270500 banana production, it is calculated that Turkey approximately has 550000 tons of banana waste. Methane gas and energy amounts that can be produced from this waste are determined.

[5] *Necmettin Erbakan University, Department of Energy System Engineering, 42090, Meram/Konya, Turkey. hidayet@konya.edu.tr*

[6] *Corresponding author: Necmettin Erbakan University, Department of Energy System Engineering, 42090, Meram/Konya, Turkey. kmartin@konya.edu.tr*

11. INTRODUCTION

As long as technology improves, world energy demand has been rising. Most of this demand is supplied by fossil resources. But fossil fuels cause serious environmental pollution, global warming and climate change. World's energy based CO_2 emission was approximately 31 billion tones in 2010. It is estimated that this emission value will rise to 43 billion tones by 2030. Global warming and climate change, which arise from rising of CO_2 and other greenhouse gases, are a threat to water sources, agriculture areas and environment. Usage rates of fossil fuels are as follows worldwide; petrol %38, coal % 26, naturel gas %23. It is said that these usage rates will not change coming years. [1] Even if energy demand doesn't raise; petrol, coal and natural gas have approximately 50, 110 and 150 years life time respectively. [2] Fossil fuels emit CO_2 and other greenhouse gases to the atmosphere. These gases heat world's atmosphere by absorbing sun ray. The amount, or concentration, of CO_2 gas in the atmosphere has risen more than 40 percent since the industrial revolution. CO_2 concentration in the atmosphere is now at its highest point in the last 800,000 years. Each year, the CO_2 concentration increases by about 0.5 percent. [3] This situation affects human life negatively.

Because of these reasons many country try to increase the usage rate of renewable sources to generate energy. For example; EU has three important targets about energy policy. They want to carry out these targets up to 2020:

- Rising of energy efficiency by %20,
- Rising of usage rate of renewable energy sources to %20 and rising of usage rate of biofuel to at least %10,
- Decreasing of greenhouse gas emission by %20[4]

Like other country, Turkey wants to raise usage rate of renewable energy sources to supply energy demand. Turkey Tenth Progress Plan was published in 2013. In this plan there are lots of article (ex: 72, 429, 784) that is about importance of renewable energy. [5]

Table 1.The progress and targets in energy sector [5]

	2006	2012	2013	2018
Primary Energy Demand	99642	11302	123600	154000
Electric Energy Demand(GWh)	174637	241949	255000	341000
Primary Energy Consumption per Person(TEP/Person)	1,44	1,59	1,62	1,92
Electric Energy Consumption per Person(kWh /Person)	2517	3231	3351	4241
Rate of Naturel Gas in Electric Production (%)	45,8	43,2	43	41
Rate of Renewable Sources in Electric Production (%)	25,3	27	27,7	29
Electric İnstalled Power(MW)	40565	57058	58500	78000
Energy Density(TEP/1000 Dollar)[2]	0,288	0,276	0,272	0,243

Turkey National Renewable Energy Action Plan was published in December in 2014. This plan was prepared for 2013-2023 period. It says:

- Up to 2023, the usage rate of renewable sources in power generation must rise to %30 at least.
- Up to 2023, Turkey should increase the number of renewable energy installed power. So technologic and industrial progress will be contributed positively.
- Regional production based on renewable energy sources should be popularized. People should be encouraged to use renewable energy in their houses.[6]

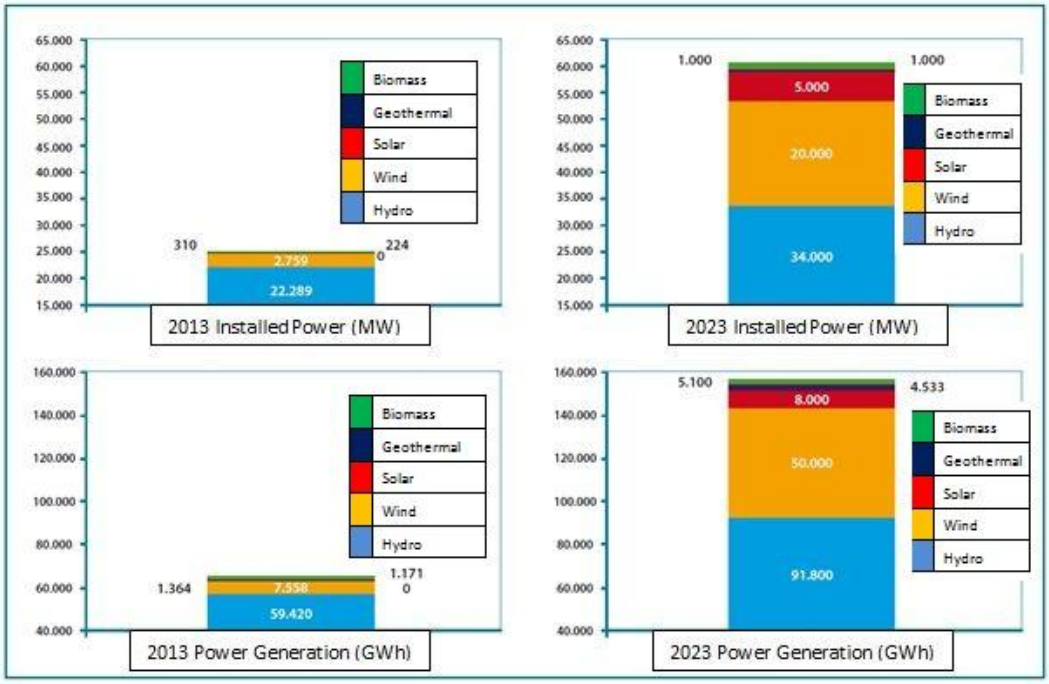

Figure 1: Power generation from renewable energy sources and installed power capacity: 2013 data and 2023 targets [6]

This subject takes part in Turkey Energy and Natural Resources Ministry 2015-2019 Strategic Plan. It was mentioned in the plan that Turkey has various renewable energy sources. These renewable energy sources should be used effectively to contribute economics. It has a strategic importance. For this reason, increasing of renewable energy sources usage rate for power generation was aimed in the plan. One of the targets of the plan was to use renewable energy as thermal energy sources. [7]

Renewable Energy Sources Installed Power(MW)	**Base Year 2013**	**2015**	**2017**	**2019**
Hydraulic	22289	25000	27700	32000
Wind	2759	5600	9500	10000
Geothermal	311	360	420	700
Solar	-	300	1800	3000
Biomass	237	380	540	700
At the End of Period Rate of Renewable Energy Sources at Heat Production (%)	Base Year 2013		2019	
	2		3	

Table 2: Renewable energy source installed power value (planned) [7]

Although Turkey doesn‘t have substantial fossil energy sources, it has significant renewable energy sources. We should use these sources effectively and add new ones to them. If so, Turkish economy is affected positively. This study is a part of master‘s thesis named ―The Manufacturing of Pilot Scale Biogas Reactor and Investigation of Biogas Production from Banana Waste”. In this study biogas production potential from banana waste of Turkey is investigated.

12. MATERIALS AND METHODS

12.1. The structure of banana

Banana has two stem. One of them is main stem. The other one is fake stem. Main stem under the soil is perennial. Other stem which is above the soil is an annual plant. Main stem has an eight or ten year‘s lifespan. Lots of fake stems occur from main stem. These fake stems are cut except one. So, this stem grows well. Fake stem can reach 7-8 meters tall. After harvest, the fake stem is waste. Fake stem has also lots of leafs. After harvest, these leafs are wastes too. These wastes are leaved in the field by breaking up into small pieces at current situation. These wastes have a potential of biogas production.

12.2. Banana production areas in Turkey

Banana is grown both in greenhouses and in open air fields in Turkey. Greenhouses give optimum growing habitat to banana. Table 3 shows banana production areas and amount of product.

TURKEY BANANA PRODUCTION		
YEAR	AREA(DECARE)	PRODUCTION(TONNE)
1990	13 720	36 000
1991	13 090	35 000
1992	11 320	20 000
1993	10 800	18 000
1994	12 000	30 000
1995	11 500	31 000
1996	11 650	32 600
1997	11 900	28 000
1998	11 930	32 000
1999	12 270	34 000
2000	17 250	64 000
2001	18 750	75 000
2002	23 850	95 000
2003	25 200	110 000
2004	30 000	130 000
2005	36 000	150 000
2006	39 168	178 205
2007	44 098	189 107
2008	43 258	201 115
2009	43 338	204 517

2010	44 279	210 178
2011	45 074	206 501
2012	44 923	207 727
2013	46 700	215 472
2014	53 497	251 994
2015	58 380	270 500

Table 3: Turkey banana production [8]

12.3. Determination of banana waste and biogas potential

12.3.1. Determination of banana waste

Banana production is done south coast of Turkey at a 200 km line widely. This line includes some district of Antalya and Mersin. These districts are Alanya (Antalya), Gazipaşa (Antalya), Anamur (Mersin) and Bozyazı (Mersin). Banana is grown at open air fields in Alanya and Gazipaşa. It is mostly grown in greenhouses in Bozyazı and Anamur. It is possible to harvest twice a year in greenhouses. Waste/product ratio is equal to 2. [9] The amount of annual product was 270500 tons so the amount of annual waste was approximately 550000 tons in 2015.

12.3.2. Determination of biogas potential

It is not an effective method to use only banana waste to produce biogas. In a study it is said that optimum mix ratio is %30 banana waste and %70 cattle manure.[10] Sözer and Yaldız mentioned that dry matter rate of banana waste is %88,45 of the waste and organic dry matter rate is %85,51of dry matter. The amount of methane is %51, 1 of biogas. The feedstock specific methane production ratio is calculated as 0,149 L g^{-1} odm^{-1} d^{-1}. [10]

13. RESULTS

- Annual amount of waste:$550000x10^3$ kg
- Amount of dry matter: $550000x10^3x0,8845=486475x10^3$ kg
- Amount of organic dry matter: $486475x0,8551=415984x10^3$ kg
- Amount of methane: $0,149x415984x10^3=61981731$ m^3
- Amount of biogas: $61981731/0,5111=121271240,46$ m^3

Biogas can be converted to heat energy by burning directly. It can be converted to electric energy by using a gas engine or a generator. But before using it in engines, it should be separated from destructive gases like H_2S, CO and CO_2. [11] Energy amount of 1 m^3 biogas is 6 kWh. [12] So the amount of energy that can be produced from this potential is 727, 63 GWh/year.

14. CONCLUSIONS

This calculated energy potential is a considerable energy amount. Turkey should use its renewable energy sources to decrease energy dependence. Each region has different renewable energy sources in Turkey. One of the sources is banana waste. Banana production area is getting rising every year. So the amount of banana waste is getting rising too. This waste should be used for energy production in south of Turkey.

ACKNOWLEDGMENT

The authors would like to acknowledge Necmettin Erbakan University Scientific Research Projects Office and Necmettin Erbakan University OYP Coordination Office for the financial support given.

REFERENCES

[1] The BİLGİUSTAM website. [Online]. Available: http://www.bilgiustam.com/fosil-yakitlarin-gelecegi-ve-cevresel-etkileri/
[2] Energy İnstitute website. [Online]. Available: http://enerjienstitusu.com/2011/05/23/dunya-enerji-kaynaklarinin-100-yillik-omru-kaldi
[3] The NSF website. [Online]. Available: https://ncar.ucar.edu/learn-more-about/climate
[4] Turkish EU Ministry website. [Online]. Available: http://www.ab.gov.tr/index.php?l=1&p=80
[5] Turkey Progress Ministry Tenth Progress Plan 2014-2018 (2013)
[6] Turkey Energy and Naturel Sources Ministry Renewable Energy General Diractorate Turkey National Renewable Energy Action Plan 2013-2023 (2014)
[7] Turkey Energy and Naturel Sources Ministry 2015-2019 Strategic Plan
[8] TÜİK website. [Online]. Available: (http://www.tuik.gov.tr)
[9] Jing Y.T., Chin L.L., Keat T.L., Kok T.T., Subhash B.," Banana biomass as potential renewable energy resource: A Malaysian case study", Renewable and Sustainable Energy Reviews, vol.14, pp. 798–805, 2010
[10] Sözer S., Yaldız O., ―A research on determination of biogas production from mixture of banana greenhouse wastes and cattle manure under mesophilic conditions", Akdeniz Univercity Faculty of Agriculture, vol. 24(2), pp. 75-78, 2011
[11] Üçgül İ., Akgül G., ―Biomass Technology", Journal of YEKARUM, vol. 1(1), pp. 3-11, 2010
[12] Yaldız O., ―Biogas Technology", Akdeniz Universıty , edition number. 78, Antalya, Turkey, 2004

Examining of Design Spectrum with Peak Period,Vs 30 Values Related by Eurocode 8: Case Study of İzmir Bay and Surrounding Area

Mustafa Akgün[7], *Aykut Tunçel*[2]

Abstract

Site class and peak period values must be described in detail on the construction area while designing earthquake resistant buildings. In this context, the depth of the bedrock determines the scope of work to be done. The distinction between bedrock and site is made on the basis of S-wave velocity values. Today, according to Eurocode 8 (EC8) regulations if the average depth of the bedrock is 30 meters or less, Vs30 velocities and peak period (T0) values are considered together while defining the ground response spectra. Thus, with respect to the site response spectrum it can be ensured possibility of using table values. However, as described in the EC8 earthquake regulations when T0> 1 sec and Vs30 <300 m/s condition was achieved the ground is defined as S1 and S2. This means that the long-period site response spectrums must be defined by making additional studies in these areas. With this definition, the calculation of earthquake loads can be ensured for particularly high-rise buildings safer. In this context, the creation of the site model and the site transfer function must be calculated by in-situ studies for the site class with S1-S2 feature. In this study, data was collected from the vicinity of the Gulf of Izmir sampled with regional 1 km intervals. Changes at Vs30 values obtained from the MASW study and changes at T0 values obtained from Quasi Transfer Spectrum are mapped. The areas contain S1 and S2 site classes based on the EC8 earthquake regulations are determined by examining these maps. Then at these areas the site and the engineering-seismic bedrock depths have been identified by obtaining S-wave velocity changes in the vertical direction using SPAC study results. Site thickness in areas defined as S1 and S2 determined much more than 30 meters (average 250m.-300m.) according to the obtained results.

Keywords: QTS, İzmir.

15. INTRODUCTION

In the preliminary estimation of the earthquake-ground common dynamic behaviour spectrum during an earthquake according to Eurocode 8 regulations Vs30 speed value with the peak period (T0) values are widely used. According to Eurocode 8 earthquake regulations when T0> 1 sec and Vs30 <300 m / sec in the ground condition it is defined as S1 and S2. In the regions with these characteristics long-period ground response spectra must be identified. So, today, the dominant high-rise buildings for earthquake loads calculated using the spectrum of safer. For this, on the S1-S2 featuring grounds, ground and bedrock models should be created and the transfer functions dependent to these models should be calculated with in-situ studies. The most important concept in the creation of the ground bedrock model is to select appropriate exploratory depth. For this purpose, 3 component measurements are widely done by using the Nakamura single station mikrotremor technique. Then, T0 values are calculated from the obtained quasi transfer spectrums. Past studies demonstrated that the thickness of ground is greater than 30 m in areas where the T0>1 (Akgün et al., 2013, Teves and Costa, 1996). In this study, Multi-channel Analysis of Surface Waves (MASW) method and Mikrotremor method studies have been made at approximately 380 points on the grounds around the Gulf of Izmir with a scale of 1*1 km. Changes on the obtained T0 and Vs30 values are examined and S1 and S2 ground classes according to Eurocode 8 earthquake regulations was determined. Thus, it is commonly provided that defining the ground class as well as the prior knowledge about ground transfer functions at microzonation studies.

16. GEOPHYSICAL STUDIES

In the study area, microtremor and masw method measurements were made at approximately 380 points using 1*1 km grid. Field studies of the masw method are completed by using Geometrics Geode 24 channel seismometer with 4.5 Hz P geophones. Three-component CMG-6TD velocity recorder was used for microtremor studies while the recording time was achieved as 30 minutes sampled at 100 Hz. The results of the study are commonly mapped and given at figures 1, 2, 3, 4 and 5.

[7] *Corresponding author: Dokuz Eylül University, Department of Geophysics Eng., 35160, Buca/İzmir Turkey.* cevdet.ozdag@deu.edu.tr

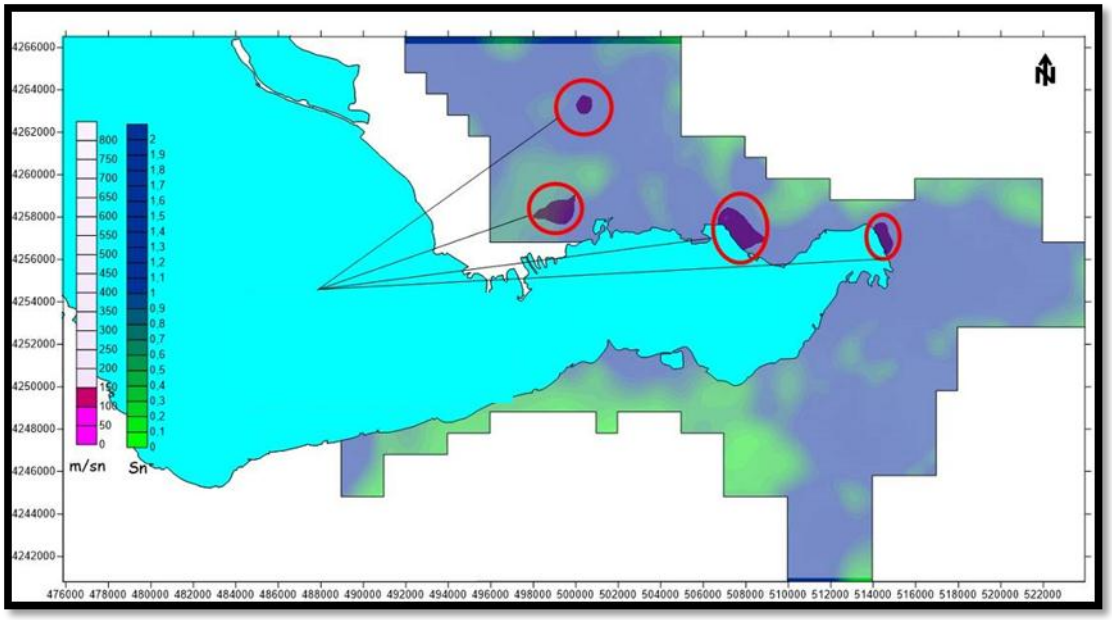

Figure 1. Common results for Vs30<150 m/sec

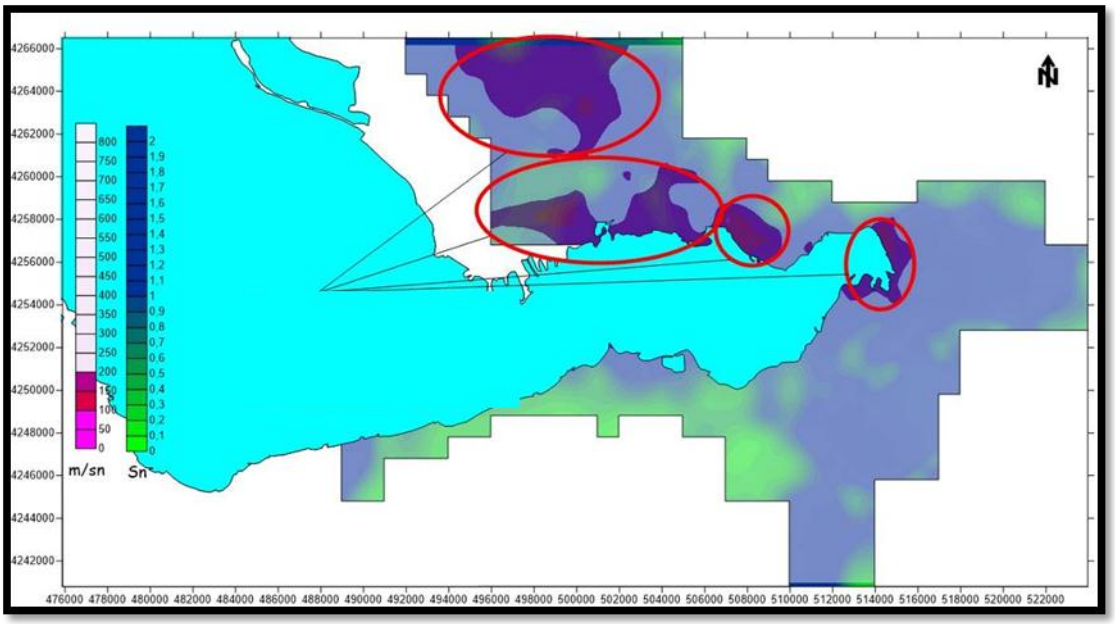

Figure 2. Common results for Vs30<200 m/sec

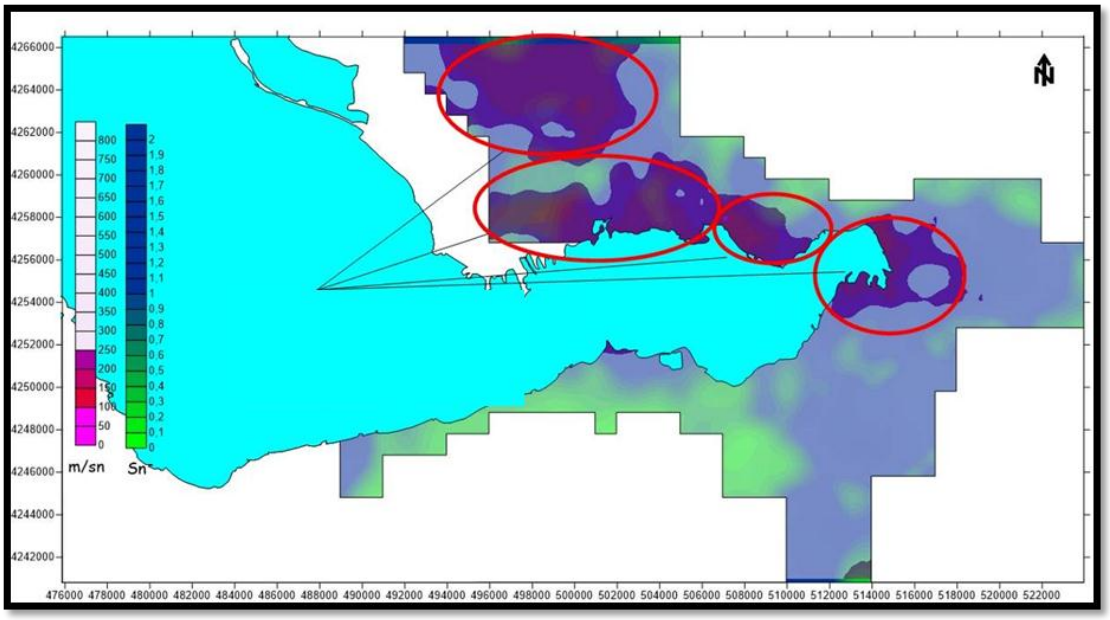

Figure3. Common results for Vs30<250 m/sec

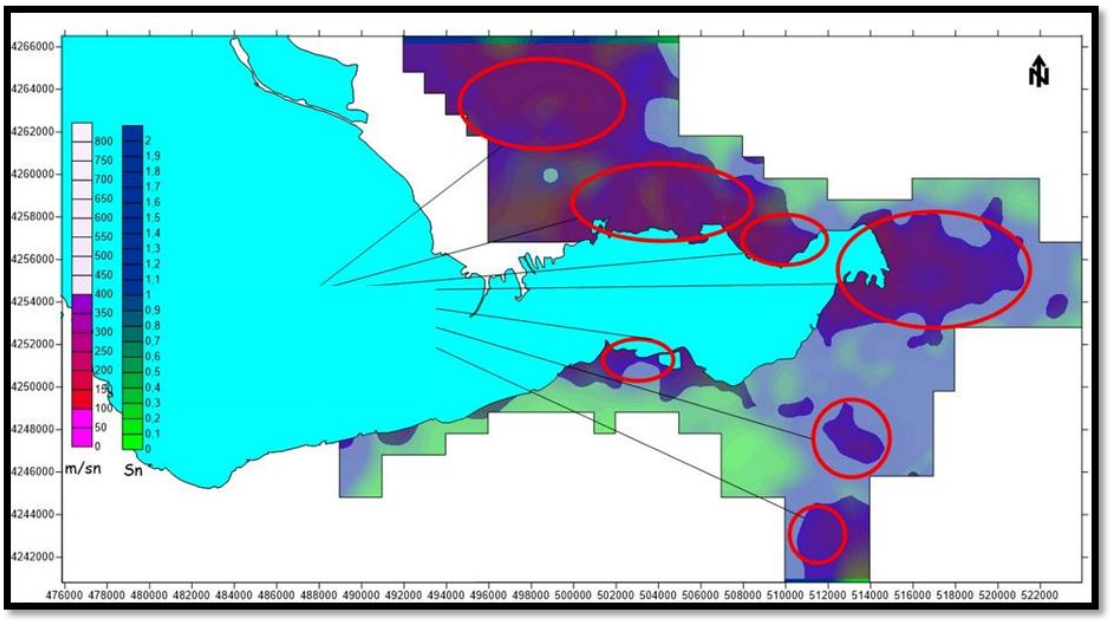

Figure 4. Common results for Vs30<400 m/sec

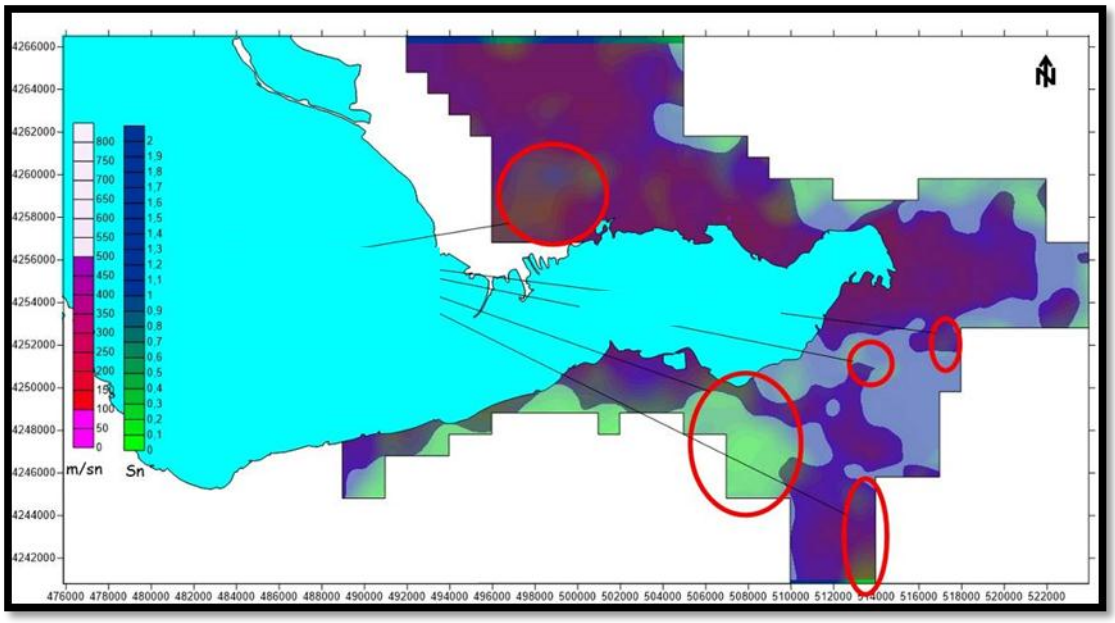

Figure 5. Common results for Vs30<500 m/sec

17. CONCLUSION

When defining the common behaviour of the earthquake-ground-structure, S1 and S2 ground classes have a special importance. The response spectra calculated using ground models obtained with in-situ measurements must used rather than theoretical models of ground response spectra on such grounds. This study subject must be based on when planning the microzoning studies. Also it is very important to calculate the ground response spectra at the locations which Vs30<300 m/sec and T0>1 second. The most economical way of approaching these conditions is to commonly use the T0 (peak period) and the S wave velocity values. According to the results of this study, around the Gulf of Izmir Vs30 velocity values are determined smaller than 300 m/s and T0 values were determined greater than 1 sec as given in the figures (Figure 1, 2, 3, 4 and 5). What this means that in these areas Eurocode 8 and TDY 2007 regulations will be insufficient. Especially where high-rise buildings are widespread it is necessary to generate long period spectrums in the metropolitan area of Izmir city.

ACKNOWLEDGMENT

This study has been achieved under the scope of No: 106G159 The Scientific and Technological Research Council of Turkey (TUBITAK) project. We would like to thank all the project team for the help on data collecting.

REFERENCES

[42]. Akgün, M., Gönenç, T., Pamukçu,O., Özyalın, Ş., Özdağ, Ö.C., (2013a), Integrated Geophysical Methods For The Determination Of Engineering Bedrock: İzmir New City CenterMühendislik Ana Kayasının Belirlenmesine Yönelik Jeofizik Yöntemlerin Bütünleşik Yorumu: İzmir Yeni Kent Merkezi Uygulamaları, Turkish Journal of Geophysics(in Turkish), doi 13.b02 jeofizik-1304-12

[43]. Bonnefoy-Claudet S, Cotton F and Bard PY (2006a), ―The Nature of Noise Wavefi eld and Its Applicationsfor Site Effects Studies: A Literature Review," Earth-Science Reviews, 79: 205–227.

[44]. Bonnefoy-Claudet S, Cornou C, Bard PY, Cotton F, Moczo P, Kristek J and Fäh D (2006b), ―H/V Ratio: aTool for Site Effects Evaluation Results from 1-D noise Simulations," Geophysical Journal International, 167: 827–837.

[45]. D'Amico V, Picozzi M, Albarello D, Naso G and Tropenscovino S (2004), ―Quick Estimates of Soft Sediment Thicknesses from Ambient Noise Horizontal to Vertical Spectral Ratios: a Case Study in Southern Italy," Journal of Earthquake Engineering, 8(6): 895–908.

[46]. Delgado J, Casado CL, Lopez Giner J, Estevez A, Cuenca A and Molina S (2000), ―Microtremors as a Geophysical Exploration Tool: Applications and Limitations," Journal of Pure and Applied Geophysics,157:1445–1462.

[47]. Field E and Jacob K (1993), ―The Theoretical Response of Sedimentary Layers to Ambient Seismic Noise," Geophysical Research Letters, 20(24): 2925–2928.

[48]. Field EH, Clement AC, Jacob KH, Aharonian V, Hough SE, Friberg PA, Babaian TO, Karapetian SS,Hovanessian SM and Abramian HA (1995), ―Earthquake Site-response Study in Giuari (Formerly Leninakan) Armenia Using Ambient Noise Observations," Bulletin of the Seismological Society of America, 85(1): 349–353.

[49]. Gosar A (2007), –Microtremor HVSR Study for Assessing Site Effects in the Bovec Basin (NW Slovenia)Related to 1998 Mw 56 and 2004 Mw 52 Earthquakes," Engineering Geology, 91: 178–193.
[50]. Gosar A and Martinec M (2009), –Microtremor HVSR Study of Site Effects in the Ilirska Bistrica Town Area (S Slovenia)," Journal of Earthquake Engineering, 13:50–67.

Relationship Between Soil Deformation, Quasi Transfer Spectrum and Soil-Bedrock Models : Case Study of İzmir Bay and Surrounding Area

Mustafa Akgün[8], Özkan Cevdet Özdağ[2], Aykut Tunçel[3], Ümit Büyükboyacı[4]

Abstract

Buildings during the earthquake remain under the force of inertia, defined as seismic forces. The magnitude of this force will affect the changes of the amplitude frequency spectrum that occurs in the source until it reaches to the ground surface of earthquake waves. During the earthquake, when the seismic force has reached or exceeds the endurance limit of the structure and the floor, structural damage begins to occur due to the earthquake motion. Earthquake force varying as a dynamic load that depends on time and space may behave as elastic, elastoplastic or plastic in the lateral direction of the site. These events pushing the limits of endurance are basically associated with displacement of soil-structure intersection during the earthquake. The endurance limit of the soil-structure intersections joint movement is defined as strain. Nowadays weight and height of the structures is gradually increasing, to perform site dynamic analysis using site-bedrock models which are appropriate to the construction area are important. The site-bedrock model must be obtained up to a necessary depth (Vs>760 m/s) to perform site dynamic analysis. In this study, at east of the Gulf of Izmir stretching NW-SE direction approximately on a 10 km long profile, seismic wave velocities (Vp,Vs) were obtained by geophysical studies. Thickness depth, and density parameters are obtained by using seismic velocities, and the 2-dimensional (2D) site-bedrock model as was created. The relationship between the lateral deformation changes and Kg values at the ground surface were examined

.**Keywords:** QTS, İzmir.

18. INTRODUCTION

Seismic bedrock (Vs>3000 m/s) and soil (Vs<760 m/s) are defined for deformation changes on ground surface as a results of earthquake-ground common behavior. Amplitude frequency values of seismic waves change while energy of earthquake wave don't change according to e seismic impedance between the layers where earthquake wave pass (Yalçınkaya 2004). Deformation changes are influenced by thickness, density, elastic properties etc. parameters.of remaining medium between ground and engineering bedrock (Vs>760 m/s) during earthquake-ground common behavior. According to these results, soil-bedrock models must be defined as original determination in study area fore earthquake ground common behavior.

The most important parameters of modeling are P and S wave velocities which change parameters of earthquake waves , density and the lateral and vertical direction changing of these parameters. But for this changes, obtaining study of P and S waves must carry out up to a depth of change will be determined based on seismic impedance (Akgun et al. 2013 a. and b.)This means that the bedrock soil models should not be selected randomly and investigation depth should not be limited with 30m.

The main reason of so much importance of these parameters is change of horizontal peak acceleration (PGA) which affect the building on ground depending on layer thickness and seismic velocities.All of these concepts are analyzed in both the defination of observational and theoretical transfer functions and soil bedrock models.

[8] *Corresponding author: Dokuz Eylül University, Department of Geophysics Eng., 35160, Buca/İzmir Turkey. cevdet.ozdag@deu.edu.tr*

Transfer function is defined as used function for defination of amplitude frequency changes in seismic waves depending on seismic impedance changes and this function is considered to be equivalent with horizontal / vertical spectral ratio (Quai Transfer Spectrum) obtained from Nakamura (1989).

This means that horizontal/vertical spectral ratios spectrums obtanined from Nakamura (1989) can be used as observational data. According to Herak (2008)'s definitions, theoretical transfer spectrums can be calculated (Akgun et al. 2013, Akgun et al. 2013b) Herak 2008).

In this study, for the soils in the Izmir Bay surroundings, theoretical soil transfer functions are calculated using P and S wave velocities, layer thickness and density and they are compared observed Quasi Transfer Spectrum obtained microtremor measurements. Lastly optimized soil-bedrock models are presented by this comparing.

19. APPLICATION

Descriptions of the observational and theoretical transfer spectrum calculation is given below for Observational Quasi Transfer Spectrum (vertical / horizontal ratio).

2.1. Observational horizontal / vertical ratio calculations

with studies, obtained by Nakamura method of horizontal / vertical spectral ratios have been shown to provide preliminary information on regional effects of ground-bedrock (M.Akgün 2013)

According to Nakamura method(1989), the horizontal component spectrum of the ground is divided into a vertical component spectrum. The dominant ground vibration period is determined. In addition, theoretically dominates the ground vibration frequency ,the thickness of ground and shear wave velocity is defined below.

$$f_0 = V_S/4_H \quad (1)$$

In the observational transfer function, amplitude changes are affected by the frequency changes. Frequency changes are also affected by the thickness of the substrate. As a result, during the earthquake, increased frequency of earthquake energy can be identified by the Quai Transfer spectrums. Low frequency‘s amplitude values identifies the impact of the deeper layers and high frequency‘s amplitude values identifies the impact of the near-surface layers.

2.2. The theoretical horizontal / verticalratio calculations

On the theoretical work, the ground is comprised of horizontal, homogeneous, isotropic and viscoelastic layers and seismic waves move in the vertical direction. We accept it. Also bedrock-ground concept and P, S waves are used. Theoretical amplitude spectrum is calculated and compared (figure 1) according to the following flow chart (Herak 2008). In this comparison, theoretical ground transfer function and the observational transfer function are approximated with least squares method. Thus, ground model is optimized. The theoretical ground transfer functions are calculated according to Tsai 1970 approaches.

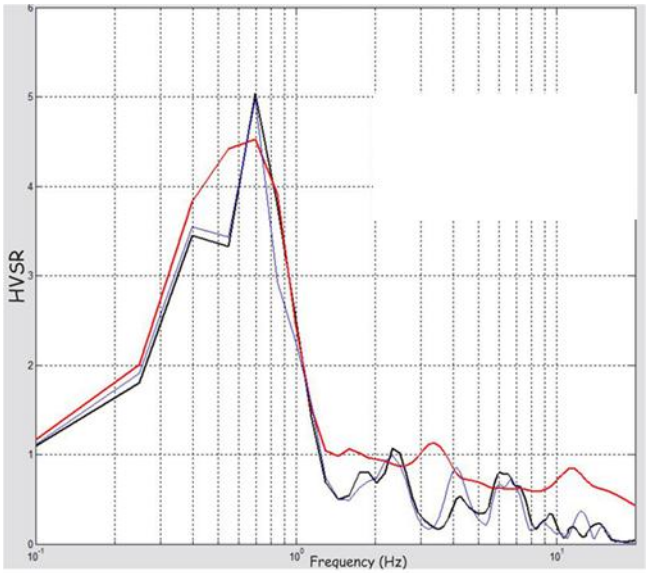

Figure 1.Comparison of observational and theoretical ground transfer function

Figure 2. SPAC Study Geometry

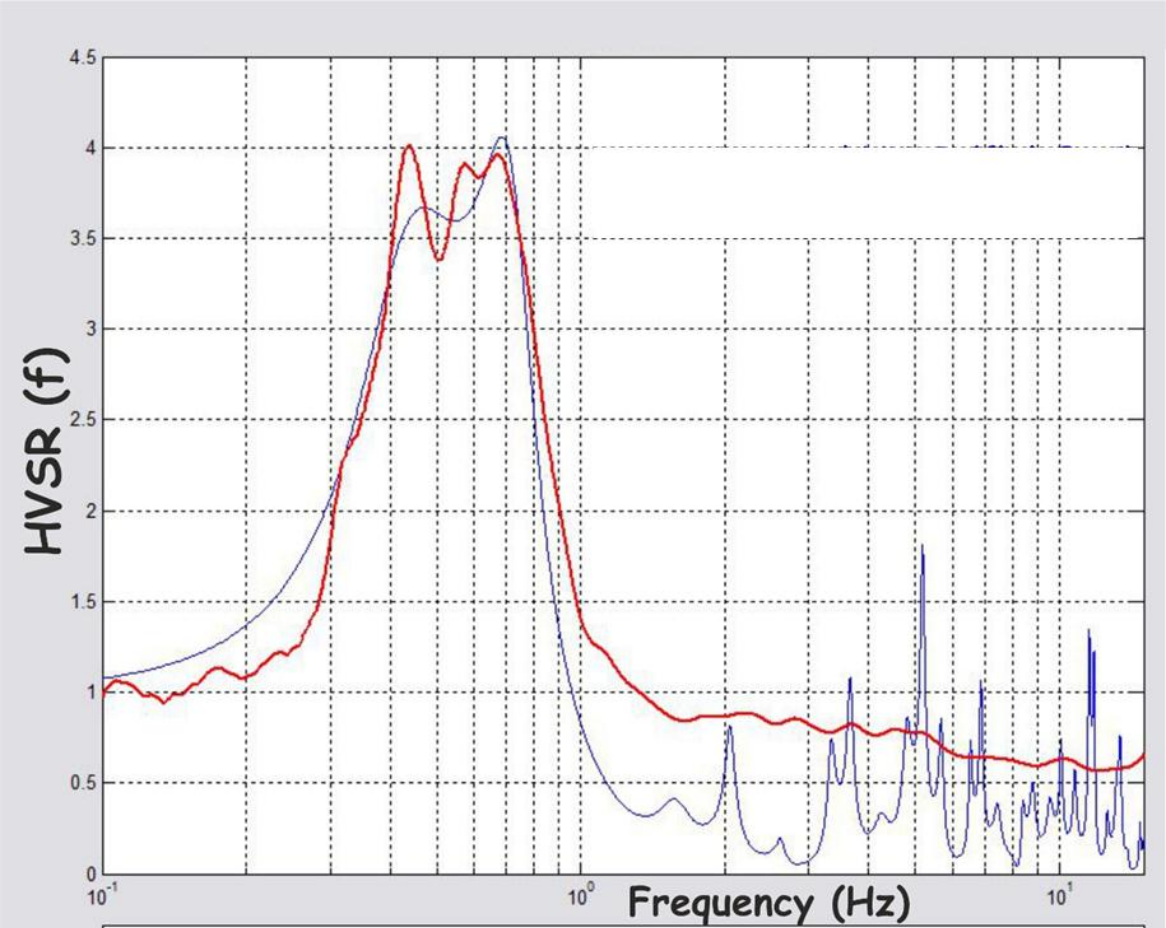

Vp	Vs	rho	D	Qp	Qs
1124	319	1.70	5.0	134	30
200	50	1.98	15.0	61	12
1270	318	1.93	50.0	150	30
1290	323	1.70	30.0	150	30
1400	352	2.01	85.0	150	30
2049	805	2.30	92.0	150	30
2268	525	1.85	28.0	144	30
3500	810	2.34	999.0	999	999

Vp	Vs	rho	D	Qp	Qs
1300	300	1.83	5.0	130	30
1200	220	1.69	15.0	120	22
1500	280	1.79	50.0	150	28
1900	480	2.05	30.0	190	48
1800	370	1.92	85.0	180	37
2250	435	2.00	92.0	225	43
3000	600	2.17	28.0	300	60
3500	810	2.34	999.0	999	999

Figure 3. Observational and Theoretical HVSR Comparison ve Ground Model Optimized

20. CONCLUSION

In this study, for around of Izmir Bay to the grounds, P and S wave velocities,layer thicknesses and densities are obtained from using in theoretical and observational Quai Transfer Spectrum calculations. With Quai Transfer Spectrums comparison, optimized ground-bedrock model samples are given. Peak period values, also it is larger average 1.5 sec. by Quasi Transfer Spectrum HVSR obtained.

This means that, the ground surface velocity and displacement effect will be dominant for the earthquake-soil-structure common behavior. If peak period value is bigger than 1 sec. , the ground is thicker tham 30 m. and soil classification in the regulation does not apply to ground response spectrum definitions. At some point peak period values are bigger and there are multiple peaks. This means that, there are multi border to creating seismic impedance changes. If ground-engineering bedrock models create, those limits must be considered. According to peak period-amplitude seismic waves changes, earthquake waves changes begins seismic bedrock upper limit(Vs>3000 m/sec. and average 1200 m. depth). According to S wave velocity change, ground (Vs <760 m / sec.) thickness changes 100-400m. and engineering bedrock (3000 m / sec.> Vs> 760 m / sec.)

depth of 100-400 meters. According to the definition of ground from defining the S-wave velocity in the vertical direction, Bay North and East of the ground thickness is greater than the southern part.

Another important result obtained from this study, the ground in Izmir Bay, velocity spectrum for earthquake-resistant design should be used. The reason for this is the inadequate in the calculations of the earthquake acceleration spectrum. Therefore both time history work and velocity records must be used together. In theoretical calculations, transition to velocity the acceleration spectrum will cause incorrect calculation. Therefore, the data velocity must be obtained directly from the seismic movement.

REFERENCES

[1] Akgün, M., Gönenç, T., Pamukçu,O., Özyalın, Ş., Özdağ, Ö.C., Mühendislik Ana Kayasının Belirlenmesine Yönelik Jeofizik Yöntemlerin Bütünleşik Yorumu: İzmir Yeni Kent Merkezi Uygulamaları, Jeofizik Dergisi, doi 13.b02 jeofizik-1304-12, 2013a.

[2] Akgün, M., Gönenç, T., Tunçel, A., Pamukçu, O., A multi-approach geophysical estimation of soil dynamic properties in settlements: a case study in Güzelbahce-İzmir (Western Anatolia), J. Geophys. Eng., 10 (2013b.) 045001 doi:10.1088/1742-2132/10/4/045001

[3] Herak, M., Model HVSR-A Matlab® tool to model horizontal-to-vertical spectral ratio of ambient noise, Computer and Geosciences, 34, 1514-1526. 2008

[4] Nakamura, Y., A method for dynamic characteristics estimation of subsurface using microtremor on the ground surface, Quarterly report of the Railway Technical Research Institute 30:1, 25-33. 1989.

[5] Nath, S.K.., Seismic Microzonation Framework – Principles & Applications,| Proceedingsof Workshop on Microzonation, Indian Institute of Science, Bangalore, pp 9-35 2007.

[6] Tsai, N.C., (1970), A note on the steady-state response of an elastic half-space. Bulletin of the Seismological society of America 60, 795–808.

[7]Yalçınkaya, E., Bir boyutlu modeller için zemin büyütmesine etki eden parametrelerin incelenmesi. İstanbul Üniv. Müh. Fak. Yerbilimleri Dergisi, C. 17, S. 1, SS. 47-56. 2004.

Nonlinear Buckling Analysis of Eccentrically Loaded T-Sections

Mustafa Durmaz[9], AyÇeDaloğlu [10]

Abstract

Single steel T-sections are widely used as chord and web members in trusses. Despite the fact that T-sections are readily available commercially and can be easily obtained by cutting standard I-sections through the middle of the web, the failure behavior of these members when subjected to a compressive force is still not fully understood as corroborated by the numerous different design approaches for these members in various national specifications for steel structures.

An efficient nonlinear finite element model is provided to understand the behavior of eccentrically loaded single T-sections. Theoretical buckling and the experimental failure loads of pin ended, concentrically loaded T-sections were predicted by eigenvalue and load-deformation analyses of various models developed in ABAQUS 6.13. The T-sections were modeled by shell elements considering geometrically and materially nonlinear behavior. Initial imperfections, end support conditions, geometry and material property variation of the T-sections were included differently in each model. The load-carrying capacity of eccentrically loaded single T-sections are investigated by performing an extensive parametric study obtaining the most realistic estimations. It is seen that compression capacities of eccentrically loaded T-sections are overestimated according to TS 648.

Keywords: Thin-Walled Members, T-sections, Buckling, Finite Element Method, Nonlinear Analysis, TS 648

21. INTRODUCTION

This paper deals with hot-rolled T-section members and their failure behavior under eccentrically applied compression load. Despite the fact that T-sections are readily available commercially and can be easily obtained by cutting standard I-sections through the middle of the web, the failure behavior of these members when subjected to a compressive force is still not fully understood as corroborated by the numerous different design approaches for these members in various national specifications for steel structures.

T-sections are singly symmetric and hence, the critical overall buckling modes in compression are the flexural buckling mode in the plane of symmetry and the flexural-torsional buckling mode. At short and intermediate column lengths, the critical overall buckling mode is the flexural-torsional mode which, at intermediate and long lengths, may change to the minor axis flexural mode. The flexural-torsional mode consists of coupled flexure about the axis of symmetry and torsion about the shear center. At short lengths, torsion dominates the flexural-torsional mode and in the limit where the length approaches zero, the flexural-torsional mode becomes the torsional mode.

Experiments on T-section columns appear to be limited to those presented by Kitipornchai and Lee [1]. Numerical studies have been undertaken by Kitipornchai et al [2] and Dinis et al [3]. In the absence of comprehensive experimental data, this paper first presents a finite element model (FEM) calibrated against the tests by Kitipornchai and Lee [1] and subsequently a parametric study of the strength of eccentrically loaded T-section columns covering a wide range of geometries. The paper then compares the numerical strengths obtained and test strengths with strength predictions by the Turkish specification, TS 648 [4] for hot-rolled and fabricated steel structures, and suggests more accurate design approaches than those currently.

22. EXPERIMENTAL TEST

The finite element model was calibrated by comparing ultimate strength data with the test strengths reported by Kitipornchai and Lee [1].

Three cross-sections were tested by Kitipornchai and Lee [1], as shown in Figure 1. The sections were obtained by cutting three I-sections lengthwise through the center of the web so as to produce two T-sections for each length of I-section, resulting in a total of six T-section specimens. The cross-section dimensions and column lengths are shown in Table 1. The measured values of Young‘s modulus and yield stress were 214 GPa and 300 MPa respectively.

[9] *Corresponding author: Gümüşhane University, Faculty of Engineering and Natural Sciences, Department of Civil Engineering, 29100, Gümüşhane, Turkey.* mustafadurmaz@gumushane.edu.tr

[10] *Karadeniz Technical University, Faculty of Engineering, Department of Civil Engineering, 61080, Trabzon, Turkey.* aysed@ktu.edu.tr

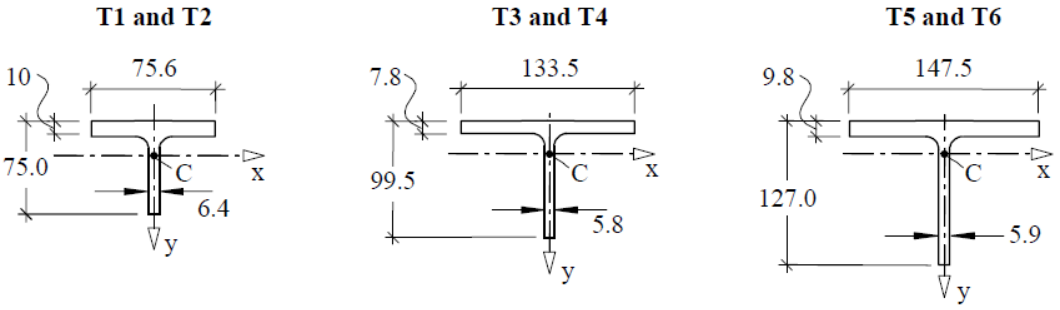

Figure 4. Cross-section geometries of the columns tested by Kitipornchai and Lee [1], dimensions in mm.

Table 2. Geometric properties and failure loads of T-section members tested by Kitipornchai and Lee [1].

Sample	B (mm)	T (mm)	H (mm)	T_w (mm)	L (mm)	A (mm^2)	P_f (kN)	P_{FEM} (kN)	P_f/P_{FEM}
T1	75,6	10,0	75,0	6,4	685	1172	315	325,4	0,97
T2	75,6	10,0	75,0	6,4	785	1172	320	319,8	1,00
T3	133,5	7,8	99,5	5,8	1785	1573	371	403,5	0,92
T4	133,5	7,8	99,5	5,8	1985	1573	385	381,2	1,01
T5	147,5	9,8	127,0	5,9	1785	2137	519	551,0	0,94
T6	147,5	9,8	127,0	5,9	1985	2137	513	532,8	0,96

3. FINITE ELEMENT MODELING

3.1. General

In this study, the finite element program, ABAQUS 6.13 [5] was used in the analysis of plain T-section columns tested by Kitipornchai and Lee [1]. The model used the nominal sizes, initial local and overall geometric imperfections, and material properties. Finite element analysis for buckling requires two types of analyses. The first is known as eigenvalue analysis that estimates the buckling modes and loads. Such an analysis is a linear elastic analysis performed using the (*BUCKLE) procedure available in the ABAQUS library with the live load applied within the step. The buckling analysis provides the factor by which the live load must be multiplied to reach the buckling load. For practical purposes, only the lowest buckling mode predicted from the eigenvalue analysis is used. The second is called load-displacement nonlinear analysis and follows the eigenvalue prediction. It is necessary to consider whether the postbuckling response is stable or unstable.

3.2. Finite Element Type and Mesh

It is mentioned in the ABAQUS manual that the four-noded doubly curved shell element with reduced integration S4R is suitable for complex buckling behavior. The S4R element has six degrees of freedom per node and provides accurate solutions to most applications. The element also accounts for finite strain and is suitable for large strain analysis. Since buckling of plain angle columns is very sensitive to large strains, the S4R element was used in this study to ensure the accuracy of the results. In order to choose the finite element mesh that provides accurate results with minimum computational time, convergence studies were conducted. It is found that a 10 mm x 10 mm (length by width) ratio provides adequate accuracy in modeling the angles.

3.3. Boundary Conditions and Load Application

Following the experimental tests, the ends of the columns were free to rotate and fixed to translate in any direction except for the displacement at the loaded end in the direction of the applied load. The nodes other than the two ends were free to translate and rotate in any direction. The load was applied in increments using the modified RIKS method available in the ABAQUS library. The RIKS method is generally used to predict unstable and nonlinear collapse of a structure such as postbuckling analysis. It uses the load magnitude as an additional unknown and solves simultaneously for loads and displacements. The load was applied as static uniform loads at each node of the loaded end which is identical to the experimental investigation. The nonlinear geometry parameter (*NLGEOM) was included to deal with the large displacement analysis.

3.4. Material Modeling

The reported stress-strain curves for angle specimens were used in the analysis. The material behavior provided by ABAQUS allows for a multilinear stress-strain curve to be used. The first part of the multilinear curve represents the elastic part up to the proportional limit stress with measured Young‘s modulus and Poisson‘s ratio equal to 0.3. Since the analysis of postbuckling involves large in-elastic strains, the nominal (engineering) static stress-strain curve was converted to a true stress and logarithmic plastic strain curve.

3.5. Modeling of Initial Local and Overall Geometric Imperfections

Both initial local and overall geometric imperfections are found in columns as a result of the fabrication process. Hence superposition of local buckling mode as well as overall buckling mode with measured magnitudes is recommended for accurate finite element analysis [6]. These buckling modes can be obtained by carrying eigenvalue analysis of the column with very high b/ t ratio and very low b/ t ratio to ensure local and overall buckling occurs, respectively. Only the lowest buckling mode (eigenmode 1) is used in the eigenvalue analysis. This technique is used in this study to model the initial local and overall imperfections of the columns. Since all buckling modes predicted by ABAQUS eigenvalue analysis are generalized to 1.0, the buckling modes are factored by the measured magnitudes of the initial local and overall geometric imperfections.

4. RESULTS AND DISCUSSIONS

4.1. Comparison of experimental results with finite element analysis results

In the verification of the finite element model, a total of 6 hot-rolled steel plain T-section columns were analyzed. The incremental plasticity models obtained from the true stress–strain curves were used in the FEM for the corresponding test series. A scale factor of 1/1500 of the specimen length was used in modeling the geometric imperfections of the columns. A comparison between the experimental results and the results of the finite element model is carried out. The main objective of this comparison is to verify and check the accuracy of the finite element model. The comparison of the ultimate loads P_f and P_{FEM} is shown in Table 1. Figure 2 plotted the relationship between the ultimate load and the column effective length L_{eff}=L for T-sections reported by Kitipornchai and Lee [1], where L actual column length. The column curves show the experimental ultimate loads together with that obtained by the finite element method. It can be seen that good agreement has been achieved between both results for most of the columns.

The mean value of the P_f/P_{FEM} ratio is 0.967 with the corresponding coefficients of variation (COV) of 0.0012 for T-sections reported by Kitipornchai and Lee [1]. Generally, very good agreement has been achieved for most of the columns. Two modes of failure have been reported by Kitipornchai and Lee [1], and verified by the finite element model. The failure modes are the flexural buckling and flexural-torsional buckling.

Figure 3 shows the ultimate load against the axial shortening behavior of column T2 that has a length of 785 mm. The curve has been predicted by the finite element model and compared with the test results. The experimental ultimate load was 320 kN compared with 319.8 kN predicted by the finite element analysis. The failure mode of the test specimen T2 was reported as a flexural-torsional buckling. The same failure mode has been confirmed numerically by the model as shown in Fig. 4.

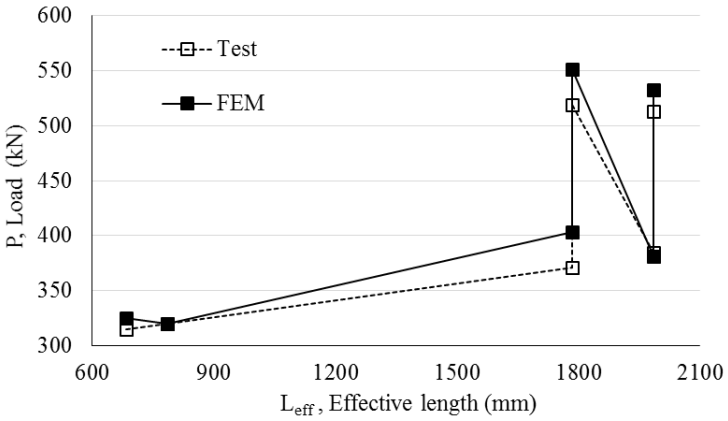

Figure 2. Comparison of experimental results with FEM results.

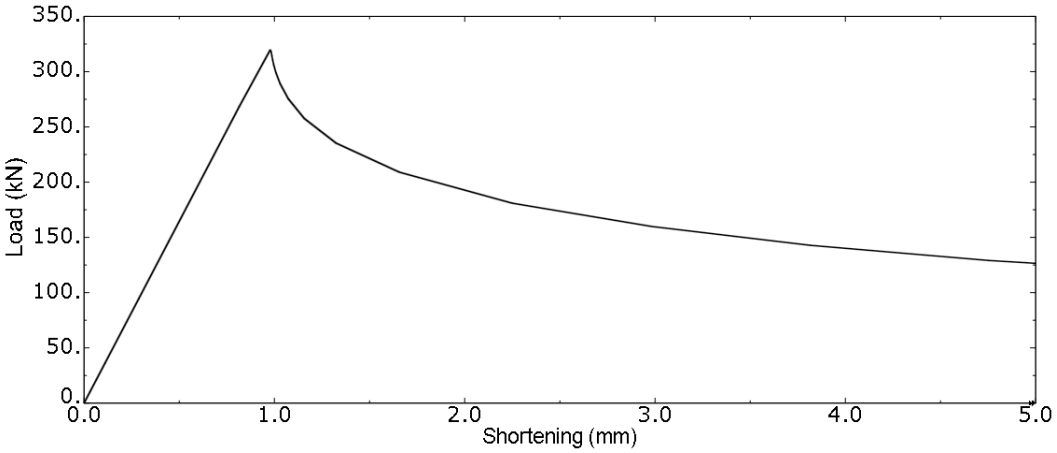

Figure 3. Load-axial shortening curve for T2.

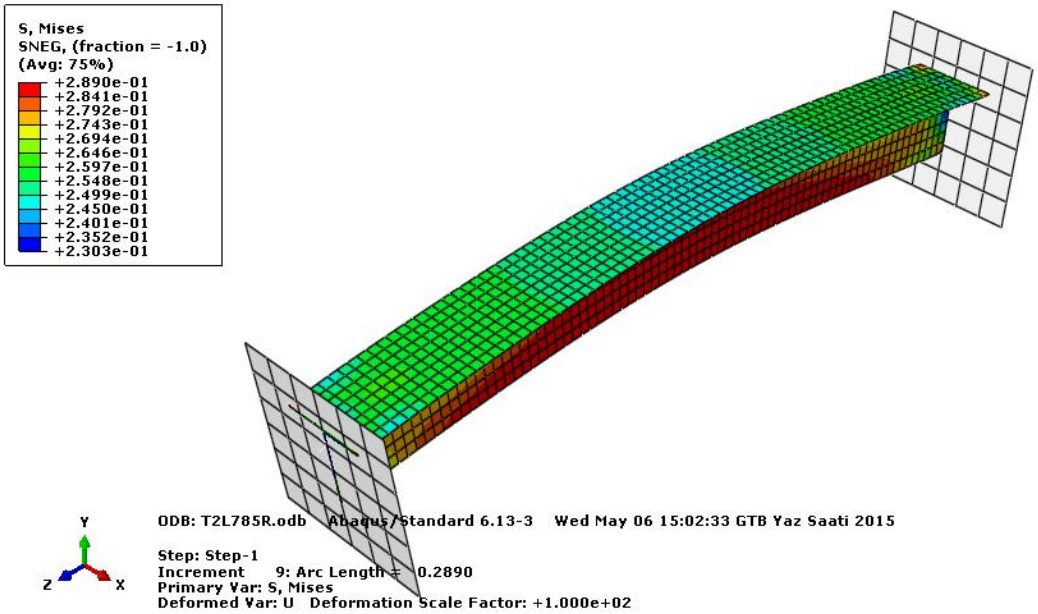

Figure 4. Failure mode of column T2.

4.2. Design Rules

In the current Turkish Standard, TS 648, the expressions governing the working stress design of a column member subjected to eccentric compression load or concentric compression load and biaxial bending moments are given as follows:

$$\frac{\sigma_{eb}}{\sigma_{bem}} + \frac{C_{mx}\sigma_{bx}}{\left(1-\frac{\sigma_{eb}}{\sigma_{ex}'}\right)\sigma_{Bx}} + \frac{C_{my}\sigma_{by}}{\left(1-\frac{\sigma_{eb}}{\sigma_{ey}'}\right)\sigma_{By}} \le 1.0 \quad (1)$$

$$\frac{\sigma_{eb}}{0.6\sigma_a} + \frac{\sigma_{bx}}{\sigma_{Bx}} + \frac{\sigma_{by}}{\sigma_{By}} \le 1.0 \quad (2)$$

where

ζ_{eb} : computed axial stress,

ζ_{bem} : axial compressive stress that would be permitted if axial load alone existed,

ζ_{bx}, ζ_{by} : computed compressive bending stresses at the point under consideration,

ζ_{Bx}, ζ_{By} : compressive bending stress that would be permitted if bending moment alone existed. The stresses are determined considering all failure modes including plastic yielding, lateral torsional buckling, and local buckling.

ζ_{ex}', ζ_{ey}' : factor of safety times the Euler buckling stresses in the plane of bending,

C_m : reduction factor used to modify the amplification factor $1/[1 - \zeta_{eb} / \zeta_e']$.

4.3. Parametric Study and Discussions

It is shown that the FE model closely predicted the behavior of plain T-section columns compared with the test results. Hence parametric studies were carried out to study the effects of load eccentricity on the strength and behavior of T-section columns. A total of 6 plain T-section columns was performed in the parametric study. Three series of columns T1-T2, T3-T4 and T5-T6 were studied. All T-sections had same geometric properties as the test specimens. The load eccentricity with respect to the major principal axis, e_x and the load eccentricity with respect to the minor principal axis, e_y were selected as (18.9, -13.3), (33.4, -16.8) and (36.9, -20.5) for series T1-T2, T3-T4 and T5-T6, respectively. T1-T2 series of columns consists of two column lengths of 685, and 785 mm, whereas T3-T4 and T5-T6 series of columns consists of two column lengths of 1785, and 1985 mm. The maximum initial overall geometric imperfection magnitude was taken as L/ 1500, where L=column length. The residual stresses were not considered since its effect on the column capacity and load-shortening behavior is negligible. The measured stress strain curves of series T1-T2, T3-T4 and T5-T6 were used in all parametric studies. A summary of the parametric study results is presented in Table 2. Slenderness and the ultimate loads (P_{fem-e}) of the T-sections are given in Table 2.

The results of the parametric study are compared with the design strengths obtained using the Turkish Standard, TS 648 (1980). It can be seen that the TS 648 design strengths ($P_{TS648-e}$) are generally quite conservative for T-section columns as shown in Table 2.

Table 2. Parametric study results of eccentrically loaded T-sections.

Specimen	L (mm)	λ	e_x (mm)	e_y (mm)	P_{test} (kN)	P_{fem-e} (kN)	$P_{TS648-e}$ (kN)	P_{fem-e}/P_{TS648e}
T1	685	39	18,9	-13,3	315	132,0	52,7	2,50
T2	785	45	18,9	-13,3	320	126,1	52,5	2,40
T3	1785	64	33,4	-16,8	371	162,5	69,9	2,32
T4	1985	71	33,4	-16,8	385	154,4	66,7	2,31
T5	1785	51	36,9	-20,5	519	230,7	98,9	2,33
T6	1985	57	36,9	-20,5	513	220,5	95,2	2,32

5. CONCLUSIONS

This paper provides an efficient nonlinear finite element model for understanding the behavior of eccentrically loaded single T-sections. Theoretical buckling and the experimental failure loads of pin ended, concentrically loaded T-sections were predicted by eigenvalue and load-deformation analyses of various models developed in ABAQUS 6.13. The T-sections were modeled by shell elements considering geometrically and materially nonlinear behavior. Initial imperfections, end support conditions, geometry and material property variation of the T-sections were included differently in each model. The load-

carrying capacity of eccentrically loaded single T-sections are investigated by performing an extensive parametric study obtaining the most realistic estimations. The results of the parametric study are compared with the design strengths obtained using the Turkish Standard, TS 648. It is seen that the TS 648 design strengths are quite conservative for T-section columns.

ACKNOWLEDGMENT

The work described in this paper was supported by the Research Foundation at Gümüşhane University. The writers would like to gratefully acknowledge this support. (Project No. 13.F5110.02.06)

REFERENCES

[51]. Kitipornchai, S., & Lee, H. W. (1986). Inelastic experiments on angle and tee struts. *Journal of Constructional Steel Research*, *6*(3), 219-236.
[52]. Kitipomchai, S., Al-Bermani, F. G., & Chan, S. L. (1990). Elasto-plastic finite element models for angle steel frames. *Journal of Structural Engineering*, *116*(10), 2567-2581.
[53]. Dinis, P. B., Camotim, D., & Silvestre, N. (2010). On the local and global buckling behaviour of angle, T-section and cruciform thin-walled members.*Thin-Walled Structures*, *48*(10), 786-797.
[54]. Turkish Standard (1982). *Building code for steel structures*, TS 648, Turkish Standards Institution, Ankara, Turkey.
[55]. ABAQUS Standard User‘s Manual. (2013). Hibbit. Karlsson and Sorensen. Inc. Vols. 1. 2 and 3. Version 6.13.
[56]. Ellobody, E., & Young, B. (2005). Behavior of cold-formed steel plain angle columns. *Journal of structural engineering*, *131*(3), 457-466.

Nonlinear Buckling Analysis of Cold-Formed Channel Sections

Mustafa Durmaz[11], AyÇeDaloğlu [12]

Abstract

The main objective of this paper is to provide an efficient and accurate finite element model to understand the behavior of cold-formed steel channel columns. The effects of initial local and overall geometric imperfections have been taken into consideration in the analysis. Failure loads and buckling modes as well as load-shortening curves of plain channel columns were investigated in this study. The nonlinear finite element model was verified against experimental results. The finite element analysis was performed on plain channels compressed between pinned ends over different column lengths, and column curves were obtained. An extensive parametric study was carried out using the finite element model to study the load eccentricity on the strength and behavior of channel columns. The column strengths predicted from the finite element model were compared with the design strengths calculated using the European Code, EN 1993-1-3 Eurocode 3: Design of steel structures - Part 1-3: General rules - Supplementary rules for cold-formed members and sheeting, for cold-formed steel structures.

Keywords: Cold-Formed Steel Channels, Buckling, Nonlinear Finite Element Analysis, EN 1993-1-3

23. INTRODUCTION

Finite element analysis (FEA) of cold-formed structures plays an increasingly important role in engineering practice, as it is relatively inexpensive and time efficient compared with physical experiments, especially when a parametric study of cross-section geometries is involved. Furthermore, it is difficult to investigate the effects of geometric imperfections and residual stresses of structural members experimentally. Therefore, FEA is more economical than physical experiments, provided that the finite element model (FEM) is accurate. Hence, it is necessary to verify the FEM with experimental results. In general, FEA is a powerful tool in predicting the ultimate loads and complex failure modes of cold-formed structural members. In addition, local and overall geometric imperfections, residual stresses and material non-linearity can be included in the FEM.

The purpose of the paper is to develop an accurate FEM to investigate the strengths of pin-ended cold-formed plain channel columns. The finite element analysis program ABAQUS 6.13 [1] was used for the numerical investigation. The FEM was verified against the cold-formed channel column tests conducted by Young and Rasmussen [2]. The FEM included geometric and material non-linearities.

24. EXPERIMENTAL TEST

The test program described in Young and Rasmussen [2] provided experimental ultimate loads and failure modes for cold-formed plain channel columns compressed between pinned ends. The test specimens were brake-pressed from high strength zinc-coated grade G450 structural steel sheets having nominal yield stress of 450 MPa and specified according to the Australian Standard AS 1397 [3]. The test program comprised two series of plain channels. The channel sections had a nominal thickness of 1.5 mm and a nominal width of the web of 96 mm. The nominal flange width was either 36 or 48 mm and was the only variable in the cross-section geometry. Accordingly, the two test series were labeled P36 and P48 where ―P" refers to ―plain" channels. The average values of measured cross-section dimensions of the pin-ended test specimens are shown in Table 1 using the nomenclature defined in Figure 1. The specimens were tested at various column lengths ranging from 280 to 1565 mm. The measured cross-section dimensions of each specimen are detailed in Young and Rasmussen [2].

Table 1. Average measured specimen dimensions and material properties

Test series	Specimen dimensions				Material properties			
	B_f (mm)	B_w (mm)	t (mm)	r_i (mm)	E (GPa)	$\sigma_{0.2}$ (MPa)	σ_u (MPa)	ε_u (MPa)
P36	36.8	96.9	1.51	0.85	210	550	570	10
P48	49.6	95.4	1.52	0.85	210	510	540	11

[11] *Corresponding author: Gümüşhane University, Faculty of Engineering and Natural Sciences, Department of Civil Engineering, 29100, Gümüşhane, Turkey.* mustafadurmaz@gumushane.edu.tr

[12] *Karadeniz Technical University, Faculty of Engineering, Department of Civil Engineering, 61080, Trabzon, Turkey.* aysed@ktu.edu.tr

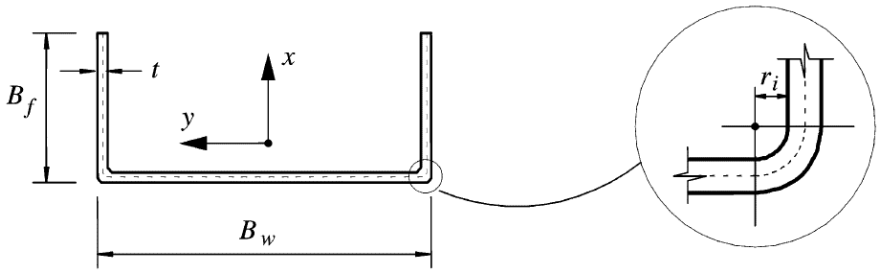

Figure 1. Definition of symbols

The material properties determined from coupon tests are also summarized in Table 1. The table contains the measured static 0.2% tensile proof stress ($\zeta_{0.2}$) and the static ultimate tensile strength (ζ_u) as well as the Young's modulus (E) and the elongation after fracture (ε_u) based on a gauge length of 50 mm. The coupons were taken from the center of the web plate in the longitudinal direction of the finished specimens. The coupon dimensions conformed to the Australian Standard AS1391 [4] for the tensile testing of metals using 12.5 mm wide coupons of gauge length 50 mm. The coupons were tested in an Instron TT-KM 250 kN capacity displacement controlled testing machine using friction grips to apply loading at a constant speed of 1 mm/min. The static load was obtained by pausing the applied straining for one minute near the 0.2% proof stress and the ultimate tensile strength. This allowed the stress relaxation associated with plastic straining to take place. The stress–strain curves obtained from the coupon tests are detailed in Young and Rasmussen [2].

Residual stress measurements were conducted on a companion series of tests of lipped channel specimens by Young and Rasmussen [2, 5]. The plain and lipped channel specimens were cut from the same batch of structural steel sheets and break pressed from the same machine. The membrane and the flexural residual stresses were found to be less than 3% and 7% of the measured 0.2% tensile proof stress, respectively. Hence, the residual stresses were deemed negligible compared with the 0.2% tensile proof stress. Local and overall geometric imperfections were measured prior to testing for the tested columns. The measured maximum local imperfections were found to be of the order of the plate thickness at the tip of the flanges for the two test series. For the pin-ended specimens, the maximum overall minor axis flexural imperfections at mid-length were 1/2200 and 1/1500 of the specimen length for Series P36 and P48, respectively. The measured local and overall geometric imperfection profiles are detailed in Young and Rasmussen [2, 6].

A 250 kN servo-controlled hydraulic actuator was used to apply compressive axial force to the specimen. The tests were controlled by incrementing the shortening of the specimen. This allowed the tests to be continued into the post-ultimate range. Readings of the applied load were taken approximately 1 min after applying an increment of compression, hence allowing the stress relaxation associated with plastic straining to take place. Consequently, the loads recorded were considered to be static loads. The pin-ended bearings were designed to allow rotations about the minor axis while restraining major axis rotations as well as twist rotations and warping. Details of the test rig are given in Young and Rasmussen [7]. The experimental ultimate loads (P_{test}) of the test specimens are shown in Table 2. The test specimens were labeled such that the test series, type of boundary conditions and specimen length could be identified from the label. For example, the label "P36P0815" defines the specimen belongs to the test Series P36, the fourth letter "P" indicates that the specimen is pin-ended, and the last four digits are the specimen length of 865 mm.

Table 2. Geometric properties and failure loads of U-section members tested by Young and Rasmussen (1998).

Specimen	B_f (mm)	B_w (mm)	t (mm)	r_i (mm)	L (mm)	A (mm^2)	P_{test} (kN)
P36P0280	36,9	96,6	1,51	0,85	280	247	55,2
P36P0315	37,0	96,8	1,50	0,85	315	245	52,1
P36P0815	36,8	97,5	1,51	0,85	815	249	40,9
P36P1315	37,0	96,6	1,50	0,85	1315	245	27,0
P48P0300	49,6	94,8	1,51	1,46	300	279	45,2
P48P0565	49,8	94,5	1,53	1,48	565	283	38,6
P48P1065	50,0	94,2	1,52	1,48	1065	282	33,9
P48P1565	49,4	95,1	1,52	1,47	1565	281	31,2

3. FINITE ELEMENT MODELING

3.1. General

In this study, the finite element program, ABAQUS 6.13 [1] was used in the analysis of cold-formed plain channel columns tested by Young and Rasmussen [2]. The model used the nominal sizes, initial local and overall geometric imperfections and material properties. Finite element analysis for buckling requires two types of analyses. The first is known as eigenvalue analysis that estimates the buckling modes and loads. Such an analysis is a linear elastic analysis performed using the (*BUCKLE) procedure available in the ABAQUS library with the live load applied within the step. The buckling analysis provides the factor by which the live load must be multiplied to reach the buckling load. For practical purposes, only the lowest buckling mode predicted from the eigenvalue analysis is used. The second is called load-displacement nonlinear analysis and follows the eigenvalue prediction. It is necessary to consider whether the postbuckling response is stable or unstable.

3.2. Finite Element Type and Mesh

It is mentioned in the ABAQUS manual that the four-noded doubly curved shell element with reduced integration S4R is suitable for complex buckling behavior [1, 8, 9]. The S4R element has six degrees of freedom per node and provides accurate solutions to most applications. The element also accounts for finite strain and is suitable for large strain analysis. Since buckling of plain angle columns is very sensitive to large strains, the S4R element was used in this study to ensure the accuracy of the results. In order to choose the finite element mesh that provides accurate results with minimum computational time, convergence studies were conducted. It is found that a 10 mm x 10 mm (length by width) ratio provides adequate accuracy in modeling the channel columns.

3.3. Boundary Conditions and Load Application

Following the experimental tests, the ends of the columns were free to rotate and fixed to translate in any direction except for the displacement at the loaded end in the direction of the applied load. The nodes other than the two ends were free to translate and rotate in any direction. The load was applied in increments using the modified RIKS method available in the ABAQUS library. The RIKS method is generally used to predict unstable and nonlinear collapse of a structure such as postbuckling analysis. It uses the load magnitude as an additional unknown and solves simultaneously for loads and displacements. The load was applied as static uniform loads at each node of the loaded end which is identical to the experimental investigation. The nonlinear geometry parameter (*NLGEOM) was included to deal with the large displacement analysis.

3.4. Material Modeling

The material behavior provided by ABAQUS allows for a multilinear stress-strain curve to be used. The first part of the multilinear curve represents the elastic part up to the proportional limit stress with measured Young's modulus and Poisson's ratio equal to 0.3. Since the analysis of postbuckling involves large in-elastic strains, the nominal (engineering) static stress-strain curve was converted to a true stress and logarithmic plastic strain curve. The true stress (ζ_{true}) and plastic true strain (ε^{pl}_{true}) were calculated using Equations 1. and 2.

$$\sigma_{true} = \sigma(1+\varepsilon) \quad (1)$$

$$\varepsilon^{pl}_{true} = \ln(1+\varepsilon) - \sigma_{true}/E \quad (2)$$

where E = Young's modulus, and ζ and ε = measured nominal (engineering) stress and strain based on the original cross-section area of the coupon specimens as detailed in Young and Rasmussen [2]. The engineering stresses and strains were obtained from tensile coupon tests. The coupon specimens were loaded at a constant speed of 1 mm/min.

Figure 2 shows the measured engineering and true stress–strain curves for the test Series P36. The incremental plasticity model required the portion of the true stress–strain curve from the point corresponding to the last value of the linear range of the engineering stress–stain curve to the ultimate point of the true stress–strain curve, as shown in Figure 2. The Poisson's ratio was taken as 0.3 and the measured Young's modulus as shown in Table 1 was used in the FEM.

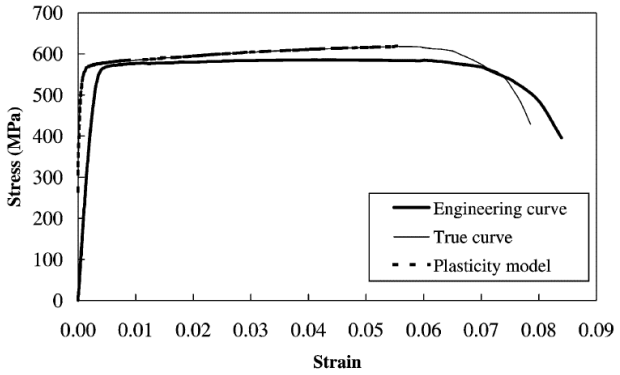

Figure 2. Modeling of material plasticity for test Series P36

3.5. Modeling of Initial Local and Overall Geometric Imperfections

The geometric imperfections were included in the FEM by using a linear perturbation analysis. The main purpose of the perturbation analysis was to establish probable buckling modes (eigenmode) of the column. The eigenmode was then scaled by a factor (scale factor) to obtain a perturbed mesh of the column for the non-linear analysis. Eigenmode 1 was used in the FEM, in which local or overall buckling mode was predicted from the analysis.

4. RESULTS AND DISCUSSIONS

4.1. Comparison of experimental results with finite element analysis results

In the verification of the finite element model, a total of 8 cold-formed steel plain channel columns were analyzed. The incremental plasticity models obtained from the true stress–strain curves were used in the FEM for the corresponding test series. A scale factor of 25% of the plate thickness was used in modeling the geometric imperfections of the columns. A comparison between the experimental results and the results of the finite element model is carried out. The main objective of this comparison is to verify and check the accuracy of the finite element model. The ultimate loads (P_{fem}) predicted by the

FEA are compared with the experimental ultimate loads (P_{test}) as shown in Table 3 for Series P36 and P48, respectively. The mean values of the P_{test}/P_{fem} ratio are 1,014 and 1,046 with the corresponding coefficients of variation (COV) of 0,0016 and 0,0096 for Series P36 and P48, respectively. Generally, good agreement has been achieved for most of the columns. Three modes of failure were reported by Young and Rasmussen [7] and verified by the finite element model. The failure modes are the local buckling, flexural buckling and flexural-torsional buckling.

Table 3. Comparison between Test and FE Results

Specimen	B_f (mm)	B_w (mm)	t (mm)	r_i (mm)	L (mm)	A (mm^2)	P_{test} (kN)	P_{fem} (kN)	P_{test}/P_{fem}
P36P0280	36,9	96,6	1,51	0,85	280	247	55,2	54,1	1,02
P36P0315	37,0	96,8	1,50	0,85	315	245	52,1	53,2	0,98
P36P0815	36,8	97,5	1,51	0,85	815	249	40,9	38,3	1,07
P36P1315	37,0	96,6	1,50	0,85	1315	245	27,0	27,3	0,99
Mean									1,014
COV									0,0016
P48P0300	49,6	94,8	1,51	1,46	300	279	45,2	47,0	0,96
P48P0565	49,8	94,5	1,53	1,48	565	283	38,6	39,5	0,98
P48P1065	50,0	94,2	1,52	1,48	1065	282	33,9	31,6	1,07
P48P1565	49,4	95,1	1,52	1,47	1565	281	31,2	26,6	1,17
Mean									1,046
COV									0,0096

Figure 3 plotted the relationship between the ultimate load and the column effective length L_{eff}=L for channels reported by Young and Rasmussen [2] where L actual column length. The column curves show the experimental ultimate loads together with that obtained by the finite element method. It can be seen that good agreement has been achieved between both results for most of the columns.

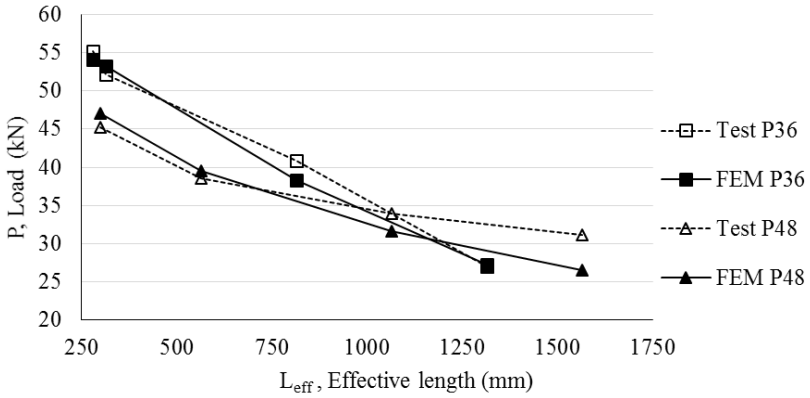

Figure 3. Comparison of experimental results with FEM results.

Figure 4 shows the ultimate load against the axial shortening behavior of column P48P0565 that has a length of 565 mm. The curve has been predicted by the finite element model and compared with the test results. The experimental ultimate load was 38,6 kN compared with 39,5 kN predicted by the finite element analysis. The failure mode of the test specimen P48P0565 was reported as a flexural buckling. The same failure mode has been confirmed numerically by the model as shown in Figure 5.

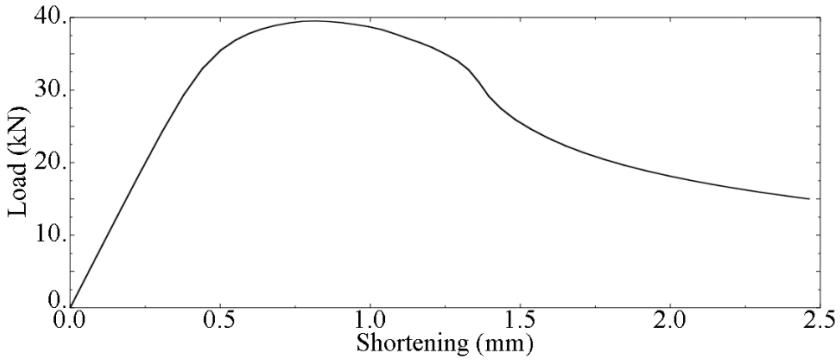

Figure 4. Load-axial shortening curve for P48P0565.

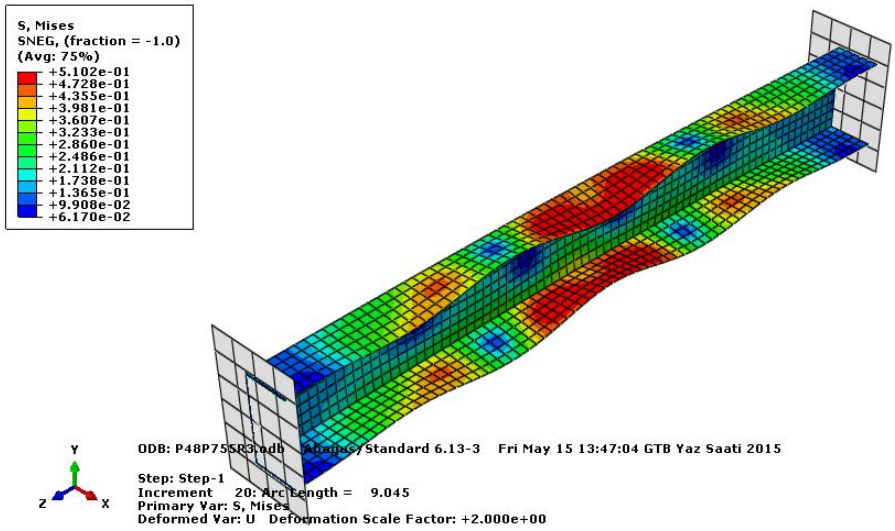

Figure 5. Failure mode of column P48P0565.

4.2. Design Rules

EN1993-1-3 [10] represents the unified European Code for cold-formed steel design, and contains specific provisions for structural applications using cold-formed steel products made from coated or uncoated thin gauge hot or cold-rolled sheet and strip. In EN1993-1-3, cross sections subject to combined axial compression N_{Ed} and bending moments $M_{y,Ed}$ and $M_{z,Ed}$ should satisfy the criterion:

$$\frac{N_{Ed}}{N_{c,Rd}} + \frac{M_{y,Ed} + \Delta M_{y,Ed}}{M_{cy,Rd,com}} + \frac{M_{z,Ed} + \Delta M_{z,Ed}}{M_{cz,Rd,com}} \leq 1.0 \qquad (3)$$

in which

N_{Ed} : design value of the compression force,

$N_{c,Rd}$: design compression resistance of a cross section,

$M_{y,Ed}$: applied bending moment about the major axis,

$M_{z,Ed}$: applied bending moment about the minor axis,

$M_{cy,Rd,com}$: moment resistances for the maximum compressive stress in a cross section that is subject only to moment about the y-y axis

$M_{cz,Rd,com}$: moment resistances for the maximum compressive stress in a cross section that is subject only to moment about the z-z axis

The additional moments $\Delta M_{y,Ed}$ and $\Delta M_{z,Ed}$ due to shifts of the effective centroidal axes should be taken as:

$$\Delta M_{y,Ed} = N_{Ed} \cdot e_{Ny} \quad (4)$$

$$\Delta M_{z,Ed} = N_{Ed} \cdot e_{Nz} \quad (5)$$

in which e_{Ny} and e_{Nz} are the shifts of y-y and z-z centroidal axis of the effective cross section relative to the gross cross section.

If $M_{cy,Rd,ten} \leq M_{cy,Rd,com}$ or $M_{cz,Rd,ten} \leq M_{cz,Rd,com}$ the following criterion should also be satisfied:

$$\frac{M_{y,Ed} + \Delta M_{y,Ed}}{M_{cy,Rd,ten}} + \frac{M_{z,Ed} + \Delta M_{z,Ed}}{M_{cz,Rd,ten}} - \frac{N_{Ed}}{N_{c,Rd}} \leq 1.0 \quad (6)$$

in which

$M_{cy,Rd,ten}$: design moment resistance of a cross section for maximum tensile stress if subject only to moment about the y-y axis,

$M_{cz,Rd,ten}$: design moment resistance of a cross section for maximum tensile stress if subject only to moment about the z-z axis.

4.3. Parametric Study and Discussions

It is shown that the FE model closely predicted the behavior of plain U-section columns compared with the test results. Hence parametric studies were carried out to study the effects of load eccentricity on the strength and behavior of U-section columns. A total of 8 plain U-section columns was performed in the parametric study. Two series of columns P36 and P48 were studied. All U-sections had same geometric properties as the test specimens. The load eccentricity with respect to the major principal axis, e_x were selected as 10.27 and 11.97 for series P36 and P48, respectively. P36 series of columns consists of four column lengths of 280, 315, 815, and 1315 mm, whereas P48 series of columns consists of four column lengths of 300, 565, 1065, and 1565 mm. A scale factor of 25% of the plate thickness was used in modeling the geometric imperfections of the columns. The residual stresses were not considered since its effect on the column capacity and load-shortening behavior is negligible. The measured stress strain curves of series P36 and P48 were used in all parametric studies. A summary of the parametric study results is presented in Table 4. Slenderness (λ) and the ultimate loads (P_{fem-e}) of the U-sections are given in Table 4.

The results of the parametric study are compared with the design strengths obtained using the European Code, EN1993-1-3. It can be seen that the EN1993-1-3 design strengths ($P_{EN-1993-1-3}$) are generally quite conservative for U-section columns as shown in Table 4.

Table 4. Parametric study results of eccentrically loaded U-sections.

Specimen	L (mm)	λ	e_x (mm)	P_{fem-e} (kN)	$P_{EN1993-1-3}$ (kN)	P_{fem-e}/ $P_{EN1993-1-3}$
P36P0280	280	42	10,27	25,50	12,1	2,11
P36P0315	315	45	10,27	25,20	12,1	2,08
P36P0815	815	90	10,27	18,60	12,1	1,54
P36P1315	1315	134	10,27	18,70	12,1	1,55
P48P0300	300	31	11,97	24,90	13,2	1,89
P48P0565	565	48	11,97	26,70	13,2	2,02
P48P1065	1065	80	11,97	16,80	13,2	1,27
P48P1565	1565	111	11,97	13,40	13,2	1,02

5. CONCLUSIONS

This paper provides an efficient nonlinear finite element model for understanding the behavior of eccentrically loaded single U-sections. Theoretical buckling and the experimental failure loads of pin ended, concentrically loaded U-sections were predicted by eigenvalue and load-deformation analyses of various models developed in ABAQUS 6.13. The U-sections were modeled by shell elements considering geometrically and materially nonlinear behavior. Initial imperfections, end support conditions, geometry and material property variation of the U-sections were included differently in each model. The load-carrying capacity of eccentrically loaded single U-sections are investigated by performing an extensive parametric study obtaining the most realistic estimations. The results of the parametric study are compared with the design strengths obtained using the European Code, EN1993-1-3. It is seen that the EN1993-1-3 design strengths are quite conservative for U-section columns.

ACKNOWLEDGMENT

The work described in this paper was supported by the Research Foundation at Gümüşhane University. The writers would like to gratefully acknowledge this support. (Project No. 13.F5110.02.06)

REFERENCES

[57]. ABAQUS Standard User‘s Manual. (2013). Hibbit. Karlsson and Sorensen. Inc.. Vols. 1. 2 and 3. Version 6.13.
[58]. Young, B., & Rasmussen, K. J. (1998). Tests of fixed-ended plain channel columns. *Journal of Structural Engineering*, 124(2), 131-139.
[59]. Australian Standard. (1993). *Steel Sheet and Strip—Hot-dipped Zinc-coated or Aluminium/Zinc-coated*. AS 1397. Standards Association of Australia. Sydney. Australia.
[60]. Australian Standard. (1991). *Methods for Tensile Testing of Metals*. AS 1391. Standards Association of Australia. Sydney. Australia.
[61]. Young, B., & Rasmussen, K. J. R. (1995a). Compression Tests of Fixed-Ended and Pin Ended Cold-Formed Lipped Channels. Research Report-University of Sydney School of Civil and Mining Engineering R.
[62]. Young, B., & Rasmussen, K. J. R. (1995b). *Compression tests of fixed-ended and pin-ended cold-formed plain channels*. Research Report-University of Sydney School of Civil and Mining Engineering R.
[63]. Young, B., & Rasmussen, K. J. (1999). Behaviour of cold-formed singly symmetric columns. *Thin-walled structures*, 33(2), 83-102.
[64]. Nandula. R. (1998). *Finite Element Analysis of Eccentrically Loaded Angles*. M.S. Thesis. University of Windsor. Windsor. Ontario. Canada.
[65]. Young, B., & Yan, J. (2002). Finite element analysis and design of fixed-ended plain channel columns. *Finite elements in analysis and design*, *38*(6), 549-566.
[66]. CEN (2006). *Eurocode 3: Design of steel structures. Part 1-3: General Rules. Supplementary rules for cold-formed thin gauge members and sheeting*, EN 1993-1-3:2006. European Committee for Standardization, Brussels, Belgium.

Heat Transfer and Entropy Generation Analysis of Nanofluids Flow over Backward-Facing Step

Recep Ekiciler [13], Kamil Arslan[14]

Abstract

A numerical investigation of heat transfer and entropy generation in laminar forced convection of Al_2O_3/water, TiO_2/water and ZnO/water nanofluids flow over backward facing step are presented. This study is performed for understanding the effects of types of nanofluids on heat transfer and entropy generation. The Reynolds number was ranged from 75 to 225. Both of the step height and inlet height of the duct were 4.8 mm. As the downstream wall was subjected to constant and uniform heat flux of 2000 W/m^2, the other walls were insulated. The nanoparticles volume fractions were kept constant at 4.0%. The average Nusselt number and average Darcy friction factor were obtained for each nanofluids. Also, entropy generation due to the convective heat transfer and friction were presented for used nanofluids.

Keywords: Nanofluid, Backward facing step, Entropy generation, Convective heat transfer, Laminar flow, Second law analysis.

25. INTRODUCTION

Many studies in engineering area involve fluid flow and heat transfer inside a duct. To analyze the energy transfer in a thermal system, the first law of thermodynamics is always used. However, the investigation of exergy or irreversibility of a thermal system requires the second law analysis, relating to an entropy generation in fluid flow and heat transfer processes. The total entropy generation consists of the entropy generation due to viscous friction between the wall and the fluid, and that due to heat transfer across finite temperature differences between the wall and the fluid [1].

The entropy generation due to flow and heat transfer has been studied in the literature. Jarungthammachote [1] studied the entropy generation of laminar flow in hexagonal duct. Water and engine oil was used as working fluid. The effects of aspect ratio of the hexagonal duct were investigated on entropy generation. He obtained that fluid properties significantly affect the entropy generation. Total entropy generation of engine oil is higher than water. Also, it was found that entropy generation increases with increasing the aspect ratio but when values of aspect ratios are higher than 2.642 and 2.627. Razavi et al. [2] numerically investigated the flow and heat transfer characteristics and entropy generation in a 3D rotating curved duct. The effects of Dean number, non-dimensional wall heat flux, and force ratio on entropy generation due to heat transfer and fluid friction. They obtained that entropy generation due to fluid friction increases with increasing force ratio and Dean number. But entropy generation due to heat transfer decreases with increasing the force ratio and Dean number.

There are a few studies about entropy generation in ducts having backward facing step in the literature. Abu-Nada [3] studied entropy generation due to heat transfer and fluid flow over backward facing step for various expansion ratios. It was found that as the Reynolds number increases, the total entropy generation increases. Total entropy generation decreases for lower Reynolds number and higher expansion ratios. Abu-Nada [4] numerically investigated the second law analysis of laminar flow over backward facing step. The aim of the study was understood the destruction of the useful energy in separated flow. Local entropy generation distribution was presented. The results show that entropy generation increases with increasing the Reynolds number and Brinkman number. In addition, the local entropy generation number has a maximum value at the section where the flow separated and reduces to the downward of the step.

The entropy generation due to flow and heat transfer of some nanofluids under different conditions has been studied in the literature. Zhao et al. [5] numerically investigated the effects of Al_2O_3/water nanofluid on heat and entropy generation in three dimensional flat tube. They applied constant heat flux to the flat tube. It was investigated that the effects of nanoparticle volume fraction and size, temperature, and Reynolds number on heat transfer and entropy generation. It was found that increasing nanoparticle volume fraction increases the heat transfer. In addition, they obtained that nanoparticle volume fraction decreases the total entropy generation in the flat tube. Mah et al. [6] investigated the effects of the viscous dissipation on entropy generation using Al_2O_3/water nanofluid in circular microchannels. It was obtained that the entropy generation significantly increases as the viscous dissipation effect is taken into account for fully developed forced convection of Al_2O_3-water nanofluid flow through circular microchannels. Purohit et al. [7] investigated the laminar forced convective heat transfer of ZrO_2-water and TiO_2-water nanofluid flow. They reported that the entropy generation slightly decreases with nanoparticle

[13] *Corresponding author: Karabuk University, Mechanical Engineering Department, 78050, Karabuk, Turkey.* recepekiciler@karabuk.edu.tr
[14] *Karabuk University, Mechanical Engineering Department, 78050, Karabuk, Turkey.* kamilarslan@karabuk.edu.tr

addition to base fluid under same Reynolds number. Cho et al. [8] studied a numerical simulation using Al_2O_3/water nanofluid in an inclined wavy-wall cavity under natural convection condition. The effects of cavity inclination angle, nanoparticle volume fraction, Rayleigh number was investigated on entropy generation in the simulations. The results show that distributions of flow streamlines and local entropy generation is effected by inclination angle of cavity. Also, they obtained that as increasing the nanoparticle volume fraction, total entropy generation decreases.

There is no study as reviewed literature about backward facing step using nanofluid on entropy generation and heat transfer. The present study deals with 2D laminar forced convective flow over a backward-facing step (BFS) in a horizontal rectangular cross-sectioned duct by using Al_2O_3/water, TiO_2/water and ZnO/water nanofluids. Results of interests such as Nusselt number, Darcy friction factor, Bejan number and entropy generation due to heat transfer and fluid friction distributions for laminar forced convection flow over a horizontal BFS are reported to illustrate the effect of types of nanofluids on these parameters.

26. MATHEMATICAL MODELING

26.1. Geometrical Configuration

A duct having backward facing step was modeled to analyze in this study. Both the step height (s) and inlet height (h_s) of the duct were 4.8 mm. Total length (H) of duct was 9.6 mm. As the downstream wall was subjected to constant and uniform heat flux, the other walls were insulated. The schematic diagram of the backward facing step is presented in Figure 1.

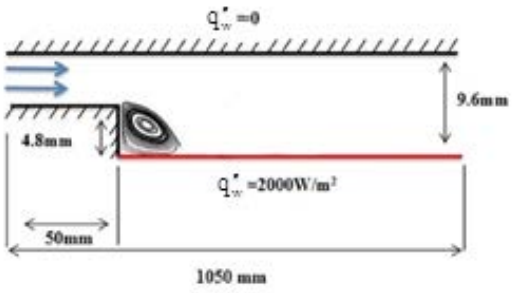

Figure 1. Schematic diagram of the backward facing step

26.2. Governing Equations and Boundary Conditions

In the mathematical modeling of single-phase steady-state incompressible laminar flow, the following governing equations are used.

Contunity: $$\frac{\partial u}{\partial x}+\frac{\partial v}{\partial y}=0 \quad (1)$$

x-momentum: $$\rho\left(u\frac{\partial u}{\partial x}+v\frac{\partial u}{\partial y}\right)=F_x-\frac{\partial p}{\partial x}+\mu\left(\frac{\partial^2 u}{\partial x^2}+\frac{\partial^2 u}{\partial y^2}\right) \quad (2)$$

y-momentum: $$\rho\left(u\frac{\partial v}{\partial x}+v\frac{\partial v}{\partial y}\right)=F_y-\frac{\partial p}{\partial y}+\mu\left(\frac{\partial^2 v}{\partial x^2}+\frac{\partial^2 v}{\partial y^2}\right) \quad (3)$$

Energy: $$\rho Cp\left(u\frac{\partial T}{\partial x}+v\frac{\partial T}{\partial y}\right)=k\left(\frac{\partial^2 T}{\partial x^2}+\frac{\partial^2 T}{\partial y^2}\right)+2\mu\left\{\left\{\left(\frac{\partial u}{\partial x}\right)^2+\left(\frac{\partial v}{\partial y}\right)^2\right\}+\mu\left\{\left(\frac{\partial u}{\partial y}+\frac{\partial v}{\partial x}\right)^2\right\}\right. \quad (4)$$

Entropy: $$\dot{S}'_{gen}=\frac{k}{T_b^2}\left[\left(\frac{\partial T}{\partial x}\right)^2+\left(\frac{\partial T}{\partial y}\right)^2\right]+\frac{\mu}{T_b^2}\left\{2\left[\left(\frac{\partial u}{\partial x}\right)^2+\left(\frac{\partial v}{\partial y}\right)^2\right]+\left(\frac{\partial u}{\partial y}+\frac{\partial v}{\partial x}\right)^2\right\} \quad (5)$$

In the governing equations, the buoyancy effect, viscous dissipation and radiation heat transfer are assumed to be negligible. Constant inlet velocity is applied and the inlet velocity can be calculated by specified Reynolds number as follows.

$$U_{inlet}=\frac{\mu Re}{\rho D_h} \quad (6)$$

where μ [Pa.s] is the viscosity, ρ [kg/m^3] is the density of the nanofluid. D_h is the hydraulic diameter and D_h=H.

Constant heat flux of 2000 W/m^2 is applied to the downstream wall of backward facing step.

26.3. Thermophysical Properties

To solve the governing equations, the thermophysical properties of nanofluid should be defined. The effective density and specific heat of nanofluids can be defined with following equations [9]

$$\rho_{eff} = \varphi\rho_s + (1-\varphi)\rho_f \tag{7}$$

$$(Cp)_{eff} = \frac{(1-\varphi)(\rho C_p)_f + \varphi(\rho C_p)_s}{(1-\varphi)\rho_f + \varphi\rho_s} \tag{8}$$

where φ is the nanoparticle volume fraction, C_P [J/kgK] is the specific heat. The subscripts *eff*, *s* and *f* denote effective, nanoparticle and base fluid, respectively.

The effective thermal conductivity of nanofluids can be calculated by the following equation is given by Vajjha and Das [10] as:

$$k_{eff} = k_{static} + k_{brownian} \tag{9}$$

The k_{static} is presented by Ghasemi and Aminossadati [11] as:

$$k_{static} = k_f \left[\frac{(k_s + 2k_f) - 2\varphi(k_f - k_s)}{(k_s + 2k_f) + \varphi(k_f - k_s)} \right]$$

Thermal conductivity resulting from Brownian motion is offered by Vajjha and Das [10] as:

$$k_{brownian} = 5x10^4 \beta\varphi\rho_f Cp_f \sqrt{\frac{KT}{\rho_s d_p}} f(T,\varphi) \tag{10}$$

where

$$f(T,\varphi) = (2.8217x10^{-2}\varphi + 3.917x10^{-3})\frac{T}{T_o} + (-3.0669x10^{-2}\varphi - 3.91123x10^{-3}) \tag{11}$$

where T is the fluid temperature, T_o is the reference temperature and K is the Boltzman constant.

Corcione [9] presented viscosity of nanofluid equation as:

$$\frac{\mu_{eff}}{\mu_f} = \frac{1}{1 - 34.87(d_p / d_f)^{-0.3}\varphi^{1.03}} \tag{12}$$

where

$$d_f = \left[\frac{6M}{N\pi\rho_{fo}} \right]^{1/3} \tag{13}$$

where μ_f and μ_{eff} are viscosity of base fluid and nanofluid, respectively. d_f is the base fluid equivalent diameter and d_p is diameter of nanoparticle. N is the Avogadro number, M is the base fluid's molecular weight, and ρ_{fo} is the mass density of the base fluid calculated at T=293 K. The nanoparticle diameters were taken as 25 nm, 50 nm and 80 nm for Al_2O_3, TiO_2 and ZnO, respectively.

The effective thermal expansion of nanofluid is presented by Corcione [9] as:

$$\beta_{eff} = \frac{(1-\varphi)(\rho\beta)_f + \varphi(\rho\beta)_s}{(1-\varphi)\rho_f + \varphi\rho_s} \tag{14}$$

Thermal expansion value of Al_2O_3, TiO_2 and ZnO can be calculated from $\beta_s = 8.4407(100\varphi)^{-1.07304}$, $\beta_s = 6.6E-4(100\varphi)^{0.121}$ and $\beta_s = 8.4407(100\varphi)^{-1.07304}$, respectively.

Average Nusselt number, Darcy friction factor and heat transfer coefficient are calculated as:

$$Nu = \frac{hD_h}{k} \tag{15}$$

$$f = \frac{\Delta P(D_h / L)}{\rho U^2_{inlet} / 2} \tag{16}$$

$$h = \rho U_{inlet} A_c C_p (T_{mo} - T_{mi}) / A_s (T_w - T_m) \tag{17}$$

where ΔP [Pa] is the pressure difference between inlet and outlet of the duct, L [m] is the total length of the duct, A_c [m^2] is the cross-sectional area of the duct, T_{mo}, T_{mi} and T_w [K] are mean temperatures of outlet, inlet and heated wall temperature of duct, respectively.

The entropy generation per unit length for internal flow can be written as follows [12]

$$\dot{S}'_{gen} = \dot{S}'_{gen,heat\ \ transfer} + \dot{S}'_{gen,fluid\ \ friction} \tag{18}$$

$$\dot{S}'_{gen} = \frac{q''^2 \pi D_h^2}{kT_b^2 Nu} + \frac{8\dot{m}^3 f}{\pi^2 \rho^2 T_b D_h^5} \tag{19}$$

The Bejan number is defined as the ratio of heat transfer irreversibility to total irreversibility due to heat transfer and fluid friction and can be written as follows,

$$Be = \frac{\dot{S}'_{gen,heat\ \ transfer}}{\dot{S}'_{gen,heat\ \ transfer} + \dot{S}'_{gen,fluid\ \ friction}} \tag{20}$$

The thermophysical properties for base fluid and nanoparticle are given in Table 1.

Table 1. Thermophysical properties for base fluid and nanoparticles [13, 14]

Material	$\rho(kg/m^3)$	$C_P(J/kgK)$	$k(W/mK)$	$\mu(Ns/m^2)$
Water	997	4179	0.613	0.000855
TiO_2	4174	692	8.4	-
Al_2O_3	3970	765	40	-
ZnO	5600	495.2	13	-

26.4. Numerical Method and Code Validation

Hexahedral mesh distribution was utilized in the modeling of backward facing step. Finite volume method was used to carry out the numerical computation. The governing equations were solved with appropriate boundary conditions. SIMPLE algorithm was implemented to resolve velocity and pressure coupling. To discretize the momentum and energy equation, Green Gauss Cell Based Method was applied. The convergence criterion of 10^{-6} was used in the iteration of governing equations. No convergence problems were observed during the calculations.

The mesh independence study was performed for the duct having backward facing step by refining the mesh number until the variation in both average Nusselt number and average Darcy friction factor were less than 0.08%. To obtain the optimum mesh number, a grid independence study was conducted using eight different mesh numbers changing from 3.4×10^2 to 5.7×10^5 for Re=225. Changing of average Nusselt number and average Darcy friction factor values with mesh number for pure water flow is given in Figure 2 as an illustration. It was observed that a further refinement of mesh number from 4.4×10^4 to 5.7×10^5, the changing of average Nusselt number and average Darcy friction factor is negligible. If Figure 2 is observed, optimum mesh number with minimum computational time and maximum accuracy approximately can be seen at 4.4×10^4.

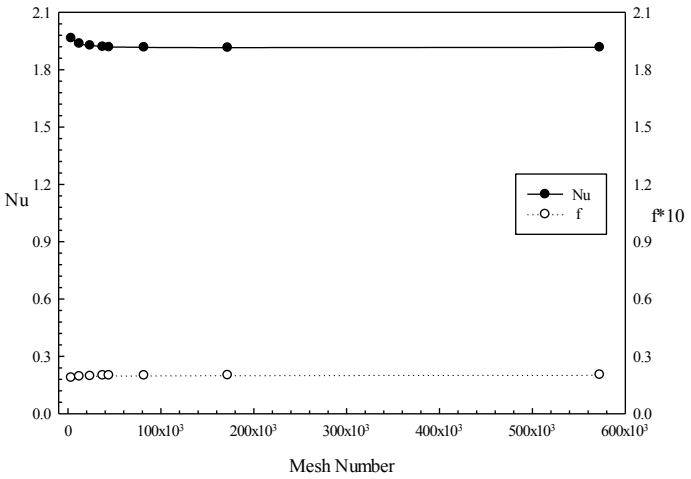

Figure 2. Mesh independency validation

To validate the code, the numerical results were compared with the data given by Togun et al. [15] and illustrated in Figure 3. As can be seen from Figure 3, the results obtained by present study show good agreement with the results obtained by Togun et al. [15].

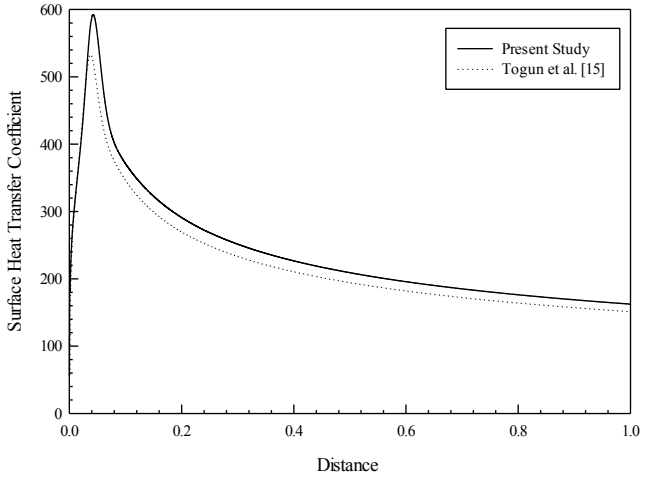

Figure 3. The comparison of the surface heat transfer coefficient values obtained by present study with that of Togun et al. [15] at Re=225

27. RESULTS

Laminar forced convection flow and heat transfer characteristics of three types of nanofluids (Al_2O_3/water, TiO_2/water and ZnO/water) over a two-dimensional horizontal backward facing step was numerically investigated. The effects of the nanoparticle volume fractions on the average Nusselt number and average Darcy friction factor are presented in Figure 4 and Figure 5, respectively. Figure 4 shows the average Nusselt number distributions for different Reynolds number and nanofluids. The average Nusselt number increases with increasing Reynolds number. Al_2O_3/water nanofluid has the highest Nusselt number compared with the other nanofluids. Also, pure water has the lowest Nusselt number. Figure 5 presents the average Darcy friction factor distributions for various Reynolds number and nanofluids at constant nanoparticles volume fractions of 4.0%. The average Darcy friction factor decreases with increasing the Reynolds number. Also, the average Darcy friction factor are not affected by the types of nanofluids.

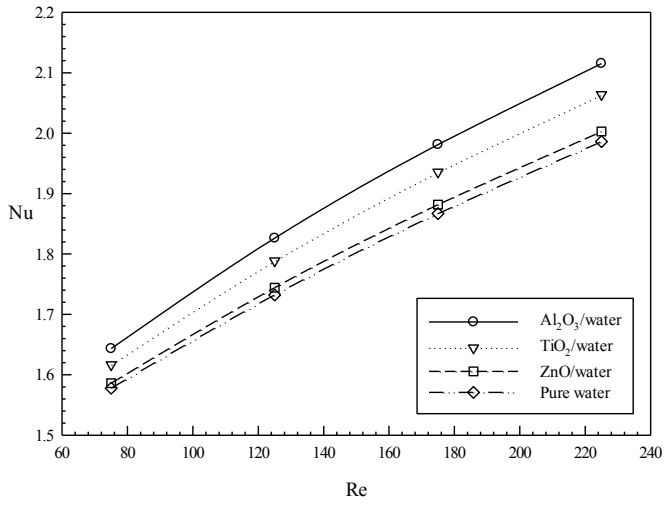

Figure 4. Changing of average Nusselt number with Reynolds number and nanofluid type

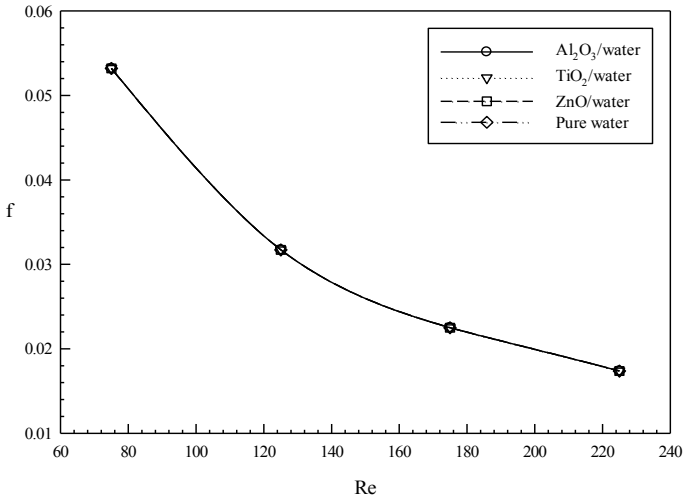

Figure 5. Changing of average Darcy friction factor with Reynolds number and nanofluid type

Figure 6 shows the entropy generation distributions due to heat transfer with varying Reynolds number for Al_2O_3/water, TiO_2/water, ZnO/water nanofluids at constant nanoparticles volume fractions of 4.0% and pure water. As can be seen from Figure 6, the entropy generation due to the heat transfer decreases with increasing the Reynolds number for all nanofluids. Al_2O_3/water nanofluid, which has the highest average Nusselt number, has the lowest entropy generation distributions at the Re=225 due to heat transfer. Pure water, which has the lowest average Nusselt number, has the highest entropy generation due to heat transfer for all Reynolds number.

Figure 7 shows the entropy generation distributions due to fluid friction with varying Reynolds number for Al_2O_3/water, TiO_2/water, ZnO/water nanofluids at constant nanoparticles volume fractions of 4.0% and pure water. Entropy generation due to fluid friction increases with increasing the Reynolds number. It can be seen from the figure that, entropy generation due to fluid friction effects increases especially at high Reynolds number. Al_2O_3/water nanofluid has the highest entropy generation due to fluid friction. Because of the higher velocities of Al_2O_3/water nanofluid than the other nanofluids, Al_2O_3/water nanofluid has lower bulk temperature. As can be seen Eq. 19, entropy generation due to fluid friction increases with decreasing the bulk temperature.

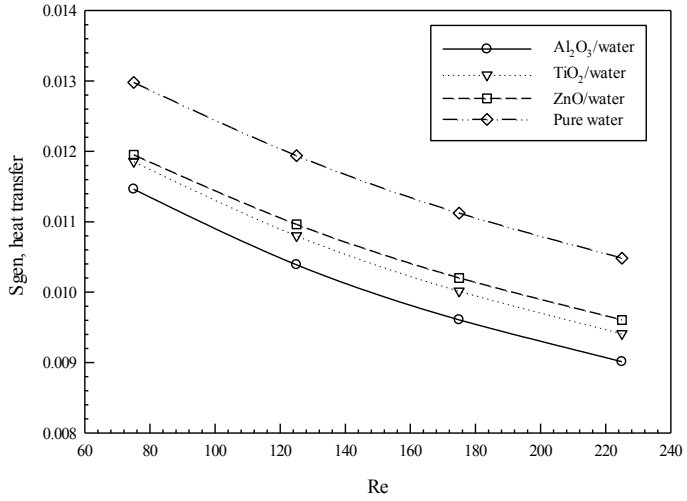

Figure 6. Entropy generation distributions due to heat transfer for different nanofluids

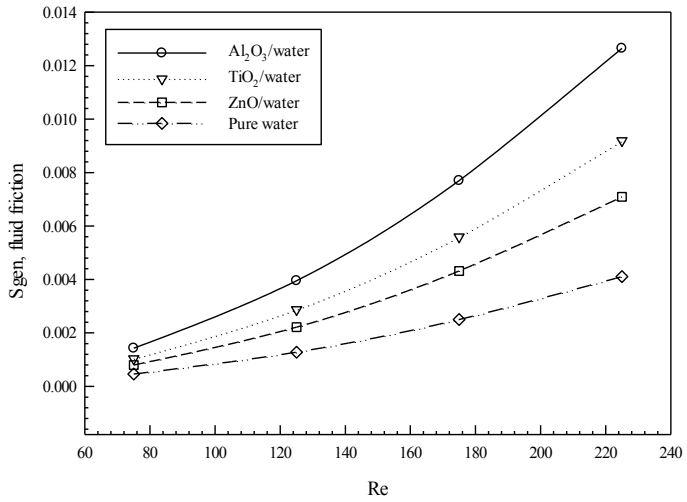

Figure 7. Entropy generation distributions due to fluid friction for different nanofluids

Figure 8 presents the total entropy generation distributions for different nanofluids. It can be obtained forom the figure that total entropy generation increases with increasing Reynolds number for all nanofluid types. Total entropy generation distributions have the same trend with entropy generation due to fluid friction which is dominant in comparison to entropy generation due to heat transfer. Al_2O_3/water nanofluid has the highest value of total entropy generation.

Figure 9 shows the Bejan number variations with Reynolds number. The Bejan number decreases with Reynolds number increases, due to the increase in entropy generation because of fluid friction.

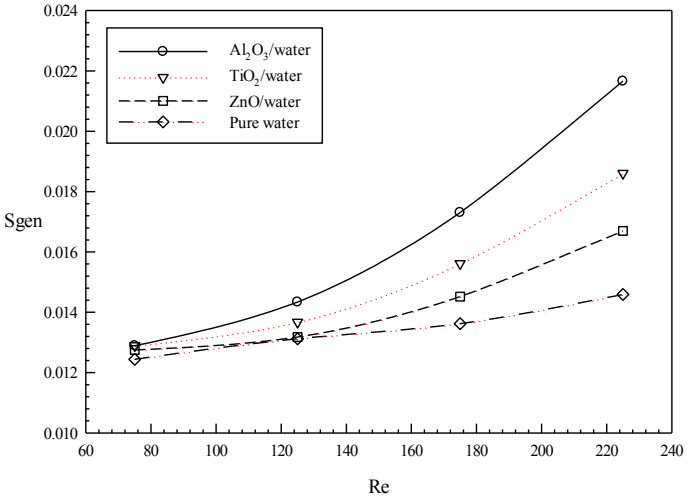

Figure 8. Total entropy generation distributions for different nanofluids

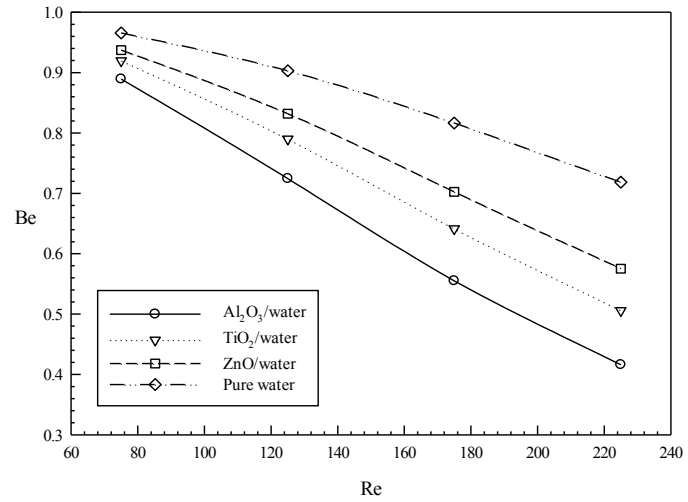

Figure 9. Bejan number distributions for different nanofluids

28. CONCLUSIONS

Numerical simulation of steady state laminar forced convection flow and heat transfer in a 2D duct having backward-facing step (BFS) was presented. Also, entropy generation was analyzed for Al_2O_3/water, TiO_2/water, ZnO/water nanofluids. Effect of Reynolds number and types of nanofluids on convective heat transfer and entropy generation were investigated in detail. It was noticed from the numerical simulation results that Al_2O_3/water nanofluid enhances heat transfer much more in comparison to the other nanofluids. The average Nusselt number increases with increasing the Reynolds number. Also, average Darcy friction factor decreases with increasing Reynolds number. There is no effect of changing of nanoparticle volume fractions on average Darcy friction factor. It was also noticed that, Al_2O_3/water nanofluid has the lowest entropy generation.

REFERENCES

[67]. S. Jarungthammachote –Entropy generation analysis for fully developed laminar convection in hexagonal duct subjected to constant heat flux", *Energy,* vol. 35, pp. 5374-5379, 2010.
[68]. S. E. Razavi, H. Soltanipour, P. Choupani, –Second law analysis of laminar forced convection in a rotating curved duct", *Thermal Science*, vol. 19, pp. 95-107, 2015.
[69]. E. Abu-Nada, –Entropy generation due to heat and fluid flow in backward facing step flow with various expansion ratios", *Int, J. Exergy*, vol. 3(4), 2006.
[70]. E. Abu-Nada, –Numerical prediction of entropy generation in separated flows", *Entropy*, vol. 7(4), pp. 234-252, 2005.

[71]. N. Zhao, J. Yang, H. Li, Z. Zhang, S., ―Numerical investigations of laminar heat transfer and flow performance of Al_2O_3–water nanofluids in a flat tube", *International Journal of Heat and Mass Transfer*, vol.92, pp. 268–282, 2016.
[72]. W.H. Mah, Y.M. Hung, and N. Guo, ―Entropy generation of viscous dissipative nanofluid flow in microchannels", *International Journal of Heat and Mass Transfer*, vol. 55, pp. 4169-4182, 2012.
[73]. N. Purohit, V.A. Purohit, and K. Purohit, ―Assessment of nanofluids for laminar convective heat transfer: A numerical study", *Engineering Science and Technology, an International Journal*, vol. 19, pp. 574-586, 2016.
[74]. C.C. Cho, C.H. Chiu, C.Y. Lai, ―Natural convection and entropy generation of Al_2O_3–water nanofluid in an inclined wavy-wall cavity", *International Journal of Heat and Mass Transfer*, vol. 97, pp. 511-520, 2016.
[75]. M. Corcione, ―Heat transfer features of buoyancy-driven nanofluids inside rectangular enclosures differentially heated at the sidewalls", *Int. J. Therm. Sci.,* vol.49, pp. 1536–1546, 2010.
[76]. R. S. Vajjha, D. K. Das ―Experimental determination of thermal conductivity of three nanofluids and development of new correlations", *Int. J. Heat Mass Transfer,* vol.52, pp. 4675–4682, 2009.
[77]. B. Ghasemi, S. M. Aminossadati, ―Brownian motion of nanoparticles in a triangular enclosure with natural convection", *Int. J. Therm. Sci.*, vol. 49, pp. 931–940, 2010.
[78]. A. Bejan, *Entropy generation through heat and fluid flow*, John Wiley& Sons, 1982.
[79]. F. P. Incropera, D. P. DeWitt, ―Introduction to Heat Transfer 3rd ed.", *John Wiley&Sons Inc.*, New York, pp. 75-370, 1993.
[80]. B. H. Salman, H. A. Mohammed, A. S. Kherbeet, ―Heat transfer enhancement of nanofluids flow in microtube with constant heat flux", *International Communications in Heat and Mass Transfer*, vol, 39, pp. 1195–1204, 2012.
[81]. H. Togun, T. Abdulrazzaq, S. N. Kazi, A. Badarudin, M. K. A. Ariffin, M. N. M. Zubir, ―Numerical study of heat transfer and laminar flow over a backward facing step with and without obstacle", *International Journal of Mechanical, Aerospace, Industrial, Mechatronic and Manufacturing Engineering*, vol. 8, 2014.

Dielectric Measurements of Cactus using Arch Free Space Method at X-Band Frequencies

Ediz Delihasanlar[15], *Ahmet Hayrettin Yüzer*[16]

Abstract

This paper presents the measurement of dielectric constant of Opuntia which is one of the cactus species. The Opuntia has flat parallel surface and about 2.5cm length spines and there is no research in literature about dielectric measurement of Opuntia. Arch free space measurement method was utilized to measure the dielectric constant of Opuntia in the frequency range from 8.5 to 12 GHz (X-band). Effect of spines on dielectric constant is also showed. The measurement system was set up with two horn antennas, one of them is receiver and other is transmitter, a network analyzer, sample holder, arch-type metal structure and a computer. The error coefficients were identified by TRL calibration technique (Thru, Reflect and Line standard). After calibration, the accuracy of the system was checked by using samples whose dielectric properties are known. The network analyzer was used to measure S-parameters of Opuntia in an X-band. The dielectric constant was calculated by using the measured S-parameters by oblique incidence wave theory.

Keywords: Arch free space measurement, dielectric measurement, oblique incidence wave theory, Opuntia cactus, TRL calibration

29. INTRODUCTION

The measurement of complex dielectric properties of materials (ε_r : permittivity and μ_r : permeability) has gotten growing significance in the material science, absorber development, military, communication, biomedical research, industrial production etc. These research and development fields use electrical or magnetic characteristics of the materials which are decipherable from dielectric measurement[1]–[4].

Vegetation covers a large portion of the earth. The dielectric properties of vegetation at radio frequency have a great impact on radar system. A good understanding of the dielectric characteristic of vegetation is a big importance because these properties are very helpful for earth resources monitoring, management and remote sensor design[5]–[8].

In the literature, determination of dielectric constant of Opuntia has not been conducted. It has a large (about 2.5 cm length), sharp spines sparse structure, effect on the dielectric constant was also investigated. Opuntia, which is one of the cactus families, has a big enough flat surface area that provides the necessary conditions for measurement.

In the dielectric measurement techniques, free space arch method is selected for its own properties and advantages. Firstly, it allows to modeling shield application condition for incident electromagnetic waves at different angles. Secondly, the method enables to survey anisotropic materials depending on wave polarization. Next, this technique has non-destructive and non-contacting measurement characteristic. Moreover, opposite to the free-space transmission technique, there is no standing wave effect. After then the method makes it possible to measure both complex permittivity and complex permeability at high temperatures[9], [10]. In the course of measurement; frequency, angle of incident electromagnetic waves and polarization are collected. Finally, dielectric constant of Opuntia is calculated.

Section 2 describes details on the oblique incidence wave theory. Section 3, following a short explanation of sample preparation, outlines the method that is implemented for the permittivity measurement by using the free space arch method. Moreover measurement set up and calibration techniques are introduced. Section 4 discusses the measured results and conclusion.

[15] *Corresponding author: Karabuk University, Department of Electric-Electronics Engineering, 78000, Karabuk, Turkey.* edizdelihasanlar@karabuk.edu.tr

[16] *Karabuk University, Department of Electric-Electronics Engineering, 78000, Karabuk, Turkey.* hayrettinyuzer@karabuk.edu.tr

30. THEORY

At the medium$_0$ - medium$_1$ boundary, a part of oblique incidence electromagnetic plane wave is reflected and the other part of wave is transmitted into the medium$_1$. Electromagnetic wave, which is transmitted to the medium$_1$, is again reflected and transmitted at the other of medium$_1$. That's continues forever and shown in Figure 5. Sum of reflection coefficient is calculated by using the equation given in (1) as explained in [11],

$$\Gamma_{(\omega)} = \frac{1 - e^{-2\gamma d/\cos\theta_t}}{1 - \Gamma_{01}^2 e^{-2\gamma d/\cos\theta_t}} \Gamma_{01} \quad (1)$$

Where θ_t represents transmitted angle, d represents the thickness of medium$_1$, Γ_{01} represents reflection coefficient from medium$_0$ (free space) to medium$_1$, γ represents medium$_1$ propagation constant. Mathematical definition of γ is given in (2).

$$\gamma = j\omega\sqrt{\mu_1 \varepsilon_1} \quad (2)$$

Where $\varepsilon_1 = \varepsilon_0 \varepsilon_r$ is effective dielectric permittivity of medium$_1$. Angles of Reflected and Transmitted wave depend on two medium permittivity and permeability (Snell's law).

$$\frac{\sin\theta_t}{\sin\theta_i} = \frac{\sqrt{\varepsilon_0}}{\sqrt{\varepsilon_0 \varepsilon_r}} \quad (\mu_0 = \mu_1) \quad (3)$$

θ_i is incidence angle, ε_0, ε_1 and μ_0, μ_1 are permittivity and permeability of medium$_0$ and medium$_1$, respectively. Fresnel law of refraction coefficient for vertical polarization can be summarized as

$$\Gamma_{01\perp} = \frac{\cos\theta_i - \sqrt{\varepsilon_r - \sin\theta_i{}^2}}{\cos\theta_i + \sqrt{\varepsilon_r - \sin\theta_i{}^2}} \quad (4)$$

for horizontal polarization as

$$\Gamma_{01\parallel} = \frac{-\varepsilon_r \cos\theta_i + \sqrt{\varepsilon_r - \sin\theta_i{}^2}}{\varepsilon_r \cos\theta_i - \sqrt{\varepsilon_r - \sin\theta_i{}^2}} \quad (5)$$

Medium$_1$ complex dielectric constant is given as in (6)

$$\varepsilon_r = \varepsilon_r' + j\varepsilon_r'' \quad (6)$$

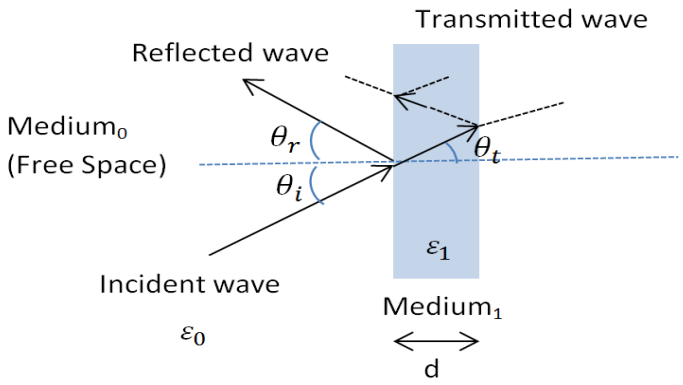

Figure 5. Reflection from medium$_1$

31. SAMPLE PREPARATION and METHOD of MEASUREMENT

3.1. Sample Preparation

A cactus, which can be adapted to live in very hot and dry environments, is a member of the plants. It is known as conserved water source and has different spines of leaves. There are about 1800 species of cactus in nature and each of them has a different shape and size. Some of the most well-known species of cactus are Opuntia and Peyotl. Opuntia, in Figure 2, is source of food and Peyotl is used in medicine [12].

To achieve accurate measurement using arch free space measurement method, some requirements must be satisfied. One of them is sample‘s surface and its size. The sample should be flat and parallel-surfaced and size of sample should be bigger than wavelength of the measurement because of effect of scattering from the sample boundary. To lessen scattering effect, sample size ought to be twice wavelength of the measurement[1], [10]. Opuntia is selected for fulfilling the necessary requirements.

Figure 6. Opuntia

3.2. Measurement Set up

The set up consists of an Agilent network analyzer (VNA), two coaxial cables, two horn antennas and arch-type metal structure. Vertical polarized horn antennas are used in the measurement setup as given in the Figure 3. Firstly, the VNA is calibrated with using two port calibration and then TRL (Through-Reflect-Line) calibration technique. Calibration step details are defined at next section. After calibration, Styrofoam substrate was used to check the accuracy of the measurement set up. The overall error for the substrate dielectric measurement was calculated to be ±%5 on average. After the measurement system is verified, S-parameters of the Opuntia were taken by using VNA. Only $S_{21}(\Gamma_{(\omega)})$ is required to determine the complex dielectric properties of Opuntia with using oblique incidence wave theory.

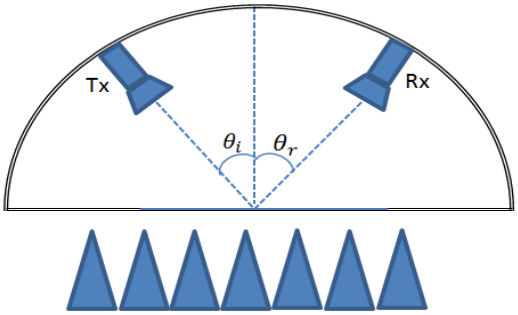

Figure 7. Representation of arc free space measurement system

3.3. TRL Calibration

In order to get accurate result a good enough calibration is needed. The TRL calibration technique, which is mostly used in literature, is illustrated in Figure 8. It has 3 steps, which are thru, reflect and line standard, for determining the error coefficients. Thru standard must be far field. The distance between two horn antennas for far field has to be more than $2\left(\frac{D^2}{\lambda}\right)$ (D: largest dimension of horn antenna aperture, λ: wavelength). Before reflect standard measurement, the transmitter and receiver antennas have to be moved back by the thickness of the metal plate. During the line standard, two antenna are moved away as $(n\left(\frac{\lambda}{4}\right)$, n=0,1,2…) wavelengths after then back in the original position [13]–[17].

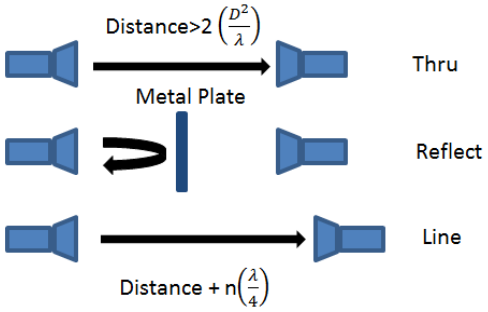

Figure 8. TRL calibration

32. RESULT and CONCLUSION

4.1. Dielectric Measurement Results

Total reflection coefficient obtained from the arch free space measurement depends on free space time domain method. This set up is especially suitable for non-destructive and non-contacting measurement of materials[18]. The measurement set up, as illustrated in Figure 9, was created with ($\theta_i = \theta_r = 44^o$), vertical polarized horn antennas and arch-type metal structure. The dielectric constant of Opuntia is calculated by using the S_{21} in oblique incidence wave theory in the frequency range from 8.5 to 12 GHz.

Figure 9. Arch free space measurement set up

The obtained value of real part of dielectric constant of Opuntia, which is with spines structure, is shown in Figure 10. Real part of dielectric constant (ε_r') of Opuntia with spines whereas the obtained value of real part of dielectric constant (ε_r') Opuntia, which is without spines structure, is indicated in Figure 11.

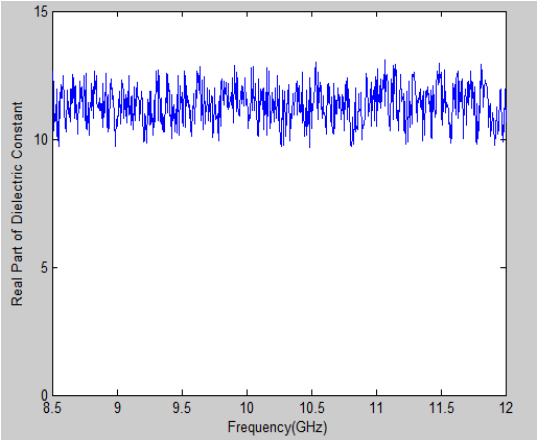

Figure 10. Real part of dielectric constant (ε_r') of Opuntia with spines

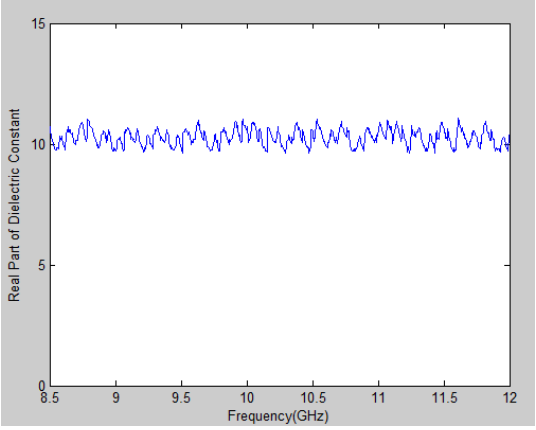

Figure 11. Real part of dielectric constant (ε_r') of Opuntia without spines

4.2. Conclusion

The dielectric constant of water is konwn about 78. Opuntia stores water inside itself so it was expected to obtain the high dielectric constant. The dielectric constant of Opuntia with spines and without spines was swinging about 11.30 and about 10, respectively. Spiny structure of Opuntia in the measurements was found to affect on dielectric constant ±10-15%.

This constant should not be used as actual dielectric constant but this constant is a good approximate approach for the exact values of the material properties in determination propagation constant on the environment.

According to the mentioned theory three parameters (reflection coefficient($\Gamma_{(\omega)}$), thickness (d) of the medium$_1$ and dielectric constant (ε_r)) are important because if two of them are known, other one can be easily calculated.

This method needs to develop to sum up total reflection coefficient and to use transmission coefficient during the dielectric constant calculation.

In future work, cactus with a lot of spines and more suitable in terms of size and surface, will be experimented for free space measurement. Moreover, effect of humidity and temperature will be researched.

ACKNOWLEDGMENT

This work was supported by Research Fund of the Karabuk University. Project Number: KBU-BAP-15/2-YL-08

REFERENCES

[1] V. V. V. and V. K. V. L.F. Chen, C.K. Ong, C.P. Neo, –Microwave Electronics: Measurement and Materials Characterization.,” in *West Sussex, U.K.:Wiley*, 2004.

[2] K. C. Yaw(Rohde&Schwarz), –Measurement of dielectric material properties Application Note,” in *Measurement Techniques*, 2006, pp. 1–35.

[3] A. Note, –Measuring Dielectric Constant with the HP8510 Network Analyzer The Measurement of Both Permittivity and Permeability of solid Metarials,” .

[4] F. H. Wee, P. J. Soh, a. H. . Suhaizal, H. Nornikman, and a. a. . Ezanuddin, –Free space measurement technique on dielectric properties of agricultural residues at microwave frequencies,” *2009 SBMO/IEEE MTT-S Int. Microw. Optoelectron. Conf.*, no. 1, pp. 183–187, 2009.

[5] U. C. Hasar, –Accurate complex permittivity inversion from measurements of a sample partially filling a waveguide aperture,” *IEEE Trans. Microw. Theory Tech.*, vol. 58, no. 2, pp. 451–457, 2010.

[6] B.-K. Chung, –Dielectric Constant Measurement for Thin Material At Microwave Frequencies,” *Prog. Electromagn. Res.*, vol. 75, pp. 239–252, 2007.

[7] T. Baum, L. Thompson, and K. Ghorbani, –Complex dielectric measurements of forest fire ash at X-band frequencies,” *IEEE Geosci. Remote Sens. Lett.*, vol. 8, no. 5, pp. 859–863, 2011.

[8] T. Oguchi, M. Udagawa, N. Nanba, M. Maki, and Y. Ishimine, –Measurements of dielectric constant of volcanic ash erupted from five volcanoes in Japan,” *IEEE Trans. Geosci. Remote Sens.*, vol. 47, no. 4, pp. 1089–1096, 2009.

[9] N. Dvurechenskaya, –Advantages and Disadvantages of the Free-Space Arch Method Used for Investigation of Shielding Materials at Low Gigahertz Frequencies,” no. 01, pp. 790–795, 2011.

[10] A. Technologies, –Agilent Basics of Measuring the Dielectric Properties of Materials Application note,” 2014.

[11] Y. H. and M. Nakhkash, –Characterisation of layered dielectric medium using reflection coefficient,” vol. 34, no. 12, pp. 1207–1208, 1998.

[12] –Cactus.” [Online]. Available: ?cactus?,https://en.wikipedia.org/wiki/Cactus#cite_note MerriamWebster -3.

[13] A. H. Boughriet, C. Legrand, and A. Chapoton, –Noniterative stable transmission/reflection method for low-loss material complex permittivity determination,” *IEEE Trans. Microw. Theory Tech.*, vol. 45, no. 1, pp. 52–57, 1997.

[14] D. K. Ghodgaonkar, V. V. Varadan, and V. K. Varadan, –Free-Space Measurement of Complex Permittivity and Complex Permeability of Magnetic Materials at Microwave Frequencies,” *IEEE Trans. Instrum. Meas.*, vol. 39, no. 2, pp. 387–394, 1990.

[15] D. K. Ghodgaonkar, V. V. Varadan, and V. K. Varadan, –A Free-Space Method for Measurement of Dielectric Constants and Loss Tangents at Microwave Frequencies,” *IEEE Trans. Instrum. Meas.*, vol. 38, no. 3, pp. 789–793, 1989.

[16] I. Rolfes and B. Schiek, –Advances in Radio Science Calibration Methods for Microwave Free Space Measurements Microwave methods free,” *Adv. Radio Sci.*, vol. 2, pp. 19–25, 2004.

[17] L. S. Rocha, C. C. Junqueira, E. Gambin, A. N. Vicente, A. E. Culhaoglu, and E. Kemptner, –A free space measurement approach for dielectric material characterization,” *2013 SBMO/IEEE MTT-S Int. Microw. Optoelectron. Conf.*, pp. 1–5, 2013.

[18] I. Vilovi, R. Na, Z. Šipuš, and N. Burum, –A Non-destructive Approach for Extracting the Complex Dielectric Constant of the Walls in Building,” no. September, pp. 10–12, 2008.

Functionally Graded Materials

T.Varol[17], A.Canakci[1], S.Özkaya[1], F.Erdemir[1]

Abstract

This article reviews the current status of the functionally graded materials (FGMs) such as types, fabrication methods and application areas. Functionally graded materials (FGMs) are special materials which incorporation two or more materials by varying gradually in specific properties such as heat conductivity, specific heat, and density. FGM properties (physical and mechanical properties) vary in space to meet the specific requirements due to the gradual change in composition. FGMs have great potential in applications where the operating conditions are severe, including impact plates, bearing materials, biomedical implants and heat exchanger tubes. After a brief introduction to the origin of the FGM concept, the review shows some specific examples of FGMs which are present in nature and human body. The present study provides new contributions of recent works aimed at the further development of new FGMs for increasing their engineering applications. Moreover, this review is intended to gain the readers a new perspective for the variety of studies and applications related to functionally graded materials.

Keywords: Functionally graded materials (FGMs), casting, powder metallurgy, biomaterials

33. INTRODUCTION

Functionally Graded Materials (FGMs) present a gradient of composition, phase, porosity or texture and theses materials have a gradient of properties such as density, hardness, electrical and thermal conductivity and fracture toughness. In other words, the desired physical and mechanical properties of FGMs can be provided for different direction through the alteration of weight percentage or volume fractions of the reinforcing materials (Fig. 1). The development and fabrication of FGMs which have different functional properties within one engineering material are a significant scientific progress for defense, biomaterial (Fig. 2), nuclear energy and aircraft industries. The definition of functional gradient expresses a chemical composition gradient chancing along x and y axes [1-3].

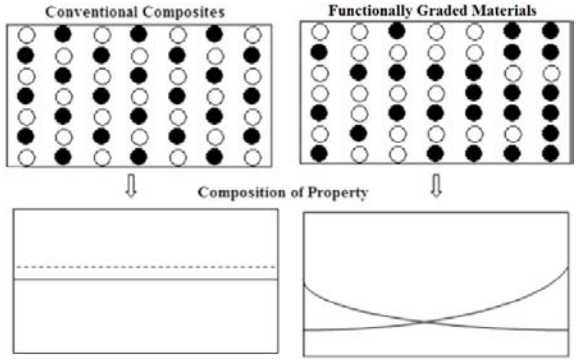

Fig. 1. Alteration of properties in conventional composite and FGMs [4]

[17] *Aykut Canakci: Karadeniz Technical University, Metallurgy and Materials Engineering, Trabzon, Turkey, aykut@ktu.edu.tr*

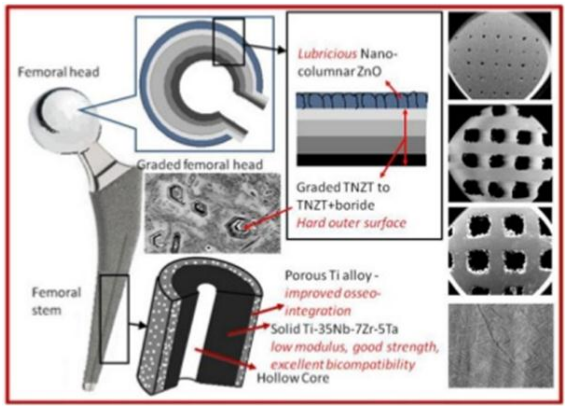

Fig. 2. Functionally graded implants [5]

In fact, the term of functionally graded materials is not a new concept for nature and human body. Examples of natural FGMs are shown in Fig. 3 [6/Varol 2016]. A tooth has gradual structure which changes from nerves to hard enamel layer (Fig. 3a). In addition, our skin has similar FGM structure with changing layers (Fig 3b).

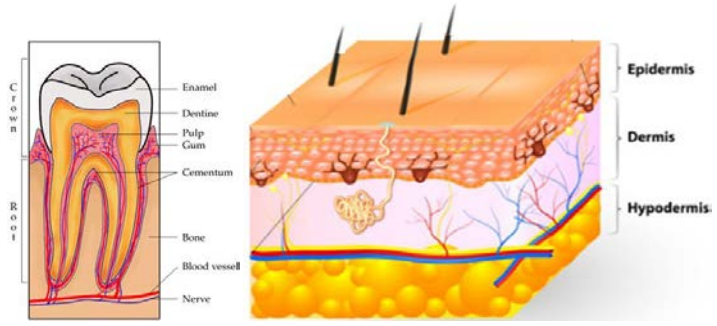

(a) (b)

Fig. 3. Examples of FGM in the human body [7-8]

The first examples of functionally graded composites with a graded structure were shown in theoretical papers by Bever and Duwez [9], and Shen and Bever [10] in 1972. However, the development process was slow due to some problems such as non suitable fabrication methods, the level of material science and lack of research center with FGM at that time. The development process, which contains advances of manufacturing processes and engineering materials, took about fifteen years until establishment of a national research center on FGMs in Japan. The study of development of FGM materials and diversification of production methods has been continued since that time [11]. To increase the use of functionally graded materials in the engineering applications and to maintain the material‘s properties during continue its mission, the physical and mechanical properties should be at the desired level in the engineering materials. Therefore, the present review discusses production methods, application and the relationships between type and properties of functionally graded materials.

2. Processing techniques of functionally graded materials (FGMs).

2.1. Powder Metallurgy

The PM technique has several advantages compared to other manufacturing processes. For example, process temperature of PM is lower than that of melting methods. That is why undesired phases between the matrix phase and the reinforcement phase are eliminated. Moreover, distribution of reinforcement particles in PM is better than that of casting processes. Another significant feature is the ability to produce near net shape parts, which is cost effective. Some materials, such as metal matrix

composites, contact materials alloys and functionally graded materials can be produced successfully via the PM technique [12]. Powder metallurgy (PM) technique, which includes three main steps: mixture or preparation of initial powders, cold pressing (forming-green compacts) and sintering process, can be used successfully to fabricate functionally graded materials. Powders of many metals, alloys, compounds and ceramic materials with particle sizes ranging from nanometers to several hundred micrometers are available from industrial sources or may be produced by the methods developed over decades in the field of PM [11]. In the powder metallurgy method, (a) porosity gradients can be obtained either by the deposition of powder mixtures with different particle shape or by varying the deposition parameters including the use of space holders, (b) Gradients may be created in chemical composition of single phase materials: gradient of chemical composition is provided during the deposition of particle within die using different composition of initial powders, (c) Gradients of the volume content of phases and grain size gradients can be obtained in two or multiphase materials: microstructure, which has two or more phases with gradients in volume content or in grain size, can be fabricated by using combinations of phases which includes include metal-metal, metal-ceramic and ceramic-ceramic systems [11]. Fig. 4 shows main steps of powder metallurgy method.

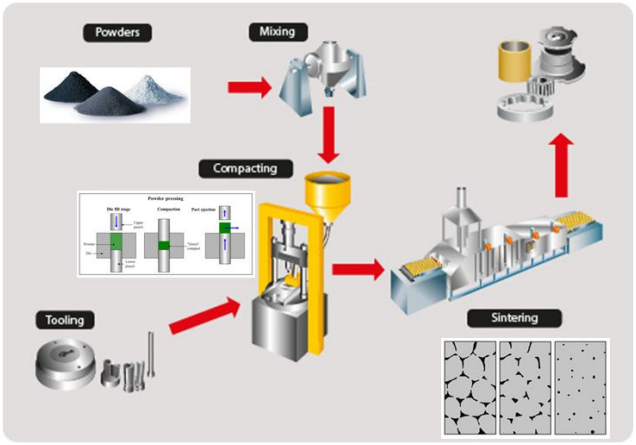

Fig. 4. The stages of powder metallurgy method

Erdemir et al. [13] studied that characterization on the Al2024/SiC functionally graded materials (FGMs) with different numbers of graded layers and different amounts of SiC fabricated by powder metallurgy method (Fig. 5). According to their results, a maximum bending strength of 1400 MPa was obtained for two-layered FGMs which contained 40% SiC (wt.%). They reported that the increase in microhardness values and intermetallic formation play a major role on the improvement of mechanical properties of the composites.

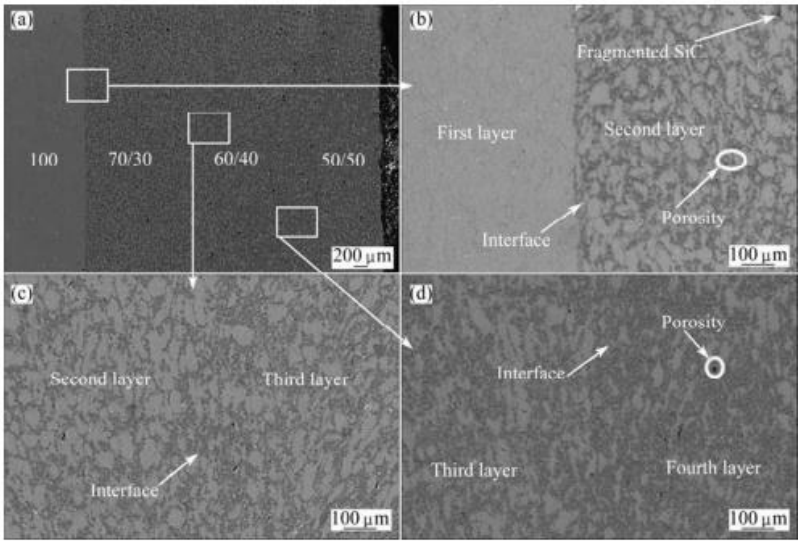

Fig. 5. The microstructures of Al2024/SiC functionally graded composites [13]

Hussain et al. [14] investigated on the fabrication of hydroxyapatite functionally graded materials reinforced with 316L and CNTs by powder metallurgy (Fig. 6a). They reported that the densification of FGMs improved with an increase in the nano HA concentration, but it declined at higher

concentrations. According to their research, CNT particles were well dispersed in the matrix and took an active part in crack bridging, which yielded a high value of fracture toughness for the composite layers (Fig 6b).

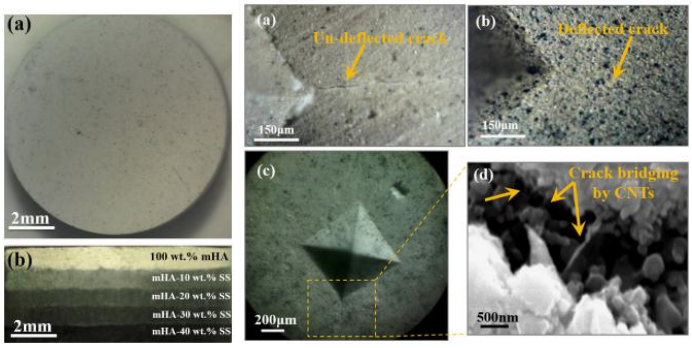

Fig. 6. Functionally graded biomaterials produced by powder metallurgy [14]

2.2. Deposition techniques

2.1. Vapor deposition techniques

Chemical vapor deposition (CVD) and physical vapor deposition (PVD) methods are known widely as vapor deposition techniques used for the production of functionally graded materials. In this method, the materials in a vapor state are condensed through condensation, chemical reaction, or conversion to form a solid material. These techniques are also used to form coatings to improve the mechanical, electrical, thermal, optical, corrosion resistance, and wear properties of the matrix materials [4]. CVD and DVD methods can provide single layer, multilayer, composite, and functionally graded coating materials with well controlled dimension and unique structure at low processing temperatures. CVD technique is one of the main processing methods for the deposition of thin films and coatings for a wide range of applications, including refractory ceramic materials (B_4C, Al_2O_3 SiC, and ZrO2) used for hard armor coatings and bearing materials, metallic films (Au, Cu, Al, Pt and Mo) for protection against corrosion and oxidation and layered materials (Al-B_4C, Al-SiC- Al-Al_2O_3, Cu-Al_2O_3 and Mg-SiC) to improve surface properties (hardness, conductivity and oxidation) [15]. The relatively low deposition temperature (200-500°C) allowing most industrially important substrate materials to be coated are one of the advantages of PVD method [16]. PVD has been used widely for production of thin hard coatings which utilized for many applications to improve friction and wear resistance of tools and mechanical components. For example, PVD multi layers are extensively used for coating of cutting tool materials such as lathe, drill and milling tools (Fig. 7).

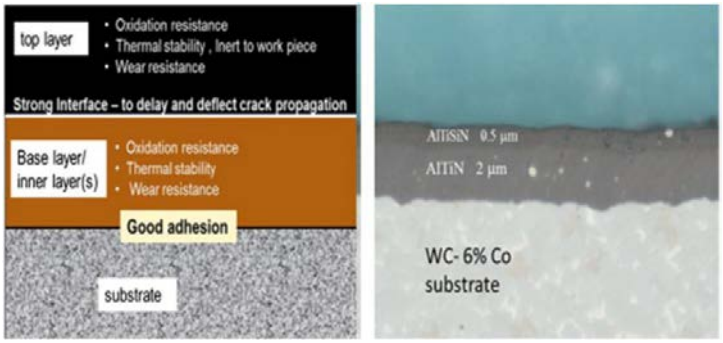

Fig. 7. (a) Conceptual design of the multilayer coating. (b) A double layer coating, with a base layer of Al-TiN and an outer layer of Al-Ti-SiN [17]

2.3. Centrifugal casting

The effect of gravitational force has been used for through spinning of the mold to produce functionally graded material in centrifugal casting method (Fig.8). This method is exclusively used for the production of cylindrical parts. The molten metal is discharged in a rotating mold and solidification of

molten metal provides during rotating of mold. Centrifugal casting has some advantages such as low porosity, high mechanical properties and uniform microstructure. The compositional gradient has been mainly obtained by the difference in the centrifugal force which is produced by the difference in density between the molten metal and solid particles [4, 18, 19].

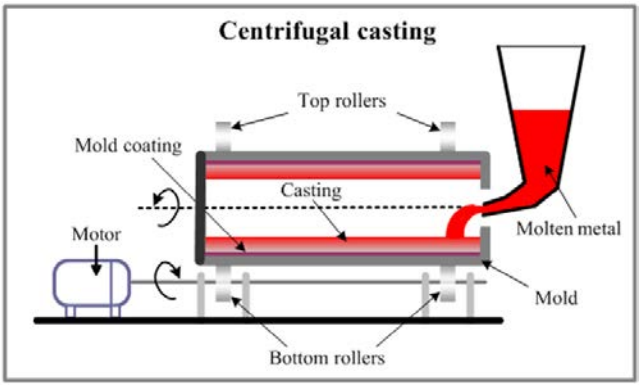

Fig. 8. Centrifugal casting process [20]

Rajan et al. studied on the characterization of centrifugal cast functionally graded aluminum-silicon carbide metal matrix composites. They stated that maximum of 45 and 40% SiC particles are obtained near the outer periphery of the SiC reinforced Al matrix functionally graded composites (Fig. 9). The maximum hardness obtained at the outer periphery after heat treatment for Al356-SiC and Al2124-SiC functionally graded composites are 155 BHN and 145 BHN respectively (Fig. 10) [21].

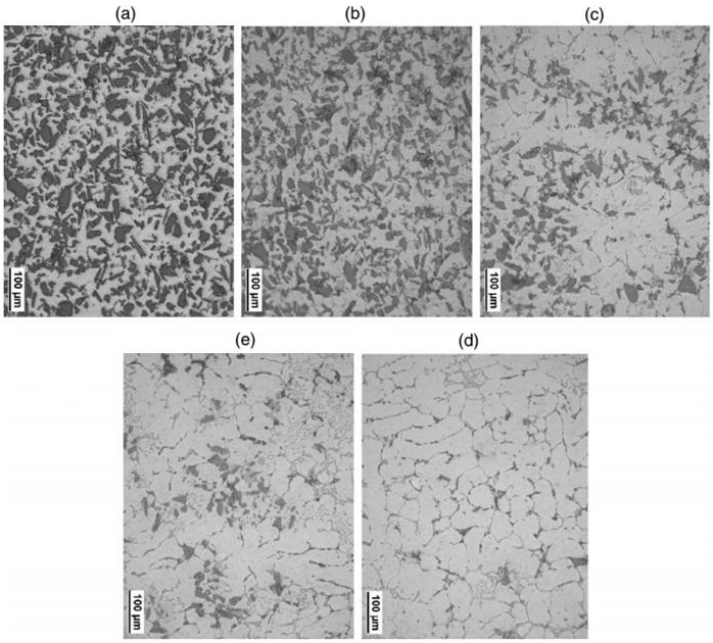

Fig. 9. Microstructures of Al2124-SiC functionally graded composites : from the outer periphery to the inner periphery, (a) 1 mm, (b) 1.5 mm, (c) 2.5 mm,

(d) 5 mm, (e) 12.5 mm [21/Rajan 2010]

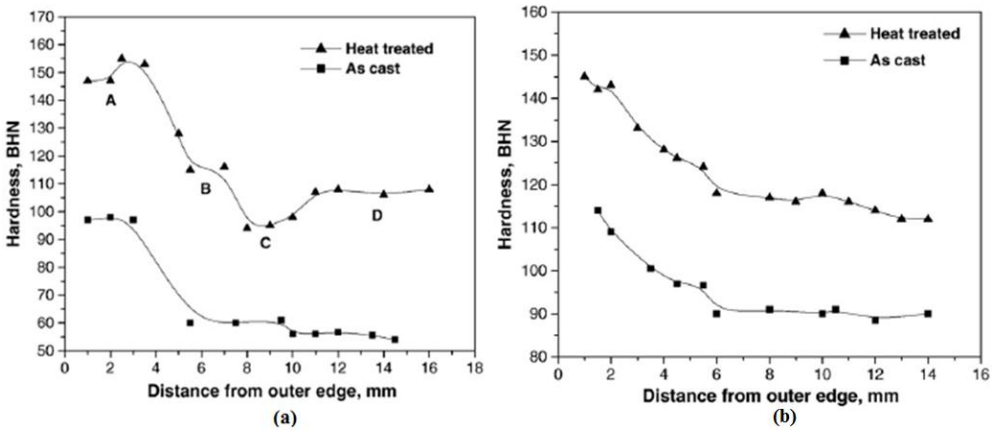

Fig. 10. The change of hardness from outer edge of (a) Al356-SiC functionally graded and (b) Al2024-SiC composites. [21]

Melgarejo et al. [22] investigated The microstructure and tribological performance of compositionally and functionally graded Al-Mg/AlB_2 metal-matrix composites (MMCs) produced by centrifugal casting. They reported that the highest wear volume was found on the 0 mm section of the FGMs, where the AlB_2 particle content is the lowest. The wear rate decreased as a function of radial distance, with the 20 mm section exhibiting the smallest wear volume (or the highest wear resistance) [Fig. 11].

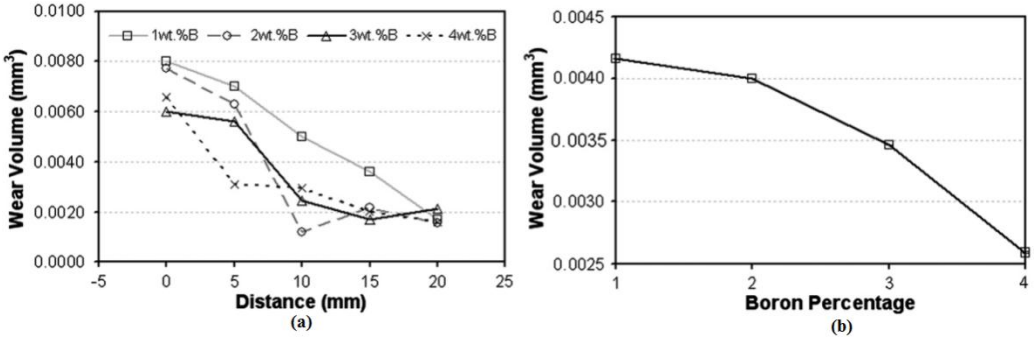

Fig. 11. The change of wear volume for the various composite samples after pin-on-disk wear tests performed under identical conditions (a) FGMs with various initial boron contents as a function of radial distance (b) gravity casting as a function of boron content [22]

3. CONCLUSIONS

Functionally graded materials are one of the important engineering materials but the properties of producing these materials changes with fabrication method, matrix and reinforcement type and interface between layers. The great potential of FGM use not only in the field of defense but also broadly accepted in aerospace and biomaterials applications. FGM's seems to be very promising in the medical field applications like dentistry, artificial and bones. There is a need of some improvement in

the techniques to get the guaranteed distribution of properties throughout the structure with more reliability and predictability although many fabrication techniques of FGM are available.

References

[1] C. Morin, S. Le Gallet, M. Ariane and F. Bernard, ―Spark Plasma Sintering tool design for preparing alumina-based Functionally Graded Materials," Ceramics International 42, pp. 3056-3063, 2016.

[2] M. Tokita, Chapter 11.2.3-Spark plasma sintering (SPS) method systems and applications, In: Shigeyuki Somiya (ed.), Handbook of Advanced Ceramics, 2nd ed., Materials, Applications, Processing and Properties, 2013.

[3] Z.J. Zhou, S.X. Song, J. Du, Z.H. Zhong and C.C. Ge, ―Performance of W/ Cu FGM based plasma facing components under high heat load test," Journal of Nuclear Materials 363-365, pp. 1309-1314, 2007.

[4] A. Gupta and M. Talha, ―Recent development in modeling and analysis of functionally graded materials and structures," Progress in Aerospace Sciences, 79 pp. 1-14, 2015.

[5] Http://research.unt.edu./İses/advanced-metallic-materials

[6] T. Varol, ―The Fabrication and Characterization of Nano Particle Reinforced-Copper Matrix Functionally Graded Electrical Contact Materials, PhD Thesis, Karadeniz Technical University, Trabzon, Turkey, January, 2016.

[7] C.Y. Chu, T.C. Kuo, S.F. Chang, Y.C. Shyu and C.P. Lin, ―Comparison of the microstructure of crown and root dentin by a scanning electron microscopic study," Journal of Dental Science, 5, pp. 14-20, 2010.

[8] S.H. Mathes, H. Ruffner and U.G. Hausner, "The use of skin models in drug development," Advanced Drug Delivery Reviews, 69-70, pp. 81-102, 2014.

[9] M.B. Bever and P.F. Duwez, "Gradients in composite materials," Mater. Sci. Eng. 10, pp. 1-8, 1972.

[10] M. Shen and M.B. Bever, Gradients in polymeric materials, J. Mater. Sci. 7, pp. 741-746, 1972.

[11] B. Kieback, A. Neubrand and H. Riedel, "Processing techniques for functionally graded materials," Materials Science and Engineering A, 362, pp. 81-105, 2003.

[12] A. Canakci, T. Varol, H. Cuvalci, F. Erdemir and S. Ozkaya, "Development and characterization of bronze-Cr-Ni composites produced by powder metallurgy," Science and Engineering of Composite Materials, 22, 425-432, 2015.

[13] F. Erdemir, A. Canakci and T. Varol, "Microstructural characterization and mechanical properties of functionally graded Al2024/SiC composites prepared by powder metallurgy techniques," Trans. Nonferrous Met. Soc. China, 25 3569-3577, 2015.

[14] M. A. Hussain, A. Maqbool, F. A. Khalid, M. U. Farooq, I. H. Abidi, N. Bakhsh, W. Amin and J. Y. Kim, "Improved sinterability of hydroxyapatite functionally graded materials strengthened with SS316L and CNTs fabricated by pressureless sintering," Ceramics International 41, pp. 10125-10132 2015.

[15] K. L. Choy, "Chemical vapour deposition of coatings," Progress in Materials Science, 48, pp. 57–170, 2003.

[16] T. Bjork, R. Westergard, S. Hogmark, J. Bergstrom and P. Hedenqvist, "Physical vapour deposition duplex coatings for aluminium extrusion dies," Wear, 225-229, pp. 1123-1130, 1999.

[17] A. Inspektor, P. A. Salvador, "Architecture of PVD coatings for metalcutting applications: A review," Surface & Coatings Technology, 257, pp. 138-153 2014.

[18] Y. Watanabe, N. Yamanaka, Y. Fukui, —Control of composition gradient in a metal-ceramic functionally graded material manufactured by the centrifugal method," Composites A, 29, 595-601, 1998.

[19] Y. Watanabe, N. Yamanaka, Y. Fukui, —Microstructures and mechanical properties of functionally graded materials fabricated by a centrifugal method," Rec. Res. Dev. Metall. Mater. Sci. 4, pp. 51-93 2000.

[20] [Online] Available: Functionally graded materials, Substech.com

[21] T. P. D. Rajan, R. M. Pillai, B. C. Pai, —Characterization of centrifugal cast functionally graded aluminum-silicon carbide metal matrix composites," Materials Characterization, 61, pp. 923-928, 2010.

[22] Z. H. Melgarejo, O. M. Suarez, K. Sridharan, —Microstructure and properties of functionally graded Al-Mg-B composites fabricated by centrifugal casting," Composites: Part A 39, pp. 1150-1158, 2008.

Kyrgyz Orthography and Morphotactics with Implementation in NUVE

Züleyha Yiner[18], Atakan Kurt[19], Kalmamat Kulamshaev[3], Harun R. Zafer[4]

Abstract

This paper describes Kyrgyz morphology using the two level model of Koskemnieni with an implementation in the NUVE framework. The morphology is given in 2 steps: morphophonemic processes and Kyrgyz morphotactics. Morphophonemic processes are described by the two level orthographic rules that are indeed lexical-to-surface transformations. Then Kyrgyz morphotactics -the rules of ordering the morpheme affixations- are defined as finite state machines(FSA). The implementation requires the orthography in the form of two level rules, the morphotactics in the form of a FSA along with a root/stem lexicon, and a suffix dictionary. NUVE framework, which is the successor to our previous machine translation framework DILMAC, is used for morphological parsing and morphological machine translation. The Turkish morphology is already available in NUVE. This new description will enable the implementation of a morphological machine translator between Kyrgyz and Turkish languages.

Keywords: DILMAC**,** Kyrgyz, NUVE, machine translation, Turkish, two-level morphology

34. INTRODUCTION

Two-level morphology [82], a computational model, has been used to define the morphology of agglutinative languages. Publicly available tools like PC-KIMMO [83] can be used to implement a two level morphology.

Two level morphological model has been applied to a number of languages including non-agglutinative ones such as those by Alam for Japanese [84], by Antworth for English [85], by Kim for Korean [86], by Oflazer for Turkish [87], Turkmen by Tantuğ [88] and Shylov [89], by Zafer for Kazakh [90], by Görmez for Kyrgyz [91] languages and so on.

In this paper, we study the morphology of Kyrgyz language which is a member of Turkic language family and spoken by nearly 5 million people. The members of Turkic language family are Turkish, Turkmen, Kazakh, Uzbek, Azerbaijani, Kyrgyz and some other 20 languages. These Turkic languages have a lot in common from phonological, morphological and syntactic aspects. Kyrgyz is an agglutinative language in which words are formed by productive affixations of derivational and inflectional morphemes to the word root or stems. A number of morphophonemic processes occur during these affixations in which a set of orthographic rules define the modifications to affixes when realizing the surface forms of words.

Our ongoing project is the development of a web-based machine translation system between Kyrgyz and Turkish which started out with DILMAC framework. We recently switch to a brand new framework to overcome some of the difficulties with DILMAC.

There have been a number of projects or studies aiming at translation among Turkic languages. One of them is implemented by Hamzaoğlu [92] for Azerbaijani-Turkish. The other translation system is Crimean Tatar-Turkish developed by Altıntaş [93]. DILMAC [94] is Turkic languages machine translation system while it originally was for translation between Turkmen and Turkish. There is another work for Turkmen- Turkish machine translation by Tantuğ [88]. A machine translation between Uyghur and Turkish language implemented in DILMAC by Keskin [95].

This paper is organized as follows: in Section 2 Kyrgyz orthography is described by using two-level rules. In Section 3, morphophonemıc processes are explained in NUVE framework and the implementation in NUVE is given Section 4. Conclusion and future work is in the last section.

[18] *Corresponding author: Istanbul University, Department of Computer Engineering, 34320, Avcilar/İstanbul, Turkey.* zuleyha.yiner@istanbul.edu.tr

[19] *Istanbul University, Department of Computer Engineering, 34320, Avcilar/İstanbul, Turkey.* atakan.kurt@istanbul.edu.tr

[3] *Fatih University, Department of Contemporary Turkic Languages, 34500, Buyukcekmece/İstanbul, Turkey.* kkulamshaev@fatih.edu.tr

[4] *Marmara University, Department of Computer Engineering, 34718, Kadikoy/İstanbul, Turkey.* harunzafer@gmail.com

35. KYRGYZ ORTHOGRAPHY

Kyrgyz is officially written in Cyrillic alphabet. In this paper we use both Cyril and Latin alphabets for clarity. The implementation is actually done in Cyril, where our previous implementation of Kyrgyz morphology in DILMAC framework was only in Latin. Cyrillic Kyrgyz alphabet is given in Table 3 that shows the Latin transliterations as well.

Table 3. Cyrillic script and Latin transcription for Kyrgyz

Cyrillic	Latin	Cyrillic	Latin	Cyrillic	Latin
А а	A a	Л л	L l	Ф ф	F f
Б б	B b	М м	M m	Х х	X x
В в	V v	Н н	N n	Ц ц	Ts ts
Г г	G g	Ң	ň	Ч ч	Ç ç
Д д	D d	О о	O o	Ш ш	Ş ş
Е е	E e/ye	Ө ө	Ö ö	Щ Щ	Şç şç
Ё ё	Yo yo	П п	P p	Ъ	apostrophe
Ж ж	J/C j/c	Р р	R r	Ы ы	I ı
З з	Z z	С с	S s	ь	soft sign
И и	İ i	Т т	T t	Э э	E e
Й й	Y y	У у	U u	Ю ю	Yu yu
К к	K k	Ү ү	Ü ü	Я я	Ya ya

Two level morphology of Koskemnieni [96] is quite useful for modelling morphology of agglutinative languages. In this approach, both orthographic rules are defined using two level rules and derivational/inflectional morphotactics are defined using FSAs. Lexical and surface forms is two forms that are used for representing a word in this model. The transformations between from these two forms are defined with two-level orthographic rules. These rules can be formalized as:

- **a:b => LC_RC**: lexical *a* corresponds to surface *b* only if (=>) it occurs given left context (LC) and the right context (RC). This realization occurs only under this condition, but not always.
- **a:b <= LC_RC**: lexical *a* always corresponds to surface *b* if it follows the left context (LC) and/or precedes the right context (RC) under this condition or other different conditions.
- **a:b <=> LC_RC**: lexical *a* corresponds to surface *b* always and only if it follows the left context (LC) and/or precedes right context (RC) under only this condition.
- **a:b \ <= LC_RC**: lexical a is never realized as surface b in the given left context (LC) and right context (RC).

Kyrgyz alphabet has 20 consonants and 8 vowels. Also there are double phonemes in Kyrgyz words of Russian origin: /ë/(yo), /ц/(ts), / щ /(şç), /ю/(yu), /я/(ya). We use a sub set of letters - called meta phonemes - when expressing orthographic rules. These meta phonemes are given below:

Consonants: C = {b, c, ç, d, f, g, x, k, l, m, n, ň, p, r, s, ş, t, v, y, z}

Voiceless Consonants: C_{ts} = {ç, f, x, k, p, s, ş, t, ts, şç} = {ч, ф, х, к, п, с, ш, т, ц, щ}

Voiced Consonants: C_t = {b, c, d, g, l, m, n, ň, r, v, y, z} = {б, ж, д, г, л, м, н, ң, р, в, й, з}

Vowels: V = {a, e, ı, i, o, ö, u, ü} = {a, e, ы, и, о, ө, у, ү}

Back Vowels: V_b = {a, ı, o, u} = {a, ы, о, у}

Back unrounded vowels: V_{bu} = {a, ı} = {a, ы}

Back rounded vowels: V_{br} = {o, u} = {o, y}

Front Vowels: V_f = {e, i, ö, ü} = {e, и, ө, ү}

Front unrounded vowels: V_{fu} = {e, i} = {e, и}

Front rounded vowels: V_{fr} = {ö, ü} = {ө, ү}

I = {ı, i, u, ü} = {ы, и, у, ң}

A = {a, e, o, ö} = {а, е, о, ө}

L = {l, d, t} = {л, д, т}

G = {g, k} = {г, к}

N = {n, d, t} = {н, д, т}

B = {b, p} = {б, п}

D = {d, t} = {д, т}

U = {u, ü} = {у, ң}

O = {o, ö} = {о, ө}

R = {r, y} = {р, й}

Y = {oo, öö, uu, üü} = {оо, өө, уу, ңң}

36. MORPHOPHONEMIC PROCESSES

A number of morphophonemic processes take place during derivation or inflection of a word in Kyrgyz similar to those in Turkish including vowel drops, consonant drops, vowel changes as in vowel harmony rules, consonant changes as in consonant harmony rules, etc. These rules express the conditions in which these modifications occur. Below they are given as two level orthographic rules along with a few examples.

36.1. Vowel Drops

Vowel drops occur in different places. For example, when a suffix starting with a vowel is affixed to a stem ending with a vowel, the vowel of the suffix is dropped.

V:0 => V +:0 _

Here 0 is a temporary placeholder symbol in the intermediate level between lexical and surface levels which is automatically deleted on the surface. + indicates a morpheme boundary. In the tables below, the first and second rows contain the lexical and the surface forms of examples, meanwhile the first and second columns of the tables contain the examples in Cyril and Latin versions. An explicit formulation of lexical form along with meaning in English are given in the third column.

ене+Ім	ene+Im	N(mother)+Poss1PS
ене00м	ene00m	енем (my mother)
ата+Ін	ata+Iй	N(father)+ Poss2PS
ата00н	ata00й	атан (your father)

The last vowel of certain words drops when they are affixed with a suffix starting with or containing a vowel. A similar rule applies to Turkish words describing organs of the head such as ağız (mouth), burun (nose), alın (forehead) etc.

еми+GI	emi+GI	N(now)+Relative
ем00ки	em00ki	емки (now)
мойун+Ім(моюн+Ім)	moyun+Im	N(nec)+ Poss1PS
мой0н0ум	moy0n0um	атан (my neck)

36.2. Vowel Harmony

Kyrgyz has vowel harmony similar to the one in Turkish where the last vowel in the stem may modify the vowels in the suffixes affixed to the stem under certain conditions. This situation is called vowel agreement between the stem and the suffixes. There are two types of vowel harmony: palatal and labial. However, the vowel harmony rules don‘t apply to many words borrowed from foreign languages such as Russian, Arabic, English etc.

36.2.1. Palatal Harmony

Kyrgyz language divides vowels into palatal (front) and velar (back) vowels as shown in the table below.

Table 4. Kyrgyz vowels (Latin in parenthesis)

	Unrounded		Rounded	
Front	е,э (e)	и (i)	ө (ö)	ү (ü)
Back	а (a)	ы (ı)	о (o)	у (u)

In short, this rule requires that front vowels should be followed by front and back vowels should be followed by back vowels in a word.

I:ı => V:V_{bu} C* +:0 C*_

I:i => V:V_{fu} C* +:0 C*_

A:e => V:V_{fu} C* +:0 C*_

In these rules * denotes zero or more occurrence of the preceding letter, in this case an optional consonant.

```
кыз+Iм          kız+Im          N(daughter)+Poss1PS
кыз0ым          kız0ım          кызым (my daughter)

ене+cI          ene+sI          N(mother)+Poss3PS
ене0си          ene0si          енеси (her/his/its mother)
```

36.2.2. Labial Harmony

Labial harmony states that preceding back vowels *o* and *u* should be followed by *ı*, and preceding front vowels *ö* and *ü* should be followed by *i* respectively. Palatal harmony takes precedence over labial harmony if both applies.

I:u => V:V_{br} C* +:0 C*_

I:ü => V:V_{fr} C* +:0 C*_

```
суу+cIз         suu+sIz         N(water)+ NtoAdj

суу0суз         suu0suz         суусуз (without water)

күч+cIз         küç+sIz         N(power)+ NtoAdj

күч0суз         küç0süz         күчсуз (powerless)
```

ö or *ü* should be followed by an *ö*:

A:ö => [ö|ü] C* +:0 C*_

```
үй+DA           üy+DA           N(home)+Locative case

үй0дө           üy0dö           үйдө (at home)
```

a, *ı* or *u* should be followed by an *a*:

A:a => [a|ı|u] C* +:0 C*_

```
ал+BA           al+BA           V(take)+ Negative

ал0ба           al0ba           alba (do not take)
```

The lexical A in a suffix is changed to *a*, when that suffix is affixed a stem whose last vowel is a front unrounded vowel.

```
ел+DA           el+DA           N(hand)+Locative case

ел0де           el0de           елде (on hand)
```

The o vowel is followed by an o. The lexical A is changed to o in the following rule.

A:o => o C* +:0 C*_

```
кол+LAr          kol+LAr          N(arm)+Plural
кол0дор          kol0dor          колдор (arms)
```

36.3. Consonant Drops

The consonant `l` at the end of the one syllable stems drops, if the stem takes the +Ip adverb suffix [97].

l:0 => C*VC* _ +:0 Ip

```
ал+Ип            al+Ip            V(take)+Ip
а000п            a000p            ап (by taking)
```

When a suffixed starting with an s is affixed to a word ending with a consonant, the s at the beginning of the suffix drops.

s:0 <=> C +:0 _I

```
жүрөк+cI         cürök+sI         N(heart)+Poss3PS
жүрөг00ү         cürög00ü         жүрөгү (her/his/its heart)
```

36.4. Consonant Harmony

In Kyrgyz, consonant harmony is enforced strictly [97]. In short voiceless consonants should be followed by voiceless one, otherwise those voiced consonants are converted to voiceless counterparts. Below are the set of voiced (C_t) and voiceless (C_{ts}) consonants (ts and sç phonemes are considered voiceless).

When adding suffixes with the initial meta consonants L, N, D, G, B to stems ending with voiceless consonants, Kyrgyz harmonizes (changes) the initial consonants with respect to final consonant in the stem as shown in the rules below.

When a suffix starting with lexical L is affixed to a stem ending with a vowel or voiced consonant r, or y, lexical L is converted to *l*.

L: l => [V|R] +:0 _

```
ене+LAp          ene+LAr          N(mother)+Plural
ене0лер          ene0ler          енелер (mothers)
```

In a similar rule a lexical N is realized as *t* on the surface when a suffix starting with N is affixed to a stem ending in a voiceless consonant:

N: t => C_{ts} +:0 _

```
таш+NI           taş+NI           N(stone)+Accusative case
таш0ты           taş0tı           ташты (the stone)
```

A lexical D is realized as *t* on the surface in a similar case.

D: t => C_{ts} +:0 _

```
китеп+DA         kitep+DA         N(book)+Locative Case
китеп0те         kitep0te         китепте (in the book)
```

A lexical G is realized as *k* on the surface in the same case.

G: k => C_{ts} +:0 _

```
жыгач+GA         cıgaç+GA         N(tree)+Dative Case
жыгач0ка         cıgaç0ka         Жыгачка(to tree)
```

A lexical B is realized as *p* on the surface in the same case.

B: p => C_{ts} +:0 _

```
айык+BAc        ayık+BAs       V(heal)+Verbal Adjective

айык0пас        ayık0pas       айык0пас(unhealable)
```

37. NUVE FRAMEWORK AND IMPLEMENTATION

NUVE is a generic top-down morphologic parser and machine translation framework developed primarily for Turkic Languages which can be used for any other agglutinative language. It is an open source project developed by Harun Reşit ZAFER with C# on .NET platform. Turkish morphology is already specified in NUVE. In NUVE no programming is required to implement a morphology, because everything is specified in a set of files: root and suffix lexicons, orthographic rules and morphotactic rules. NUVE has a number of properties that makes it easier to describe morphology than its predecessor DILMAC [94].

- It is possible to define suffixes written separately which may look like words in the text
- It is possible to handle multi-word expressions which are the basic units of translations

The specification of Kyrgyz in NUVE proceeds in four steps:

1. A lexicon in CSV format is prepared. The lexicon is organized as root (or stems), surfaces, POS, rules.

2. A suffix lexicon in CSV format is prepared. The suffix lexicon is organized as Id, lexical form, suffix group, rules and surfaces.

3. Two level orthographic rules are specified in the *orthography.xml* file. An example rule and its specification is given below. The XML tags are self-explanatory.

D: t => C_{ts} +:0 _

D: d => [C_t|V] +:0 _

```
<rule id="DONUSUM_D" phase="2">
 <description>after voiceless consonant D => t, after voiced consonant and vowels D=>d, </description>
  <transformation morpheme="This" action="Replace" operandOne="D" operandTwo="т" flag="all">
    <conditions flag="Or">
      <condition morpheme="Previous" operator="LastLetterEquals" operand="кпстфхцчшщц" />
    </conditions>
  </transformation>
 <transformation morpheme="This" action="Replace" operandOne="D" operandTwo="д" flag="all" />
 </rule>
```

Figure 12. An example of orthographic rules in NUVE

4. The morphotactics of the language is specified as a FSA in the morphotactics.xml file. A small portion of the morphology file is given for the FSA in Figure 13**Error! Reference source not found.**.

```
<morphology lang="Kg-KG">
<suffixGroups>
        <suffixGroup name="ISIM_SAHIPLIK">
                <suffix>IC_SAHIPLIK_BEN_(I)m</suffix>
                …
                <suffix>IC_SAHIPLIK_ONLAR_LArI</suffix>
        </suffixGroup>
        …
</suffixGroups>
<graph>
        <source id="ISIM">
                <target id="IC_COGUL_LAr"/>
                <targetGroup id="ISIM_SAHIPLIK"/>
```

```
                    …
            </source>
    …
    </graph>
```

Figure 13. A small part of morphotactics.xml file

The initial state is [Nominal Root] which is defined as source in morphology.xml. The next state can be [Plural] state by taking suffix +LAr. Another intermediate state is when taking one of possessive suffixes [Noun+LAr+(I)m].

Finite state machines are used for representing morphotactic rules. An FSA is a directed graph consisting of a set of states (rectangles) and a set of transitions (arrows) between these states. Transitions are the edges of graph and labeled with suffixes defining in what order those morphemes can be affixed to a word. The initial state represents root words from a lexicon and their part of speech such as noun, verb, adverb, adjective, etc. And it is represented by rectangles. The intermediate state, in a way, represents partial words and their part of speech and is shown by rounded rectangles. Final states (double circles) represent full word formations of roots starting with initial states, going through intermediate states (partial word formations) until a final state is reached. A small part of nominal morphotactics of Kyrgyz is given in Figure 14.

Here is a sample for inflection of noun *iş* (business): *işteribizdegi* (the one that in our business)

work	+N	+Plural	1.Plu. Poss.	+Locative	+Relative
iş	+0	+LAr	+IbIz	+DA	+GI
iş	+0	+ter	+ibiz	+de	+gi
иш	+0	+тер	+ибиз	+де	+ги

Due to space limitation, we only give a simple example for how multi-word expression is taked as a single word. Example is inflection of *kara teke süz-*(get into trouble) in simple past tense for 3 rd person singular that is *kara teke süzdübü* (did he get into trouble).

get into trouble	+V	+Past tense	+Question
kara teke süz	+0	+DI	+BI
kara teke süz	+0	+dü	+bü
кара теке сүз	+0	+дү	+бү

Below is an example for suffix which are seen separately in surface form. This example is verb inflection of *al* (take) in present continuous tense for 1st person singular: *alıp catamın* (I am taking)

take	+V	+Present Cont.Tense	Verbal Adverb	Person Suffix
al	+0	+Ip_cat	+A	+mIn
al	+0	+ıp0cat	+a	+mın
ал	+0	+ып жат	+а	+мын

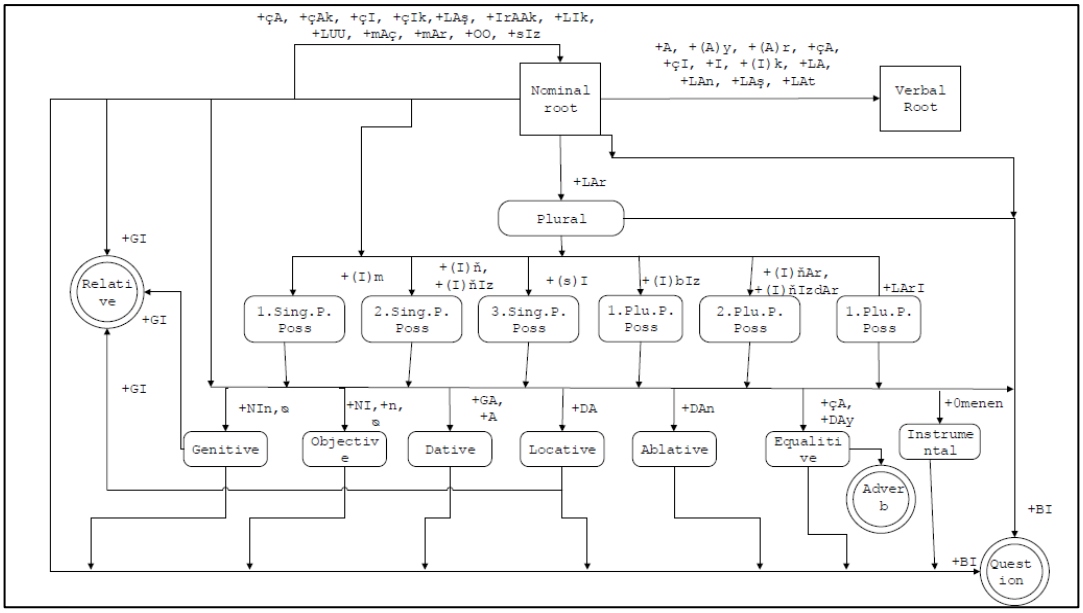

Figure 14. Partial nominal morphotactics for Kyrgyz

Below we give a screen shot of the generator where orthographic rules are tested. In the text input box, a root or stem from the root lexicon along with a number of morphemes (suffixes) are specified. System generates the surface form from the given lexical form of the word as shown in Figure 15**Error! Reference source not found.**. Morphological parsing is shown in Figure 16Figure 16 where a surface form is given in the text box and resulting morphological parsers are listed below.

In Figure 15 and Figure 16, we can see generation and parsing of *–işteribizdegi*" (the one that in our business).

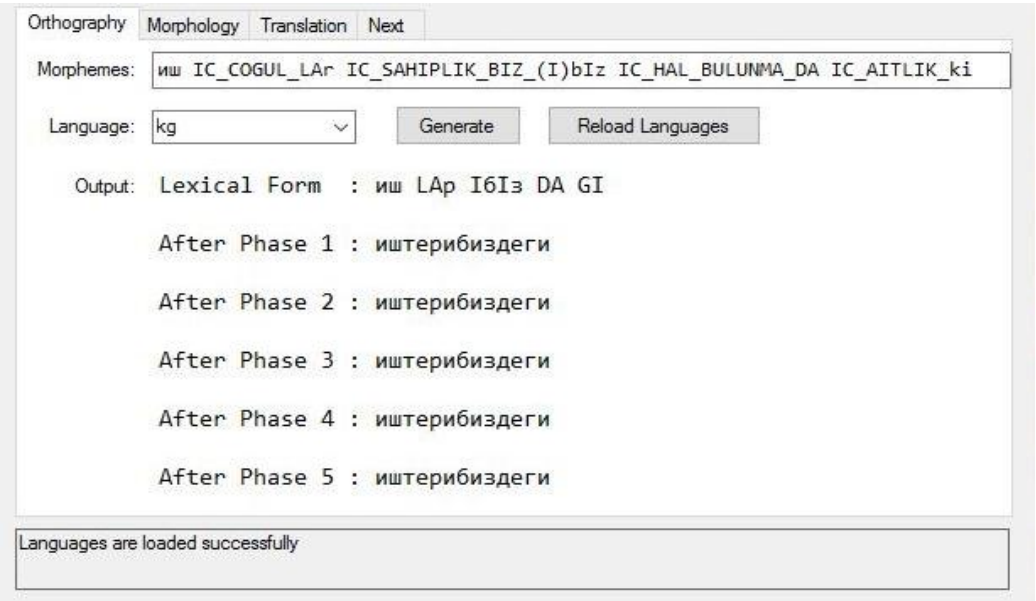

Figure 15. Morphological generation in NUVE

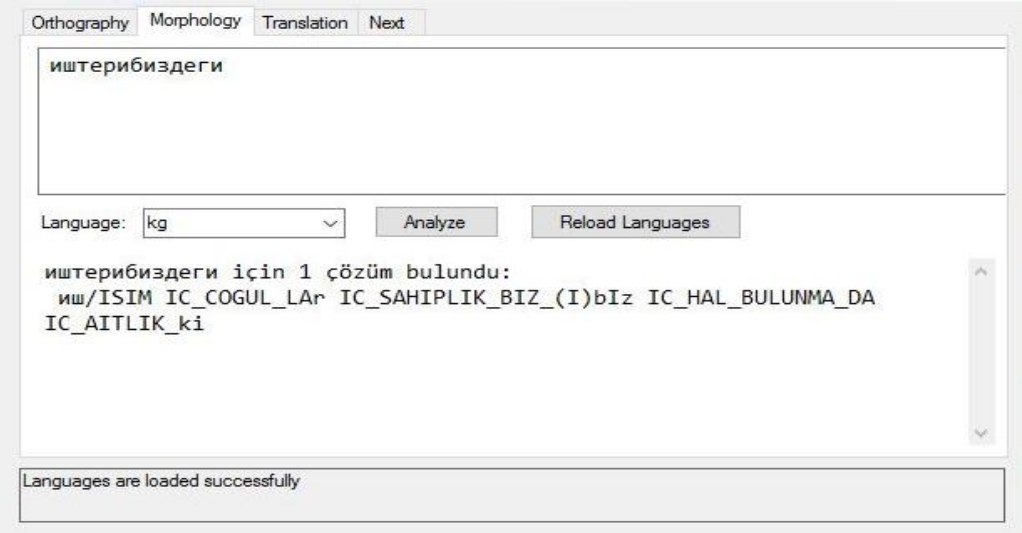

Figure 16. Morphological parsing in NUVE

38. CONCLUSION

The morphological description is one of the first steps in studying a language in computational linguistics. The morphological parsing is also used in further linguistically processing such as syntactic and semantic analysis. In this paper we give a concise presentation of a two level description of Kyrgyz morphology in terms of orthographic rules and FSAs which are implemented using a new NUVE machine translation framework for agglutinative languages.

We this implementation we are able (i) specify Kyrgyz in original Cyrillic alphabet (ii) parse words with multi suffixes written separately (ii) process multi word expressions as a single word. This paper presents an important step in our Kyrgyz Turkish machine translation project. We have so far Turkish and Kyrgyz morphological generation and parsing. We are currently testing Kyrgyz morphology with a comprehensive nearly fifty thousand root lexicon.

REFERENCES

[82]. Koskenniemi, K., ―Two-Level Morphology: A General Computational Model of word-form recognition and production", Tech. Rep. Publication No. 11, Department of General Linguistics, University of Helsinki, 1983
[83]. Karttunen L., (1983) ―PC-KIMMO: A General Morphological Processor", In Texas Linguistics Forum 22, pp.165-186.
[84]. Alam, Y.S., ―Two-level Morphological Analysis of Japanese", Texas Linguistics Forum 22, pp. 229-252, 1983
[85]. Antworth, E.L., ―PC-KIMMO: A Two-level Processor of Morphological Analysis", Summer Instıtute of Linguistics, Dallas, TX., 1990
[86]. Kim, D. B., Lee S. J., Choi, K.S., and Kim, G.C., ―A two-level morphological analysis of Korean", In Proceedings of the 15th conference on Computational linguistics - Volume 1 (COLING '94), pp. 535-539,1994
[87]. Oflazer K., ―Two-Level Description of Turkish Morphology", Lit. Linguist. Comput., vol. 9, no. 2, p. 13, 1994
[88]. Tantuğ A.C., Adalı E. & Oflazer K.,―Computer Analysis of the Turkmen Language Morphology". In: FinTAL, Lecture Notes in Computer Science, pp. 186-193. Springer.2006
[89]. Shylov M., ―Two Level Turkmen Morphology and a Turkmen Turkish Machine Translation", Master's Thesis, Fatih University, Istanbul, Turkey, 2010
[90]. Zafer H.R, et al, ―Two-Level Description of Kazakh Morphology", 1st International Conference on Foreign Language Teaching and Applied Linguistics, 2011
[91]. Görmez Z., Ünlü Baki S., Kurt A., Kulamshaev K. & Kara M.,"An Overview of Two-Level Finite State Kyrgyz Morphology", Aydin, Turkey, 2011
[92]. Hamzaoğlu, I., ―Machine translation from Turkish to other Turkic languages and an implementation for the Azeri language". Master's thesis, Bogazici University, 1993
[93]. Altıntaş K & Çicekli İ.," A Morphological Analyser for Crimean Tatar". In: Pro-cedings of the 10th Turkish Sym on AI and NN TAINN pp 180-189, North Cyprus, 2001
[94]. Shylov M., ―Dilmaç: Turkish and Turkmen Morphological Analyzer and Machine Translation Program", Master _s Thesis,Fatih University, Istanbul, Turkey, 2008
[95]. Keskin R., ―Two Level Uyghur Morphology and Uyghur Turkish Machine Translation", Master's Thesis, Fatih University, Istanbul, Turkey, 2012
[96]. Oflazer K., Göçmen E. & Bozşahin C., ―An Outline of Turkish Morphology", Report on Turkish Natural Language Processing Initiative Project, 1994
[97]. Çengel H. K., Kırgız Türkçesi Grameri (Ses ve Şekil Bilgisi), 2005
[98]. H. R. Zafer, ―Nuve: A Natural Language Processing Library for Turkish in C#" [Online]. Available: https://github.com/hrzafer/nuve. [Accessed: 05-Jul-2015].

Improve the Classification Success of Fatty Liver Disease by Using Feature Weighting Method

Yavuz Ünal[20], Kemal Polat [21], Mustafa Çapraz[3], Aylin Çapraz[4]

Abstract

This study aimed to increase the performance of classification of fatty liver disease by using one of the feature weighting methods, fuzzy c-means clustering based feature weighting method. To classify the fatty liver disease, eleven different blood test analysis values such as AST, ALT, LDL, and HDL were used as feature vector. Data set was obtained from the specialists at Amasya University Sabuncuoğlu Şerefeddin Research and Application Hospital. Firstly, raw data of 300 patients was classified by means of five different classification algorithm such as k nearest neighbor (k-NN), Multi-Layer Perceptron (MLP), support vector machine (SVM), Naïve Bayes and decision Tree. Then, these classified data was weighted by means of fuzzy c-means clustering based feature weighting method and was once again classified by means of the aforementioned five different classification algorithms. Results showed that 60% of the classification success of fatty liver illness increased up to the level of 90%.

Keywords: feature weighting, machine learning, fuzzy c-means clustering, fatty liver

39. INTRODUCTION

Liver has numerous important duties in our body such as decontamination of harmful substances in blood, turning what we eat into energy. While performing its duties, it is considered normal in this life-sustaining organ to have a little fat[1].

Abnormal fat deposits in liver cells are called fatty liver or ~~h~~epatosteatosis". Although seen quite often, fatty liver is extremely an issue that needs to be taken seriously because this fatty liver problem may trigger an inflammatory reaction which could also cause cirrhosis[2].

There could be many reasons of fatty liver. The most often causes are excessive use of alcohol, obesity and malnutrition habits.

Malnutrition, sedentary lifestyles and alcohol use, nowadays, cause this disease to be seen quite often in developed countries[3].

Disease diagnosis via machine learning methods has been one of the most widely used methods for the last 20 years[1].

In this study, whether patients have fatty liver disease was determined via the machine learning method through data obtained from blood values. Firstly, raw data of 300 patients was classified by means of five different classification algorithm such as k nearest neighbor (k-NN), Multi-Layer Perceptron (MLP), support vector machine (SVM), Naïve Bayes and decision Tree. Then, these classified data was weighted by means of fuzzy c-means clustering based feature weighting method and was once again classified by means of the aforementioned five different classification algorithms.

40. MATERIALS AND METHODS

In this part, the data used in the study were touched on with the methods we used.

40.1. Database

The data used in the study were obtained from Sabuncuoğlu Şerefeddin Research and Application Hospital, Amasya University. The data from 300 patients were used. Simple statistical values of these patients are given in Table 1.

Table 5. Statistical Values of the Patients

Text	Text

[20] *Corresponding author: Amasya University, Department of Computer Engineering, 34220, Amasya, Turkey. yavuz.unal@amasya.edu.tr*

[21] *Bolu Abant İzzet Baysal University, Electrical and Electronics Engineering Department, Faculty of Engineering, kemal_polat2003@yahoo.com*

[3] *Amasya Universiy Sabuncuoğlu Şerefeddin Research and Application Hospital, mustafa.capraz@amasya.edu.tr ,Amasya Turkey.*

[4] *Amasya Universiy Sabuncuoğlu Şerefeddin Research and Application Hospital,draylincapraz@yahoo.com, Amasya, Turkey*

The number of patients	300
Age average	54.4
Male	146
Female	154

The data included into the classification are blood values. These values are 11 in total: AST, ALT, GGT, LDH, T.BIL, ALP, TKOL, TG, LDL, HDL and Grade.

Table 2. Statistical Values of Blood Values

Text	Min.	Max.	Mean	StdDev
AST	11	102	35.853	18.457
ALT	17	114	42.251	18.656
GGT	24	164	52.639	26.529
LDH	84	302	194.321	39.109
TBIL	0.41	1.4	0.863	0.233
DBIL	0.21	1.21	0.644	0.263
ALP	12	185	97.9	17.237
TKOL	11	369	233.201	49.472
TG	105	620	291.415	120.7
LDL	100	280	170.585	40.403
HDL	20	84	38.492	12.541

These data were additionally classified in 3 grades as Grade 1, Grade 2 and Grade 3. There are 108 patients in Grade 1, 107 patients in Grade 2 and 85 in Grade 3.

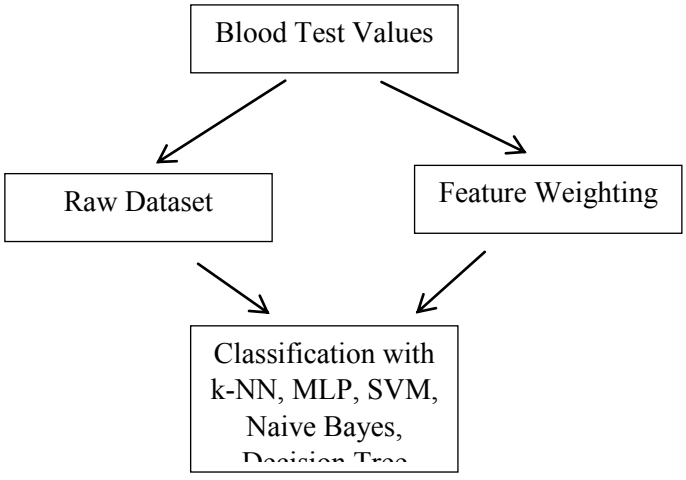

Figure 1. The flow chart of this study

The flow chart of the study conducted is given in Figure 1. The data obtained from the patients were accordingly classified first as raw without weighing. Feature weighting method (FCM) was then applied, and results are indicated in the relevant part.

40.2. Feature weighting

The success of classification algorithms generally depends on the quality of data operated on. If the data is not proper, classification algorithms may underachieve or get less intelligible results. In order to increase the success of data classification, various data preprocessing methods are used. Therefore, data preprocessing are of quite importance for classification algorithms. One of the data preprocessing methods is data or feature weighting. By the weighting, an increase for an easier data classification is targeted [4].

Fuzzy C means feature weighting, one of the data weighting methods, was used in this study.

Fuzzy C-Means Feature Weighting Method:

FCM based feature weighting method was explained in details in our previous studies. Thus, it will be briefly mentioned.

The main aims of FCM clustering algorithm are both to transform a linearly non-separable dataset to a linearly separable one and to increase the distinguishing performance between classes. In order to make these processes happen, the clustering centres of features have been found. Then, the ratios of centres of features to the means of features have been calculated and these ratios have been multiplied with each datum in features dimension by dimension [5].

The FCM is briefly explained as follows: FCM is one of the most popular fuzzy clustering algorithms [6]. FCM was realised by Bezdek [7]. FCM attempts to find a partition for a set of data points $x_j \in R^d, j = 1,\ldots,N$ while minimising the cost function (Equation 1) [8].

$$J(U,M) = \sum_{i=1}^{c} \sum_{j=1}^{N} (u_{i,j})^m D_{ij} \quad (1)$$

where $U = [u_{i,j}]_{cxN}$ is the fuzzy partition matrix and $u_{i,j} \in [0,1]$ the membership coefficient of the *j*th object in the *i*th cluster (Xu and Wunsch 2005); $M = [m_1,\ldots,m_c]$ the cluster prototype matrix; $m \in [1,\infty]$ the fuzzification parameter; and $D_{ij} = D(x_j, m_i)$ the distance measure between x_j and m_i [5].

40.3. Feature Classification

The aim of machine learning algorithms is to allocate objects in classes, based on measurements conducted on the objects [5].

In this study, k-NN, MLP, SVM, Naïve Bayes and Decision Tree were used as classification algorithms.

The classification algorithms that we used in the study are explained briefly as they are the popular ones.

40.4. k-NN Classifier

After applying feature weighting method (FCM) on the data, they were classified with k-NN algorithm. k-NN is the simplest one amongst all machine learning algorithms. To put it simply, it works with the principle of considering the distance of k piece with the distance of the previous data which is intended to be classified. Of distance measurements, generally Euclid Distance can be used. Euclid Distance formula [9];

$$d(i,j) = \sqrt{\sum_{k=1}^{p} (x_{ik} - x_{jk})^2} \quad (2)$$

k value was determined as 1 in the study.

40.5. MLP Classifier

An Artificial Neural Network (ANN) is a mathematical model consisting of inter-correlated elements that have a similar structure with human brain. An artificial neural network is trained with the most appropriate data samples in order to explain the relation between inputs and outputs. That way, when a new entry is checked in the trained artificial neural network, correct and proper outputs can be acquired [10], [11].

The artificial neural network model used in our study to classify the data is multilayer perceptron model. Parameters in this model are;

The used activation function: Sigmoid

The learning rate: 0.3.

The momentum rate: 0.2.

The number of epochs: 500.

40.6. SVM Classifier

Another method used for classification problems is Support Vector Machines (SVM). This method fulfill classifications by means of a linear or non-linear function. Support Vector Machines are based on the principal of estimation of the best function to separate the data. The data have different properties according to linear separability and linear non-separability [12],[13],[14].

40.7. Naïve Bayes Classifier

It is used for statistical techniques in classification processes. One of these is the naïve bayes classifier. If the occurrence of an event depends on the existence of some conditions, ~~"c~~onditional probability" is in the question.

$$P(A|B) = \frac{P(B|A)P(A)}{P(B)} \quad (3)$$

$P(A|B)$; The occurrence probability of the event A when the event B occurs.

$P(B|A)$; The occurrence probability of the event B when the event A occurs.

$P(A)$ and (B) ; Prior probability of the events A and B. [15].

40.8. Decision Tree Classifier

Another data classification method is the decision tree. Decision tree is like flowcharts. Each qualification is represented by a node. Branches and leaves are the elements of the tree. The latest structure is the ~~"l~~eaf", the top structure is the ~~"r~~oot" and the ones in between are called the ~~"b~~ranches". The decision trees provides an appropriate substructure in order to apply classification algorithms.

One of the most important problems with decision trees is the question of what criterion the branching will be based on from any root.

In our study, C4.5 decision tree algorithm was used. This algorithm is of the ones based on entropy [15].

41. RESULTS

3.1 *Performance measures*

As the performance measures, the classification accuracy have been used and explained as follows. In training and testing 10 cross-fold validation has been used.

The confusion matrix is shown in Table 3 (actual vs.predicted) and the other parameters which are computed using confusion matrix are shown with the following formulas.

Classification accuracy(%):

$$\frac{TP+TN}{TP+FP+TN+FN} x100 \quad (4)$$

Table 3. Confusion matrix

Confusion matrix	No	Yes
No	TN	FP
Yes	FN	TP

Note: TP,TN,FP and FN denote True positive, true negatives, false poisitives and false negatives

Before weighting, blood values from 300 patients were classified via k-NN, MLP, SVM, Naïve Bayes and Decision Tree algorithms. Then, they were weighted with feature weighing method (FCM) and classified via k-NN, MLP, SVM, Naïve Bayes and Decision Tree algorithms. Acquired results are given in tables below. Classification accuracy of raw dataset classified with k-NN algorithm is, accordingly, 43.81%. For the dataset weighted with FCM, 86.95% classification accuracy was obtained, which is high. Classification accuracies of raw and weighted datasets classified with k-NN can be seen in Table 3.

Table 3. The results obtained in the classification of raw and weighted datasets using k-NN classifier

Used dataset	**Classification accuracy (%)**
Raw dataset	43.81
Weighted dataset	86.95

Classification accuracy of raw data classified with MLP algorithm is 49.16%. As for the data weighted with FCM, a high classification accuracy, 89.96%, was obtained. Classification accuracies of raw and weighted datasets classified with MLP can be seen in Table 4.

Table 4. The results obtained in the classification of raw and weighted datasets using MLP classifier

Used dataset	**Classification accuracy (%)**
Raw dataset	49.16
Weighted dataset	89.96

Classification accuracy of raw data classified with SVM algorithm is 55.18%. As for the data weighted with FCM, a high classification accuracy, 86.28%, was obtained. Classification accuracies of raw and weighted datasets classified with SVM can be seen in Table 5.

Table 5. The results obtained in the classification of raw and weighted datasets using SVM classifier

Used dataset	**Classification accuracy (%)**
Raw dataset	55.18
Weighted dataset	86.28

Classification accuracy of raw data classified with Naïve Bayes algorithm is 55.18%. As for the data weighted with FCM, a high classification accuracy, 87.62%, was obtained. Classification accuracies of raw and weighted datasets classified with Naïve Bayes algorithm can be seen in Table 6.

Table 6. The results obtained in the classification of raw and weighted datasets using Naïve Bayes classifier

Used dataset	Classification accuracy (%)
Raw dataset	55.18

Classification accuracy of raw data classified with decision tree algorithm is 55.18%. As for the data weighted with FCM, a high classification accuracy, 92.30%, was obtained. Classification accuracies of raw and weighted datasets classified with decision tree algorithm can be seen in Table 7.

Table 7. The results obtained in the classification of raw and weighted datasets using Decision Tree classifier

Used dataset	Classification accuracy (%)
Raw dataset	50.50
Weighted dataset	92.30

Therefore, the best classification accuracy was obtained from decision tree algorithm with 92.30%. Besides, classification accuracy of weighted data almost doubled the raw data. In cases in which classification of medical data is not easy, it is clearly seen that weighting substantially increases the classification success.

ACKNOWLEDGMENT

This study was supported by Scientific Research Projects, Amasya University, within the scope of FMB-BAP 15-0158 project number.

REFERENCES

[99]. S. E. Seker, Y. Unal, Z. Erdem, H. E. Kocer ―Correlation Between Liver Analysis Outputs ―, SCI 2013 (System, Control and Informatics) Proceedings of the 2013 *International Conference on Systems, Control and Informatics (SCI 2013)*, Venice, Italy, Sept, 28-29, 2013, ISBN: 978-1-61804-206-4 , pp. 217-222.

[100]. G.Li, Y.Luo,W. Deng, X. Xu,A. Liu and E.Song , ―Computer Aided Diagnosis of Fatty Liver Ultrasonic Images Based on Support Vector Machine", *30th Annual International IEEE EMBS Conference*, Vancouver, British Columbia, Canada, August 20-24, 2008.

[101]. C. Wang, T. Chen, K., Chen, C. Lu. ―Classification of Nonalcoholic Fatty Liver Ultrasonography by Significant Image Features", *IEEE 2nd International Symposium on Next-Generation Electronics (ISNE)* - February 25-26 , Kaohsiung , Taiwan.

[102]. K. Polat, The Investigation of Effect of Data Pre-Processing Techniques To Classification Accuracy On Medical Diagnosis In Biomedical Signals, PhD. Thesis. Selçuk University, 2008, Konya.

[103]. K. Polat , Classification of Parkinson's disease using feature weighting method on the basis of fuzzy C-means clustering

[104]. Höppner, F., Klawonn, F., and Kruse, R. , *Fuzzy Cluster Analysis: Methods for Classification, Data Analysis,and Image Recognition*, New York: Wiley, 1999.

[105]. Bezdek, J.C. , *Pattern Recognition With Fuzzy Objective Function Algorithms*, New York: Plenum Press 1981.

[106]. Xu, R., and Wunsch II, D. , „Survey of Clustering Algorithms', IEEE Transactions on Neural Networks, 16, 645–678, 2005.

[107]. N. Cheung, ―Machine learning techniques for medical analysis ", School of Information Technology and Electrical Engineering, BsC thesis, University of Queenland, 19 Oct. 2001.

[108]. C.M. Bishop, *Neural Networks for Pattern Recognition*, Oxford University Press, New York, 1995.

[109]. S. Haykin, Neural Networks: A Comprehensive Foundation, 2nd ed., Prentice-Hall, India, 1998.

[110]. V. Vapnik, O. Chapelle, Boundsonerror expectation for support vector machines, Neural Comput. 12(9)(2000) 2013–2036.

[111]. C. Huang, L.S.Davis and, J.R.G.Townshend, An assessment of support vector machines for land cover classification, *Int.J.RemoteSens*.23(4)(2002) 725–749.

[112]. S. Abe, *Support Vector Machines For Pattern Classification*, Springer, London, 2005.

[113]. Y. Özkan, *Data Mining Methods*, Papatya Publisher.2008 (in Turkish)

Proper Mesh Size Determination of Melamine Impregnated Paper (MIP) in Particleboard Manufacturing as an Adhesive Replacement

İbrahim Halil BaĞboğa[22], Fatih Mengeloğlu[23], Kadir KarakuŞ[24], İlkay Atar[25]

Abstract

This study investigated the proper mesh size and rate of waste melamine impregnated paper (MIP) in particleboard manufacturing. First, waste melamine impregnated paper (MIP) granulated in Pulverizator with cooling capabilities into the flour form. Three different sizes (small (passed from 0,1mm sieve), medium (between passed from 0,6mm and stayed on 0,1mm sieve) and large (between passed from 4mm and stayed on 0,6mm sieve)) and four different rates (%10, 15, 20, 25) of MIP were used in this study. Mechanical and physical properties including bending strength, modulus of elasticity, internal bond strength, surface stability, thickness swelling and water absorption of the samples were determined according to TS EN 310, TS EN 319, TS EN 311 and TS EN 317 standards, respectively. Based on the results, mesh size and rate of MIP had significant effect on all mechanical and physical properties investigated. The best result was obtained when 25% small size MIP was used. As a result, small size MIP might be utilized as an adhesive replacement in particleboard manufacturing providing economic and environmental benefits.

Keywords: Melamine impregnated paper waste, mechanical and physical properties, mesh size

42. INTRODUCTION

Melamine impregnated paper (MIP) is decorative paper for wood based boards. Those papers are used for surface coating on boards. The main aim of the coating is to have a better visual for wood based board products. In addition, it helps to keep humidity at the best levels for products. The coating also approves the mechanical properties and bans the nocuous gases releasing such as formaldehyde, pesticides, etc. [1]. Two and half million of MIP wastes occur for a year during the coating in a middle density board plant which uses 420 million m2/year MIP, approximately.

Wood based panels generates wastes such as chips with resin, melamine impregnated paper (MIP), non-standard board, etc. Portion of them were reused in manufacturing panels while some other were utilized for generating energy [2]. MIP contains chemicals (adhesives, curing agents, crosslinking agents, etc.) and it is not suitable for generating energy through burning them. It is required special running boilers at higher temperatures [3]. Researches have looked for alternatives to utilize these wastes. Ayrılmış [4] grinded MIP with hammer-mill the size of 2-3mm and utilized them with glued fibers in fiberboard manufacturing. It was reported that mechanical properties approved with the adding of MIP. In another study, Alpar and Winkler [5] have used MIP powder in the manufacture of particleboard as a both filler and adhesives. As a result, no significant differences were found between particleboard manufactured with UF adhesives and the one with MIP powder. In this study, single-layer particleboards were manufactured and there is no information about MIP size. Commercial particleboards have three layers.

In this study, proper mesh size and rate of waste melamine impregnated paper (MIP) to be used in particleboard manufacturing was investigated. On this purpose, three-layers particleboards were manufactured with three different sizes (small, medium and large) and four different rates (%10, 15, 20, 25) of MIP for this study. Mechanical and physical properties of the samples were determined according to TS EN 310, TS EN 319, TS EN 311 and TS EN 317 standards.

43. EXPERIMENTAL

43.1. Materials

Particleboards were manufactured utilizing waste melamine impregnated paper (MIP) and 2 different types of chip (fine and coarse). MIP waste, which obtained when the neat décor papers were impregnated (in the impregnation line) with melamine

[22] *Corresponding author: Kahramanmaras Sutcu Imam University, Department of Forest Product Engineering, 46100, Onikişubat/Kahramanmaraş, Turkey. ihbasboga@ksu.edu.tr*

[23] *Kahramanmaras Sutcu Imam University, Department of Forest Product Engineering, 46100, Onikişubat/Kahramanmaraş, Turkey. fmengelo@ksu.edu.tr*

[24] *Kahramanmaras Sutcu Imam University, Department of Forest Product Engineering, 46100, Onikişubat/Kahramanmaraş, Turkey. karakus@ksu.edu.tr*

[25] *Kahramanmaras Sutcu Imam University, Department of Forest Product Engineering, 46100, Onikişubat/Kahramanmaraş, Turkey. iatar@ksu.edu.tr*

urea formaldehyde and other chemicals, was got from Kastamonu Integrated Adana MDF Facility. Chips were obtained from Kastamonu Integrated Tarsus Particleboards Facility.

43.2. Particleboard Manufacturing

Waste melamine impregnated paper (MIP) granulated in Pulverizator with cooling capabilities into the flour form. Three different sizes (small (passed from 0,1mm sieve), medium (between passed from 0,6mm and stayed on 0,1mm sieve) and large (between passed from 4mm and stayed on 0,6mm sieve)) and four different rates (%10, 15, 20, 25) of MIP were used for this study. Twelve different particleboards with three layers (two surface layers and one core layer) were manufactured. Fine chips were utilized in surface layers while coarse ones in core layer. Same rate and size of MIP was used for all layers for each board. The core layer was accounted for 67% of the total board weight. Surface layers were contained 33% of the total board weight. The experimental design of the study was presented Table 1.

Table 6. Manufacturing schedule of Particleboards

Board-ID	MIP Size	MIP (%)	Chip (%)
1	Small	10	90
2	Small	15	85
3	Small	20	80
4	Small	25	75
5	Medium	10	90
6	Medium	15	85
7	Medium	20	80
8	Medium	25	75
9	Large	10	90
10	Large	15	85
11	Large	20	80
12	Large	25	75

Depending on the formulation chips and MIP were dry-mixed in a high-intensity mixer to produce a homogeneous blend. The blends were laid into frame of 500mm x 500mm. A hot press was used for forming of particleboards (0,5-4,8 MPa). The target thickness was 19mm. Pressing time and temperature were 240s and 200 °C, respectively. After pressing, particleboards were conditioned at a temperature of 20 °C and 65% relative humidity. The conditioned boards were cut from four edges and grinded until their thickness was 18mm. Then test samples were cut according to TS EN standards.

43.3. Particleboard testing

Testing of the samples was conducted in a climate-controlled testing laboratory. Densities were measured by air-dried density method according to the TS EN 323 standard. Bending strength, modulus of elasticity, internal bond strength, surface stability, thickness swelling and water absorption of the samples were determined according to TS EN 310, TS EN 319, TS EN 311 and TS EN 317 standards, respectively. Five samples for each group were tested. Mechanical properties testing were performed on Zwick Z010 (10KN).

43.4. Data analysis

Design-Expert® Version 7,0,3 statistical software program was used for statistical analysis.

44. RESULTS AND DISCUSSION

Particleboards were produced in the density range of 565-672 kg/m^3. In this study, mechanical (bending strength, modulus of elasticity, internal bond strength and surface stability) and physical (thickness swelling and water absorption) properties of all samples were determined. All values of the particlesboards produced with MIP were summarized in Table 2. The arithmetic mean and standard deviation values were given for each group in the table. ANOVA (analysis of variance) were performed and Interaction graphs (Figure 1-3) were presented.

Table 2. Mechanical properties of Particleboards

Group ID	Bending strength (MPa)	Modulus of elasticity (MPa)	Internal bond strength (MPa)	Surface stability (MPa)	Thickness swelling (%)	Water absorption (%)
1	13.67 (1.51)*	2312,24 (139,97)	0,418 (0,06)	1,02 (0,04)	17,74 (3,10)	94,01 (7,15)
2	15,7 (2,47)	2646,76 (359,12)	0,483 (0,078)	1,31 (0,14)	12,52 (1,24)	80,92 (6,64)
3	17,63 (5,34)	2664,39 (487,88)	0,518 (0,172)	1,19 (0,24)	10,32 (2,16)	90,29 (15,09)
4	18,22 (5,79)	2801,54 (593,49)	0,652 (0,199)	1,31 (0,35)	8,51 (1,10)	67,82 (6,45)
5	7,16 (0,71)	1687,39 (94,04)	0,046 (0,009)	0,39 (0,03)	32,89 (1,62)	107,73 (5,97)
6	8,59 (1,78)	1664,08 (207,26)	0,082 (0,029)	0,56 (0,08)	32,50 (4,34)	101,81 (6,28)
7	9,73 (1,76)	1889,16 (256,09)	0,167 (0,033)	0,53 (0,05)	17,89 (2,12)	72,63 (0,66)
8	10,02 (1,39)	1982,99 (438,84)	0,238 (0,046)	0,98 (0,12)	13,68 (0,52)	99,34 (6,22)
9	5,02 (1,78)	718,98 (457,70)	0,028 (0,004)	0,27 (0,15)	62,80 (3,49)	100,84 (2,08)
10	8,76 (2,27)	1854,80 (300,44)	0,128 (0,034)	0,53 (0,07)	30,57 (3,10)	102,92 (11,43)
11	9,80 (3,71)	1945,76 (498,16)	0,117 (0,028)	0,55 (0,03)	22,58 (2,51)	82,97 (2,00)
12	10,25 (1,29)	1986,02 (166,67)	0,192 (0,017)	0,68 (0,23)	16,75 (0,72)	71,93 (2,58)
Standard	≥ 13	Min. 1600	≥ 0,35	≥ 0,8	Max. 15	Max. 80

* Values in parenthesis are standard deviations.

The graph of internal bond strength was given in Figure 1. Based on results, MIP size and rate has significant effect on internal bond strength (P <0.0001). All produced particleboards with small size MIP powder provided better internal bond strength than the others. In addition, each group, which produced with small sizes MIP, was provided standards requirements. It is thought that the small particles were properly dispersed among chips in the mat. However, the both particleboards produced with medium and large MIP did not meet the standard requirements.

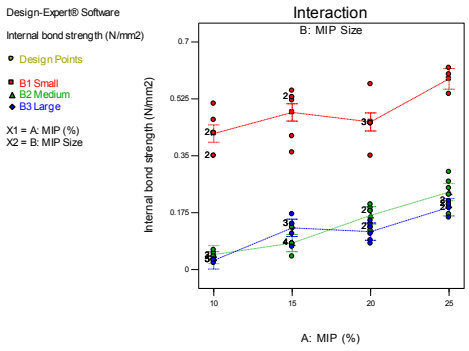

Figure 17. Interaction graphs of internal bond strength

Interaction graphs of bending strength and modulus of elasticity are shown in Fig. 2a and Fig. 2b, respectively. To mention of bending strength, MIP size is significantly important (P<0.0001). The best results were obtained manufactured particleboards with small size and 25% rate of MIP. All the boards, which produced with small size MIP, provided bending strength required values on standards while the others were dissatisfy. MIP size is also statistically important for modulus of elasticity (P<0.0001). If the interaction graphs for modulus of elasticity in the Fig. 2b will be examined, it will observed that with the addition of small size MIP, first it was increasing than values got slightly changed.

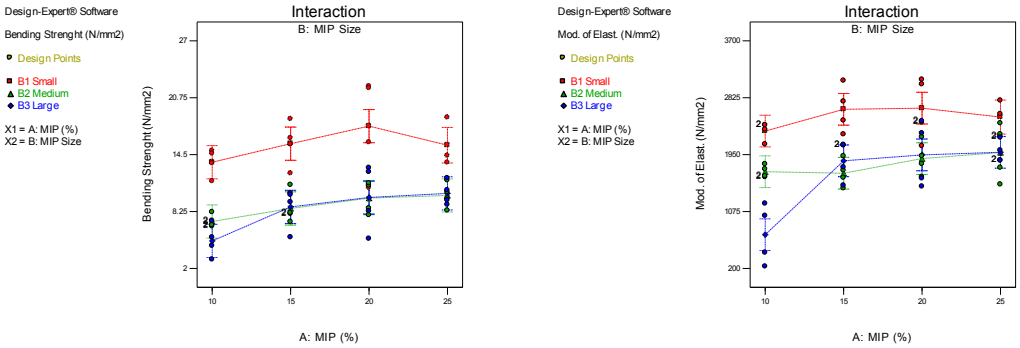

Figure 2. (a) Interaction graphs of bending strength *(b) Interaction graphs for modulus of elasticity*

Interaction graphs of thickness swelling, water absorption, surface stability and density are shown in Fig. 3a, Fig. 3b, Fig. 3c and Fig. 3d, respectively.

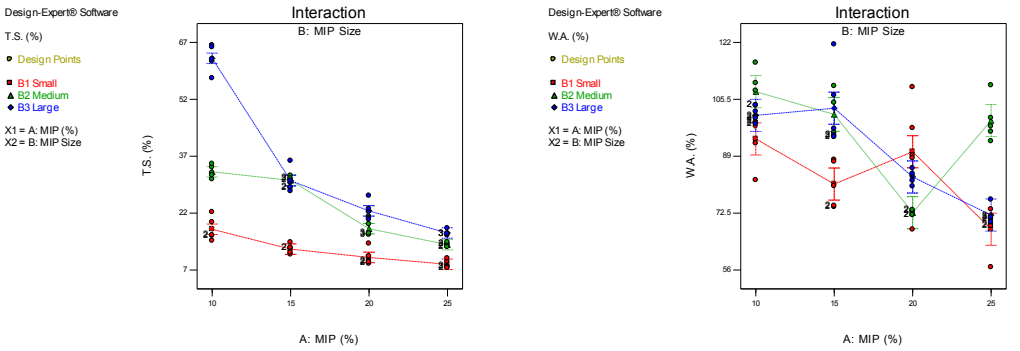

Figure 3. (a) Interaction graphs of thickness swelling *(b) Interaction graphs of water absorption*

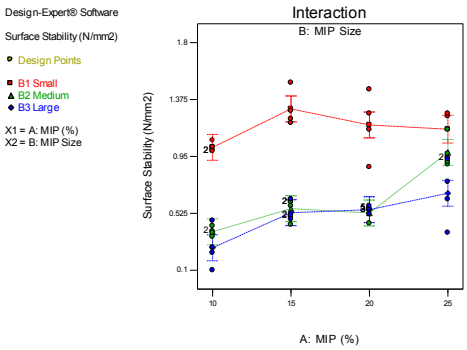

(c) Interaction graphs of surface stability

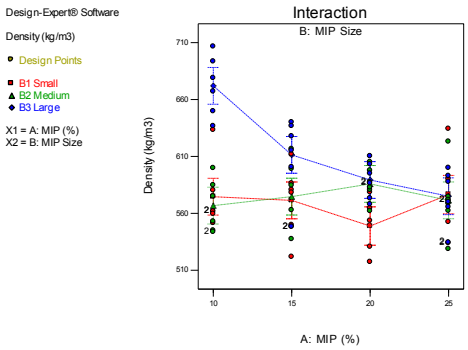

(d) Interaction graphs of density

Only the 25% small size MIP contained board‘ satisfied the requirements for both thickness swelling and water absorption. When the size of MIP gets smaller, specific surface area contrarily is large. That causes better adhesion between chips. It might the reason why the medium and large size MIP did not satisfy the requirements.

As shown in figure 3C., the best results obtained from small size MIP boards. It might explain with better distribution and also better adhesion. All the produced boards has nearly same density.

Moreover, all the data and standard requirement were summarized in Table 3. Values matching standards was painted in green and if not, it was painted in red.

Table 3. Summary of Mechanical and Physical properties of Particleboards

SIZE	RATE	B.S.	M.E.	I.B.S.	S.S.	W.A.	T.S.
Small	%10						
	%15						
	%20						
	%25						
Medium	%10						
	%15						
	%20						
	%25						
Large	%10						
	%15						
	%20						
	%25						
Standard Values		≥ 13	Min. 1600	≥ 0,35	≥ 0,8	Max. 80	Max. 15

B.S.: Bending Strength

M.E.: Modulus of Elasticity

I.B.S.: Internal Bonding Strength

S.S.: Surface Stability

W.A.: Water Absorption

T.S.: Thickness Swelling

In this study, the best MIP size and rate were investigated. It can observe from Table 3 that the best result was obtained from small size MIP and 25% rate. That board provided all standards requirements. Furthermore, the particleboards, which produced with small size MIP and 15%, 20% rates, were also over the standards except water absorption properties.

45. CONCLUSIONS

In this research, it was observed that the size and rate of waste melamine impregnated paper were statistically important for mechanical and physical properties of particleboards. Usage of the small size of MIP increased mechanical and physical properties of particleboards. All the rates for small size MIP reached the requirement values without water absorption and thickness swelling properties. However, other particleboards manufactured with medium and large size of MIP dissatisfied standards requirement for mechanical properties except modulus of elasticity.

Waste Melamine Impregnated Papers (MIP) was successfully utilized as an adhesive in manufacturing of Particleboard and the following conclusions were reached;

1. The board produced with 25% small size MIP, provided better mechanical and physical properties compared to other rates and sizes,
2. All boards with small size MIP provided required mechanical properties,
3. All boards with small size MIP might be utilized in particleboards manufacturing for dry areas.

As a result, the utilization of the proper size and rate of MIP waste in particleboards industry could provide extra income for manufacturers and clear environment for the people.

ACKNOWLEDGMENT

This study was supported by Ministry of Science, Industry and Technology in Ankara. Project number: 870.STZ.2015. Authors would also like to thank Kastamonu Integrated Adana MDF Facility for providing waste melamine impregnated paper (MIP) and chips.

REFERENCES

[114]. G. Nemli, S. Yıldız, E.D. Gezer, *Effects of melamine raw paper weight, varnish type and the structure of continuous pressed laminated (CPL) on the physical, mechanical properties and decay resistance of particleboard,* International Biodeterioration & Biodegradation, (56), pp. 166-172, 2005.
[115]. F. Mengeloglu, F. Bozkurt, I.H. Başboğa, Ö. Yüce, *Waste Melamine Impregnated Paper (Mip) In Thermoset And Thermoplastic Based Composites,* Pro Ligno, 11(4), pp. 165-172, 2015. Online Issn: 2069-7430.
[116]. M.C. Barbu, M. Steinwender, *The state of the art for the environmental protection in the European wood based panels industry,* Pro Ligno, 5(2), pp. 85-96, 2009.
[117]. N. Ayrılmış, *Enhancement of Dimensional stability and mechanical properties of light MDF by Adding melamine resin impregnated paper waste,* International Journal of Adhesion & Adhesive, 33:4549, 2012.
[118]. T. Alpar, A. Winkler, *Recycling of Impregnated Décor Paper in Particleboard,* Acta Silv. Lign. Hung., (2), pp. 113-116, 2006.
[119]. TS EN 310, Wood based panels determination of modulus of elasticity in bending and of bending strenght, TSE, Ankara, 1999.
[120]. TS EN 311, Wood-based panels - Surface soundness - Test method, TSE, Ankara, 2005.
[121]. TS EN 317, Particleboards and fibreboards – Determination of swelling in thickness after immersion in water, TSE, Ankara 1999.
[122]. TS EN 319, Particleboards and fibreboards- Determination of tensile strength perpendicular to the plane of the board, TSE, Ankara, 1999.
[123]. TS EN 323, Wood- Based panels- Determination of density, TSE, Ankara, 1999.

Arduino Based Wall Plug Control by Android Mobile Device

Kubilay TaŞdelen[26], Muhammed Hasan Tanrıöven[1], Cem Aybey[1], Sancar Kayalar[1]

Abstract

The idea of controlling the existing manually controlled devices remotely, make the life easier. Apart from the convenience, some systems become a lot more secure when monitored and controlled by such systems. The security issues cannot be easily monitored and tracked, when using traditional methods while remote controlling allows us to be able to see what is going on without really interfering with the system and take the necessary precautions before its too late. The protection of electrical devices is provided through some mechanical fuses. These mechanical fuses are not convenient when they are desired to be controlled remotely, due to the mechanical properties of the components and their likelihood of failure. Some devices may draw more current than desired from the power line. It is because of the devices present in the system such as motors, heaters. When such an event happens, it is expected to damage the wires that carry the power, the device itself or even to humans. With this project, the electrical devices which draw current from the 220V single phase line can be controlled in terms of preventing them from drawing more current than desired. When the current exceeds the limit, system can be protected by terminating the system. An Android device is used to monitor the drawn current values. The values that are read by the current sensor are processed by Arduino and sent to the Android device. The same software allows us to open/close the plugs and any problem that may occur can be prevented by doing so. With this study, all devices that are run from the single phase power line can be controlled remotely, and the users are warned/protected against the possible leakage currents. It is expected that the damages that can be harmful and fatal can be minimalized

Keywords: Remote Control, Wall Plug, Current Sensing, Android Application

46. INTRODUCTION

Electrical energy is one of the most essential concepts since all the devices, from the most complicated ones that are in the industry to the most basic household devices are run by the electrical energy. And the engineers and researchers are working on controlling the existing systems remotely as the technologic advancements are being applied to the everyday households more and more. And the since electrically run devices are everywhere, security is becoming an important issue to be considered. Namely electric shocks can be very harmful, even fatal and it also can damage the device itself. Figure 1 shows the mortality database of WHO due to electric shocks.

[26] *Corresponding author: Süleyman Demirel University, Faculty of Technology Merkez Isparta, 32000 Kayıköy/Isparta Merkez/Isparta, kubilaytasdelen@sdu.edu.tr , hasantanrioven@sdu.edu.tr , cemaybey@gmail.com, sancar_air@gmail.com*

[2]

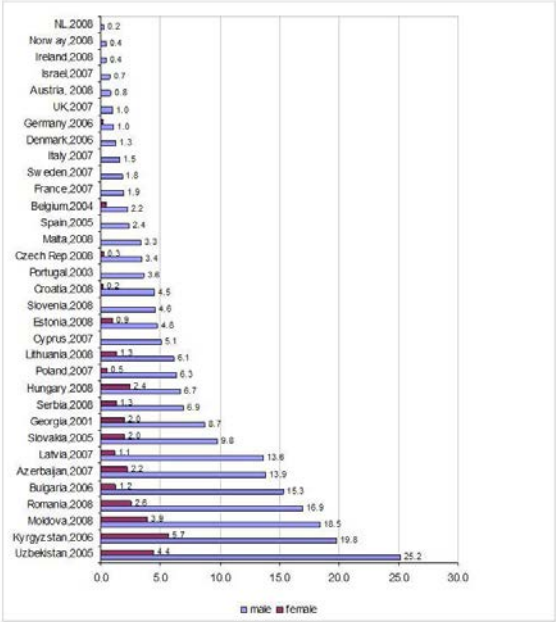

Figure 1. Data from the detailed mortality database of WHO reveals that mortality from electrical injuries

The monitoring process that has been achieved in this study refers to all kinds of industrial establishments. By the help of such a monitoring system, without really interfering with the system, the likelihood of the damages can be prevented. Automatic control applications such as smart home systems are using Arduino, and the need of using a PC is eliminated. This reduces the cost of the system significantly while the system maintains to perform the dedicated tasks. Data from multiple sensors can be obtained and processed simultaneously with success. In [1], such a smart home system was presented for the aspects such as feasibility, functionality and effectiveness. This kind of control systems are generally being developed for the home and SOHO environments [2]. The systems do not only consist the hardware, but also for the sake of convenience, some software are used to develop user interfaces. Different kinds of techniques such as Android, iOS, Windows Symbian, JAVA are used to keep track of the installed systems as well as providing the user an easier way to use and control the whole system [3]. But as the smartphones are on the rise, adopting these kind of systems to the cell phones are, for now, will provide most feasible interface that meets the demands. Both the smart home systems and robotics are controlled by the aid of Android OS very easily [4]. But being interested in controlling the current that flows through a device is not so common among the published papers related to such control systems although it poses a big problem.

As the current overflow and the faulty currents damage the equipment and worst of all, can cause serial damages to people, even death. So, having such a system is really beneficial. In order to satisfy this need, such a system is developed. The idea that lies behind this study is that the equipment that is connected to the automation systems in the industry can be controlled remotely in terms of current flow control, apart from the use of the regular fuse techniques. The current flow is read by the current sensor, and by the help of Arduino, the data is sent to the Android device where one can control the system via Bluetooth modules. This system also can limit the amount of current that flows. System can be further developed by the aid of wireless modules, as the scope of this study is only to demonstrate that such a system is convenient for further developments.

47. MATERIALS AND METHODS

The study that is presented in this article has been dedicated to perform a specific task. Such systems are called embedded systems. Embedded systems can come out in many forms during our daily life. There are various ways to build an embedded system and one of the most convenient ways to do it is by

the aid of the microcontrollers. Microcontrollers are used to perform complicated tasks in an automated fashion. There are various types of microcontrollers that can be used. Arduino is a physical programming card that has a microcontroller on board (i.e. Atmega 8, 168 and 328). Arduino also has many types that are commercially available.

Arduino like microcontroller boards have been used to develop systems. There are numerous articles that involves Arduino at some part of the study have been published. In various types of projects, from the ones that involve robotics to the ones that involves signal processing, Arduino provides a firm grip to handle the problems [5], [6].

The Android OS is an open source operating system primarily used in mobile devices. Written primarily in Java and based on the Linux operating system, it was initially developed by Android Inc. and was eventually purchased by Google in 2005. Android OS is a very useful tool to commercialize and make this study more feasible. Providing user friendly interfaces is very easy when Android OS is concerned. As there are cellphones everywhere, adjusting the system to be controlled by using the cellphone is very convenient [7].

As stated above, the current control and the limitation is the main issue in this study. To be able to achieve this goal, the current values need to be read and implemented within success. ACS712 current sensor is a sensor that is available for this kind of study. ACS712 provides economical and precise solutions for AC or DC current sensing in industrial, commercial, and communications systems. Typical applications include motor control, load detection and management, switched-mode power supplies, and overcurrent fault protection, which shows that is is most suitable to use in this context. The device consists of a precise, low-offset, linear Hall sensor circuit with a copper conduction path located near the surface of the die. Applied current flowing through this copper conduction path generates a magnetic field which is sensed by the integrated Hall IC and converted into a proportional voltage. Device accuracy is optimized through the close proximity of the magnetic signal to the Hall transducer. For more detailed information, the datasheet is available online [8].

The relays are controlled from the android device via Bluetooth, if they are in the open state, the current value is read. The current values that are acquired by the current sensor is displayed in the interface. If the current value is more than the limit that is set by the user, the system is shut down to prevent likely damages. The system continuously reads the amount of current and as long as the desired level of amount of current is not at hand, the system stays inactive. The flowchart of the system is shown in Figure 2.

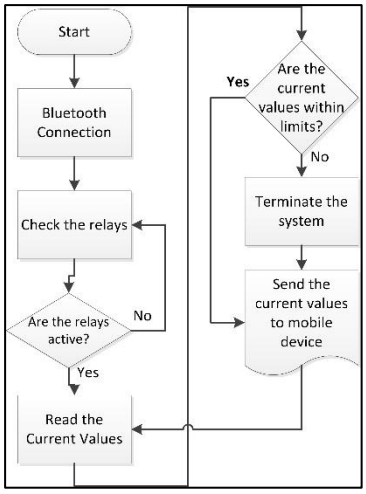

Figure 2. Flowchart of the system

The current sensor senses the current flow in the system and converts the current value so that the Arduino can read it. The processing takes places in the microcontroller and the data is sent to the Android device via Bluetooth modules. The control process of the relays is performed by the user with the Android device, so that the related relay can be opened and closed.

The Android interface of the system is presented in Figure 3. The relays have buttons as OPEN/CLOSE, and the number of relays that are present are shown on the screen. The first step to activate the software is the blue button above the relay sequence, which is connection to the Bluetooth module. After the connection the states of the relays are shown, open relays are indicated as green, and closed relays are indicated as red.

Figure 3. Interface

Beneath the yellow line that is written —amount of current that is drawn from the main power line, the actual current that is drawn is displayed in Figure 4.For the testing purposes, the limit value is set to be 9.2A. As the current value exceeds 9.2A, the system terminates and the possible damages were successfully prevented. Figure 5 shows that the system is terminated after overflow is detected

Figure 4. 2.11 A. of current is drawn, relay 1 and relay 4 are functional

Figure 5. System is terminated after the current value is more then the limit value

48. RESULTS AND DISCUSSION

In this study, the current limitation via the presented study is successfully demonstrated. Mostly for the industrial purposes, the current overflow is an unwanted situation. For a safer and uninterrupted working process, all kinds of unwanted and

unexpected factors should be eliminated. This study provides a safe wall plug system that can be monitored and controlled via an Android device through the Bluetooth modules. The current values are read by the current sensor which is connected to the Arduino programming card. The test results that are obtained showed that to use such a system will prevent the likely problems that are aimed to be solved at the beginning.

49. CONCLUSION

This study shows that, the existing problems regarding the overdrawing current from the power line can be simply avoided by replacing the existing wall plugs with the study that is presented in this article. The articles that have been published about current limitation, fault current detection systems are based on sophisticated technologies [9] while this work promises a simpler and cheaper solution. The system needs further improvements as the Bluetooth module which is used for the communication between Arduino and the Android device has a limited range. The authors only aimed to show that such a study can satisfy a need, and open for further developments. The modules that can enhance the communication range can be added to the system in order to provide the user to be able to monitor the system from more distant places.

REFERENCES

[124]. Shiu Kumar, ―Ubiquitous smart home system using Android Application" , International Journal of Computer Networks & Communications (IJCNC) Vol.6, No.1, January 2014
[125]. S.K.Tso, B.L.Luk, W.H. Choy, K.P. Liu, C.S. Chow, K.F. Leung, G. Lee, F. Yau and C.W. Lam, ―An intelligent networking and automation system for home and SOHO environments" The fourth International Conference on Control and Automation (ICCA'03), 10-12 June 2003, Montreal Canada.
[126]. Sharon N. Panth, Mahesh Narandas Jivani, ―Device Control in Ad-hoc Network Environment by using moSync for multiple platform mobile application development" ---S. Zhang, C. Zhu, J. K. O. Sin, and P. K. T. Mok, ―A novel ultrathin elevated channel low-temperature poly-Si TFT," *IEEE Electron Device Lett*., vol. 20, pp. 569–571, Nov. 1999.
[127]. Nicolas Oros, Jeffrey L. Krichmar, ―Smartphone Based Robotics: Powerful, flexible and Inexpensive Robotics for hobbyists, educators, students and researchers", CECS Technical Report, 13-16 November 26, 2013.
[128]. Chinmay Kulkarani, Suhas Grama, Pramod Gubbi Suresh, Chaitanya Krishna, Joseph Anthony, ―Surveillance robot using Arduino Microcontroller, Android APIs and Internet", 2014 First International Conference on Systems Informatics, Modeling and Simulation.
[129]. M. K. D. Ulaganathan, C. Saravanan, Olivia Ramya Chitrajnan, ―Cost-effective perturb and Observe MPPT Method using Arduino Microcontroller for a Standalone Photo Voltaic System" International Journal of Engineering Trends and Technology (IJETT) – Volume 8 Number 1- Feb 2014
[130]. Takashi Minato, Michihiro Shimada, Hiroshi Ishiguro Shoji Itakura, ―Development of an Android Robot for Studying Human-Robot interaction", Innovations in Applied Artificial Intelligence, Vol. 3029 pp 424-434
[131]. AVS712 Datasheet, Allegro.
[132]. Chin-Chang Hsu, Yen-Shin Lai, Bo Yuan Chen ―Novel Current Limitation Technique without Current Feedback for Digital-Controlled Battery Charger in UPS Applications" 2010, IEEE, 978-1-4244-5287-3/10 pp 4351-4355

River Simulation in GIS Software

M. Kazım. YETIK[1], Mehmet. YUCEER[2], Erdal. KARADURMUS[3]

Abstract

In human life water pollution is gradually becoming one of the major issue, so that to follow river quality control is very important in the world at present time. CIS software provides many important facilities to river quality control and model simulation and to follow the system for decision makers.

CIS software allows extensive presentation method and many visual effects to follow river system with remote monitoring facilities of the river. For these reasons, in this study written program represents an interactive and friendly Graphical User Interface (GUI) for decision makers.

For this purpose, Yeşilırmak river simulation program (AKAB) was written by using QUAL2E (river simulation model) as base program in MATLAB. In this work, AKAB program integrated in CIS program than all of them organized to represent the river situation for decision makers. They can follow the river pollution parameters in river line on the map. At the same time, this program provides statistical analysis and graph of water pollution parameters of river. This program shows river line with different color and its color is changing with the value of selected parameters on the map. Thus the program provides a user friendly GUI for decision makers.

Keywords*: GIS, Simulation, river quality control, Qual2E*

50.

51. 1.INTRODUCTION

The reliable assessment of water quality conditions in river streams has become a necessity for resource management and environmental control purposes. Water quality models should be able to predict consequences of planning scenarios and pollutant levels in receiving streams so that water quality standards can be met. The experimental work for collection of water quality data is relatively expensive requiring a quite large, sophisticated work force and equipment. Routinely collected data from surveys designed to check basin wide water quality for regulatory compliance are usually inadequate because they usually lack some of the critically important, but not easy-to-measure, constituents. Therefore a thorough account of real water conditions is needed for model calibration and verification. In the most recent extensive review on in-stream water quality modeling, Cox (2003)[1] selected 6 models with different degree of complexity in conceptualization and solution for detailed comparison, namely SIMCAT, TOMCAT, QUAL2E, QUASAR, MIKE-11 and ISIS, Among those selected, first three were steady state and the remaining were of dynamic character. SIMCAT and TOMCAT were stochastic models, while all the others being of mechanistic type. It is stated that the most widely used water quality model in the world was QUAL2E. Cox (2003)[1] concludes that all models contain assumptions and limitations that need to be understood if meaningful interpretations of the model simulations are to be made, and it is unfair to set one model against another in terms of broad applicability, but that a model of intermediate complexity, such as QUASAR, is generally well suited to simulate dissolved oxygen (DO) in river systems.

Only few reports are available in the current literature on integrated software development for river water quality monitoring. Indeed, to be mentioned in this regard are only Marsili Libelli et al.'s work. Their first attempt (Libelli et al. 2001)[2] towards geographical processing of environmental information was the development of a Dynamic Data Exchange (DDE) system between ArcVIEW and MATLAB. The test case was from a small river reach in Tuscany. They later (Marsili Libelli et. al. 2002)[3] approached the case from a different point of view, i.e. Developing the integrated package in entirely MATLAB environment by making use of Mapping Toolbox of MATLAB^{TM}. The software was tested with data from two small river reaches in Tuscany. They later extended their work to create an internet-based decision support system

Ganapathy, C. & Ernest A.N.S. (2004)[4] prepared water quality assessment using web based GIS and distributed Database Management System. The Spatial Decision Support System was developed for this study on the Lower Rio Grande river basin

52. 2.WATER QUALITY MODEL

There are some different water quality models, with some of them having already received extensive application. The situation of the art in river water quality modeling was summarized by Rauch et al. (1998)[5] with particular reference to coupling the river water quality models with models describing emissions from the drainage system and sewerage system. This paper explained and defined some issues related to the practical use of the river quality models. As for model identification and testing the authors (Rauch et al. 1998)[5] argue that in many practical applications of water quality models, heuristic approaches are followed to defined which parameters to adjust and to obtain a good fit, choosing parameter values manually

rather than by automated numerical techniques. Some of these procedures are difficult to perform and may lead to unrealistic parameter sets. Rauch et al. (1998) listed software product and compared 10 important software products from QUAL2 to WAP5 and Salmon-Q, with respect to some features related to hydrodynamics and transport, model structure and analytic features. According to them AQUASIM and DESERT software offer parameter estimation capability. AQUASIM is applicable to a wide class of aquatic systems, and its use for parameter identification of activated sludge models is discussed with a relatively simple example of a denitrification process.

According to Shanahan et al. 1998 [6] that the U.S. EPA‘s QUAL2 model is almost the standard for river water quality modeling. Cox (2003) [1] also notes that water quality modeling is an active area of research around the world, and underlines that only few papers refer to specific models with majority of the papers reporting applications with EPA‘s QUAL2E.

5.

53. 3.CASE STUDY: APPLICATION TO YESILIRMAK RIVER IN TURKEY

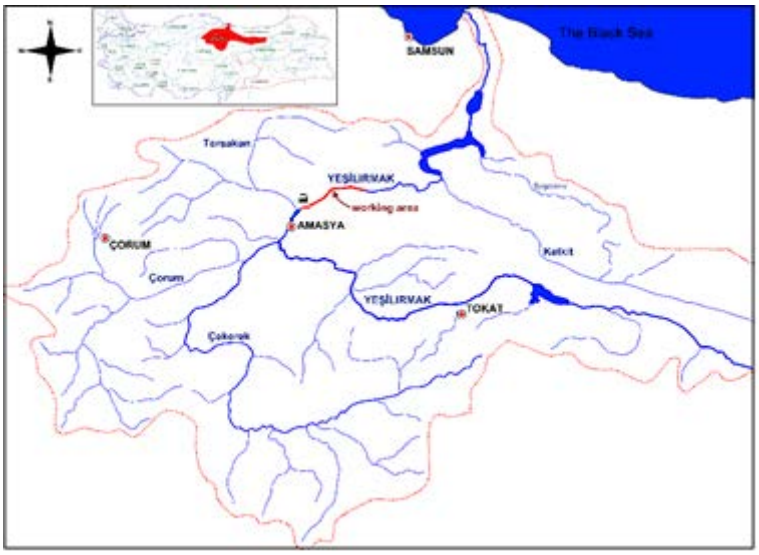

Figure. 1. Yesilirmak river basin and the study area.

6.

7. The created software was tested with off line data collected from field studies where is around the city of Amasya along Yesilirmak river in Turkey. Yesilirmak is one of the major rivers in Turkey with 450 km length, and a basin of 36114 km^2 comprising 4.63% of the territorial area of Turkey. Figure 1 shows the river map (basin).The study area started from the location 8.9 km east of the city center where a baker yeast plant was situated. The treated wastewater of this plant was considered as a point source to the river. The river water was sampled at 7 different locations in the downstream direction towards the Durucasu gauging station of State Hydraulic Works (DSI) and the town of Tasova. During the dynamic sample collection period, the effluent from the wastewater treatment plant of a baker yeast production plant was being discharged right beyond the starting point as shown in Figure. 2. Therefore, the results of the study indicated the extent of the pollution caused by the discharge from this industrial plant. In the simulations, addition of this discharge was considered as a continuous disturbance to the system, and its effect on the water quality, thus, was determined. Table 1 gives the characteristics of discharge from this local industrial plant.

Table 1. Characteristics of discharge from the local baker yeast plant variables to waste water of baker yeast plant

Variables	Waste water of baker yeast plant
Temperature (°C)	25.3
Flow (m^3/s)	0.25
Ammonia-N (mg/l)	27.4
Nitrite-N (mg/l)	1.3
Nitrate-N (mg/l)	52
Organic-N (mg/l)	0
Organic-P (mg/l)	0.52
Dissolved-P (mg/l)	12.4
BOD_5 (mg/l)	210
DO (mg/l)	7.2
Coliform (colonies/100 ml)	2900
Chloride (mg/l)	0

The initial conditions of the river and the characteristics of the point source as measured from points 1 and 2 indicated in Figure 2 were introduced into the written software, and dynamic simulation was run.

8.

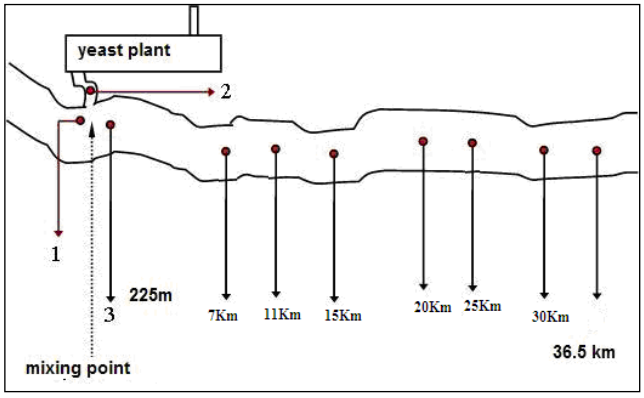

Figure. 2. Experimental study area for model verification, and sample collection points (distances indicated are measured from point 1).

Pollution level in Yesilirmak affects the agricultural and rural development directly by distorting the ecological balance. The basin of this river is a predominantly rural area and suffers from quite high level of pollution, in particular from agriculture, urban and industrial sources. When physical, chemical, organic and bacteriological parameters are considered, water quality of the river is classified in III and IV level according to the Water Pollution Control Act of Turkey,. An interactive river management decision support system for the region in order to protect the river from pollution becomes very important for sustainable development in the future. Therefore, Yesilirmak was chosen as the study area, where our previous studies had also been concentrated.

9. For field data collection, the concentrations of ten water-quality constituents indicative of the level of pollution in the river were determined either on-site by portable analysis systems or in laboratory after careful conservation of the samples.

10.

11. 4.MODELLING STUDIES

12. A new GIS platform integrated with a water quality model in MATLAB. In this work, a software has been developed in order to follow and analyse the river water quality in GIS platform. The program was particularly designed to simulate Yesilirmak river in Turkey. The software allows user interaction and visual effects so that the predictions for pollution constituents can be represented on a digital map of the river. ArcMap™ 9.1 was used as the GIS software. The River Stream Dynamic Simulation (RSDS) software previously developed in MATLAB™ in our research group Yuceer et al. (2007)[7] was used as the water quality model, and software was incorporated into the GIS platform. An essential factor in combining a MATLAB model with a GIS system is integrating the geographical data river pollution variables that are handled in MATLAB. Our research group used the data transfer strategy represented in Figure 3, which shows that the ASCII formatted text files were the medium of transfer between GIS (ArcMap™) and MATLAB™ ArcMap™ employs database files for displaying the digital maps. Microsoft ACCESS™ was employed as the database handling platform.

13.

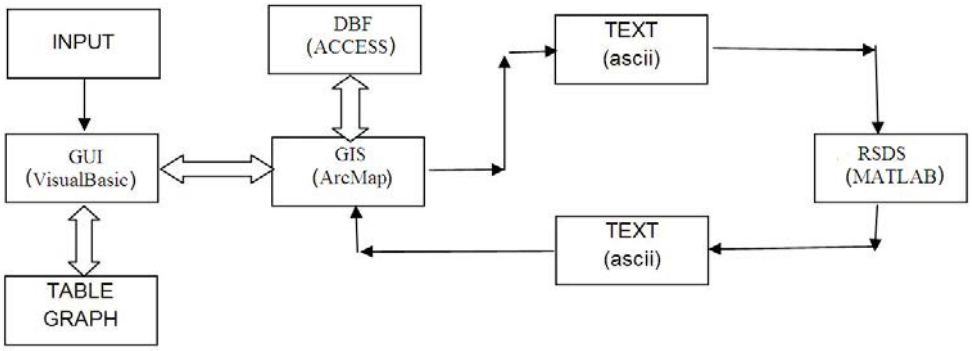

14.

Figure 3: Coordination of program

15.

All windows and menus of the GUI were designed in Visual Basic editor of ArcMap, they are illustrated in the following figure. The opening menu of the program is depicted in Figure 4 together with the input sheet for entering initial water quality conditions. The table on the left hand side of the window lists the water quality variables that can be monitored on the screen. Prior to any run for simulation and prediction, the user is expected to enter the initial water quality conditions at starting point of working area where the simulation will begin. If there is a point source to the river, it can also be taken into account and respective values can be entered via additional input sheets that will open.

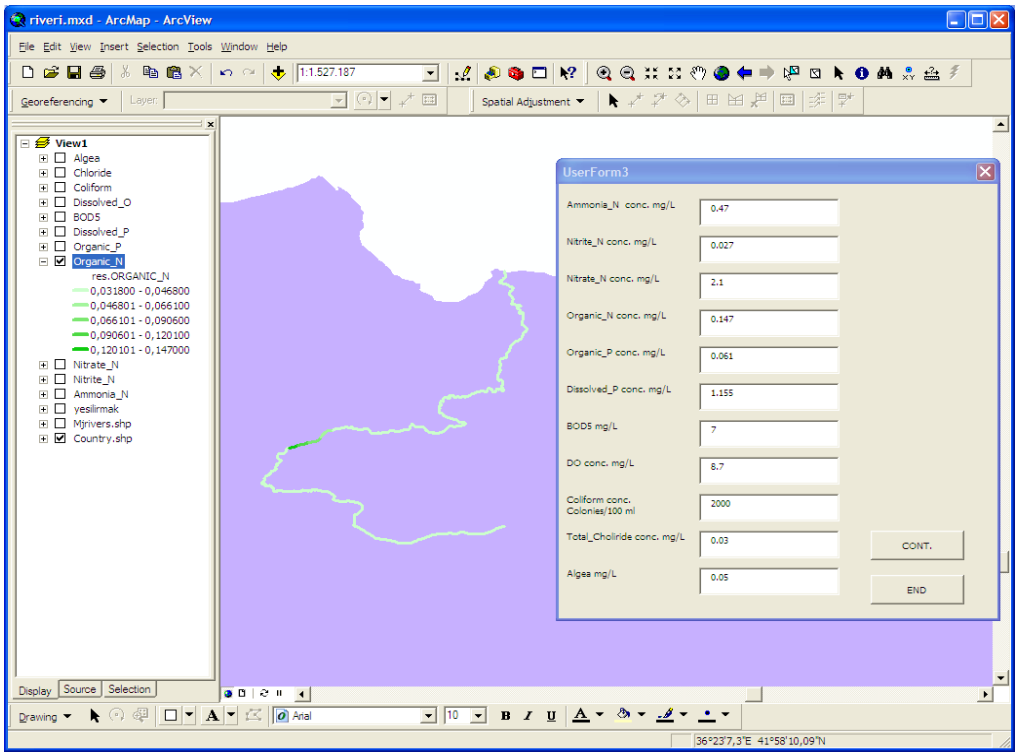

Figure 4. View of the starting menu of the software (with the map of Yesilirmak river indicating the study area, and user input sheet)

Once the simulation is run, the user can select any variable from the list, shown in left hand side of the menu, to be displayed in table or graphical form.

The working area was divided into 100 parts of equal length to calculate and illustrate water quality variables, and thus the user can follow the concentration of the selected quality variable in different color at desired locations on map. The geographical point where the variables are sought is selected by the movement of the mouse along the river displayed on map.

It then becomes possible to follow the water quality in terms of the selected pollutants along the river. For example, Figure 5 depicts the change in the ammonia nitrogen concentration following a point source. With this feature, the simulation results are linked to the GIS database, and thus the user can easily follow the spatial distribution of the major constituents of river water quality. It is also possible to display more than one quality variable in graphical or table form at any location indicated.

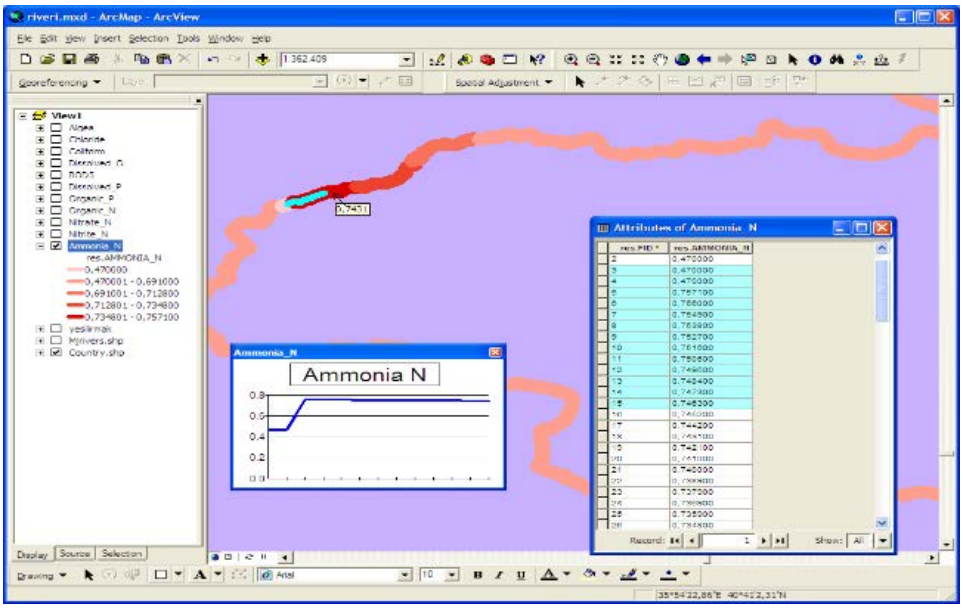

Figure. 5. Water quality display in table and graph form on the map.

16.

17. In Figure. 6 the list on the left hand side shows the water quality variables considered. The user can select a location on the river map by moving the mouse, and if it is a point on the river the data table associated with this particular location opens on the screen. On the other hand, if the user scans a region along the river, the software allows the user to see the changes in the concentration of the selected quality variables along this site by different colors. The color intensity on the map changes from light to dark with increased concentration, and this feature makes keeping track of water quality very easy. The user can select the concentration range (maximum and minimum values) and the number of intervals between. The color codes corresponding to those selected concentrations may be also determined by the user. If no choice has been made, the software picks up the maximum and minimum concentration values encountered in the simulations, and allocates five intermediate color codes (as default) to 5 intermediate values between the maximum and minimum. This feature of the GUI is illustrated in Figure 6. It is also possible to see the changes in concentration in graphical form.

18.

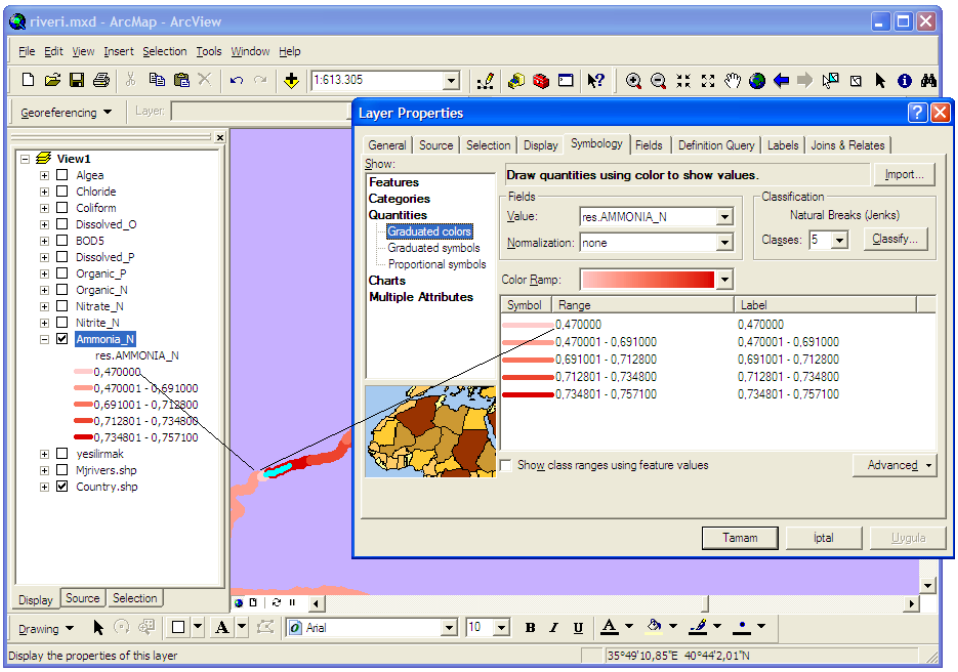

Figure 6. Selection of color codes between maximum and minimum concentration intervals.

Mean absolute percentage error values were calculated for quantitative evaluation and comparison. Table 2 indicates that, except nitrite nitrogen and chlorine, the predicted values of all quality variables are in compliance with experimental values. Figure 9 presents the predicted water quality results in tabulated form as a function of geographical space indicated on the first row. The columns represent the water quality variables predicted. The water quality data displayed can be viewed in graphical form or as colour-coded displays on the river map.

19.

Table 2. Absolute Average Deviation (AAD) values for comparison of pollution variables

Water Quality Variables	**(AAD %)**
Ammonia Nitrogen	2.86
Nitrite Nitrogen	29.59
Nitrate Nitrogen	2.71
Organic Nitrogen	9.01
Organic Phosphorus	2.09
Dissolved Phosphorus	1.89
BOD	5.49
Dissolved Oxygen	0.64
Coliform	6.87
Chloride	20.19

Predictions from the software were compared to field data for a section of 36.5 km of the river after the point source. Measured and predicted profiles of the pollution variables are shown in Figures 7–8.

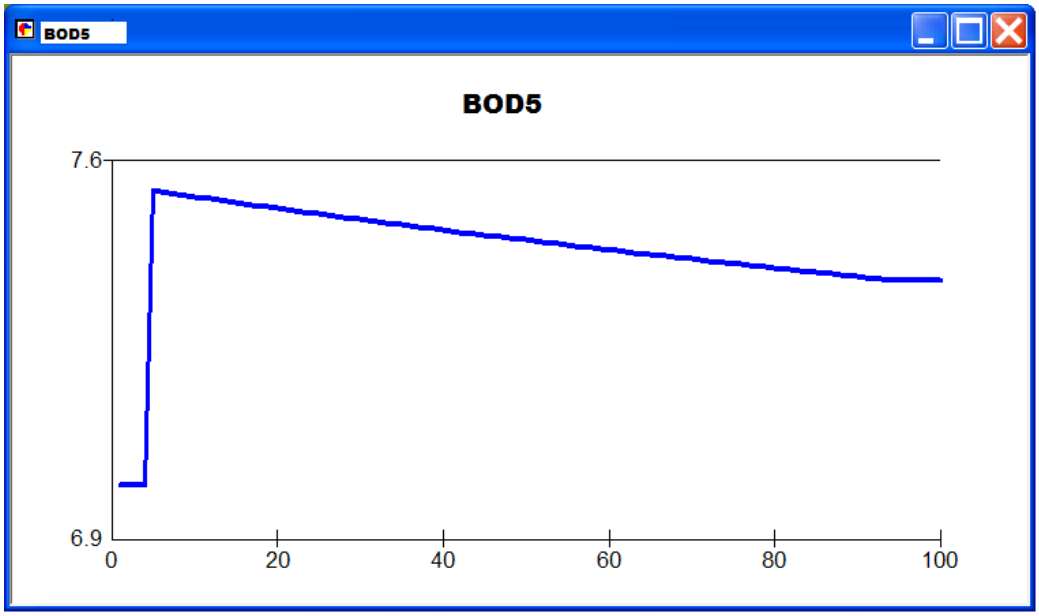

Figure 7. BOD5 concentration

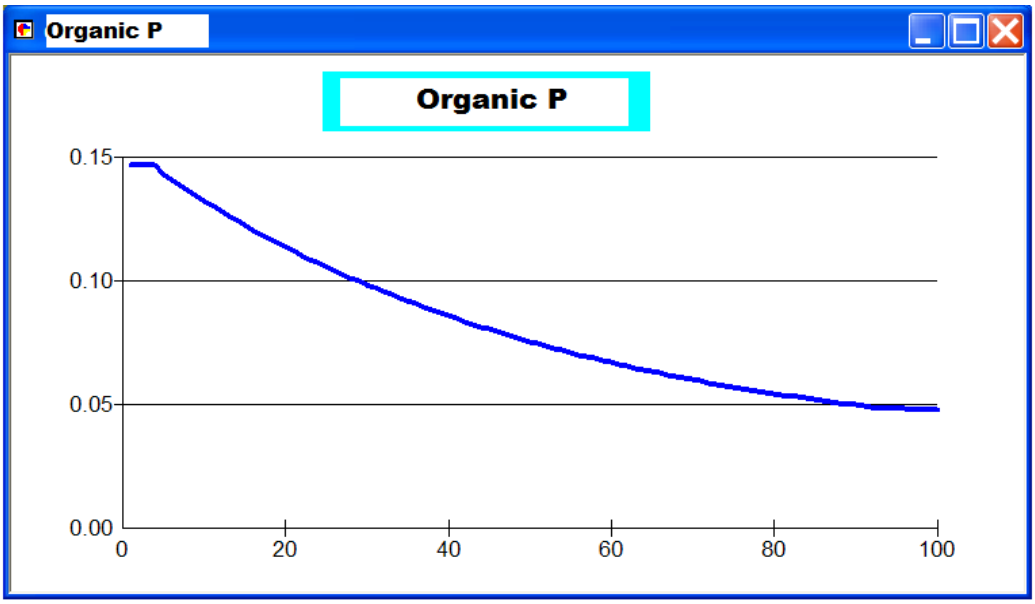

Figure 8. Organic P concentration

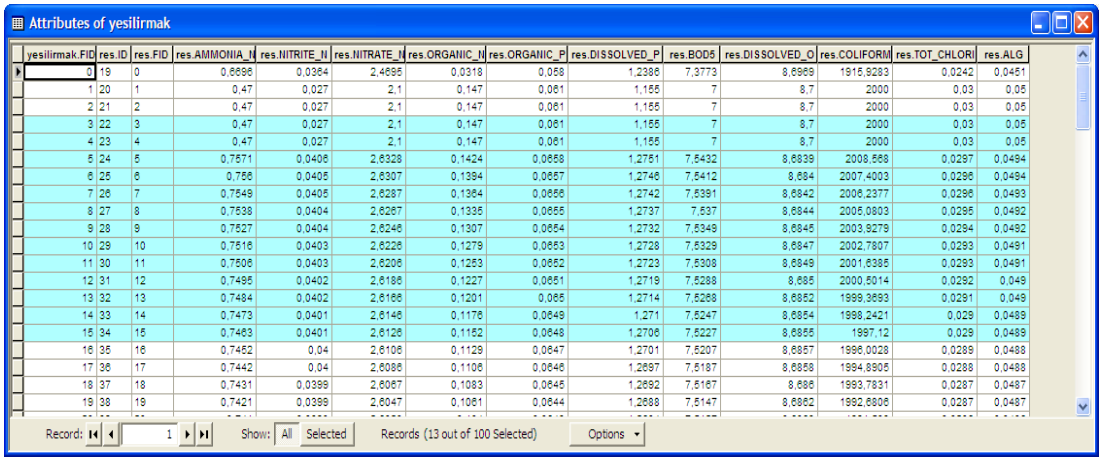

yesilirmak.FID	res.ID	res.FID	res.AMMONIA_N	res.NITRITE_N	res.NITRATE_N	res.ORGANIC_N	res.ORGANIC_P	res.DISSOLVED_P	res.BOD5	res.DISSOLVED_O	res.COLIFORM	res.TOT_CHLORI	res.ALG
0	19	0	0,6696	0,0364	2,4695	0,0318	0,058	1,2386	7,3773	8,6969	1915,9283	0,0242	0,0451
1	20	1	0,47	0,027	2,1	0,147	0,061	1,155	7	8,7	2000	0,03	0,05
2	21	2	0,47	0,027	2,1	0,147	0,061	1,155	7	8,7	2000	0,03	0,05
3	22	3	0,47	0,027	2,1	0,147	0,061	1,155	7	8,7	2000	0,03	0,05
4	23	4	0,47	0,027	2,1	0,147	0,061	1,155	7	8,7	2000	0,03	0,05
5	24	5	0,7571	0,0406	2,6328	0,1424	0,0658	1,2751	7,5432	8,6839	2008,568	0,0297	0,0494
6	25	6	0,756	0,0405	2,6307	0,1394	0,0657	1,2746	7,5412	8,684	2007,4003	0,0296	0,0494
7	26	7	0,7549	0,0405	2,6287	0,1364	0,0656	1,2742	7,5391	8,6842	2006,2377	0,0296	0,0493
8	27	8	0,7538	0,0404	2,6267	0,1335	0,0656	1,2737	7,537	8,6844	2005,0803	0,0295	0,0492
9	28	9	0,7527	0,0404	2,6246	0,1307	0,0654	1,2732	7,5349	8,6845	2003,9279	0,0294	0,0492
10	29	10	0,7516	0,0403	2,6226	0,1279	0,0653	1,2728	7,5329	8,6847	2002,7807	0,0293	0,0491
11	30	11	0,7506	0,0403	2,6206	0,1253	0,0652	1,2723	7,5308	8,6849	2001,6385	0,0293	0,0491
12	31	12	0,7495	0,0402	2,6186	0,1227	0,0651	1,2719	7,5288	8,685	2000,5014	0,0292	0,049
13	32	13	0,7484	0,0402	2,6166	0,1201	0,065	1,2714	7,5268	8,6852	1999,3693	0,0291	0,049
14	33	14	0,7473	0,0401	2,6146	0,1176	0,0649	1,271	7,5247	8,6854	1998,2421	0,029	0,0489
15	34	15	0,7463	0,0401	2,6126	0,1152	0,0648	1,2706	7,5227	8,6855	1997,12	0,029	0,0489
16	35	16	0,7452	0,04	2,6106	0,1129	0,0647	1,2701	7,5207	8,6857	1996,0028	0,0289	0,0488
17	36	17	0,7442	0,04	2,6086	0,1106	0,0646	1,2697	7,5187	8,6858	1994,8905	0,0288	0,0488
18	37	18	0,7431	0,0399	2,6067	0,1083	0,0645	1,2692	7,5167	8,686	1993,7831	0,0287	0,0487
19	38	19	0,7421	0,0399	2,6047	0,1061	0,0644	1,2688	7,5147	8,6862	1992,6806	0,0287	0,0487

Figure 9. Simulation results in tabulated form.

In addition that researcher can calculate the selected parameters average values, variance and standard deviation from these result table by using GUI of program. An addition that the above tables vales transferred to excel sheets to researcher who can make necessary analyses with excel easly.

20. 5.CONCLUSION

Although many models have been developed, they appear to be available to limited number of professionals who are capable of using and interpreting water quality simulation models. However, increased awareness in surface water pollution dictates that these models be used by non-experts who may be interested in knowing the consequences of various scenarios on river pollution. Availability and affordability of GIS systems offer alternative solutions to this problem.

Starting from this point, a software integrating a Geographical Information System and a water quality model in a single convenient package has been developed in this study. The effects of a discharge on the river can be predicted by simulation and the results are displayed on the map. The software was tested off-line with data collected from field measurements on Yesilirmak river in Turkey.

The integration strategy developed and the GUI created provide an interactive environment for the user and will help decision making process in river basin management systems, and can be fairly easily adapted to other rivers.

The results indicated that the model was able to satisfactorily estimate the water quality along the downstream section of a point load.

In our ongoing work, the software has been implemented for one more river than real time applications whose results will be reported later.

REFERENCES

[133]. [1] B. A. COX: A Review of Available in-stream Water Quality Models and Their Applicability for Simulating Dissolved Oxygen in Lowland Rivers. Sci Total Environ, 314–316(1), 335 (2003).
[134].
[135]. [2] S. MARSILLI-LIBELLI, E. CAPORALI, S. ARRIGHI, C. A. BECATELLI: Georeferenced Water Quality Model. Water Sci Tech, 43(7), 223 (2001).
[136].
[137]. [3] S. MARSILLI-LIBELLI, G. PACINI, C. BARRESI, E. PETTI, F SINACORI: An Interactive Georeferenced Water Quality Model. In: Proc. of the 5th International Conference on Hydroinformatics, Cardiff, UK, 2002
[138].
[139]. [4] C. GANAPATHY, A. N. S. ERNEST: Water Quality Assessment Using Web Based GIS and
[140]. Distributed Database Management Systems. Environ Informatics Archives, 2, 938 (2004).
[141].
[142]. [5] Rauch, W., Henze, M., Koncsos, L. Reichert, P., Shanahan, P., Somlyody, L. and Vanrolleghem, P. (1998). River water quality modelling: I. State of the art. IAWQ Biennial Int. Conf. Vancouver-Canada, 21-26.
[143].
[144]. [6] Shanahan, P., Henze, M., Koncsos, L. Rauch, W., Reichert, P. Somlyody, L. and Vanrolleghem, P. (1998). River water quality modelling: II. Problems of the art. IAWQ Biennial Int. Conf. Vancouver-Canada, 21-26.
[145].
[146]. [7] Yuceer, M., Karadurmus, E. and Berber, R. (2007). Simulation of River Streams: Comparison of a New Technique to QUAL2E. Mathematical and Computer Modelling. 46, 292–305.

Control of Power Electronic Interface for a Stand-Alone Photovoltaic System

Evren Isen[27]

Abstract

This paper presents a single-phase stand-alone PV system. The system includes ten PV panels that are connected in series and parallel. Each panel has 260W power and 38.3V open circuit voltage. Five panels are connected in series, thus 192V output voltage can be obtained. The total system power is 2.6 kW in ideal standard test conditions, 1000 W/m^2 and 25^{0}C. A DC/DC converter is used for maximum power point tracking (MPPT). It controls the output power of panels. The extracted power from PV panels is injected into DC-link that includes batteries. In the next stage of the system, a single-phase inverter is utilized to feed the local load. It is controlled with sinusoidal pulse width modulation technique to regulate the output voltage. At the output stage, a transformer increases the inverter output voltage to required load voltage level and provides galvanic isolation. The system is investigated for energy efficiency and load energy sustainability with different input power values. Protection parameters of DC/DC converter and inverter are used to investigate the system. The sinusoidal voltage is produced by inverter at the output for the load while the input power is at sufficient level. It is seen that the output energy and the input energy are interrupted because of unbalance power flow. The investigation shows that MPPT controller and inverter selection has important role for system energy efficiency and energy sustainability of the load.

Keywords: MPPT, photovoltaic system, stand-alone inverter.

54. INTRODUCTION

Alternative energy sources such as solar and wind energy has becoming steadily more popular due to diminishing of fossil fuels, increasing of CO_2 emission and energy demand. Therefore, grid-connected and stand-alone photovoltaic (PV) systems are installed to support the power network and to supply the energy to rural areas that are far away from power network. The total installed capacity at the end of 2015 is reached to 227,1 GW in the world. China, Germany, Japan, USA and Italy are the first countries that have the most cumulative capacities with 43,6 GW, 39,37 GW, 34,4 GW, 25,6 GW and 18,9 GW, respectively. Turkey has installed 208 MW PV system in 2015. The evolution of PV installation in 2000-2015 is seen in Figure 18 [1]. As seen from the figure, PV system installation increases steadily in the world.

In the literature there are many studies based on stand-alone and grid-connected PV systems. In this study, a single-phase stand-alone PV system that provides energy to residential house is presented. Different topologies are installed in PV systems [2]. A DC-DC buck converter is used to charge the battery, and another DC-DC Boost converter provides maximum power point tracking (MPPT) and charges the DC-link. An inverter injects the energy to the load and grid from DC-link. At the output stage, a transformer is utilized in case of grid connection [3]. A cascaded multilevel inverter includes DC-DC converter with high frequency transformer is used for isolation and to reduce the transformer size and total harmonic distortion of output voltage [4].

Maximum power point tracking is the most important point in PV systems. Different algorithms are used for this issue [5], [6]. Widely used methods are perturb and observe (P&O) and incremental conductance in the literature. P&O algorithm is also called ―hill-climbing" and widely used in stand-alone PV systems because of its simplicity. In this method, the last perturbation and the last sign of power increment are used to determine the next step. If the power difference is positive, the perturbation should be kept in the same direction [7], [8]. Otherwise, direction should be changed. It continues to the maximum power point. The other method, incremental conductance, checks the slope of the power vs. voltage (current) curve. The point that has zero slope of the curve indicates the maximum power extraction [9], [10]. Furthermore, fuzzy and neural based MPPT algorithms are used to improve the performance [11]-[15].

[27] *Corresponding author: Kirklareli University, Department of Electrical & Electronics Engineering, Kirklareli, Turkey.*
evren.isen@klu.edu.tr

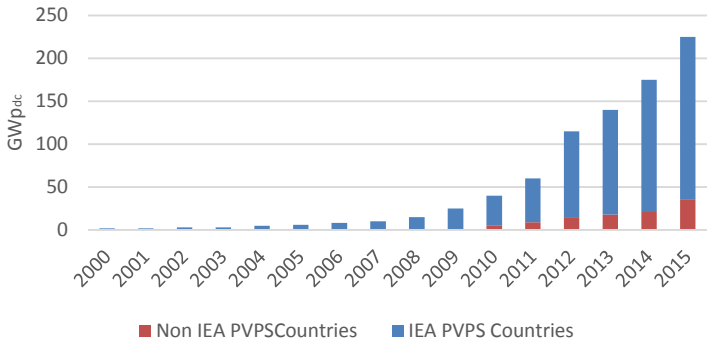

Figure 18. Evolution of PV Installation [1]

In this study, single-phase stand-alone PV system is simulated for different radiation values. A DC/DC buck converter is utilized to control the output power of panels for MPPT. The energy extracted from panels is stored in battery, and it is used to produce AC output voltage by an inverter. At the output stage, a transformer is utilized to increase the voltage that is required for the load. The MPPT control and inverter is controlled with voltage protection parameters to investigate system energy efficiency and load energy sustainability.

55. SYSTEM TOPOLOGY AND CONTROL PRINCIPLE

The proposed single-phase stand-alone PV system is given in Figure 19. The system is fed by ten PV panels. There are two parallel connected groups, and each includes five serial connected panels. Therefore, total output voltage and current are increased. The electrical specifications of PV panels are given in Table 7. Each panel has 260 W_p power in theoretically. Therefore, the total output power reaches to 2.6 kW. The electrical characteristic of the panel is given in Figure 20. As seen from the figure, output power changes depending on the panel voltage, thus maximum power point tracking algorithm is used in converter control.

Table 7.Electrical specifications of PV panel (KU260-6MCA)

Parameter	Value	Unit
P_{max}	260	W
V_{mp}	31	V
I_{mp}	8.39	A
V_{oc}	38.3	V
I_{sc}	9.09	A

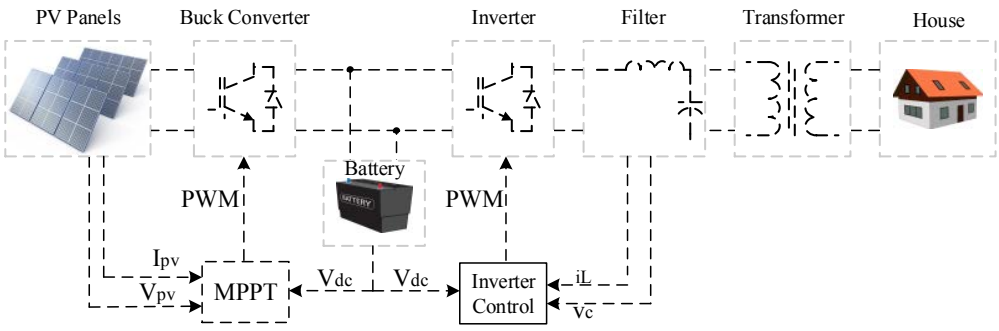

Figure 19. Block diagram of the system

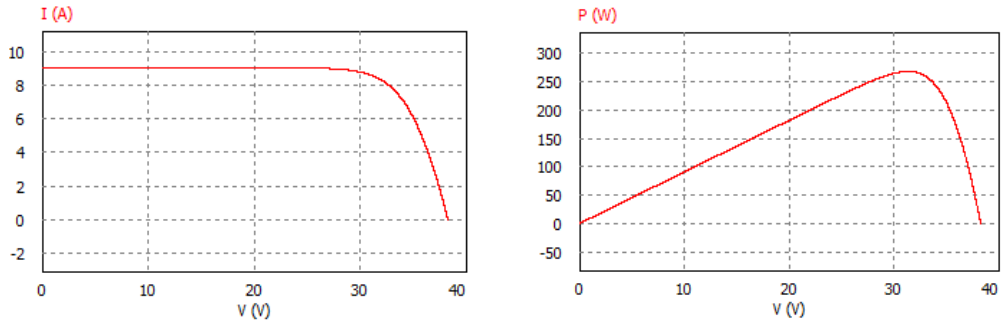

a) V x I *b) V x P*

Figure 20. Output characteristics of a PV panel

PV systems have several power electronics converter to control the power flow. In the proposed system, there are two converters. A DC/DC buck converter is utilized at the output of PVs. It controls the power extraction from panels depending on MPPT algorithm. Therefore, the maximum power can be produced although the weather conditions change, such as temperature and radiation. The algorithm calculates the maximum power for the different weather conditions. It is used in buck converter control. Topology of the buck converter is seen in Figure 21. The semiconductor switch is controlled by DC-PWM. As converter controls the output power of panels, reference value is adjusted in MPPT algorithm. Duty cycle is changed depending on the reference voltage to ensure MPPT.

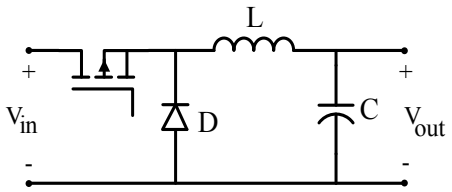

Figure 21. DC/DC buck converter

The converter is controlled by DC-PWM, and reference value is adjusted with P&O algorithm for MPPT. The algorithm flowchart is given in Figure 22. This algorithm is widely used for stand-alone applications because of its simple implementation. Output voltage and current of panels are measured to calculate instantaneous power. The difference between the instantaneous and previous sampled value of voltage and power is calculated. Duty cycle of semiconductor switch is changed depending on the state of output power and voltage to control the output voltage. The duty cycle (D) is increased or decreased by ΔD as seen in Figure 22.

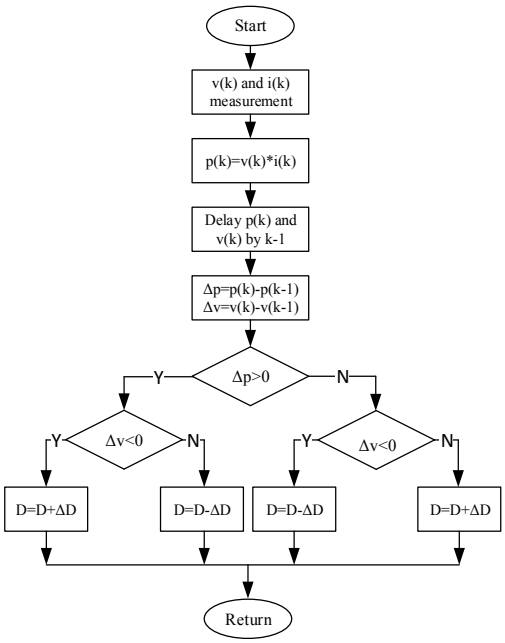

Figure 22. P&O algorithm flowchart

Third stage of the system includes storage elements. The energy extracted from panels is injected to DC-link that includes battery. The battery supplies energy to the system when solar energy is not enough for the load. It also feeds the load when the

buck converter stops running because of operating principle. The battery voltage in the system is 24V. A bulky capacitor is used for modelling of the battery.

The DC energy stored in batteries is injected to the load via an inverter and a transformer. Single-phase four-switch inverter is utilized after the DC-link. Inverter converters the DC voltage to AC voltage. The topology of the inverter is seen in Figure 23. Output of the inverter is filtered by LC filter. Inductor filters the AC current while capacitor filters the AC output voltage. The output of the system is connected to load via transformer. It provides the required voltage to the load boosting the capacitor voltage.

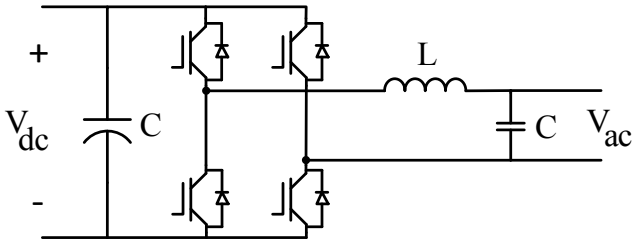

Figure 23. Single-phase inverter

56. SIMULATION STUDY

The proposed single-phase stand-alone PV system is simulated in PSIM. The schematic is seen in Figure 24. PV panels block consists of ten panels that includes two groups. Each group has five series connected panel, and two groups are connected in parallel. The second block is buck converter that controls the PV panel power. The operating principle of the converter to extract maximum power from PV panels. Additionally, it has parameters for battery protection. In PV system converter market, there are many MPPT controllers, and they have different protection parameters. In the proposed system, the protection parameters of the controller (buck converter) are 27.8 V and 25 V. If battery voltage reaches to 27.8V, the controller stops working to protect the battery. In this state, power demand of the load is smaller than the sum of produced power from panels and battery power. When the controller stops, load power is supplied from battery. Therefore, battery voltage decreases to 25 V, and it runs again at this voltage. The simulation result for this state is seen in Figure 25. In the first 7 ms, output power of panels increases to 2.6 kW, while 2 kW load is fed by battery. Therefore, battery voltage decreases to 25.5 V from 26 V. After that time, as the produced PV power is higher than the load voltage, battery voltage starts increasing. When the battery voltage reaches to 27.8 V, controller stop working, thus output power of panels decreases to zero. While buck converter does not run, load power is supplied from battery. It causes a decreasing at the battery voltage to 25 V. At the last interval, controller operates again when the battery voltage is 25 V. Therefore, battery starts to be charged again. In the time interval that MPPT controller does not operate, the energy can be produced from PV panels does not be used. It decreases the energy efficiency.

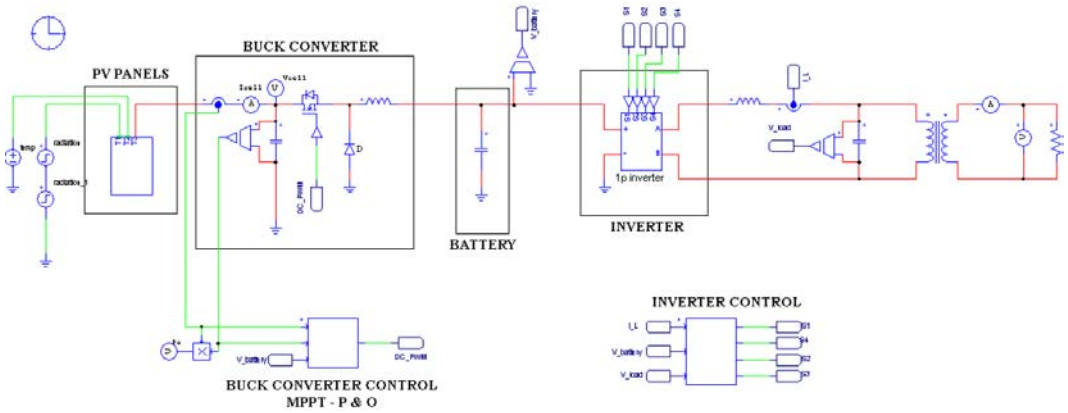

Figure 24. System simulation schematic

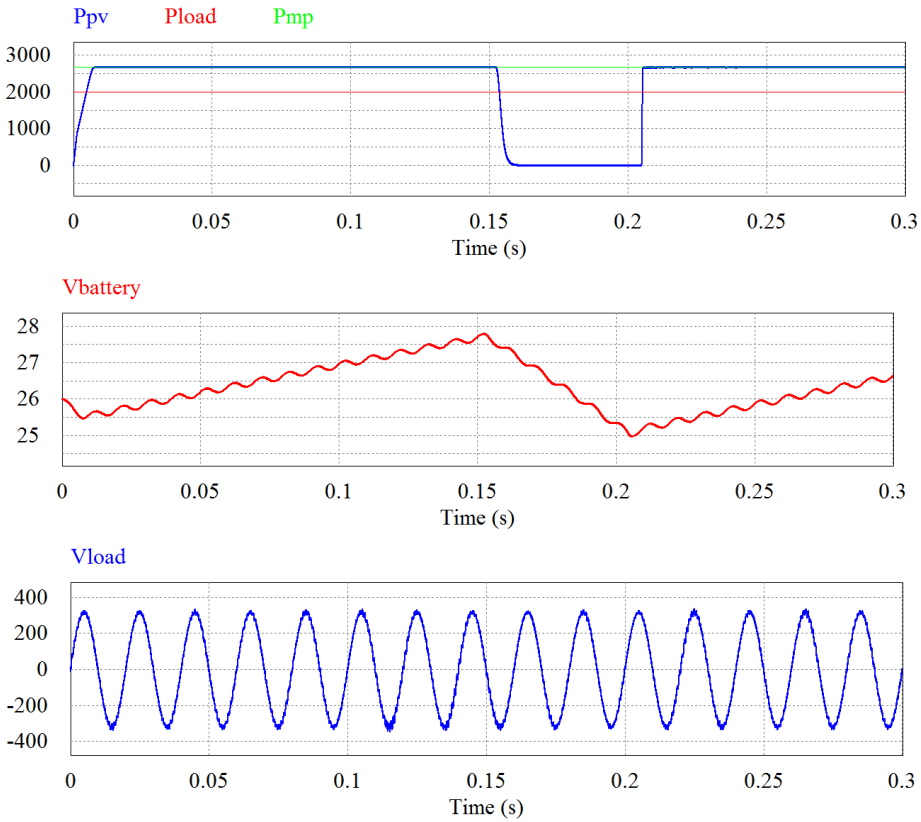

Figure 25. MPPT controller protection principle

Inverter is utilized after DC-link. It converts DC voltage to AC voltage. It regulates the load voltage by SVPWM control technique with current and voltage loops. The battery voltage changes depending on the power balance between input and output. Input power changes with weather conditions such as temperature and radiation. Therefore, inverter control algorithm should be included protection parameters. The lower voltage causes disturbed voltage at the output, and the higher voltage break the semiconductors down of the inverter. The parameters of the inverter in the proposed system are 20.3V shutdown voltage and 25.2V restart voltage. Inverter stops running at 20.3 V and restarts at 25.2 V as seen in Figure 26. When the inverter stops, the load cannot be fed. It affects the energy sustainability negatively.

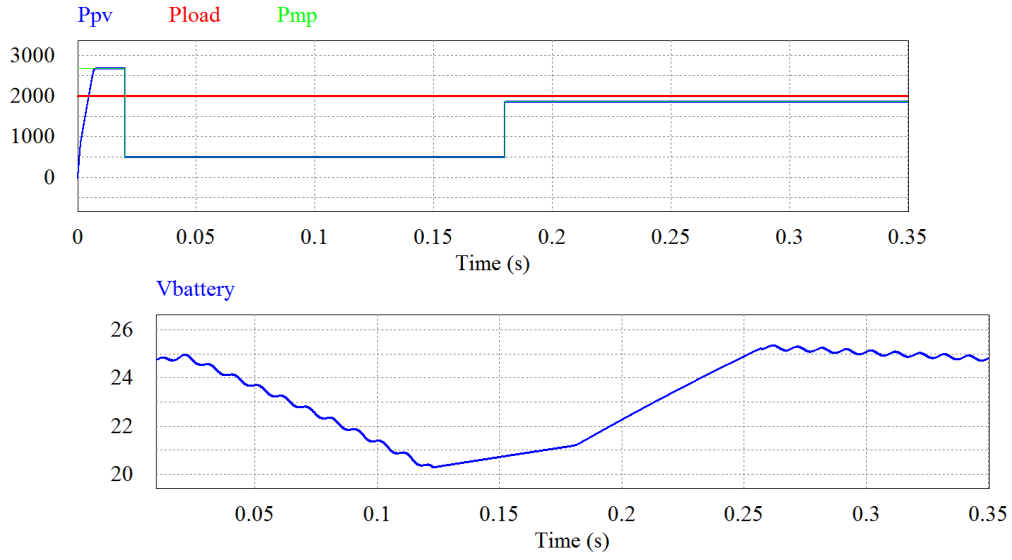

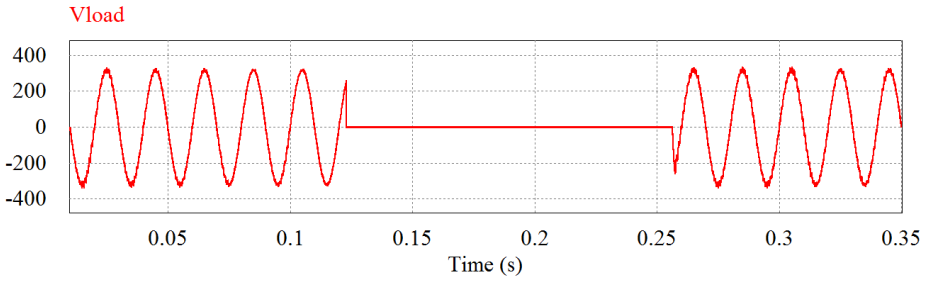

Figure 26. Inverter protection principle

57. CONCLUSIONS

In this study, a single-phase stand-alone PV system that has 2.6 kW power capability is simulated. The system includes a DC/DC buck converter, 24 V battery as a storage element, a single-phase inverter and a transformer. Perturb & Observe maximum power point tracking is implemented with a DC/DC buck converter (MPPT controller). The buck converter and inverter are controlled with DC-PWM and SPWM, respectively. In each converter control principle, battery voltage protection is considered. MPPT controller observes the battery voltage for overvoltage protection. Controller stops working at over voltage 27.8 V and keeps stopping until the voltage decreases to restart voltage 25 V. Inverter control checks the battery voltage for deep charge protection. It stops working to protect the battery and to guarantee the output voltage because inverter needs a specific minimum DC voltage to produce required load voltage. Therefore, inverter stops working at 20.3 V, and restart at 25.2 V. The simulation results shows that load is fed by the system. However, the unbalance power between the input and output power demand affect power flow. It indicates the importance of sizing of the system element. Solar energy capability of the system location and load power demand should be considered in PV panels and battery sizing to guarantee power producing from panels in maximum duration and feeding the load without interruption. The protection parameters of converters also should be taken into account for converter selection.

REFERENCES

[1] PVPS, I., Trends in photovoltaic applications. Survey report of selected IEA countries between 1992 and 2013, Report IEA-PVPS T1-25; 2014.
[2] M. Islam, S. Mekhilef and M. Hasan, "Single phase transformerless inverter topologies for grid-tied photovoltaic system: a review", Renew. Sustain. Energy Rev., vol. 45, 2015, pp. 69-86.
[3] H. Chaves, J. Grigulo, L. Bertagnolli and L.A.C. Lopes, "2-stage grid-connected and stand-alone PV inverter implemented with a renewable energy developer's KIT", IEEE International Instrumentation and Measurement Technology Conference, 2014, pp. 631-636.
[4] M. Sadikin, T. Senjyu and A. Yona, "High-Frequency Link DC for Power Quality Improvement of Stand-Alone PV System in Cascaded Multilevel Inverter", IEEE 10th International Conference on Power Electronics and Drive Systems, 2013, pp. 597-601.
[5] U.S. Patel, D. Sahu and D. Tirkey, "Maximum Power Point Tracking Using Perturb & Observe Algorithm and Compaare With Another Algorithm", International Journal of Digital Application & Contemporary Research, vol. 2, no. 2, 2013.
[6] T. Esram and P. L. Chapman, "Comparison of Photovoltaic Array Maximum Power Point Tracking Techniques", IEEE Transactions on Energy Conversion, vol. 22, no. 2, 2007, pp. 439-449.
[7] P. Kinjal, K. B. Shah and G. R. Patel, "Comparative Analysis of P&O and INC MPPT Algorithm for PV System", International Conference on Electrical, Electronics, Signals, Communication and Optimization, 2015, pp. 1-6.
[8] M. Killi and S. Samanta, "Modified Perturb and Observe MPPT Algorithm for Drift Avoidance in Photovoltaic Systems", IEEE Transactions on Industrial Electronics, vol. 62, no. 9, 2015, pp. 5549-5559.
[9] P. Q. Dzung, L. D. Khoa and H. H. Lee, "The New MPPT Algorithm using ANN-Based PV", International Forum on Strategic Technology, 2010, pp. 402-407.
[10] N. E. Zakzouk, M. A. Elsaharty, A. K. Abdelsalam, A. A. Helal and B. W. Williams, "Improved performance low-cost incremental conductance PV MPPT technique", IET Renewable Power Generation, vol. 10, no. 4, 2016, pp. 561-574.
[11] A. I. Dounis, S. Stavrinidis, P. Kofinas and D. Tseles, "Fuzzy-PID controller for MPPT of PV system optimized by Big Bang-Big Crunch algorithm", IEEE International Conference on Fuzzy Systems, 2015, pp. 1-8.
[12] M. A. A. M. Zainuri, M. A. M. Radzi, A. C. Soh and N. A. Rahim, "Development of adaptive perturb and observe-fuzzy control maximum power point tracking for photovoltaic boost dc-dc converter", IET Renewable Power Generation, vol. 8, no. 2, 2014, pp. 183-194.
[13] H. Hassan, M. A. Geliel and M. A. Zeid, "A Proposed Fuzzy Controller for MPPT of A Photovoltaic System", IEEE Conference on Energy Conversion, 2014, pp. 164-169.
[14] L. Jie and C. Ziran, "Research on the MPPT Algorithm of Photovoltaic System Based on PV Neural Network", Chinese Control and Decision Conference, 2011, pp. 1851-1854.
[15] L. M. Elobaid, A. K. Abdelsalam and E. E. Zakzouk, "Artificial neural network-based photovoltaic maximum power point tracking techniques: a survey", IET Renewable Power Generation, vol. 9, no. 8, 2015, pp. 1043-1063.

Static Analysis of Higher Order Shear Deformable FGM Timoshenko Beam

Özgür Demir[28], Gökhan Ceylan[29], Mustafa TaÇkın[30]

Abstract

Functionally graded materials (FGM) have properties that change gradually within the microstructure of the material. This enables the structure to have much better material properties than of its counterparts of metal and ceramic. In this study, static analysis of a simply supported Timoshenko beam has been investigated using higher order shear deformation theory. Numerical implementation has been done by using Ritz method and Finite element method considering the material properties vary alongside the beam according to the power-law. Approximation functions that are used in both transverse and longitudinal displacement of the cross sections are considered trigonometric. The governing equations and boundary conditions are derived from principle of virtual work. Transverse and longitudinal deflections, stresses and strains are examined for different power law values. It has been found that the power law coefficient which determines the metal/ceramic ratio in the beam is an important factor in designing a structure and increased power law coefficients yield better bending rigidity.

Keywords: FGM Materials, Ritz Method, Higher Order Shear Deformation Theory, Finite Element Analysis, Power Law

58. INTRODUCTION

Advanced composites are one of the many developing areas in terms of structural analysis. Different composites provide different material properties which can be used in various situations. Functionally graded materials (FGM) are one of the types of advanced composites which have significant advantages among others such as high stiffness ratio, high fracture and crack strength and most importantly, advanced thermal resistance that can be useful in many areas such as aerospace and military applications. They have properties that changes gradually within the microstructure of the material. This enables the structure to have much better material properties than of its counterparts which are usually ceramic based materials and metals.

There have been several studies about functionally graded materials in recent years. However there are only a few studies considers using the higher order shear deformation theory which was suggested by Reddy [1]. Higher order theory represents the kinematics of the body better and results in more accurate interlaminal stress distributions[1] Thus, it does not require the shear correction factor for in-plane calculations. Chakraborty et al. developed a new beam element to study the thermo-elastic behavior of functionally graded structures using the first order shear deformation theory [2]. Shi et al. implemented finite element method to calculate the strain expressions and nodal displacements of a FGM beam by using two different models [3]. Aydogdu and Taskin performed free vibration analysis of FGM‘s and presented linear frequencies of simply supported beams [4]. Kadoli et. al studied the static behavior of FGM‘s under ambient temperatures by assuming the material properties vary continuously in the vertical direction[5]. Huu-Tai Thai and Seung-Eock Kim used higher order shear deformation theory for performing the bending and free vibration analysis of FGM plates [6]. Wattanasakulpong et al. [7] investigated the thermal buckling and elastic vibrations of a functionally graded beam using third-order shear deformation theory.

The ways to determine the method in which the material properties vary alongside the the structures differs in terms of the type of FGM. There are several methods such as exponential theory, power law, modified rule of mixtures, Mori-Tanaka method and so on. Sankar [8] used exponential method, while Şimşek and Reddy [9] used a modified couple stres theory to determine the material properties. Several other researchers such as Kien [10], Simsek [11], Thai [12], Ebrahimi [13] used power law in which the material properties vary in the z- direction according to a power law coefficient. Stochastic micromechanical methods are also used by Rahman and Chakraborty [14] which involves non-homogeneous, non-Gaussian random field representation of phase volume fractions and random variable description of constituent material properties.

In this study, static analysis of a functionally graded Timoshenko beam has been considered. Higher order shear deformation theory is used to examine the vertical and transverse deflections as well as rotations of the body with respect to reference plane. Numerical implementation has been done by using Ritz method and Finite element analysis considering the material properties vary alongside the beam according to the power-law. Approximation functions that are used in both transverse and

[28] *Corresponding author: Yildiz Technical University, Department of Naval Architecture and Marine Engineering, Beşiktaş/İstanbul, Turkey. ozgurd@yildiz.edu.tr*

[29] *Turkish Naval Academy Department of Naval Architecture and Marine Engineering, Tuzla/İstanbul, Turkey. gceylan@dho.edu.tr*

[30] *Yildiz Technical University, Department of Naval Architecture and Marine Engineering, 34220, Beşiktaş/İstanbul, Turkey. mtaskin@yildiz.edu.tr*

longitudinal displacement of the cross sections are considered trigonometric. The governing equations and boundary conditions are derived from principle of virtual work. Transverse and longitudinal deflections, stresses and strains are examined for different power law values.

59. MATHEMATICAL FORMULATION

59.1. Displacement field of a functionally graded beam

The displacement field of a functionally graded beam based on the higher order theory given below [1],

$$u(x,z) = u_0 + z\Phi(x) - \alpha(\frac{\partial w_0}{\partial x} + \Phi)z^3 \tag{1}$$

$$w(x,z) = w_0(x) \tag{2}$$

where u and w are the axial and vertical displacements and Φ is the rotation along the y axis. h represents the thickness of the beam and α=4/3h2. It is assumed that no displacement along the y axis occurs due to the bending of the beam, thus υ terms are omitted.

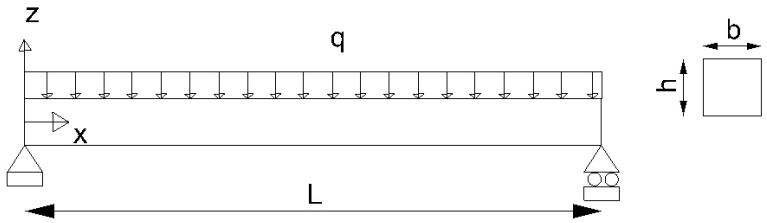

Figure 1. A Simply supported FGM beam subjected to distributed load

Strain equations can be evaluated using the displacement field are written as follows,

$$\varepsilon_{xx} = \frac{\partial u(x,z)}{\partial x} = \frac{\partial u_0(x,z)}{\partial x} + z\frac{\partial \Phi(x)}{\partial x} - \alpha\left[\frac{\partial^2 w_0(x)}{\partial x^2} + \frac{\partial \Phi(x)}{\partial x}\right]z^3 \tag{3}$$

$$\gamma_{xz} = \frac{\partial u(x,z)}{\partial z} + \frac{\partial w(x,z)}{\partial z} = (1-3\alpha z^2)\left[\Phi(x) + \frac{\partial w_0(x)}{\partial x}\right] \tag{4}$$

Normal and shear strain energies based on the higher order theory suggested by Reddy [1] is given below;

$$U_1 = \int\left[\sigma_{xx}(\varepsilon_{xx}{}^{(0)} + z\varepsilon_{xx}{}^{(1)} - c_1 z^3 \varepsilon_{xx}{}^{(3)}) + (\gamma_{xz}{}^{(0)} + z^2\gamma_{xz}{}^{(2)})\right]dxdydz \tag{5}$$

which leads to,

$$U_1 = \frac{b}{2}\int_0^L\left[\begin{array}{l}(\varepsilon_m{}^T A_{xx}\varepsilon_m + \varepsilon_b{}^T D_{xx}\varepsilon_b + \varepsilon_{hs}{}^T\alpha^2 H_{xx}\varepsilon_{hs} + \gamma_{xz}{}^T S_{xx}\gamma_{xz} + \\ 2\varepsilon_m{}^T B_{xx}\varepsilon_m - 2\varepsilon_b{}^T\alpha F_{xx}\varepsilon_b - 2\varepsilon_m{}^T\alpha E_{xx}\varepsilon_m\end{array}\right]dx \tag{6}$$

In this equation A_{xx}, $B_{xx}, C_{xx}, D_{xx}, E_{xx}, F_{xx}, H_{xx}$ are different stiffness elements that can be represented as,

$$(A_{xx}, B_{xx}, D_{xx}, E_{xx}, F_{xx}, H_{xx}) = \sum_{n=1}^{N}\int_{-h/2}^{h/2}(1, z, z^2, z^3, z^4, z^6)(Q_{xx})dz \tag{7}$$

and

$$S_{xx} = \sum_{n=1}^{N} \int_{-h/2}^{h/2} (1 - 3\alpha^2 z^2)(Q_{xz})dz \tag{8}$$

Axx: extensional stiffness, Bxx: bending-extension coupling stiffness, Dxx:bending stiffness, Exx:warping-extension coupling stiffness, Fxx: warping-bending coupling stiffness, Hxx:warping-higher order bending coupling stiffness and Sxx:shear stiffness respectively. Qxx and Qxz are represented as the effective elastic and shear modulus of the beam are evaluated in below.

$$Q_{xx} = \frac{E}{1-\nu^2} \qquad Q_{xz} = \frac{E}{2(1+\nu)} \tag{9a-b}$$

59.2. Constitutive Equations

Constitutive equations that are used in classical beam theory are valid for functionally graded materials too. However, since they consist of two different material (usually ceramic and metal) effective material properties need to be determined in order to implement the Hooke‘s law. In this study, it is considered that the material properties change in the z direction along the thickness of the beam by following power law.

$$E(z) = (E_m - E_c)\left(\frac{z}{h} + 0.5\right)^k + E_c \tag{10}$$

$$\nu(z) = (\nu_m - \nu_c)\left(\frac{z}{h} + 0.5\right)^k + \nu_c \tag{11}$$

$$G(z) = \frac{E(z)}{2(1+\nu(z))} \tag{12}$$

Here E(z), υ(z) and G(z) represents the effective material properties of a FGM beam. k is a non negative power law coefficient which determines the material variation along the thickness of the beam.

59.3. Boundary Conditions and System of Equations

In this study simply supported boundary conditions are evaluated. The boundary conditions for the simply supported beam are;

$u_0(x) = 0$ for x=0 (13a)

$w_0(x)=0$ for x=0 and x=L (13b)

In order to satisfy the kinematic boundary conditions, trigonometric displacement and rotation functions are selected which are expressed as series in below.

$$w_0(x) = \sum_{n=1}^{N} X_n \mathrm{P}_n(x)$$

$$u_0(x) = \sum_{n=1}^{N} Y_n R_n(x) \qquad (14\ a\text{-}b\text{-}c)$$

$$\Phi(x) = \sum_{n=1}^{N} Z_n S_n(x)$$

Here P, R and S are trigonometric trial functions which are given below.

$$P_n(x) = \sin(\frac{n\pi x}{L})$$

$$R_n(x) = \sin\frac{(2n-1)\pi x}{L} \qquad (15\ a\text{-}b\text{-}c)$$

$$S_n(x) = \cos(\frac{n\pi x}{L})$$

By assuming X, Y and Z are unknown functions and using the minimum potential energy theory, the system of equations can be written as follows.

$$\begin{bmatrix} [K_{uu}] & [K_{uw}] & [K_{u\gamma}] \\ [K_{wu}] & [K_{ww}] & [K_{w\gamma}] \\ [K_{\gamma u}] & [K_{\gamma w}] & [K_{\gamma\gamma}] \end{bmatrix} \begin{Bmatrix} X \\ Y \\ Z \end{Bmatrix} = \begin{Bmatrix} F_1 \\ F_2 \\ F_3 \end{Bmatrix} \qquad (16)$$

60. NUMERICAL RESULTS AND DISCUSSION

Numerical studies are carried out to determine and analyze the static deflections in a FGM beam composed of Aluminum (Al) and Zirconium Oxide (ZrO_2) Material properties of both elements are given below.

Table 8 Material Properties of the FGM beam

Material	Elastic Modulus	Shear Modulus	Poisson Ratio
Aluminum(Al)	70 GPa	28 GPa	0,3
Zirconium	200 GPa	---	0,3

Oxide (ZrO_2)

First, a beam which has a thickness/length ratio of 1/3 is considered. Length of the beam is 0.3 m and the width and thickness is 0.1 m respectively. It is assumed that the beam has been subjected to distributed load of 0.01 kN/m^2 along its length. It has a rectangular cross section and the width is constant. For displacement analysis, values are calculated for the mid-plane which has the material properties calculated by power law.

In Figure 1 and 2 deflections on the middle of a simply supported FGM beam are shown for 4 different power law value. It can be seen that the power law coefficient k is an important factor in the analysis. As the power law coefficient increases, the deflection in the mid-plane decreases. Since the power law coefficient is related to the rigidity of the material, this result is expected. For instance, if we take the power law coefficient zero, the material properties goes to being fully metal. As the coefficient increases, ceramic ratio in the beam increases and bending rigidity is expected to be higher than the full metal case. The results in both Finite Element Method and Ritz Method are given in Table 2.

Table 9 Displacement Results

	Vertical displacement values(m)							
	k=0.3		**k=0.5**		**k=0.9**		**k=1.5**	
L(m)	**FEM**	**Ritz**	**FEM**	**Ritz**	**FEM**	**Ritz**	**FEM**	**Ritz**
0	0	0	0	0	0	0	0	0
0.05	0.000912	0.000835	0.000816	0.000754	0.000728	0.00067	0.000675	0.000609
0.1	0.001458	0.001415	0.001305	0.001278	0.001166	0.001137	0.00108	0.001035
0.15	0.001641	0.001616	0.001468	0.00146	0.001311	0.001299	0.001215	0.001183
0.2	0.001458	0.001416	0.001305	0.001278	0.001166	0.001137	0.00108	0.001035
0.25	0.000912	0.000836	0.000816	0.000754	0.000728	0.00067	0.000675	0.00061
0.3	0	0	0	0	0	0	0	0

If we plot the displacement values for different k coefficients, we can see that as the power law coefficient increases, the deflection in the mid-plane decreases in both methods. This shows that the power law coefficent is directly related to the rigidity of the material.

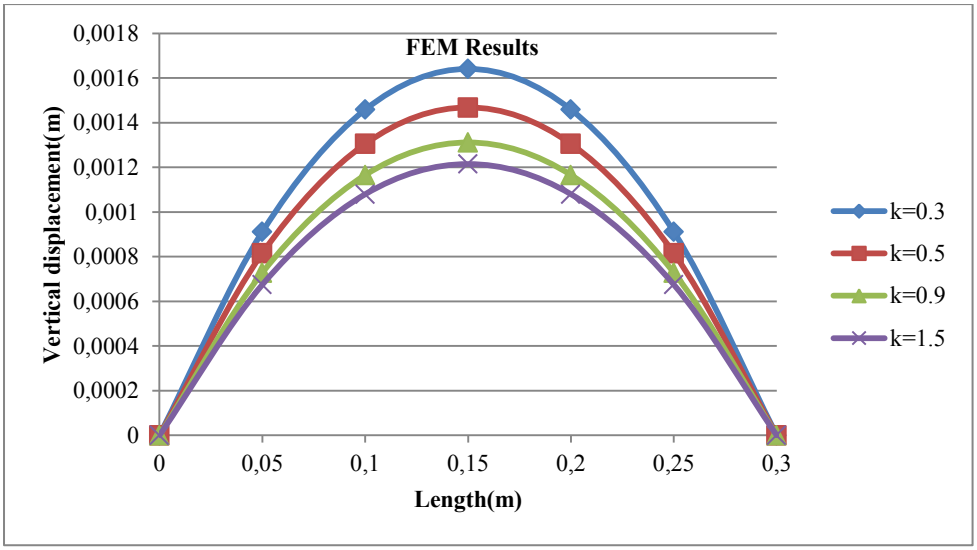

Figure 2 FEM Results

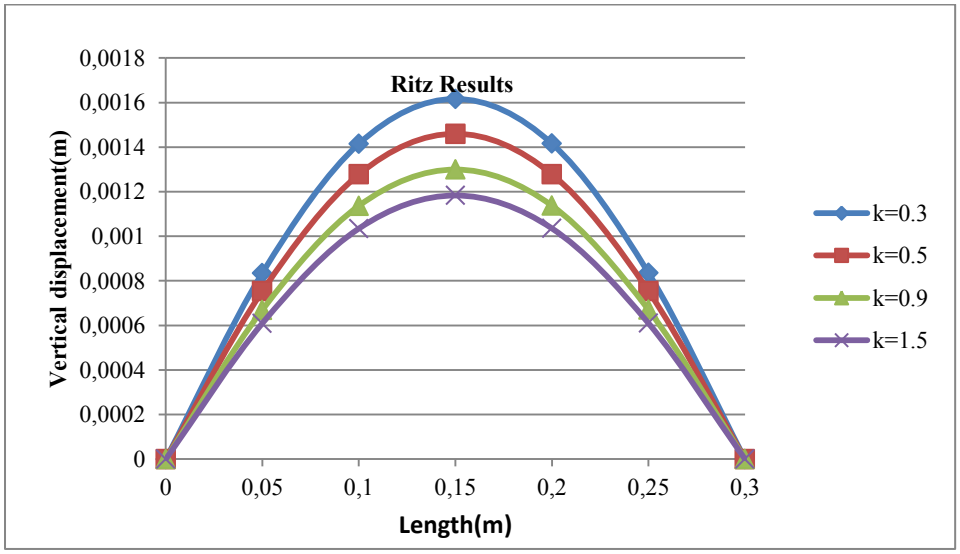

Figure 3 Ritz Results

61. CONCLUSION

Static analysis of a simply supported FGM beam is investigated using both Ritz Method and Finite Element Analysis. The characteristic functions that are used in Ritz Method are expressed as trigonometric and deflections in mid-plane is calculated. The material properties are assumed to vary continuously along the thickness of the beam according to power law. Deflections in mid-plane are calculated for different power law coefficients. The analysis showed that the power law coefficient which determines the metal/ceramic ratio in the beam is an important factor in designing a structure. Increased power law coefficients yield better bending rigidity. Thus the material can be tailored to have the required material properties by changing the power law coefficient.

REFERENCES

[147]. J.N.Reddy, Laminated Composite Plates and Shells.
[148]. A. Chakrabortya, S. Gopalakrishnana, J.N. Reddy, A new beam finite element for the analysis of functionally graded materials. International Journal of Mechanical Sciences, 519-539, 2003. vol. 61.

[149]. G. Shi, K. Y. Lam, T. E. Tay, On efficient finite element modeling of composite beams and plates using higher-order theories and an accurate composite beam element. Composite Structures (41), 159-165, 1998.
[150]. M. Aydogdu, V. Taskin, Free vibration analysis of functionally graded beams with simply supported edges. Materials and Design (28), 1651-1656, 2007.
[151]. Ravikiran Kadoli , Kashif Akhtar , N. Ganesan, Static analysis of functionally graded beams using higher order shear deformation theory. Applied Mathematical Modelling (32), 2509-2525, 2008.
[152]. Huu-Tai Thai, Seung-Eock Kim, A simple higher-order shear deformation theory for bending and free vibration analysis of functionally graded plates. Composite Structures (96), 165-173, 2013.
[153]. N. Wattanasakulpong, B. Gangadhara Prusty, D.W.Kelly, Thermal buckling and elastic vibration of third-order shear deformable functionally graded beams. International Journal of Mechanical Sciences (53), 734-743, 2011.
[154]. B.V. Sankar, An elasticity solution for functionally graded beams. Composites Science and Technology (61), 689-696, 2001.
[155]. M. Simsek, J.N. Reddy, Bending and vibration of functionally graded microbeams using a new higher order beam theory and the modified couple stress theory.
[156]. Nguyen Dinh Kien, Large displacement behaviour of tapered cantilever Euler–Bernoulli beams made of functionally graded material. Applied Mathematics and Computation (237), 340-355, 2014.
[157]. M. Simsek, Vibration analysis of a functionally graded beam under a moving mass by using different beam theories. Composite Structures (92), 904-917, 2010.
[158]. T.P.Vo, Huu-Tai Thai, T. Nguyen, A. Maheri, J.Lee, Finite element model for vibration and buckling of functionally graded sandwich beams based on a refined shear deformation theory. Engineering Structures (64), 12-22, 2014.
[159]. Farzad Ebrahimi, Large amplitude nonlinear vibration analysis of functionally graded Timoshenko beams with porosities. Acta Astronautica (116), 117-125, 2015.
[160]. S.Rahman, A.Chakraborty, A stochastic micromechanical model for elastic properties of functionally graded materials. Mechanics of Materials (39), 548-563, 2007.

Analysis of Wind and Wave Climate along the Coasts of the Black Sea

R. Emre Çakmak[31], Bilal Bingölbali[32], Adem Akpınar[33]

Abstract

The wind and wave conditions of Black Sea coasts have been modelled using the third generation wave model SWAN forced with the CFSR winds over a period of 31 years (1979-2009). The SWAN model has been adapted and validated for the Black Sea within the TUBITAK Project [1]. In this study, long-term time series of the CFSR winds and simulated waves are processed to determine the statistical properties of these wind waves in six locations close to the shore. Annual and seasonal wind and wave rose diagrams, probability and cumulative distribution plots, and the relationship between H_{m0} and T_{m02} at the locations selected are discussed. Monthly variations of the arithmetic monthly average H_{m0} values during 31 years and the highest, mean, and lowest maximum values obtained using yearly maximum values of each month during 31 years are examined. Extreme value analysis results for waves using the yearly maximum values simulated during 31 years is also discussed for all locations.

Keywords: *Black Sea, extreme waves, SWAN, wind and wave climate,*

62. INTRODUCTION

Determining wind and wave climate have an important place in all oceanographic activities. In particular, extreme wave estimation becomes crucial for the design of offshore or coastal structures together with the wind wave climate. For an accurate assessment of the wind wave climate and extreme value analysis, long-term observation data is required. Wind measurements are usually available, however wave measurement is difficult and has a high cost. Therefore, numerical wave hindcasting models are used to fulfil this deficiency of missing wave data.

Even if there are many studies about wind and wave climate in the Black Sea, these studies have been limited to a specific region. For instance, Valchev et al. [2] simulated the wind wave characteristics in the western Black Sea shelf by using SWAN model forced with data of coarse resolution global atmospheric reanalysis for the period of 1958-2007 and they assessed wind and wave climate of the region. Özhan and Abdalla [3] produced the wind and deep sea wave atlas that is included statistics of long term and extreme value analyses at the southern coasts of the Black Sea.

In this study wind and wave climate over the entire Black Sea basin using long-term simulation results of the calibrated and validated numerical wave model (SWAN) in the locations selected were determined.

63. MATERIALS AND METHODS

63.1. Data Used and Locations

There are the short-time wave measurements in a few locations in the Black Sea and they are not sufficient to make reliable wave climate study. Therefore, the wave data that is required for wind wave climate study was produced with the help of SWAN model forced with the CFSR wind fields along the Black Sea in six locations. Detailed information about the theoretical background of the third-generation numerical wave model SWAN (Simulating Waves Nearshore) was given in [4], [5], [6], and [7]. Setting of all physical phenomena and coefficients of their application, calibration, and validation of the model were presented in Akpınar et al. [1] and [8].

The CFSR wind fields at a height of 10 m was used for generation of waves and performing of wind climate study. The grid spacing of 1 hourly wind speeds are 0.3125° in both latitude and longitude. Bathymetry of the Black Sea domain for the wave model was obtained from GEBCO (General Bathymetric Charts of the Ocean) has a global 30 arc-second interval grid (Figure 1).

The names and the coordinates of the locations indicated on the map (Figure 1) are given in the Table 1.

Table 1. Names and coordinates of the selected locations

Location	Name	Coordinates

[31] *Uludag University, Department of Civil Engineering, 16059, Bursa, Turkey. remrecakmak@uludag.edu.tr*

[32] *Uludag University, Department of Civil Engineering, 16059, Bursa, Turkey. arda_bilal_49@hotmail.com*

[33] *Corresponding author: Uludag University, Department of Civil Engineering, 16059, Bursa, Turkey. ademakpinar@uludag.edu.tr*

1	Sinop-Inceburun	42.20 N – 35.00 E
2	Rize - Findikli	41.30 N – 41.00 E
3	Krasnodar - Krai	44.00 N – 39.00 E
4	Yalta - Simeiz	44.30 N – 34.00 E
5	Northwest BlackSea	45.00 N – 31.00 E
6	Burgas – Rezovo	42.00 N – 28.50 E

63.2. Methods

This section provides information on the analyses performed in.

63.2.1. Rose Diagrams

Together with the wind and wave roses (Figure 1) covering all of the data, seasonal wind and wave roses (Figure 2) are drawn for 31 years. Wind and wave roses are plotted to determine directions of the dominant wind and waves and distribution of their magnitudes. Wind speeds were classified as lower than 2.5 m/s, 2.5 m/s to 20 m/s by 2.5 m/s intervals and higher than 20 m/s. Significant wave heights were classified as lower than 0.5 m, 0.5 m to 4 m by 0.5 m intervals and higher than 4 m. Angle axis of the rose diagram is divided into 16 directions at angles of 22.5 degrees. In addition to these, calm percentages were given according to decided limit values for wind speed and wave height, respectively 5 m/s and 0.5 m.

63.2.2. Probability and Cumulative Distributions

Probability distribution of the wave heights are calculated based on Rayleigh distribution that is most appropriate to wave statistics as mentioned in [9]. Then, Rayleigh cumulative distribution has been found and compared with the actual cumulative distribution.

63.2.3. H_{m0} and T_{m02} Relation Graphs

Scatter plot of significant wave heights versus corresponding mean wave periods is drawn without any classification based on directions for 31 years wave data. Then, equation that representing the relationship is obtained by fitting appropriate curve depending on the first degree power function and goodness of fit (r-square value) is given.

63.2.4. Extreme Value Analysis

Annual maximum values of the H_{m0} are extracted from the overall data for six locations. Gumbel Type-I largest extreme probability distribution method is applied using these values. First, non-exceedance probabilities of H_{m0} values are calculated. Then, reduced y variate values are calculated and the linear graph of y variate versus H_{m0} values is obtained. Finally, return periods corresponding to the y values are added into the diagram. In the diagram the horizontal axis is constructed at a double log scale. The vertical axis is linear. Non-exceedance probability $F(H_{m0})$

$$F(H_{m0}) = \frac{m-\alpha}{N+\beta} \quad (2)$$

where m is rank of ascending order of H_{m0} values, N is total number of data, α is location factor, and β is scale factor. Reduced variate y calculated by

$$y = -\ln(-\ln(F(H_{m0})). \quad (3)$$

Beside these, curves showing 90% confidence interval were also added to the chart.

64. RESULTS AND DISCUSSION

Rose diagrams based on all data are given in Figure 1. Each rose diagram represents the location to which it is attached. Wind roses are presented on the upper map and wave roses are presented on lower map. Waves which can be generated by the winds blowing from the sea side are observed in the wave rose diagrams.

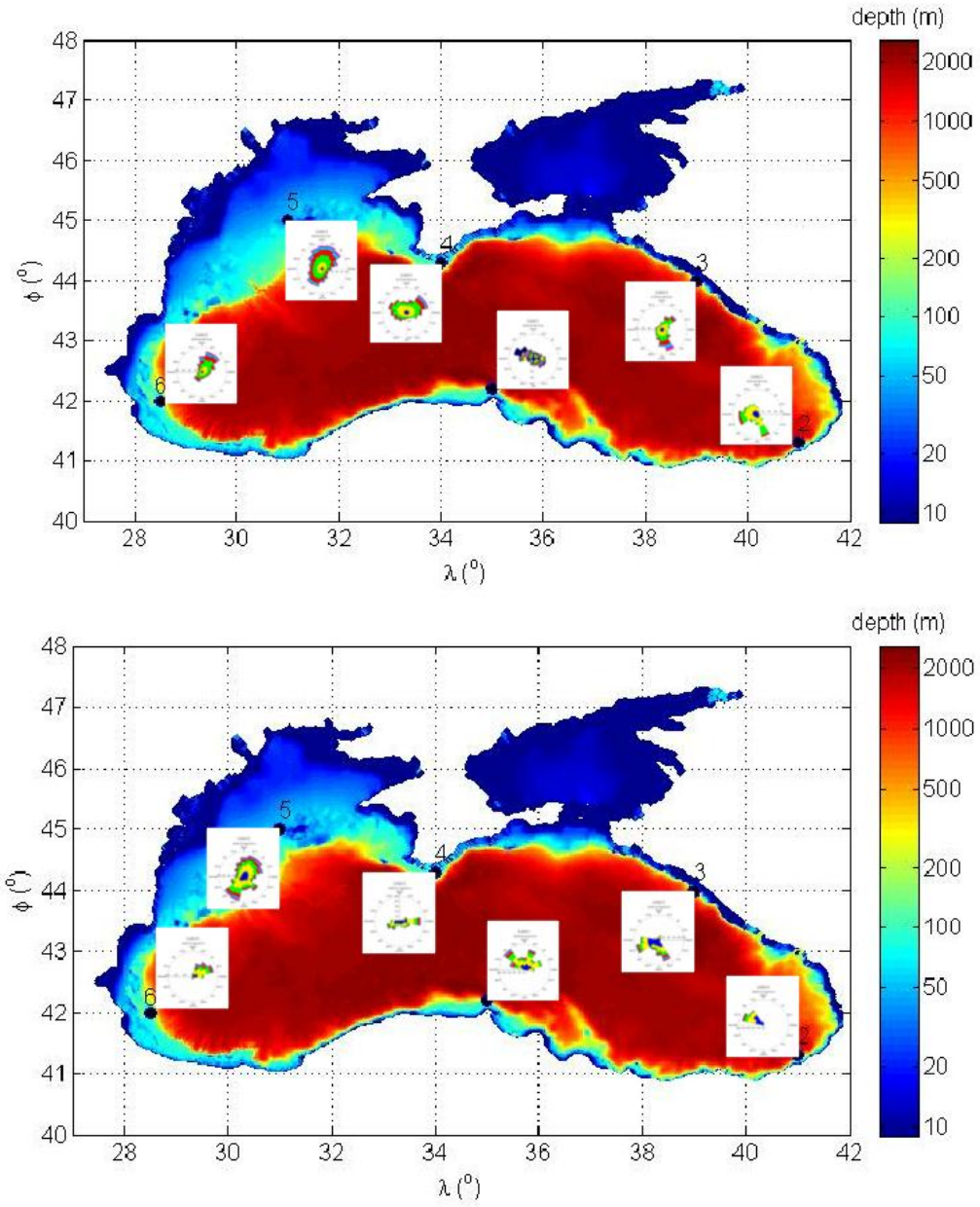

Figure 1. Bathymetry of the study area, locations, and wind (upper) and wave (lower) roses at the location

Seasonal rose diagrams are given in Figure 2 only for location 1 for the sake of the page layout. According to the wind rose diagrams most frequently blowing winds are from WNW and its secondary direction is ESE. Probabilities of occurrence are almost similar for these directions in autumn (10%) and spring (12%). Most frequent blowing winds were seen from WNW and its neighbour directions in summer. In winter secondary frequent blowing winds turn to southern directions. Strong winds blow mostly from NW – W and ESE.

Southern part of the location stand land side thus, wave has not occurred. For all seasons, most probable and strong waves come from NW due to the long fetch distance and blowing winds especially, in winter most severe waves were observed. Secondary dominant waves come from NNE and ENE directions. Considering the all rose diagrams, waves are looking agreeable to the winds blowing from sea side.

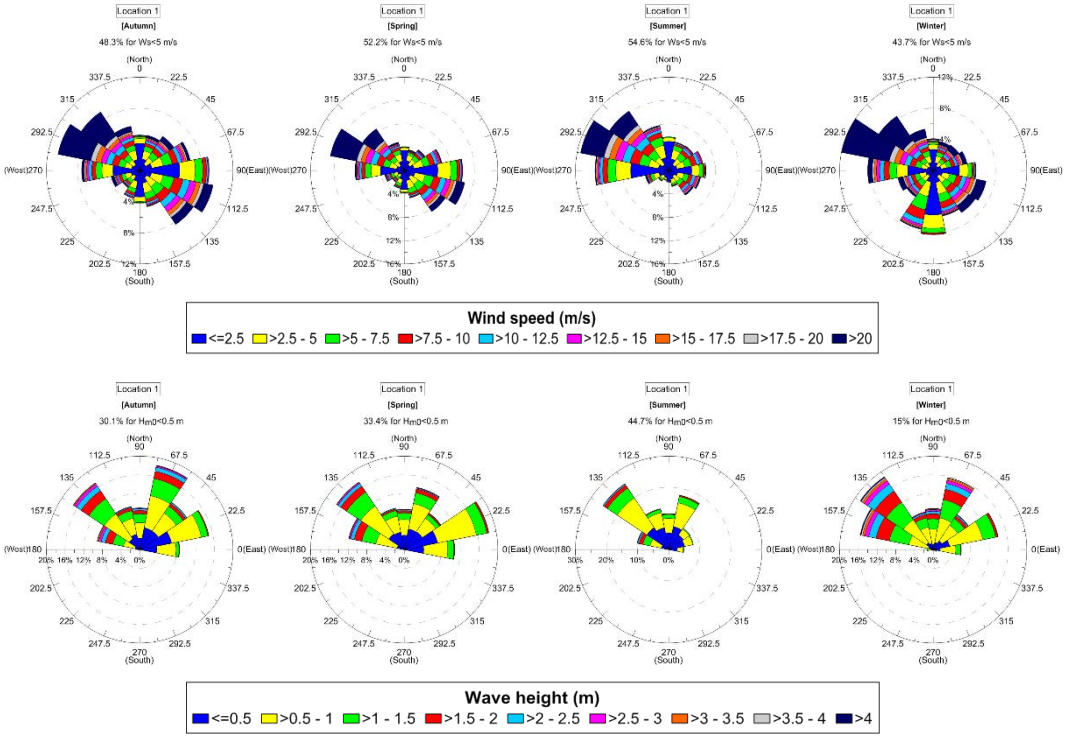

Figure 2. Seasonal wind (upper) and wave (lower) rose diagrams at location 1

Probability and cumulative distributions are presented in Figure 3. Most frequent waves can be seen when probability distributions are viewed. At locations 1, 3 and 4, approximately 50% of the total waves (in 31 years) are about 1.2 m. At location 2, most frequent wave heights (about 65% of total) are smaller than 1 m. About 40% of waves are around 1.5 m at location 5 and 6. Moreover, pdf graph shows the maximum wave heights for 31 years at all locations.

Red line shows actual cumulative distribution and green line shows Rayleigh cumulative distribution in the figure. Median wave heights are similar for both Rayleigh and actual distributions at all locations except location 3. It is also clear to see that the actual cumulative distributions reach the higher probability value smoothly than the Rayleigh cumulative distributions.

The relations between H_{m0} and T_{m02} are given in Figure 4. Equation of the appropriate representing curve of the scatter data and goodness of fit (r-square) are shown in the figure. The first striking case is diffuse scattering caused by using long-term data regardless of direction. Nevertheless, the goodness of fit values (changing 0.62 to 0.80) are slightly acceptable and constants of the equations are similar to the equations in the literature. Moreover, scatter points approach to the fitted curve at higher values, especially at locations 4, 5 and 6.

Extreme outliers are presented in Figure 5. Monthly averages are calculated as the arithmetic averages of all the significant wave heights during the month for 31 years. Highest maximum indicates the highest value of the annual maximum values observed in that month for 31 years. Lowest maximum means the lowest value of the annual maximum values observed in that month for 31 years. Mean maximum indicates the mean value of the annual maximum values observed in that month for 31 years. The monthly averages remain at a level of 1 m, however decrease slightly during summer months. Other extreme outliers vary severely from month to month, particularly the highest maximum value. Higher values were observed in winter with the highest maximum value of 8 m at location 6.

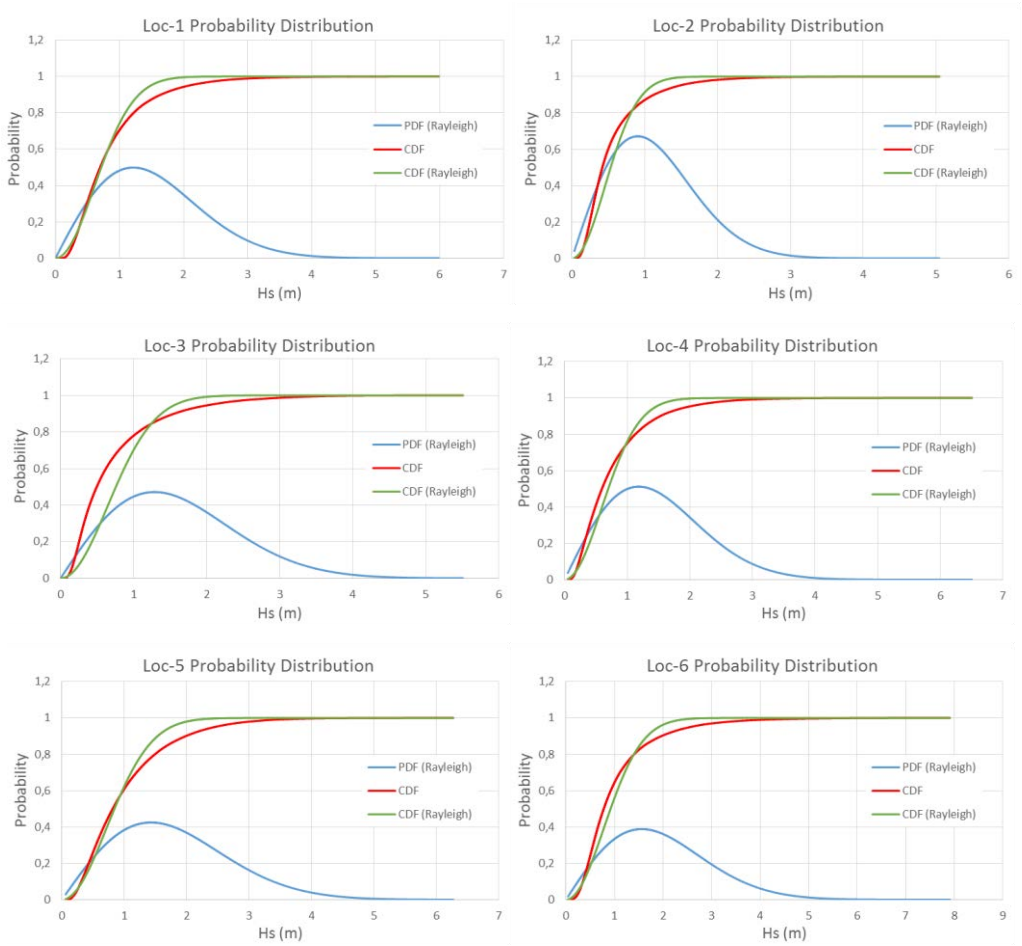

Figure 3. Rayleigh probability (blue line), Rayleigh cumulative probability (green line), and actual cumulative (red line) distributions of the wave heights for 31 years at all locations

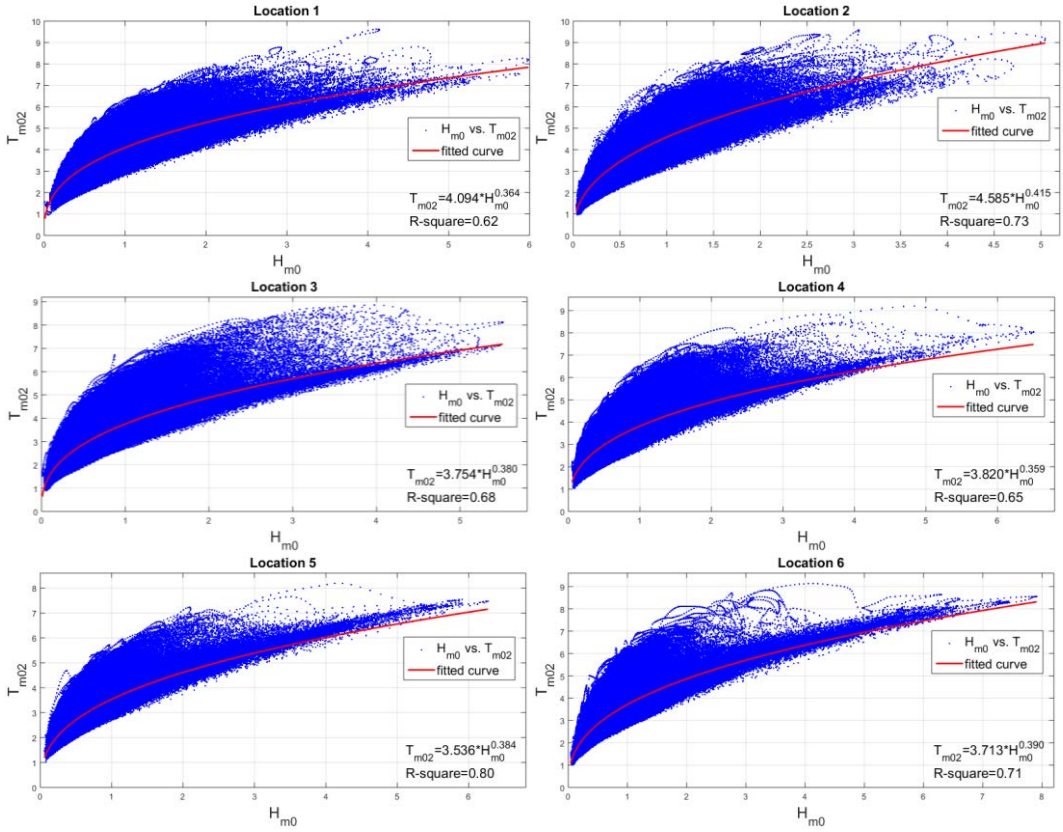

Figure 4. Relationship between Hm0 and Tm02 at all locations

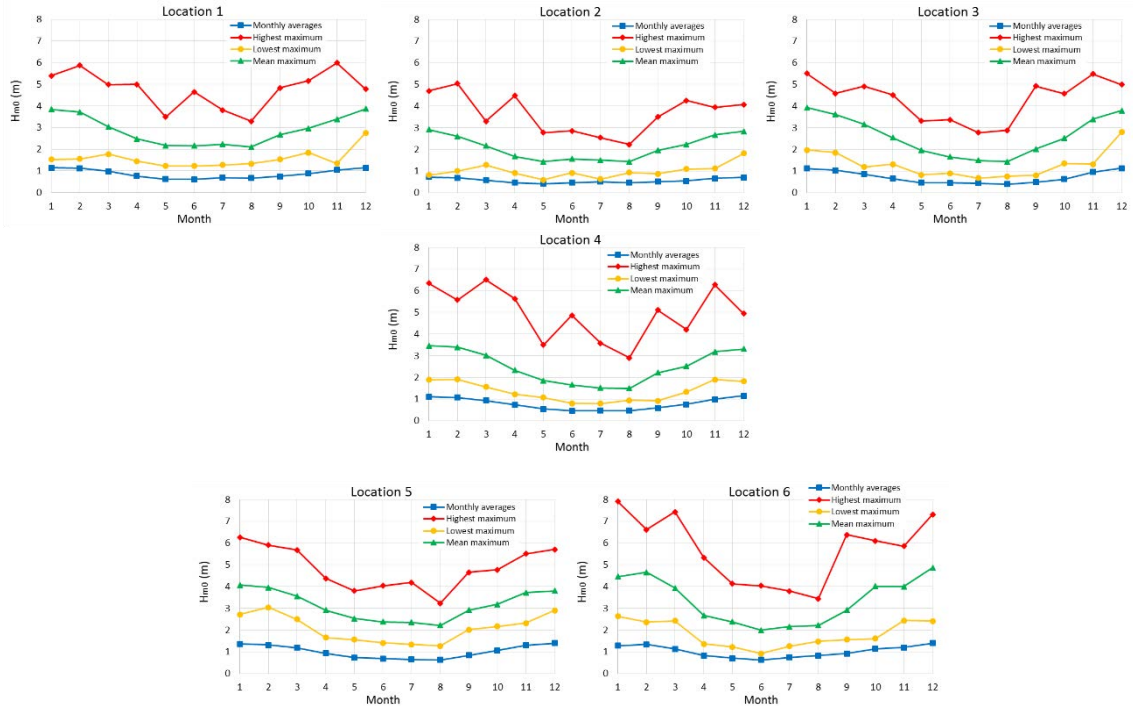

Figure 5. Monthly averages of all data and monthly highest, lowest, and mean extreme values of annual maximum values during 31 years

Largest extreme value probability statistic graphs are given in Figure 6 based on annual maximum wave data for 31 years without irrespective of direction. Intended H_{m0} value associating with the return period can be read with the help of fitted red

line that is obtained using reduced y variate and H_{m0} values. Dashed lines are showing limits of 90% confidence intervals. Significant wave heights with different return periods determined based on fitted red line in Figure 6 are given in Table 2 for all locations. 100-yr return values of significant wave heights vary between 6.5 – 9.0 m. 100-yr significant wave height is at least 5.62 m at location 2 and highest at location 6 with 9.04 m.

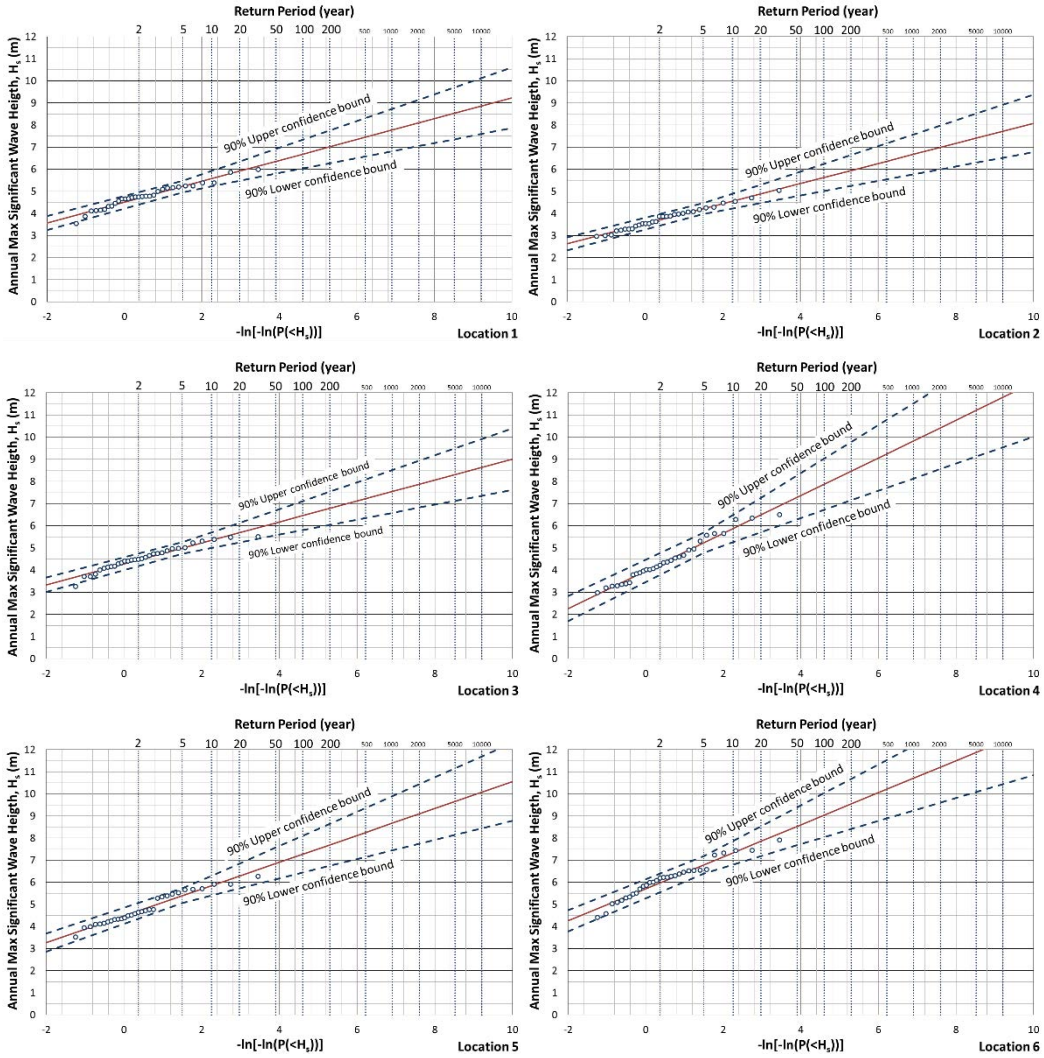

Figure 6. Gumbel Type-I largest extreme value probability distribution

Table 2. H_{m0} (m) values for different return periods

Location	Return period (year)						
	2	**5**	**10**	**20**	**50**	**100**	**200**
1	4.76	5.22	5.57	5.91	6.35	6.68	7.01
2	3.70	4.22	4.56	4.88	5.31	5.62	5.94
3	4.49	4.99	5.35	5.69	6.13	6.46	6.79
4	4.23	5.24	5.87	6.49	7.28	7.87	8.46
5	4.64	5.39	5.85	6.28	6.85	7.27	7.69
6	6.19	6.79	7.33	7.86	8.53	9.04	9.54

65. CONCLUSION

Some statistical analyses were subjected to the available CFSR wind and simulated wave data. In particular, more detailed study (probability distributions, extreme value analyses etc.) was done for the wave data. Waves have been found to be compatible with the wind data depending on the fetch and orography when the rose diagrams examined. Higher wind speeds and wave heights are observed in autumn and winter seasons. The actual distribution of the wave data is looking similar with the Rayleigh distribution of it. When available data are analysed according to the largest value analysis, location 6 located in the south western part of the Black Sea has higher wave heights. In addition to available data analysis, location 6 gives higher significant wave heights in the estimation of higher return levels of H_{m0}.

In future studies, statistical analysis will be conducted with using different distributions and compared with each other. These distributions will be applied based on different directions. In addition, peak over threshold method will be applied for estimating extreme significant waves with high return periods.

ACKNOWLEDGMENT

Special thanks from the author go to TUBITAK (The Scientific and Technological Research Council of Turkey) for its supporting our Project under the grant number 214M436.

REFERENCES

[161]. A. Akpınar, S. Bekiroglu, GPh. VanVledder, B. Bingölbali, "Temporal and Spatial Analysis of Wave Energy Potential Along the Southern west Coasts of the Black Sea," Project Number: 214M436, TUBITAK Project, 2015 (In Progress).
[162]. N. Valchev, I. Davidan, Z. Belberov, A. Palazov, and N. Valcheva, "Hindcasting and Assessment of the Western Black Sea Wind and Wave Climate," J. Environ. Prot. Ecol., vol. 11, pp. 1001-1012, 2010.
[163]. E. Özhan, and S. Abdalla, "Turkish Coast Wind and Deep Water Wave Atlas", Middle East Technical University, Civil Engineering Dept., Ocean Eng. Research Center, Ankara, Applied Project Rep., 1999.
[164]. L. H. Holthuijsen, N. Booij, and R. C. Ris, "A spectral wave model for the coastal zone," in Proc. 2nd International Symposium on Ocean Wave Measurement and Analysis, 1993, New Orleans, Louisiana, New York, p. 630–641.
[165]. R. C. Ris, L. H. Holthuijsen, and N. Booij, "A third-generation wave model for coastal regions: 2 Verification," J. Geophys. Res., vol. 104 (C4), pp. 7667–7681, 1999.
[166]. N. Booij, L. H. Holthuijsen, and R. C. Ris, "A third-generation wave model for coastal regions. Model description and validation," J. Geophys. Res., vol 104 (C4), pp. 7649–7666, 1999.
[167]. M. Zijlema, and A. J. Van der Westhuysen, "On convergence behaviour and numerical accuracy in stationary SWAN simulations of nearshore wind wave spectra," Coast. Eng., vol. 52 (3), pp. 237–256, 2005.
[168]. A. Akpınar, GPh. VanVledder, M. I. Kömürcü, and M. Özger, "Evaluation of the numerical wave model (SWAN) for wave simulation in the Black Sea," Continental Shelf Research, vol. 50-51, pp. 80-99, 2012.
[169]. *M. S. Longuet-Higgins,* "On the statistical distributions of sea waves," *J. Mar. Res.*, vol. 20, pp. 245-265, 1952.

ICENS
INTERNATIONAL CONFERENCE ON ENGINEERING AND NATURAL SCIENCES
24-28 May 2016 /Sarajevo

Investigation Of The AA1050 Aluminum Alloy With AISI 304 Austenitic Stainless Steel Sheets Are Joined By Friction Stir Spot Welding Method

Hasan KAYA, Alı OZ, Abdullah DEMIR, Mehmet UCAR, Ramazan SAMUR

Department of Machine and Metal Technology, Asim Kocabiyik Vocational School of Higher Education, Kocaeli University, TR-41800, Kocaeli, TURKEY, hasan.kaya@kocaeli.edu.tr
Department of Automotive, Vocational School of Higher Education, Mehmet Akif Ersoy University TR-Burdur, TURKEY, alioz@mehmetakif.edu.tr
Department of Mechanical Engineering, Faculty of Technology, Marmara University, TR-34730 Istanbul, TURKEY, ademir@marmara.edu.tr
Department of Automotive Engineering, Faculty of Technology, Kocaeli University, TR-41380, Kocaeli, TURKEY, ucarm@kocaeli.edu.tr
Department of Materials and Metallurgy, Faculty of Technology, Marmara University, TR-34730 Istanbul, TURKEY, rsamur@marmara.edu.tr

Abstract

The welding region of AA1050 aluminum sheet sample coated with copper-based powder through high velocity oxygen fuel (HVOF) powder spraying method when aluminum alloy with AISI 304 austenitic stainless steel sheets combined through friction stir spot welding. In characterization studies, the microstructural features of welded parts were obtained using both light and scanning electron microscopes and the mechanical properties were determined using Vickers hardness, tensile tests. The microstructure, mechanical and corrosion properties of the welded joints were analyzed.

Keywords: Friction stir spot welding (FSSW), Dissimilar materials

1. INTRODUCTION

It was determined that intermetallic compounds such as $Al_{13}Fe_4$ and Al_5Fe_2 formed in joint face of friction stir lap welding of 3mm-thick AA5083 aluminum compound and St-12 carbon steel. In welded regions, mechanic locking, diffusion, and chemical bound formation were observed. Since the thickness of intermetallic compounds in joint face is approximately 10 micron, other authours [1] have determined that it didn‘t decrease the endurance of welded joint. Watanabe et al. have reported that, by reaching the findings corroborating the formation of FeAl and $FeAl_3$ among intermetallic compounds, these intermetallic compounds decreased the mechanic properties of welded joints [2]. Traditionally, the electric resistance welding is a connection method that is widely used in automotive industry. Its superior properties such as rapid welding procedure, easy execution of welding in any position, and suitability for automatization bring it to the forefront [3]. Besides these superiorities, in connecting the AL and steel by using electric resistance welding method, a thick intermetallic reaction layer affecting the properties of joint parts emerges [4]. Despite that, in friction stir welding method, it is possible to joint different materials such as Al/Fe and Al/Cu, it is not easy to create durable joint parts because the deformation characteristics vary significantly at the temperature of friction stir welding. It has been reported that better FSW configuration has been achieved when the welding equipment penetrated into soft material [5]. Among the materials constituting the majority of studies, both of soft steel and austenitic steel have relatively low yield strength. The number of studies on welding the aluminum compounds, as the preferred lightweight vehicle structures that are discussed widely, with high-strength steels by using friction stir welding in literature is very limited. Advanced High Strength Steels (AHSS) have higher mechanic strength and operational hardness rate that have been achieved via many microstructures. The Advanced High Strength Steels are divided into 4 main groups as double-phased steels (DP), transformation induced plasticity (TRIP), complex phased steels (CP) and martensitic steels [6]. Esmaeili et al. have studied AA1050 aluminum compound and brass via the friction stir welding method. They have reported that the tensile strength of the joint decreased as the rotation speed of the equipment increased. They have explained this mechanism with the thickening of intermetallic layer and removal of finned composite structure [7]. Because of their high performance, the aluminum compound/steel hybrid compositions are widely used in different industrial areas. By decreasing the thickness of the components, the lightweight structures can be designed. It has been seen that such designs can only be manufactured by connecting the thin aluminum and steel sheets having different chemical compositions via the advanced welding methods such as friction stir welding [8].In proportion to fusion welding, the friction stir welding is of significant superiorities such as low energy intake, short duration of procedure, minimum shock, and relatively lower welding temperatures. For this reason, FSW has been developed for aviation, automotive, maritime, and nuclear systems. Friction stir welding requires friction stir equipment consisting of a shoulder and a penetrator tip. By rotating at the desired speed, the equipment unites at the desired welding spot and brings the desired solid-state heat and angle of welding. Rotating tip moves along the welding axis. When the temperature of tip and

shoulder rubbing on the material increased at the desired temperature level, then the welding of sheets can be started. Due to the temperature caused from the friction, the materials soften before reaching their melting point.In this study, it was aimed to joint AA1050 aluminum compound and AISI 304 stainless steel material, which have different chemical compositions, via friction stir welding, and then to analyze. The microstructure of the joint region of welded materials, which have different chemical structures, was examined. Moreover, the changes in micro-hardness and tensile strength of the welded regions were examined. The diffusion transitions between the copper-based coating in joint surface of AA1050 aluminum compound and AISI 304 stainless steel were determined and analyzed via EDS and XRD analyses [9].

2. Experimental

2.1. The design of the materials to be joined by friction stir spot welding

In this research, 2 mm-thick copper based coated AA1050 aluminum alloy sheet and 1mm-thick AISI 304 stainless steel sheet were used. 2x100x300 mm joint configuration was used for the fabrication of friction stir welding (FSSW) joints. Before FSSW process, the surface of aluminum plate was coated with copper based powder in a depth of 80µm using HVOF process (Figure. 2.,Tab.5). The chemical composition and mechanical properties of AA1050 aluminum alloy and AISI 304 stainless steel are given in Tabs. 1-4 respectively. Both sheets were cleaned well using emery paper and acetone before each experiment. Schematic view of the FSSW and position of sample in fixture are also illustrated in (Figure. 3). The FSSW tool had a 10 mm diameter shoulder and an unthreaded conical pin tip length with 2.7 mm and 3.1 mm respectively. A tool with a conical tip diameter of 10 mm was used and pin was tapered from 4.5 to 3 mm. During the welding process, the angle of tool tilt with respect to the work piece surface was kept constant at 0° (Figure. 3).

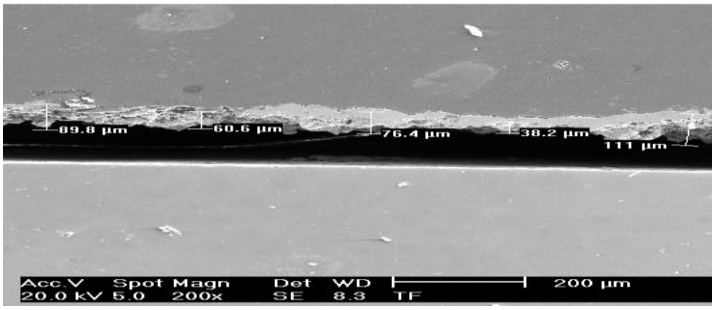

Figure 1. a-The AA1050 2mm-thick copper based coated aluminum alloy and b-1mm-thick AISI 304 stainless steel sheet.

Table 1. Chemical composition (wt. %) of 2-mm-thick AA1050 aluminum alloy used in this study

Al	Si	Fe	Cu	Zn	Ti
Bal	0.08	0.27	0.02	0.02	0.02

Table 2. Mechanical properties of AA1050 aluminum alloy used in this study

E (GPa)	Ultimate tensile strength (MPa)	Elongation (%)
69	58	40

Table 3. Chemical composition of 1-mm-thick AISI 304 stainless steel sheet (wt%) [10]

Fe	Si	P	S	V	Cr	Mn	Al	Co	Ni	Cu	Zn	C
70.94	0.22	0.04	0.04	0.08	17.55	1.61	0.07	0.14	7.96	0.92	0.11	0.05

Table 4. Mechanical properties of the used AISI 304 stainless steel metallic sheets[8]

Sheet Thickness (mm)	Density (g/cm3)	Young's modulus (GPa)	Tensile Strength (MPa)	Elongation (%)	Yield strength (MPa)
1	8	190	520	45	240

2.2. High velocity oxygen fuel (HVOF) sprayed copper-based powder coating on welding regions of aluminum alloy AA1050

Thermal spraying is a well established means of forming relatively thick coatings. In particular, high velocity oxy fuel (HVOF) spraying has been developed into a reliable technique to apply hard, tribologically superior and well adherent metallic and composite cermets coatings to a great variety of metallic surfaces. Among the thermal spraying techniques, HVOF is effectively used to prepare coatings with dense structure at a particle velocity of above 700 m/s [11]. The HVOF thermal spray method is cost effective and has been applied to copper-based coatings.

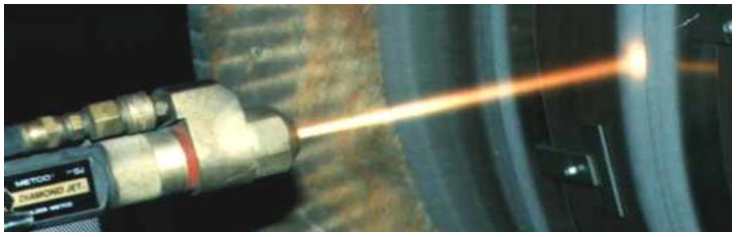

Figure 2. HVOF process used in the present study [12]

Copper-based powder is often used as the corrosion and bond strength-enhancing layer. copper-based powder coatings deposited by means of HVOF thermal spray, onto AA1050 aluminum alloy substrate. The morphology and chemical composition of the phases that are present in the coatings were characterized by means of SEM, EDS techniques. The results show that the nanostructured coating has excellent mechanical properties due to the microstructural homogenization and the well preserved nanostructure characteristic of the ball milled powders.

Table 5. High velocity oxygen fuel (HVOF) spray process parameters

Powder spray process parameters	**HVOF process**
Spray gun type	Metco Diamond Jet
Spray distance	300 mm
Spraying rate	5.3 kg/h
oxygen pressure	9.30 atm
Nitrogen pressure	3.4 atm
Flammable gas species	Natural Gas
The coating powder	copper-based

2.3 Tool tip geometry, design of materials to manufacturing and machining production

HB44UF Carbide tool material is very fine (ultrafine) particles have a structure. having balanced wear resistance and ductility values HB44UF is an ideal quality. It is especially ideal for high speed tool with a quality that can be processed hardened steels up to 64 HRC.

Table 6. Tool profile and the experimental parameters used in friction stir spot welding

Friction Stir Spot Welding Sheets	**Friction Stir Spot Welding Tool Profile**	**Tool Rotational Speed (rpm)**	**Tool Penetration Depth Rate (mm/min)**	**Dwell Time (s)**	**Tool Penetration Depth (mm)**
AA1050/AISI304 Steel	Conical	2000	12.5	6	2.7
AA1050/AISI304 Steel	Conical	2000	12.5	9	3.1

2.4. The design of steel mould used in welding and machining process to manufacturing production and use on milling machines

Figure 3. The milling machine used for friction stir spot welding process

3. Results and Discussion

3.1. Performing tensile testing after welding

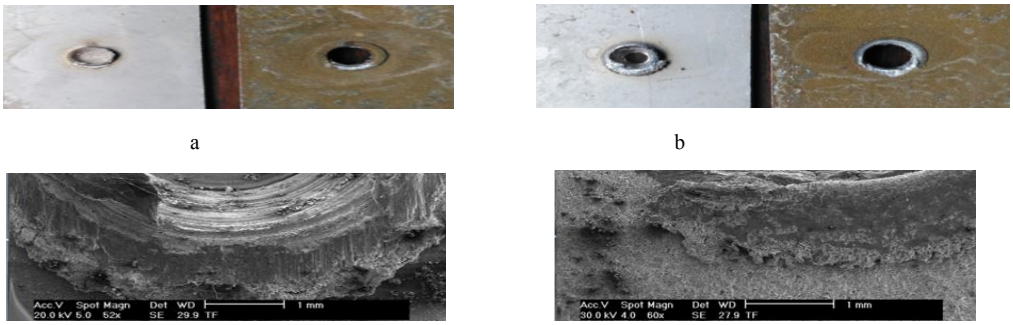

a b c d

Figure 4. Fractured specimens after tensile test for FSSW welds. a,b- Low fracture energies with an interfacial britle pullout failure mode. Rotational speed 2000 rpm, welding speed 12.5 mm/min, penetration depth 2.7mm and dewell time 6s c,d- A very robust producing high fracture energies with a ductile pullout failure mode. Rotational speed 2000 rpm, welding speed 12.5 mm/min, penetration depth 3.1mm and dewell time 9s.

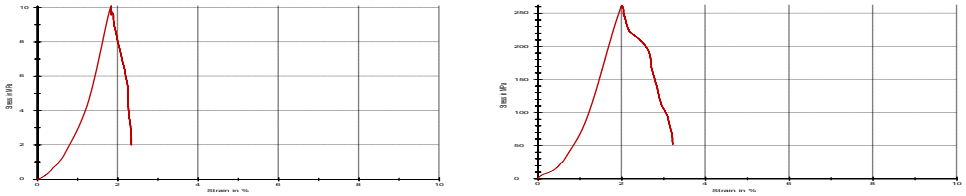

a b

Figure 5. Tensile strength and strain graph of pin penetration depth and dwell time. a- Low FSSW shear strength and failure energies b- High FSSW shear strength and failure energies.

Tablo 7. Tensile strength change with tool penetration depth and dwell time.

Welded Materials	Dwell time s	Tool Penetration Depth (mm)	Tensile strength (MPa)
AA1050/AISI304 Stainless Steel	6	2.7	10
AA1050/AISI304 Stainless Steel	9	3,1	262

It is the fact that the chemical compositions of the materials jointed via friction stir spot welding method and the copper-based surface coating material are completely different. The practice of connecting different materials is generally utilized in connecting different materials such as Al-Mg and Al-steel coated with copper-based material. The diffusion occurring at the interface during welding procedure and the formation of errors such as intermetallic compounds and cracks are not similar with those occurring during welding the materials having same chemical compound. The existence and morphology of such welding defects may significantly affect the mechanic performance of joint parts. The formation of welding defects indicates that it is due to the material used, welding equipment, and practice. The strong welding joints of different materials can be achieved via the design of appropriate processes. Intermetallic compounds that may occur in interface were used in order to eliminate the welding defects, while the copper-based coating material was used in order to prevent the cracks to improve the diffusion. The micro-structure and mechanic properties comprising as a result of designed welding parameters, the conditions of welded samples connected to the sampling container, and the interfacial conditions between material to be welded and friction stir welding equipment were examined. In weldability of different materials such as AA1050 aluminum alloys and AISI 304 stainless steel, the maximum increase in strength was achieved via the penetration depth of equipment under the effects of copper-based coating material and diffusion (Figures. 4b,d and 5b)(Table.7) [15].

3.2. Scanning electron microscope (SEM) macro and microstructure and XRD analysis

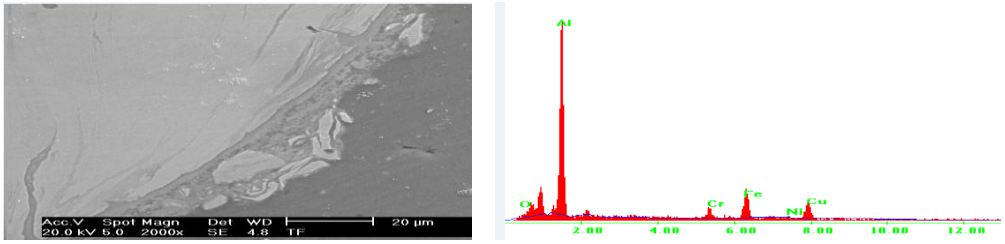

a b

Figure 6. a- Friction stir spot welding interface *stir zone of coper coated AA1050 aluminum alloy with AISI 304 welded by FSSW.b- EDS analysis*

results of friction stir spot welding interface *stir zone of coper coated AA1050 aluminum alloy with AISI 304 welded by FSSW.*

An alternative way for connecting the AA1050 aluminum alloys and AISI 304 stainless steel, which have different chemical compositions, is to coat the welding region of AA1050 aluminum alloys. As the parameter in welding process, the different penetration depths and waiting durations were taken (Table. 6). In order to increase the temperature higher than 450˚C during the welding procedure, the total procedure duration is 6s and 9s. High tensile strength during the connection procedure was achieved via copper-based coating and regional plastic deformation. Moreover, together with the chemical bound between the copper-based powder coating and AA1050 aluminum sheet, the increase in surface area of AA1050 /AISI 304 couple, and the increased temperature in interface, the activation of atomic copper, nickel and aluminum diffusion seems enough for high quality of welded connection (Figures. 6a and 7a,b).

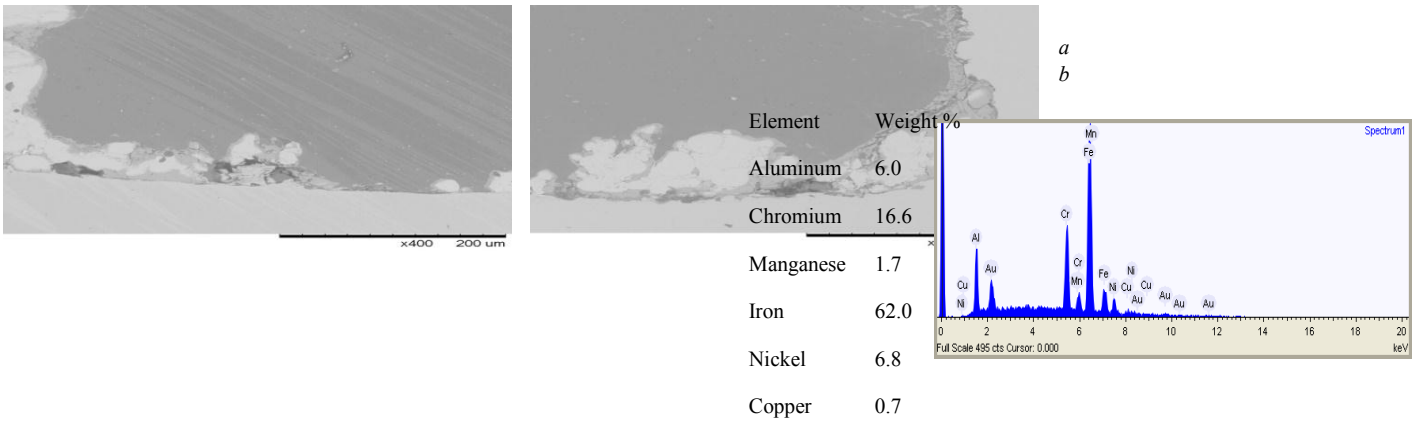

Figure 7. (a) Left corner of SEM image and (b) Right corner of SEM image, (c) and (d) EDS analysis results of general friction stir spot welding interface *stir zone of coper coated AA1050 aluminum alloy with AISI 304 welded by FSSW.*

It can be said that the increase in intermetallic layer thickness emerging as a result of Fe-Al and Cu-Al diffusion towards both of copper-based coated AA1050 aluminum sheet and AISI 304 stainless steel is positively related with regional plastic deformation due to enough heat intake (Figures. 6a and 7a,b). In connecting the AA1050 aluminum compound coated with copper-based powder coating and the AISI 304 stainless steel, which have different chemical composition, the use of friction stir welding method seems useful due to its advantages such as perfect connection performance with 262MPa tensile strength value (Figure. 5b), weight efficiency, simplicity of procedure, and long durability [8].In connecting via the friction stir spot welding method, the perfect connection was achieved by the penetration of conic tip into the aluminum sheet 2.7 mm and 3.1 mm towards the stainless steel. The XRD analyses indicate the formation of Fe_4Al_{13}, Fe_2Al_5, $FeAl_3$,CuNi and NiAl intermetallic compounds (IMC) at the certain thickness on joint face (Figure. 8). Because the desired temperature couldn‘t be reached via friction stir spot welding method in 2.7mm-deep connection procedure and consequently the diffusion and plastic deformation mechanisms couldn‘t reach at the desired level (Figure. 4a,c), the weak tensile strength 10MPa could be achieved through the weak mechanic adhesion between copper-based powder coated AA1050 aluminum compound and AISI 304 stainless steel sheets (Figure. 5b). In this study, since the HB44UF carbide equipment material was used, the equipment could penetrate into AISI 304 stainless steel sheet during the procedure without being exposed to severe corrosion. Previous studies of Chen and Nakata are in parallel with our study [16].

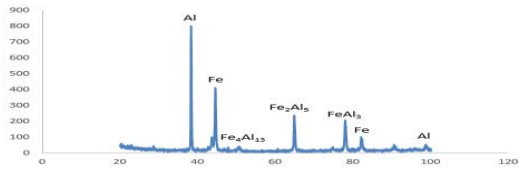

Figure 8. XRD pattern showing IMC phases (Tool Dwell time 9s and Penetration Depth of 3.1mm)

3.3. Microhardness distributions analysis effects of tool penetration depth on microhardness of the FSSW joint in AA1050 aluminum alloy and AISI 304 stainless steel sheets

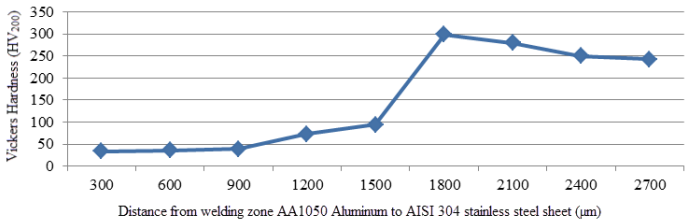

Figure 9. Microhardness distributions of the FSSW joint in coper coated AA1050 aluminum alloy to AISI 304 stainless steel sheet (Dwell time 9s and Penetration Depth of 3.1mm)

The Vickers hardness tests on the cross-sectional of the welds were carried out using an Vickers hardness testing machine according to the ASTM: E384-11.Microhardness variation across the aluminum/steel interface at the center line (Dewell time 9s and Penetration Depth of 3.1mm). The hardness values of the welded connection, starting from the AA1050 aluminum main material, were measured in horizontal, vertical and transverse directions in the way representing the aluminum and steel materials and connection interface by using Vickers hardness measurement method. The hardness measurements were started from the AA1050 aluminum main material to copper-based coating, which was affected from thermodynamic heat as a result of rotating friction effect of the tip and exposed to plastic deformation, and then connection interface of AISI 304 stainless steel and finally to the AISI 304 stainless steel material affected from the temperature by using Vickers method with 0.3 mm spacing. The hardness values showed gradual increase starting from the copper-coated AA1050 aluminum main material to intermetallic connection interface. XRD analyses indicate the formation of Fe_4Al_{13}, Fe_2Al_5, $FeAl_3$ and CuNi intermetallic compounds (IMC) in connection interface at certain thicknesses (Figure. 8). The formation of intermetallic friable phases at the connection interface and plastic deformation of AISI stainless steel material indicate the rapid increase in hardness value due to the diffusion of small particles into the connection interface and AA1050 aluminum material (Figures. 6a and 9). It should be emphasized that this rapid increase in hardness is because of the presence of intermetallic compounds (IMCs). It is possible to state that, in connection procedure performed with maximum penetration depth of 3.1mm, a friable structure formed in soft aluminum matrix because of the diffusion of AA1050 aluminum material, copper coating material and the AISI 304 stainless steel material, which emerged mainly due to the plastic deformation, into the connection interface [17].

3.4. Corrosion measurement and analysis

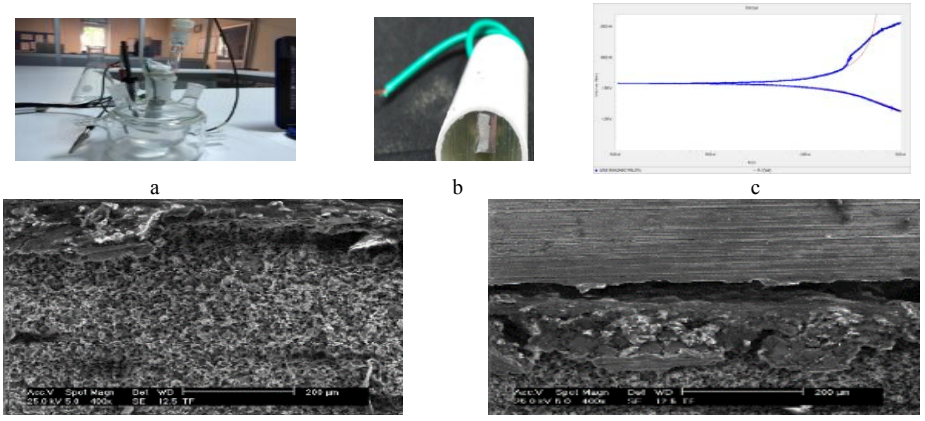

Figure 10. a- Corrosion measurement device b- Corrosion measurement sample c-Potentiodynamic polarization Tafel curves of welded interface regions along with the BM d,e- The general welded zones after corrosion test along with the BM and interface SEM micrograph

Figure. 10d shows the images of the general welded zones after corrosion test along with the BM and interface. The pitting is due to the local dissolution of the matrix as a result of galvanic coupling between copper and AISI 304 stainless steel particles and surroundings AA1050 aluminum matrix. The AA1050 aluminum BM and interface regions have corroded very severely and pits are seen throughout the surface. Also in The AA1050 aluminum BM and welded interface, the rate of attack is very high (Figures. 10d,e). In the AISI 304 stainless steel BM, only a few pits are seen. It can further be seen that the density and size of pits in AA1050 aluminum BM and interface regions are higher in comparison to AISI 304 stainless steel HAZ and BM weld regions. Galvanic coupling between copper and AISI 304 stainless steel particles and surroundings matrix is the main reason for corrosion in the interface welding zone of copper coated AA1050 aluminum alloy. Distribution of copper and AISI 304 stainless steel particles throughout the stir zone increases the sites for galvanic cell and hence decreases the corrosion resistance.

4. Conclusion

It was aimed in this study to improve the mechanical strength of the joints of copper-based coated AA1050 low strength aluminum alloy sheet to AISI 304 stainlees steel joined with friction stir spot welding by altering the chemical composition of the weld spots. In this context, the plate weld suface of AA1050 aluminum alloy sheets, were coated with 80µm copper-based powder material using high velocity oxy-fuel thermal powder spraying (HVOF) method.

1. The copper-based powder coating was founded in chemical bond with AA1050 aluminum sheet. AA1050 / AISI 304 the growth of a pair of mating surface areas with rising temperatures at the interface; atomic copper, nickel and aluminum diffusion is the activated, it is sufficient to maintain a high quality of welded joints (Figure 7a,b).

2. XRD analysis of the joint interface Fe_4Al_{13}, Fe_2Al_5, $FeAl_3$ and CuNi of the intermetallic compounds (IMC) refers to the formation (Figure. 8).

3. The friction stir spot welding process can not reach a sufficient temperature with 2.7mm depth of plunge and diffusion and plastic deformation mechanisms in parallel is performed at the desired level. While poor mechanical hold so brittle rupture mode of the interface 10 MPa could be obtained a low tensile strength (Figures. 4a,c and 5a). However, it reached a sufficient temperature and 3.1mm depth of diffusion bonding and plastic deformation mechanisms in parallel took place at the desired level. Tensile strength of 262 MPa tensile ductile mode could be achieved with excellent combination performance (Figures. 4b,d and 5b).

4. It should be emphasized that this rapid increase in hardness is because of the presence of intermetallic compounds (IMCs). It is possible to state that, in connection procedure performed with maximum penetration depth of 3.1mm, a friable structure formed in soft aluminum matrix because of the diffusion of AA1050 aluminum material, copper coating material and the AISI 304 stainless steel material, which emerged mainly due to the plastic deformation, into the connection interface [17].

5. Galvanic coupling between copper and AISI 304 stainless steel particles and surroundings matrix is the main reason for corrosion in the interface welding zone of copper coated AA1050 aluminum alloy. Distribution of copper and AISI 304 stainless steel particles throughout the stir zone increases the sites for galvanic cell and hence decreases the corrosion resistance (Figures. 10d,e)[18].

Acknowledgements
Asst.Prof.Dr.SAMUR acknowledges the support by Marmara University, Scientific Research Projects Department (BAPKO), Project FEN-C-YLP-030114-0014.

Note: The responsible translator for English language is Dr. O.Faruk CANTEKİN, School of Foreign Languages, Gazi University, Turkey.

REFERENCES

[1] Y.C.Chen, K.Nakata, Effect of tool geometry on microstructure and mechanical properties of friction stir lap welded magnesium alloy and steel,Mater.Des.30 (2009)3913–3919.
[2] T. Watanabe, H. Takayama, A. Yanagisawa, J. Mater. Proc. Technol. 178 (2006)342–349.
[3] C. Connolly, Friction spot joining in aluminium car bodies, Ind. Robot 34 (2007)17.
[4] R. Qiu, C. Iwamoto, S. Satonaka, Interfacial microstructure and strength of steel/aluminum alloy joints welded by resistance spot welding with cover plate,J. Mater. Process. Technol. 209 (2009) 4186.
[5] W.B. Lee, S.B. Jung, Mater. Res. Innovat 8 (2004) 93.
[6]. Kuziak R, Kawalla R, Waengler S. Advanced high strength steels for automotive industry. Arch Civ Mech Eng 2008;8:103–17.
[7] Esmaeılı A, Besharatıgıvı M K, Rajanı Z. A metallurgical and mechanical study on dissimilar friction stir welding of aluminium 1050 to brass (CuZn30) [J]. Materials Science and Engineering A, 2011, 528: 7093−7102.
[8] Z. Huang, J. Yanagimoto, Journal of Materials Processing Technology, Dissimilar joining of aluminum alloy and stainless steel thin sheets by thermally assisted plastic deformation 225 (2015) 393–404.
[9] H. Uzun et al. , Friction stir welding of dissimilar Al 6013-T4 to X5CrNi18-10 stainless steel , Materials and Design 26 (2005) 41–46.
[10] R.P.Mahto et al., A study on mechanical properties in friction stir lap welding of AA 6061-T6 and AISI 304, Materials Science & Engineering A 652 (2016)136–144.
[11]. Asma Salman, Brian Gabbitas, Peng Cao, Deliang Zhang, Tribological Properties Of Ti(Al, O)/Al_2O_3 Composite Coating By Thermal Spraying, International Journal Of Modern Physics B Vol. 23, Nos. 6 & 7 (2009) 1407–1412.
[12]. Çamcı,Ş.,Ustaoğlu,G.,Güler,S., Isıl Püskürtme Yöntemiyle Tungsten-Karbür Kaplama, M.Ü.T.E.F.Metal Eğitimi Bölümü Bitirme Tezi, İstanbul(2004).
[13] Tran, V., Pan, J., 2010. Fatigue behavior of dissimilar spot friction welds in lap-shear and cross-tension specimens of aluminum and steel sheets.International Journal of Fatigue 32, 1167-1179.
[14] A.K. Lakshminarayanan, V.E. Annamalai, K. Elangovan, Identification of optimum friction stir spot welding process parameters controlling the properties of low carbon automotive steel joints, j m a t e r r e s t e c h n o l . 2 0 1 5;4(3):262–272.
[15] Nilesh Kumar, Wei Yuan, Rajiv S. Mishra, Friction Stir Welding of Dissimilar Alloys and Materials, A volume in Friction Stir Welding and Processing 2015, Pages 71–114.
[16] Y.C. Chen, K. Nakata, Effect of tool geometry on microstructure and mechanical properties of friction stir lap welded magnesium alloy and steel,Mater. Des. 30 (2009) 3913-3919.
[17] S.Bozzi, a L. Helbert-Etter, T.Baudin, B.Criqui, J.G.Kerbiguet, Intermetallic compounds in Al6016/IF-steel friction stir spot welds, Mater. Sci.Eng. A527 (2010)4505–4509.

[18] H. Mındıvan et al. ,Microstructure, Mechanical And Corrosion Properties Of Friction Stir Welded AA1050 Aluminum Alloy Coated With Nickel Powder By High Velocity Oxy Fuel (HVOF) Process, 4th International Conference on Welding Technologies and Exhibition (ICWET'16)11-13 May 2016, Gaziantep-Turkey

CORRESPONDENCE ADDRESS: Ramazan SAMUR, Department of Materials and Metallurgy, Faculty of Technology, Marmara University, TR-34730 Istanbul, TURKEY, rsamur@marmara.edu.tr,GSM: +905325480919.

Application of Statistical Process Control (SPC) for Manufacturing of GGG50 Spheroidal Graphite Cast Iron

Metin Uçurum[1], Murat Çolak[2], Mehmet Çınar[1]

Abstract

Spherodized graphite cast iron, having carbon content and silicium for various reasons including the manipulation of properties required to achieve desired microstructures. One of important preferred cast irons is GGG50 in industry. Carbon Equivalent (CE) is an empirical value in weight percent, relating the combined effects of different alloying elements such as C, Si and P. Statistical Process Control (SPC) is an effective powerful methodology for analyzing, monitoring, managing, and improving process performance. In this study, the XmR control chart and process capability index method was applied to data set of CE values for a GGG50 manufacturing company's product, and the result were interpreted.

Keywords: Spherodized graphite cast iron, Carbon Equivalent (CE), Statistical Process Control (SPC)

66. INTRODUCTION

Spheroidal cast iron is an iron carbon based material, the carbon being present mainly in the form of spheroidal graphite particles. Spheroidal cast iron is also known as ductile, and less commonly as nodular iron. This spheroidal graphite is already present as cast state, and characterizes the material properties of spheroidal cast iron. Due to the nodular shape of the graphite, the notch effect is minimized. Thereby, high values for tensile strength and elongation at fracture are achieved [1]. Cast iron has become a popular cast metal material which is widely applied in modern industrial production, because of its low cost and desirable properties such as good cast ability, convenient machining property, better wear resistance, etc [2]. Nowadays nodular cast irons are significant and preferred type of cast irons. Nodular cast irons that are similar to steels from the point of mechanical properties are most popular engineering materials; at the same time they are similar to cast irons from the point of chemical and physical properties. Most preferred nodular cast irons are respectively GGG40, GGG50, GGG60 and GGG70 in industry [3].

Statistical process control (SPC) is the application of statistical methods to the monitoring and control of a process to ensure that it operates at its full potential to produce conforming product. Under SPC, a process behaves predictably to produce as much conforming product as possible with the least possible waste. While SPC has been applied most frequently to controlling manufacturing lines, it applies equally well to any process with a measurable output. Key tools in SPC are control charts and cause & effect diagrams, focused on continuous improvement [4].

[1]*Corresponding author: Bayburt University, Department of Industrial Engineering, 69000, Bayburt, Turkey.* mucurum@bayburt.edu.tr

[2]*Bayburt University, Department of Material Science and Nanotechnology Engineering, 69000, Bayburt, Turkey.* mcolak@bayburt.edu.tr

[1] *Bayburt University, Department of Industrial Engineering, 69000, Bayburt, Turkey.*
mcinar@bayburt.edu.tr

One of the most commonly employed pair of charts is the X bar-chart and the mR-chart. Through the use of control charts, similar gains can be realized in the manufacturing sector. Users of control charts report savings in scrap, including material

and labor, lower rework costs, reduced inspections, higher product quality, more consistent part characteristics, greater operator confidence, lower trouble shooting, reduced completion time, faster deliveries and others [5].

The aim of this study is determination of the lower control limits (LCL), upper control limits (UCL) and process capability indexes (Cp, Cpk_1 and Cpk_2) of the results for CE (Carbon Equivalent Number) values for GGG50 spheroidal graphite cast iron obtained from a plant in Turkey. The statistical determinations with mean chart (X), moving range (mR) method and process capability index were used for showing differences between in CE values.

67. EXPERIMENTAL

The composition of cast iron (CI) varies significantly depending upon the grade of pig iron used in its manufacture. CI contains carbon in the range of ~2 to 4 wt%. The mode and concentration of carbon in the CI is controlled to produce various grades of CI, which differ significantly in their mechanical properties and weldability. The CE of a CI helps to distinguish the gray irons, which cool into a microstructure containing graphite, and the white irons, where the carbon is present mainly as cementite. The CE is defined in Equation (1).

$$CE\ (wt\%) = C + (Si+P)/3 \quad (1)$$

A high cooling rate and a low CE favor the formation of white CI whereas a low cooling rate or a high CE promotes gray CI [6].

The purpose of this study is to apply statistical process control techniques for a GGG50 Spheroidal Graphite Cast Iron Plant in Turkey. In the calculations, X and mR control chart was established in order to determine whether the results from CE analysis of GGG50 in a metal mill were under control or not. One sample was obtained for one day during 210 days and the CE analysis were conducted X and mR control charts. The formulations of XmR are given in Table 1.

Table 1. XmR Control chart limits [7]

Chart type	Central line	Lower control limit	Upper control limit
Averages, $\bar{X}$	$\bar{X}$	$\bar{X}$-2.66*$\bar{R}$	$\bar{X}$+2.66*$\bar{R}$
Ranges, $\bar{R}$	$\bar{R}$	0	3.27*$\bar{R}$

In control charts created for quality features of products, the following points are important [8]

- Two thirds of the point should be on the central line or near the central line.
- The number of points near control limits should be at minimum level.
- The points should randomly fall below or above central limits and should be balanced.
- There should be no points outside control limits

Process capability is one of the important items in a production. A process may be controlled statistically, but its products may not be in the range being considered by the customer. The highest and the lowest tolerance ranges were treated as the

controlled upper and lower specification limits (USL and LSL, respectively) in the calculation of C_p and C_{pk} values. Using process capability indices, a specific production range can be determined for a component as a fraction of its tolerance range. Production process capability can be identified using C_p index:

$$Cp = \frac{USL-LSL}{6\sigma} \quad (2)$$

Considering C_p formula, decreasing the range of production process is one of the factors effective on improving C_p index. Thus, the smaller process dispersion or is, the higher production process capability is. C_p index, independent of production process range is placed in which part of tolerance range, can have numbers larger than one, i.e., it may be $C_p>1$ while all produced components are outside of the tolerance range. Due to this defect in Cp, another index is introduced to consider the production process dispersion, as well as to evaluate the process location to tolerance range. This factor, called C_{pk}, is displayed as follows:

$$Cpk = \min[\frac{USL-\mu}{3\sigma}, \frac{\mu-USL}{3\sigma}] \quad (3)$$

where the μ is arithmetic mean and ζ standard deviation. Different values calculated for Cp and Cpk index indicate process state as follows:

1- Cp>1 has process capability for producing a component in the range being considered by the customer
2- Cp =1 has process capability for producing a component in the range being considered by the customer with the probability of producing a defective component
3- Cp<1 has not process capability for producing a component in the range being considered by the customer and a defective component is certainly produced by this process [9].

68. RESULTS

The following calculations for X and mR charts were done and the details were given in Table 2. As seen in Figure 1, on the X chart for CE values, most of the values are above or below the center line, exhibiting a random and balanced distribution. Three points are on the outside of lower control limit. However, on the mR chart for CE value in Figure 2, six point is seen on the outside of upper control limit and the other points are seen to display normal and regular distribution, near the center line.

Table 2. Control chart values of CE for $\bar{X}$ and R

X Chart	Lower Control Limit=4.34-2.66*0.08=4.13
	Center Line=4.34
	Upper Control Limit=4.34+2.66*0.08=4.55

	Lower Control Limit=0
R Chart	Center Line =0.08
	Upper Control Limit=3.27*0.08=0.026

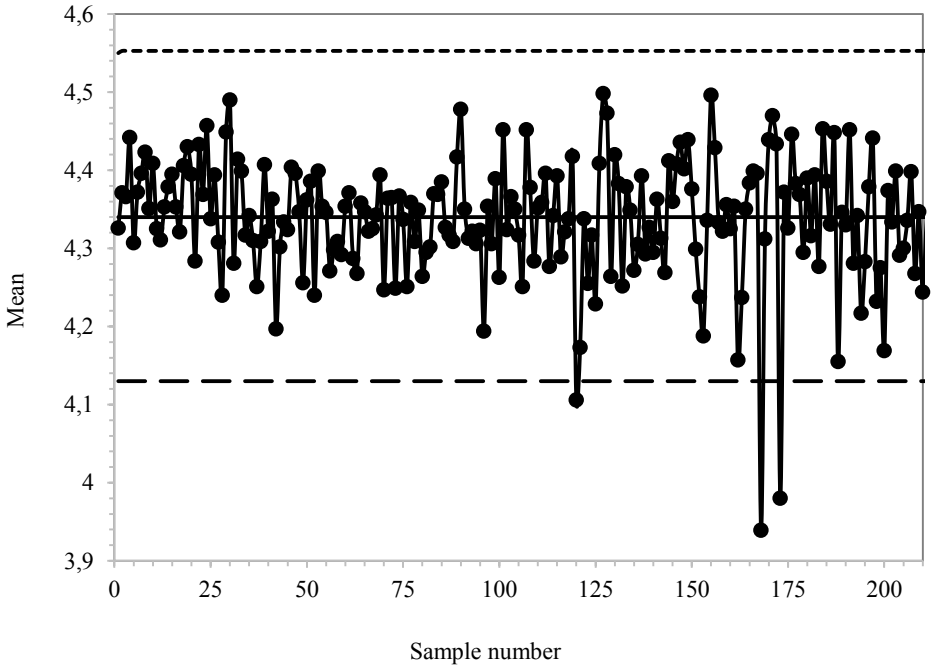

Figure 1. X chart for CE

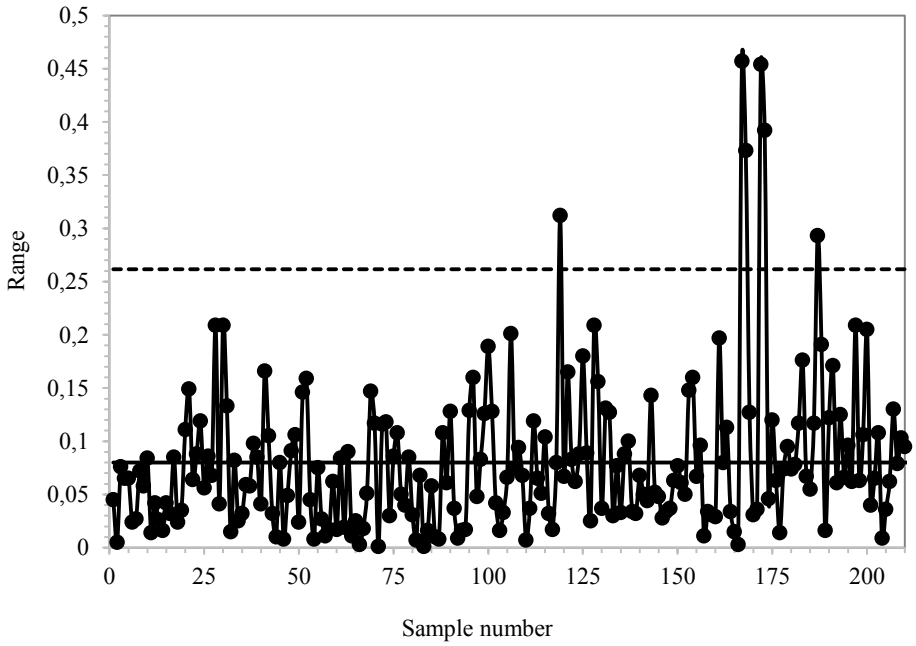

Figure 2. R chart for CE

Process capability indexes that are an overview and available statistic science for process performance gives us useful knowledge to analyze process capability or incapability. The USL and LSL as expected values for calculations indexes were obtained from the management of the plant. The calculated capability indexes for CE were given in Table 3. The Cp/Cpk values after performing the few iterations of data collection were greater than 1.0 and hence the process was declared as a capable process for important color parameters such as CE value of products, index values were under 1.0. In general, it was determined that the plant was adequate for produce GGG50.

Table 3. Capability indexes for CE

USL	4.0
LSL	4.8
Cp	1.71
Cpk_1	1.46
Cpk_2	1.97

69. CONCLUSIONS

In this study, control charts and process capability analysis of statistical quality control methods have been utilized to reach at the following conclusions:

-when XmR control charts created with CE values of GGG50 produced at the plant are examined, it is observed that it is near the central line. That is, the weaknesses of the plant were not determined.

-the calculated C_p values (1.71 for CE) for important parameters of GGG50 products are upper than 1.0. Meanwhile, the C_{pr1} and C_{pr2} values (1.46 and 1.97) are greater than 1.0. Therefore, it can be said that the process is adequate.

REFERANCES

[1] http://www.claasguss.de/html_e/pdf/THBl2_engl.pdf

[2] X. Tong, H. Zhou, L.Ren, Z. Zhang, W. Zhang and R. Cui, *Effects of graphite shape on thermal fatigue resistance of cast iron with biomimetic non-smooth surface*, International Journal of Fatigue 31/4, 668-677, 2009.

[3] L. Collini, G. Nicoletto, R. Konecna, *Microstructure and mechanical properties of pearlitic gray cast iron*, Materials Science and Engineering A, 488, 529–539, 2008.

[4] D.R. Prajapati, *Implementation of SPC Techniques in Automotive Industry: A Case Study*, International Journal of Emerging Technology and Advanced Engineering Website:, Volume 2, Issue 3, March 2012.

[5] D.C S Summers, *Quality,* Pearson Prentice Hall, 4th Edition, 2006.

[6] R. Singh, *Cast Iron Metallurgy*, Materıals Performance September 2009

[7] T. Özdemir, *İstatistikî Süreç Kontrolü*, İS 432 —İstatistikî Kalite Denetimi Dersi— notu. 2003

[8] H. Ipek, H. Ankara, H. Özdağ, *The Application of Statistical Process Control*, Minerals Engineering, Vol. 12, No. 7, pp. 827-835, 1999

[9] H. Haghighi, A.A. Shahkarami, F. Shahkarami, M. Shakeri and R. Najizadeh, *Statistical Quality Control Tools; Practical approach*, 1st Edition, Industrial management organization Publishing, 1994.

The Effect Of Drill-Hole Pattern On Fragmentation And Overburden Costs In Gle Open Pit Mines In Turkey

Onder Uysal[34]

Abstract

The drilling and blasting processes carried out in Garp Lignite Enterprise (GLE) open pit mines in Turkey and the effects of these processes on stripping costs have been examined. Three different drill-hole patterns were drilled then blasted using spacing and burdens of 7x6m, 7x5m and 6x5m respectively. The research study was carried out for a period of three months during which time the effect of drilling pattern on the size distribution of muck pile for each drill-hole pattern (as a measure of fragmentation) was determined. In addition, stripping unit costs were calculated for each drill-hole pattern. The results of this study, demonstrate that the drill-hole pattern does have a have direct effect on fragmentation and thus also will have a significant impact on stripping costs.

Keywords: drill-hole pattern, fragmentation, stripping cost.

70. INTRODUCTION

An open pit mine operation typically consists of drilling, blasting, loading and hauling activities. Drilling and blasting is an important step of this process chain. It has a direct impact on fragmentation, muck pile shape, looseness and dilution, each of which can affect the efficiency of subsequent processes and their costs [1]. Other important steps are loading and hauling. When it is considered that open pit mine planning is moving towards ever deeper excavations, importance of drilling and blasting becomes apparent. The cost of loading is a function of the size distribution of the muck pile, which in term depends on the specifications of explosive and drill-hole pattern. Poor fragmentation which gives rise to a large percentage of over size blocks of rock, resulting in longer loading times as well as an increase in energy required in both crushing and grinding which in turn leads to a decrease in productivity and increase in the cost of these processes [2,3].

Size distribution of muck pile after blasting is extremely important in mining. Expanded blast hole burden and spacing results in an increase in the drill ratio (volume of rock blasted divided by the total length drilled i.e. cubic metres per metre) as each specific blast hole influences an increased volume of rock with a resultant increase in average particle size [4,5]. Whilst oversize fragmentation increases the costs of downstream processes, undersized fragmentation increases the cost of drilling and blasting [6,7,8,9,10,11,12]. The relationships between fragmentation and these costs are shown in Figure 1 [13]. Drilling-blasting and loading-hauling costs were defined as total cost in Figure 1. The aim should be to minimise the total cost of production and combination, part of which will be to determine the optimum fragmentation required, always bearing in mind that the cheapest form of rock breakage is most likely to be by drilling and blasting.

In this study, a three-month study was conducted in GLE open pit mine. Blasting processes in 3 different drill-hole patterns have been carried out in one month intervals. The drill-hole patterns used were 7m x 6m, 7m x5 m and 6m x 5m (spacing x burden). Initially, size distribution analysis for each drill-hole pattern was carried out and the effect of changes in drill-hole pattern over fragmentation was determined. The software package (SPLIT) was used in assess size distributions contained in each muck pile photographed. Subsequently, the cost of drilling, blasting, loading and hauling was calculated and unit stripping cost was determined.

[34] *Corresponding author: Dumlupinar University, Department of Mining Engineering, Kutahya, Turkey.* onder.uysal@dpu.edu.tr

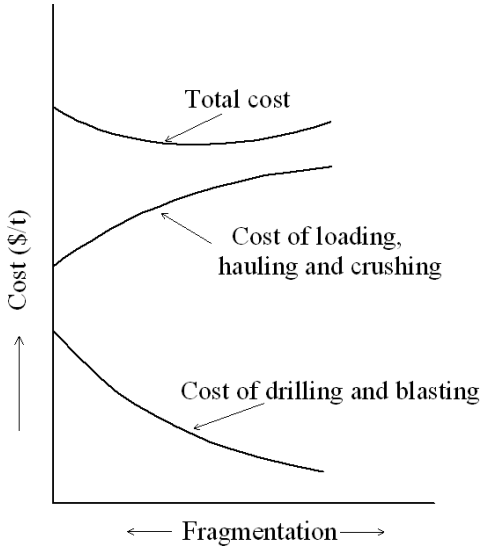

Figure 1. The effect of fragmentation on cost in open pit mine

2. INFORMATION ON THE PIT

A specific loading bench within GLE open pit mine was selected for the study. The formation of the area is made up the marl of which some geo-mechanical features are listed in Table 1. The loosening operation is carried out by blasting. Loading shovels with 4-6 m^3 capacity were used to excavate the rock into 22-50 m^3 capacity dump trucks. The average distance from the loading face to the overburden dump was about 1450 meters (200-2700 m). The thickness of the overburden was about 10 m. The bench height was 7.5 m and the slope of excavation face was 80°.

Table 1. The Geo-Mechanical Properties of the Marl.

Density (g/cm^3)	2.75
Schmidt hardness	42.6 (Strong)
Unaxial compressive strength (MPa)	24.31
Indirect tensile strength (MPa)	2.19
Cohesion (MPa)	32
Internal friction angle (°)	30

3. THE DETERMINATION OF SIZE DISTRIBUTION OF MUCK PILE

In this study size distribution has been assessed by means of the software called SPLIT [14,15]. In order to determine the size distribution, photographs of the each muck pile formed as a result of a specific blast were taken. These photographs were then transferred into the computer and evaluated by SPLIT software computer programme to determine the size distribution. Figure 2 shows a sample muck pile and Figure 3 shows the size distribution of this muck pile. These procedures where repeated 10 times for each hole-pattern. The average size distributions pertaining to the three different are shown in Figure 4. This clearly shows that a change in spacing and burden results in considerable differences in size distribution. The smaller drill-hole patterns result in smaller fragmentation size[16].

Figure 2. A sample muck pile.

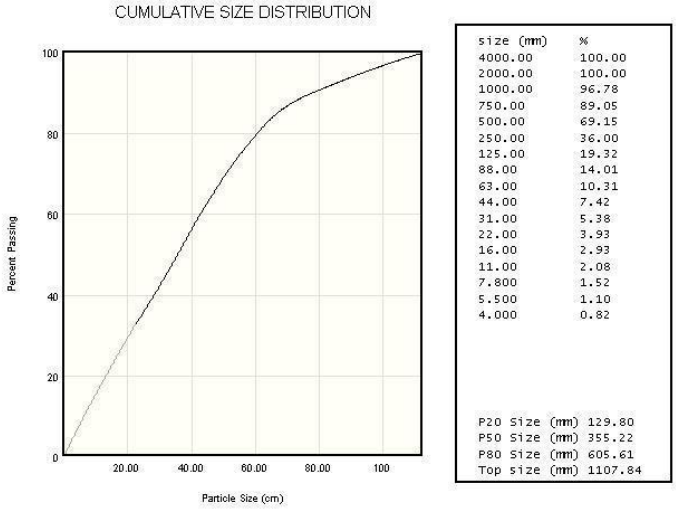

Figure 3. The size distribution of the muck pile in Fig. 2.

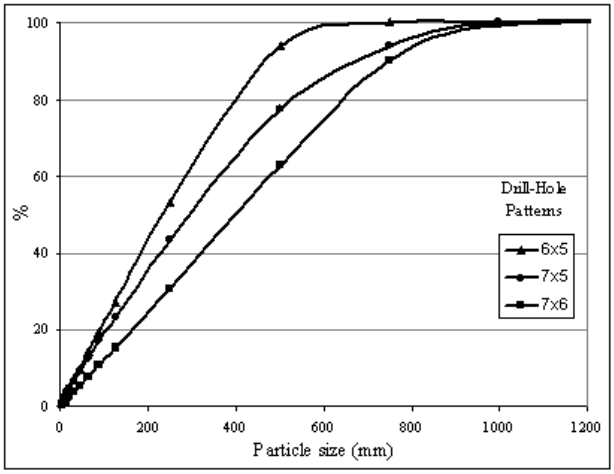

Figure 4. Average size distributions for different drilling patterns

4. STRIPPING COST

The costs of drilling and blasting, loading and hauling for the 3 drill-hole patterns were calculated to determine the extent to which the drill-hole pattern influenced the stripping cost. The calculations include only the costs of explosive and fuel-oil. Other expenditure such as labour which is the same for every period was excluded from the calculations. The same equipment was used at every observation period. The 7m x 6m drill-hole pattern resulted in 745000 m^3 of blasted rock, the 7m x 5m drill-hole pattern resulted in 847695 m^3 of blasted rock, and in 6m x 5m drill-hole pattern resulted in 614241 m^3 of blasted rock.

4.1. Drilling and Blasting Costs

During the whole study, the holes were drilled in the form of double row, with the second row being offset by half the spacing. Each hole was 15.24 mm in diameter and 8.5 in length. All holes were loaded identically with a main charge of 62.5 kg of ANFO, 0.5 kg of dynamite was used as a primer and then initiated by a single delay detonator. Table 2 contains information as to the drilling and blasting parameters recorded as well as their respective values.

Table 2. Data Related to Drilling and Blasting Processes for Drilling Patterns

	Drilling pattern		
	7mx6m	**7mx5m**	**6mx5m**
Stripping amount (m^3)	745000	847695	614241
Number of the holes	1848	2480	2058
ANFO (kg)	109275	142850	109900
Dynamite (kg)	955	1210	973
Fuse (unit)	1848	2480	2058
Fuel oil consumption of the drillers (l)	10810	14287	11137
Drilling ratio (m^3/m)	47.43	40.21	35.11
Blasting ratio (m^3/kg)	6.82	5.93	5.59

As seen from Table 2, as the drilling ratio decrease, overburden per hole decreases and the amount of ANFO used for m^3 overburden increases.

Table 3 shows drilling and blasting unit costs for each term by combining the data given in Table 2 with the explosive and fuel costs given below.

ANFO : 0.58 $/kg

Fuse : 1.33 $/unit

Dynamite : 2.38 $/kg

Fuel : 1.50 $/litter

As is seen in Table 3, as spacing and burden decreases, there occurs an increase in drilling and blasting unit cost since the volume blasted by each hole decreases (i.e a decrease in the drilling ratio). However as the charge weight per hole remains the same the blasting ratio (i.e volume of rock disrupted divided by the charge weight per hole) also decreases.

Table 3. Drilling and Blasting Costs

	Drilling pattern					
	Total Cost ($)			Unit Cost ($/m^3)		
Material	**7mx6m**	**7mx5m**	**6mx5m**	**7mx6m**	**7mx5m**	**6mx5m**
Explosive						
ANFO	63380	82853	63742	0.085	0.098	0.104
Fuse	2458	3299	2737	0.003	0.004	0.004
Dynamite	2273	2880	2316	0.003	0.003	0.004
Fuel (for drillers)	19644	21431	16706	0.026	0.025	0.027
TOTAL	87755	110463	85501	***0.117***	***0.130***	***0.139***

4.2. Loading and Hauling Costs

In the mine, the excavators with 4, 5.8, 6, 6.2 and 7.3 m^3 capacity were used for loading. In hauling, trucks with 22, 24, 28 and 50 m^3 capacity were used. Total amount of fuel-oil equipments used in all loading and hauling and unit costs are given in Table 4. As clearly shown from the data in Table 4, as the drilling ratio decrease, loading and hauling unit cost also decrease. While the unit cost for 7m x 6m drilling pattern is 0.554 $/$m^3$, the unit cost for 6m x 5m drilling pattern is 0.482 $/$m^3$. The reason for this is that the size of average fragment that emerges out of blasting becomes smaller as both spacing and burden decrease. With the result that the loading and hauling processes become more efficient. In addition, decreases in the percentages of large blocks and a reduction in ―de formation" combine to make loading and hauling more efficient.

Table 4. Fuel Consumptions and Costs on Loading and Hauling Processes

	Drilling pattern		
	7mx6m	7mx5m	6mx5m
Loading			
Fuel consumption (litter)	141684	119830	107953
Unit fuel consumption (l/m^3)	0.190	0.185	0.176
Unit cost ($/m^3)	0.285	0.278	0.264
Hauling			
Fuel consumption (litter)	133206	139403	88979
Unit fuel consumption (l/m^3)	0.179	0.164	0.145
Unit cost ($/m^3)	0.269	0.246	0.218
Loading-Hauling unit cost ($/m^3)	***0.554***	***0.524***	***0.482***

4.3. Stripping Unit Costs

Table 5 lists the stripping unit costs which are calculated by considering fuel-oil consumption and explosive used only in drilling, blasting, loading and hauling by means of the unit costs given in Table 3 and 4. As it can be seen in Table 5, there is a negative correlation between drill-hole geometry and drilling-blasting, whereas there is a positive correlation between drill-hole geometry and loading-

hauling. In terms of stripping cost, while the total unit cost for 7mx6m drilling pattern was 0.671 $/m^3, this cost was 0.654 $/m^3 for 7mx5m drilling pattern and decreased to 0.621 $/m^3 for 6mx5m.

Table 5. Stripping Unit Costs

	Drilling pattern		
	7mx6m	**7mx5m**	**6mx5m**
Costs ($/m^3)			
Drilling and blasting	0.117	0.130	0.139
Loading	0.285	0.278	0.264
Hauling	0.269	0.246	0.218
TOTAL	***0.671***	***0.654***	***0.621***

CONCLUSION

In this study, the effects of different drill-hole changes on fragmentation and stripping cost in an open pit have been investigated. This was achieved by selecting three different blasting drill hole patterns: 7m x 6m, 7m x 5m and 6m x 5m. For each case, blasting have been carried out for a period of one month. Size distribution analysis were done in order to identify the effect of drill-hole pattern on fragment size, and the results show a marked decrease in average fragment size occurs when smaller spacing and burden were used in blasting. Moreover, a decrease in toe formation was also observed during the field observation with smaller spacing and burden.

The stripping costs for each case were also determined. In these calculations, only fuel and explosive costs were included since these are the costs which are affected mostly by drill-hole pattern changes. For each pattern, drilling-blasting, loading and hauling unit costs including explosive and fuel costs were calculated. The results show that drilling and blasting cost increases as spacing and burden decreases because more holes are drilled and thus more explosive is needed in order to blast the same volume. However, the opposite is true when considering the loading and hauling costs. Loading and hauling costs decrease as spacing and burden decreases. The reason for this is that as average fragment size becomes smaller, loading and hauling become more efficient.

When stripping unit costs for each pattern were calculated, it was possible to see that stripping unit cost decreases as the drill ratio decreases. While the stripping cost for 7m x 6m drilling pattern was 0.671 $/m^3, this cost decreased to 0.654 $/m^3 for 7m x 5m drilling pattern and to 0.621 $/m^3 for 6m x 5m drilling pattern.

In open pit mines today, stripping ratio is high, and competition if fierce. Therefore, it is extremely important to carry out operations at the lowest possible unit cost. This study clearly demonstrates that it is possible to increase profit by changing drill-hole pattern. However this is only possible if the whole drilling, blasting, loading, hauling, crushing and grinding are optimised as one process. It is folly to try to minimise one unit cost (e.g. drilling and blasting) without fully examining the effects that this has on other stages of the production process...

REFERENCES

[1]. Kanchibotla SS. Optimum Blasting ? Is it minimum cost per broken rock or maximum value per broken rock. *Fragbalst*, 2003, 1:35-48.

[2]. Bilgin HA. Açık Ocak ve Taşocaklarında Patlatma", in Eskikaya S et al, editors. *Maden Mühendisleri için Açık Ocak İşletmeciliği El Kitabı. Ankara* TMMOB, Maden Mühendisleri Odası, 2005, p.231-313.

[3]. Workman L, Eloranta J. Saving money from the start: a look at effects of blasting on crushing and grinding efficiency and energy consumption – E&T Blasting. *Pit & Quarry*, 2004.

[4]. Bilgin HA. Açık İşletmelerde Patlatma Sorunları ve Tasarımı. *TKİ Eğitim Semineri,* No:2, ODTÜ, 1988, Ankara.

[5]. Erkoç OY. Kaya Patlatma Tekniği. *Çelikler Matbaacılık*, İstanbul, 1990, 164

[6]. Kanchibotla SS, Valery W, Morrell S. Modelling fines in blast fragmentation and its impact on crushing and grinding. Proc. Explo-99 Conf. Kalgoorlie, 1999.

[7]. Kojovic T, Kanchibotla SS, Poetschka N, Chapman J. The effect of blast design on the lump-to-fine ratio at Marandoo iron ore operations. Proc. Mine to Mill Conf., Brisbane, 1998.

[8]. Floyd J. Improving low -grade ore recovery with the use of efficient blasting techniques. Proc. Mine to Mill Conf., Brisbane, 1998.

[9]. Simkus R, Dance S. Tracking hardness and size: Measuring and monitoring ROM ore properties at Highland valley copper. Proc. Mine to Mill Conf.,Brisbane, 1998.

[10]. Scott A, Kanchibotla SS, Morrell S. Blasting for Mine to Mill Optimisation. Proc. Explo-99 Conf. Kalgoorlie, 1999.

[11]. Nielsen K. The economic consequences of drill hole deviation in crushed aggregate production. Proc. Explo-99 Conf. Kalgoorlie, 1999.

[12]. Grundstrom C, Kanchibotla SS, Jankovich A, Thornton D. Blast Fragmentation for Maximising the Sag Mill Throughput at Porgera Gold Mine. Proc. 28th ISEE Conf, Orlando, 2001.

[13]. Hoek E, Bray J. Rock Slope Engineering. IMM 3rd Edition, 358, 2001, London.

[14]. Girdner K, Kemeny J, Srikant A, McGill R. The Split System for Analyzing the Size Distribution of Fragmented Rock. Proceedings of the Fragblast-5 Workshop on Measurement of Blast Fragmentation, A.A. Balkema, Montreal, Quebec, Canada, 1996, 101-108.

[15]. Kemeny JM, Girdner K, BoBo T. New Advances in Digital Image Analysis Software to Quantify the Size Distribution of Fragmented Rock. MINNBLAST 99, 1999, 27-43.

[16]. Unlu A.O. TKI-Garp Linyitleri İşletmesi Açık Ocaklarında Delik Geometrisinin Parça Boyutu ve Dekapaj Maliyeti Üzerindeki Etkisi (In Turkish). M.Sc. Dissertation, (unpublished), Graduate School of Natural and Applied Sciences, Dumlupinar University, Kutahya, 2006, 73 pp.

Investigating the Electromagnetic Shielding Effectiveness Simulations of Metal Composite Fabrics

Ruslan Abdulla[35], Ediz Delihasanlar[36], F.Gamze Kızılçay Abdulla[3], A.Hayrettin Yüzer[4]

Abstract

This paper presents the investigation of electromagnetic shielding effectiveness (EMSE) simulation of weft knitted fabric made of yarns blended with metal fiber filaments 50μm in diameter. In researches related with this study, the EMSE are mainly obtained by experimental testing and no suitable fabric structure design for simulation is available. It is hard to design and draw the fabric in 3D. Thus fabric structures are generally regarded as metal plane or metal plain with some apertures on it. This may result in inaccurate readings of shielding effectiveness (SE) values. In this study, in order to accomplish this problem and minimize the error, the weft knitted fabric structure with inserted copper wire and 2mm^2 apertures, was designed both as metal plain with apertures on it and a real structure of the fabric, where one continuous yarn forms courses across the fabric, on simulation software Computer Simulation Technology (CST) Studio. Afterwards, SE simulations had been carried out for both models and the results had been compared with each other. The results indicate that the SE values of former model are not compatible with those obtained from experiments carried out in literature and they are far more than the values obtained from the knitted fabric model. Both aspects show that for SE simulations metal planes cannot be substituted as fabrics' structures.

Keywords: conductive fabric, electromagnetic shielding, shielding fabric simulation

71. INTRODUCTION

From the beginning of 20thcentury with the growth of technology development in industry and improvements in economic conditions resulted in the growth of electrical devices. In spite of the fact that the use of these devices eases our lives, it is commonly believed that electromagnetic waves emitted from these devices are harmful to human health. There are still ongoing researches investigating the harmful effects of media due to electrical energy consumption. In the aspect of gathered data from related articles, it is obvious that the electromagnetic waves should be analyzed in deep and we should protect ourselves from its possible negative effects [1]-[3].

Shielding is a very popular method of ensuring electromagnetic compatibility and protecting electronic and electrical equipment as well as human beings against radiated electromagnetic energy [4]. Shields are used either to isolate a space or media from outside sources of electromagnetic radiation. The way how it is done is to put shielding material or barrier between source and victim. By this means, electromagnetic interference between source and victim is prevented due reduce in exposed electromagnetic fields strength [5].

In order to evaluate shielding effectiveness of materials several number of simulation software can be used such as CST Studio, HFSS, FEKO and etc. Simulating EMSE values of different type of conductive fabrics is an essential step of this subject. It is seen from the literature that researchers developing such shielding fabrics are willing to compare the simulation results to those obtained from theoretic calculation methods and experiments. However, because of complex structure of fabric it is hard to design the conductive fabric in 3D. Thus, fabric structures are generally regarded as metal plane or metallic rectangular meshes. Liu et.al. [6] stated that the conductive fabrics consists of many

[35]*Corresponding author: Karabük University, T.O.B.B. Technical Sciences Vocational School, 78000, Karabük/Turkey.* ruslanabdulla@karabuk.edu.tr

[36,4]*Karabük University, Engineering Faculty, 78000, Karabük/Turkey.*

[3]*Süleyman Demirel University, Engineering Faculty, 32200, Isparta/Turkey.*

independent yarns and there are many interstices in the fabric. The electromagnetic wave can produce conventional angel reflections in the fabric. They concluded that SE computation of the metal shield is not suitable for shielding fabrics. After what by considering the physical features of fabric they succeeded to derive own theoretical calculation method from present SE equations for metal shields(Figure1(a),(b)). Pocai and Bottari [7] figured out that conducting fabrics could be realized as metallic rectangular meshes. In addition to this, Perumalraj ve Dasaradan [4] also simulated metallic rectangular meshes with many apertures (0, 5, 10, 15, 20 and 25 aperture/cm^2) as if they were conductive fabrics used as a sample in their experiments. (Figure1(a),(c)).

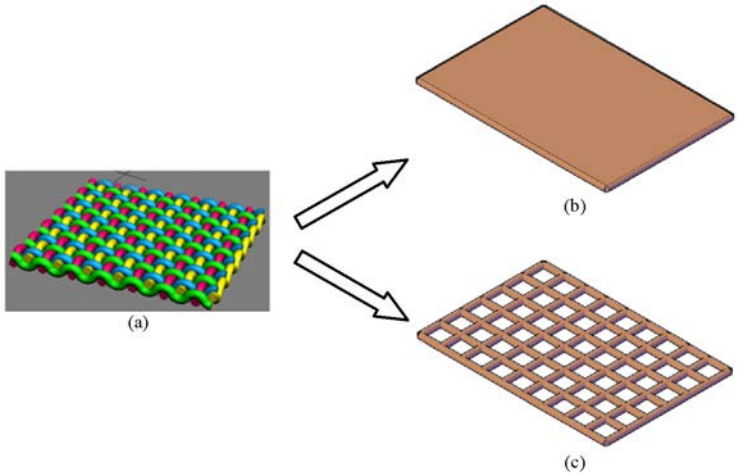

Figure 1. Geometry of (a) regular fabric, (b) fabric substituted as metal plane, (c) fabric substituted as metallic rectangular meshes

This kind of approaches may give unreliable shielding effectiveness values read from the simulations. Thus, analyzing the real physical geometry of conductive fabric during the experiments is very important issue. For this reason in this study as a sample, weft knitted fabric had been chosen and designed in 3D with the help of AutoCAD Mechanical 2014 software. At the last stage in order to simulate shielding behavior of the fabric, design file had been exported from the AutoCAD and then imported to the simulation software CST Studio where we got final SE simulation results. The same procedure had been applied to a model in which the fabric realized as rectangular meshes (Figure 1-(a), (c)). All simulations were performed in the frequency range from 1.7 to 2.6GHz which includes many commercial bands such as 1800MHz GSM, 2100MHz 3G, 2400MHz Wi-Fi, microwave ovens and etc.[3],[8]. Transmission and shielding efficiency were evaluated from S parameter simulations. Results obtained from both models had been compared with each other.

72. THEORETICAL ANALYSIS

2.1. Shielding Effectiveness

Shielding Effectiveness of a material is the ratio of the power received with and without a material present for the same incident power.

$$SE = 10\log\left(P_1/P_2\right) \tag{1}$$

The shielding can be divided into reflection loss, absorption and multiple reflections. The SE of a material is given by the equation [8]

$$SE = R + A + B \qquad (dB) \tag{2}$$

where R represents the reflection loss, A represents the absorption loss, and B represents the correction factor due to multiple reflections within the shielding material. The term B is often neglected due to the extreme small size of term. Thus shielding generally relies on reflection and absorption loss.

2.2. S - Parameters

As a result of simulations, complex scattering parameters (S-parameters) i.e. S_{11} (or S_{22}) and S_{12} (or S_{21}) which conveniently correlated with reflection (R) and transmission (T), were analyzed . Both reflection and transmission coefficients are given by $R = \left|S_{11}\right|^2$ and $T = \left|S_{21}\right|^2$ respectively. The absorption coefficient A can be obtained from the simple relation

$A+R+T=1$ indicating that the absorbed power is $A=1-R-T$. The eventual equations for shielding effectiveness can be derived as [9]-[10]

$$SE_{RL}=10\log\left(1-10^{\frac{S_{11}}{10}}\right) \tag{3}$$

$$SE_{AL}=10\log\left(\frac{10^{\frac{S_{12}}{10}}}{1-10^{\frac{S_{11}}{10}}}\right) \tag{4}$$

Where S_{11} and S_{12} are evaluated measured scattering parameters by the software. SE_{RL} and SE_{AL} are reflection loss and absorption loss respectively.

73. DESIGN AND SIMULATIONS

3.1. Weft Knitted Fabric

Weft knitting is a construction process in which the fabric is made by a yarn forming loops across the width or around a circle; each yarn is fed at more or less a right angle to the direction in which the fabric is formed [11].The stitch of yarns that forms the geometry of weft knitted fabricis shown in Figure 2 with 3D views.

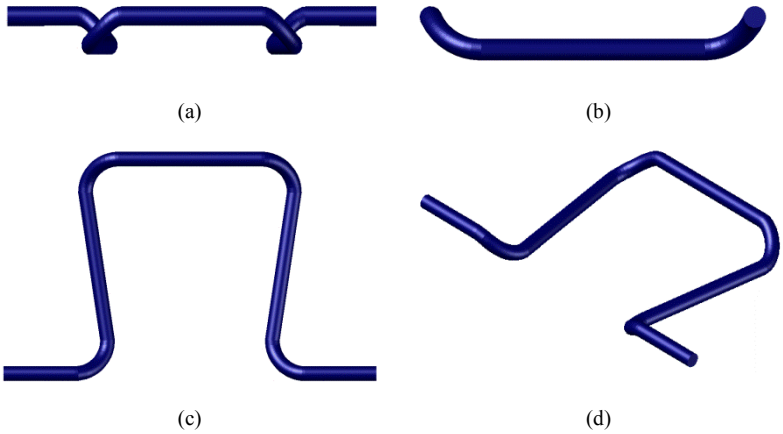

Figure 2. Weft knitting stitch (a) top, (b)left side, (c)front, d)isometric views

Weft knitted fabric and rectangular mesh were designed in the same dimensions (109.22x54.61cm) which is the recommended dimensions in WR430 waveguide system. The metal composite yarns were arranged with interval of around2mm (stitch size) to obtain open grid structure. The metal was chosen as copper with 50µm in diameter. Having superior electrical properties, copper has better reflection loss than do lower conductive materials. This makes copper to be used widely in composite conductive fabrics.

The open grid structure of the typical composite fabrics is presented in Figure3.

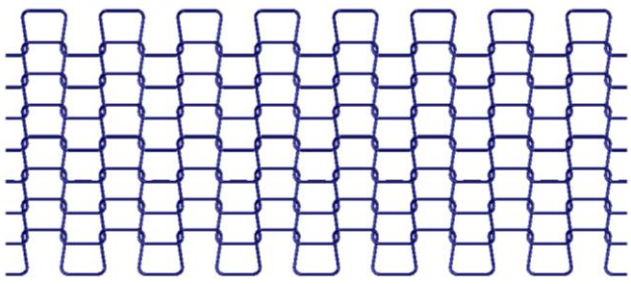

Figure3. Weft knitted fabric geometry

Rectangular meshes as an equivalent metal shield model had been drawn with the same conductor diameter and aperture size of knitted fabric structure. In contrast to knitted fabric in meshes 3rd dimension referring to the thickness of fabric is only straight line with size of the conductor diameter.

3.3. Simulations

The files with 3D designs prepared on AutoCAD software is exported as SAT file. Afterwards, this file had been imported into CST Studio. Material property of both designs had been changed to a copper. To satisfy the terms of WR340 waveguide system, the boundary conditions had been applied to the design with relevant properties. The simulation results are shown in Figure 4.

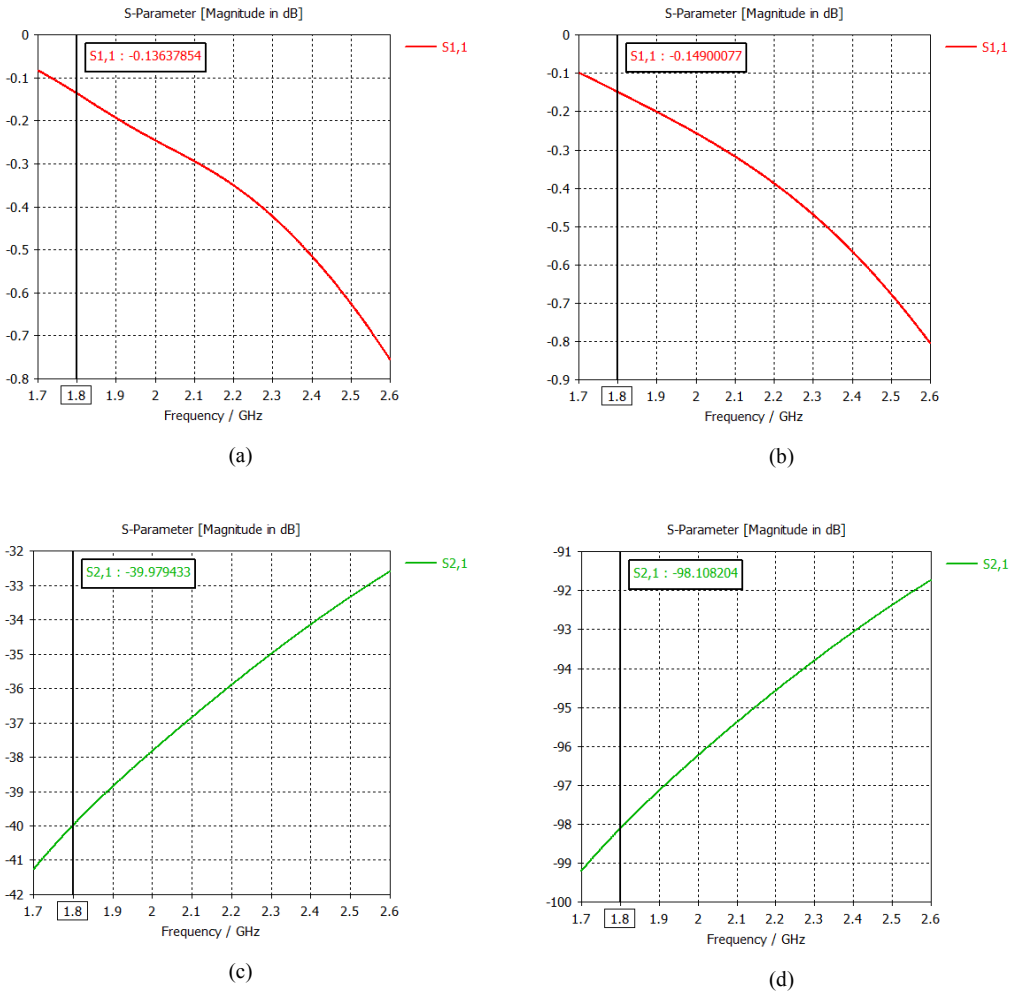

Figure4. (a) S_{11} values of knitted fabric structure, (b) S_{11} values of metallic rectangular meshes, (c) S_{21} values of knitted fabric structure, (d) S_{21} values of metallic rectangular meshes

Substituting S_{11} and S_{21} values of both models into the equation 3 and 4 it was seen that at frequencies of 1.8GHz and 2.4GHz SE values of knitted fabric were about 39.97dB and 34.12dB while for the same frequencies, the SE values obtained by rectangular meshes were 98.10dB and 92.9dB respectively. It was also observed that for each model in both reflection and absorption loss values was a slow decrease causing a decrease in total SE.

74. RESULTS AND DISCUSSIONS

The SE values obtained by the equivalent model are far more than the values obtained from the knitted fabric. Moreover, the results of equivalent model are not compatible with those obtained from experiments carried out in literature. Thus, it can be concluded that, for shielding fabric simulations the metal planes with apertures namely rectangular meshes cannot be substituted as fabrics‘ structures.

The output of this study represents a contribution to knowledge in composite shielding fabric simulations. Our future work will include related measurements as well as simulations for more complicated shielding fabric structures.

REFERENCES

[1]. World Health Organization,2012. Establishing a Dialogue on Risks from Electromagnetic Fields, 65s.Geneva, Switzerland.

[2]. Chung, D.D.L. , –Materials for Electromagnetic Interference Shielding", *Journal of Materials Engineering and Performance*, vol. 9, no.3, pp350-354,January 2000.

[3]. Özdemir,H., Uğurlu, Ş.S., Özkurt,A., 2015. Electromagnetic Shielding of Textured Steel Yarn Based Woven Fabrics Used for Clothing. *Journal of Industrial Textiles*, 45(3), pp416-436.

[4]. Perumalraj, R., Dasaradan, B.S., Electromagnetic Shielding Effectiveness of Doubled Copper-Cotton Yarn Woven Materials, *Fibres & Textiles in Eastern Europe* 2010, Vol. 18, No. 3(80) pp74-80.

[5]. Sevgi, L., Elektromanyetik Uyumluluk Elektromanyetik Kirlilik, Yapım Matbaa, İstanbul, 2000.

[6]. Liu, Z., Wang, X.C., Zhou, Z., Computation of shielding effectiveness for electromagnetic shielded blended fabric, *Przeglad Elektrotechniczny* ISSN 0033-2097,R.89 NR 3a, 2013.

[7]. Pocai, M.R., Bottari, E., Electromagnetic Characterization of Protective Clothing,*International Symposium on Electromagnetic Compatibility*, 1999,pp516-519,Tokyo..

[8]. Clayton, R.P., *Introduction toElectromagnetic Compatibility*, 2nd ed., USA, John Wiley & Sons Inc., 2006.

[9]. Drinovsky, J., Kejik, Z., Electromagnetic Shielding Efficiency Measurement of Composite Materials. *Measurement Science Review*, 2009, 9(4), pp109-112.

[10]. Mathew, K.T., Kalappura, U.G., Augustine, R., Polyaniline Based Materials for Efficient EMI Shielding, *International Union of Radio Science-URSI*,2008,Chicago.

[11]. Marjory, L.J., *Introductory Textile Science*, 3rd ed., USA, Holt, Rinehart and Winston, 1977.

ICENS
INTERNATIONAL CONFERENCE ON ENGINEERING AND NATURAL SCIENCES
24-28 May 2016 /Sarajevo

Numerical Estimation of NOx Emissions with ANN Utilizing Fuel Properties and Combustion Indicators in a CI Engine

Cafer Budak[37], Faruk Erken[2], Hüseyin Aydın[3]

Abstract

Emissions of nitrogen oxides (NOx) are main important pollution emissions, which are mainly caused by compression ignition (CI) engines. NOx emissions are one of the greenhouse emissions that lead to global warming. They also lead to acid rain thus damage land and human health. Therefore, NOx emissions should be decreased in CI engines. For these reasons, exploration of the reasons of NOx formation in CI engines is an important issue. In this study, numerical estimation of NOx formation in a CI engine with Artificial Neural Network (ANN) by focusing on combustion outputs the real engine works and fuel properties. Combustion parameters such maximum in-cylinder pressure (Pmax), temperature (T) and heat release, crank angle position of peak pressure CA_{Pmax}, and engine load, and fuel properties such as O_2 content, were selected as input values while NOx formations at certain loads was observed as the output value. The level of NOx values were successfully estimated by ANN with accuracy above 90%.

Keywords: NOx emissions, CI engines, Diesel fuel, ANN

[37] *Corresponding author: Batman University, Faculty of Engineering and Architecture, Department of Electrical Electronics Engineering, 72100, Batman, Turkey, cafer.budak@batman.edu.tr*

[2] *Kastamonu University, Faculty of Engineering and Architecture, Department of Electrical Electronics Engineering, 37200, Kastamonu, Turkey ferken@gmail.com*

[3] *Batman University, Faculty of Engineering and Architecture, Department of Mechanical Engineering, 72100, Batman, Turkey, huseyin.aydin@batman.edu.tr*

1. INTRODUCTION

75. NOx emissions are one of the greenhouse emissions that lead to global warming. Emissions of nitrogen oxides (NOx) are main important pollution emissions, which are mainly caused by compression ignition (CI) engines. They also lead to acid rain thus damage land and human health. Therefore, NOx emissions should be decreased in CI engines.

76. NOx emissions in internal combustion engines are caused by certain reasons such as in-cylinder flame temperature and duration in such high temperatures [1]. Local or global homogenous high temperature environments in the combustion chamber are the places that formation of NOx occurs. Heat release rate for each crank angle proportionally affects the temperature rise in the combustion chamber. The increase of heat release simultaneously increases the in-cylinder pressure [2]. Therefore both parameters are known to be indicators of NOx formation. Besides the increase of heat release and pressure increase the temperature values inside the cylinder that eventually result in NOx formation. All of these parameters in combustion engine are mainly affected by the load applied to the engine. When the load of the engine increased the amounts of fuel burned is increased proportionally that results in the higher amounts of heat released and pressure rise and thus the increased operation temperature [3]. Therefore the operation load is one of the main contributors of NOx formation.

77. The crank angle position that peak pressure occurs on which are seen to be one of the other indicators of NOx formation. The early peak pressure position of each cycle symbolize that heat release rate are higher probably due to ignition delay of fuels used. The delayed ignition points are attributed to the fuel properties such as cetane number, oxygen content etc. Higher O_2 content that is the indicator of the lambda (λ) values are seen to be one of the main other reasons of the NOx formation that is also known to increase in-cylinder temperature.

78. For all above mentioned reasons NOx formation in an internal combustion engine, in-cylinder pressure, temperature and heat release, and crank angle position of peak pressure and fuel properties such as O_2 content are selected to calculate the NOx formation by ANN.

2. ARTIFICIAL NEURAL NETWORK

79. Artificial neural networks that was carried out by people (for example, the product of actual brain function) that can learn events, is a computer system that will determine how the responses to events generated from the environment. These systems are further developed nowadays.

80. There are two important stages in neural networks, and the first of them is learning the second is test phase. The reaching of the network to the correct weights means that the samples to reached to the ability of generalizations about the event that representing. This generalization feature is called network learning [4].

81. Test examples are shown to the network. It produces output for these examples that is not seen by using the connection weights determined during network training. Accuracy of the resulting output provides information about the learning network. The level of accuracy of performance of education also indicates how well the education as well [4].

2.1. Training of Neural Networks

82. The basic steps of the neural network training used in this study can be summarized as follows:

83. In the process of developing a neural network we need to give the following decisions in accordance with the architecture and function of the network that is each a stage [5].

a) Selecting of the network architecture and determining the structures specifications (number of layers, the number of hidden layer, the neurons in input layer and the number of neurons in the output layer etc.)

b) Determining of the characteristic properties of the neurons function

c) Selection of Learning algorithm and identification of parameters

d) Training and generating test data

e) Training of the network in different load level

f) Conversion of to the experimental results into a column vector form applying them to the neural network at input layer.

84.

3. ARCHITECTURE OF NEURAL NETWORK MODELS

85. When estimating the NOx values by the ANN, the main important parameters that effect the NOx formation such as, Load, P_{max}, $CA_{Pmax,}$ T and Lambda values are obtained experimentally. Then the network is trained by using these parameters. Therefore, the input parameters in the ANN calculations are;

- Load
- Pmax
- T (temperature)
- λ
- CA_{Pmax},

86. The network calculated the weights of each parameter. The output parameter of the constructed ANN was designed to be NOx level. The block diagram of the structure of the constructed ANN is presented in Figure 1.

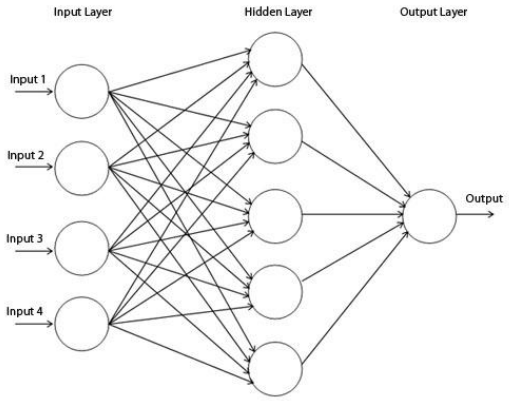

Figure 1: Structure for NOx estimator in ANN

87. The neural network model was trained with backpropagation algorithms. The designed neural network is multilayer feed-forward network that consist of an input layer and an output layer. As can be seen in Figure 2, the designed two layer feed-forward network has an input layer that consist of purelin neurons and an output layer that consists of purelin neurons. There are five neurons in input and one neuron in output. Purelin (linear) activation function was used as the activation function.

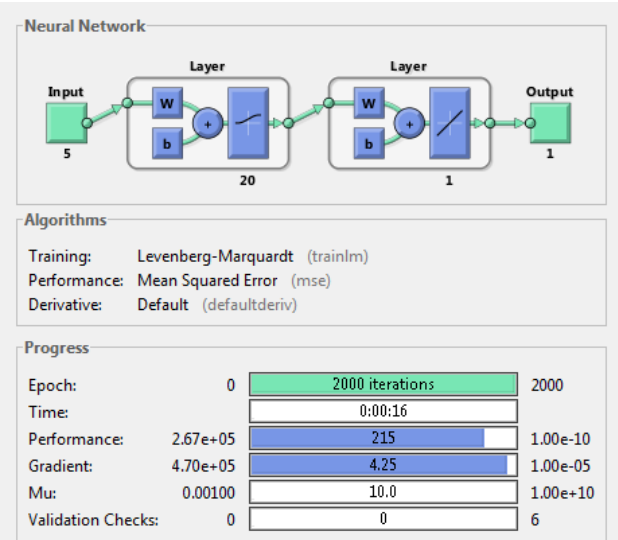

Figure 2. Training network

88. In the study, various types of training rules were testified in order to train the network and the Levenberg-Marquardt (LM) rule provided best results and was used for estimations [6].

89. After completing the training with the experimental results, in order to testify the accuracy of the network, outputs from the experimental real data mining and outputs from the calculations of ANN was compared and used to construct figure. As can be seen in Figure 3, the NOx emissions were successfully estimated.

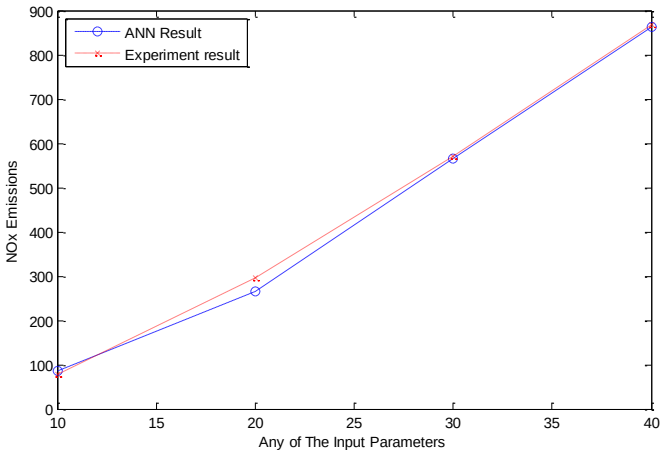

Figure 3: Estimated ANN output for NOx

Table 1. The trained network and experimental result

Experimental result NOx	ANN NOx estimation	Estimation rate %
77	84	91
297	266	89
571	565	98
869	862	99

The results of trained network and experimental result were compared in Table 1. The ANN results were considerably similar to experimental results.

4. CONCLUSIONS

Even though it is possible to experimentally measure the NOx emissions in internal combustion engines by emission devices it is both an expensive method and requires many efforts. The NOx emissions can also be estimated by ANN mathematically with high average accuracy level of 95% instead of experimental results. Also the number of testes can randomly be increased in accordance with random values of engine operation parameters or fuel specifications.

In this study, numerical estimation of NOx formation in a CI engine with ANN by focusing on combustion outputs of the real engine works and fuel properties. Combustion parameters such maximum in-cylinder pressure (Pmax), temperature (T) and

heat release, crank angle position of peak pressure CA_{Pmax}, and engine load, and fuel properties such as O_2 content, were selected as input values while NOx formations at certain loads was observed as the output value. The level of NOx values were successfully estimated by ANN with accuracy above 90%.

REFERENCES

[170]. Heywood JB. Internal Combustion Engine Fundamentals, McGraw-Hill, New York, 1988.
[171]. H. Aydin ―Combined effects of thermal barrier coating and blending with diesel fuel on usability of vegetable oils in diesel engines", Applied Thermal Engineering 51:623-629, 2013
[172]. E.F. Obert, Internal Combustion Engines and Air Pollution, Intext Educational Publishers, New York (1973).
[173]. M., Hagan H Demuth., and M. Beale, Neural Network Design, PWS Publishing Company and Thomson Asia, 2002.
[174]. C. Budak, M. Türk, A. Toprak, "Reduction in impulse noise in digital images through a new adaptive artificial neural network model" Neural Computing and Applications, 26, 4, pp 835-843, 2015
[175]. M.T. Hagan, M. Menjah, ―Training feedforward networks with the Marquardt algorithm", IEEE Transactions on Neural Networks, 5, 989-993, 1994

An Adaptive Torque Ripple Reduction Method in Hysteresis Current Controlled Permanent Magnet Synchronous Motor

Faruk Erken[38], Cafer Budak[39]

Abstract

In this study an adaptive method is used to minimize torque ripple in hysteresis current controlled Permanent Magnet Synchronous Motor (PMSM). This method is based on injection of appropriate current harmonics to motor in order to obtain minimum torque ripple. In the applied method appropriate amplitude and phase values of predetermined harmonic orders are weighted with the applied adaptive method. The weights of injected current harmonic values are online updated by orthogonal projections onto convex sets, according to the gradient of torque ripple. The validity of the applied method is presented with simulation studies.

Keywords: PMSM, torque ripple, hysteresis current control, adaptive control

5. INTRODUCTION

Permanent magnet synchronous motors (PMSMs) are used in several industrial applications due to their high efficiency, high-power density and high torque-to-inertia ratio, when compared with other machines, in recent years. One of the main problems of the PMSM drive is the generated torque ripple. These ripples are emerged periodically in motor speed and thus limit their usage in high precision applications [1-2].

There are various sources such as cogging, flux harmonics, current unbalancing and ripples stemming from measurement and control system which contribute to torque ripples [1-2].

Torque ripple minimization methods concentrate on two categories. In the first category torque ripple reduction methods are composed of different motor design methods, and the second category make use of various motor control strategies [2]. As the vector control methods of PMSM, Field Oriented Control (FOC) method and Direct Torque Control (DTC) method are generally used. The electromagnetic torque is controlled indirectly by the control of the current components in FOC method. Most of the motor control strategies are based on the control of stator current. These methods aim to implement optimal currents to obtain minimum torque ripple [3]. In one of the method individual back EMF harmonics are used to determine stator current. The methods using pre-programmed current harmonic techniques based on pre-determined values are not adequate for various operating conditions of the motor [4]. Iterative Learning Control (ILC) method is based on a dynamic torque controller and the conventional current controller. The dynamic torque controller produces the reference current iteratively by comparing the desired motor torque with the instantaneous motor torque to decrease the torque error [5]. The repetitive current control method uses modified q-axis current to obtain optimal currents [6]. In the other study an artificial neural network based method is presented. In this method optimal stator currents are determined to provide the desired torque (or speed), besides minimum ohmic losses [7].

[38] *Corresponding author: Kastamonu University, Faculty of Engineering and Architecture, Department of Electrical Electronics Engineering, 37200, Kastamonu, Turkey ferken@gmail.com*

[39] *Batman University, Faculty of Engineering and Architecture, Department of Electrical Electronics Engineering, 72100, Batman, Turkey, cafer.budak@batman.edu.tr*

At the beginning the direct mean torque control method was presented for the induction machine and then it was applied to PMSMs. The DTC method is based on selecting of optimum voltage vector according to flux and torque error for producing the desired torque. DTC can be realized easily by means of its simple structure. Besides, small amount of calculation time and fast torque response can be achieved. However compared with FOC, DTC generates large torque ripple, variable switching frequency and acoustic noises [8].

Linear and nonlinear current controllers are used as the current control methods. Hysteresis Current Control Method is a current control method used in voltage source inverters. In this method, instantaneous values of phase current taken by a feedback loop are compared with the reference sine wave produced in desired amplitude and frequency by the control circuit, in the hysteresis band. Here PWM hysteresis current control is preferred due to its fast dynamic response and it doesn‘t need any information of the system parameters. Moreover, this method is popular because of easily implementation to control system. However, its variable switching frequency causes to various switching losses [9].

In the present paper an adaptive method is used to minimize torque ripple by injection of appropriate current harmonics in hysteresis current controlled PMSM. In the method, the current harmonic orders to be injected are used from predetermined values. The 1st, 2nd, and 6th and other multiples of sixth harmonics are dominant in the synchronous rotating reference frame. While the 1st and 2nd order harmonics result from the current measurement error, the 6th and other multiples of the sixth harmonics generally result from magnetic flux distribution on air gap. In the applied method, the 6th harmonic order is used for minimization of torque ripple [2].

6. PMSM MOTOR MODEL

In the study the motor is assumed to be a surface-mounted three-phase PM synchronous motor and a PM rotor. The stator voltage equation in the abc frame can be expressed as;

$$\begin{bmatrix} v_a \\ v_b \\ v_c \end{bmatrix} = R_s \begin{bmatrix} i_a \\ i_b \\ i_c \end{bmatrix} + \frac{d}{dt} \begin{bmatrix} \psi_a \\ \psi_b \\ \psi_c \end{bmatrix} \quad (1)$$

Where, R_s is a stator resistance and i_a, i_b, i_c are stator currents. Stator flux can be expressed as follows;

$$\begin{bmatrix} \psi_a \\ \psi_b \\ \psi_c \end{bmatrix} = \begin{bmatrix} L_{aa} & M_{ab} & M_{ac} \\ M_{ba} & L_{bb} & M_{bc} \\ M_{ca} & M_{cb} & L_{cc} \end{bmatrix} \begin{bmatrix} i_a \\ i_b \\ i_c \end{bmatrix} + \psi_m \begin{bmatrix} \cos\theta_e \\ \cos(\theta_e - 2\pi/3) \\ \cos(\theta_e + 2\pi/3) \end{bmatrix} \quad (2)$$

Where, L is a stator self-inductance, M is a stator mutual-inductance and ψ_m is PM flux. The mechanical equation of motor can be represented as;

$$T_e = T_y + J\frac{d\omega_r}{dt} + B_m\omega_r \quad (3)$$

In the equation T_e is electromagnetically developed torque, T_y is load torque, J is moment of inertia, B_m is friction coefficient and ω_r is angular speed of motor. Because of these values are varying depending on θ_e, solving these equations becomes difficult. In order to facilitate solving the equation d-q axis transformation is performed. As a result of this transformation, inductance matrix parameters become constant coefficients.

The transformed values of d-q axis voltages and electromagnetic torque;

$$V_d = r_s . i_d + L_d \frac{d}{dt} i_d - \omega_r L_q i_q \quad (4)$$

$$V_q = r_s . i_q + L_q \frac{d}{dt} i_q + \omega_r L_d i_d + \omega_r \psi_m \quad (5)$$

$$T_e = \frac{3}{2} p\left[\psi_m i_q + (L_d - L_q) i_d i_q\right] \quad (6)$$

In the Eq. (6), p shows the number of pole pairs. In the electromagnetic torque equation the first term is the torque that generated by PM magnets, and the second term represents reluctance torque. Since d axis inductance and q axis inductance are considered equal in d-q reference frame, reluctance torque is assumed as zero in surface mounted PMSM.

7. HYSTERESIS CURRENT CONTROL METHOD

In the hysteresis modulation method, reference current of desired magnitude and frequency produced by the controller is compared with the actual motor current in the hysteresis band. As shown in Figure 1, upper switch of the inverter arm is turned off and the lower switch is turned on when the current exceeds the upper limit of the hysteresis band. In a similar way the lower switch of the inverter arm is turned off and the upper switch is turned on when the current drops to below the lower limit of the hysteresis band. Thus the reference current keeps tracking the actual current within the hysteresis band.

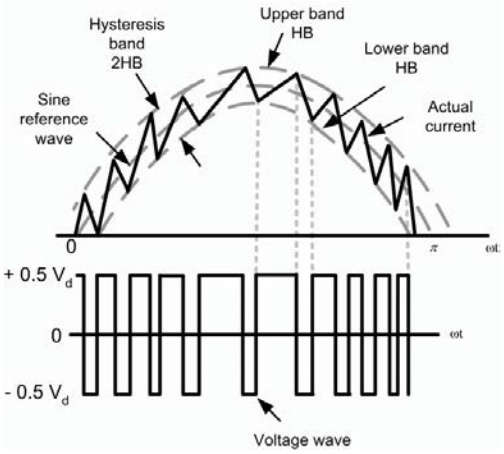

Figure 1. Hysteresis current controller basic scheme

The Hysteresis Current Control of PMSM is shown in Figure 2. In the method, reference d-q axis currents obtained by means of PI controllers are converted to reference phase currents. These reference currents are compared with the actual motor current in the hysteresis band.

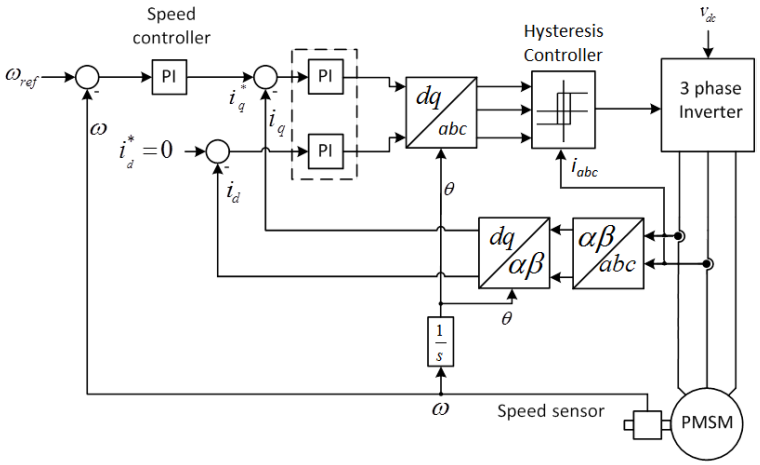

Figure 2. Hysteresis current control of PMSM

8. ADAPTIVE TORQUE RIPPLE REDUCTION METHOD

Non-sinusoidal flux density distribution around the air gap causes torque ripple in the PMSMs. These ripples appear as multiples of sixth harmonics in the d-q reference frame. Since these harmonic orders are the most common cause of torque ripples it is decided to inject 6th order harmonic to motor. Applied method is based on determining appropriate amplitude and phase values of this harmonic order. Injected current harmonic can be represented as;

$$x_h = x_m \sin(h\theta + \varphi) \quad (7)$$

where x_m shows the amplitude, h shows the harmonic order and φ shows the phase angle. If the sine expression is resolved;

$$x_m \sin(h\theta + \varphi) = x_m[\sin(h\theta)\cos(\varphi) + \sin(\varphi)\cos(h\theta)] \quad (8)$$

If it is accepted $x_m \cos(\varphi) = w_1$ and $x_m \sin(\varphi) = w_2$;

$$x_m \sin(h\theta + \varphi) = w_1 \sin(h\theta) + w_2 \cos(h\theta) \quad (9)$$

As seen, harmonic components at desired amplitude and phase can be acquired when sine and cosine terms are weighted with appropriate values. These values are termed as weights and these weights are estimated with proposed adaptive weight update algorithm. The weights of harmonic components are updated according to their contribution in the error term. The error term is obtained from the gradient of the torque error. Torque equation in surface mounted PMSM;

$$T_e = \frac{3}{2} p[\psi_m i_q] \quad (10)$$

If q-axis current is compensated by injecting the appropriate current harmonics, torque ripple will reduce. Corresponding block diagram is shown in Figure 3.

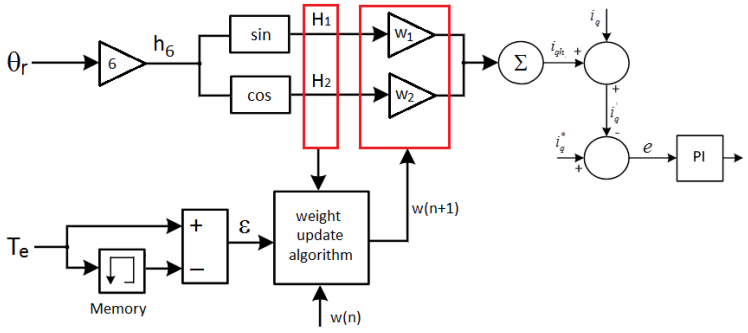

Figure 3. Adaptive torque ripple reduction method

8.1. Weight Update Algorithm

The orthogonal projection onto convex sets based weight update algorithm is applied. Let $H_1, H_2, \ldots, H_N$ be the sub-values corresponding to different harmonics. Ideally, weighted decision values of harmonic components should be equal to the decision value of $\hat{y}(x, n)$, which represents the hyper-plane in N dimensional space $\mathbb{R}^N$.

$$\hat{y}(x, n) = H^T(x, n)w(n) = \sum_i w_i(n)H_i(x, n) \quad (11)$$

At a time step n, the error can be written as the difference between its actual value and its estimation value of y. Weights are updated by minimizing the mean-square-error (MSE):

$$e(x,n) = y(x,n) - \hat{y}(x,n) \quad (12)$$

$$\min_{w_i} E\left[\left(y(x,n) - \hat{y}(x,n)\right)^2\right], i = 1, \dots N \quad (13)$$

where E symbolizes the expectation operator. Taking the derivative with respect to weights and equating to zero;

$$-2E\left(e(x,n)H_i(x,n)\right) = 0 \qquad i = 1, \dots N \quad (14)$$

If it is applied Wiener solution to a set of N equations;

$$w(n+1) = w(n) + \lambda e(x,n)H_i(x,n) \qquad i = 1, \dots N \quad (15)$$

If in Eq. 14, the step size λ, replaced by;

$$\lambda = \frac{\mu}{\|H(x,n)\|^2} \quad (16)$$

$$w(n+1) = w(n) + \mu \frac{e(x,n)}{\|H(x,n)\|^2} H(x,n) \quad (17)$$

The above weight update algorithm, which is similar to the normalized LMS algorithm, is obtained. The symbol μ is an update parameter and this parameter is selected inversely proportional according to the injected harmonic frequency.

9. SIMULATION RESULTS

Surface mounted PMSM is used in the simulation. In the proposed control method switching frequency of the motor driver and DC link voltage are selected as 15 kHz and 100V, respectively in the simulation.

Simulation results of motor torque, are presented in Figure 4 for the conditions 100 rad/s, 5 Nm load condition and the algorithm is enabled at t=3s.

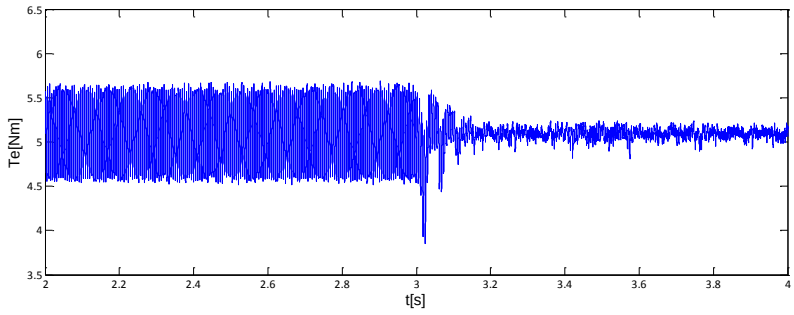

a)

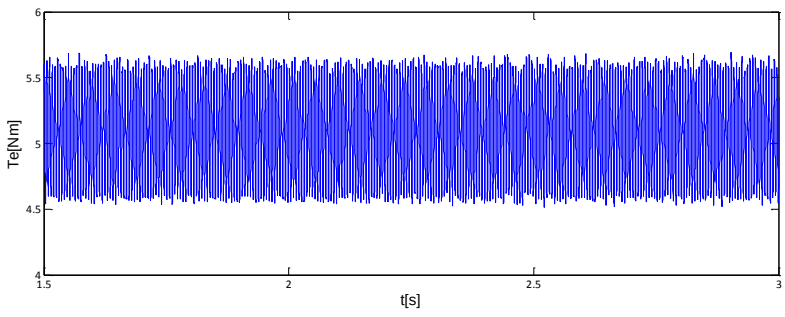

b)

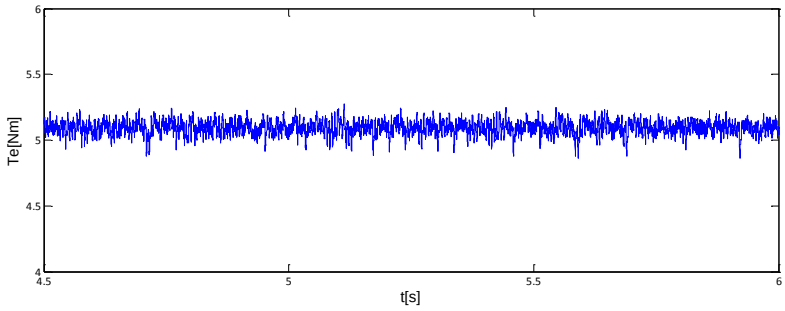

c)

Figure 4. Simulation results of torque at 100 rad/s, 5 Nm load condition

a)Motor torque when the algorithm enabled at t=3s

b)Motor torque when algorithm is disabled

c)Motor torque when algorithm is disabled

As can be seen, the torque ripples are periodic and generally in the 6th harmonic orders. As shown in the Figure 4 the torque ripples decrease rapidly with the applied method based on μ updating parameter. The harmonic spectrums are computed as percent of effective values of harmonics to DC component. Figure 5 shows that 9.2% ripple in the 6th harmonic is effectively eliminated with the proposed method.

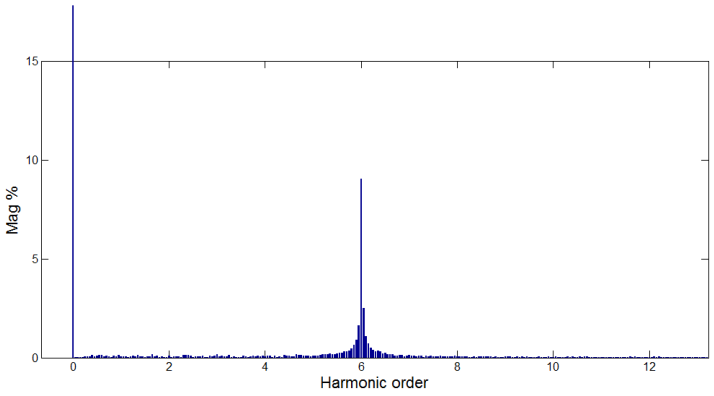

a)

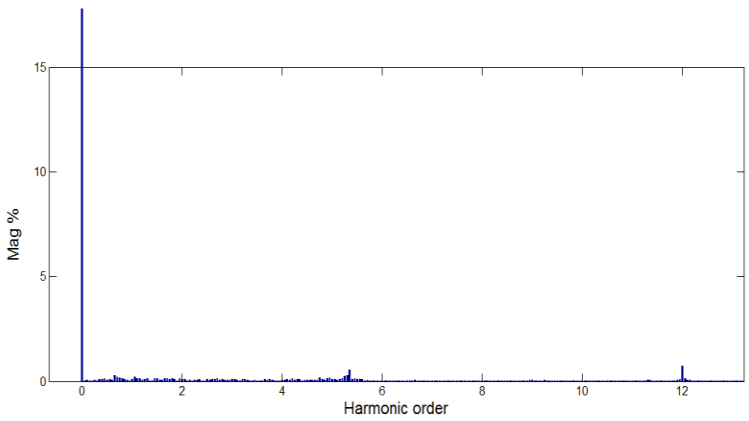

b)

Figure 5. Harmonic spectrum of torque

a)When algorithm is disabled

b)When algorithm is enabled

10. CONCLUSIONS

In the present study an adaptive torque ripple reduction method for decreasing torque ripple of the hysteresis controlled PMSM that is based on injection of appropriate current harmonic has been proposed. In the method, weights of predetermined the 6th harmonic order components are estimated based on gradient of torque values. Weights are updated according to the contribution of harmonic components to the error. The simulation results show that the torque ripples are reduced expeditiously with the presented method.

REFERENCES

[176]. Jahns, T.M., Soong,W.L.: ―Pulsating torque minimization techniques for permanent magnet ac drives – a review", IEEE Trans Ind. Electron., 43, pp. 321–330, 1996

[177]. Erken F, Öksüztepe E, Kürüm H, ―Online Adaptive Decision Fusion Based Torque Ripple Reduction in Permanent Magnet Synchronous Motor", IET Electric Power Applications, 10, 3, pp.189-196, 2016

[178]. Chapman, P.L., Sudhoff, S.D., Whitcomb, C.A.: ―Optimal current control strategies for surface-mounted permanent-magnet synchronous machine drives", IEEE Trans. Energy Convers., 14, (4), pp. 1043–1050, 1999

[179]. J. Y. Hung and Z. Ding, ―Design of currents to reduce torque ripple in brushless permanent magnet motors," Proc. Inst. Elect. Eng.—Elect. Power Appl., vol. 140, no. 4, pp. 260–266, Jul. 1993.

[180]. Xu, J.X., Panda, S.K., Pan, Y.J., et al.: ―A modular control scheme for PMSM speed control with pulsating torque minimization", IEEE Trans Ind. Electron., 51, pp. 526–536, 2004

[181]. Mattavelli, P., Tubiana, L., Zigliotta, M.: ―Torque-ripple reduction in PM synchronous motor drives using repetitive current control", IEEE Trans. Power Electron., 20, (6), pp. 1423–1431, 2005

[182]. Flieller, D., Nguyen, N.K., Wira, P., et al.: ―A self-learning solution for torque ripple reduction for nonsinusoidal permanent-magnet motor drives based on artificial neural networks", IEEE Trans. Ind. Electron., 61, (2), pp. 655–665, 2014

[183]. Morel, F., Xuefang, L. S., Retif, J. M., Allard, B., ―A Predective Current Control Applied to a Permanent Magnet Synchronous Machine, Comparison with a Classical Direct Torque Control", Science Direct Electric Power Systems Research 78, p. 1437-1447, 2008

[184]. Soliman H. M., S.M.EL. Hakim, ―Improved Hysteresis Current Controller to Drive Permanent Magnet Synchronous Motors through the Field Oriented Control", International Journal of Soft Computing and Engineering, vol. 2, 4, pp. 40-46, 2012

The Development of Well Information System Using GIS: A Case Study of the Raman Oil Field in Turkey

Bayram Ali MERT[1], Emine AVCI[2]

ABSTRACT

The oil industry has wide and difficult administration substructure which should be followed at all stages from drilling to the pipelines of system, and from refining to the end user. Moreover, it is seen that GIS is used in many different disciplines as an effective data management tool successfully. Because of the increasing popularity and the functional development of GIS in recent years, many petroleum companies have started using the technology as the preferred tool for planning, analysis, and management. Within this frame, the aim of the study is to establish GIS-based well information system. For this purpose, firstly, tabular and graphical data were created by analyzing the drill holes data and the map materials such as topographical, geological, drilling locations, porosity distribution, permeability distribution, reservoir thickness, pipelines and the site plans of the Raman oil field in Turkey, and then they were combined under the GIS environment. For this reason, the graphical and the non-graphical data and the logical and the topological relations between these data; the relational database management system (RDBMS) was established with the possibility of processing as integrated and therefore, carrying out the analysis based on the position. Thanks to RDBMS, conditional analysis were performed on graphical and tabular database then it was presented that all attributes in the database or other statistical information that can be created with the questioning can be reached on the wells which are selected from screen. Consequently, an information standard was formed by terming system and connection elements easily and quickly. Thus, the complexity and clutter of data was prevented. Owing to the instant monitoring of attributes that contain the maintenance and repair information available in the database, it is obvious that operating costs will be reduced in the long term.

Key words: *Raman Oil Field, GIS, Reservoir Evaluation, Reservoir Management*

1. INTRODUCTION

The importance of data and information is increasing every day. Moreover, GIS is a useful technology to manage and organize information effectively. GIS is a computer system capable of assembling, storing, manipulating, and displaying layers of geographically referenced information [1,2,4]. In GIS, each layer of spatial data is linked to corresponding tabular information. Each object on the map layers has location-coordinate information in which the objects are defined and expressed on the map. Oil and gas data is strongly connected to geography which is identified according to their locations, such as **oil exploration, pipeline construction and the environment.** GIS applications in the oil and gas industry can serve multiple purpose. A **geodatabase can be used to store, collect and visualize the physical location of pipelines, wells and spatial data.** Non-spatial information such as leases, date of installation and pipe material can also be added in attribute data. This can be useful to better understand when pipelines are in need of maintenance or repair. Topological relationships can be maintained to ensure data quality. Definition queries can be performed to differentiate pipelines with attribute data. Other useful analytics information can be analyzed. For example, you can compare the amount of pipeline by type in specific locations. All of these features are spatial in nature. GIS in oil and gas industry is a rapidly growing field of interest. Because of the increasing popularity many petroleum companies have started using the technology as the preferred tool for planning, analysis, and management. Although GIS has been used in many operations, the purpose of this study is to develop a well information system to enable engineers to collectively instant monitoring of attributes, reduce the operating costs.

2. DESCRIPTION OF RAMAN OIL FIELD

Raman oil field, which is the first discovered oil field in Turkey, is located in Southeast Turkey. The oil field, discovered in 1940, located at the north of Hasankeyf districts of Batman city, covers an approximate surface area of 36 km^2 (Figure 1). The Raman Oil Field is located in southeast Turkey. It is roughly outlined by an east-west trending, double-plunging anticline. The structure was discovered by surface geological mapping of the Midyat Limestone Formation which outcrops in the uppermost envelope of the anticline. The anticline rises approximately 200 m above the surrounding plateau of the karstic Midyat limestones to form the Raman Mountain [5].

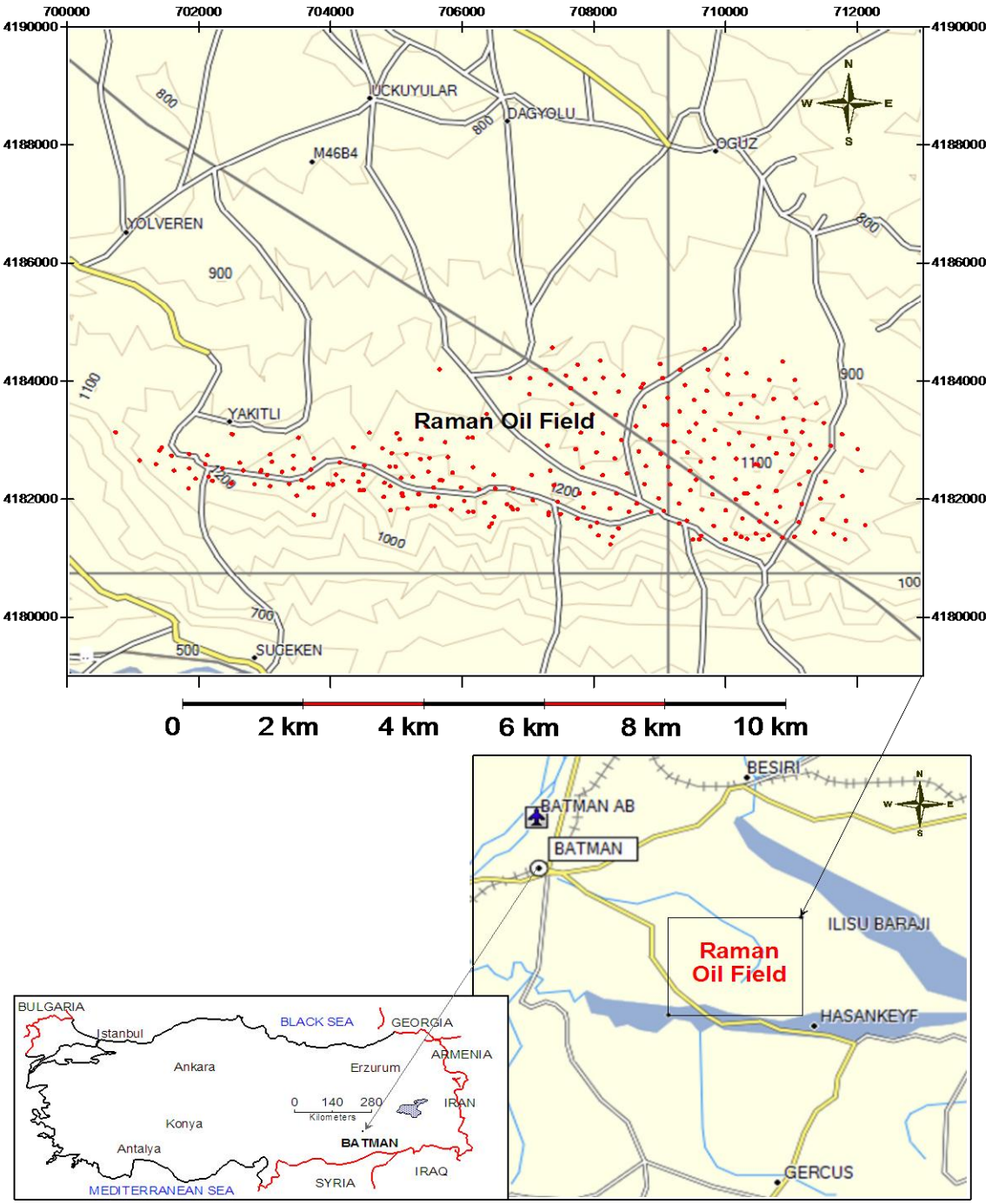

Figure 1. Location map of Raman Oil Field

During much of the Paleozoic and Mesozoic periods, the study area was in the unstable shelf region lying between the Arabian shield and associated stable shelves to the south, and the mobile Alpine geosyncline to the north. The Persian Gulf geosyncline (Taurus- Zagros geosyncline) passed through eastern and northern Southeast Turkey until Cretaceous time when the Paleozoic and early Mesosoic tectonic patterns were destroyed. This break-up of pre-existing patterns caused some of the Cretaceous and Tertiary sedimentary rocks to have depositional aspects and trends different from those of the older strata. The existing sedimentary rock sequence in the study area is composed predominantly of Paleozoic clastics, Mesozoic carbonates and Tertiary clastics and carbonates [5].

From 1940 date Raman field has continued to be developed and as of 2014, a total of 267 wells were drilled in the field, 214 of them are in production and because of various reasons the other wells were excluded [8]. The oil produced is collected at two stations. After water separation, oil is pumped to Batman. The waste water decomposed is pressed back into wells by waste water systems installed in stations [7]. Raman is the second biggest oil field in Turkey with 600 MMbbls of original oil in place (OOIP). 6,000 bbls per day of oil is produced from 140 oil producers. 75,000 bbl per day of produced water is injected to aquifer by 13 water disposal wells [3].

The field has average 18° API degree heavy crude oil. The total proven reserves of the Raman oil field are around 400 million barrels (55×10^6 tonnes) [5]. The field measures about 15 km long and 4 km wide. Average field porosity is around 14% [4, 6, 7]. Within the studies to increase production in the field, injection of the polymer gel which it prevents the arrival of water was carried out in total 22 wells in Raman field in 2014. As a result of application, 5 wells which they were abandoned were put into production again, additional a total of 90 thousand barrels oil production has been achieved by the well made application by the end of the year [7].

The field is an east-west trending double plunging anticline located in southeast Turkey. The main producing carbonate reservoir is the member of the Karababa formation. Oil-bearing lenses of the Garzan limestone formation of the overlying sequence provided reservoir capacity in the northern and eastern parts only [4].

The main productive zone in the Raman field is the Mardin formation. The Mardin Group consists of four formations. From bottom to top these are the Areban Formation, Sabunsuyu Formation, Derdere Formation and Karababa Formation. The Mardin Group represents a fairly continuous sedimentary sequence deposited from Aptian to at least the end of Turonian time [4]. However, the Garzan formation is also productive areally depending on the evolution of fractures and porosity in the east and north of the field. Because of low porosity and permeability the first 3-10 meters of the Mardin formation is non-productive. Under this non-productive zone there is, on average, a 20-25 meter productive zone in the Mardin formation. The porosity changes from 14-20 % in the Mardin formation productive zone and 10-25 % in the Garzan formation productive zone. The production mechanism is a strong water drive. Original reservoir pressure is about 1300 psi at the -200 m datum depth. Pressure is now 1100-1150 psi areally. The original WOC is -300 m. [3].

3. DEVELOPMENT OF WELL INFORMATION SYSTEM

Establishing the framework of the GIS database and entering the data into the database is the most important and most time and effort requiring part of the project. These stages were determined by the followings in the given order:

- ✓ generating graphical data,
- ✓ generating tabular data,
- ✓ establishing database management system.

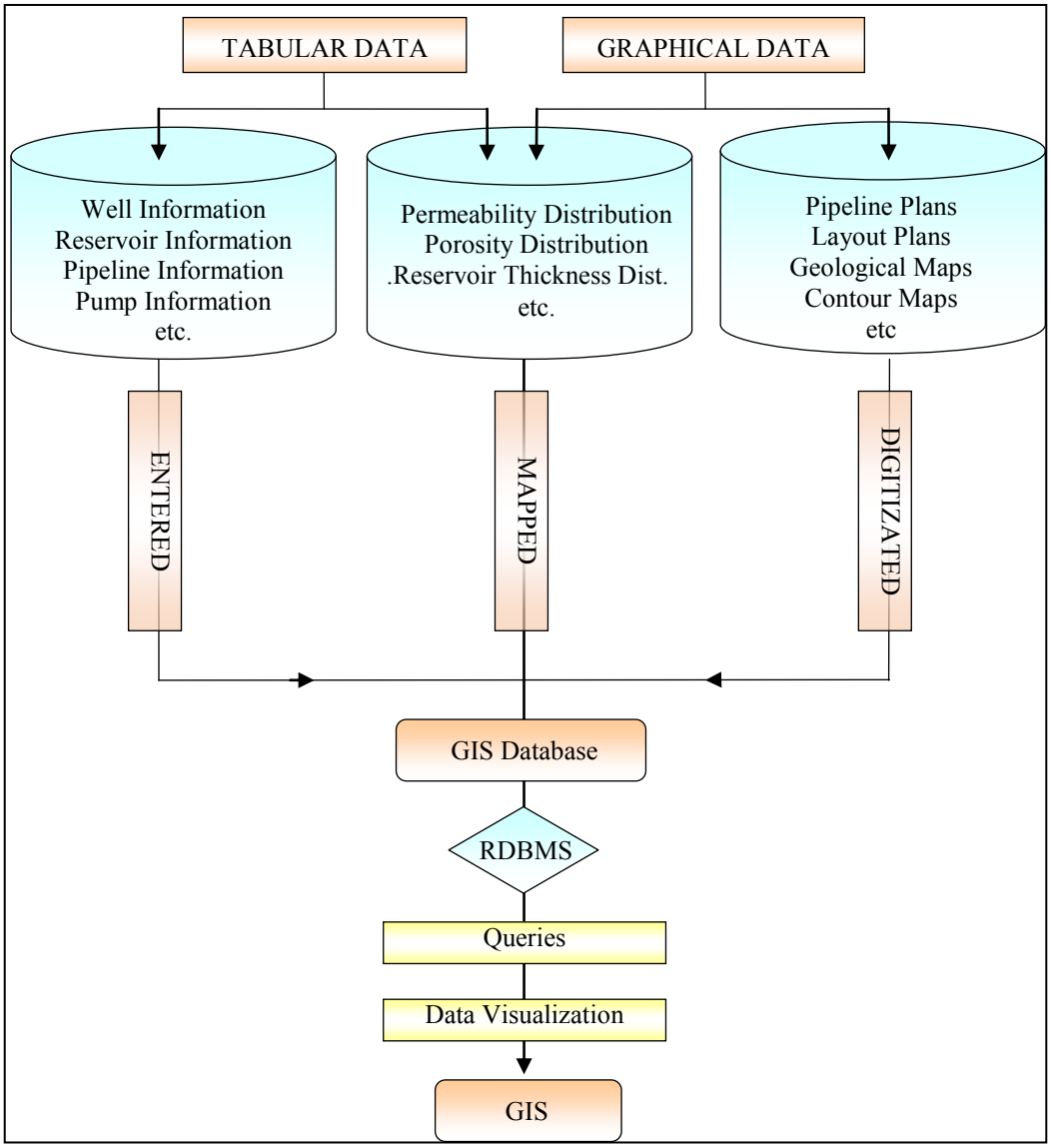

Figure 2. General flow chart of the study.

In the process of formation of graphical data, firstly 1/25.000 scale topographic maps with sheet numbers of M46/B3-B4, were transferred to computer media using a scanner with a resolution of 600 dpi. After that, by positioning the map on the planar projection within the 37th Zone – 39th Central Meridian in the UTM projection system and in line with the ED50 ellipsoid with the MapInfo 9.0 software, it was converted into Turkish Coordinate System. During the digitization process, each element class of different types on the map was classified on different layers. With a similar principle, contour lines, pipelines, well site lines were included in the

system by digitization of Google maps and topographic maps. The coordinates of wells extracted from Keskin and Can [4] and google map(Figure 3-5). As a result of digitization process, 267 well site locations have been digitized and a graphical database of the study has been formed.

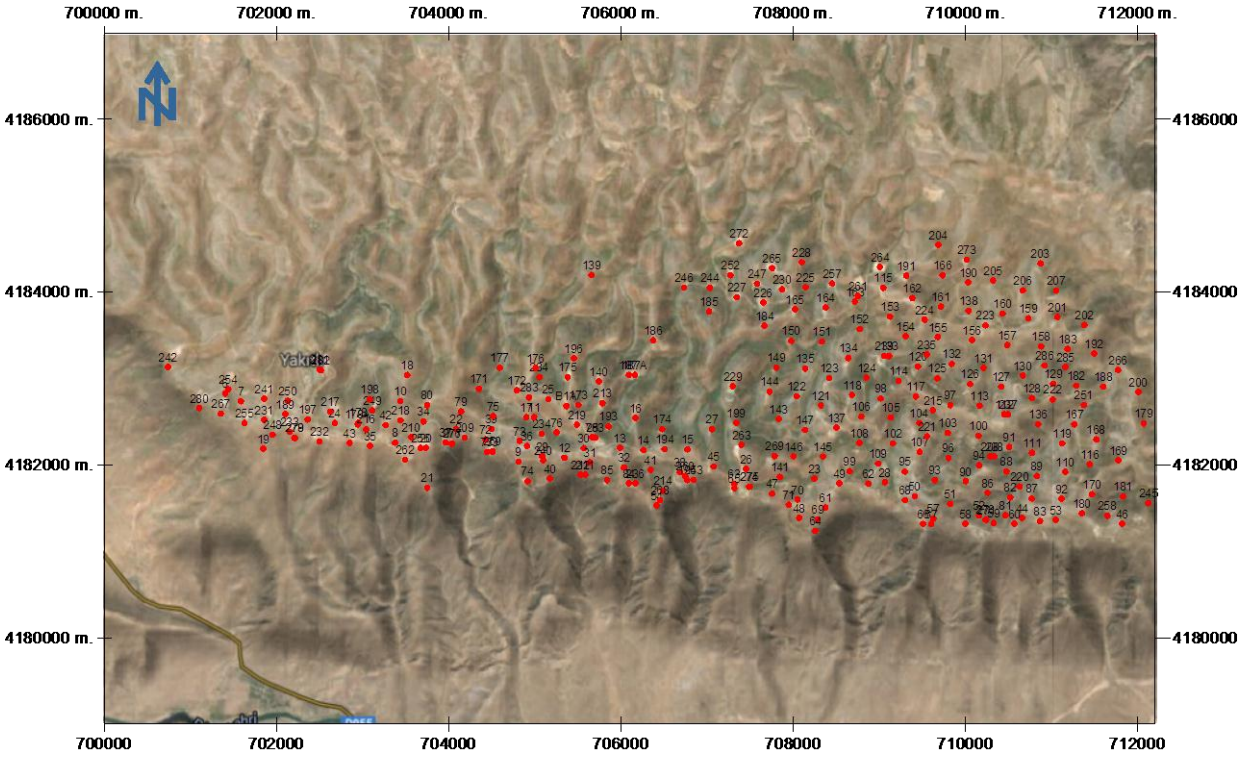

Figure 3. The google map of Raman oil field

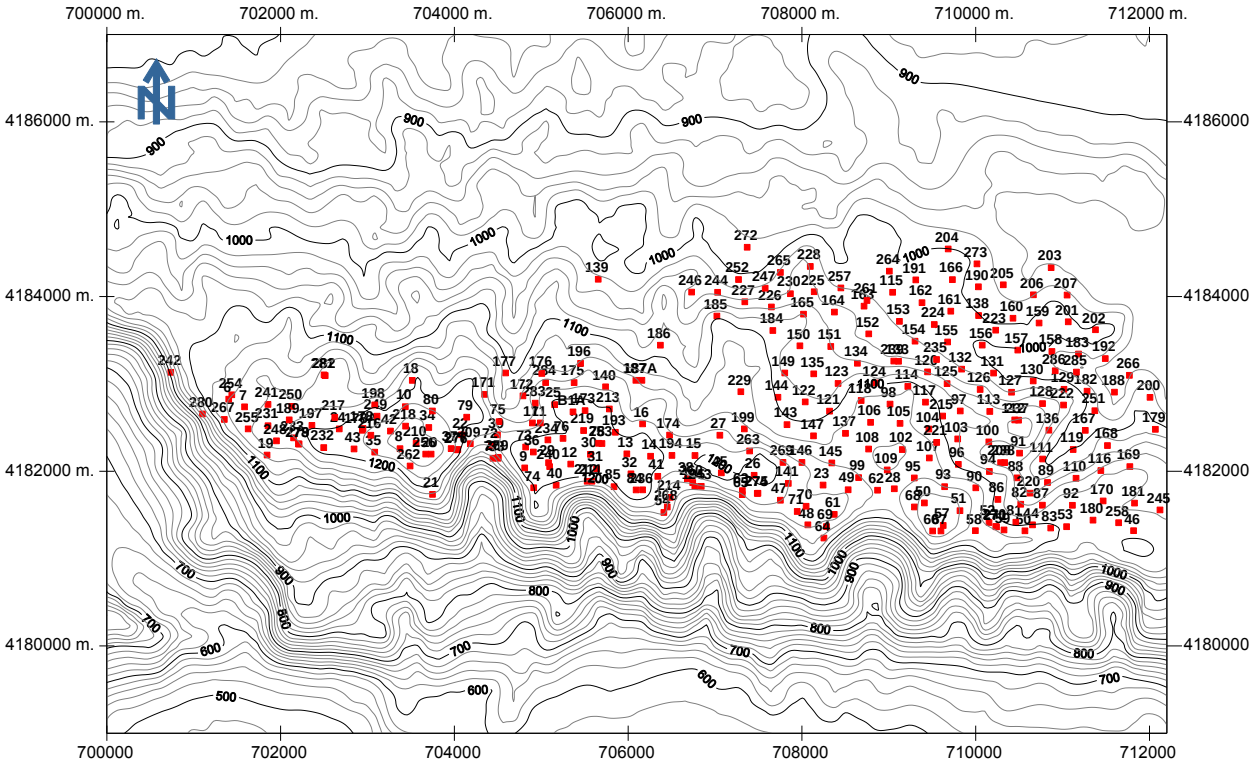

Figure 4. The contour map of Raman oil field

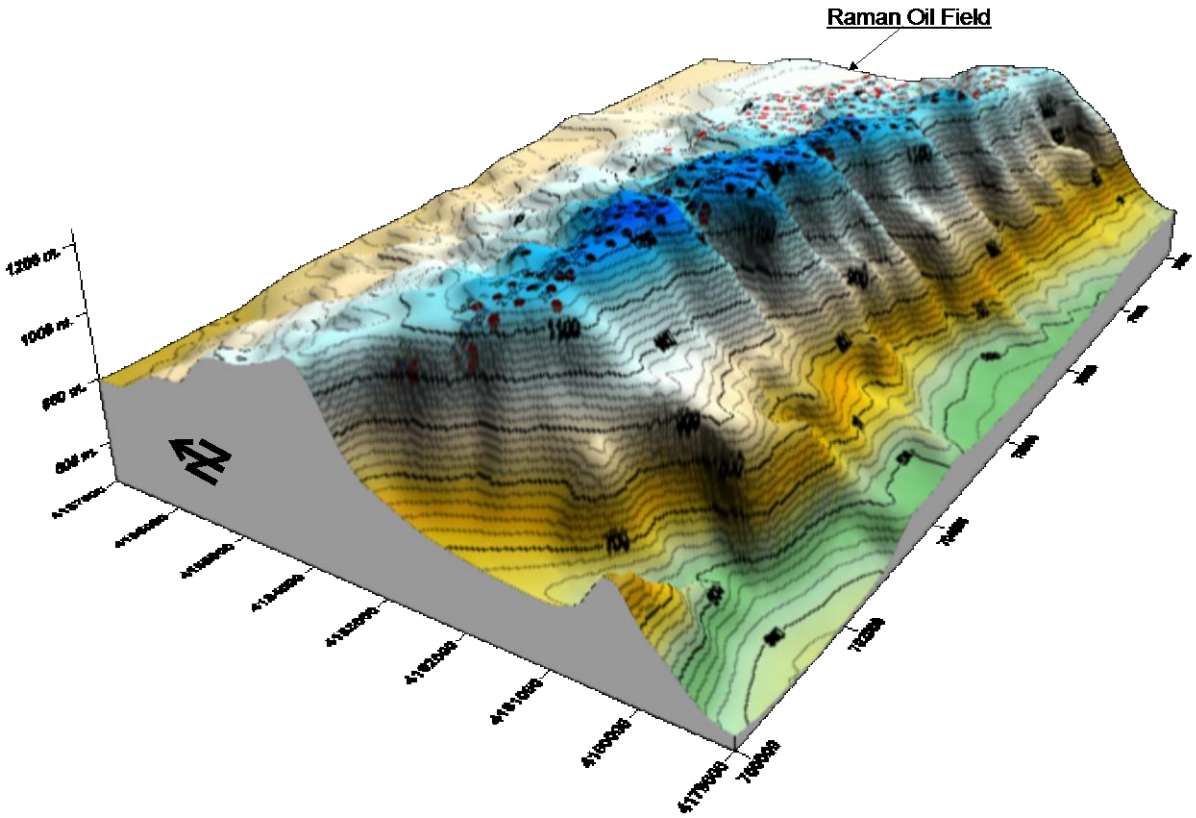

Figure 5. The surface map of Raman oil field

Preparing the tabular data that include the attributes of the digitized graphical data constitutes a significant part of this study. In this context, several attributes, such as API Gravity, Spesific Gravity, Viscosity, Bubble Point Pressure Gas/Oil Ratio, Water of Formation Salinity, Water of Formation Rezistivity, Rate of sulfur, Freeze Point, Yield Point, Flash Point, Calorific Value, which a production well has the all parameters was presented in the databases. (Figure 6-7).

Finally, the tabular and graphical data were combined under the GIS environment. For this reason, the graphical and the non-graphical data and the logical and the topological relations between these data; the relational database management system (RDBMS) was established with the possibility of processing as integrated and therefore, carrying out the analysis based on the position. The relational database management system (RDBMS) allows flexible data extraction, called a ‗query', with a single criterion or multiple criteria, based on structured query language (SQL). It can store and manage the geographic data, as well as implementing logic operations, for example, building relationships between data types, such as topologies and geometric networks, validating data, and controlling access [9]. Thanks to RDBMS, conditional analysis performed on graphical and tabular database then it was presented that all attributes in the database or other statistical information that can be created with the questioning can be reached on the wells which are selected from screen.

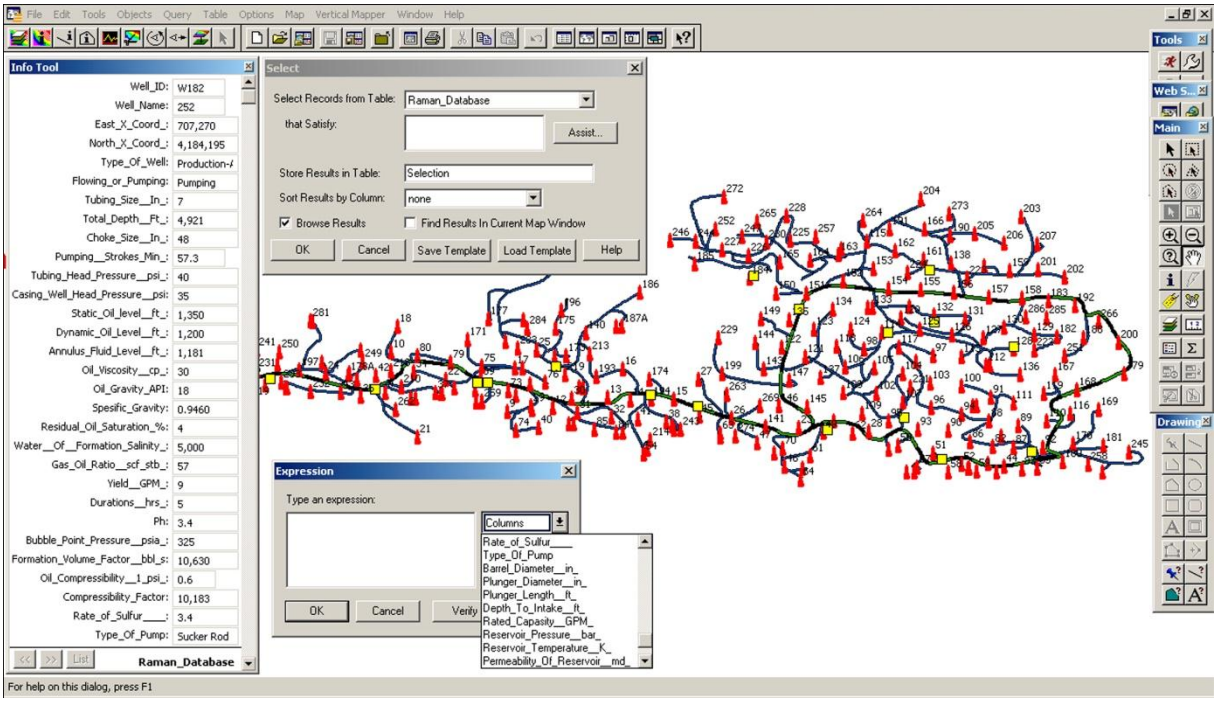

Figure 6. The screen capture of program

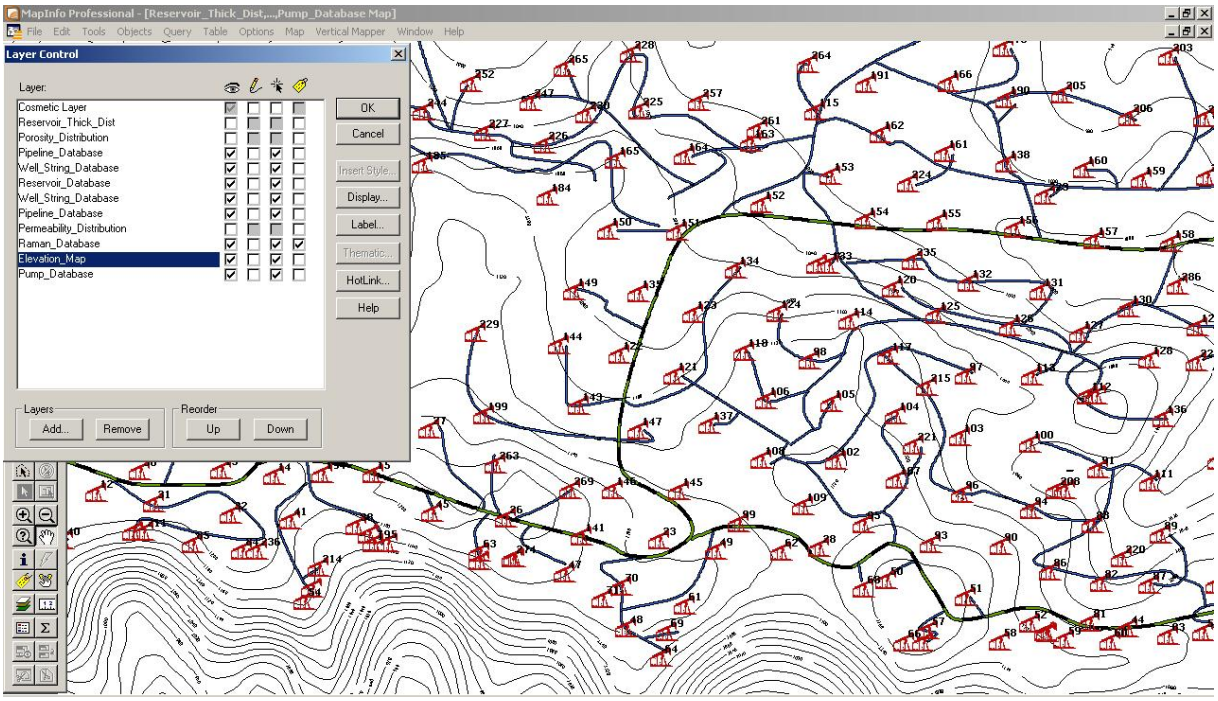

Figure 7. The screen capture of database

4. CONCLUSIONS

In this study, Well Information System was developed for the Raman Oil Field with the possibility of processing as integrated and therefore, carrying out the analysis based on the position. Thanks to system, conditional analysis were performed on graphical and tabular database then it was presented that all attributes in the database or other statistical information that can be created with the questioning can be reached on the wells which are selected from screen. Consequently, an information standard was formed by terming system and connection elements easily and quickly. Thus, the complexity and clutter of data was prevented. Owing to the instant monitoring of attributes that contain the maintenance and repair information available in the database, it is obvious that operating costs will be reduced in the long term.

REFERENCES

[1]. G.F., Bonham-Carter, *Geographic Information Systems for Geoscientists: Modeling with GIS, Computer Methods in the Geosciences*, 1st ed., D. F. Merriam, Jr., Ed. New York, USA: Pergamon, 1994.

[2]. E.J.M., Carranza, *Geochemical anomaly and mineral prospectivity mapping in GIS*, 1st Edition, M. Hale, Jr., Ed., Handbook of Exploration and Environmental Geochemistry, Elsevier Science, Amsterdam, Nederland, 2008.

[3]. M., Demir, N. N. S., Topguder, M., Yilmaz, Y., Ince, U., Karabakal and J. H., Gould ―Water shutoff gels improved oil recovery in naturally fractured Raman heavy oilfield," in SPE Russian Oil and Gas Technical Conference and Exhibition. Society of Petroleum Engineers, 2008, p. 1-11.

[4]. J.R., Harris and M., Sanborn-Barrie, ―Mineral potential mapping: examples from the Red Lake Greenstone Belt, Northwest Ontario,". In: Harris, J.R. (Ed*.), GIS for the Earth Sciences. Geological Association of Canada,* pp. 1–21, 2006.

[5]. G. Keskin, and C. Can, ―Upper Cretaceous carbonate reservoirs of the Raman field, southeast Turkey". Carbonates and Evaporites, volume 1, pp. 25-43, March, 1986.

[6]. E. Özgür, ―Upstream Petroleum Law and activities in Turkey," *Energy Policy*, vol: 88, pp.131-137, Jan. 2016.

[7]. ―TPAO (2014)a," 2014 Annual Report, TPAO Headquarters, Ankara, Turkey. [Online]. Available: *www.tpao.gov.tr/tp5/docs/rapor/TP-2014-YILLIK-RAPORU.pdf*

[8]. ―TPAO (2014)b," Raman Field Annual Report, TPAO Batman Region Headquarters , Batman, Turkey.

[9]. B. A., Mert, and A. Dag, ―Development of a GIS-based information system for mining activities: Afsin-Elbistan lignite surface mine case study," *International Journal of Oil, Gas and Coal Technology*, vol: 9, pp. 192-214, 2015.

Finite Elements Modelling of the Gas Metal Arc Welding Process

Gökhan Biçer[40], Ġsmail Tirtom[1], Essam Abo-Serie[1]*

Abstract

Gas Metal Arc Welding (GMAW) operation has been modeled in ABAQUS using its welding interface extension. The welding operations and their application for a variety of metal manufacturing are briefly stated in the paper. The GMA welding operation in 3D finite element (FE) models are presented. FE simulations were carried out to examine the stress-strain distributions and metal distortions due to thermal expansions around welding line of the sample. The impact of operation parameters and geometry of the weldment have been evaluated with and without the consideration of residual stresses and strains induced from the forming processes prior to welding. Based on the given welding parameters, the simulation evaluates the welding material properties and the internal stresses in addition to the expected distortion. For this reason, finite element analysis applied on the welding process can be used not only to have better understanding of the GMAW operations but also can be a useful mathematical tool for future process development and control with the view of optimizing welded product properties and quality.

Keywords: GMAW, welding material distortion, welding simulation, welding in ABAQUS

90. INTRODUCTION

Gas Metal Arc Welding (GMAW) is one of the most widely used methods for joining metals. In spite of the numerous advances in the science and technology of welding, still defected weld is common and it is still representing, in many cases, the weakest area. To identify the quality of welding a non-destructive test techniques such as ultrasonic or radiography are commonly used. However, these techniques are not efficient or economic as defected welding parts are discarded wasting material, man power and time. Being able to understand the main factors affecting welding quality is crucial to optimize the welding parameters particularly for intelligent robotic welding.

For robot welding quality control, surface temperature during the welding process has been realised for long time as indicative parameter and to detect perturbations that result in faults during the arc welding process [1,2]. Arc misalignment, groove geometry faults, variations in penetration and impurities were discernible in distinctly different ways that can be related to weld pool temperature and its surrounding area. Previous studies used point IR sensors to measure the temperature as indicative of penetration depth [3]. As the temperature distribution curve become widened and the maximum temperature increases, the welding penetration becomes deeper [4]. Welding temperature fields can be investigated by contact-free temperature measurement in welding and to attained cooling curves using thermocouples [5]. The temperature was therefore used as a method of controlling the position of the arc and the penetration depth of the weld. Although temperature measurements were early used to predict the welding or control the welding quality, more recently, analytical and computational predictions of surface temperature have become common practice.

Early studies suggested an analytical heat conduction model for predicting the temperature of bidirectional multi-pass welding pieces with short seam lengths. The model was then validated using thermocouples [6]. Further studies examined temperature distribution of transient temperatures simulations and calculated the residual stresses in welding plates. Thermo mechanical and 3-D nonlinear thermal welding simulations were also used to stipulate temperature and residual stress distributions [7]. The accuracy of the predicted temperature distribution depends on the material properties and their variation with temperature. However, high temperature material properties are either difficult to obtain or do not exist for many materials. A study has been carried out to investigate the effect of each temperature-dependent material property on the transient temperature, residual stress and distortion in computational simulation of welding process. The study showed that except for the yield stress, using material properties at the room temperature gives reasonable predictions for the transient temperature fields, residual stress and distortion [8].

[40] *Mevlana University, Department of Mechatronics Engineering, 42003, Selçuklu/Konya, Turkey.* [*] *Corresponding author, gbicer@mevlana.edu.tr*

2. MODEL SIMULATION CONDITIONS

In this study, a simulation using welding interface extension in ABAQUS is carried out to predict the temperature and stress changes in the welding seam and the surrounding region of butt-welding joints. The butt-welding joint consists of two AISI 304 stainless steel sheets. Each sheet has the same dimension; 100 mm x 50 mm x 4 mm and each side of the two sheets have half v-shaped (45^o) inclination. Gas Metal Arc Welding (GMAW) method with Ar-CO_2 mixture is used as a shielding gas. Table 1 shows the main operating conditions for the welding process and the sheet metal material properties at different temperatures while Fig. 1 shows a schematic sketch of the two thin plates that are used in the simulation.

Temp	Mass Density	Young's Module	Poission Ratio	Expansion Coeff Data
C	kg/m^3	Pa	v	Alpha (l/K)
100	7,15E-09	28900000	0.3	6,68E-06
200	7,10E-09	28450000	0.3	6,71E-06
300	7,05E-09	28030000	0.3	6,91E-06
400	7,00E-09	27580000	0.3	7,09E-06
500	6,95E-09	27030000	0.3	7,26E-06
600	6,90E-09	26280000	0.3	7,43E-06
700	6,85E-09	25260000	0.3	7,60E-06
800	6,80E-09	23910000	0.3	7,77E-06
900	6,75E-09	22200000	0.3	7,93E-06
1000	6,70E-09	20140000	0.3	8,08E-06
1100	6,65E-09	17800000	0.3	8,21E-06
1200	6,60E-09	15290000	0.3	8,32E-06
1300	6,55E-09	13420000	0.3	8,42E-06
1400	6,50E-09	11580000	0.3	8,21E-06
1500	6,45E-09	9788000	0.3	7,99E-06

Temp	Conductivity
C	W/m.C
32	0.000694
212	0.000681
392	0.000646
572	0.000611
752	0.000563
932	0.000507
1112	0.000451
1292	0.000433
1472	0.000333

Temp	Specific Heat
C	J/kg.C
167	0.116
347	0.123
437	0.126
527	0.131
617	0.136
707	0.14
887	0.155
1067	0.169
1247	0.184
1337	0.2
1427	0.149

Table 1- Thermal physical properties and mechanical properties of selected material in ABAQUS (AISI type 304).

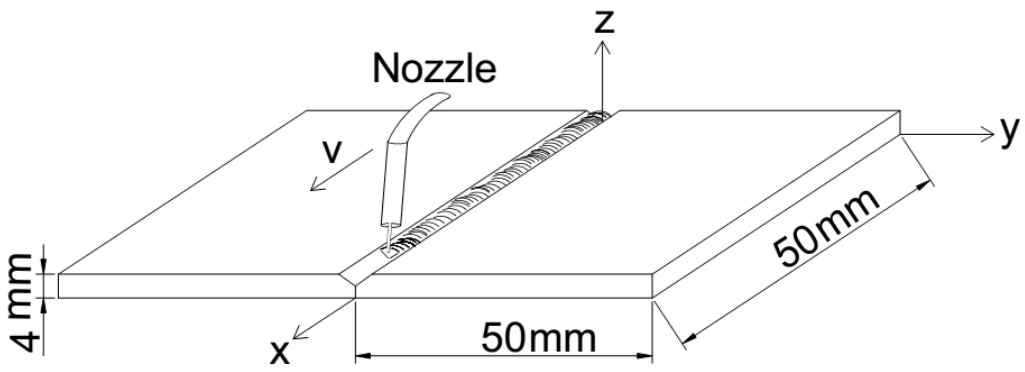

Fig. 1 – Schematic image of thin plates.

2.1. 3D FINITE ELEMENT (FE) MODEL

The aim of the simulation is to identify the temporal and spatial distribution of the temperature and stress during the welding process. The weld torch is simulated by applying a prescribed temperature of a magnitude slightly higher than the melting temperature at the boundary between the beads involved in the current weld pass and the neighboring region. The torch application and cool down regions are both analyzed through transient heat transfer steps. The two thin sheets are drawn and the welding seam is divided into 16 equal parts as shown in Figure 2. After identifying the base and welding material properties, a fine mesh is applied to the two metal pieces and the seam. To have accurate temperature distribution mesh is further refined in the seam region where temperature gradient is expected to be high. Therefore; the meshes are not equal in each region but more fine at the welding seam region as shown in Figure 3. Mesh expansion is applied to gradually increase the mesh from the high temperature gradient region at the seam to the rest of the metal sheet. The mesh size is also significantly reduced in Y direction since the temperature is changing significantly along the sheet thickness.

Having completed the drawing and meshing of the FE model, the thermal, physical and mechanical properties of the material are assigned. These values of the properties [9] are used for the AISI type 304 stainless steel and the welding material. Effect of temperature on properties is taken into account as listed in Table 1 [10]. Isotropic thermal conductivity with a uniform density is assigned to both the base and welding seam.

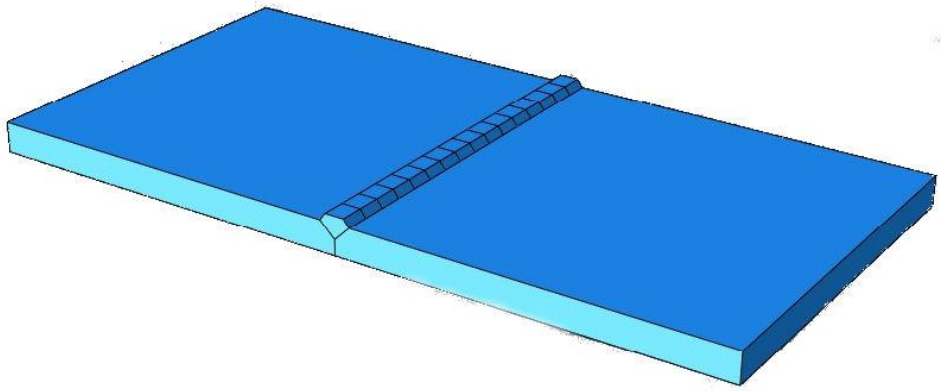

Fig. 2 – Whole drawing of the thin plates and welding seam.

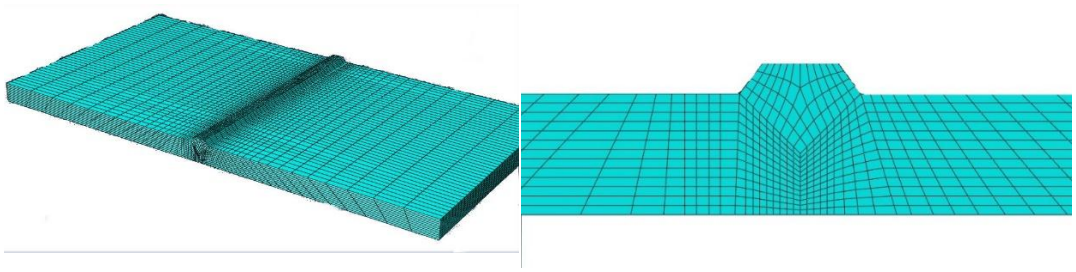

a) b)

Fig. 3 – Mesh used in the simulation.

During welding, the governing equation for transient heat transfer analysis is given by

$$\rho c \frac{\partial T}{\partial t}(x, y, z, t) = -\nabla \cdot \vec{q}(x, y, z, t) + Q(x, y, z, t)$$

Where ρ is the density, c is the specific heat capacity, T is the current temperature, q is the heat flux, Q is the internal heat generation rate. The non-linear isotropic Fourier heat flux constitutive equation is employed:

$$\vec{q} = -k\nabla T$$

where k is the temperature-dependent thermal conductivity.

ABAQUS Welding Interface (AWI) plugin is added to the main program. The Plugin has 5 different sections that required to be filled in together with the boundary conditions before running the simulation. In the first section, welding seam and maximum weld temperature are set to a value of 1500 ^{o}C. The second section which is the pass control is the most important step in welding simulation. In this section, the torch time step increment, maximum number of increments and the maximum allowed temperature are defined. In this section, moreover, the heat transfer coefficient and temperature are defined at the surface boundaries. In this work, a value of 0.025 mW/mm^2 K is set for the heat transfer coefficient and a temperature of 21 ^{o}C for all surfaces (Front, Back, Front, Top and Sides). Radiation is neglected to minimize the computation time. The third step is the number of passes or step to complete the simulation. The fourth step defines the heat transfer element type and a linear heat transfer model is selected, heat-transfer output properties are also chosen. In the final section, the model is generated. A summary of the conditions used in the simulation is listed in Table 2.

Parameters	Units	Value
Current	A	24
Voltage	V	200
Thickness	mm	4
Metal Initial Temp.	^{0}C	21.1
Welding wire - Welding Pool Distance	mm	10
Max. Weld Temp.	^{0}C	1500

Table 2 – Boundary Conditions of the Simulation.

3. RESULTS AND DISCUSSIONS

Spatial temperature distribution during welding of the 4 mm thin stainless steel plates is shown in Fig. 5. The temperature distribution shows that at the arc location a local melting occurs with the highest possible temperature. It can be noticed that there is a symmetry for the temperature distribution on both sides of the seam due to equal heat transfer resistance. However, this is not the case for the area upstream and downstream the welding torch location. Downstream the torch, the temperature gradient is much steeper. This asymmetric temperature distribution is the reason for the metal distortion or thermal stress during the welding process as a result of the various expansion values. The temperature distribution of the isothermal lines is similar to that obtained by the infrared camera as shown in Figure 6. Although a direct comparison has not been carried out at this stage, the team is currently working towards validating that results and correlating the temperature distribution to the depth of penetration as similar to what is found experimentally [4].

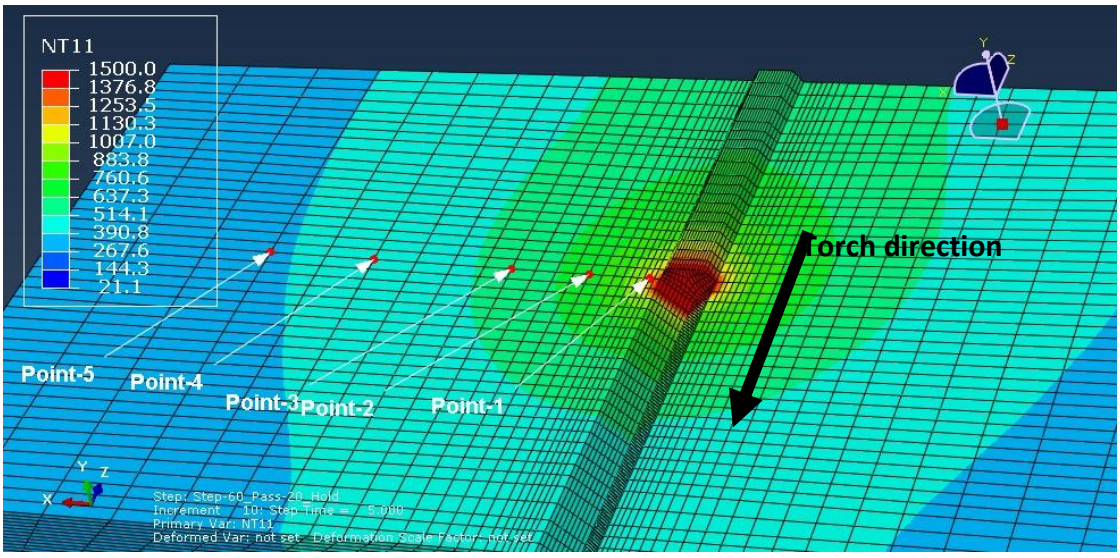

Fig. 5– Spatial surface temperature distribution during the welding process.

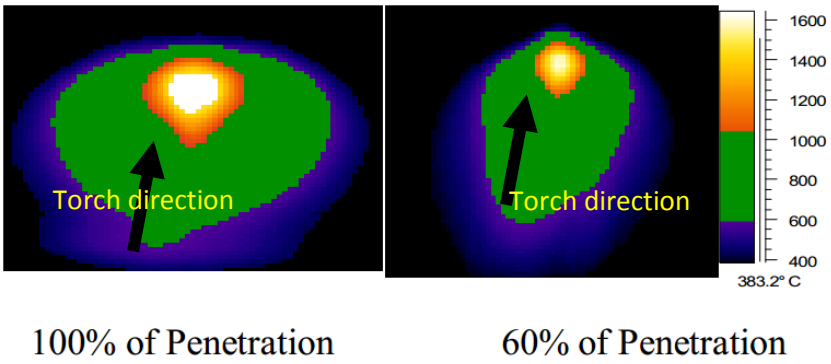

Fig. 6 – Isothermal temperature distribution using infrared camera [xx2].

The temporal distribution of the welding temperature at point 1, 2, 3, 4 and 5 for a duration of 450 s is shown in Figure 7. It can be seen from these selected points in the simulation that the rate of temperature increase of the point located on the seam becomes very steep as the torch passing through to reach its highest temperature in approximately 200 s. Further away from the welding seam, the curve for each point is less inclined than the closer one. After passing the maximum temperature all points are cooled and tried to attain thermal equilibrium state. The temperature difference between point 1 and point 5 reaches a value 100 ^{o}C after 250 s from the time when point 1 reaches its maximum temperature.

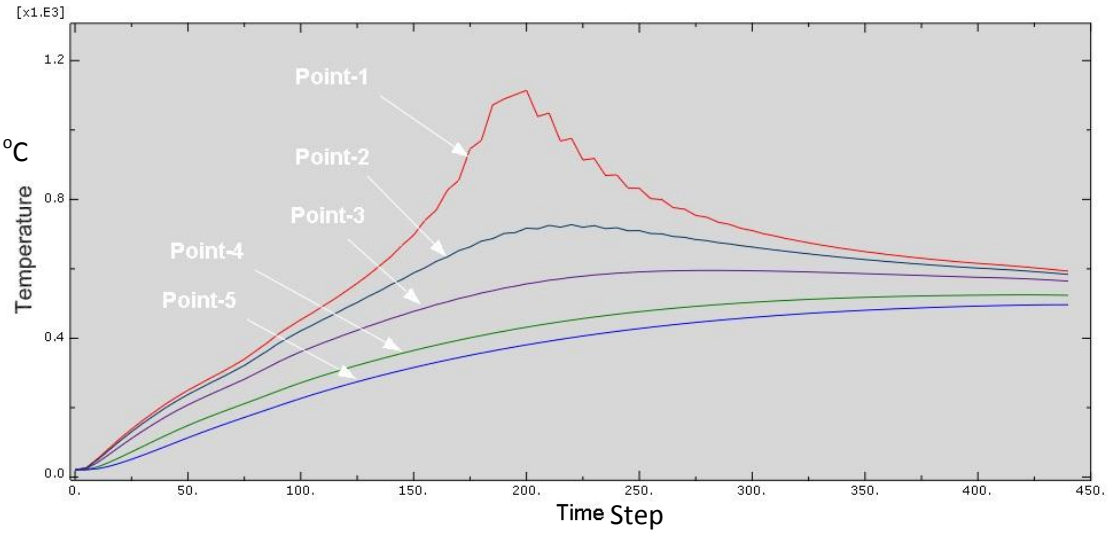

Fig. 7–Temporal temperature distribution of points 1, 2, 3, 4 and 5.

At the bottom side of the plate a spatial temperature distribution similar to that at the top surface is noticed but with lower temperature value as shown in Figure 8. To further investigate the temporal variation of the temperature in the bottom surface a line has been selected and a 3D graph has been plotted to show how the temperature varies along that line with time as shown in Figure 9. The variation in temperature is giving an indication of how the material is tending to change its shape due to the thermal expansion.

The graph also shows relatively fast gradient of temperature when the torch pass above that line. Approximately 100 second after the torch passes the seam location, the temperature becomes almost homogeneous. The fast change in temperature not only results in higher thermal stresses but also can lead to a change in the micro structure of the material. As the material properties are non-linear, this hypothesis will have some error, however it is small and can be neglected in most of practical applications.

In Fig. 10, total distortion of the welded part is shown during the welding operation (10 times enlarged). With this simulation, before welding the part where can be fixed points and due to the connection point, we can predict how the stress affected the part. Connection types and welding‘s effect can be seen in fig. 10.

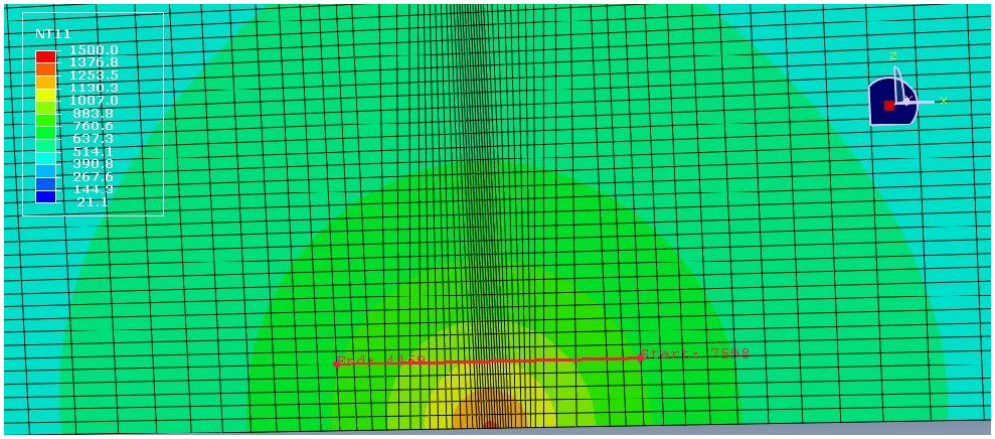

Fig. 8– 20mm straight line on the bottom side of the pieces.

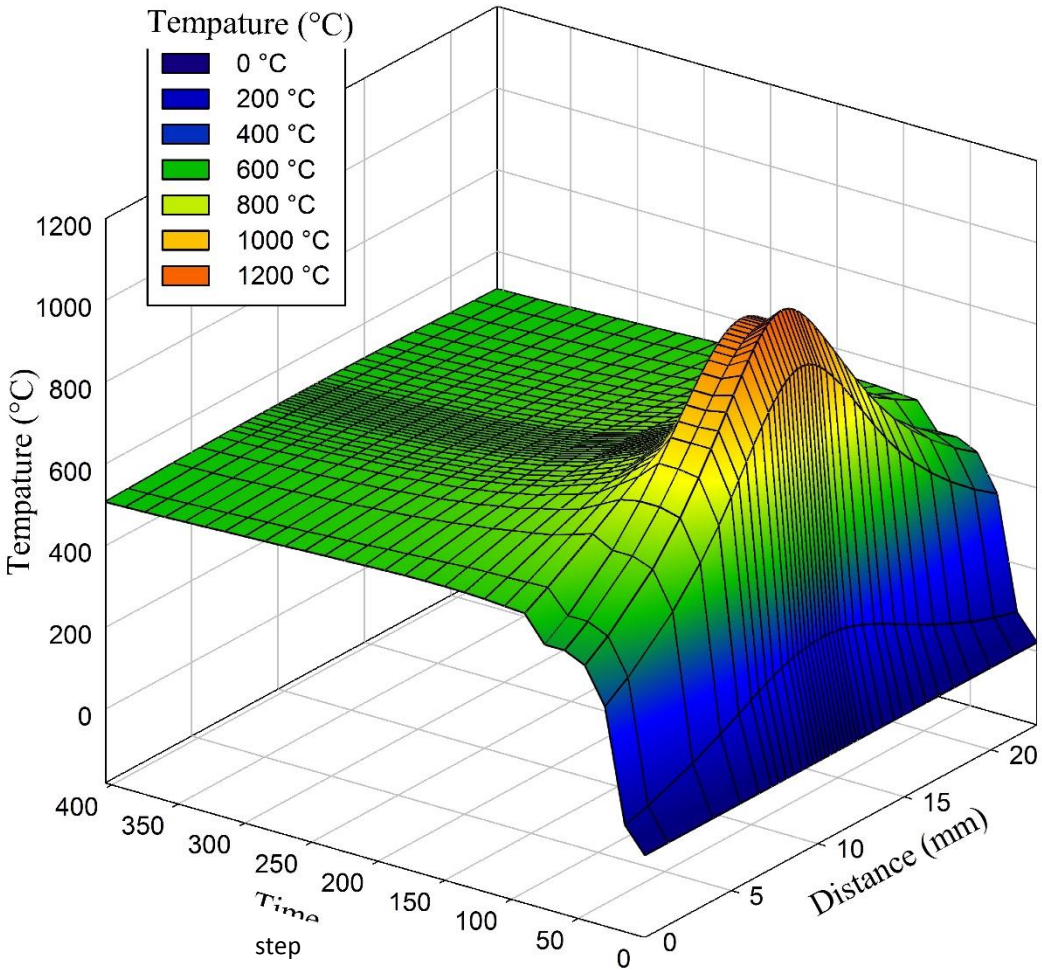

Fig. 9 – Temperature variation across the seam at the bottom of the plate during the welding.

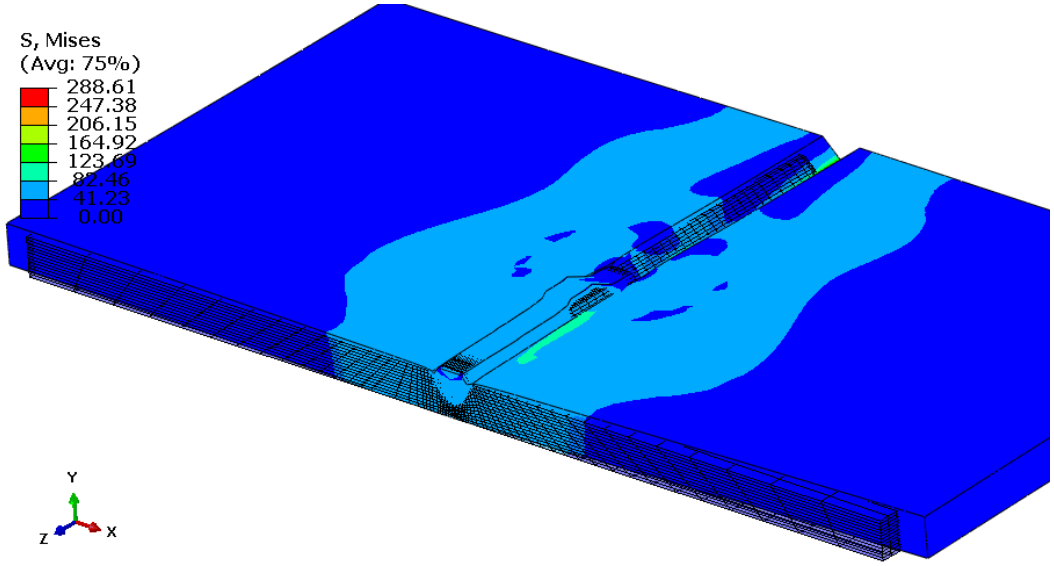

Fig. 10- Total distortion (10 times enlarged) and V. Mises stress distribution during the welding.

4. CONCLUSIONS

Temporal and spatial temperature and stress distributions are predicted successfully using ABAQUS welding interface in a 4 mm plates of material AISI type 304 stainless. The results show a temperature distribution similar to the published experimental data obtained by infrared camera. The simulation is therefore can be useful to study the effect of welding on material micro structure change and to predict the welding quality. Further work is needed to numerically validate the model, and to examine the mode for different operating conditions. And also for future work, connectiong types will be investigated for minimum deformation during welding.

5. ACKNOWLEDGEMENT

The authors would like to acknowledge the financial support from The Turkish National Research Council through the project No. 114M756.

6. REFERENCES

[1] Chin, B.A., Madsen, N.H. and Goodling, J.S.: Infrared thermography for sensing the arc welding process. the Annual AWS Convention, Philadelphia, Pa., April (1983).

[2] Murugan, S., Kumar, P.V., Raj, B., Bose, M.S.C.: Temperature distribution during multi-pass welding of plates. Int. J. Press. Vessel Pip. 75, (1998), 891–905.

[3] Song J.B., Hardt D.E.: Estimation of weld bead depth for in-process control. in: Danai K., Malkin S. (Eds), Automation of Manufacturing Processes, ASME, New York, (1990) 39-45,.

[5] Liang, G., Yuan, S.: Study on the temperature measurement of AZ31B magnesium alloy in gas tungsten arc welding. Mater. Lett. 62, (2008), 2282–2284.

[6] Kasuya, T., Hashiba, Y., Ohkita, S., Fuji, M.: Heat conduction analysis of bidirectional multi-pass welding with short bead lengths. Sci. Technol. Weld. Join. 5, (2000), 215–220.

[7] Zhu, X.K., Chao, Y.J.: Numerical simulation of transient temperature and residual stresses in friction stir welding of 304L stainless steel. J. Mater. Process. Technol. (2004), 146, 263–272.

[8] Zhu, X.K., Chao, Y.J.: Effects of temperature-dependent material properties on welding simulation. Comput. Struct. 80, (2002), 967–976.

[9] M.J. Attarha, I. Sattari-Far.: Study on welding temperature distribution in thin welded plates through experimental measurements and finite element simulation. Journal of Materials Processing Technology, (2011) 211. 688–694.

[10] Metals Handbook, American Society for Metals, Metals Park, Ohio 44073, 1985.

CORRESPONDENCE ADDRESS: Gökhan BİÇER, Mevlana University, Yeni İstanbul Cad. No: 235, gbicer@mevlana.edu.tr

SHORT BIOGRAPHIES

Gökhan BİÇER – Project researcher and teaching assistant at Mevlana University.

İsmail TİRTOM - Ismail Tirtom is currently working at Mevlana University, Mechatronics Engineering Department as an Assistant Professor. He obtained his doctorate from Tohoku University, Mechanical Engineering in 2008; master degree from Izmir Institute of Technology, Materials Science and Engineering and bachelor's degree from Ege University, Mechanical Engineering.

Essam ABO-SERİE–was born in Cairo-Egypt, 1967. He obtained BSc with honors in 1989 and MSc in 1995 from Cairo University, Mechanical Power Engineering. He completed his PhD from Imperial College, Mechanical Engineering London in 2004. His major study is focusing on optical techniques and different industrial applications. Dr. Abo-Serie is a fellow of the Higher Education Academy in UK (FHEA) and a member of Institute of Physics IOP, Society of Automotive Engineers SAE, ILASS Europe, Egyptian Society of Mechanical Engineers, Engineering Society of Mechanical Engineering ESME and a reviewer for different international journals. He is currently Associate Professor at Mevlana University, Turkey.

Lightweight Design of Vehicle Energy Absorbers Using Steel, Aluminum and Magnesium Alloys

Emre Demirci[41], *Ali Rıza Yıldız*[42]

Abstract

Nowadays, lightweight vehicle component designs are very important for fuel efficiency and low emissions in automotive industry. The carmakers need to develop innovative safety systems to meet new international crash test regulations like ECE, Euro NCAP, NHTSA. Energy absorbers are one of the passive safety systems used in the vehicles. In this study, crash performances of the energy absorbers with different materials like SPC 440 steel, Al 7108 – Al 7003 aluminum alloys and AM60 magnesium alloys are investigated numerically. According to finite element analysis results, crash performance parameters such as total energy absorption, specific energy absorption and reaction forces are compared for the mentioned materials. Although energy absorption capability of the steel energy absorber is better than aluminum and magnesium absorbers, the energy absorbers made of lightweight materials can absorb more energy per unit mass of material than the SPC steel. This advantage of the lightweight alloys has been encouraging automakers to use them in designing of structural vehicle components.

Keywords: Aluminum and Magnesium Alloys, Crash Analysis, Energy Absorbers, Lightweight Design

91. INTRODUCTION

The design of lightweight vehicle components is driven by many competing criteria such as car safety, improved performance, fuel efficiency and low emissions in automotive industry. The carmakers need to develop innovative safety systems to meet new international crash test regulations like ECE, Euro NCAP, NHTSA standards. While adding new safety systems, the carmakers also need to reduce fuel consumption and CO_2e emissions. Weight reduction is one of the best solutions for reducing fuel consumption and emissions [1]-[6].

In recent years, there is a great deal of interest in low density materials, such as aluminum and magnesium alloys for vehicle weight reduction [7]. Body and chassis components constitute nearly half of the vehicle's weight. Low density materials can be used in different components such as safety systems for lightening the weight of chassis and body structure.

In automotive industry, vehicle safety systems can be handled in two classes: Active safety systems and passive safety systems. Active safety systems intervene before an accident occurs. Passive safety systems are the components that protect occupants during a crash. Energy absorbers is one the passive safety systems in automotive industry that also known as crash boxes. The main purpose of using energy absorbers is to control the kinetic energy of the car during crash while preventing the peak reaction force. Crash performance of the energy absorbers has been determined in different research works in the literature [1],[2],[8]-[12].

In this study, crash performances of the energy absorbers with different materials like conventional SPC 440 steel, Al 7108 – Al 7003 aluminum and AM60 magnesium low density alloys are investigated numerically. Crash performances of conventional steel and low density alloys are compared and usages of low density materials as an energy absorber are investigated.

92. ENERGY ABSORBERS AND CRASHWORTHINESS PARAMETERS

The energy absorber is the vehicle safety system component that is used to convert the kinetic energy into another form of energy dissipated in plastic deformation. Other function of the energy absorbers is to reduce the peak reaction force to protect occupants from serious damages while crash occurs. In this work, square, rectangular, circular and polygonal cross section energy absorber geometries were designed in CAD software. Figure 1 shows the geometric forms of energy absorbers. All energy absorbers have same length of cross-section $s = 200$ mm, length of tube $L = 180$ mm and thickness $t = 1.5$ mm.

[41] *Corresponding author: Bursa Technical University, Department of Mechanical Engineering, 16330, Bursa, Turkey.* emre.demirci@btu.edu.tr

[42] *Bursa Technical University, Department of Mechanical Engineering,* aliriza.yildiz@btu.edu.tr

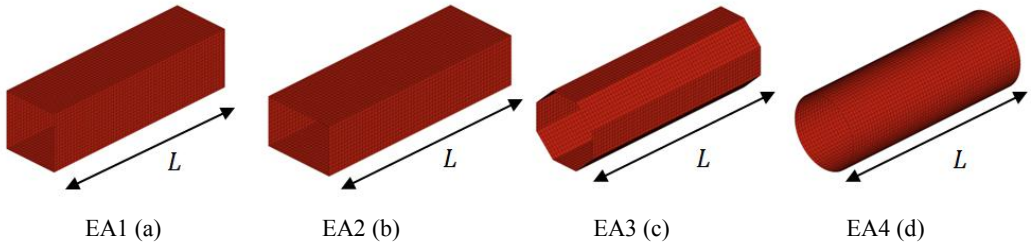

Figure 1. Different energy absorber geometries; (a) Square, (b) Rectangular, (c) Polygonal, (d) circular

In the literature there are several criteria for defining crash parameters and crash performance of energy absorbers [9]. Some of these criteria are listed below that are used in this study:

92.1. Total Energy Absorption

Total energy absorption can be defined as the work done by crush load during the impact [11]. Figure 2 shows the area under the load and displacement curve which represents the total energy absorption. The area can be calculated as:

$$E_T = \int_{S_i}^{S_l} F \cdot dS \tag{1}$$

Where E_T is the total energy absorption, F is the crush load and S is the displacement. S_i is the initial length of crushed zone and S_l is the length of crushed zone of energy absorber.

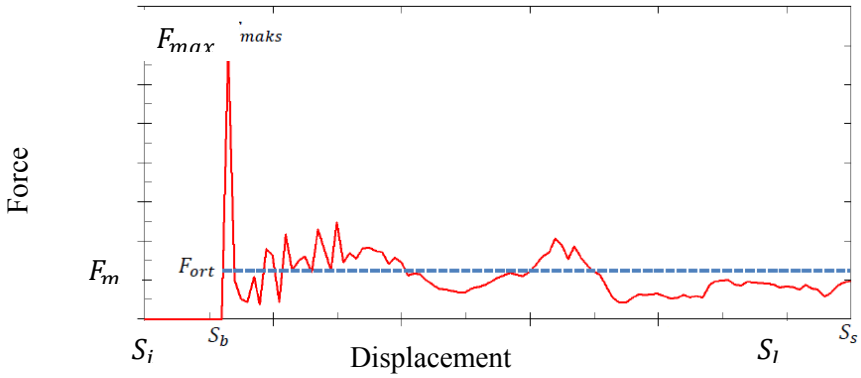

Figure 2. A typical load-displacement curve

92.2. Peak Crush Force and Mean Crush Force

During the first steps of impact, maximum reaction force occurs on energy absorber because of the axial loadings. This maximum reaction force is called peak crush force (F_{max}) in the literature [12]. The peak crush force should be as low as possible to protect occupants from serious damages while crash occurs.

The mean crush force (F_m) can be defined by dividing the total energy absorption (E_T) by the total displacement (S) and given as:

$$F_m = \frac{E_T}{S} = \frac{E_T}{S_l - S_i} \tag{2}$$

92.3. Specific Energy Absorption

The specific energy absorption (E_m), also called the energy absorbed per unit mass is calculated by dividing the total energy absorption (E_T) by the mass of undeformed energy absorber.

$$E_m = \frac{E_T}{m} \tag{3}$$

These formulations are used as crashworthiness parameters to define crash performance of an energy absorber.

93. FINITE ELEMENT MODELS AND CRASH ANALYSIS

The designed energy absorber models are imported in to HyperMesh Ls-Dyna interface and finite element models are created. Meshing of the energy absorbers is carried out using shell elements of size 3mm x 3mm. In this study, Energy absorbers are

fixed at one end and axially crashed by a movable rigid wall from the other end. The rigid wall modelled as 200 kg and moved at a speed of 15 m/s. The finite element model of EA3 can be seen in Figure 3. The contact between energy absorbers and rigid wall is defined with –Automatic Single Surface" card in Ls-Dyna [13].

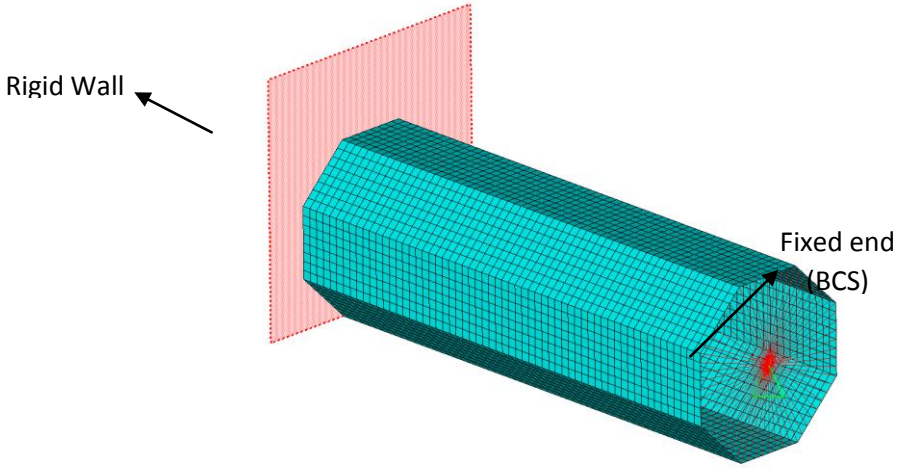

Figure 3. A Finite element model of EA3

MAT 24 - Piecewise linear isotropic plasticity material cars is selected in Ls-Dyna for dynamic crash analysis. The plastic deformation characteristics of the materials are defined with effective true stress-true strain curves. The main aim of this study is to compare crash performance of conventional steel and low density materials. In order to do this, conventional SPC 440 steel, Al 7108 – Al 7003 aluminum alloys and AM60 magnesium alloy were defined as energy absorber material in finite element model. Some mechanical properties of used materials are given in Table 1 and effective true stress-true strain curves are shown in Figure 4.

Table 10. Mechanical properties of used steel and low density materials

Material	Young's Modulus (GPa)	Density (kg/m^3)	Poisson's Ratio
SPC440	206	7850	0.3
Al7108	71	2770	0.33
Al7003	71	2770	0.33
AM60	45	1700	0.35

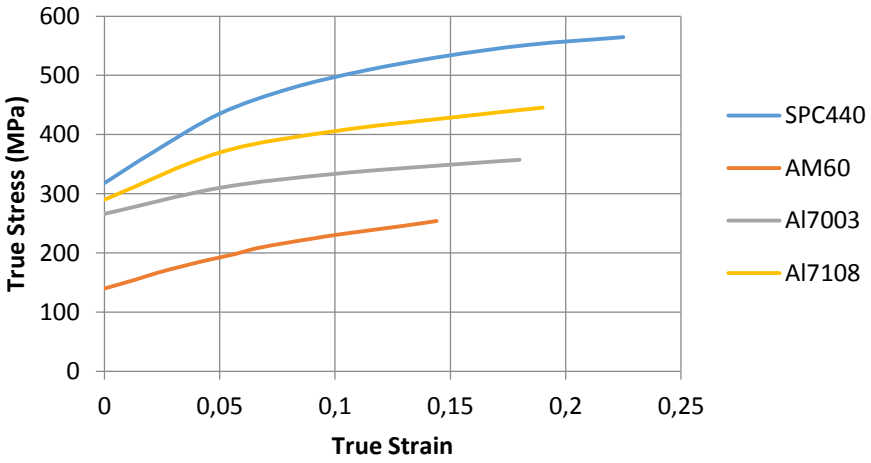

Figure 4. True stress – strain curve of used steel and low density materials

The crash analyses of the all models are done in Ls-dyna. Energy absorption and crush force values are calculated for 130 mm deformation. The specific energy absorptions of all models are calculated for all materials. The mass of undeformed energy absorbers are: 0,4435 kg for SPC 440 steel, 0,1596 kg for aluminum alloys and 0,0979 kg for magnesium alloy. The results and comparison of materials are shown in Table 2.

Table 2. Crash analysis results of all energy absorber models

		MATERIAL			
		SPC440	**Al7003**	**Al7108**	**AM60**
EA1	Energy Absorption (kJ)	8,50	4,36	4,56	2,45
	Peak Crush Force (kN)	136,72	80,33	89,96	43,33
	Specific Energy Absorption (kJ/kg)	19,16	27,32	28,57	25,02
EA2	Energy Absorption (kJ)	6,76	3,07	3,69	2,25
	Peak Crush Force (kN)	139,21	85,36	94,01	44,87
	Specific Energy Absorption (kJ/kg)	15,24	19,24	23,12	22,98
EA3	Energy Absorption (kJ)	11,15	4,94	5,79	3,47
	Peak Crush Force (kN)	154,08	90,24	98,68	46,38
	Specific Energy Absorption (kJ/kg)	25,14	30,95	36,28	35,44
EA4	Energy Absorption (kJ)	10,49	4,71	5,63	3,41
	Peak Crush Force (kN)	143,72	78,04	87,13	43,61
	Specific Energy Absorption (kJ/kg)	23,65	29,51	35,28	34,83

Absorbed energy – displacement graph is shown in Figure 5 and reaction force – displacement graph is shown in Figure 6 for selected energy absorber model EA3. The graphs show the crash characteristic of different materials.

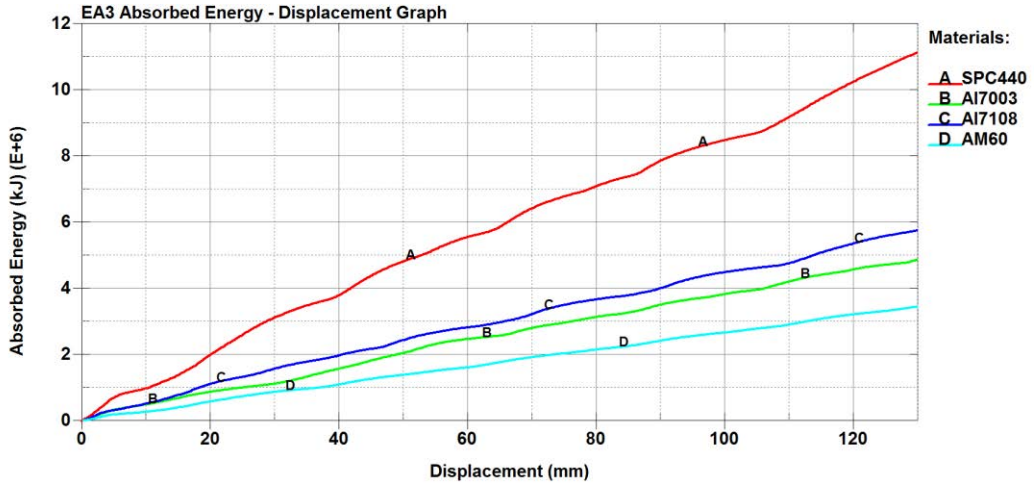

Figure 5. Absorbed energy – displacement graph of EA3 for all materials

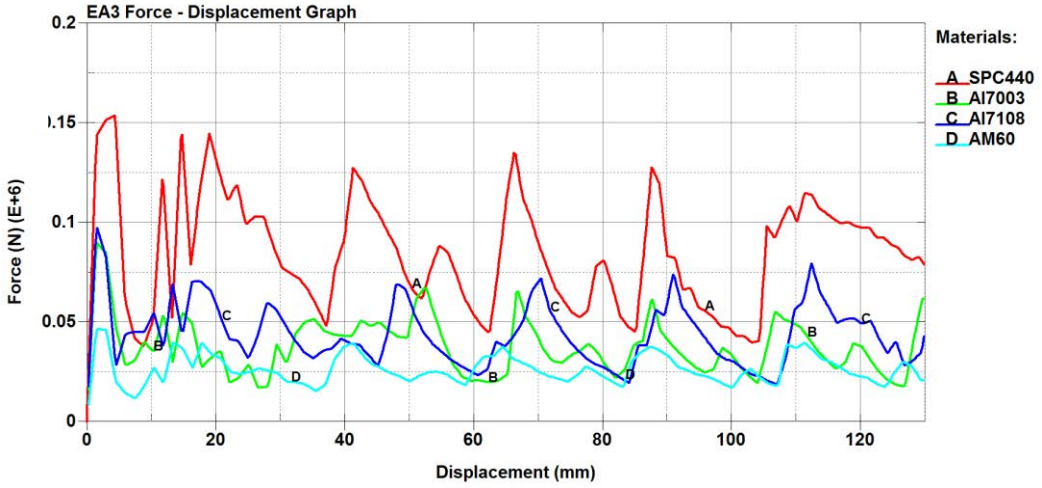

Figure 6. Force – displacement graph of EA3 for all materials

94. CONCLUSIONS

In this study, crash performances of the energy absorbers with different materials like SPC 440 steel, Al 7108 – Al 7003 aluminum alloys and AM60 magnesium alloys are investigated numerically. According to finite element analysis results, crash performance parameters such as total energy absorption, specific energy absorption and reaction forces are compared for the mentioned materials. The main points of the results are explained below:

- The total energy absorptions and the specific energy absorptions of polygonal and circular energy absorbers are better than square and rectangular energy absorbers for all used materials. This means that crash performances of polygonal and circular energy absorbers are better.
- The crush shape of energy absorber for all used materials are similar that can be seen in Figure 6. Energy absorber is exposed to local buckling for all used materials.
- Although energy absorption capability of the SPC440 steel energy absorber is better than aluminum and magnesium absorbers, the energy absorbers made of low density materials can absorb more energy per unit mass of material than the SPC steel. Al 7108 energy absorber has the maximum specific energy absorption for all energy absorber models.
- This advantage of the aluminum and magnesium alloys has been encouraging automakers to use them in designing of lightweight structural vehicle components and reduce to fuel consumption and emissions.

REFERENCES

[185]. A.R. Yildiz, E. Kurtulus, E. Demirci, B.S. Yildiz, S. Karagoz, ~~–~~Optimization of thin-wall structures using hybrid gravitational search and Nelder-Mead algorithm, *Materials Testing*, vol. 58, no. 1, pp. 75-78, 2016.

[186]. E. Demirci, A.R. Yildiz, ―Improving the vehicle crash safety with high performance energy absorbers", *Engineer & the Machinery Magazine*, vol. 56, no. 663, pp. 40-45, 2015.
[187]. A.R. Yildiz, K. Solanki, ―Multi-objective optimization of vehicle crashworthiness using a new particle swarm based approach", *International Journal of Advanced Manufacturing Technology*, vol. 59, pp. 367-376, 2012.
[188]. M. Kiani, A.R. Yildiz, ―A comparative study of non-traditional methods for vehicle crashworthiness and NVH optimization", *Archives of Computational Methods in Engineering*, DOI: 10.1007/s11831-015-9155-y, 2015.
[189]. C.M. Tamarelli, *The Evolving Use of Advanced High-Strength Steels for Automotive Applications*, Michigan, USA: Steel Market Development Institute, 2011.
[190]. S. Keeler, M. Kimchi, *Advanced High-Strength Steels Application Guidelines Version 5.0*, World Auto Steel, 2014.
[191]. J. Rowe, *Advanced Materials In Automotive Engineering*, Philadelphia, USA: Woodhead Publishing, 2012.
[192]. M. Langseth, ―Crashworthiness of Light-weight Automotive Structures 2001-2006", NorLight Conference, Tron, 2003.
[193]. G. Nagel, ―Impact and Energy Absorption of Straight and Tapered Rectangular Tubes", PhD Thesis, The School of Civil Engineering Queensland University, Queensland, 2005.
[194]. A.A.A. Alghamdi, ―Impact and Energy Absorption of Straight and Tapered Rectangular Tubes", *Thin-Walled Structures*, vol. 39, pp. 189-213, 2001.
[195]. A. Chathbai, ―Parametric Study of Energy Absorption Characteristic of a Rectangular Aluminum Tube Wrapped With E-Glass/Epoxy", Master Thesis, Wichita State University, Mechanical Engineering Department, Kansas, USA, 2007.
[196]. S.Y. Jin, W. Altenhof, ―Comparison of the Load/Displacement and Energy Absorption Performance of Round and Square Aa6061-T6 Extrusions Under a Cutting Deformation Mode", International Journal of Crashworthiness, vol. 12, no. 3, pp. 265-278, 2007.
[197]. Livermore Software Technology Corporation, Livermore, ―Ls-Dyna Keyword User's Manual Volume I", California, 2012.

On the Investigation of a Novel P&O MPPT Algorithm Based on Extraterrestrial Irradiance for PV Systems

Said Mahmut Çınar[43], *Sedat Bakım*[44]

Abstract

To produce the electrical energy from the sun, photovoltaic (PV) panels use. The output of the PV panels has nonlinear characteristics due to unstable variations of solar radiations, and ambient temperatures. To maximize the efficiency of the PV systems, the PV panels should be operated in maximum power point (MPP). There are a lot of algorithms such as Perturb and Observe (P&O), Incremental Conductance (INC) and Hill Climbing (HC) etc. for maximum power point tracking (MPPT) for the PV systems. Because of its simple structure, P&O algorithm is widely used for MPPT. In this study, a novel P&O type MPPT algorithm based on extraterrestrial irradiance is proposed for the PV systems. The proposed P&O algorithm has low computational complexity, easily implementable and, requirement of a few measurement parameters. Steps of the proposed P&O algorithm are; i. A look-up table that gives the MPP parameters of the PV panel versus irradiance is computed, ii. The extraterrestrial irradiance values are calculated for given date and location, iii. MPP parameter of PV panel is derived from the look-up table. iv. Traditional P&O algorithm is started to tracking from the derived MPP. The proposed P&O and traditional P&O algorithms were tested on a platform arranged in MATLAB/Simulink environment. MPP catch time of the proposed P&O algorithm and steady-state performance was examined in test experiments. Moreover, the energy efficiency of the proposed P&O algorithm was investigated in case of long time operation. The results showed that the proposed P&O algorithm has shorter the MPP catch time than the traditional P&O algorithm and power oscillations can be reduced by small perturbation step. The energy efficiency of the PV system can be increased thanks to small the MPP catch time.

Keywords: Extraterrestrial irradiance, PV panel, P&O, MPPT

95. INTRODUCTION

Today, the studies related to renewable energy are popular because of the decreasing in fossil fuel reserves. Sun irradiance is converted to electric energy by PV panels. Because of the PV panels‘ efficiency is about 20% they should be operated at maximum power point (MPP) for increasing the efficiency of PV panels. There are a lot of MPPT methods such as incremental conductance (INC), P&O and hill climbing (HC) [1-3]. Literature survey of this methods involved is given below.

Salah C. B. and Quali M. in their study, proposed MPPT controllers for PV systems, designed with fuzzy logic and artificial neural network methods. In both of these controllers, solar radiation and PV cell temperature are taken as inputs. From the simulation and experimental results, it is observed that fuzzy logic and artificial neural network controllers operate with higher performance than the known MPPT methods [4]. Bendib B. and his colleagues in their study presented a fuzzy logic based smart MPPT for the PV system independent from the network. From the simulation results, it is observed that the fuzzy logic controller is more stable than the traditional P&O technique in changing environmental conditions [5].

Hassan Fathabadi propose a MPPT algorithm that uses PV current and voltage in various meteorological conditions for PV systems. Test results are showed that this algorithm catch the MPP in short time. Angel-Antonio et al. present a new MPPT method that can be applied to PV inverters and charge converters. Thanks to irradiance sensors, their MPPT method shows the good dynamic response according to other four MPPT methods.

Though there are many novel methods in the literature, no algorithm tracking MPP by using extraterrestrial irradiance has been seen. In this study, initial value in the P&O algorithm, depending on extraterrestrial radiation, was ensured to be determined in a position close to MPP and so, MPP finding time of algorithm could be decreased substantially. The proposed P&O algorithm was tested by using the solar radiation data obtained on a sunny day on June 10, 2015 in Afyonkarahisar region and the extraterrestrial radiation derived on the same date. The principle of the proposed P&O algorithm is given below in detail and then, the results obtained from simulation studies are presented.

[43] *Corresponding author: Afyon Kocatepe University, Department of Electrical Engineering, 03200, Merkez/Afyonkarahisar, Turkey. smcinar@gmail.com +90 272 2281423*

[44] *Afyon Kocatepe University, Department of Electrical Engineering, 03200, Merkez/Afyonkarahisar, Turkey. sedat_bakim@hotmail.com*

96. METHOD

In PV systems, to run the PV panel at MPP, a DC/DC converter should be connected between the PV panel and load. With changing the duty cycle of converter, impedance balancing is made and operating of PV panel at MPP is ensured. The duty cycle of the converter is regulated by means of a controller. The controller is placed in a control loop composed of PV panel, DC/DC converter, and load. In the control loop the reference operating point (MPP) is not known before and parameters of this point vary when compared to parameters like irradiance, junction temperature and load type.

There are a lot of MPPT techniques in the literature for tracking MPP. The required features for MPPT algorithms can be ranged as follows; i: they are realized simply, ii: it needs parameter measurement in the least possible number, iii: it catches the MPP in a short time, iv: it has a lesser calculation work load. As P&O can meet most of the features set forth above, it is among the mostly demanded algorithms in the literature. In this study, a new algorithm enabling the P&O algorithm to start tracking from a point close to MPP is proposed. The parameters of this point close to MPP can be determined simply depended on extraterrestrial radiation and P&O algorithm starts tracking from that point. In this way, MPP finding time of proposed P&O algorithm can be shortened substantially when compared to traditional P&O algorithm. The flow chart of the proposed MPPT algorithm is given in Figure 1.

In the algorithm, firstly, the look-up table that gives the MPP current against the solar radiation of PV panel to be used in the system is established.

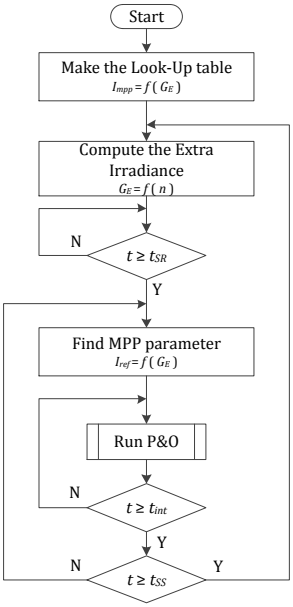

Figure 1. The flow chart of proposed algorithm

The look-up table contained MPP current values versus the irradiance can be generated to using equations 1-9 (Table 1). I_{mpp} values given here were derived for 200-1000 W/m^2 solar radiation range for Isofoton ISF-250 model PV panel. In case of using different PV panel, look-up table can be easily regenerated.

Table1. PV panel look-up table

G_E [W/m^2]	I_{mpp} [A]
200	1.63
210	1.72
220	1.8
…	…
…	…
990	8.09
1000	8.17

Calculation formulas of MPP according to the alteration of solar radiation values are provided below:

$$P_{tip} = V_{oc} \cdot I_{sc} \quad (1)$$

Equation 1 indicates the typical power of the PV panel. The typical power of the panel at a given radiation intensity equation (2) calculated.

$$P_{tip}(\xi) = P_{tip}(\xi_{stc}) \cdot \Delta\eta(\xi) \cdot \xi \quad (2)$$

where; ξ shows the relative 1000W/m^2 radiation intensity and is determined by the basic value. For example, 800W/m^2 for radiation $\xi = 0.8$ .The typical maximum power of PV panels known of equation (3) with can be found.

$$P_{\max}(\xi) = P_{tip}(\xi) \cdot FF \quad (3)$$

where; FF is described as the fill factor of PV panel and calculated in equation (4).

$$FF = \left(V_{mpp} \cdot I_{mpp}\right) / \left(V_{oc} \cdot I_{sc}\right) \quad (4)$$

PV panel maximum power point current (I_{mpp}), maximum power point voltage (V_{mpp}) and open circuit voltage (V_{oc}) respectively, can be calculated with equation (5), (6) and (7).

$$I_{mpp}(\xi) = \xi \cdot I_{mpp}(stc) \quad (5)$$

$$V_{mpp}(\xi) = P_{\max}(\xi) / I_{mpp}(\xi) \quad (6)$$

$$V_{oc}(\xi) = P_{tip}(\xi) / I_{sc}(\xi) \quad (7)$$

Equation (7) using $V_{oc}(\xi)$ calculated to being asked $I_{sc}(\xi)$ is required value. The following equation (8) and (9) can easily calculated using the equations.

$$V_{oc}(\xi) = V_{oc}(stc) \cdot \Delta\eta \quad (8)$$

$$I_{sc}(\xi) = P_{tip}(\xi) / V_{oc}(\xi) \quad (9)$$

After the generating the look-up table, next step is calculated the extraterrestrial irradiance for specific location. The extraterrestrial irradiance values can be easily calculated from sun geometry and detailed information is given in [8]. In proposed P&O algorithm, the MPP current is found for extraterrestrial irradiance value and P&O algorithm is started with this MPP current. Finally P&O algorithm is run to catch MPP.

97. EXPERIMENTAL RESULTS

In experiments the dynamical and steady state response of the proposed P&O algorithm is tested. Also the energy efficiency of the PV system for long time operation is examined for the case that the PV panel is in the uniform irradiance. The DC/DC converter is restart during the day, four times for comparing the MPP catch time of the algorithms. Moreover to detect the effects of MPP finding times and the ossilations of power, the value of (the perturbation step of the P&O algorithm) is set to two different values (0.01 and 0.001). The simulations are run for sunny whether conditions. Figure 2 represents the alteration of output power of the PV panel under sunny wheather condition run.

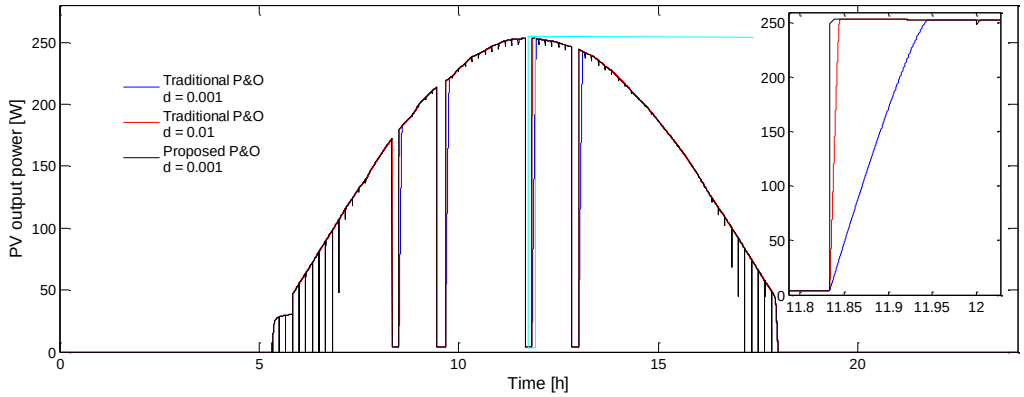

Figure 2. Alteration of PV output power versus time of day for sunny day

The alteration of PV output voltages are presented in Figure 3 for the investigated algorithms. It can be seen, in case of proposed P&O algorithm is used, the value of parameter is set to 0.01, the magnitude of osscilation is obtained around 10mV whereas in case the value of parameter is set to 0.001 the magnitude is decreased considerably (around 1mV).

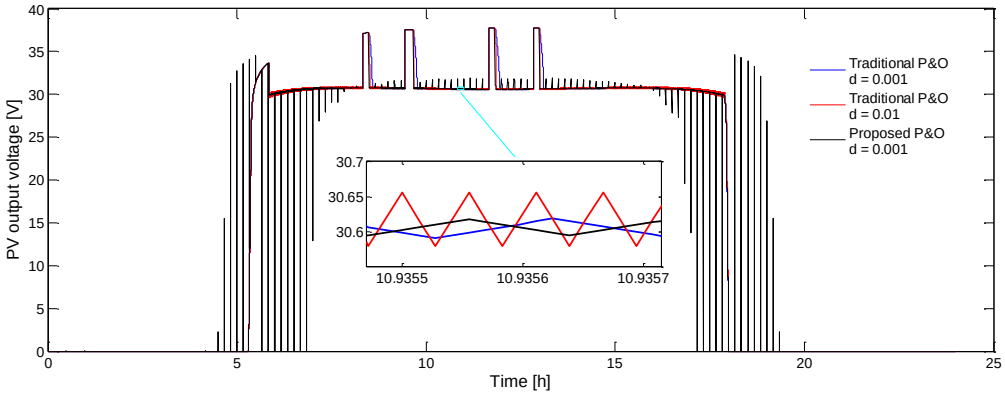

Figure 3. Alteration of PV output voltage versus time of day for sunny day

The calculated efficiencies of the PV are compared in Table 3, in case of the proposed P&O algorithm and the traditional P&O algorithm is run. Two different step sizes (0.01 and 0.001) are considered while simulations. It is obtained that proposed P&O algorithm outperforms the traditional P&O algorithm with 0.15%.

On the other hand in case the step sizes of the algorithms are tune to 0.001 it is obtained that proposed P&O algorithm outperforms the traditional P&O algorithm with 1.5%. Moreover it is obvious from Table 3 that the performance of proposed P&O algorithm is much more increased for clear day conditions since the general characteristic of global solar radiations are similar to extraterrestrial radiation values for clear days.

Table 2. Energy efficiency of PV system for proposed and traditional P&O algorithms

	d = 0.01 June 10	d = 0.001 June 10
Traditional P&O	85.65	84.18
Proposed P&O	85.80	85.71
Difference	0.15	1.53

CONCLUSİON

In this study, a novel P&O MPPT algorithm 2015 according to which the extraterrestrial irradiance is designed and tested for June 10, 2015.The energy efficiency of the proposed P&O algorithm was investigated in case of long time operation (during the day). The energy efficiency of the PV system can be increased thanks to small the MPP catch time. The considering different atmospheric conditions in further studies the proposed P&O algorithm is comparable with other algorithms. Also extraterrestrial radiation intensity performance by applying other algorithms can be observed that the maximum power point tracking.

ACKNOWLEDGMENT

This study is supported by Afyon Kocatepe University Scientific Research Projects Council under 15.FEN.BİL.30 project.

REFERENCES

[198]. P. Bhatnagar and R. K. Nema, ―Maximum power point tracking control techniques: State-of-the-art in photovoltaic applications," Renew. Sustain. Energy Rev., vol. 23, pp. 224–241, Jul. 2013.
[199]. T. C. Esram Pl; PN - IC -, ―Comparison of photovoltaic array maximum power point tracking techniques," Ieee T Energy Conver; , vol. 22, no. 2, pp. 439–449, 2007.
[200]. B. Subudhi and R. Pradhan, ―A Comparative Study on Maximum Power Point Tracking Techniques for Photovoltaic Power Systems," Sustain. Energy, IEEE Trans., vol. 4, no. 1, pp. 89–98, 2013.
[201]. C. Ben Salah and M. Ouali, ―Comparison of fuzzy logic and neural network in maximum power point tracker for PV systems," Electr. Power Syst. Res., vol. 81, no. 1, pp. 43–50, Jan. 2011.
[202]. B. Bendib, F. Krim, H. Belmili, M. F. Almi, and S. Boulouma, ―Advanced Fuzzy MPPT Controller for a Stand-alone PV System," Energy Procedia, vol. 50, pp. 383–392, 2014.
[203]. H. Fathabadi, ―Novel fast dynamic MPPT (maximum power point tracking) technique with the capability of very high accurate power tracking." Energy, 94, 466-475. 2016.
[204]. Á. A. Bayod-Rújula, & J. A. Cebollero-Abián, ―A novel MPPT method for PV systems with irradiance measurement," Solar Energy, 109, 95-104. 2014.
[205]. E. Akarslan, F. O. Hocaoğlu, & R. Edizkan, ―A novel M-D (multi-dimensional) linear prediction filter approach for hourly solar radiation forecasting," Energy, vol. 73, pp. 978–986, 2014.

A Novel Method for Reactive Power Control Relays

Hasan Dirik[45], Cenk Gezegin[46]

Abstract

Reactive power is a kind of power that is desired not to be drawn from a grid by loads. Minimizing the reactive power drawn from the point of common coupling by the customers that have the rated values above some certain values is mandatory due to some legal obligations. In practice, the compensation of reactive power has been conventionally achieved by switching the contactors in order to activate or deactivate the capacitors. There, the control signals of contactors are produced by a reactive power control relay. In this paper, a novel method for the determination of capacitors that must be activated or deactivated in order to provide reactive power compensation by reactive power control relays is presented. The method, unlike existing classical methods that use the values of powers, performs grid side reactive power compensation by controlling the values of inductive/capacitive reactances. For this purpose, firstly, total reactance values of load + capacitor banks are computed by using voltages and currents of grid side and then, necessary switching actions are fulfilled. Developed method provides fairly good reactive power compensation both in the case voltages deviate from their rated value and even in the presence of harmonics. The validity of the suggested method is demonstrated by simulations that have been done in Matlab/Simulink environment.

Keywords: *Reactive Power Control Relay, Reactive Power Compensation, Conventional Compensation, Reactance*

98. INTRODUCTION

Various loads that have windings in their internal structure for magnetizing have to draw a kind of power called reactive power in order to work. In real, this power cannot be transformed to any form of energy but have to be drawn by the loads that have coils or windings in order to work. Motors, transformers, arc furnaces, and self-ballasted lamps are of the significant loads. In the systems having no reactive power compensation, the inductive or ohmic-inductive loads have to take the required reactive power from grids. Reactive power drawn from grid limits the power transmission capacity of conductors by increasing the amount of current, increases the active power or energy loss of grids and causes significant drops in the voltage amplitude applied to other loads. When transmission level is taken into consideration, reactive power contributes to voltage instability significantly [1]. Because of these reasons, reactive power factor compensation is mandatory for the consumers having power rate above a certain value in our country and in the world [2].

Synchronous condensers, static condensers and capacitor banks are main alternatives for reactive power compensation. Among them the most traditional and commonly used method is shunt capacitor banks that are controlled by reactive power control relays and have been used since 1914 [3]. Reactive power control relays compute the required reactive power by using the sampled values of current and voltage. Then they find the capacitor banks corresponding to this reactive power and activate or deactivate these capacitors via contactors. Therefore, they try to approximate the reactive power drawn from grid to zero and make power factor one.

The most significant problems of reactive power control relays that are used for the compensation of the reactive power are harmonics in current and voltage, unstable amplitude of voltage, and unbalanced load currents. Reactive power produced by capacitor banks is directly proportional with the terminal voltage of them. This means that reactive powers of each capacitor banks will deviate when the amplitude of voltages changes [4]. Unbalanced load currents necessitate some capacitor banks that must be used for compensation to be single phase in addition to the other three phase capacitor banks. Load currents and/or voltages containing harmonic components necessitate using a method such as Fast Fourier Transform (FFT) instead of a simple method for the computation of reactive power

[45] *Corresponding author: Vocational School, Department of Electric and Energy, Sinop University, Sinop, Turkey, hasan_dirik@hotmail.com*
[46] *Technical Sciences Vocational School, Department of Electric and Energy, Amasya University, Amasya, Turkey, cenkgezegin@gmail.com*

corresponding to the fundamental components. In classic reactive power control relays, Discrete Fourier Transform (DFT) and FFT algorithms are used for harmonic analysis. As an alternative to these algorithms, there are also some studies suggesting Goertzel algorithm which can reach to the result with less computation [5, 6].

In this study a novel method that is developed to be used in reactive power control relays is suggested. The method finds the value of capacitor banks that must be switch on/off for reactive power compensation by using directly total reactance of load+capacitor banks without computing the powers that as classical methods do. Reactance value of capacitor banks computed by the method coincides to fundamental value of voltages and currents. From this aspect, the method is not affected by harmonics. In the calculation of the value of capacitors corresponding to fundamental component, differential equation algorithm (DEA) has been used.

99. REACTANCE COMPUTATION BASED ON DEA

In this section, a parallel version of differential equation algorithm which is used R and L parameters of a load via voltage and current samples is described.

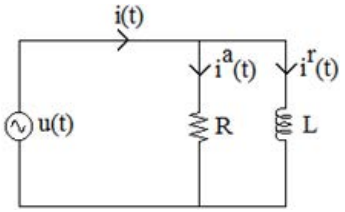

Figure 1. Equivalent circuit of single-phase source-Load

Using the equivalent circuit of single-phase source-load system given in Figure 1, source current can be written in terms of parallel branch currents as in the (1).

$$i(t) = i^a(t) + i^r(t) \tag{1}$$

This equation turns into (2) if we replace the current on the left side with its equivalent.

$$i(t) = \frac{u(t)}{R} + \frac{1}{L} \cdot \int u(t) \tag{2}$$

Taking derivatives of the last equation in the consecutive two intervals we get the following two equations.

$$i(t_2) - i(t_1) = \frac{1}{R}[u(t_2) - u(t_1)] + \frac{T_s}{2L}[u(t_2) + u(t_1)] \tag{3}$$

$$i(t_3) - i(t_2) = \frac{1}{R}[u(t_3) - u(t_2)] + \frac{T_s}{2L}[u(t_3) + u(t_2)] \tag{4}$$

In these equations, instead of R and L, if we write

$$G = \frac{1}{R} \tag{5}$$

$$H = \frac{1}{L} \tag{6}$$

and compute G and H, Eqs. (7) and (8) are obtained.

$$G=\frac{(u(t_3)+u(t_2))\cdot(i(t_2)-i(t_1))-(u(t_2)+u(t_1))\cdot(i(t_3)-i(t_2))}{(u(t_3)+u(t_2))\cdot(u(t_2)-u(t_1))-(u(t_2)+u(t_1))\cdot(u(t_3)-u(t_2))} \quad (7)$$

$$H=\frac{2}{T_s}\frac{(u(t_2)-u(t_1))\cdot(i(t_3)-i(t_2))-(u(t_3)-u(t_2))\cdot(i(t_2)-i(t_1))}{(u(t_3)+u(t_2))\cdot(u(t_2)-u(t_1))-(u(t_2)+u(t_1))\cdot(u(t_3)-u(t_2))} \quad (8)$$

This method that provides to compute the equivalent circuit parameters of a load using three voltage and current samples in (7) and (9) can be entitled as short windowed DEA for parallel equivalent of load [7-10]. If load current contains harmonics, computed values of G and H will not be constant and thus, results will be incorrect. So, in order to find real values of G and H, these values are passed through a moving average filter that has a window width of one cycle. That is, in order to find G and H values, consecutive N-number of G and H that correspond to one cycle are used in

$$G_{ort}=\frac{1}{N}\sum_{k=1}^{N}G(k) \quad (9)$$

$$H_{ort}=\frac{1}{N}\sum_{k=1}^{N}H(k) \quad (10)$$

and thus, harmonic free G and H values are obtained.

100. REACTIVE POWER CONTROL RELAY ALGORITHM

Single-phase equivalent of the source-load and reactive power compensation system is given in Figure 2.

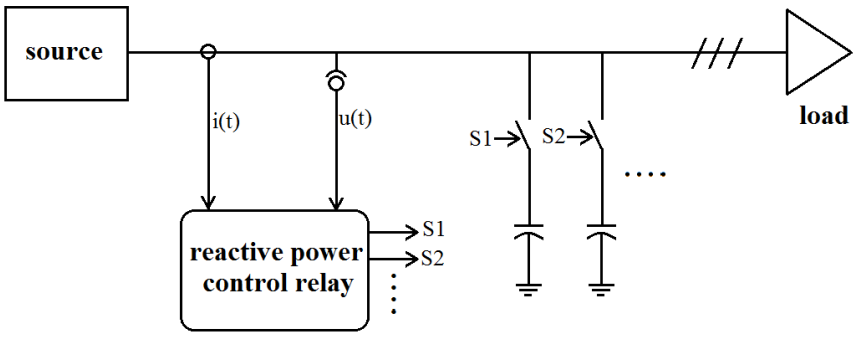

Figure 2. Single-phase equivalent of the source-load and reactive power compensation system

Reactive power control relays, in order to meet the reactive power required by the loads, enable or disable proper capacitor banks. In this way, they try to set power factor to one or close to 1 by compensating the reactive power requirements of loads. Reactive power compensation is the process of converting ohmic-inductive character of loads to ohmic at side of grid in terms of impedance. That means that a load with uncompensated impedance Z as in (11) is converted to new impedance as given in (12) after reactive power compensation.

$$Z=R+jX_L \quad (11)$$

$$Z = R \tag{12}$$

To do this, a capacitor must be connected to the load given in Figure 1. For unity power factor, the reactance value of capacitor must be equal to inductive reactance.

$$X_L = X_C \tag{13}$$

From the last equation, value of capacitor that ensure unity power factor is obtained as

$$C = \frac{1}{2 \cdot \pi \cdot f \cdot X_C} \tag{14}$$

In real compensation systems, this process is executed via reactive power by a reactive power control relay. In this paper, it is suggested the usage of impedance for the determination of capacitor values instead of reactive powers. Here, reactive power control relay switch on and/or off capacitor banks so that total impedance of load+capacitors is brought closer to zero.

Steps of the method are as follows:

1. Consecutive H values along with one-cycle are computed by using current and voltage samples of each phase measured at the grid side in Eq. (8). (H_a, H_b, H_c)

2. H values of each phase free from harmonics are obtained by using Eq. (10). ($H_{ort\text{-}a}$, $H_{ort\text{-}b}$, $H_{ort\text{-}c}$)

3. Inductive reactance values of each phase seen by the relay are computed by the following equation. ($X_{relay\text{-}a}$, $X_{relay\text{-}b}$, $X_{relay\text{-}c}$)

$$X_{relay} = \frac{2 \cdot \pi \cdot f}{H_{ort}} \tag{15}$$

4. The smallest reactance is determined.

$$X_{L3} = \min\left(X_{relay-a}, X_{relay-b}, X_{relay-c}\right) \tag{16}$$

This value is the part of impedance that must be compensated by the 3-phase capacitor banks by relay.

5. Value of X_{L3} indicates the degree of compensation. If this value is negative, this means there is an excessive compensation. If this value is positive, this means deficient compensation and if this value equal to zero, this means that there is a full compensation.

a) In the case of excessive compensation, either no any capacitor is disabled or the smallest active capacitor is switched off according to the degree of excess.

b) If deficient compensation is determined, either no any capacitor is enabled or the smallest non-active capacitor is switched on according to the degree of excess.

c) If full compensation is determined, this means any action of switch on or off is not required.

6. Uncompensated parts of reactance for each phase are determined by using the following equation. ($X_{L1\text{-}a}$, $X_{L1\text{-}b}$, $X_{L1\text{-}c}$)

$$X_{L1} = X_{relay} - X_{C3} \quad (17)$$

7. The capacitors that has the nearest value to the uncompensated reactance are determined and then, they are switched on or off by following the way given in 5 for each phase separately. ($X_{C1\text{-}a}$, $X_{C1\text{-}b}$, $X_{C1\text{-}c}$)

8. The process is stopped for at least one cycle and then passed to 1.

101. SIMULATIONS

In this section, a simulation of the suggested method that explained above has been given. The simulation of the method has been done in Matlab/Simulink environment. Grid voltages that used in the simulation have been selected to be in the form of pure sinusoid and 3-phase load currents have been selected in three different forms for three simulation intervals. As in the first time interval, load currents are pure sinusoidal and balanced, in the second time interval, load currents has been selected to be sinusoidal and unbalanced. In the last time interval of simulation, load currents contain harmonics and are unbalanced. Equations of 3-phase voltages used in the simulation are given in Eqs. (18) - (20).

$$u_a(t) = 311\sin(314t) \quad (18)$$

$$u_b(t) = 311\sin(100\pi t - \frac{2\pi}{3}) \quad (19)$$

$$u_c(t) = 311\sin(100\pi t + \frac{2\pi}{3}) \quad (20)$$

Equations of load currents in the first, second and third time intervals of simulation are also given in Eqs. (21) – (29) respectively.

$$i_{a1}(t) = 25\sin(100\pi t - \pi/3) \quad (21)$$

$$i_{b1}(t) = 25\sin(100\pi t - \frac{2\pi}{3} - \pi/3) \quad (22)$$

$$i_{c1}(t) = 25\sin(100\pi t + \frac{2\pi}{3} - \pi/3) \quad (23)$$

$$i_{a2}(t) = 25\sin(100\pi t - \pi/3) \quad (24)$$

$$i_{b2}(t) = 15\sin(100\pi t - \frac{2\pi}{3} - \pi/3) \quad (25)$$

$$i_{c2}(t) = 20\sin(100\pi t + \frac{2\pi}{3} - \pi/3) \quad (26)$$

$$i_{a3}(t) = 25\sin(100\pi t - \pi/3) + 10\sin(300\pi t - \pi/3) + 5\sin(500\pi t - \pi/3) \quad (27)$$

$$i_{b3}(t)=15\sin(100\pi t-\frac{2\pi}{3}-\pi/3)+10\sin(300\pi t-\frac{2\pi}{3}-\pi/3)+5\sin(500\pi t-\frac{2\pi}{3}-\pi/3) \quad (28)$$

$$i_{c3}(t)=20\sin(100\pi t+\frac{2\pi}{3}-\pi/3)+10\sin(100\pi t+\frac{2\pi}{3}-\pi/3)+5\sin(100\pi t+\frac{2\pi}{3}-\pi/3) \quad (29)$$

In the compensation system, three 3-phase capacitors at the rates of 33µF, 66 µF and 132 µF has been used. Also, for each phases, two single-phase capacitors at the rates of 33µF and 66 µF has been used. Grid voltages and load currents that have been used in the simulation lasting 0.6 second are given in Figures 3 and 4.

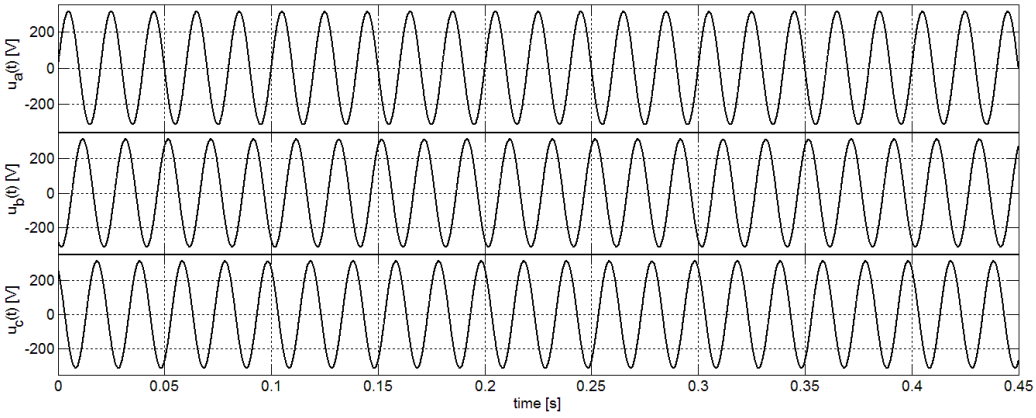

Figure 3. Grid voltages that were used in the simulation

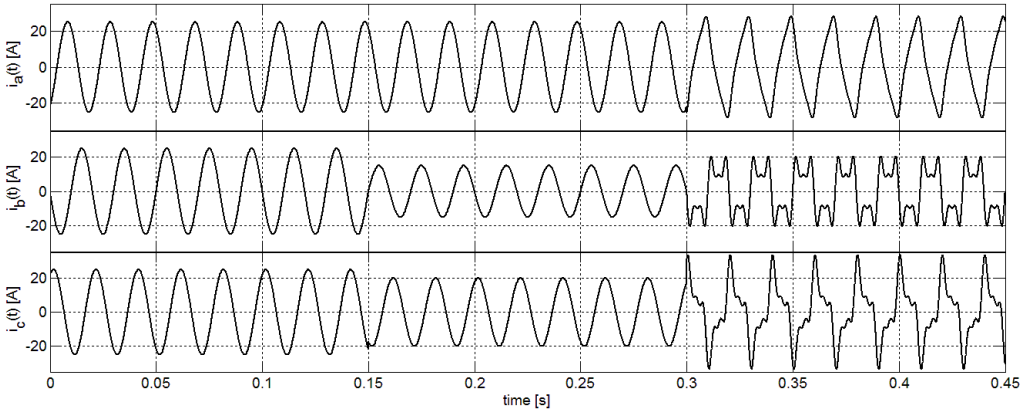

Figure 4. Load currents that were used in the simulation

Active, reactive powers and power factors of each phases of load during the simulation are given in Figure 5.

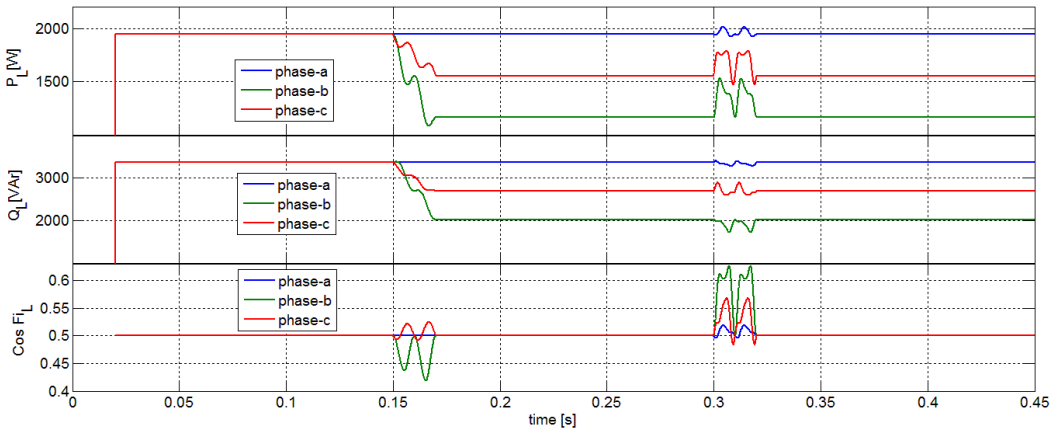

Figure 5. Active, reactive powers and power factors of each phases of load

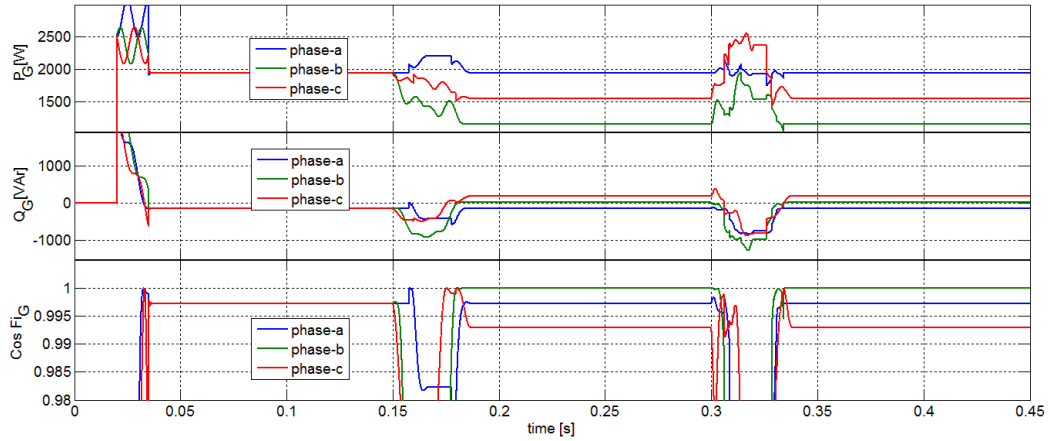

Figure 6. Simulation results for active, reactive powers and power factors of the suggested method at the grid side

Simulation results for active and reactive powers and power factors at the grid side are given in Figure 6. As can be seen from this figure, suggested reactive power control relay algorithm can provide to be performed accurately the compensation even in the case of unbalanced currents with harmonics. While power factors of each phases are 0.5 at the load side, these values have been increased above 0.99. Also, the values of reactive power for each phase have been reduced from about 2000-3500 VAr to about 250 VAr. Due to the feature of the method that allows to compute reactance of each phase independent of harmonics, power factors could be kept to very close to one.

102. CONCLUSIONS

In this paper, a novel reactive power control relay working method for reactive power compensation is suggested. The method uses inductive/capacitive reactance values differing from classical relay methods. For the determination of reactance values, a new form of DEA that is developed for parallel equivalent load is utilized. Unbalanced loads and currents containing harmonics do not affect the performance of the suggested method. As can be seen from the simulation, while the power factor of the load is about 0.5, this value could be kept above 0.99 by using the suggested method even in the case of currents that are unbalanced and harmonic containing. Simulation results have also show that the suggested method reaches results with less computation as compared to FFT methods which is used in classic relays.

REFERENCES

[1]. A. Mohanty, M. Viswavandya, S. Mohanty, P. K. Ray, S. Patra, –Modeling, simulation and optimization of robust PV based micro grid for mitigation of reactive power and voltage instability", *International Journal of Electrical Power and Energy Systems*, Vol. 81, pp. 444-458, October 2016.

[2]. Elektrik Şebeke Yönetmeliği, 28.05.2014 tarih ve 29013 sayılı resmi gazete, 2014, EPDK

[3]. J. Dixon, L. Moran, J. Rodriguez and R. Domke, "Reactive Power Compensation Technologies: State-of-the-Art Review," in *Proceedings of the IEEE*, vol. 93, no. 12, pp. 2144-2164, Dec. 2005

[4]. Şekkeli, M. ve Adak, S., –Yeni Bir Yaklaşımla Reaktif Güç Kontrol Rölesi Dizaynı ve Uygulaması", *KSÜ. Fen ve Mühendislik Dergisi*, 9 (1), 2006.

[5]. I. K. Kiran and J. Laxmi. A, –Shunt versus Series Compensation in the Improvement of Power System Performance", *International Journal of Applied Engineering Research*, vol. 2 (1), 2011, pp. 28–37.

[6]. A. Özdemir, –**A reactive power control relay design with a new approach**", *ELECTRICAL ENGINEERING*, Vol. 88, pp. 133-140, JAN 2006

[7]. Akke, Magnus, and James T. Thorp. "Some improvements in the three-phase differential equation algorithm for fast transmission line protection." *IEEE Transactions on Power Delivery,* 13.1 (1998): 66-72.

[8]. Shehab-Eldin E. H., McLaren P. G., 1998. Travelling wave distance protection-problem areas and solutions, *IEEE Transactions on Power Delivery*, vol.3, no.3, 894-902.

[9]. Pathirana V., McLaren P. G., Dirks E., 2002. Investigation of a hybrid travelling wave/impedance relay principle, CCECE 2002, *IEEE Canadian Conference on Electrical and Computer Engineering*, Winnipeg, Canada, 12-15 May 2002, vol.1, 48-53.

[10]. Phadke A. G., Thorp J. S., 1994. Computer Relaying for Power Systems, 2nd Edition, Research Studies Pres Ltd., Taunton, Somerset, England.

The Modeling of Groundwater Quality Parameters Used in Agricultural Irrigation Depending on Many Years

M. Cüneyt BAĞDATLI[47]

Abstract

The quality of agricultural irrigation water in agricultural production is one of the most important factors. In this context, the opening of the observation wells for monitoring groundwater quality is extremely important. In this study, Turkey's Nevşehir province in intensive farming a groundwater levels in the area to monitor the quality parameters of the State Hydraulic Works (DSI) was carried out in accordance with the data obtained from observation wells by drop. Water quality parameters measured in a total of 10 observation wells made in the years 1997 to 2013 were examined in this context, depending on the time. As quality parameters, pH, EC, Na, K, Ca, Mg, HCO_3, Cl, SO_4, NO_2, Sodium Absorbsion Rate (SAR), B, Na%, statistically using a water class and hardness of time depending on the linear regression approach as it modeled. As a result of this study; Irrigation water quality parameters have been identified strong relationships depending on the time (pH; R^2=0.87, EC; R^2=0.80, Mg; R^2=0.87, Na; R^2=0.88, K; R^2=0.92, HCO_3; R^2=0.81, B; R^2=0.82, Ca; R^2=0.68, Cl; R^2=0.66, SO_4; R^2=0.92, Na%; R^2=0.25, SAR; R^2=0.86, and water hardness; R^2=0.92). Irrigation water as the class average was found C_3-S_1. Each chemical parameters of the linear regression model with linear equations are created. Heavy fertilizing and agricultural sprayings with rainfall and irrigation washed into the ground water conducted in agricultural areas affect the water quality negatively. Instead of chemical fertilizers and pesticides in this context organic origin on the quality of the application making the ground water will be caused to positive effects

Keywords: *Groundwater Quality, Agricultural Irrigation, Turkey*

103. INTRODUCTION

Water resources are dwindling along with global warming in the world. The population growth rate is parallel to the need for intensive agricultural production in order to meet the food needs. Water the plants as living things is the source of life is inevitable in the development of an entry. Making effective irrigation in order to receive adequately the efficiency of agricultural production is extremely pivotal in this regard. However, when used for irrigation must be especially suitable for agricultural production in the properties of the quality of underground water resources. In this sense, it reduces the efficiency of agricultural water quality is poor and may even make agriculture made.

Corresponding author: The University of Nevşehir Hacı Bektaş Veli, Department of Biosystem Engineering, 50300, Nevşehir/Turkey, e-mail:cuneytbagdatli@gmail.com

Turkey have 98 billion m^3 surface and 12 billion m^3 groundwater which consists of 110 billion m^3, nearly three-quarters of the total water resources used for irrigation. Above ground used for irrigation and constantly keep under control the exchange of knowledge and quality of groundwater resources is important for the sustainability of land and water resources [11].

It must be examined in terms of quality parameters before being used in the production of agricultural water resources. In this study, a valve taken from groundwater observation wells irasat between the years 1997-2013, some agricultural irrigation water to 10 water quality parameters in the example were investigated. The resulting water quality in exchange for some of the parameters in size between that of linear regression analysis with the province and the year has been determined.

2. MATERIALS AND METHODS

This study was conducted to model the change to the years between the years 1997-2013 some groundwater parameters from a groundwater observation observation station in of Nevsehir Province, Derinkuyu District of Turkey. The workspace and location detail can be seen on the map presented in Figure 1.

Figure 1. The Location of Research Area (Derinkuyu District in Nevşehir Province of Turkey)

The study area is an area of intense agricultural production made with 308 208 ha. Irrigation water is particularly welcomed the groundwater in this area. Derinkuyu district summers are hot and dry, winters are cold and rainy carries the terrestrial climate.

Long annual average total rainfall of 421 mm in the area of research. The minimum temperature in the summer is of 7.7 ^{0}C while the maximum temperature was recorded as 33.5 ^{0}C in long years [1]. The area of 445 km^2 area of research is the height above sea level is 1.300 meters.

This study was conducted in groundwater measurements given in Table 1. Irrigation water in the irrigation water samples taken from groundwater wells in relationship to the value specified ICP / AES devices have been detected. Irrigation water quality parameters were used for evaluation of the approach outlined by the researchers [2, 3, 8]. In terms of water quality classification of irrigation water EC value is determined by considering the class of water [9]. In Addition to, The datas on the groundwater quality parameters in this study were obtained from the State Hydraulic Works (DSI) in TurkeySodium Adsorption Ratio (SAR): It contained in the irrigation water for the calculation Na (meq/l), Ca (meq/l) and Mg (meq /l) should be known concentrations ofions. Thus Na cation ratio of Ca and Mg cations of the SAR value is calculated by the formula given in equation1 [9].

$$SAR = \frac{Na^{+}}{\sqrt{(Ca^{++} + Mg^{++})/2}} \quad \text{.....(1)}$$

Irrigation water quality characteristics of the course of change in some years were analyzed by linear regression model [10].

104. RESULTS AND DISCUSSION

In this study, groundwater observation well in a total of 10 measurements made between the years 1997 to 2013 set quality parameters and the values obtained are presented in detail in Table 1.

Table 1. Some Quality Parameters of the Groundwater Used in Agricultural Irrigation

Measurement Dates	pH	EC x 10^6	Cations (meq/l)				Anions (meq/l)				Total	% Na	Sodium Absorbsion Ratio SAR	Hardness(fs)	B (ppm)	Water Class
			Na	K	Ca	Mg	CO_3	HCO_3	Cl	SO_4						
29.05.1997	6,85	851	1,78	0,20	3,18	2,15	0,00	6,73	0,85	0,26	7,95	24,35	1,09	24,80	1,1	C2-S1
17.09.1997	6,60	840	1,85	0,24	3,88	2,35	0,00	6,20	0,90	0,30	7,30	22,24	1,05	24,90	1,1	C3-S1
14.09.1998	6,54	759	1,89	0,28	3,53	2,20	0,00	6,23	0,95	0,33	7,34	23,92	1,12	25,30	1,1	C3-S1
27.09.2002	6,39	750	2,01	0,29	3,60	2,00	0,00	6,40	0,98	0,51	7,79	25,44	1,20	26,20	1,1	C2-S1
24.06.2003	6,20	760	2,17	0,30	4,81	1,98	0,00	6,50	0,98	0,60	9,46	23,43	1,18	32,60	1,2	C3-S1
16.09.2010	6,15	730	2,18	0,34	4,48	1,90	0,00	7,00	0,99	0,62	8,86	24,49	1,22	33,40	1,4	C3-S1
16.09.2011	6,12	709	2,20	0,38	4,50	1,89	0,00	7,10	1,00	0,68	7,52	24,53	1,23	35,96	1,3	C2-S1
13.06.2012	6,05	710	2,21	0,39	4,62	1,80	0,00	7,20	1,10	0,70	7,48	24,50	1,23	37,10	1,5	C2-S1
06.09.2012	6,02	705	2,23	0,40	4,70	1,79	0,00	7,30	1,20	0,74	7,76	24,45	1,24	38,20	1,3	C2-S1
04.09.2013	6,00	700	2,30	0,40	4,86	1,70	0,00	7,45	1,30	0,78	8,91	24,84	1,27	38,28	1,4	C3-S1

As a result of the quality measurements made in the groundwater it is varied between 6.00-6.85 pH. This water samples are seen that acidic character. When looking at the EC value 700-850 µs cm^{-1} have varied. In terms of salinity of the water it is generally seen to fall within the third class water quality. Sodium (Na) values are measured in terms of 1.78-2.30 meq / l varies between. Potassium (K) and the value of 0.20-0.40 meq / l is changed.

Calcium(Ca) in the irrigation water and the value of 3.18-4.86 meq/l, ranged. Magnesium (Mg) value of 1.70-2.35 meq/l have varied. Carbonate (CO_3) was observed in water to measure the value never made in this date. Bicarbonate (HCO_3) When the value of 6.20 -7.45 meq / l is determined that the change. Chlorine (Cl) values of 0.85-1.30 meq /l ranged. Looking at this in terms of value first Class chlorine enters the water quality class.

Sulfate (SO_4) value is of 0.26-0.78 meq/l varies between. When the Na value varies between the 22.24-24.84%. In this context, in terms of % Na in the water supply it is emerging as a result of entering the first grade water quality class.

Sodium absorption ratio (SAR) varies between 1.05-1.27 water hardness in the history of the measurement of irrigation water to look at the situation when it is determined that varied between 24.80-38.28 fs.

Boron in groundwater (B) is the amount of views between 1.1-1.4 ppm that showed increasing this change. Boron value in terms of agricultural production in areas held until the groundwater from the cultivation of plants with medium and durable is recommended. When the class was determined that irrigation water is often made into quality class C_3S_1 class in the groundwater.

Measurements to determine whether they show any variability between the measurements made history of underground irrigation water quality parameters for regression analysis was performed. The mathematical model between each parameter measurement date as a result of It was obtained. pH, EC, Na and measurement dates between regression equation graphs for K values in Figure 2 are presented separately.

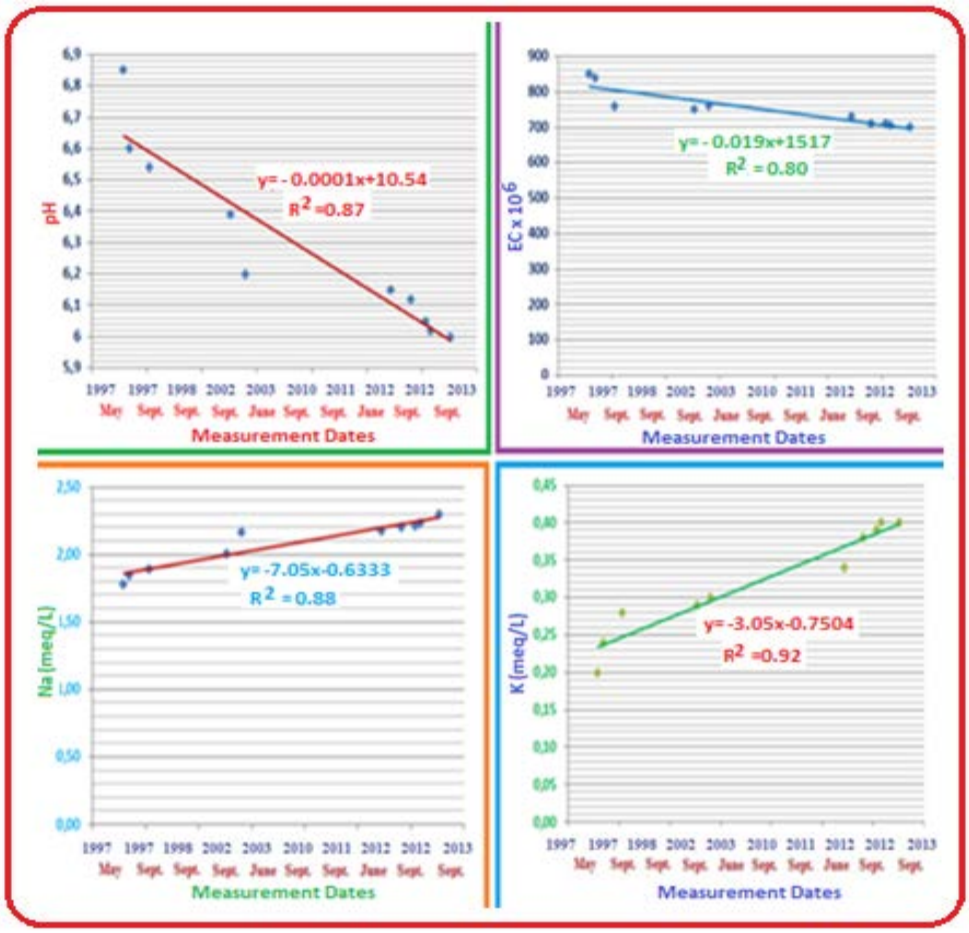

Figure 2. Regression Modelling for pH,EC, Na and K depending on measurement dates

Figure 2 shows the pH of the measurement date as shown (1997-2013) (y= -0.0001x + 10.54) relationship was found. A strong correlation between the pH value measurement, such as R^2=0.87 tarhih were obtained. In short, the measurement dates were obtained in a linear decrease in the pH value increases. When the EC value (y = -0.019x+1517) were obtained in the form of a mathematical model. The R^2= 0.80 was found to be a strong relationship between the EC value measurement dates. Sodium value (y = -7.05x - 0.6333) was obtained in the form of an equation. R^2 =0.88 is seen to be a linear and strong relationship.

The potassium value (y= -3.05x - 0.7504) was obtained linear equations. where in R^2 =0.92 is observed that there is a strong relationship. Calcium, magnesium, bicarbonate and chlorine values between measurement dates regression equation graphs in Figure 3 are presented separately.

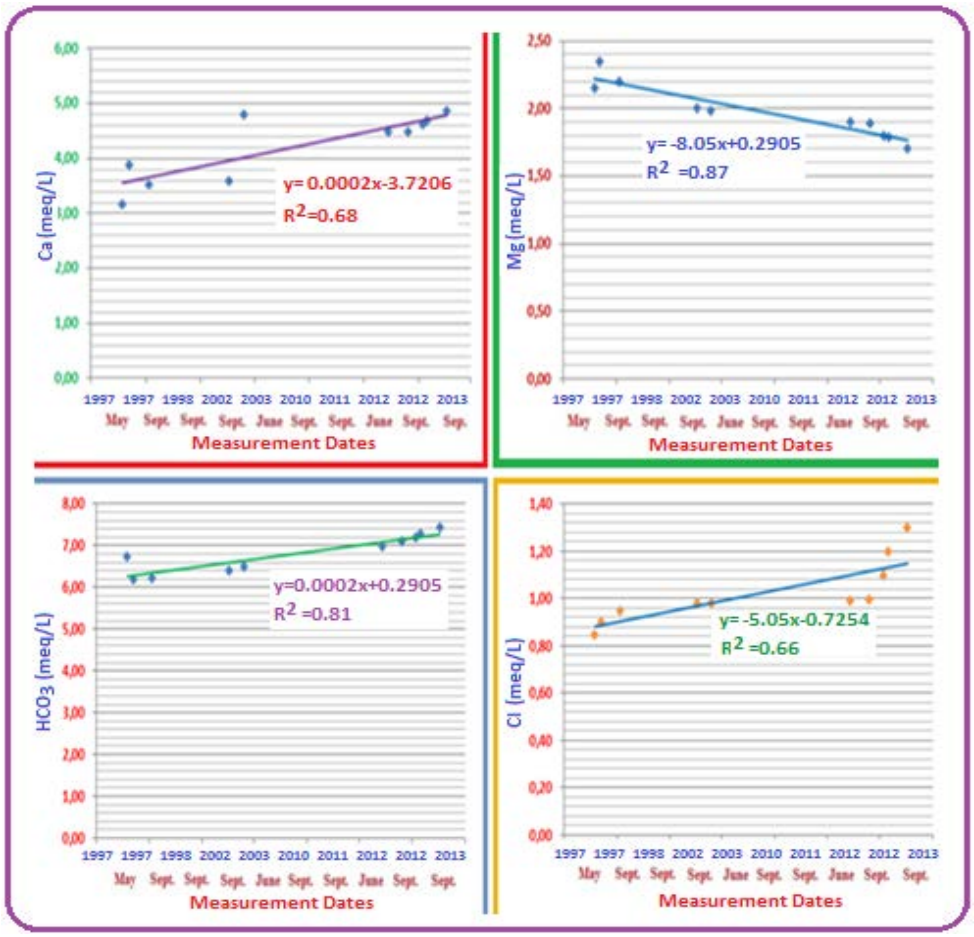

Figure 3. Regression Modelling for Ca, Mg, HCO_3 and Cl depending on measurement dates

As shown in Figure 3 with a value of between calcium measurement date (y=0.0002x - 3.7206) relationship was found. R^2=0.68 Calcium was as a strong correlation between the measurement values were obtained. In short, the measurement date is obtained in a linear increase in calcium increases. When the magnesium value (y= -8.05x+29.05) was obtained in the form of a mathematical model. R^2 =0.87 the Magnesium value is the measurement date are shown to have a strong relationship.

Bicarbonate value (y =0.0002x + 0.2905) was obtained in the form of an equation. R^2 =0.81 is seen to be a linear and strong relationship. The value chlorine of (y = -5.05x - 0.7254) was obtained linear equations. wherein R^2=0.66 is observed that there is a strong relationship.

Sulfate, % sodium, sodium absorption ratio and regression equation between the measurement date for graphics boron values in Figure 4 are presented separately.

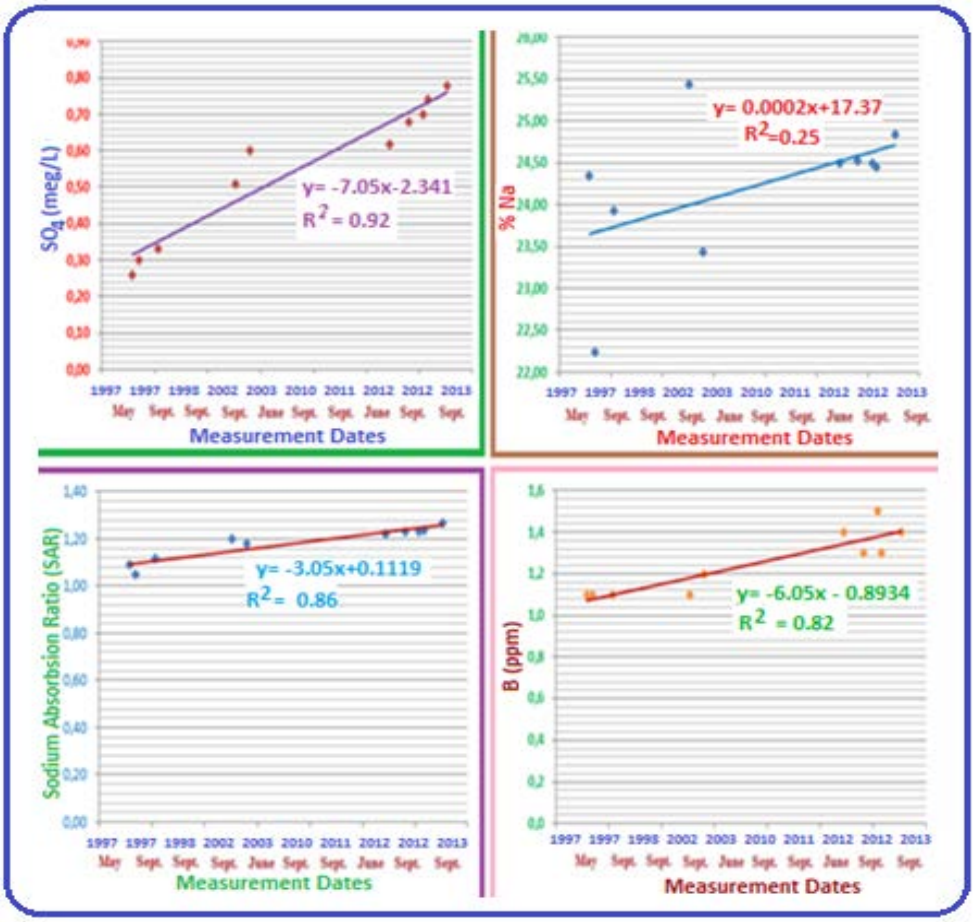

Figure 4. Regression Modelling for SO_4, % Na, Sodium Absorbsion Rate and B depending on measurement dates

As shown in Figure 4 between measurement, The sulfate value (y= -7.05 -2.341) relationship was found. R^2 = 0.92, Sulfate as a strong correlation between the measurement values were obtained . In short, the measurement date for increased sulfate is obtained in a linear increase. When the percent Sodium value (y =0.0002x+17.37) was obtained in the form of a mathematical model. R^2 =0.25 is a weak correlation was found between the percentage of sodium value measurement dates.

The measurement dates of the sodium absorption ratio variable from (y= -3.05x+0.1119) was obtained in the form of an equation. R^2= 0.86 is seen to be a linear and strong relationship. The value Boron (y = -6.05x-0.8934) was obtained linear equations. where in R^2= 0.82 is observed that there is a strong relationship.

Regression equations, graphs obtained in order to determine the relationship between measurement dates for irrigation water hardness values are presented in Figure 4.

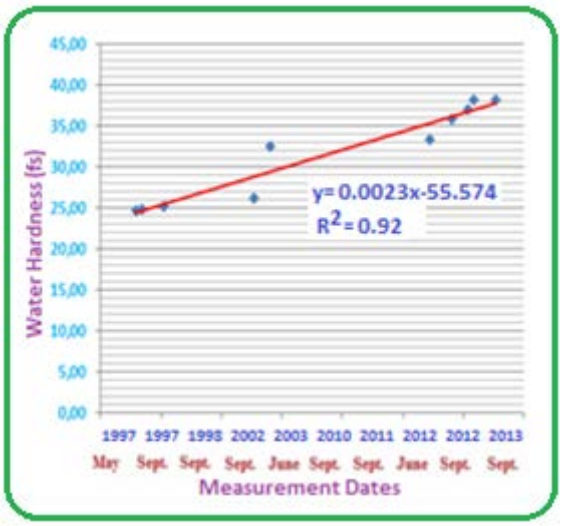

Figure 5. Regression Modelling for Water Hardness

Between hardness with measurement dates (y= 0.0023x - 55 574) was obtained in the form of a linear equation. it is determined that there is a strong relationship in the form of R^2=0.92 .While these values are low hardness in 1997 showed a significant upward trend in 2013. The evaluation of groundwater resources in terms of water quality and in particular to investigate whether it is appropriate to agricultural production is extremely important. Chemical fertilizers and washing with precipitation reaching the ground water with the use of pesticide chemicals adversely affect the quality of water. In this sense, Turkey has carried out for the determination of groundwater quality in many similar studies. Some of these include;

Based on the results obtained from the study; investigated samples were generally including usable irrigation water class in terms of pH values. According to the results, appears that the samples usually contains meduam and high salinity concentration. After comparison of the maximum allowable irrigation water according to the evaluation of heavy metals and toxic elements, irrigation water limit values do not exceed for Fe and B elements, but the other parameters (Cu, Zn, Mo, Ni, Pb, Cr, Co and Cd) were generally exceeds. It is observed that the results of water analysis among terms and sampling pints are different [4].

By researchers; Drinking in a study conducted in Turkey's Manisa Province and use irrigation water fall from the deep wells obtained, winter and early summer, including water samples at three different periods were taken and their toxic effect may be trace elements (Pb, Cd, As, Hg, Cr, Sa, Sb, Fe, Cu, Mn, Ba, Zn and B) changes investigated. The results were not found in all wells in the Sa and Sb elements are found to be below the allowable maximum limit values for concentrations of other elements [5].

Researchers have investigated the NO_3 content of water wells in the region in Turkey's Antalya Kumluca For this purpose, they took water samples from 20 wells in this region. In these water samples EC, NO_3, NH_4 analysis made; [NO_3-N] +[NH_4]% and NO_3-N are calculated. As a result, water is positively correlated with EC between NO_3 and water wells in the area have found that the pollution reached a very important level [6].

Researchers; Turkey's Manisa Province from 23 deep wells in Saruhanlı plains in the analysis conducted on water samples taken in three separate periods; Examples of pH values that vary over a wide range, such as 6.5-8.47; Examples of basic and medium irrigation usually towards the end of the process were found to be strongly basic reaction. The electrical conductivity(EC) of water samples in the same survey values determined between 375-2200 µs cm^{-1} borders; C_3S_1 of their %42.02; while% 57.97's C_2S_1has been reported to be involved in irrigation class [7].

3.CONCLUSIONS

As a result of years of research by the value obtained it was found to be a strong relationship. The only reason for the high value of some of the one factor in this rise can be shown as the increasing use of pesticides and chemical fertilizers. Underground water is not an infinite resource. Especially in chemical applications are made to land in adversely affect groundwater with precipitation. For this chemical in agriculture using reduction and agricultural production, especially with good agricultural practices and making controlled with supervision it is emerging as an unavoidable reality.

REFERENCES

[1]. M. C. Bağdatlı, K. Bellitürk, A. Jabbari, "Possıble effects on soıl and water resources observed in Nevşehir province in long annual temperature and raınfall changing", Eurasian Journal of Forest Science, 3(2): 19-27. 2015

[2]. R.S. Ayers, and D.W. Westcot, "Water Quality for Agriculture"Irrigation and Drainage Paper 29, rev. 1, Food and Agriculture Organization of the United Nations, Rome, 1994.

[3]. R. S. Ayers "Quality of Water for Irrigation" Journal of the Irrigation and Drainage Div., ASCE. Vol 103, No. IR2, p. 140. 1977.

[4]. F. Aydoğan, K. Bellitürk, and M.T. Sağlam, "The Assesment of Irrigation Water Salinity and Heavy Metal Contents of Some Selected Resources in Edirne Region" Journal of Tekirdağ Agricultural Faculty (JOTAF), Tekirdağ, 11 (2): 27-37, 2014.

[5]. Y. Sekin, A. Eryurt, N. Bağdatlıoğlu, Manisa Bölgesi Yeraltı Sularında Mevsimsel Değişiklikler: İz Elementler, 1. Çevre ve Jeoloji Sempozyumu (Yeraltı Suları ve Çevre Sempz.) Bildiriler Kitabı, 255-262,21-23March,İzmir/Turkey,2001.(in turkish)

[6]. M. Kaplan, S. Sönmez, S. Tokmak, Antalya-Kumluca Yöresi Kuyu Sularının Nitrat İçerikleri, Turkish Journal of Agriculture and Forestry, 23, 309-313. 1999. (in turkish)

[7]. Ü. Altınbaş, S. Anaç, D. Anaç, H.Z. Can, "The Effect of Ground Water Salinity on Satsuma Mandarins: Preliminary Results" Second Intern. Symp. on Irrigation Hort. Crops, Chania, Crete, Greece. 1996.

[8]. B.L. Sharp, "Inductively coupled plasma atomic emission spectrometry(ICP-AES)" pp.63-109. Soil Analysis Modern Instrumental Techniques 2nd Ed. Keith A. Smith. Marcel Dekker. 659 pp. 1991.

[9]. L.A. Richards, Diagnosis and Improvement of Saline and Alkali Soils.Agriculture Handbook No: 60, U.S.A., 150p. 1954.

[10]. E. Frank, Jr. Harrell, "Regression Modeling Strategies Book", Springer Series in Statistic, Section Edition, 2015.

[11]. Ş., Aşık, M. Avcı, B. Okur, B. Yağmur, S. Delibacak, B.S. Karataş, "Menemen Ovası Yer altı Suyu Kalitesinin Belirlenmesi Üzerine Bir Araştırma. Ege Üniv. Bilimsel Araştırma Proje Kesin Raporu, Proje No: 2001-ZRF-055,İzmir/Turkey, 2004. (in Turkish).

Analyses of SO_2 Index and SO_2 Extreme Value Index for Karabük Province

Ali CAN[48],

Abstract

The Air Quality Index known as the Pollutant Index is used for preventing action to limit their activities exceeded to the some leve of pollutants. Air is polluted continuously by means of antropogenic sources. As the air is polluted, the atmosphere could be a serious problem for the human healths. One of the most important gaseous pollutants is the SO_2. The SO_2 is a highly soluble in water and body fluids. It is also very bad effect on the respiratory system of the body. Its effect is, however, short and severe.

Karabük Province is a famous province for iron and steel industry. There are 3 air quality measurement stations. In this study, the last 2 years SO_2 values of these 3 station were studied, Sulphur Dioxide Index (Is) and Sulphur Dioxide Extreme Value Index (Es) were calculated then finally the seasonal and annual results were analyzed.

The SO_2 Index is the root-sum-square (RSS) value of hourly SO_2 concentration data. The sulphur dioxide Index is the RSS value of individual terms corresponding to the secondary standards. The RSS value is used to ensure that the index value is greater than 1, if one of the Environmental Protection Agency (EPA) standard values is exceeded. The index is not only considered the annual value, but also the 24 hours and 3 hour SO_2 averages are also used for the calculation of Indexes. In the second methodology, the maximum values of 24 and 3 hour averages were used for the calculations and the pollutant accumulation capacity were considered. The annual, seasonal and daily results are showing some fluctuations. The fluctuations are mainly depends on industrial processes and meteorology. The wind and rain are very affective in winter season.

Keywords: SO_2 Emission, Sulphur Dioxide Index, Sulphur Dioxide Extreme Value Index

105. INTRODUCTION

The air pollution is one of the most important environmental problems of the industrialized provinces. Because of harmful effect of air pollution on human beings, it could create a public pressure on the industries to find a solution for their emissions or to decrease it on a level which is not harmful for human beings, animal and plant life [1]. It is not very difficult to understand how air has been polluted while the emission emitted from the plumes and disappeared with the wind. If the meteorological conditions are not suitable for the emission dispersion, then the limitation of wasted emissions onto atmosphere will decrease its inverse effects [11]. The development of the new technologies is not a complete solution for the entire air pollution problem; however, some level of pollution inverse effect is controlled with the technological improvement [8].

The polluted air is including many air pollutants such as particulate matter, carbon monoxide, nitrogen dioxide, ozone and sulphur dioxide. The concentrations of pollutants are changing considerable due to its emissions sources. The entire inverse affect of these pollutant are evaluated by using Air Quality Index (AQI). AQI has been devised for categorizing the air quality measurements of pollutants by one composite number [1], [9]. The Air Quality Index (AQI) can be estimated through a formula, based on comprehensive assessment of concentration of air pollutants, which can be used to characterize the status of air quality at a given location [6]. There are many AQI used in the world. All are different in concept and presentation, however, indices strongly based on health impact [2].

For any pollutant, air quality criteria may refer to different types of effects. Effects are described as the air level of a pollutant reaches or exceeds specific concentrations for a particular time period [10]. The Environmental Protection Agency (EPA) criteria for the pollutants are leading the standards. The standards are also consistent with the meteorological fundamentals and experimental methods as well as health impact [3].

One of the most important gaseous pollutants is the SO_2. The SO_2 is a highly soluble in water and body fluids. It is also very bad effect on the respiratory system of the body. Its effect is, however, short and severe [11]. The SO_2 present in atmosphere comes mostly from natural sources. The human contribution is, however, especially related to combustion processes addressed to sulphur content on fuels [5].

Although the six pollutants measurements are required for the AQI studies, this study is just the evaluation of the SO_2 hourly concentrations at 3 stations in Karabük province between 1st day of 2014 to last day of 2015. The SO_2 index (I_s) and SO_2 Extreme Value Index (E_s) values is being calculated and considered for the study.

[48]*Corresponding author: Karabuk University, Engineering Faculty, Mechanical Engineering Department, Balıklar Kayası Mevkii, Karabük, 78100, Turkey. alican@karabuk.edu.tr*

106. METHODOLOGY

Karabük Province is one of the famous provinces for iron and steel industry. There are 3 air quality measurement stations. In this study, the last 2 years SO_2 values of these 3 station were studied and Sulphur Dioxide Index (I_s) and Sulphur Dioxide Extreme Value Index (E_s) were calculated and analyzed. The air quality data, dated from 1st day of 2014 to last day of 2015, of Karabük Province are gathered from the "Air Quality Monitoring Network" web pages of Ministry of Environment and Urbanization [7]. Then, the indexes are calculated owing to the EPA primary and secondary SO_2 standards [4].

The SO_2 Index is the root-sum-square (RSS) value of hourly SO_2 concentration data. The sulphur dioxide Index is the RSS value of individual terms corresponding to the secondary standards. The RSS value is used to ensure that the index value is greater than 1, if one of the Environmental Protection Agency (EPA) standard values is exceeded. The index is not only considered the annual value, but also the 24 hours and 3 hour SO_2 averages are used for the calculations [9].

The SO_2 index (I_s) is defined as (1);

$$I_s = [\left(\frac{C_{sa}}{S_{sa}}\right)^2 + K_1\left(\frac{C_{s24}}{S_{s24}}\right)^2 + K_2\left(\frac{C_{s3}}{S_{s3}}\right)^2]^{0.5} \quad (1)$$

and the SO_2 Extreme Value index (E_s) is defined as (2);

$$E_s = [\left(\frac{A_{s24}}{S_{s24}}\right)^2 + \left(\frac{A_{s3}}{S_{s3}}\right)^2]^{0.5} \quad (2)$$

A_{s24} is the accumulation of those observed 24-h concentrations that exceed the secondary standard and is expressed mathematically as (3);

$$A_{s24} = \sum_i K_i (C_{s24})_i \quad (3)$$

where, K_i is 1 if $(C_{s24})_i \geq S_{s24}$ and is 0 otherwise, A_{s3} is the accumulation of values of those observed 3-h concentration that exceed the secondary standard and is expressed mathematically as (4);

$$A_{s3} = \sum_i K_i (C_{s3})_i \quad (4)$$

K_i is 1 if $(C_{s3})_i \geq S_{s3}$ and is 0 otherwise, and that is,

C_{sa} : arithmetic mean observed concentration of sulfur dioxide,

S_{sa} : annual secondary standard value (i.e., 0.02 ppm or 60 µg/m^3),

C_{s24} : maximum observed 24-h concentration of sulfur dioxide,

S_{s24} : 24-h secondary standard value (i.e., 0.1 ppm or 260 µg/m^3),

C_{s3} : maximum observed 3-h concentration of sulfur dioxide,

S_{s3} : 3-h secondary standard value (i.e., 0.5 ppm or 1300 µg/m^3),

K_1 : 1 if Cs24≥ Ss24 and is 0 otherwise,

K_2 : 1 if Cs3≥Ss3 and is 0 otherwise.

107. RESULT AND DISCUSSION

The hourly SO_2 concentrations are fluctuating considerably throughout the years. During the winter season, the concentration is determined as higher than that of summer. Moreover, the annual SO_2 concentration of station 3 is higher compared to the other stations and the hourly SO_2 concentrations even in summer for the whole year are very high. All three stations are affected by the pollutant sources. The main pollutant sources in Karabük are industries, road transportation and households. The trends are not enough for commenting whether the air of the province is polluted or not. Therefore, the other scientific evaluation is also necessary and the annual pollutant average, hourly concentrations, the maximum 24 hr values and the maximum 3 hr values were also being analyzed for determining the air pollution in Karabük province.

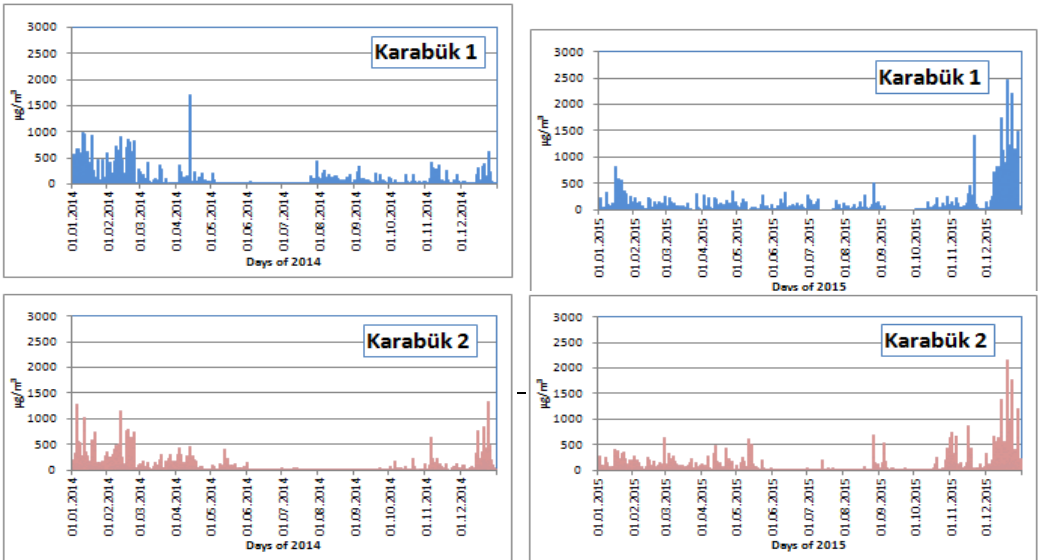

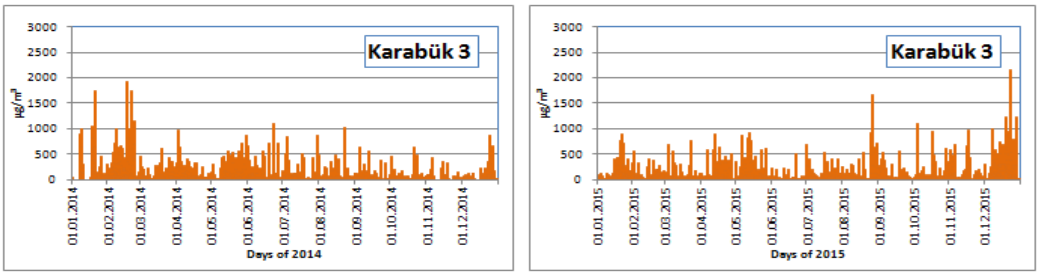

Figure 1.The daily SO_2 concentration trend at three stations in Karabük Province.

The SO_2 indexes (I_s) are calculated for three stations and these values are expected not to exceed value 1. If value 1 is exceed, than the air pollution is problem for the human health. For year 2014, only the station 3 SO_2 indexed values in January and February were exceeding, the others are, however, not. During the entire seasons in 2014, the SO_2 indexed values for station 2 and 3 are not exceeding 1. The results could be seen on Figure 2. The annual arithmetic concentration determines a constant line according to the indexes calculations. The respective index SO_2 values for station 1 and 2 are 0.4 (<1) and 0.45 (<1). However, in station 3, the index value line is higher with a value 0.69 (<1). Moreover, for 73 hrs in 6 different days, the people exposed to higher SO_2 concentrations which is bigger than 1. According to the EPA criteria, if the human beings are exposed to sulfur dioxide, lung function typically returns to normal within an hour even without medication. However, long time exposure causes wheezing, chest tightness and respiratory problem (Figure 2).

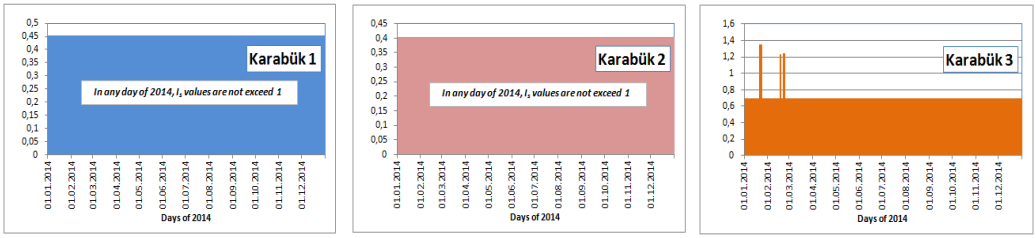

Figure 2.The 2014 SO_2 Index (Is) figures for 3 stations

For year 2015, in all 3 stations, SO_2 indexed values were exceeding 1. The results could be seen on Figure 3. The annual arithmetic concentration determines a constant line according to the indexes calculations. The annual SO_2 index line values for station 1, 2 and 3 are 0.49 (<1), 0.54 (<1) and 0.7 (<1) respectively. For station 1 measurements, the people exposed to higher SO_2 concentration with a period of 144 hrs in 12 different days. In station 2 and station 3, the duration of time that the people exposed to higher SO_2 concentrations is the same with an 64 hrs in 6 different days (Figure 3).

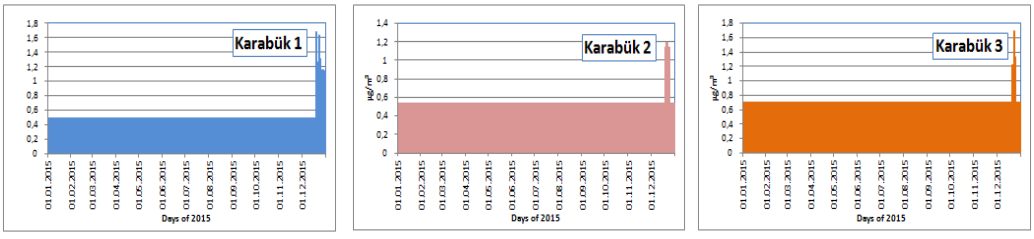

Figure 3.The 2015 SO_2 Index (Is) figures for 3 stations

The SO_2 Extreme Value Index (E_s) values are the accumulation of the ratio for the pollutants. For the pollutants, the secondary ~~–~~maximum values" are not to be exceeded more than once per year. According to the following 2014 figures, the extreme value indexes are exceeded 8 times (more than 1) for the station 3, and more precautions have to be taken in order to decrease SO_2 air pollution until the level which is not hazardous for human beings.

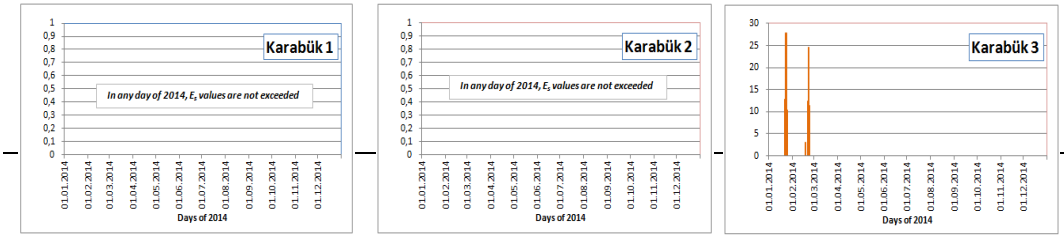

Figure 4.The 2014 SO_2 Extreme Value Index (Es) figures for 3 stations

In year 2015, the Extreme Value Indexes are exceeded more than 1 for all station. For station 1, 2 and 3, the respective extreme value indexes are exceeded 12, 9 and 8 times in different days. Therefore, it can be concluded that the Karabük province is highly SO_2 polluted province according to the EPA standards. Because, the secondary ~~"~~maximum values" are exceeded more than 1 during a year in all stations. Therefore, the precautions in order to decrease the sulphur concentrations have to be taken immediately.

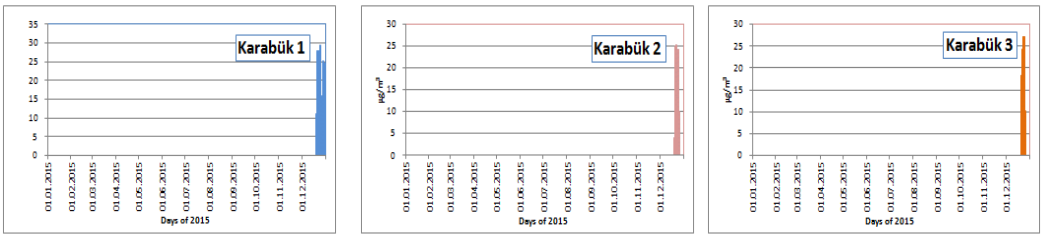

Figure 5.The 2015 SO_2 Extreme Value Index (Es) figures for 3 stations

108. CONCLUSION

Karabük Province is a famous province for iron and steel industry. There are 3 air quality measurement stations. The last 2 years SO_2 values of these 3 stations were studied and Sulphur Dioxide Index (I_s) and Sulphur Dioxide Extreme Value Index (E_s) were calculated and analyzed. The index is not only considered the annual value, but also the 24 hours and 3 hour SO_2 averages are used for the calculations. According to the analyses of both indexes, the province is polluted and SO_2 concentrations were reached and exceeded specific concentrations for 2014 and 2015 period. Although the SO_2 indexes of all three stations in 2015 were exceeding the critical values, that in 2014 were not the case and only one station is exceeding the specific concentrations. However, more precautions have to be taken in order to decrease SO_2 air pollution especially in winter season until the level which is not hazardous for human beings according to the EPA criteria.

REFERENCES

[206]. Boubel R.A., Fox D.L., Turner D.B., Stern A.C., **Fundamentals of Air Pollution** – Academic Press, Third Addition, P.3-33, 1994.
[207]. Elshout S, Léger K., Heich H., **CAQI Common Air Quality Index - Update with PM2.5 and sensitivity analysis**. Science of the Total Environment, 2014. P. 461-468.
[208]. EPA, Environmental Protection Agency - **Air Quality Index**. web address: https://www3.epa.gov/region1/aqi/ date:01.02.2016.
[209]. EPA, Environmental Protection Agency. **National Ambient Air Quality Standards NAAQS**. web address: https://www.epa.gov/criteria-air-pollutants/naaqs-table date: 01.02.2016.
[210]. Famoso F., Lanzafame R., Monforte P., Oliveri C., Scandura P. F., **Air quality data for Catania: analysis and investigation case study** 2012-2013. Energy Procedia 81, 2015. P. 644 – 654.
[211]. Kumar A., Goyal P. **Forecasting of daily air quality index in Delhi**. Science of the Total Environment, 2011. P. 5517-5523.
[212]. MEU. Ministry of Environment and Urbanization. **Air Quality Monitoring Network.** web address: http://www.havaizleme.gov.tr/Default.ltr.aspx date: 11.02.2016.
[213]. Schnelle K.B., Brown C.A., **Air Pollution Control Technology Handbook** – CRC Press – The Mechanical Engineering Handbook Series. 2002. Chapter 1. P.1-24.
[214]. Wang L.K., Pereira N.C., Hung Y., **Advanced Air and Noise Pollution Control** – Volume 2 – Handbook of Environmental Engineering. 2004. P.1-12.
[215]. Vallero D., **Fundamentals of Air Pollution** – Fourth Edition – Civil and Environmental Engineering Department - Duke University – North Caroline. 2007. P.659-677.
[216]. Vesilind P.A., **Environmental Pollution and Control** – Department of Civil Engineering Duke University – North Caroline - Ninth printing, 1980. P.111-182.

Uncertainty Analysis of Direct GHGs Emissions from Turkey's Provinces for 2000-2015

Ali CAN[49],

Abstract

The inaccuracy and imprecision in the calculations are termed as uncertainty estimates of the emission inventories. Uncertainty estimates are an essential element of the complete emission inventories. It can be seen in the range of standard deviation around the mean value of the sample and it is usually associated with different parts of the inventories. These parts are stated by IPCC (Intergovernmental Panel on Climate Change) as: Fuel Consumption Data, Emission Factors and Methodology.

The statistical differences give an indication of the uncertainties of the data. Moreover, the characteristics of the emission data are also estimated with statistical approaches. In an emission inventory, the statistical evaluation of the annual series rather than the differences is also important to understand the representativeness and appropriateness of the emission series. The CO_2, CH_4 and N_20 emission data are separately evaluated. According to the final results, the correlations between years are changing considerably. Another important statistical variable is the SEM, which is the indication of the spread of the mean. The method used in this study determines the significance of year-to-year differences and it takes into account the long-term trends in the inventories. A key issue in the compilation of uncertainties within inventories is the distinction between the –standard deviation" of the data set and the standard error of the sample mean.

The CO_2 uncertainty values are changing between highest value ∓22.07% in 2000 to lowest value ∓20.14% in 2015. The uncertainty value of CH_4 are changing between lowest value ∓30.4% in 2009 to highest value ∓35.65% in 2006 and the uncertainty value of N_2O are changing between lowest value ∓21.7% in 2013 to highest value ∓27.4% in 2011. The most important causes of uncertainties are the using IPCC emission factors which are changing considerably from local ones and the assumptions in fuel consumption data.

Keywords: CH_4, N_2O, CO_2 Emission, IPCC Method, Statistical Approach

109. INTRODUCTION

The emission inventories of countries are important tool for the future environmental planning of decision makers. However, as all environmental pollution modeling and estimations, the emission inventory has also uncertainty and it is mostly estimated according to the fuel consumption data uncertainty and emission factors uncertainty of any gases. Uncertainty value can be directed for future improvement of emissions estimations [6].

There are numerous methods for uncertainty calculations of air pollution [1]. However, for emission inventories, the uncertainty calculations can be listed into two types [7]. Eggleston et al. [4] provide an example of Monte Carlo analysis, applied to a national greenhouse gas inventory and used to estimate uncertainties both in overall emissions and emissions trends. The Monte Carlo approach consists of uncertainties in the basic data. This includes emission factors and activity data, their associated means and probability distribution functions, and any cross correlation between source categories. The other type of uncertainty is linked to the activity data and experimental results as showed by Kline and McClintock [10]. However, the lackness of empirical data of emissions causes some judgment on the uncertainty of activity data.

The inaccuracy and imprecision in the calculations are termed as uncertainty estimates of the inventories [8]. Moreover, uncertainty estimates are an essential element of the complete emission inventories [6]. It can be seen in the range of standard deviation around the mean value of the sample [12] and it is usually associated with different parts of the inventories.

The statistical differences give an indication of the uncertainties of the data. Moreover, the characteristics of the emission data are also estimated with statistical approaches [13]. By the way, the year 1990 is the base year for the Annex I countries [15].

The main purpose of this study was to investigate the uncertainty of Turkish direct greenhouse gases emission by using IPCC methodology and the sectoral fuel consumption data. The necessary data were obtained from the Can [2], emission inventories prepared by Turkish Statistical Institute and energy balance tables of Ministry of Energy and Natural Resources. The CO_2, CH_4 and N_20 emissions were calculated by using the IPCC-Tier 1 method [5], [7].

110. METHODOLOGY

The method (IPCC - Tier 1) was used to estimate the CO_2, CH_4 and N_20 emissions [5]. The IPCC Methods are designed to estimate and report on national inventories of anthropogenic greenhouse gas emissions and removals. The methods are the

[1]*Corresponding author: Karabuk University, Engineering Faculty, Mechanical Engineering Department, Balıklar Kayası Mevkii, Karabük, 78100, Turkey. alican@karabuk.edu.tr*

primary technical guidelines for the national inventories. The estimation process can be divided into some steps that lead to figures for CO_2 and non-CO_2 emissions from fuel consumption as described in [2], [3].

After calculating the CO_2, CH_4 and N_20 emissions due to the energy consumption from industrial sources, energy production, households and road transportation, the statistical methods were used to estimate the uncertainties and the accuracy of the inventories. The process is based on certain characteristics of the variables of data sets between the years and base year 1990. The total uncertainties are studied. This type of analysis yields internal errors. It means that the uncertainties are only determined from the emission data.

In these analyses, the important variables for the sample data are the mean, the standard deviation and the standard error of the mean [14]. When a particular measurement is repeated several times and random differences occur for each measurement, the probabilistic methods can be applied to analyze the uncertainties. Moreover, it is common to assume that the distribution of the emissions follow a normal distribution [8]. In this study, the probability density function of the annual emission is assumed as normally distributed and the range of uncertainty is expressed within 95% confidence intervals according to the IPCC Good Practice Guidance [6].

The probability density functions of the differences of the mean values for the emissions in years t_x and t_y is also normal with the following equations. Here, ty is the base year.

$$mean = \bar{x} - \bar{y} \quad (1)$$

where

$$\bar{x} = \frac{1}{N}\sum_{i=1}^{N} x_i \; ; \bar{y} = \frac{1}{N}\sum_{i=1}^{N} y_i \quad (2)$$

and

$$Standard\ deviation = (S_x^2 + S_y^2)^{1/2} \quad (3)$$

where

$$S_x^2 = \frac{1}{N-1}\sum_{i=1}^{N}(x_i - \bar{x})^2 \; ; \; S_y^2 = \frac{1}{N-1}\sum_{i=1}^{N}(y_i - \bar{y})^2 \quad (4)$$

then, the standard error of the mean (SEM) is given as:

$$SEM = \frac{Standard\ deviation}{\sqrt{N}} \quad (5)$$

finally, the uncertainty interval from the set of data is estimated using classical method [6], [9]

$$mean \mp SEM * t_{0.05,df} \quad (6)$$

where,

N : Sample Size

df : Degrees of freedom

t0.05,df : Student t-table value obtained from the degrees of freedom and 0.05 (95% of confidence interval) probability of a absolute value [11].

111. RESULT AND DISCUSSION

Uncertainty estimates are an essential element of the complete emission inventories. It can be seen in the range of standard deviation around the mean value of the sample [12] and it is usually associated with different parts of the inventories. For the uncertainty evaluation, the provincial base direct GHGs emission data are used. The total Turkey‘s Direct GHGs emissions increases can be seen in the following figure 1.

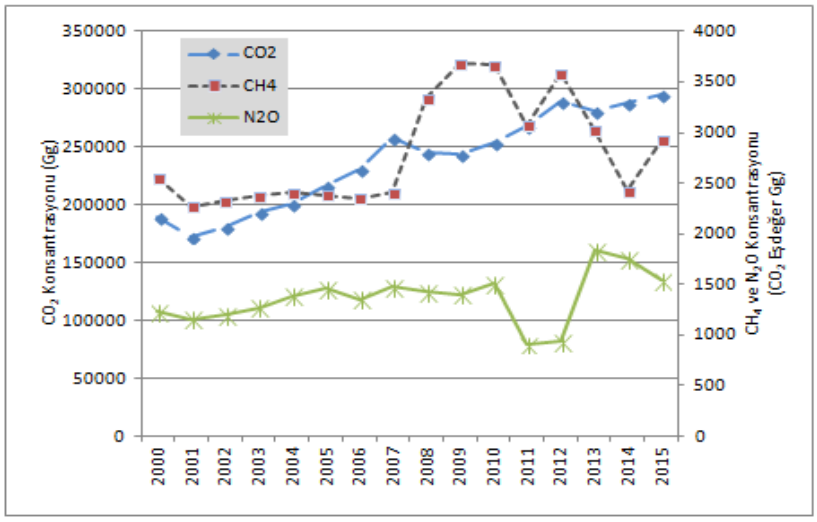

Figure11. The direct GHGs emission between 2000-2015

In year 2015, the total CO_2 equivalent emission is around 300 million tones from fuel burning in industries, thermal power plants, households and road transportation. The CO_2 equivalent emission increase is 55% in 2015 compared to the that in 2000. However, only CO_2 emission increase is observed throughout the years without any fluctuating. The CO_2 emission is increased from 193.5 million tones in 2000 to 300.5 million tones in 2015 from the above mentioned sources,. The CH_4 emission trend has also shown an increase from 2.6 million tones in 2000 to 2.9 million tones in 2015 with an 14% value. However, the emission is decreased after reaching 3.7 million tones in 2009. The N_2O emission trend is increasing constantly until the year 2010 and then it is decreased until 0.9 million tones in the following year. In 2013, the N_20 emission is reached twice of the year 2010. In 2015, the N_20 emission is increased 25% more compared to the year 2000.

By using the results of the statistical evaluations, it is concluded that the correlations between Direct GHGs emissions of the base year and that of the each related years from 2000 to 2015 are decreasing throughout the emission series. The correlations of CH_4 and N_20 emission series are also higher than that of CO_2. The highest correlation was observed in CH_4 series with 0.998 for 1990-2000 series. The smallest correlation was observed in CO_2 series for the year 2015. However, it is still high with a value of 0.943. It means, the series shows high associations (Table 1).

Table 1. Correlations between Emission Series

Paired	CO_2	CH_4	N_2O
1990-2000	0,9643	0,9980	0,9820
1990-2001	0,9693	0,9979	0,9846
1990-2002	0,9636	0,9974	0,9792
1990-2003	0,9569	0,9969	0,9791
1990-2004	0,9558	0,9966	0,9765
1990-2005	0,9545	0,9962	0,9767
1990-2006	0,9538	0,9956	0,9737
1990-2007	0,9610	0,9951	0,9742
1990-2008	0,9607	0,9951	0,9794
1990-2009	0,9659	0,9945	0,9837
1990-2010	0,9639	0,9940	0,9681
1990-2011	0,9519	0,9930	0,9722
1990-2012	0,9498	0,9925	0,9705
1990-2013	0,9477	0,9919	0,9688
1990-2014	0,9457	0,9913	0,9672
1990-2015	0,9431	0,9908	0,9652

Another important statistical variable is the SEM, which is the indication of the spread of the mean. The SEM of the annual emission series is decreasing while the number of the sample size is increasing. The SEM of the annual emission series is decreasing while the number of the sample size is increasing. Briefly, the more the data are gathered, the less the uncertainty is observed in the measurement.

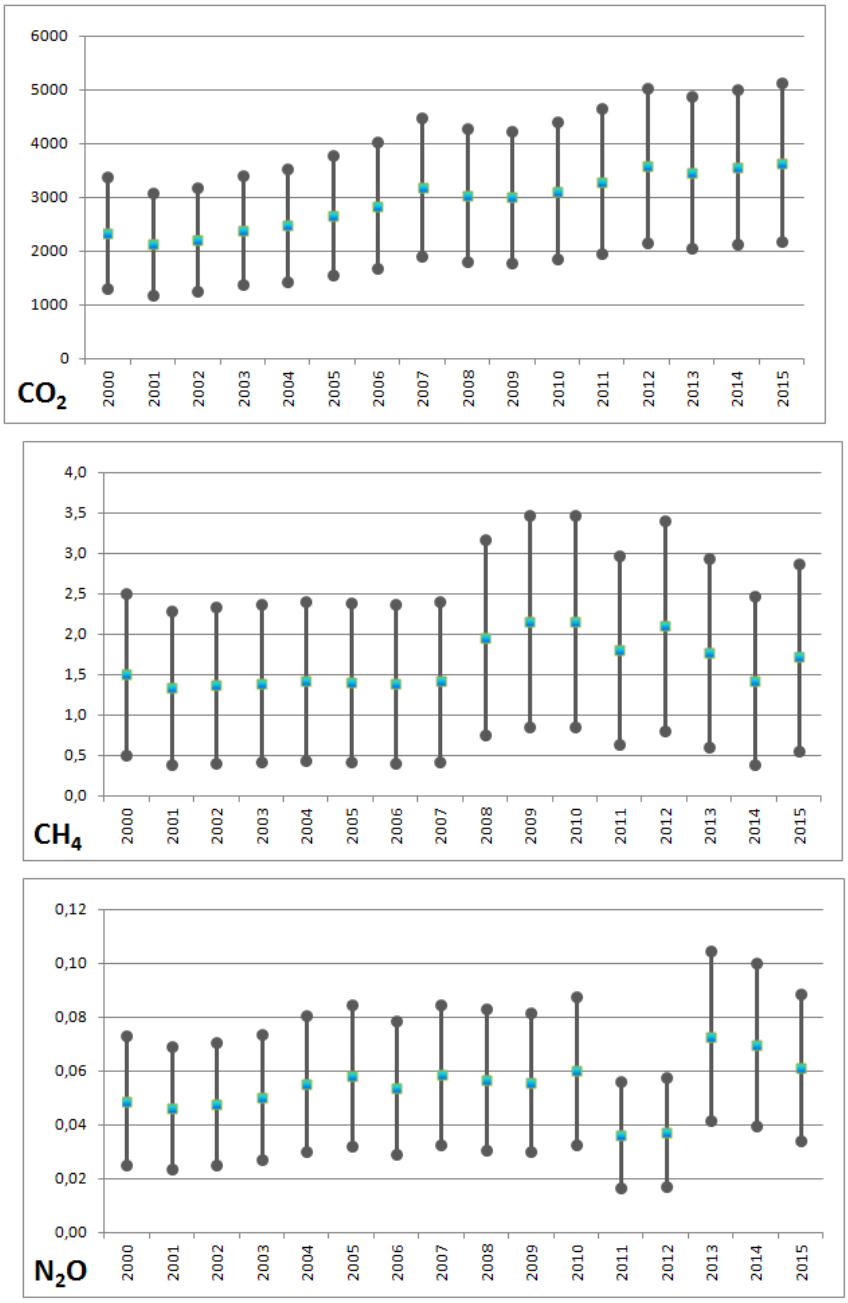

Figure 2. The Uncertainty interval of the provinces between 2000-2015

Uncertainty interval is not intended to dispute the validity of the inventory estimates, but it helps to improve the accuracy of the inventories and actual reliability of the total estimates. Under this circumstance, the uncertainty intervals are determined by using two main statistical concepts. These are the —probability density function" and —confidence intervals". Briefly, the —probability density functions" describe the ranges and the confidence intervals give the range within the underlying value. The method used in this study determines the significance of year-to-year differences and it takes into account the long-term trends in the inventories. A key issue in the compilation of uncertainties within inventories is the distinction between the —standard deviation" of the data set and the standard error of the sample mean. The use of the standard deviation to estimate the limits of the confidence interval is directly dependent on the probability distribution of the data set [2].

The highest SEM value of CO_2 is observed in 2015 with an value of 736 Gg and the average province base emission is 3655 Gg. However, highest SEM value doesn't mean highest uncertainty percent value, which is the lowest ∓20.14%. The CO_2 uncertainty values are changing between highest value ∓22.07% in 2000 to lowest value ∓20.14% in 2015. For CH_4, the highest SEM value is 0.7 Gg and the average province base emission is 2.2 Gg in 2009, and the uncertainty value are changing between lowest value ∓30.4% in 2009 to highest value ∓35.65% in 2006. For N_2O, the highest SEM value is 0.016 Gg and the average province base emission is 0.073 Gg in 2013, and the uncertainty value are changing between lowest value ∓21.7% in 2013 to highest value ∓27.4% in 2011.

Although it is recognized that there are many causes of uncertainties, most important ones in this study are believed to be due to using IPCC emission factors which are changing considerably from regional and local emission factors for some fuel types. The quality of fuel consumption data and local calorific values of fuels are also considered as the reasons for uncertainties'.

112. CONCLUSION

The method used in this study determines the significance of year-to-year differences and it takes into account the long-term trends in the inventories. A key issue in the compilation of uncertainties within inventories is the distinction between the ~~–s~~standard deviation" of the data set and the standard error of the sample mean. The CO_2 uncertainty values are changing between highest value ∓22.07% in 2000 to lowest value ∓20.14% in 2015. The uncertainty value of CH_4 are changing between lowest value ∓30.4% in 2009 to highest value ∓35.65% in 2006 and the uncertainty value of N_2O are changing between lowest value ∓21.7% in 2013 to highest value ∓27.4% in 2011. The most important causes of uncertainties are the using IPCC emission factors which are changing considerably from local ones and the assumptions in fuel consumption data.

REFERENCES

[217]. Carnevale C., Douros J., Finzi G., Graff A., Guariso G., Nahorski Z., Pisoni E., Ponche J-L., Real E., Turrini E., Vlachokostas Ch., **Uncertainty evaluation in air quality planning decisions: a case study for Northern Italy**. Environmental Science and Policy, 2016. (Article in press).
[218]. Can A., 2006. **Investigation of Turkey's Carbon Dioxide Problem by Numerical Modeling**. (Ph.D.Thesis) – METU.
[219]. Can A., Ekmekci H., 2015. **Natural gas consumption and its effect on air emission in Turkey**. ICENS 2015 Conference Book (Macedonia) – P. 26-31.
[220]. Eggleston, S.,**Treatment of Uncertainties for National Greenhouse Gas Emissions**. Report AEAT 2688-1 for DETR Global Atmosphere Division, AEA Technology, Culham, UK, 1998.
[221]. IPCC, 1996. Greenhouse Gas Inventory Reference Manual – **Revised 1996 IPCC Guidelines for National Greenhouse Gas Inventories** – Volume 3 – Intergovernmental Panel on Climate Change – Edited by Houghton J.T., et al.
[222]. IPCC - **Good Practice Guidance and Uncertainty Management in National Greenhouse Gas Inventories** – IPCC National Greenhouse Gas Inventories Programme.p.(6.1)-(6.34)., 2000.
[223]. IPCC, 2006. Greenhouse Gas Inventory Reference Manual – **2006 IPCC Guidelines for National Greenhouse Gas Inventories** - Intergovernmental Panel on Climate Change
[224]. Measurement Uncertainties for Vector Network Analysis -Measurement Analysis: **Uncertainities, Propagation of Error, Least Square Fitting, and Graphical Analysis**. http://www.rohde-schwarz.com/.../ANFileByANNoForInternet visited on August 8, 2005.
[225]. Robinson, J. M., **On uncertainty in the Computation of Global Emissions from Biomass Burning** - Climate Change.14.p.243-262.,1989.
[226]. S.J. Kline, McClintock F.A., **Describing Uncertainties in Single-Sample Experiments**. Mechanical Engineering. P.3. !953.
[227]. **Studdent t-table**. www.stst.lsu.edu/exstweb/statab/Tables/TABLES98-t-special. html - visited on August 1, 2005.
[228]. Tippet J. M., **The Certainty of the Uncertainty** – http://www. earthresearch.com/data-analysis-uncertainties.shtml visited on August 1, 2005.
[229]. **Tretment of Uncertainties for National Estimates of Greenhouse Gas Emission** – Appendix A (Methods of Assessing Uncertainties. www.aeat.co.uk/netcen/airqual/naei/ipcc/uncertainty/exsumm.html visited on August 1, 2005.
[230]. **Uncertainties and Error Propagation** – Appendix V – (Revised September 11, 2003) http://www.physicslabs.phyc.cwru.edu/MECH/Manual/Appendix_V_ Error.Prop.pdf visited on August 1, 2005.
[231]. UNFCCC, 2004. **Overview of UNFCCC Review Process and General IPCC Inventory Guidance**. http://www.earthcouncil.com/ANGEL/ - Training Course, Start: 2005, February 1 - End: 2005, March 15.

Real-Time Target Tracking Using Fast Object Detection

Muhammed Mustafa Kelek[50], Muhammet Fatih Aslan [51] Akif Durdu [52]

Abstract

In this study, Mean-shift, Cam-shift and Color Tracking algorithms which all be used in object tracking are compared in a real-time robotic application. The environment in which the robot and the object followed by robot is recorded by a camera and that data is sent to a computer through cables. To identify this object by using appropriate image process tracking, the location of the robot and the object is could be monitored at the same time. According to the results, the most effective method is shared at the discussion of the outcomes. The robot used in this application has omni-wheel and were designed in our own laboratory.

Keywords: *Target tracking, Mean-Shift, Cam-Shift, image processing, remote control, omni wheel*

113. INTRODUCTION

A new world with new technologies and rapidly advancing Science and Technology is set in. Through the help of digital image processing, the images transferred to the computer in the outside world are used in the many industrial applications. The digital image data using computer image processing techniques is improved by object recognition and object extraction. Image processing consists of a series of operations. These operations begin with the capture of the image, continues with the use of different techniques for the purpose [1].

Robots that can move independently and has their own decision-making on changing, began to be more desirable in term of services they provide. Decision-making mechanism of such autonomous robots depends on their prediction algorithms and their systems are very complicated. Cooperation of vision-based individual in depended robots was carried out by T. Schmitt and his colleagues via probabilistic state estimation [2].

International RoboCup competitions are held in different countries every year. In the football category of these competitions, image processing techniques are determined by using the objects in different colors (visual sides) [3]. This and other similar competitions for applications visual indicators instead of, the more effective will be lifted in the near future it is envisaged that the discovery of different solutions. A. Treptow et al. have performed the tracking by using particle filter function. In this way, it is demonstrated that the ball maybe tracked even in complex environment in real time. On a minimized the football field, thanks to special equipment, one can shoot the ball and score; it is decided to implement a robotic system. In such a system, Motion Analysis of objects such as the robot and the ball in a precise manner with simultaneous tracking and direction should be determined.

The image information that is received from the application environment in the computer environment is used for object tracking. The performance of the Mean-shift, Cam-shift and color tracking algorithms has been evaluated. In this way, it is induced to a smart control system which can detect the robot and the changes around it rapidly thanks to the use of the most efficient object tracking algorithm for a real time robotic football application. This statement will be discussed in the later parts of the methods that are implemented as a priority, and then the general structure of the study will be

[50] *Corresponding author: Selçuk University, Department of Electrical-Electronic Engineering, 42000, Selçuklu/Konya, Turkey. mmustafakelek@gmail.com*

[51] *Selçuk University, Department of Electrical-Electronic Engineering, 42000, Selçuklu/Konya, Turkey. fatihaslan.76@hotmail.com*

[52] *Selçuk University, Department of Electrical-Electronic Engineering, 42000, Selçuklu/Konya, Turkey. durdu.1@selcuk.edu.tr*

described. In the fifth section the results will be given. The sixth section is a discussion of the results obtained and future business planning will be described.

114. METHODS

In this study, the object tracking methods which are Mean-shift, Cam-shift and color tracking algorithms in a robotic application are performed by doing performance tests and color analysis. Therefore, the methods used in this study are described below.

114.1. Mean-Shift Method

This method is a histogram based method. The Mean shift; predicts the intensity degree of the change and united recursive progress of the format search. Mean-shift algorithm does not change the size of the frame to be followed. When using this method, the following processing steps were followed [4].

- The center point of the part to be followed is determined.
- The center of the histogram is subtracted from the designated area.
- The necessary matrix values for tracking are obtained from histogram of the location to be follow with the next frame.
- To find the new location, the Mean-shift method is called.
- After the new location is found the second process is restored.

114.2. Cam-Shift Method

Cam-shift algorithm is a histogram based method which is derived from the Mean shift algorithm. Although it is simple, Cam-shift is a quite effective color tracking techniques. In Cam-shift method, the width of the frame is followed by changing of object. When using this method, the following processing steps were followed [4].

- The center point of the part to be followed is determined.
- A mask is created by calculating the color distribution of the area that is designate as a center.
- The histogram of the area that is determined and its mask is subtracted is shown.
- The necessary matrix values for tracking are obtained from histogram of the location to be follow with the next frame.
- To find the new location, the Cam-shift method is called.
- After the new location is found the second process is restored.

114.3. Color Tracking Method

Each image can be considered as a matrix function of El. These matrix values vary depending to colors of the pixels that forms the image. A colored frame is expressed as RGB so with three colors of red, green and blue. However, sorting in the library OpenCv is BGR unlikely in Matlab. HSV is the most appropriate color space for color-based image segmentation that is used in object tracking processes. Therefore during image processing the RGB color space must be converted to the HSV color space. HSV color space was described by Smith in 1738. HSV is obtained by a nonlinear transformation from the RGB color space [5].

115. GENERAL APPLICATION DESIGN

This study consist of two phases; in the first stage the design and the integration of the robot which is used as hardware, in the second stage the most efficient algorithms is investigated as software.

During the process of combination of our robot, its wheel was designed as Omniwheel and the robot was made up as shown in Figure 2. It is shown in figure 2 that the robot can desired places in which it goes forward, backward and cross-direction; turns right and left without any rotation. To obtain the desired sensitivity is possible by increasing direction numbers with the help of software.

The robot moves faster and responds more quickly to the surrounding events by using Omniwheel. Furthermore, the Bluetooth module was used in the robot in order to communicate with the computer. In addition three motors, two motor driver cards and a micro controller (Arduino) which evaluates information provided by computer controls the movements of our robot.

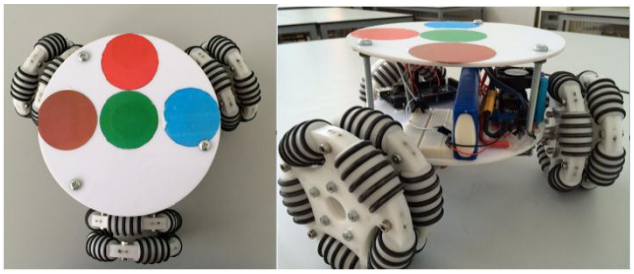

Figure 1. It is the base and side view of the robot with omniwheel used in our experiment

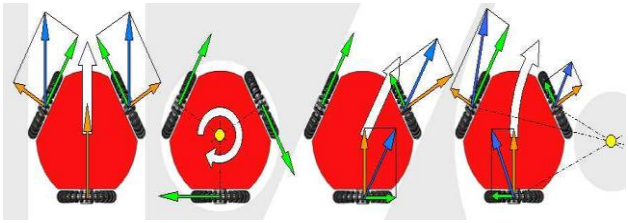

Figure 2. Motion Analysis of the robot Omniwheels

During the software process, it is provided of object tracking and controlling the robot in a faster way by evaluating images captured from camera in computer content with image processing techniques. According to the flow chart given in Figure 3, after processing the image which was received from the environment, it has been provided that the robot moves towards the object via Bluetooth.

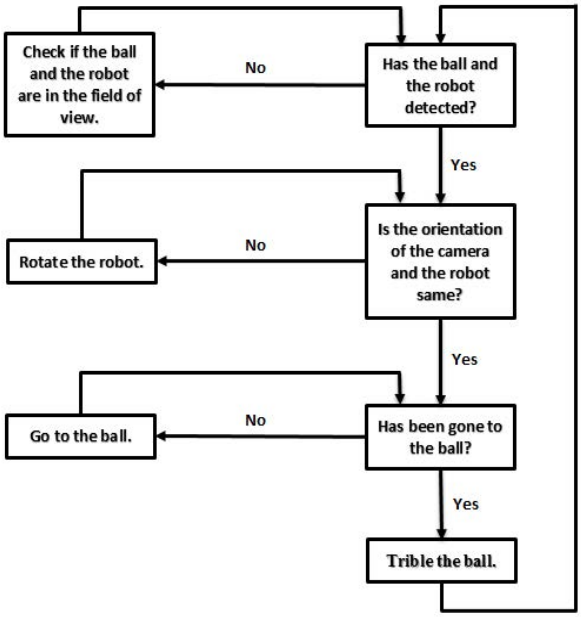

Figure 3. Flow chart

115.1. The sensation and the communication system

Different color makers were designed in order to follow the desired goals on the field [5]. Color makers was made up by gluing four different colored circular pieces on a white mica, as shown in Figure 1. The location and the orientation of the robot and of the ball on the field was detected by ceiling-mounted camera by recognition of colored signs, as shown in Figure 3. At the same time; it is provided by these colors to identify the moving object whether it is a ball or a robot. After the declarations have been made according to the flow chart given in Figure 3, using the Bluetooth communication, the ball is required to follow the motion commands are sent to the robots.

The Omni wheels are used in order to facilitate the movement of the robot is connected to DC motors, motor driver controlled by PWM (Pulse Width Modulation) signals generated by the micro controller Arduino. Simultaneous image transfer to lead to delays in the OpenCv library with the C++ language has been used. In the determination of the coordinates of the robot, the robot and the camera axis for locating the position of the ball and at the same time for the comparison of five different color perception are reviewed. The three of perceived different five colors were used to determine the orientation of the robot and to compare the axes of the robot with the axes of the camera, another color was used to determine the coordination of the robot and the last color was used as fort hat to perceive the ball. The obtained algorithm depending on the perceived colors, constitute the input data which is necessary for comparison. The screenshot of the output as the result of the study is shown in Figure 4. The shades of the colors vary according to the ambient light intensity detected by the camera. For this reason, it is necessary to define the colors again in each different environment.

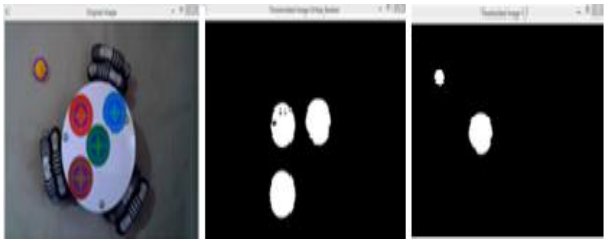

Figure 4. The image of the computer program that is used for the color recognition method

116. EXPERIMENTAL RESULTS

In this study, we used object tracking Mean-shift, Cam-shift tracking algorithms for different floors and different color and light intensities were compared.

First of all, the object tracking algorithm using color recognition process has been performed. Color recognition made by the method of this study is given in the screenshot of Figure 4. In color recognition method, the shades of the colors detected by the camera vary according to the light intensity of the ambient. For this reason, it is required to define the colors again in each environment. Color tracking method, the ambient light intensity constitutes a very great disadvantage. Therefore, there are distortions occur in the position information of the tracked object. These distortions require the use of filters such as Gaussian filters [7]. Due to the difficulties encountered in color tracking, the usability of target tracking methods in the application such as the Mean-shift and Cam-shift methods was investigated.

In a real time environment where the ball and the robot are located, in the application which the tracking of the robot on a particular orbit is taken as a basis, the results have been obtained in three methods. The ball which is normally almost constant in the Y plane and moving at a constant speed in the X plane, the changes of its position according to the three methods which has applied is shown in Figure 5.

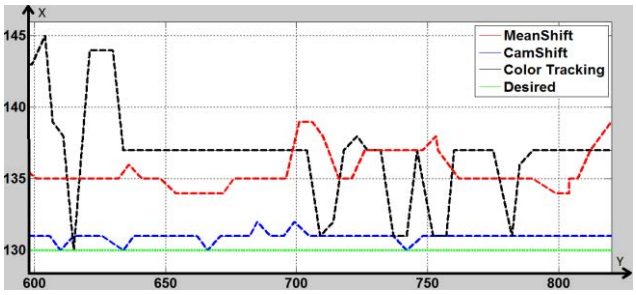

Figure 5. Comparison of methods used

As can be seen in the graph, deviations in the coordinate values of the target occur. These maximum deviations are the most in color detection method, and the least in Cam-shift method. The points that make up the curves in Figure 5 and are formed depending on the position of the ball, their average values are calculated and the percentage error values are given in Table I.

Table 1. Comparison of calculated average values of the methods used

Method	Mean Value	Percentage Error Rate
Color Tracking	135,43	4,98%
Mean Shift	134,75	4,26%
Cam Shift	130,4	1,09%

As can be seen from the graph and the percentage errors, Cam-shift algorithm is the method which has the least deviation and the highest efficiency.

117. INFORMATIONAL DISCUSSION AND CONCLUSION

In this study, the algorithms used in object tracking; color tracking and Mean-shift and Cam-shift are compared in a real-time robotic application in different floors and ambient lighting. According to the results, it is observed that the Cam-shift algorithm is more efficient. This method is preferred and an intelligent control system is carried out in the considered robotic football application. In this way, by creating a local team both in hardware and software, the aim of participating in RoboCup football category of international competitions will be possible to reach.

ACKNOWLEDGMENT

Authors are thankful to RAC-LAB for providing the trial version of their commercial software for this study.

REFERENCES

[1] Samtaş, G., Gülesin, M., ―Sayısal Görüntü İşleme Farklı Alanlardaki Uygulamaları", Mayıs 2011.

[2] Schmitt, T., Hanek, R., Beetz, M., Buck, S. and Radig, B., ―Cooperative Probabilistic State Estimation for Vision- Based Autonomous Mobile Robots". IEEE Transactions on Robotics and Automation 18(5), 670–684 (2002).

[3] https://en.wikipedia.org/wiki/RoboCup

[4] Kuyumcu, B., ―OpenCV Görüntü İşleme ve Yapay Öğrenme", 1. Baskı: Eylül 2015.

[5] Başlar, İ., ―Tüm Gökyüzü Kamerasından Alınan Görüntüler kullanılarak Bulutluluk Ölçümü Yapılması", Antalya ,Ocak 2012.

[6] Kavaklıoğlu, C., ―Akademik Araştırma Platformu Olarak Tasarlanmış Tepe Kamerası Sistemi", January 19, 2009.

[7] Kılıçaslan, İ., Erkmen, A.M., ―Parçacık Filtresi Tabanlı Dikkat Odaklamalı Görsel Hedef Takibi", Emo Ankara Şubesi Haber Bülteni, 2015/1.

An Algorithm to Determine the Ideal Hop Length for Minimum Energy Consumption in WSNs

Nukhet Sazak[1] , Ali Soner Kilinc[2]

[1] Department of Electrical and Electronics Engineering, Sakarya University, Sakarya, Turkey nsazak@sakarya.edu.tr

2 Department of Electrical and Electronics Engineering,Sakarya University, Sakarya, Turkey soner.kilinc@ogr.sakarya.edu.tr

Abstract

A wireless sensor network (WSN) consists of numerous sensor nodes operating with battery and communicating over wireless medium. The unique features of wireless sensor networks such as ease of installation, self-organization, low requirements of maintenance etc. make them have great application potential in various fields ranging from military to health applications. One of the most attractive properties of WSNs is that they can be deployed in harsh networking environments where traditional systems are difficult to be installed. However, replacing or recharging batteries of sensor nodes is quite difficult in this kind of applications. Since the WSN lifetime depends on the lifetime of the sensor nodes and a sensor node with exhausted battery is regarded as ―dead" node, energy efficiency becomes one of the most significant design issues for WSNs. The energy consumption could be minimized by adjusting the distance between the nodes which is called as hop length. In the literature, the best hop length is determined to minimize the energy consumption during data transmission for a given distance between source and destination when the sensor nodes are deployed equidistantly. In this paper, an algorithm is proposed to present the required number of sensor nodes in a simple 1-D linear WSN topology when the hardware data of the Mica2dot sensors is given. The distinctive feature of our proposed algorithm is that it gives the ideal hop number and the number of sensor nodes required for minimum energy consumption directly without calculating energy consumption values for each hop number.

Keywords: *Energy efficiency, ideal hop length, wireless sensor network.*

118. INTRODUCTION

Wireless Sensor Networks (WSNs) have a great application potential in various fields such as agricultural monitoring, industrial monitoring, military applications and health applications. A WSN is simply composed of a number of small and independent sensor nodes or called also as motes which are battery-powered and wireless communicating devices. A wireless sensor node basically is made up of a sensing unit, a transceiver, a power unit (battery) and a processing unit. According to the WSN application requirements, some special components such as location finding system, mobilizer and power generator can also be added [1].

Sensor nodes supply energy from battery for sensing data, communication and data processing. The most energy consuming activity is communication [2]. Since the sensor node with exhausted battery is assumed as ―dead" and mostly changing or recharging the battery is not possible, the efficient use of the available energy determines the lifetime of the WSN. The lesser energy consumption means the longer lifetime. Sensor nodes either send their data to the destination directly which is called as single-hop communication or they send it to the destination through the other sensor nodes and this second communication is called as multi-hop communication [2].

In recent years, many researches have been made for extending WSN lifetime. The optimization of hop length is crucial in terms of lifetime in WSNs. This paper explores the values of the hop length and hop number are optimal for minimum energy consumption and then determines the number of required sensor nodes for the application. Our aim is to determine the ideal hop length and as a result, the number of sensor nodes is calculated for minimum energy consumption. For this purpose, we have developed an algorithm for Mica2dot sensors; however, this algorithm can be applied for any type of sensors.

The remainder of the paper is organized as follows. In section 2, single-hop and multi-hop communication methods and their advantages/disadvantages are explained briefly. The multi-hop power consumption model used in this study is given with details in section 3. The analytical study realized by using this mentioned model is expressed in section 4. In section 5, results and comments are given.

119. SINGLE-HOP VERSUS MULTI-HOP COMMUNICATION

There are basically two communication types for wireless sensor networks: single-hop (also known as nonpropagating) and multi-hop (propagating) [2]. Each has their own benefits and drawbacks. While single-hop routing is shown as being more energy efficient than multi-hop one in some papers, some other authors claimed that multi-hop routing is more energy efficient than the single-hop routing [3, 4].

In a single-hop wireless sensor network, each sensor node sends its data directly to the sink. There is a direct communication between the data sender (source) and the receiver (destination) as shown in Figure 1. All the data source nodes, represented by S, send their data to the destination, represented by D, directly. Destination might be a cluster head, sink or base station. Since there is direct transmission, this type of communication has some advantages in terms of network parameters such as lower end-to-end delay, lower packet loss etc.

Single-hop WSNs have much simpler structure and control and fit into the applications of small sensing areas. On the other hand, this communication method is costly in terms of power consumption and also infeasible since the sensor nodes have restricted transmission range. The sensor nodes that are farther away from the destination might consume their energy quickly in the applications where wireless sensor nodes are deployed to cover large geographical areas and this results in limiting the lifetime of the WSN.

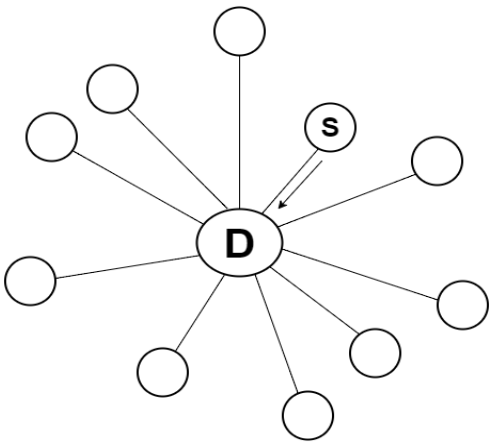

Figure 1. Single-hop wireless sensor network

Multi-hop communication is widely used in wireless sensor networks. The multi-hop communication model is represented by the sketch in Figure 2. Each source node sends its data to the destination through intermediate nodes in a multi-hop wireless sensor network. The intermediate nodes work as routers and these nodes relay the data along the routing path. Data travels from the source node hop by hop until it reaches to the destination node. Multi-hop WSNs are efficient in terms of energy usage because the average received signal power is inversely proportional to the n^{th} power of the distance. The shorter the distance is between the sensor nodes, the less energy is consumed. Multi-hop communication reduces considerably communication interference between sensor nodes competing to access the channel, particularly in highly dense WSNs [5]. In multi-hop communication, system lifetime is increased since transmissions distribute the power consumption over the sensor nodes fairly [2]. However, in a wireless sensor network with many nodes, this communication has a latency drawback. Also, if the size of the WSN is large, the sensor nodes closer to the destination node will route a large number of data and consume their restricted energy fastly.

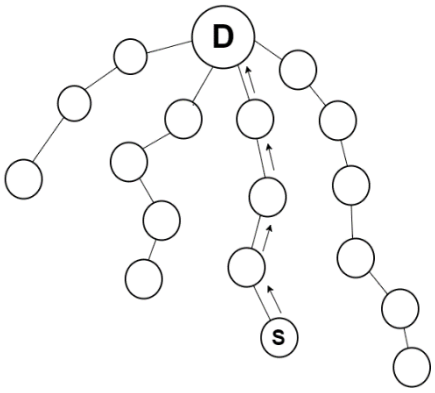

Figure 2. Multi-hop wireless sensor network

The communication could be realized either short hops or long hops in a multi-hop communication type. The optimization of the hop length might save energy and also extend the lifetime of wireless sensor networks. There are some papers analyzing the issue of hopping distance strategy in WSNs [6, 7]. If the multi-hop communication model is used, it is proved that placing the sensor nodes equally distant from the source to the destination is the optimal solution [6].

The log-distance path model has been used in [7]. In that paper, the sensor nodes are placed as long hops and short hops between the source and destination, the consumed energy is computed by changing the hop number and the ideal hop length is determined as a result of minimum energy consumption. According to the obtained results, when the number of hops increases, the hop length decreases as expected and the energy consumption decreases at the beginning but then it increases after reaching the minimum value. The hop length at which minimum energy consumption obtained is called as ideal hop length.

Wang et. al. [6] claim that they have developed a realistic power consumption model for WSN devices and also compared single-hop and multi-hop routing based on this proposed model. In this study, we use a more realistic model proposed in [6] to calculate the number of hops and the number of required sensor nodes for minimum energy consumption by considering the power specifications of commercially available Mica2dot motes. We compare the power consumption values versus hop length by using the multi-hop communication model [6] with the results of the recently proposed model [7]. We have determined that they have similar characteristics for equally placed sensor nodes.

3. MULTI-HOP POWER CONSUMPTION MODEL

First, we describe the multi-hop power consumption model used in our study. In this model, physical communication rate represented by B bits per second is assumed to be constant. The simple 1-D linear WSN with relay nodes placed equidistantly topology is shown in Figure 3. This topology includes a source node S, a destination node D and relay nodes placed equidistantly [6]. The purpose of this network is to deliver the data generated at the source node to the destination node. The intermediate sensor nodes are placed at equal hop distances across the path joining the source to the destination.

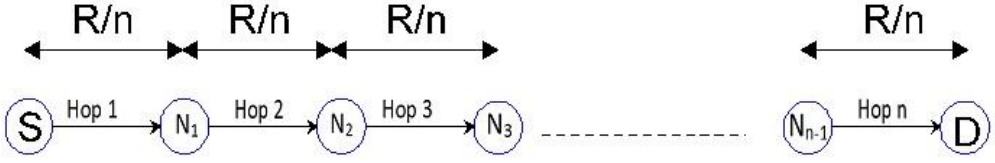

Figure 3. Multi-hop 1-D linear WSN model [6]

Relay nodes are identical and numbered as N_i , i=1,2,…. n-1. The multi-hop power consumption over a given distance with equal distance between nodes is given in eq.(1):

$$P(n) = (n-1)P_{R0} + nP_{T0} + \frac{n \times \varepsilon \times (R/n)^{\alpha}}{\eta} \qquad (1)$$

n: number of hops
P_{R0}: the power consumption of a sensor node to receive data
P_{T0}: the power consumption of a sensor node to transmit data
ε: constant
R: the distance between the source node and the destination node
R/n: the distance between each hop (hop length)
η: the drain efficiency (the ratio of RF output power to DC input power) as given by eq. (2)

$$\eta = \frac{P_{Tx}}{P_{DC}} \qquad (2)$$

α: the path loss exponent

The value of path loss exponent (α) depends on the propagation environment and its range is usually between 2 and 6 as given in Table I [7]. For free space, α is 2 and we do the analysis for α = 2 in this study.

Table I Typical values of path loss exponent [7]

Environment	**α**
Free-Space	2
Urban area LOS	2,7 to 3,5
Urban area no LOS	3 to 5
Indoor LOS	1,6 to 1,8
Factories no LOS	2 to 3
Buildings no LOS	4 to 6

4. ANALYTICAL STUDY

The flowchart of the new algorithm is presented in Figure 4. Since Mica2dot motes use CC1000 processor, the hardware values of CC1000 given in [6] are used as the input parameters. The power consumption of a Mica2dot sensor node to receive data (P_{R0}) is 22.2 mW and the power consumption of a Mica2dot sensor node to transmit data (P_{T0}) is 15.9 mW. The drain efficiency (η) is 15.7% and ε value is taken as 0.0005. The path loss exponent (α) is free space value 2 as mentioned in Section 3. Total energy consumption (P(n)) is calculated by using eq.(1) according to the number of hops (n).

First of all, distance between the source and destination is asked by the algorithm. When the distance is entered, the beginning node number is calculated by dividing this distance value to the node distance with the maximum transmission power which is 230 m for Mica2dot mote. Then, the number of nodes is increased one by one from the starting value and iteration goes on until the minimum energy value is reached. The energy consumption value decreases and after reaching its minimum value, it increases similar to the results given in [7]. Therefore there is no calculation needed anymore and the algorithm ends up.

Although Mica2dot sensor nodes are used for this study, this algorithm can be employed for any type of sensor node by using the hardware parameters related to it or this algorithm can be generalized by asking the hardware parameters of the sensor

node at the beginning. The proposed algorithm gives the ideal hop number and the number of sensor nodes required for minimum energy consumption directly without calculating energy consumption values for each hop number.

5. CONCLUSIONS

In this paper, a new algorithm is proposed for determining the ideal hop length and hop number for minimum energy consumption in WSNs by using the formula already known in the literature. In [7], the ideal hop length to reduce the energy consumption and extend the network lifetime is determined. In this paper, our algorithm defines not only the ideal hop length and as a result ideal hop number but also the number of sensor nodes required since all the sensor nodes are placed equidistantly. In future study, we will focus on developing the algorithm for more complicated node deployment scenarios.

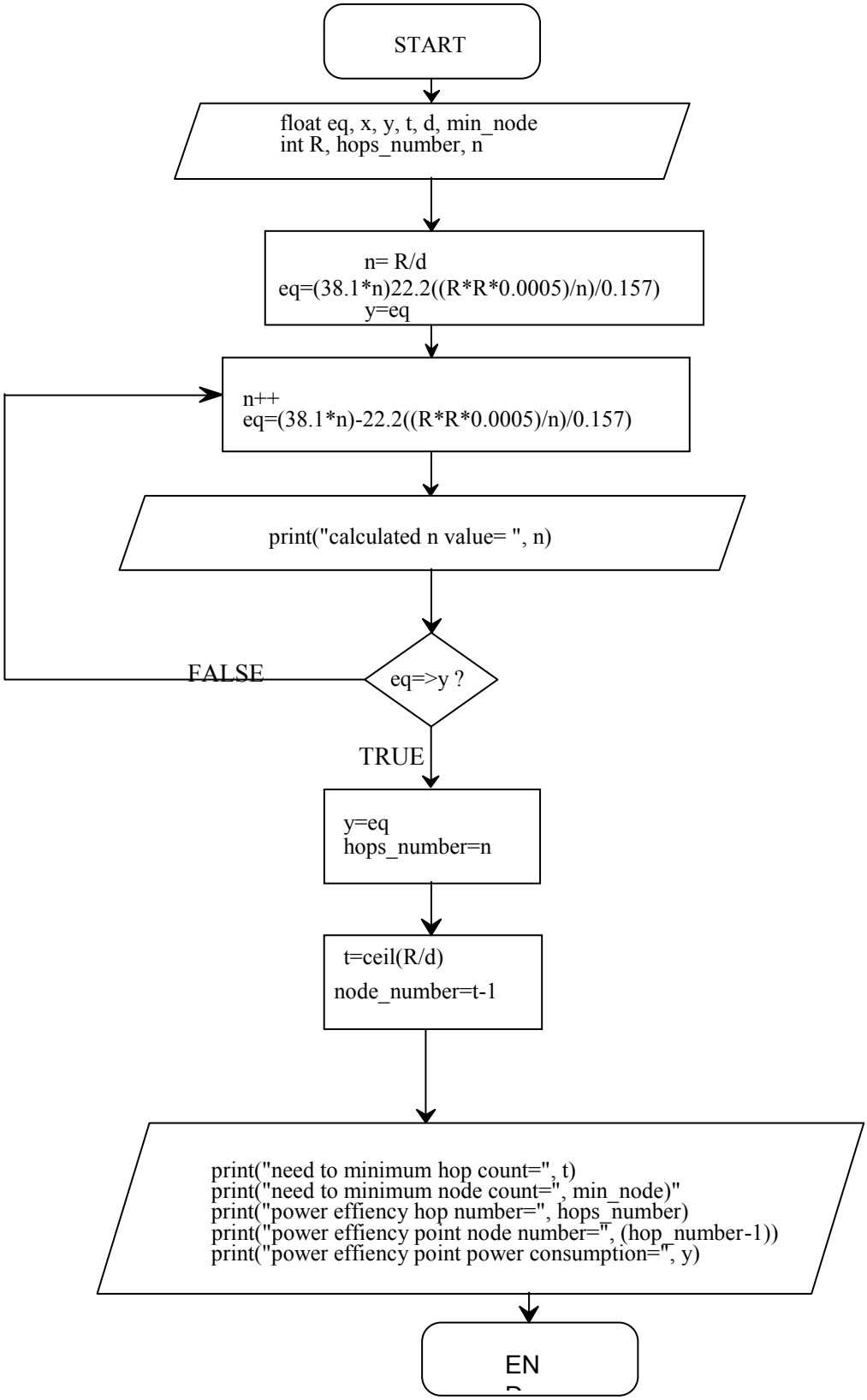

Figure 4. Flowchart of the algorithm

BIOGRAPHY

Nukhet Sazak (nsazak@sakarya.edu.tr) has been an assistant professor in Electrical and Electronics Engineering at the Sakarya University since 2012. She received MSc and PhD degrees from the department of Electrical and Electronics Engineering at Sakarya University in 2002 and 2011, respectively. Her current research interests include MAC protocols and energy efficiency in wireless sensor networks.

REFERENCES

[232]. Akyildiz, I.F., Su, W. and Sankarasubramaniam, Y., ―Wireless sensor networks: A Survey‘, Computer Networks”, vol. 38, pp. 393-422, (2002).
[233]. Ilyas, M., Mahgoub, I., ―Handbook of Sensor Networks: Compact Wireless and Wired Sensing Systems”, CRC Press, 2005.
[234]. Yin, B.L., Shi, H.C. and Yi S. (2005), ―A Two-Level Strategy for Topology Control in Wireless Sensor Networks”, Proceedings of 11th International Conference on Parallel and Distributed Systems, Fukuoka, 22-22 July 2005, 358-362. http://dx.doi.org/10.1109/ICPADS.2005.57
[235]. Haenggi, M. (2004), ―Twelve Reasons Not to Route over Many Short Hops”, Proceedings of IEEE 60th Vehicular Conference, Piscataway, 26-29 September 2004,3130-3134. http://dx.doi.org/10.1109/VETECF.2004.1404638
[236]. Sohraby, K. Minoli D., Znati, T., ―Wireless Sensor Networks: Technology, Protocols and Applications”, John Wiley & Sons Inc., 2007, http://dx.doi.org/10.1002/047011276X
[237]. Q. Wang, M. Hempstead, W. Yang, ―A Realistic Power Consumption Model for Wireless Sensor Network Devices,” In Proc. 3rd Annual IEEE Communications Society on Sensor and Ad Hoc Communications and Networks, Reston, 2006, Vol. 1, pp. 286-295.
[238]. Kheireddine, M., & Abdellatif, R., ―Analysis of hops length in wireless sensor networks. Wireless Sensor Network”, 2014, 6(6), pp. 109–117.

Failure Modes and Effects Analysis for Cogeneration Unit in a Wastewater Treatment Plant

Nazlı Gülüm MUTLU[1], Serkan ALTUNTAS[2], İlter TÜRKDOĞAN[3]

Abstract

Wastewater treatment plants (WWTPs) are established to clean wastewater for reuse. Accidents occurred in these plants highly affect system efficiency and effectiveness as well as employee health. Therefore, risk analysis in WWTPs is quite important to detect and prevent possible accidents in the manufacturing process. WWTPs compose of sub-systems such as the cogeneration system, which is one of the energy production facilities in WWTPs. Failure Modes and Effects Analysis (FMEA) is one of the well-known risk analysis methods in the literature. In this study, a real life case study is conduced to show the application of the FMEA to the cogeneration system in a wastewater treatment plant in Istanbul, Turkey. At the beginning of this study, failures are identified by a group of workers composed of engineers and technician in the cogeneration system. Then, a risk priority number is assigned to each failure to sort the failures with respect to their risky. The results of this study show that the potential accidents can be decreased by the successful application of FMEA in the cogeneration system in a wastewater treatment plant.

Keywords: Wastewater treatment plant, Cogeneration unit, FMEA, Risk analysis.

120. INTRODUCTION

The wastewater treatment plants (WWTPs) carry out the rehabilitation process after using the domestic and industrial of water source. WWTPs compose of multiple processes to treat wastewater at different stages (Wei, 2013). Substances obtained from these multiple processes are rich with respec to organic matter. Biological treatment process is executed for biogas production from organic waste substance. The biogas is one of the most suitable gas types to produce energy. The wastewater treatment plants always work 24 hours a day. These plants needs huge amount of thermal and electrical energy. Some of these energies can be provided from cogeneration plant. In a cogeneration unite, thermal energy and electricity are simultaneously generated to provide a portion of WWTPs energy needs (Havelsky, 1999). In addition to providing many advantages of this unite, any failure in process components may affect negatively all of the process. These failures are mainly based on three systems, namely mechanical, boiler, and turbine (Ramesh, 2011). These failures lead to loss of time, financial loss and efficiency loss in the cogeneration system. The possible failure that will be occur in near future should be identified previously for mitigation the losses.

[1] *Corresponding author: Yıldız Technical University, Department of Industrial Engineering, 34349, Beşiktaş / İstanbul, Turkey. ngmutlu@yildiz.edu.tr*
[2] *Yıldız Technical University, Department of Industrial Engineering, 34349, Beşiktaş / İstanbul, Turkey. serkan@yildiz.edu.tr*
[3] *Yıldız Technical University, Department of Environmental Engineering, 34220, Esenler / İstanbul, Turkey. ilter@yildiz.edu.tr*

The decision makers and engineers in WWTPs should take preventive action plans. Occupational safety can be provided by using risk analysis for the failures in the cogeneration unit.

To date, various methods have been used to evaluate the risks in the cogeneration unit in the literature. Among them, Feili et al. (2013) used the FMEA method to increase the plant security and reliability in the geothermal energy plant. Nikhil Dev (2014) developed a novel method for the assessment of reliability index for a co-generation cycle power plant (CGCPP). Ramesh (2011) conducted the reliability assessment by using fault tree analysis method (FTA) to mitigation of life cycle cost in cogeneration power plant. Chang et al. (2014) applied the FMEA method to identify the critical risk events and to predict the failures in the system to avoid/reduce the potential failure modes and their effect on operations in the process. Li and Zhou (2014) performed reliability analysis in an urban gas transmission and distribution system by using FMEA method. In addition, Lee et al. (2014) used FMEA method to identify and to evaluate possible failures in the design of dolly assembly control system of drilling top drive. Hoseynabadi et al. (2010) used the FMEA method for reliability assessment in a wind turbine design. Wessiani and Sarwoko (2015) evaluated the risk that threat the poultry feed production process and used the Fuzzy FMEA method. Details on the risk analysis in cogeneration units can be found in Cabeza et al. (2008), Eti (2007) and Ramesh (2011). In addition, Li and Gao (2010) combined failure mode and critically analysis method (FMECA) and fault tree analysis method (FTA) for reliability-centered maintenance. Mariajayaprakash and Senthilvelan (2014) used the FMEA method and Taguchi method to optimize the process parameters of screw conveyor (sugar mill boiler) with respect to the process stability, reliability and quality. Furthermore, Sutrisnoa et al. (2015) assessed the risk regarding wastes using

modified FMEA method. Silva et al. (2014) used fuzzy logic and the FMEA method to determine the potential threats for information technology systems security (ITSS). Trafialek and Kolanowski (2014) conducted the FMEA method to evaluate the risks for food security. In this study, the FMEA method is conducted to measure the risks for cogeneration power plant in WWTPs.

The rest of this study is organized as follows. The cogeneration system is introduced in Section 2. Case study is presented in Section 3. Finally, Section 4 consequences their implementation.

121. DESCRIPTION OF THE COGENERATION SYSTEM

The cogeneration unit generates heat and 5500 kVA/hour electric energy approximately with the use of fuel of nearly 1500 Nm3/hour natural gas in gas turbine for energy to be used in the wastewater treatment plant (WWTP). The WWTP is the one of the most important and big plant in Istanbul, Turkey. The temperature of flue gas coming from the turbine in WWTPs is 518 ^{o}C. This gas is used to heat the hot oil, which is required for sludge drying unit included in the WWTP. There are two auxiliary boilers which is used if the hot oil amount to be used in the WWTP increases in the system. Table 1 shows the components included in the cogeneration unit in the WWTP. As can be seen from Table 1, there are 31 components in the system. The flow relation between the system components in cogeneration system is given in Table 2. Figure 1 illustrates material flow within the thermal oil heating system and turbine system.

Table 1. The system components in the cogeneration unit

No	Component name	No	Component name	No	Component name
1	Oil filling line	12	Hot oil exchangers	23	Waste Heat recovery boiler
2	Reserve circulation pumps	13	Hot oil boiler	24	Waste Heat and Hot water boiler
3	Hot oil	14	Chimney	25	Chimney
4	Oil reserve tank	15	Heat exchangers for oil	26	Chimney
5	Gas receiver	16	Hot oil boiler	27	Hot water boiler
6	Nitrogen tube	17	Chimney	28	Auxiliary boiler
7	Expansion tank	18	Sludge drying Units	29	Boiled oil
8	Hot oil outlet collector	19	Return collector	30	Chimney
9	Biogas feed line	20	Natural gas feed line	31	Chimney
10	Biogas filter	21	Biogas feed line		

11	Burner (natural gas and biogas)	22	Turbine

Table 2. Material flow relation between the system components

From	To	From	To
1	2	15	8,16,7
2	4,19	16	17,7
3	2	18	19
4	5,7	19	5,12
5	7	20	22,27,28
6	7	21	22
7	8	22	23
9	10	23	24
10	11	24	25,26
11	13	27	28,30
12	7,13	28	31
13	7,14		

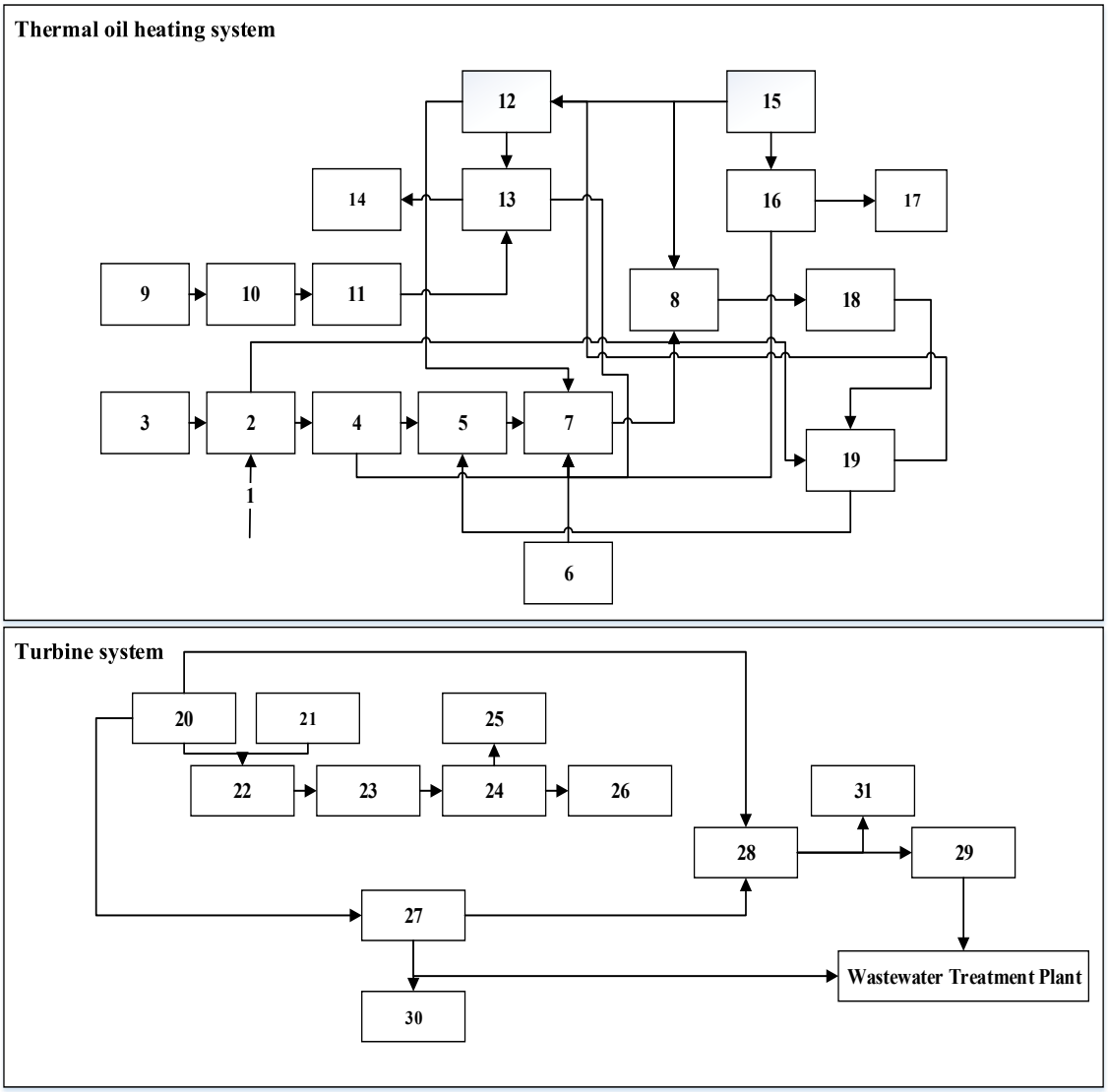

Figure 1. Material flow within the thermal oil heating system and turbine system

122. CASE STUDY

In this section, the application of the failure modes and effects analysis (FMEA) is conducted to evaluate the risks in the cogeneration unit in the wastewater treatment plant. The cogeneration system considered in this study is analyzed in two sections, namely thermal oil heating system and turbine system. As can be seen from Figure 1, these two systems have different number of sub systems denoted by 1, 2, …., 30.

At the beginning of the study, the cogeneration system and corresponding subsystem components are determined. Then, the failures are determined based on experts‘ opinion and the system database which records the failures occurred in the system. 7 experts are interviewed to gain the input data for the FMEA method. Details on these experts are given in **Table 3**. As can be seen from Table 3, the experts are from three majors, namely Mechanical Engineering, Electrical Engineering and Environmental Engineering and their experiences are between 1 to 15 years.

Table 3. The experts interviewed to obtain the failure information in the cogeneration unit

Branch	Department	Experience (year)
ME*	Breakdown and maintenance	**15**
ME*	Breakdown and maintenance of sludge digestion unit	**1**
EE*	Breakdown and maintenance	**4**
EE*	Occupational health and safety	**10**
EE*	Occupational health and safety	**9**
EE**	Department of cogeneration	**2**
ME*	Department of sludge digestion	**3**

ME: Mechanical Engineering , EE*: Electrical Engineering, EE**: Environmental Engineering*

The Risk Priority Number (RPN) is calculated based on equation (1)

$$\boldsymbol{RPN = Occurrence * Detectability * Severity} \quad \textbf{(1)}$$

Table 4 and Table 5 show the RPN for thermal oil heating system and the turbine system, respectively. The first two failures having higher the RPN for thermal oil heating system are, cracks in the boiler wall, lose of oil properties used in the all system caused by continuous circulation of the oil. The first two failures having higher the RPN for the turbine system are **sudden pressure change** and **u**ncontrolled gas supply.

Table 4. The RPN of the failure for thermal oil heating system

Risk No	**Failure Mode**	**RPN**	*Risk No*	**Failure Mode**	**RPN**
1	The failure of **Cracks in the boiler wall**	**659**	*21*	**Failure of ımpure hot oil**	**20**
2	The failure of **lose of hot oil properties**	**299**	*22*	**Malfunction of oil level gauge**	**19**
3	The failure of **contact with the air of oil**	**299**	*23*	**The failure of ball bearing diverging** in hot oil circulation pump	**17**
4	The failure of **overheating of solenoid valve**	**205**	*24*	**Disengagement of safety valve** in thermal oil heating system	**16**
5	The failure of **pressure rise in the pipeline**	**181**	*25*	**The failure of blown fuse** in boiler control dashboard	**16**
6	**Temperature deformations and surface cracks in pipes**	**177**	*26*	**The deformation of pump fan** in pilot pump	**16**
7	**Disintegration of ball bearing** at blower motor	**132**	*27*	**Deformation of coupling tires of** pilot pump	**15**
8	**The deterioration of magnetic filter** in hot oil pipeline	**94**	*28*	**Pollution of flame sensor**	**15**
9	**Breakdown of fire-proof concrete** within boiler	**69**	*29*	**Feed of low purity natural gas to the boiler**	**14**
10	Pressure, temperature **sensor failure** in hot oil collector	**69**	*30*	**The weakening of insulation materials** of the motor winding	**10**
11	**Feed of low purity biogas to the boiler**	**66**	*31*	**Wear in the pipe flange gasket**	**10**
12	**Deterioration of flange coupling** in hot oil circulating pump	**66**	*32*	**The breakage of electric motor** in biogas blower	**9**
13	**Low input gas pressure** in biogas blowers	**64**	*33*	**The failure of water condensation** in biogas and natural gas pipeline	**8**
14	**The failure of improper setting of belt pulley in biogas blowers**	**63**	*34*	**Power surge** in biogas control dashboard	**8**
15	**The failure of ball bearing diverging** in plot pump	**42**	*35*	**The failure of ball bearing diverging** in biogas blowers	**6**
16	**The failure of valve completely not closing**	**37**	*36*	**The failure of the valve** in hot oil collector	**5**
17	**Depreciation of tire** in coupling flange	**33**	*37*	**The breakage of pump shaft**	**5**

18	**Malfunctioning of valve** in input and output within oil tank	**32**	*38*	**The failure of insufficient lubrication of the valve**	**5**
19	**Malfunctioning of compensator** in hot oil circulation line	**31**	*39*	The **pressure gauge and burner** in hot water boiler	**2**
20	**The breakage of pump impeller**	**25**	*40*	**The failure of blown fuse** in solenoid valve	**1**

Table 5. The RPN of the failures for the turbine system

Risk No	**Failure Mode**	**RPN**	***Risk No***	**Failure Mode**	**RPN**
1	**Sudden pressure change**	**262**	*18*	Electrostatic **filter** failure caused by **oil filter fouling**	**39**
2	**Uncontrolled gas supply** to turbine	**216**	*19*	Electrostatic **filter failure**	**36**
3	**Electrical cable deformation**	**164**	*20*	**Compensator failure in hot oil exchanger**	**34**
4	**Oil deficiency in step-up transformer**	**148**	*21*	The failure of **deformation of coupling tires**	**33**
5	**Malfunction** of **cooling water pump**	**112**	*22*	**Pump impeller failure breakdown pump fan**	**25**
6	The failure of **butterfly valve**	**103**	*23*	The failure of **fire detector**	**24**

	in hot oil exchanger				
7	**Switch failure**	**103**	*24*	The failure of **gaskets relaxation** losing of heat exchanger gasket	**21**
8	The failure **of valve actuator**	**103**	*25*	The failure of **bearing diverging**	**17**
9	The failure **of transmitter in fire detector**	**101**	*26*	Due to heat The failure of **cracking and thining of pipeline**	**17**
10	The failure of **gas shut-off valve** in the feed line	**82**	*27*	The failure **of overcurrent circuit breaker**	**16**
11	The failure of **clogging of filter** in the natural gas turbine inlet line	**81**	*28*	**The weakening of insulation materials** of the motor winding in hot oil circulation pump	**10**
12	The failure of **sensor economic life in turbine**	**79**	*29*	The failure **of weakness in turbine main bearing**	**9**
13	The failure of **bolt loosening in oil pipeline**	**72**	*30*	The failure **of Suction Fan belt breakage**	**9**
14	The failure of **turbine cabinet pollution** caused by the clogging of air filter	**70**	*31*	**The failure of cracking in the water pipeline**	**5**
15	The failure of **coupling spring or spindle coupling settling**	**66**	*32*	The failure of breaking down **hot oil pump shaft**	**5**
16	The failure of **burning of transformer station**	**63**	*33*	The failure of **filter clogging of air pollution**	**2**
17	The failure of **high-voltage terminal box**	**44**			

123. CONCLUSION

In this study, a real life case study was conducted to show the application of the FMEA method to the cogeneration unit in the wastewater treatment plant (WWTP) in Istanbul, Turkey. Two important systems, namely the thermal oil heating system and turbine system were analyzed extensively to go into the details of the cogeneration unit in the WWTP. The possible failures were identified based on the experts‘ opinion and the system database which records the failures occurred in the system. The failures were sorted in descending order according to the risk priority number (RPN) through the use of the FMEA method for the thermal oil heating system and turbine system. The results of this study show that the decision makers or engineers can use the FMEA method to utilize occupational health and safety practices in the manufacturing system. The occupational health and safety practices will also lead to more efficient and effective process in the cogeneration unit in the WWTP.

Biography:

Nazlı Gülüm Mutlu, earned her B.Sc. with the best degree and M.Sc. in Chemical Engineering from Firat University, Elazığ, Turkey, respectively in 2010 and 2013. As a double major student, in 2011, Mutlu received her 2nd B.Sc. in Environmental Engineering from the same university. In 2015, Mutlu started her Ph.D. studies in Occupatıonal Health and Safety Programme of Department of Industrial Engineering in Yıldız Technical University, Turkey. Mutlu is a member of Chamber of Environmental Engineers.

Serkan Altuntas is an Asst. Prof. Dr. at the Industrial Engineering Department of the Yıldız Technical University in Turkey. He got his B.Sc degree in industrial engineering, from Eskisehir Osmangazi University, Eskisehir, his M.Sc degree in industrial engineering from Dokuz Eylul University in Izmir, Turkey and his Ph.D. degree in the Department of Industrial Engineering at the University of Gaziantep in Gaziantep, Turkey. His research interests include, facility layout, multicriteria decision making and technology evaluation.

İlter Türkdoğan works as an associated professor at Yıldız Technical University Environmental Engineering Department, received her BSc in Civil Engineering in 1985 from Yıldız Technical University, İstanbul, Turkey, her MSc in Civil Engineering in 1988 from Yıldız Technical University, İstanbul, Turkey and her PhD in Environmental Engineering in 1996 from Yıldız Technical University, İstanbul, Turkey. Türkdoğan is a member of Chamber of Civil Engineers.

ACKNOWLEDGMENT

The authors would like to thank the Istanbul water and sewerage services - Ataköy advanced biological wastewater treatment plant for supplying the failures related to cogeneration unit.

REFERENCES

[239]. Wei, "Modeling and optimization of wastewater treatment process with a data-driven approach", PhD (Doctor of Philosophy) thesis, University of IOWA, 2013.
[240]. Havelsky, V., –Energetic efficiency of cogeneration systems for combined heat, cold and power production", *International Journal of Refrigeration*, vol. 22, p. 479-485, 1999.
[241]. Cabeza., Z., Ridao, M., A., Alvarado, I., Camacho, E., F., –Applying Risk Management to Combined Heat and Power Plants" , *IEEE Transactions on Power Systems*, vol. 23, p. 938-945, 2008.
[242]. Eti, M.C., Ogaji, S.O.T. Probert, S.D., –Integrating reliability, availability, maintainability and supportability with risk analysis for improved operation of the Afam thermal power-station", *Applied Energy*, vol. 28, p. 202-221, 2007.
[243]. Ramesh, V., Saravannan, R., –Reliability Assessment of a Co-Generation Power Plant in a Sugar Mill Using Fault Tree Analysis", *Energy Sources*, vol. 33, p.1168-1183, 2011.
[244]. Feili, H., R., Akar, N., Lotfizadeh, H., Bairampour, M., Nasiri S., –Risk analysis of geothermal power plants using Failure Modes and Effects Analysis (FMEA) technique", *Energy Conversion and Management*, 2013, vol. 72, p. 69-76.
[245]. Ramesh, V., Saravannan, R., –Reliability Assessment of Cogeneration Power Plant in Textile Mill Using Fault Tree Analysis", *Journal of Failure Analysis and Prevention*, vol.11, p.56-70, 2011.
[246]. Li, S., Zhou, W., –Reliability analysis of urban gas transmission and distribution system based on FMEA and correlation operator", *Frontiers in Energy*, vol. 8, p.443-448, 2014.
[247]. Chang, K.H., Chang, Y.C., Lai, P., T., –Applying the concept of exponential approach to enhance the assessment capability of FMEA", *Journal of Intelligent Manufacturing*, vol. 25, Issue 6, p. 1413-1427, 2014.
[248]. Lee, S., Chu, B., Chang, D., –Risk-based design of dolly assembly control system of drilling top drive", *International Journal of Precision Engineering and Manufacturing*, vol. 15, p. 331-337, 2014.
[249]. Hoseynabadi, H., A., Oraee, H., Tavner, P.J., –Failure Modes and Effects Analysis (FMEA) for wind turbines", *Electrical Power and Energy Systems*, vol. 32, p. 817-824, 2010.
[250]. Wessiani, N., A., Sarwoko, S., O., –Risk analysis of poultry feed production using fuzzy FMEA", 2015, *Procedia Manufacturing*, vol. 4, p. 270-281.
[251]. Mandal,S., Maiti, J., –Risk analysis using FMEA: Fuzzy similarity value and possibility theory based approach", *Expert Systems with Applications*, vol. 41, p. 3527-3537, 2014.
[252]. Li, D., Gao, J., –Study and application of Reliability-centered Maintenance considering Radical Maintenance", *Journal of Loss Prevention in the Process Industries* ,vol. 23, p. 622-629, 2010.
[253]. Mariajayaprakash, A., Senthilvelan, T., –Optimizing Process Parameters of Screw Conveyor (Sugar Mill Boiler) Through Failure Mode and Effect Analysis (FMEA) and Taguchi Method", *Journal of Failure Analysis and Prevention*, vol. 14, p. 772-783, 2014.
[254]. Sutrisnoa, A., Gunawanb, I., Tangkumanc, S., –Modified failure mode and effect analysis (FMEA) model for accessing the risk of maintenance waste", *Procedia Manufacturing*, 2015, vol. 4, p. 23-29.
[255]. Silva, M., M., Gusmão, A., P., H., Poleto, T., Silva, L., C., Costa, A., P., C., S., –A multidimensional approach to information security risk management using FMEA and fuzzy theory", *International Journal of Information Management*, vol.34, p. 733-740, 2014.
[256]. Trafialek, J., Kolanowski, W., –Application of Failure Mode and Effect Analysis (FMEA) for audit of HACCP system", *Food Control*, vol. 44, p. 35-44, 2014.

ICENS
INTERNATIONAL CONFERENCE ON ENGINEERING AND NATURAL SCIENCES
24-28 May 2016 /Sarajevo

Odorus Volatile Organic Compounds Determined Inside the ISTAC Landfilling Facility and Places at Close Vicinity by Passive Air Sampling Method

Arslan Saral[*53], S. Levent Kuzu[1], ġenol Yıldız[2]*

Abstract

Volatile organic compounds (VOCs) attract the attention of the authorities due to their detrimental effects on environmental and human health. People are exposed to odor problems, which live in close vicinity of the emission sources. This is the most obvious effect of these emissions. In order to manage and control the emissions, released compounds at least should be monitored at source and receptor points. So that, source contributions can be evaluated.

Landfilling is the most frequent method used in Turkey to manage and dispose the solid wastes. Although, engineering methods during and after the landfilling process minimizes the undesired effects of the wastes in the environment, odorous compounds released to the atmosphere still remains as a serious problem. Especially, people living in the surrounding residential areas are the most vulnerable ones.

Sampling was conducted in the European side of Istanbul. Sampling points were selected to be inside the landfilling facility and residential areas where are reported to be exposed to odor from landfilling activity. Passive sampling method was used in this study. Sample tubes were placed in the area at least for ten days. Then, these tubes were brought to laboratory for further processing and quantification. VOC species were detected and quantified by GC-MS.

Total VOC concentrations were ranged between 50 and 850 ppm. The VOC species with the highest concentrations were m&p xylene, 1,2,4-trimethybenzene, 1,4-diethylbenzene, n-decane, n-undecane. Concentrations observed in summer were considerably higher than in winter. The highest concentrations were observed in active landfilling lot, leachate waste water collection tank and composting facility.

Keywords: VOC, passive sampling, landfill gas, passive sampling

124. INTRODUCTION

Investigation of volatile organic compounds (VOCs) are of scientific interest nowadays due to their toxic, carcinogen, and their odor effects [1],[2]. Long time exposure to benzene, toluene, xylene, and chlorinated compounds could yield health problems on landfilling operators [3]. Odor is occurred when insufficient oxygen is present during the decomposition of solid wastes [4]. There are some studis on the composition of landfilling gasses. In Turkey, characterization study was conducted in Izmir Harmandali landfilling area [5]. Diverse types of VOCs were identified in that study. The identified VOCs were monoaromatics, halogenated compounds, aldehydes, esters, ketones, sulfur/nitrogen containing compounds, volatile fatty acids. The main problem of these organic types are their annoying odor in urban areas [6].

The main goal of this study is to determine the VOC levels inside the landfilling facility area and in the residential zones close to the landfilling area, where people living in those areas are usually get annoyed. Finally, spatial distribution of VOCs were determined.

125. MATERIALS AND METHODS

125.1. Study Area

Landfilling facility in the European side of Istanbul is located in Kemerburgaz-Odayeri. This location is to the north of residential area of Istanbul. The prevailing wind direction in Istanbul is north-easterly. For that reason, the sampling points, apart from waste processing facilities, were selected to be the residential sites to the south of the facility. Sampling points are shown in Figure 1.

[*] *Corresponding author: Yildiz Technical University, Department of Environmental Engineering, 34220, Esenler/Istanbul, Turkey.*
saral@yildiz.edu.tr

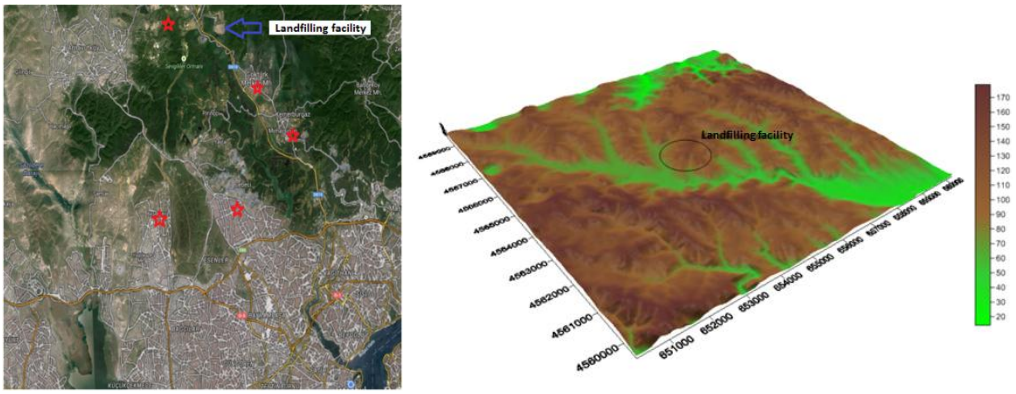

(a) *(b)*

Figure 27. (a) Map of the study area (b) Geographical properties of the study area (elevation in meters)

The red stars are the residential sites distributed in the sampling train. Geographic properties and meteorological conditions have big importance on the dispersion of the pollutants released from landfilling activities. The map showing the geographical properties of the study area in 10 km x 10km dimensions.

Meteorological data were gathered from Davis Vantage Pro-2 weather station present in Odayeri landfilling facility.

125.2. Sampling Method

The sampling was not in a single point. On the contrary, there were many sampling points distributed within a large area. So that, passive sampling method was selected. It is easy to handle passive sampling and a common method when there is large number of sampling points [7]. Sampling pump is not used so operation is cheaper than active sampling [8].

Passive sampling tubes were filled with 100 mg Carbopack-B adsorbent material and closed with fine mesh at both edges of the tube. Dept of the mesh was 1.5 cm from the edge. These tubes were delivered to the sampling location inside a falcon tubes. They were closed with telfon lids when sampling was finished and returned to the laboratory again in the falcon tubes. Sampling dates are given in Table 1.

Table 12. Sampling dates

Sampling no	Start date	Finish date
1	03.12.2014	17.12.2014
2	15.01.2015	04.02.2015
3	03.03.2015	19.03.2015
4	20.04.2015	05.05.2015
5	02.06.2015	17.06.2015
6	31.07.2015	21.08.2015
7	17.09.2015	15.09.2015
8	26.10.2015	06.11.2015
9	26.11.2015	11.12.2015

Some photos taken from the field studies are shown in Figure 2. Blank samples were taken along with the original samples in order to make quality assurance/quality control tests.

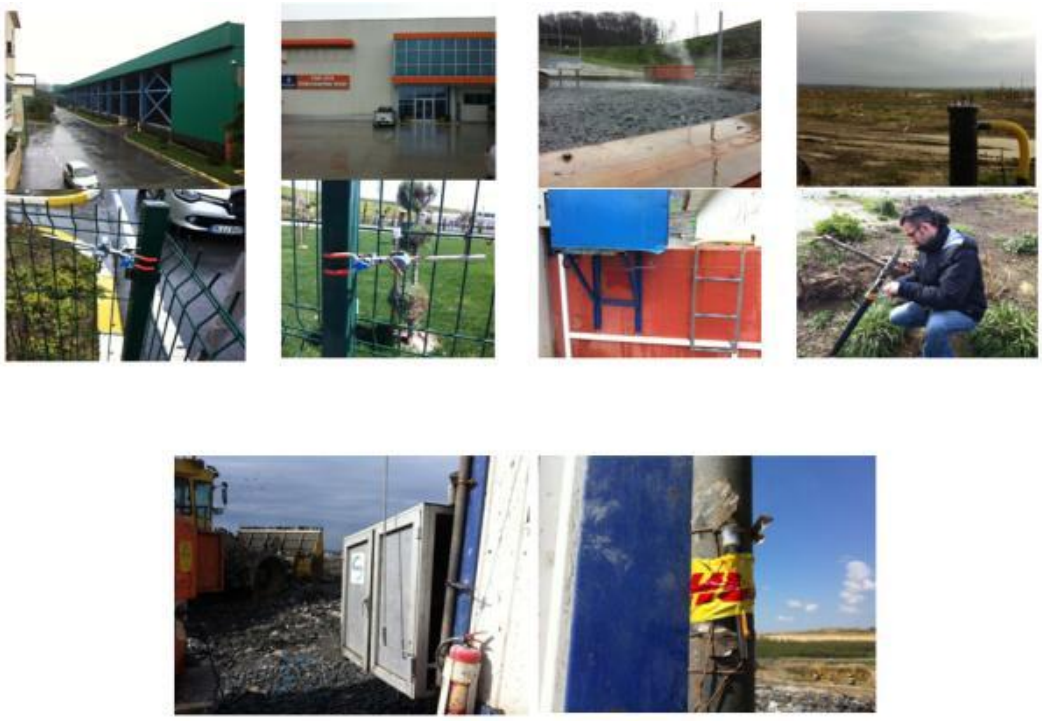

Figure 2.Pictures from field sampling studies

125.3. Sample Preparation

VOCs were adsorbed to adsorbent material at the sampling points. Their desorption was made by solvent extraction. Methanol was selected as the solvent. Chemical desorption process was realized inside the falcon tubes. Meshes of the tubes were removed and adsorbent material were poured in the falcon tubes. 2 ml of methanol was included inside the falcon tube. Then, falcon tubes were placed inside an ultrasonic bath and samples were ultrasonically extracted for 30 minutes. At the outset of each extraction, surrogate standards were included to find the recovery. After that, samples were placed into vials for gas chromatography (GC) analysis.

125.4. Gas Chromatography Analysis

Analyses were performed by Perkin-Elmer GC-MS system. The column was HP-5MS (30 m, 0.25 um, 0.25 id). Sample injection volume was 1 ml. Splitless injection was selected. Carrier gas was ultra pure helium, having pressure of 20 psi. Injector port temperature was kept at 240 ^{o}C. The oven was held 5 min at 35 ^{o}C, then temperature was raised to 110 ^{o}C at a rate of 5 ^{o}C/min. The oven was held at 110 ^{o}C for 2 min. After that, oven temperature was raised to 200 ^{o}C, at a rate of 40 ^{o}C/min. Finally, temperature was increased to 220 ^{o}C and waited there for 2 min. Total run time was 26.25 min.

In order to quantify the compounds 18 masses were investigated at two channels, which were 42, 43, 55, 57, 67 ,69, 71, 78, 83, 84, 85, 91, 92, 93, 98, 104, 105, 119. Forty different VOCs were targeted with these masses. However, 17 VOCs were regularly quantified. These species were: m-xylene, p-xylene, styrene, propylbenzene, n-decane, isopropylbenzene, alpha-pinene, beta-pinene, propylbenzene, 3,4-ethyltoluene, 1,3,5-trimethylbenzene, 1,2,4-trimethylbenzene, 1,2,3-trimethylbenzene, 2-ethyltoluene, 1,3-diethylbenzene, n-undecane.

125.5. Gas Chromatography Analysis

Blank samples were analyzed as with regular samples. Limit of detection (LOD) was calculated according to blank samples. LOD was calculated as : mean blank sample concentration plus three times of the standard deviation of the blank samples. o-xylene were used as the surrogate standard. Its average recovery efficiency was 53±11%

125.6. Calculation of the Concentrations

Concentration of VOCs were determined in liquid phase. Total air flowrate need to be known in order to find atmospheric concentrations. As the sampling was passive type, it is not accurately possible to find actual flowrate. VOCs accumulated inside the adsorbent by diffusion. Equation 1 and equation 2 are used to calculate ambient air concentrations.

$$Uptake\ rate = \frac{D\left(\frac{cm^2}{sec}\right) x A(cm^2)}{L(cm)} \quad (1)$$

$$Atmospheric\ concentration\ (ppm) = \frac{M_a(mg)}{uptake\ rate\left(\frac{ng}{ppm\ x\ min}\right) x\ t\ (\min)} \quad (2)$$

where, D is the diffusion coefficient for each VOC type, A is the cross sectional area of the sampling tube, L is the distance between the mesh and the edge of the tube, Ma is the molecular weight of the VOC in concern, and t is the sampling time.

126. RESULTS AND DISCUSSION

The results of each sampling period was shown with the spatial distribution and wind rose acquired for each sampling period. The time spent in the field for sampling no 7 was prolonged and consequently they reached to saturation. The values results for sampling no 7 was not reported for that reason. Spatial distribution of sampling no 1 is given in Figure 3

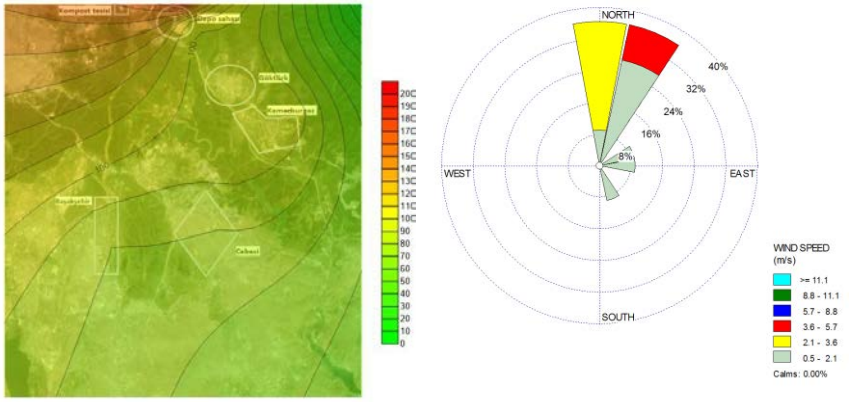

Figure 3.Sampling results of sampling no 1

Prevailing wind direction was N-NE. Wind speed was mostly below 3.6 m/sec. The highest concentration was 200 ppm. The location of the highest concentration was landfilling area. The three highest concentrations in residential areas were 90 ppm, 80 ppm, and 70 ppm for Kemerburgaz, Başakşehir, and Cebeci, respectively.

Spatial distribution of sampling no 2 is given in Figure 4.

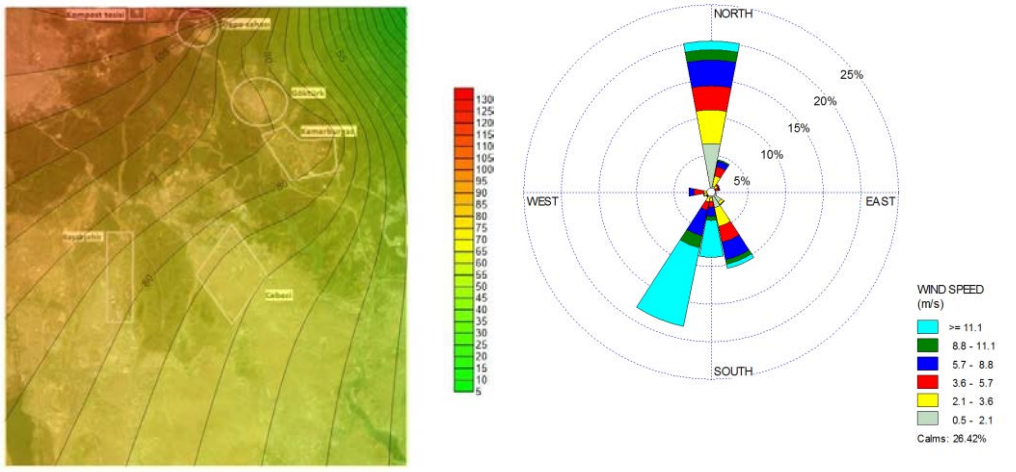

Figure 4. Sampling results of sampling no 2

Prevailing wind direction was N-SW. Wind speed was mostly above 11.1 m/sec. The wind speed was less than 0.5 m/sec during 26% of the whole sampling time. The highest concentration was 130 ppm. The location of the highest concentration was landfilling area. The three highest concentrations in residential areas were 80 ppm, for Kemerburgaz, Başakşehir, and Cebeci. It was 60 ppm in Cebeci.

Spatial distribution of sampling no 3 is given in Figure 5.

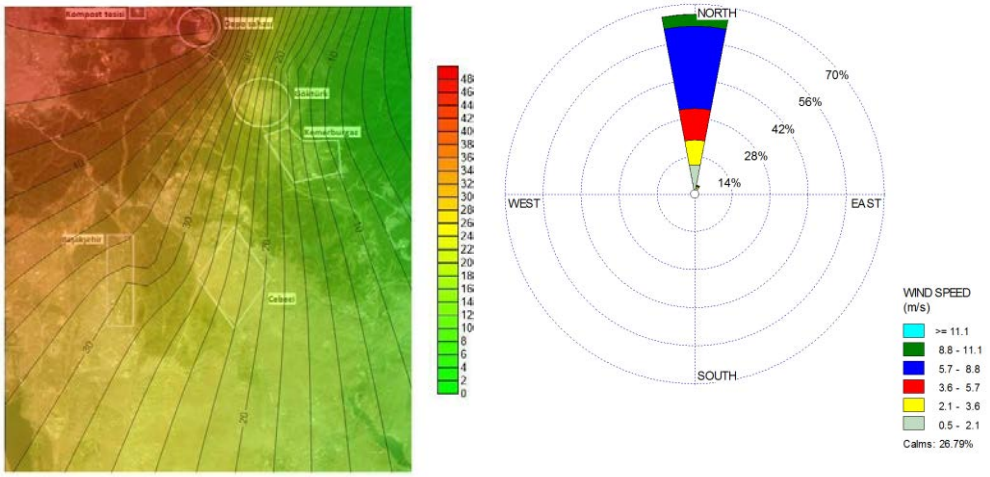

Figure 5. Sampling results of sampling no 3

Prevailing wind direction was N. Wind speed was mostly between 5.7-8.8 m/sec. The wind speed was less than 0.5 m/sec during 27% of the whole sampling time. The highest concentration was 50 ppm. The location of the highest concentration was landfilling area. The two highest concentrations in residential areas were 50 ppm for Başakşehir, and Cebeci.

Spatial distribution of sampling no 4 is given in Figure 6.

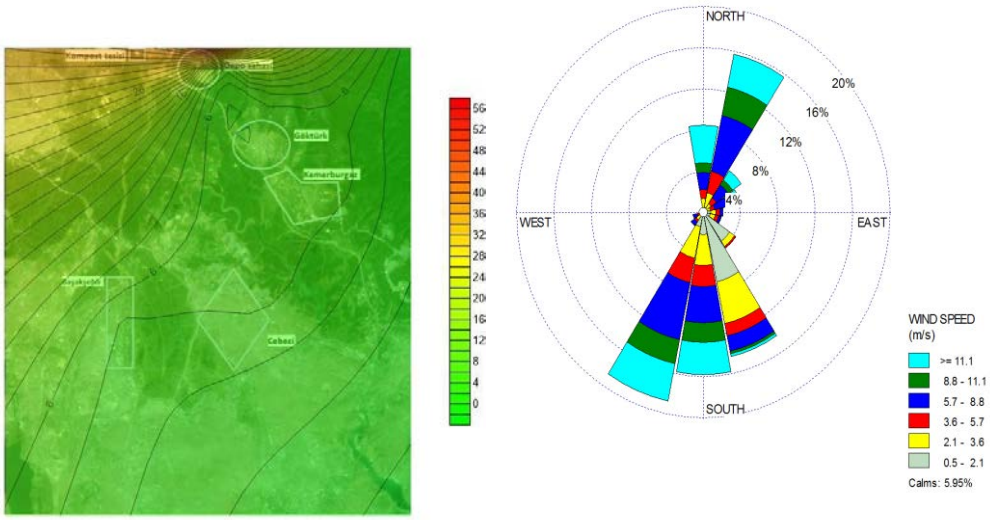

Figure 6. Sampling results of sampling no 4

Prevailing wind direction was S-SSW-NNE. Wind speed was mostly between 5.7-8.8 m/sec. The wind speed was less than 0.5 m/sec during 6% of the whole sampling time. The highest concentration was 56 ppm. The location of the highest

concentration was landfilling area. The highest concentrations in residential areas were 5 ppm Göktürk, Kemerburgaz, Başakşehir, and Cebeci.

Spatial distribution of sampling no 5 is given in Figure 7.

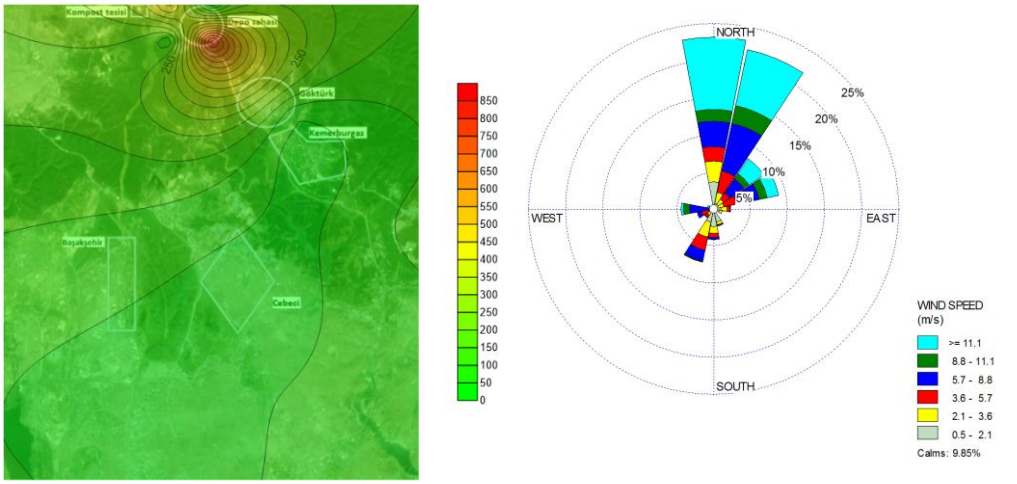

Figure 7. Sampling results of sampling no 5

Prevailing wind direction was N. Wind speed was mostly above 11.1 m/sec. The wind speed was less than 0.5 m/sec during 10% of the whole sampling time. The highest concentration was 850 ppm. The location of the highest concentration was landfilling area. Half of this concentration was observed from the composting facility. The highest concentrations in residential areas were between 50 and 100 ppm at Kemerburgaz, Başakşehir, and Cebeci‘.

Spatial distribution of sampling no 6 is given in Figure 8.

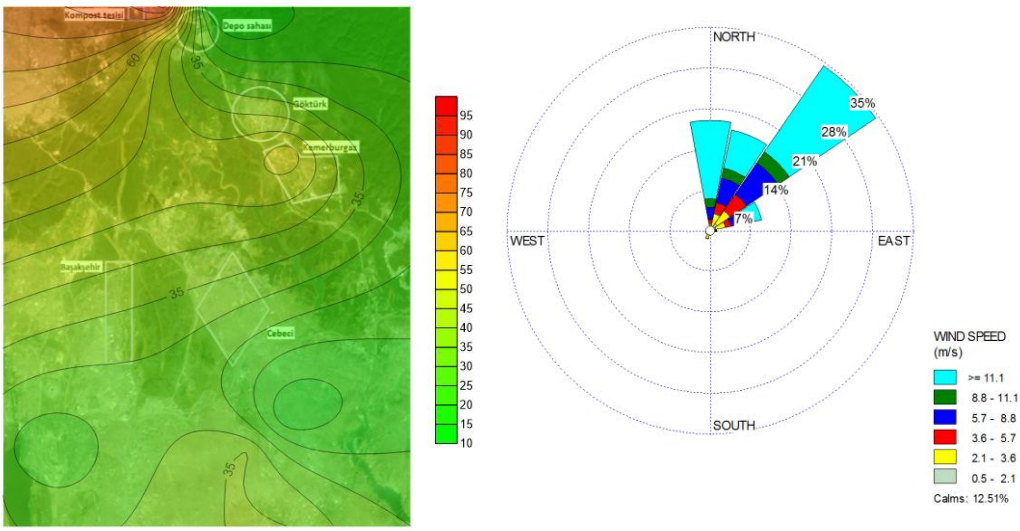

Figure 8. Sampling results of sampling no 6

Prevailing wind direction was N. Wind speed was mostly above 11.1 m/sec. The wind speed was less than 0.5 m/sec during 12% of the whole sampling time. The highest concentration was 100 ppm. The location of the highest concentration was the composting facility. VOC concentration was 60 ppm at the landfilling site. The highest concentration in residential areas was observed in Kemerburgaz as 45 ppm. The concentration was 35 ppm at between 50 and 100 ppm at Göktürk, Başakşehir, and Cebeci.

Spatial distribution of sampling no 8 is given in Figure 9.

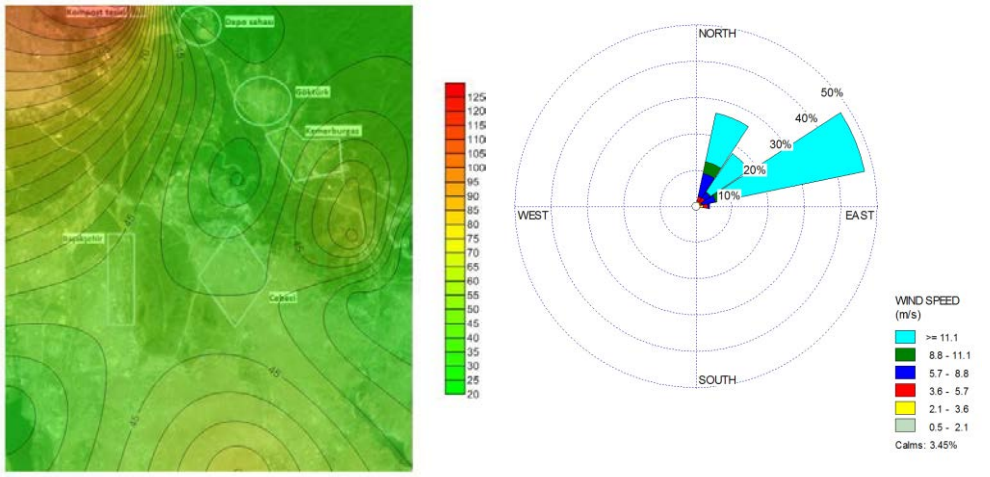

Figure 9. Sampling results of sampling no 8

Prevailing wind direction was N. Wind speed was mostly above 11.1 m/sec. The wind speed was less than 0.5 m/sec during 3% of the whole sampling time. The highest concentration was 130 ppm. The location of the highest concentration was the composting facility. VOC concentration was 45 ppm at the landfilling site. The highest concentrations in residential areas were between 35 and 50 ppm in Kemerburgaz.

Spatial distribution of sampling no 9 is given in Figure 10.

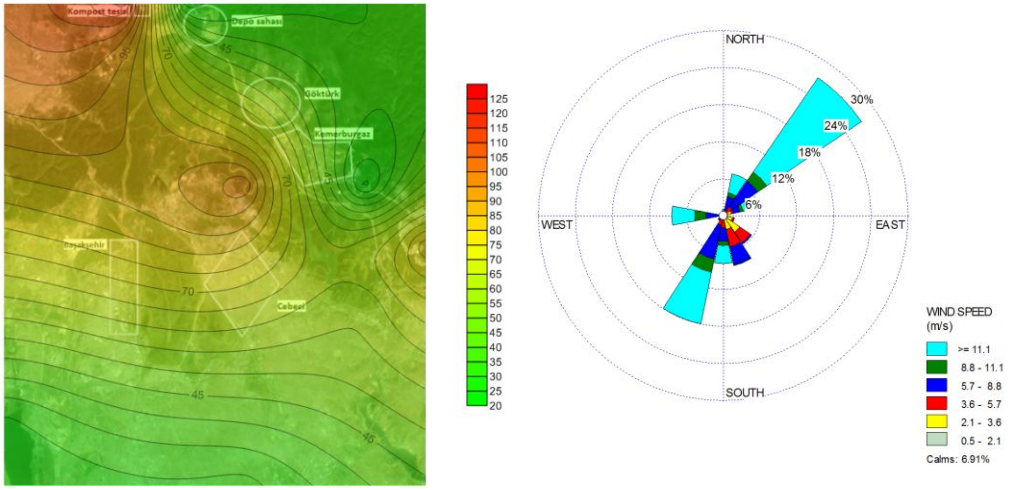

Figure 10. Sampling results of sampling no 9

Prevailing wind direction was N. Wind speed was mostly above 11.1 m/sec. The wind speed was less than 0.5 m/sec during 26% of the whole sampling time. The highest concentration was 300 ppm. The location of the highest concentration was the composting facility. The concentrations were at the same levels for the remaining places.

127. CONCLUSIONS

In this study, VOC concentrations at the waste management facilities were measured and to see their effect on residential sites, sampling was conducted at some specific residential areas. The highest concentrations were encountered mostly in landfilling area. The highest concentration was 850 ppm However, the variability was very high. Usually half of the VOC concentrations were present in residential areas. The main sources were landfilling, composting, and leachate collection tank. It is suggested to control the emissions from these sources. Daily soil can be laid in order to prevent volatilization of VOCs from landfill and operation can be made within small scale lots. Top of the leachate collection tank could be closed and emissions can be treated in a further step. The emissions of composting facility is treated by a biofilter. However, the treatment process is not working efficiently. It is suggested to revise and modify this system to control the VOCs.

ACKNOWLEDGMENT

The authors would like to acknowledge ISTAC AS for their technical support during the sampling stage.

REFERENCES

[257]. A. Saral, S. Demir, and Ş. Yıldız, –Assessment of odorous UOBs released from a main MSW landfill site in Istanbul-Turkey via a modelling approach", *J Haz Mat*, vol 168, pp 338-345, 2009.
[258]. M. A. Parra, D. Elustondo, R. Bermejo, and J. M. Santamaria, " Exposure to volatile organic compounds (UOB) in public buses of Pamplona, Northern Spain ", *Sci Tot Environ*, vol 404, pp 18-25, 2008.
[259]. S. C. Zou, S. C. Lee, C. Y. Chan, K. F. Ho, X. M. Wang, L. Y. Chan, and Z. X. Zhang, "Characterization of ambient volatile organic compounds at a landfill site in Guangzhou, South China", Chemosphere, vol. 51, pp. 1015-1022, 2003.
[260]. Q. Liu, M. Li, R. Chen, Z. Li, G. Qian, T. An, and J. Fu, "Biofiltration treatment of odors from municipal solid waste treatment plants", *Waste Management*, vol. 29, pp. 2051-2058, 2009.
[261]. F. Dinçer, M. Odabaşı and A. Muezzinoğlu, "Chemical characterization of odorous gases at a landfill site by gas chromatography-mass spectrometry", *J Chrom A*, vol 1122, pp. 222-229, 2006.
[262]. A. Muezzinoglu, "A study of volatile organic sulfur emissions causing urban odors", Chemosphere, vol. 51, pp. 245-252, 2003.
[263]. F. Karaca, "Istanbul'un tarihi yarımadasında yüzey yayılım profilinin araştırılması", *Hava Kirliliği Araştırmaları Dergisi*, vol. 1, pp. 53-65, 2012.
[264]. E. Woolfenden, "Sorbent-based sampling methods for volatile and semi-volatile organic compounds in air Part 1: Sorbent-based air monitoring options", *J Chrom A*, vol. 1217, pp. 2674-2684, 2010.

ICENS
INTERNATIONAL CONFERENCE ON ENGINEERING AND NATURAL SCIENCES
24-28 May 2016 /Sarajevo

Indoor Particle Size Distribution and Ionic Content of Particles in the Laboratory of ISTAC Composting Facility

Arslan Saral[*54], S. Levent Kuzu[1], ġenol Yıldız[2]*

Abstract

Particulate matter can be generated through several processes. Formation processes determines the size distribution of the particles. The size distribution gives us important data about the fate of the particles. Composition of the particulate matter includes forensic about their actual sources. The aim of this study is to determine the impact of composting process to laboratory indoor air quality in close proximity to composting process. For this purpose, sampling was conducted at two different points; one of them wass inside the laboratory, whereas the other one was in the composting facility.

A low volume cascade impactor was used to collect particulate matter according to their sizes. The impactor was operated for one week at each sampling point. Particles of 10 µm was dominant in the composting facility. The dominant particle size was 5.8 µm inside the laboratory. Particles were ultrasonically extracted in deionized water in order to determine ion concentrations. Ions were quantified in Dionex ICS-3000 ion chromatograph. Ca^{+2}, NH_4^+ and SO_4^{-2} were investigated. NH_4^+ and SO_4^{-2} had highest share in the finest size fraction at both laboratory and plant. Particles of 3.3 µm were enriched with Ca^{+2}. Biological decomposition products were effective in the ionic composition of the fine particles, whereas mechanically generated dusts formed the coarse particle fraction.

Keywords: Particle size distribution, ionic content, active sampling

128. INTRODUCTION

Particles in ambient air is among the major pollutants. They referred in three maim groups, which are nuclei mode, accumulation mode, and coarse mode [1]. Nuclei mode are occurred from primary formed gasses, latter they are accumulated to form accumulation mode particles. Accumulation mode particles are usually regarded to be at the proximity of 1 µm aerodymamic size. The size with the highest size is referred as coarse mode. Particle sizes bigger than 2.5 µm are considered as coarse mode. The coarse mode particles are generated through mechanical formation. This formation can either be from industrial activities or from abrasion effect of the wind. Combustion and biological activities generate fine particles (particle diameter less than 2.5 µm). The data of particle size distribution is essential to know further insights of the particle sources. In many cases atmospheric particles exhibits bi-modal size distribution [2]. Apart from biological activities, biological sources could yield coarse particles [3].

Particles carry forensic from their actual sources. The chemical compositions of the particles can be used to distinguish their actual sources. There are several studies, in which the researchers investigated both particle distribution and its composition for source estimations [4]-[6]. In those references studies authors have made comments about the possible sources of the origins of the particles. Additionally, chemical composition data of the particles gives an idea of their probable effects.

Composition of the size segregated particles serves critical data about their sources. In this study, it was aimed to determine the sources of indoor particle, related to their sizes.

129. MATERIALS AND METHODS

129.1. Sampling

Sampling was conducted inside the laboratory of ISTAC AS composting facility. An additional sampling point was in the composting plant in order to differentiate the sources. There was one more plant nearby, which is producing brick. Map of the study area is shown in Figure 1.

[*] *Corresponding author: Yildiz Technical University, Department of Environmental Engineering, 34220, Esenler/Istanbul, Turkey.*
saral@yildiz.edu.tr

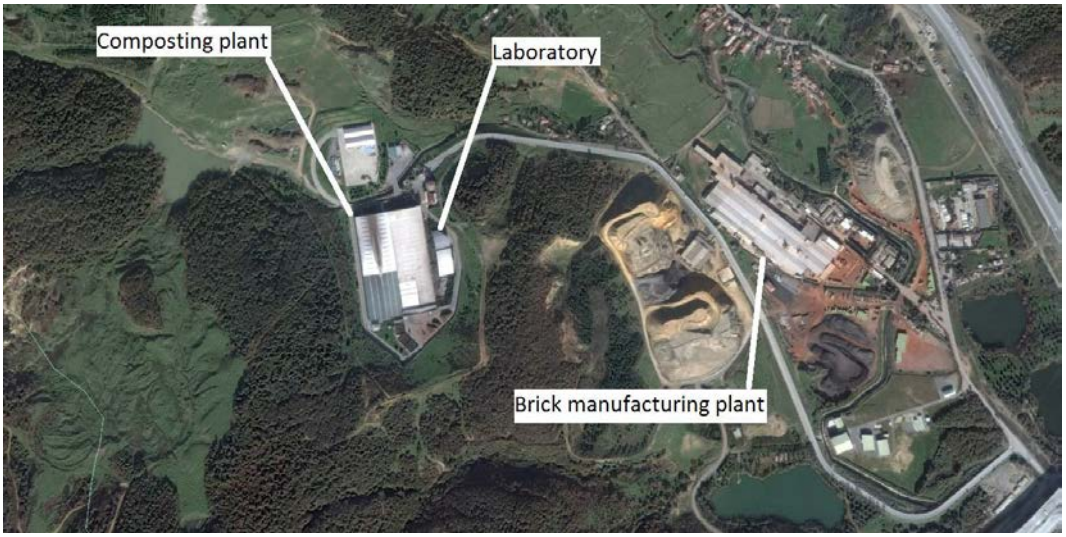

Figure 28. Study area

129.2. Sampling equipment

A low volume cascade impactor (LVCI) was used in the study to make the size segregation of the particles. LVCI was an eight-stage impactor, operated at 28.3 L/min air flow. The sampling at each point took one week in order to collect enough particle for the analyses of ions. This flowrate yielded the cut-off diameters given in Table 1.

Table 13. LVCI cut-off diameters

Stage no	Cut-off diameter (µm)
1	10
2	9
3	5.8
4	4.7
5	3.3
6	2.1
7	1.1
8	0.65

Stages of each diameter were weighed before and after the sampling in order to quantify particle mass at each stage. Further processing was applied for the determination of ions related to particles.

129.3. Sample preparation and quantification

Ionic species on the particles were eluted with deionized water [4]. 50 ml of water was used to collect all of the ions on the particles. The conductivity of the deionized water was 18.2 M.ohm.cm^{-1}. Prepared water samples were taken to vials for quantification in an ion chromatograph. The quantification results gives the concentrations in liquid medium in mg.L^{-1}. This concentration was multiplied with 50 mL to find the mass of ions at each stage.

130. RESULTS AND DISCUSSION

Particle sampling was performed inside the laboratory and plant environments with the LVCI. Particle size distribution data was gathered and source profile was investigated with the achieved particulate matter size data. The modal size distribution inside the laboratory was shown in Figure 2.

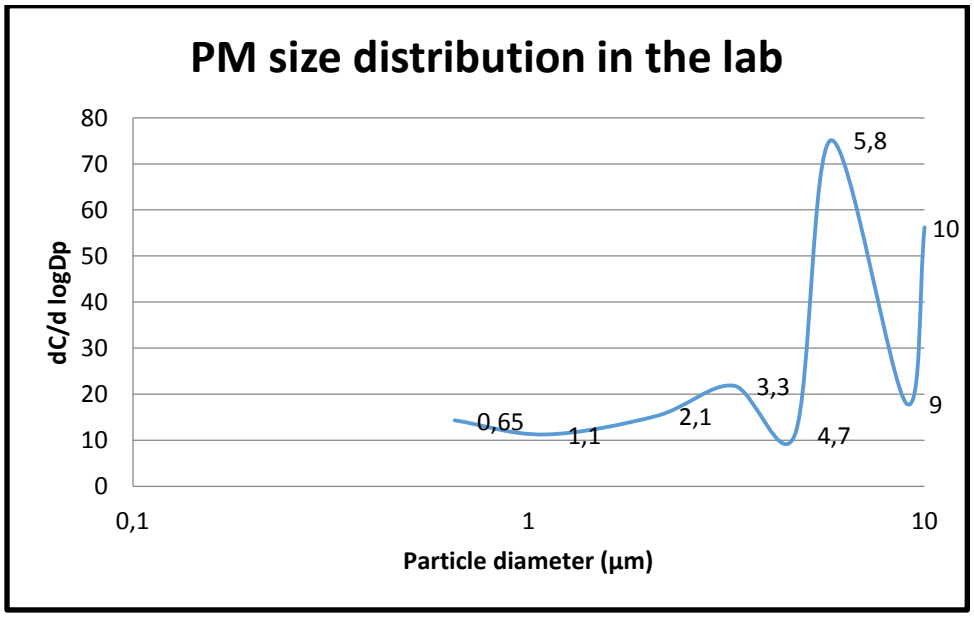

Figure 2. Particle size distribution inside the laboratory

Two peaks were observed. one of them wa at 5.8 µm, whereas the other one was at 3.3 µm. There was not an elevated trend below 1 µm particle size. It was thought that particles having diameter less than 1 µm is released from the plant. However, an additional sampling was required in order to verify this claim inside the plant. The particle size distribution inside the plant was shown in Figure 3.

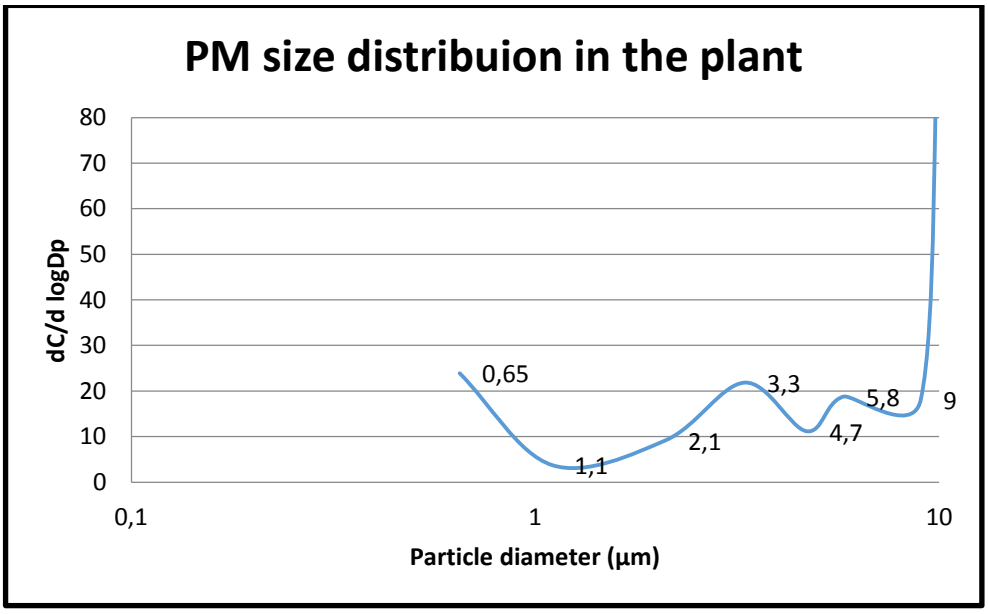

Figure 3. Particle size distribution inside the plant

In this case, there is an important increase below 1 µm particle size. This was the expected case in accordance with the nature of the process in the composting plant. Either of the samplings were shown in Figure 4 in order to make a comparison.

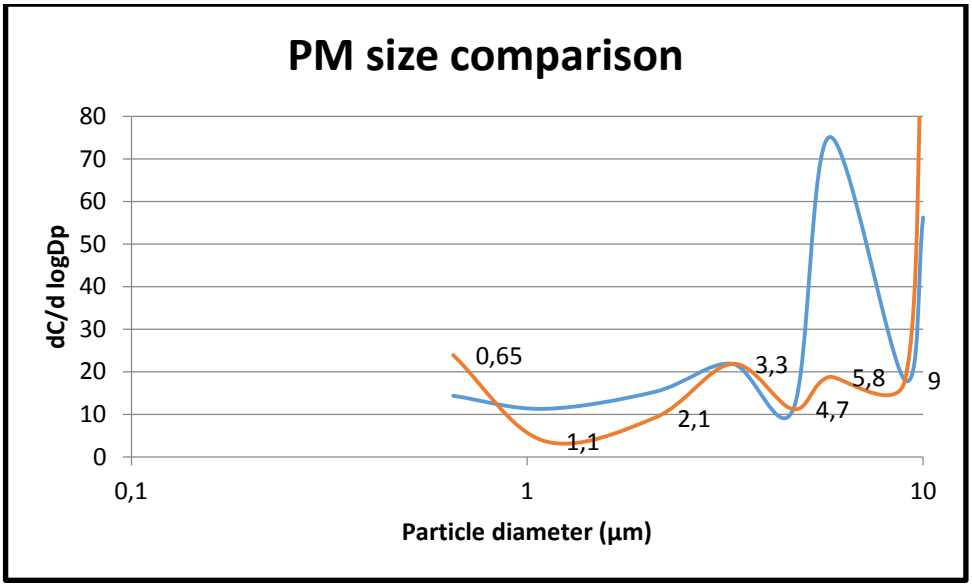

Figure 4. Comparison of particle size distribution in the plant and the laboratory

The line with blue color shows the distribution inside the laboratory, whereas the line with red color shows the distribution inside the plant. It is observed that major and minor peaks were observed at the same stages in both of the cases. However, their dominancy were different from each other. This fact tells us that same source or sources affect the two sampling points. Further comments can be made according to compositional results.

Air conditioning system is present to supply air to laboratory. The air moving to the system is pre-filtered. However it is seen that particles of 5.8 µm was from the major fractions inside the lab. It can be inferred that this filtration system is not working properly to remove the coarse particles. Coarse particles are usually originated from naturally blown dusts. In order to clarify this point, Ca^{+2} ions were investigated.

The distribution of Ca^{+2} ions at each stage is given in Figure 5.

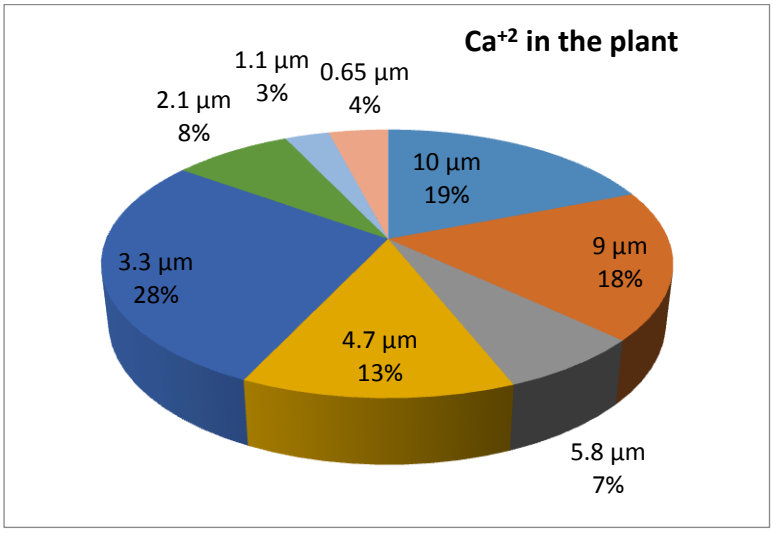

(a)

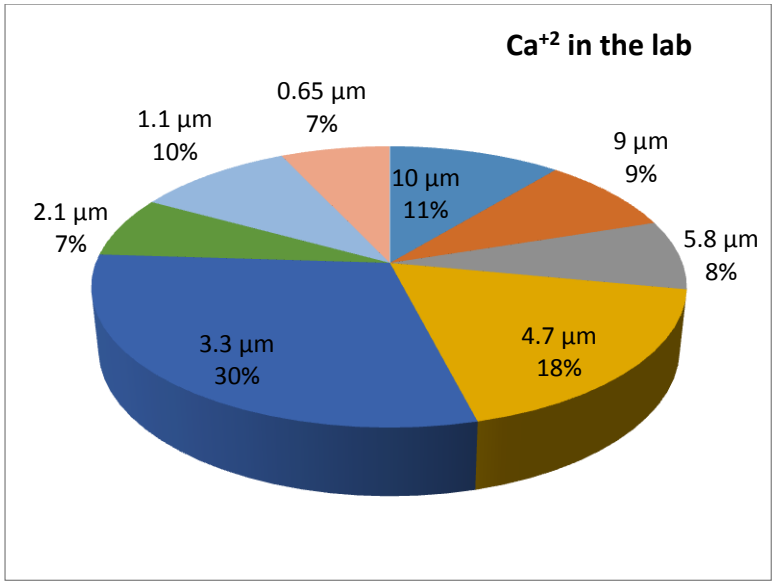

(b)

Figure 5. (a) Ca^{+2} distribution among different stages in plant (b) Ca^{+2} distribution among different stages in lab

Sodium, potassium, and magnesium ions were also quantified along with calcium ions. However there was no difference among the distribution of these species. So that, it was decided not to include them in the paper. Calcium was included as a representer to the major ionic group. Coarse particles were dominated with these ions. The previous comment during the particle size distribution, is verified according to these results.

Organic matter originated compounds such as sulfate and ammonium was enriched in the fine particle mode at both plant and the laboratory. Ammonium was solely in the fine fraction inside the plant, where dense biological activity occurs. Particles less than 0.65 µm had contribution over 80%. Distribution of the ammonium and sulfate ions among the particle sizes are shown in Figure 6.

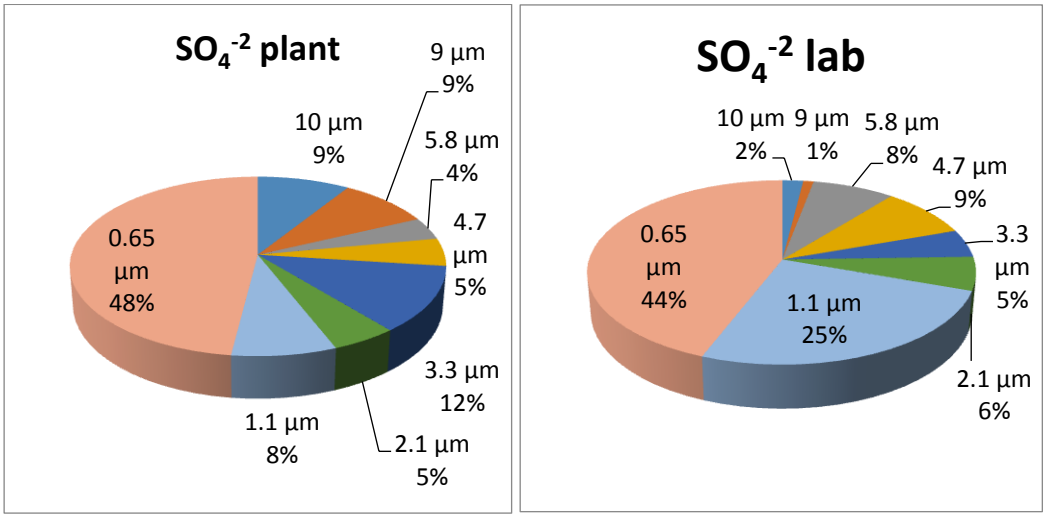

(a) *(b)*

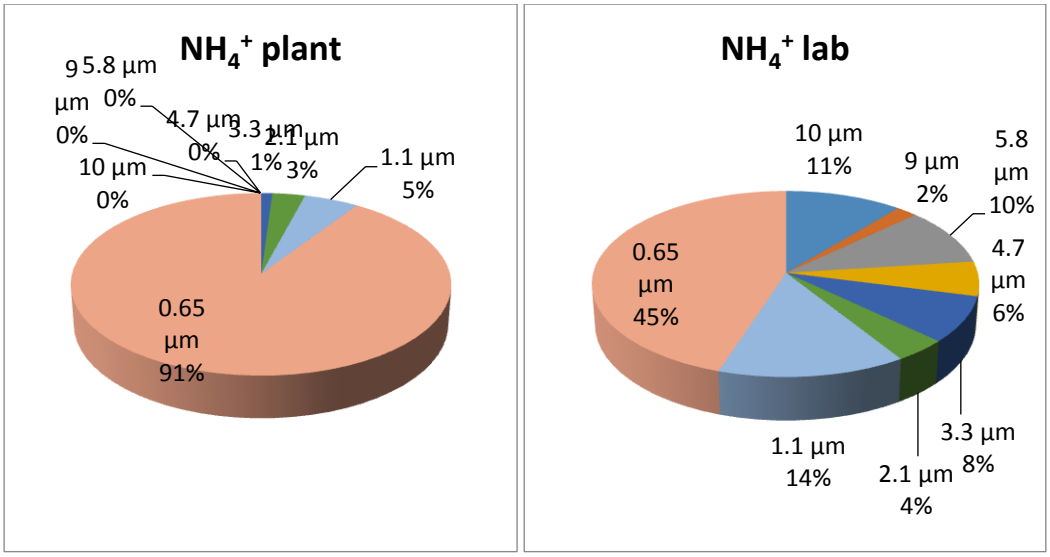

(c) *(d)*

Figure 6. (a) SO4-^{2} PM distribution in the plant (b) SO4-^{2} PM distribution in the lab (c) NH_4^+ PM distribution in the plant d) NH_4^+ PM distribution in the plant

Accumulation particles, which are equal to or less than 1 µm, are occurred through the condensation of primary gasses and humidity in the air boost their formation. Sulfate ion can further lead to acidic aerosol forms. This can cause damage on laboratory devices. According to above results, it is inferred that air conditioning is not efficiently supplied.

131. CONCLUSIONS

In this study, air sampling was conducted at two locations; inside the laboratory and composting plant. Sampling was realized by LVCI. Particle size distributions in both of the sites were revealed. Particles of 3.3 µm mass median particle diameter were mostly enriched by calcium ion. This shows the contribution from resuspension of mineral dusts. The nearby brick factory could cause this contribution. Ammonium and sulfate ions were highly enriched in fine particles at both laboratory and composting plant. However, ammonia had much more contribution from the plant itself. Almost entire ammonium ions were below 1 µm. Sulfate content of indoor particles can lead to corrosion of laboratory devices. Some suggestions are listed below in order to improve the quality of indoor air inside the laboratory.

- HEPA filters should be used to improve the filtration capacity at the inlet of the fan system. Additional carbon fitler could reduce the organic content of the air and breakthrough tests should be performed to determine the capacity of carbon filters.
- Air fed to the conditioning system should be taken from the North or East of the laboratory in order to prevent direct contamination from composting process.
- Positive pressure should be present. So that, leaks from the outside air can be prevented.
- Sufficient circulation should be present with higher air fan power.
- Dehummidification of the indoor air is essential.
- Recirculation (close circuit system) should be present in the air conditioning system.

ACKNOWLEDGMENT

The authors would like to acknowledge ISTAC AS for their technical support during the sampling stage.

REFERENCES

[265]. K. T. Whitby, W. E. Clark, V.A. Marple, G.M. Sverdrup, G. J. Sem, K. Willeke, B. Y. H. Liu, D.Y.H. Pui, " Characterization of California aerosols—I. Size distributions of freeway aerosol", *Atmos Environ*., vol. 9, pp. 463–482, 1975
[266]. L. Morawska, S. Thomas, M. Jamriska, G. Johnson, "The modality of particle size distributions of environmental aerosols", *Atmos Environ,* vol. 33, pp. 4401–4411, 1999
[267]. J. H. Seinfeld and S. N. Pandis, *Atmospheric Chemistry and Physics: from air pollution to climate change*, 2nd ed., Berlin, USA: Wiley, 2006.
[268]. S. L. Kuzu, A. Saral, S. Demir, G. Summak, G. Demir, "A detailed investigation of ambient aerosol compositions and size distribution in an urban atmosphere", *Environ Sci Pol Res*, vol. 20, pp. 2556-2568, 2013
[269]. Ü. Alver Şahin, K. Scherbakova, B. Onat, "Size distribution and seasonal variation of airborne particulate matter in five areas in Istanbul, Turkey", *Environ Sci Pol Res*, vol. 19, pp. 1198-1209, 2012
[270]. B. Onat, Ü. Alver Şahin, C. Bayat, "Assessment of particulate matter in the urban atmosphere: size distribıtion, metal composition and source characterization using principal component analysis", *J. Environ Mon*., vol.14, pp. 1400-1409, 2012

BIOGRAPHY

Prof. Dr. Arslan SARAL was born in 1969, in Trabzon. He completed his bachelor of science in Bogazici University in the Department of Chemical Engineering, in 1991. He took his master of science and philosophy of doctorate degrees, respectively in 1994 and 1999 from Yildiz Technical University Environmental Engineering Department. Since then, he has given lectures on the topic of environmental chemistry, air pollution, and air pollution control. He has published several papers in the field of air pollution and control.

ICENS
INTERNATIONAL CONFERENCE ON ENGINEERING AND NATURAL SCIENCES
24-28 May 2016 /Sarajevo

Temporal Variation of Organic and Inorganic Carbon Transport from the Southeastern Black Sea (Trabzon Province) Rivers

Sinan NACAR[55], Adem BAYRAM[2], Uğur SATILMIġ[3]

Abstract

The input of organic carbon being an indicator of organic pollution as well to the oceans provides crucial sources in food web of estuarine ecosystems. The Black Sea surrounded by six countries is the world's largest land-locked inland sea and its total length of the coastal zone is 4,340 km, of which 1,400 km is shared by Turkey. The Black Sea receives annually a considerable freshwater input from the rivers carrying substantial loads of organic matter, nutrients and anthropogenic pollutants and the coastal parts are highly affected by eutrophication.

The aim of this study is to determine the temporal variability of total carbon (TC), total organic carbon (TOC) and total inorganic carbon (TIC) carried from the eight Turkish streams to the Black Sea. The streams included in this study are Ağasar, Fol, Galanima, Değirmendere, Yomra, Karadere, Manahoz and Solaklı, within the boundaries of Trabzon Province, the most densely populated city located in the coast of Southeastern Black Sea. The water sampling studies have been monthly conducted in one station, which was selected at the point where the stream is discharged into the Black Sea, for each stream during a period of twelve months between March 2015 and February 2016.

Considering the mean values for each stream, TOC concentration fluctuated from 1.59 to 25.90 mg/L and the Stream Yomra being under immense pressure due to various kinds of anthropogenic activities among which sand and gravel mining is the most disastrous one was the most critical one. The streams showed high TC and TIC yields during the summer and autumn months, corresponding to the seasonal trend of stream discharge. It was also found that TIC comprised the majority of the total carbon concentration, with mean percentages ranging from 68.9% to 84.06% in all of the streams.

Keywords: *Black Sea, Total Organic Carbon, Trabzon streams*

132. INTRODUCTION

Water plays a vital role in all aspects of human and ecosystem survival. Unconsciously pollution of water of the rivers, lakes, seas and drinking water supplies are endangering life on earth day by day. Human activities like improper disposal of municipal and industrial effluents and indiscriminate applications of agrochemicals in agriculture are the main factors contributing to the deterioration of water quality [1]. An estimated 2 million tons of sewage and other effluents are discharged into the world's waters every day. In developing countries where over 90% of raw sewage and 70% of untreated industrial wastes are dumped into surface water sources the situation is worse [2].

The Black Sea has been increasingly threatened by nutrients carried by rivers over the past decades as a result of discharge of domestic wastes from coastal settlements and industrial areas [7]. The major rivers following into the Black Sea and their discharges are: Danube (203 km^3/yr), Dniper (54 km^3/yr), Dniesta (9.3 km^3/yr), Don (28 km^3/yr) and Kuban (13 km^3/yr). In addition to these rivers, a large number of smaller rivers along the Turkish and Bulgarian coasts contribute another 28 km^3/yr to the water budget of the sea [4]. There are several studies were made by researchers on the effect of different domestic and industrial discharges on the water quality of the Black Sea Coast of Turkey [3], [5], [6], [8], [9], [11], [13], [16], [17]. Also variation in the quality and quantity of river water has been studied worldwide in recent years [10], [14], [15].

The TC, TIC and TOC in surface waters and wastewaters are important analytical parameters describing the total content of all substances containing carbon. In practice, the TOC originated from natural and anthropogenic sources, and even if it is not directly responsible for dangers on human health, its determination is important for any kind of water that is used by public [19]. Researchers must consider that TOC depends on the kind of the measured water, but it is also affected by several parameters such as temperature, salinity, pH, microbial activity and surrounding vegetation [21].

The aim of this study is to determine the TC, TIC and TOC carried by streams located within the boundaries of Trabzon, the biggest province of the Eastern Black Sea Basin (EBSB), into the Black Sea.

133. MATERIALS AND METHODS

2.1. Study Area

[1] *Corresponding Author: Karadeniz Technical University, Faculty of Engineering, Department of Civil Engineering, 61080, Trabzon/Turkey, sinannacar@ktu.edu.tr*

[2] *Karadeniz Technical University, Faculty of Engineering, Department of Civil Engineering, 61080, Trabzon/Turkey, abayram@ktu.edu.tr*

[3] *Karadeniz Technical University, Faculty of Engineering, Department of Civil Engineering, 61080, Trabzon/Turkey, usatilmis@ktu.edu.tr*

The Black Sea is a semi-enclosed sea, whose only connection to the world's oceans is the narrow Bosphorus Channel. The area of Black Sea is $4.2*10^5$ km^2 with maximum and average depths of 2200 and 1240 m, respectively. Ninety per cent of its water mass is anoxic, thus it contains the world's largest anoxic water mass [18]. To the south, it is connected to the Mediterranean through the Bosphorus, which is the world's narrowest strait, with an average width of 1.6 km, depth of 36 m and a total length of 31 km. To the north, the Black Sea is connected with the Sea of Azov through the shallow Kerch Strait, which has a depth of less than 20 m. The Black Sea is surrounded by six countries located in Europe and Asia: Bulgaria, Georgia, Romania, Russia, Turkey and Ukraine (Figure.1). In fact, the Black Sea is influenced by 17 countries, 13 capital cities and some 160 million people [3].

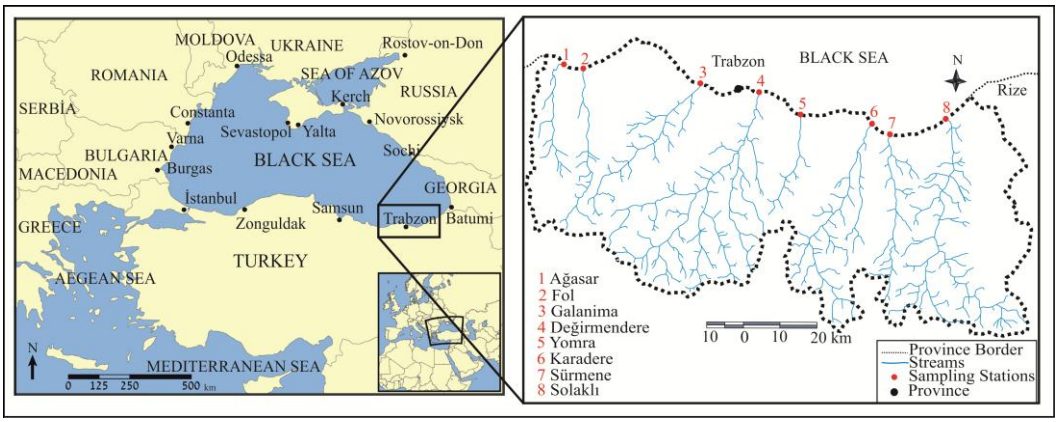

Figure 29. Study area and locations of the sampling stations

The ESBS is one of the most important hydrological basins in Turkey, and it is a major part of Caucasus Ecological Region together with Çoruh and Aras Basins [19].

Trabzon, the biggest province located in the ESBS of Turkey, lies between the 38° 30' and 40° 30' eastern longitudes and 40° 30' and 41° 30' northern latitudes. Trabzon with the area of 4,664 km^2 is a coastal city situated on the slope of the hills. The climate characteristic of the northeast coastal region of Turkey is rainy and humid. Trabzon has a typically moderate climate that is neither too warm in summers and nor too cold in winters [20].

There are many streams flowing in the boundaries of Trabzon into the Black Sea. A total of eight streams and one monitoring station for each stream were selected along the coast of Trabzon Province at the Eastern Black Sea Region of Turkey. The streams studied from the west to the east are Ağasar, Fol, Galanima, Değirmendere, Yomra, Karadere, Manahoz and Solaklı, respectively.

These streams drain the major rural, agricultural, and urban of the Eastern Black Sea Region of Turkey and discharge into the Black Sea. The main nutrient loads include domestic wastewaters, agricultural runoff and industrial effluents. The Coordinates for each station are given in Table 1.

Table 1. Coordinates of stations

Station	N			E		
Ağasar	41˚	03'	26.14"	39˚	13'	07.51"
Fol	41˚	02'	48.69"	39˚	16'	40.22"
Galanima	41˚	01'	07.80"	39˚	35'	46.20"
Değirmendere	41˚	00'	06.00"	39˚	45'	25.80"
Yomra	40˚	57'	10.80"	39˚	52'	03.00"
Karadere	40˚	56'	05.40"	40˚	03'	38.40"
Sürmene	40˚	54'	52.80"	40˚	06'	41.40"
Solaklı	40˚	56'	35.40"	40˚	16'	01.80"

2.2. Water Sampling

Water samples were collected at all eight monitoring stations monthly from March 2015 to February 2016. The surface water samples were collected in 1.0 L polyethylene bottles. Plastic sample bottles, pre-cleaned with 1M HNO_3 and rinsed with double-distilled water, were used to collect the water samples. At the point of collection, bottles were rinsed several times with water of streams and transferred to the laboratory in coolers containing icecap to reducing the degradation of samples before

analysis. At the laboratory located in Karadeniz Technical University, Hydraulic Laboratory, the water samples were immediately analyzed within 12 h of sampling.

2.3. Water Analysis

TC, TIC and TOC content of the water samples were determined with a UV-vis spectrophotometer (DR 5000) by using its cuvette-test (LCK 380, TC), according to Standard Methods [22]. TOC is calculated as the difference between the TC and TIC values. These analyses were carried out in triplicate in room temperature (21 ± 2˚C) and their mean values were presented.

134. RESULTS AND DISCUSSION

The basic statistics of TC, TIC and TOC content (mg/L) for each studied stream are given in Table 2.

3.1. The Ağasar Stream

The TC levels of the Ağasar Stream show that the content varies between 19.10 mg/L in November and 41.90 mg/L in October. The TIC content changed between 14.20 mg/L in April and 34.60 mg/L in October. Also, the TOC content of the Ağasar Stream changed between 1.59 mg/L in November and 9.06 mg/L December. TC and TIC concentrations were highest during a three-month period from August to October.

3.2. The Fol Stream

For the Fol Stream, the content of TC varies between 22.60 mg/L in April and 41.60 mg/L August. The TIC levels of Fol Stream show that the content varies between 16.60 mg/L in April and 34.30 mg/L in October. The minimum TC and TIC content were determined in April. The TOC levels of the Fol Stream show that the content varies between 6.04 mg/L in May and 15.40 mg/L in February. TC and TIC content of the Fol Stream were highest during a three-month period from August to October. Also, the lowest content of TC, TIC and TOC were determined from March to May.

3.3. The Galanima Stream

Considering the yearly mean values for the Galanima Stream, the TC concentration was determined as 42.44 mg/L with a range of 27.40-61.60 mg/L, and TIC concentration 35.68 mg/L with a range of 24.40-55.50 mg/L. The lowest TC concentration was observed in April and the highest TC concentration was observed in August. The lowest TIC concentration was observed in April and the highest TIC concentration was observed in August. The TOC concentration of the Galanima stream was measured as 6.77 mg/L and, the lowest TOC concentration (1.60 mg/L) were observed in November and the highest TOC concentration (12.70 mg/L) were observed in December. TC, TIC and TOC concentrations were lowest during a three- month period from March to May. Considering the all streams, it was seen that the Galanima Stream had maximum TC and TIC concentrations.

3.4. The Değirmendere Stream

For the Değirmendere Stream, the yearly average TC content was determined as 38.76 mg/L with a range of 20.50 mg/L (June)-57.50 mg/L (January). Yearly average TIC concentration was 29.43 mg/L with a range of 17.20 mg/L (May-June) - 48.30 mg/L (September). The yearly average TOC content of the Değirmendere Stream was determined as 9.33 mg/L. The minimum TOC concentration (3.25 mg/L) was measured in June and, the maximum TOC (21.85 mg/L) concentration was measured in January. TC and TIC content of the Değirmendere Stream were highest during a three-month period from August to October. Also, the lowest content of TC, TIC and TOC were determined from April to Jun.

3.5. The Yomra Stream

The TC levels of the Yomra Stream show that the content varies between 16.20 mg/L in July and 73.10 mg/L in September. The TIC content changed between 10.50 mg/L in July and 52.60 mg/L in Jun. Also, the TOC content of the Yomra Stream changed between 4.06 mg/L January and 25.90 mg/L in March. TC and TIC content of the Değirmendere Stream were highest during a three-month period from August to October. Considering the all streams, it was seen that the Yomra Stream had maximum TOC concentration.

3.6. The Karadere Stream

For the Karadere Stream, the yearly average TC concentration was determined as 24.64 mg/L with a range of 15.10 mg/L (April)-35.70 mg/L (October), and yearly average TIC concentration 19.88 mg/L with a range of 12.50 mg/L (April)-30.80 mg/L (October). The yearly average TOC concentration value of the Karadere Stream was measured as 4.76 mg/L and, the lowest TOC concentration value (2.26 mg/L) were observed in May and the highest TOC concentration value (8.08 mg/L) were observed in December. TC, TIC concentrations were highest during a three month period from August to October. Also, TC, TIC and TOC concentration were lowest during a three-month period from April to Jun.

3.7. The Sürmene Stream

For the Sürmene Stream, the yearly average TC value was determined as 17.53 mg/L with a range of 14.50 mg/L (February)-24.30 mg/L (October). Yearly average TIC concentration value was 13.59 mg/L with a range of 10.50 mg/L (May) - 20.70 mg/L (October). The yearly average TOC content of the Sürmene Stream was determined as 3.96 mg/L. The minimum TOC concentration (2.20 mg/L) was measured in March and, the maximum TOC (5.44 mg/L) concentration was determined in

December. TC, TIC concentrations were highest during a three month period from August to October. Considering the all streams, it was seen that the Sürmene Stream had minimum TC, TIC and TOC concentrations.

3.8. The Solaklı Stream

The TC levels of the Solaklı Stream show that the content varies between 14.20 mg/L (April) and 27.90 mg/L (October). The TIC content changed between 11.40 mg/L in April and 22.90 mg/L in October. Also, the TOC content of the Solaklı Stream changed between 2.75 mg/L April and 6.05 mg/L March. TC, TIC and TOC concentration were highest during a tree-month period from August to October and lowest during a three month period from April to Jun in the Solaklı Stream.

Table.2. Basic statistics of TC, TIC and TOC content monitored for the Southeastern Black Sea Streams

		Ağasar	Fol	Galanima	Değirmendere	Yomra	Karadere	Sürmene	Solaklı
TC (mg/L)	Mean	27.18	32.84	**42.44**	38.76	38.93	24.64	**17.53**	20.89
	Min	19.10	22.60	27.40	20.50	16.20	15.10	14.50	14.20
	Max	41.90	41.60	61.60	57.50	73.10	35.70	24.30	27.90
	SD	7.05	7.07	8.65	12.72	17.88	5.84	2.93	4.39
TIC (mg/L)	Mean	20.60	24.50	**35.68**	29.43	26.83	19.88	**13.59**	16.75
	Min	14.20	16.60	24.40	17.20	10.50	12.50	10.50	11.40
	Max	34.60	34.30	55.50	48.30	52.60	30.80	20.70	22.90
	SD	6.50	6.15	7.48	9.64	13.14	5.05	2.97	3.76
TOC (mg/L)	Mean	6.58	8.34	6.77	9.33	**12.14**	4.76	**3.96**	4.13
	Min	1.59	6.04	1.60	3.25	4.06	2.26	2.20	2.75
	Max	9.06	15.40	12.70	21.85	25.90	8.08	5.44	6.05
	SD	2.06	3.09	3.18	5.18	6.77	1.68	1.03	1.07

135. CONCLUSIONS

In this study the temporal variability of TC, TIC and TOC carried from the eight streams namely Ağasar, Fol, Galanima, Değirmendere, Yomra, Karadere, Manahoz and Solaklı, within the boundaries of Trabzon Province, to the Black Sea was investigated. The water sampling studies were monthly conducted in one station, which was selected at the near point where the stream is discharged into the Black Sea, for each stream during a period of 12 months between March 2015 and February 2016. The TC, TIC and TOC content of the water samples collected from eight stations along the coast of the Southeastern Black Sea were determined and evaluated. It was found that:

- The minimum TC concentration is determined in Solaklı Stream in April and the maximum concentration is determined in September in Yomra Stream. The minimum TIC concentration is determined in Yomra and Sürmene Streams and the maximum concentration is determined in August in Galanima Stream. Also the minimum TOC content was determined in November in Ağasar Stream and maximum content was determined in March in Yomra Stream.
- In all station, TC and TIC content show a similar trend throughout the year; start to decrease on spring, then rise during the summer and then it reached its peak in the autumn.
- TC and TIC content of stream water were highest during a three-month period from August to October for all streams while lowest from March to May for Ağasar, Fol and Galanima and from April to Jun for Değirmendere, Karadere and Sürmene streams.
- The maximum TC and TIC content are recorded in summer and autumn seasons, due to the low precipitation, where the lowest levels are determined in winter and spring because of the heavy rainfall causing dilution. But the maximum TOC content is recorded in spring.
- Considering the yearly mean values minimum TC, TIC and TOC concentration value are determined at Sürmene Stream and maximum TC and TIC value are determined in Galanima Stream, maximum TOC concentration is determined in Yomra Stream.
- Because of being under immense pressure due to various kinds of anthropogenic activities among which sand and gravel mining the TOC concentration of Yomra was recorded very high in all months.
- It is recognized that TIC generally constitutes the majority of the TC concentration with mean percentages ranging from 68.9% to 84.06% in all streams.

REFERENCES

[271]. Azizullah, A., Khattak, M. N. K., Richter, P., & Häder, D. P. (2011). Water pollution in Pakistan and its impact on public health—a review. *Environment International*, *37*(2), 479-497.

[272]. Anonymous. World Water Day 22.03.2010; 2010. Retrieved from www.worldwaterday2010.info, United Nations.
[273]. Bakan, G., & Büyükgüngör, H. (2000). The black sea. *Marine Pollution Bulletin*,*41*(1), 24-43.
[274]. Balkas, T., Dechev, G., Mihnea, R., Serbanescu, O., & Unlueata, U. (1990). State of the marine environment in the Black Sea Region. *UNEP Regional Seas Reports and Studies,124*, 47.
[275]. Bayram, A., Onsoy, H., Bulut, V. N., & Akinci, G. (2013). Influences of urban wastewaters on the stream water quality: a case study from Gumushane Province, Turkey. *Environmental Monitoring and Assessment*, *185*(2), 1285-1303.
[276]. Boran, M., & Sivri, N. (2001). Trabzon (Türkiye) İl Sınırları İçerisinde Bulunan Solaklı ve Sürmene Derelerinde Nütrient ve Askıda Katı Madde Yüklerinin Belirlenmesi. *E.U. Journal of Fisheries & Aquatic Sciences*, 18,(3-4): 343 – 348
[277]. Bozcaarmutlu, A., Sapmaz, C., Aygun, Z., & Arinç, E. (2009). Assessment of pollution in the West Black Sea Coast of Turkey using biomarker responses in fish. *Marine Environmental Research*, 67, 167–176.
[278]. Gültekin, F., Ersoy, A. F., Hatipoğlu, E., & Celep, S. (2012). Trabzon İli Akarsularının Yağışlı Dönem Su Kalitesi Parametrelerinin Belirlenmesi. *Ekoloji*,*21*(82), 77-88.
[279]. Koklu, R., Sengorur, B., & Topal, B. (2010). Water quality assessment using multivariate statistical methods—a case study: Melen River System (Turkey).*Water Resources Management*, *24*(5), 959-978.
[280]. Kumarasamy, P., James, R. A., Dahms, H. U., Byeon, C. W., & Ramesh, R. (2014). Multivariate water quality assessment from the Tamiraparani river basin, Southern India. *Environmental Earth Sciences*, *71*(5), 2441-2451.
[281]. Tuncer, G., Karakas, T., Balkas, T. I., Gökçay, C. F., Aygnn, S., Yurteri, C., & Tuncel, G. (1998). Land-based sources of pollution along the Black Sea coast of Turkey: concentrations and annual loads to the Black Sea. *Marine Pollution Bulletin*, *36*(6), 409-423.
[282]. TSWQR (2015). Turkish Surface Water Quality Regulation. Official Gazette. no: 29327, Turkey, (in Turkish).
[283]. Varol, M., Gökot, B., Bekleyen, A., & Şen, B. (2012). Water quality assessment and apportionment of pollution sources of Tigris River (Turkey) using multivariate statistical techniques—a case study. *River Research and Applications*, *28*(9), 1428-1438.
[284]. Vieira, J. S., Pires, J. C., Martins, F. G., Vilar, V. J., Boaventura, R. A., & Botelho, C. M. (2012). Surface water quality assessment of Lis river using multivariate statistical methods. *Water, Air, & Soil Pollution*, *223*(9), 5549-5561.
[285]. Wan, J., Bu, H., Zhang, Y., & Meng, W. (2013). Classification of rivers based on water quality assessment using factor analysis in Taizi River basin, northeast China. *Environmental Earth Sciences*, *69*(3), 909-919.
[286]. Bulut, V. N., Bayram, A., Gundogdu, A., Soylak, M., & Tufekci, M. (2010). Assessment of water quality parameters in the stream Galyan, Trabzon, Turkey. *Environmental Monitoring and Assessment*, *165*(1-4), 1-13.
[287]. Alkan, A., Serdar, S., Fidan, D., Akbas, U., Zengin, B., & Kilic, M. B. (2013). Physico-Chemical Characteristics and Nutrient Levels of the Eastern Black Sea Rivers. *Turkish Journal of Fisheries and Aquatic Sciences*, *13*, 847-859.
[288]. Sorokin, Y. I. (1983) The Black Sea. In Estuaries and Enclosed Seas. Ecosystems of the World, Vol. 26, ed. B. H. Ketchum, pp. 253 – 291. Elsevier, Amsterdam.
[289]. Bayram, A., Onsoy, H., Akinci, G., & Bulut, V. N. (2011). Variation of total organic carbon content along the stream Harsit, Eastern Black Sea Basin, Turkey. *Environmental Monitoring and Assessment*, *182*(1-4), 85-95.
[290]. Demirci, E., & Cuhadaroglu, B. (2000). Statistical analysis of wind circulation and air pollution in urban Trabzon. *Energy and Building, 31*, 49–53.
[291]. Visco, G., Campanella, L., & Nobili, V. (2005). Organic carbons and TOC in waters: an overview of the international norm for its measurements. *Microchemical Journal, 79(1),* 185-191.
[292]. APHA (1992). Standard methods for the examination of water and wastewater, 18th ed. Washington, DC: American Public Health Association.

New Technology Gravity Seperators in Mineral Processing

Ömer Canıeren[1], Cengiz Karagüzel[2], Ahmet Aydın[3]

Abstract

In mineral processing minerals physical, chemical and physicochemical features are utilized in order to seperate minerals from each other with industrial value and non industrial value. The specific gravity of a physical property of minerals is the most utilizied properties in mineral processing. Considering the industrial application, many gravity separators are available the used of this propertie difference. Especially it has seen that the development of new technology device intended for slime size liberalized minerals to be gained by this method.

In general, water, rarely heavy (dense) fluid, and sometimes used the air as the fluid medium in enrichment of the specific gravity difference. With this method, the separation of mineral particles are provided through specific gravity difference of particles, movement velocity of fluid medium, specific gravity and vizcosity of fluid medium, the structure and operation of the separator device, general hydrodynamic features. It has seen overmuch studies in literature related to selective separation work with different gravity separators. In these studies the parameters which effect the separation examined in detail, it has been studied to the effect of effective parameters on gain efficiency and content.

In this study, It was investigated gravity separators currently used in industrial plants and new tehnology gravity seperator. Also, the existing applications of this separator was investigated for samples of voriuos ore.

Keywords: mineral processing, beneficiation, gravity separators.

1.INTRODUCTION

Gravity separation is a beneficiation method which is utilizingspecific gravity of the mineral particles in the method. In gravity seperation, generally water, for some application heavy fluid and air are used as a fluid medium. Specific gravity of particles, movement speed in the fluid medium and their behavior, particle size, fluid density, viscosity and working conditions of separator device are effective performans of gravity separation. This method is used in enrichment of many minerals in the industry due to low investment and operating cost besides being environmentalist. Conventional methods in the enrichment by specific gravity of minerals are consist of dense medium separation, jig separation, enrichment in the laminer fluid flowing medium, Reichert cone, spiral concentrator (Humprey) and shaking table [1]. Gravity method is the cheapest method among the methods utilized in ore beneficiation. If the liberations of constituents is obtained by enough fragmentation and if the difference in specific gravity is high enough (Taggart criteria), gravity method is the first method to be chosen. Nonetheless, gravimetric separation efficiency can be decreased in fine particles (around 100um). Recently, development of new technology gravity separators (Falcon concentrators, Knelson concentrators, multi gravity separator, Kelsey jig, and the others separators; FGX separator, Floatex density separator, continuous vibrated gas-fluidized bed separator) is followed in the literature towards separation of particles to be liberated in fine sizes. In recently developed gravity separators, it is seen that medium density is changed and extra forces (centrifugal force, vibration force, air pressure) to increase the effect of gravity force are utilized (e.g. [2], [3], [4]).

In this study, industrial feasibility possible, economic and environmentalist new technology gravity separators are investigated comparatively.

2.NEW TECHNOLOGY GRAVITY SEPARATORS

135.1. 2.1. Knelson Concentrator

Knelson concentrator utilized in obtaining fine and very fine heavy minerals, which is used pre-enrichment purpose in gold and silver mining generally, whereas Knelson concentrator is used in valuable minerals of recovering from tailings in a limited number of works (e.g. [5], [6], [7], [8]). Centrifugal force equal to 60 times of gravity force is applied to particles in this separator which benefits from centrifugal force effectively. Centrifugal force (Fc) in Knelson separator is formulized as below [e.g. [5], [7]]:

$Fc = (\Pi / 6) * (dp)^3 * (\delta s - \delta 1) * ro * w^2$

Here;

Fc: Centrifugal force, $gr.cm.s^{-2}$

ro : Distance change from particle axis of rotation to its current location, cm

dp : Particle diameter, cm

δs : Particle density, $gr.cm^3$

δl : Medium density, $gr.cm^3$

w : Particle angular speed, $radyan.sn^{-1}$

Heavy and light products, feed in to the device as a pulp are separated from each other by centrifugal force. In this method, while light particles taken from products overflowed from separating cone, whereas, heavy particles accumulate on separating cone sides as layers and are taken as concentrate (Fig.1). Centrifugal force, particle size, feeding speed, wash water amount, sample acquiring time and solid concentration are known effective working parameters in Knelson separator

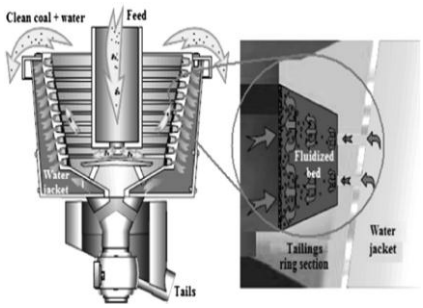

Fig. 1*. Schematic* view *of the Knelson concentrator [3].*

Laplante and et al, (1996), [6] recovered free gold from a high grade stock sample by using knelson centrifugal separator . In this study; feed rate, density, size distribution and fluidizing water pressure systematically were tested. In this study authors described that the recovery decreased slightly with decreasing fluidizing water pressure.

Greenwood and et al., (2013), [9] investigated the operating parameters of laboratory scale Knelson Concentrator on a dry basis. In this study, air was used as the fluidising medium in order to separate tungsten from silica in a synthetic ore (1%w/w tungsten), and compared to wet process. The wet processing attained a mean tungsten recovery of 94.92% (tungsten grade: 30.96%). The dry processing at two different fluidising air pressures attained a recovery of 78.53% (tungsten grade: 6.32%) and 69.90% (tungsten grade: 15.57%) at 2 psi and 3 psi respectively

Kıyak and Karaguzel, (2015) [10] investigated the effect of operating parameters such as;grinding time, particle size, G force (centrifugal force), water flow ve solid ratio for chromite tailings which contain 5% Cr_2O_3.content. In this study chromite concentrate obtained with 20% Cr_2O_3 content and 75% chromite recovery.

135.2. 2.2. Falcon Concentrator

Falcon concentrator is a gravity separator such as knelson concentrator where centrifugal force is effective. But the recovery mechanism of falcon concentrator has a little difference according to knelson. The falcon has higher rotation speed than knelson. The rotational speed of the bowl change between 0 G to 300 G by [11]. Capable of operating at a high speed of rotation and hence ‗g'' force, it enables more successfully separating for fine particles and enables higher capacity and low energy in accordance to knelson concentrator. [12]. The shematic view of the Falcon is given Fig 2.

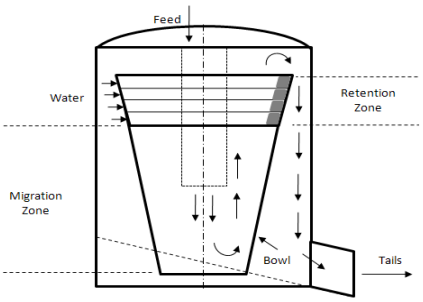

Figure 2. Schematic view of a Falcon Centrifugal Concentrator [13].

Falcon concentrator currently used in recovery of gold, silver, coal and industrial minerals. It has some advantages such as, able to use particles in size down to 15–20 micometer, relatively simple mechanically and robust, relatively high capacity, relatively low operator attention. On the other hand, generally low upgrading ratio (typically 2 to 1)and unable to see separating surfaces due to closed system [14].

Lu, et al., (2015), [15] investigated to the beneficiation of a tungsten ore bythe Falcon Concentrator and high-gradient magnetic concentrator (SLon VPHGMS). The WO_3 recovery was obtained 81.02% by using only Falcon. On the other hand

the recovery was obtained 86,72 % by using magnetic seperator due to a significant magnetic susceptibility differences between wolframite and arsenopyrite.

Liu and et al., (2006), [16] conducted to along with recovery of heavy metal from oil sand tailings by using Falcon concentrator.. Pre enrichment test results shown the recovery of the heavy minerals were 85%. But the concentrate has contain 30% bitumen. Authors recommended with improved liberation the recovery of the residual bitumen into the concentrate could be further reduced.

Oruc and et al, (2010), [17] studied to recover ultra fine coal from talings by using Falcon. Various operating and design conditions such as bowl speed (G force), water pressure, pulp solid ratio and pulp feed rate were investigated. In this study, ahydrocyclone was used for pre-enrichment with the Falcon concentrator. The test results was shown that Falcon concentrator and hydrocylon obtained clean coal with an ash value of 36% from a feed coal of about 66% ash.

Bastürkcü, (2011), [18] studied to remove pyritic sulfur from coal. The test results shown that Falcon concentrator could remove percent of 50-60 of pyritic sulfur from Tuncbilek coal under optimized conditions (74 μm, 30%, 300 G).

135.3. 2.3.Multi Gravity Seperator

The MGS combines the centrifugal motion of an angled rotating drum with the oscillating motion of a shaking table, to provide an enhanced gravity separation, particularly suited to fine particles. The principle of the separation in the MGS is based upon centifugal and gravity forces that act on particles in a slurry stream being fed and are distributed onto the inside of the drum‘s surface. With the aid of scrapers and wash water, the high spesific gravity (SG) particles migrate up the drum to discharge over the drum‘ s top lip, while the low SG particles flow in the opposite direction and discharge over the lower drum lip. Drum rotational speed or spin, drum wash water, drum tilt angle are significant operating parametres in the unit of MGS. A schematic view of MultiGravity Separator shows in Fig. 4.

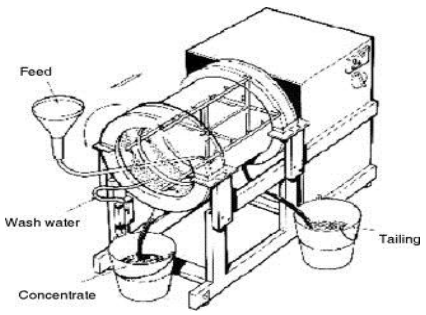

Figure 4. Schematic represantation of a Multi Gravity Seperator [3].

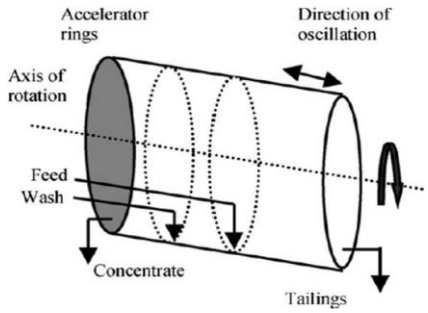

Figure 5. Particle Seperation Mechanism of Multi Gravity Seperator [3].

MGS succesfully used in recovery of cassiterite, chromite, wolfamite, graphite, mixed sulfides, and gold beneficiation [12]. It has some advantages such as very selective separation with fine-sized particles (typically -75+10 μm), high upgrading ratios (typically 20 to 1), on the other hand low capacity, mechanically quite complex and expensive, unsuited for treating coarse material are disadventages (e.g. [12], [14]).

Göktepe, (2005), [19] investigated the treatment of lead–zinc mine wastes by the multi-gravity separator. A laboratory study was carried out to find the most effective conditions using parameters such as drum angle and size fraction. The test results has demonstrated that approximately 12% of the Pb can be removed in the form of concentrate with 12% Pb content.

Özgen vd, (2012), [20] investigated the possibility of beneficiation of chromite tailings by a combination of hydrocyclone and multigravity separator (MGS).The two significant operational

parameters of hydrocyclone, which are diameter of the apex and diameter of the vortex, and the three significant operational parameters of the MGS, which are drum speed, tilt angle, and wash water, were varied and the results were evaluated. Diameter of apex of 4.8 mm, diameter of vortex of 11 mm, drum speed of 140 r/min, tilt angle of 6º, and wash water flow rate of 7 l/min have been determined as optimum levels. As a result of the experimental studies, chromite concentrate obtained with 45,76 % content and 80,94% chromite recovery from tailings.

Özgen, et., al, (2010), [21] studied to recover hard coal and lignite from tailings by using MGS. Various operating and design conditions of MGS such as, drum speed, tilt angle, shaking amplitude, wash water rate, feed rate and pulp solid ratio were investigated. A hydrocyclone was also used for pre-enrichment with the MGS. The results shown that clean lignite was obtained with 22.83% ash, and recovery of 49.32% from lignite has 66.21% ash and clean hard coal was obtained with 6.98% ash, and recovery of 85.61% from a hard coal has 28.41% ash by using hydrocylone and Multi Gravity separator.

2.4. Kelsey Jigi

The Kelsey jig, developed in the last 20 years, is the best-known example of a centrifugal jig. The principle of the Kelsey jig is similar to the conventional jigs in terms of the pulsing motion of the bed., but it is used to centrifugal ‗G'' force which increases the sensitivity of the separation for finer and similar density particles to be separated (Fig. 6) [14]. [22]. Kelsey jigi currently used in for beneficiation of ultra-fine coal (0,5-0,038 mm). Operating paremetres consist of rotation speed ,sieve size, ragging bed depth, thickness of ragging bed and pulsatition frequency and (e.g. [12], [22]).

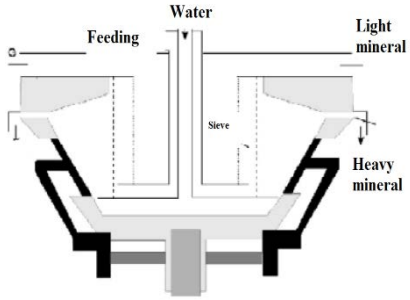

Figure 6. Schematic view of kelsey jig [12].

Singh, R.K., and Das, A., (2013), [22] investigated the effects of different process variables (rotational speed, pulsatition frequency and ragging bed depth) for beneficiation of coal by using Kelsey jig The results shown that clean coal was obtained with 21,6% ash content and recovery of 75% from coal has 27,5% ash.

3. The Other Gravity Separators

3.1. FGX Separator

The FGX dry cleaning system employs the separation principles of an autogenous medium and a table concentrator, as shown in Fig. 7. The separation process generates three products concentrate, middlings and tailing streams. Two dust collection systems are employed to clean the recycled air and to remove the dust from air being emitted into the atmosphere. The separating compartment consists of a deck, vibrator, air chamber and hanging mechanism. A centrifugal fan provides air that passes through holes on the deck surface at a rate sufficient to transport and fluidize the particles. Light particles are lifted up the back plate at a higher elevation than the dense particles As such, light particles create the upper layer of particles that are collected along the length of the table. The heavy particles are forced by both vibration and the new feeding material. The heavy particles comes to end of the table where the final refuse (tailing) is collected. Performance data for the FGX separator is currently limited to tests on Chinese coals and a few pilot-scale tests on U.S. coals. However, the separation data collected to date indicates that this system offers an attractive and cost-effective alternative to traditional coal preparation processes [23].

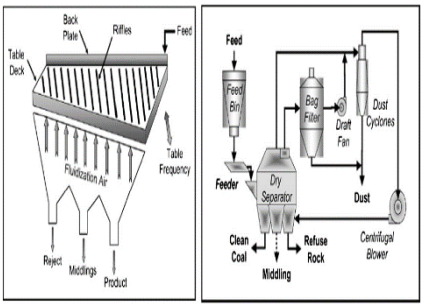

Figure 7. Schematics showing the basic operation of the FGX separator unit [3].

T.Ghosh and et al, (2014), [24] conducted to remove pyritic sulfur from sub-bituminous coal by using a pilot-scale FGX. The separation results shown that, clean coal was obtained with 7% ash content and recovery of 83% from low rank coal has 26% ash as well as, sulfur reduction and pyrite rejection were carried out.

3.2. The Floatex Density Separator

The Floatex Density Separator (FDS) is a shaker-bed based gravity separator which is used to separate different density minerals. Both the size and density have substantial influence on the separation process. The separator consists of an upper tank with a square cross-section and a lower conical section (Fig.7) As the feed enters the separator, the lighter and finer materials are carried over to the overflow by rising water. The heavier and larger materials start to settle against water through the dense suspension and deposite at the bottom forming a bed. This bed formation is similar to that formed in a typical hindered bed separator. The deposited bed materials expand into a teetered bed as a result of the rising current of water. This bed acts as an artificial heavy medium. The separator is equipped with a pressure sensor mounted at the bottom of the square tank and a control valve which is fitted at the bottom of the conical section. Separation performance of the FDS depends upon the pressure setting, teeter water, flow rate and feed characteristics [25].

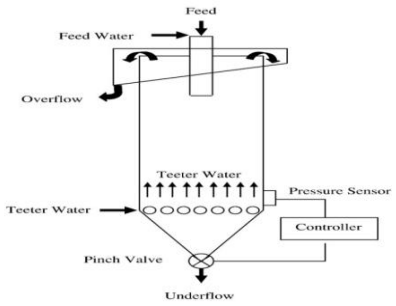

Figure 7. Schematic diagram of Floatex Density Separator [25].

Raghukumar, C., and et al, (2012), [26] conducted to recover producing sinter/ pellet concentrate by using flotex density separator.Two conceptual flow sheets have considered for the beneficiation of Indian high alumina fine iron ores The first option, consisting of followed by two stage gravity concentration results in a the concentrate was obtained with with 66.82%Fe content and recovery of 25.15%.from iron ore has 59.77 % Fe by using Floatex Density Separator and two stage gravity concentration.. In the second option, the iron concentrate was obtained with 67.77 %Fe and recovery of 28.95% from iron ore has 59.77% Fe by using magnetic separation.

3.3. Continuous vibrated gas-fluidized bed separator

Heterogeneous particles under fluidization tend to segregate by size/density [4]. When a fluidized bed is used to separate fine coal, more effort should be made to strengthen the density segregation.a narrow size range must be used for fine particles. to reduce the effect of size segregation on separation performance. But, fine coal particles are very prone to commence channeling and large bubbles in a conventional gas-fluidized bed, leading to a poor performance of density segregation. Therefore, vibration energy is introduced to eliminate the channeling and improve fluidization quality (Fig.9). A fluidized bed of fine coal under the collaborative function of air flow and vibration has a large bed expansion and gentle bubbling behavior. Fine coal particles conduct hindered settling processes under the gravity force and air drag force. Gangue particles with higher density have bigger settling acceleration than clean coal particles with lower density. Thus, gangue particles settle faster and arrive at the bottom of the bed. Finally, particles in the upper section of the bed are collected as a clean coal product[4].

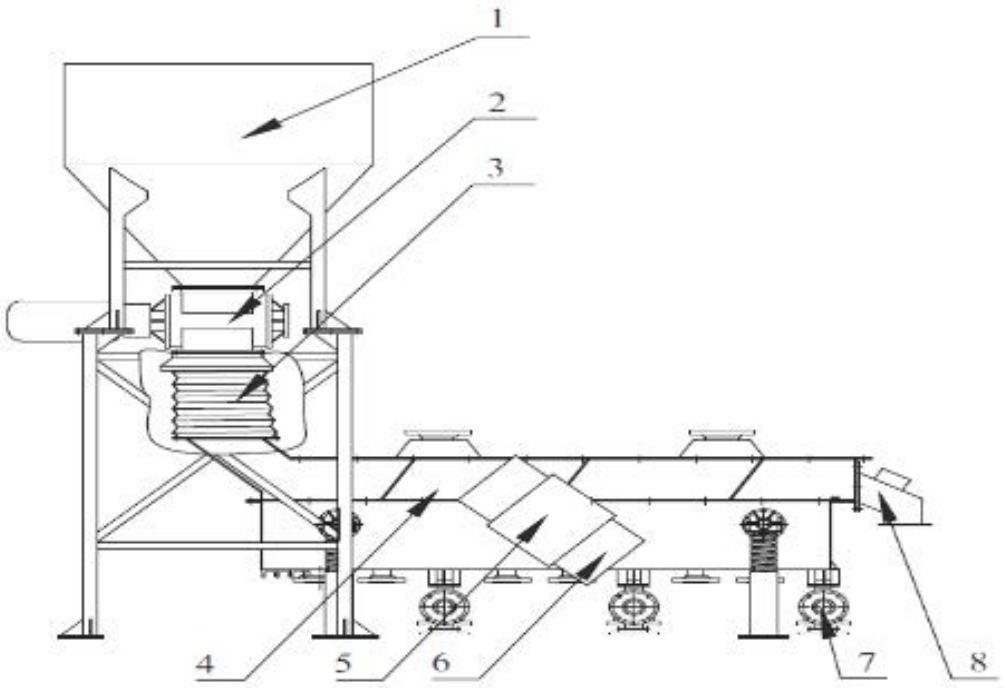

Figure 9. Mechanical structure of the continuous vibrated gas-fluidized bed separator. 1 Feed silo; 2 impeller feeder; 3 flexible coupling materials; 4 separating bed; 5 vibration motor; 6 air chamber; 7 impeller discharging device; 8 overflow discharge opening of clean coal [4].

Yang and et al, (2015), [4] developed a continuous vibrated gas-fluidized bed separator for dry beneficiation of fine coal and it use no dense medium and water. The optimal vibration angle were determined in the range of [63^o, 68^o]. The optimal feeding velocity was determined as 0.280 kg/s. The beneficiation performance was also evaluated by separating 3 + 1 mm fine coal. The results show that the probable error, E, is 0.225, indicating that a continuous separator can achieve a satisfactory performance of fine coal dry beneficiation.

4.CONCLUSION

In these study; working principles, working parameters and enrichment sizes of new technology gravity separators are investigated. And also it has been investigated in enrichment of which kind of ore with these devices. Literature reviews conducted that Falcon and Knelson concentrators are preferred in gold, silver and platinum group while multi gravity separator used for metalic group (cassiterite, tin, kromit, volframit) recovery. On the other hand, Kelsey jig is chosen in fine coal enrichment. The other gravity devices (FGX separator, Floatex density separator, continuous vibrated gas-fluidized bed) also used coal and metallic ore recovery. New technologies gravity devices that use very large area is also used for the evaluation of ore tailings. While gravity separator selecting, conditions must be taken into consideration at the facility. The variable parameters of the separator must be tested. And also, further studies on the gravity separator are necessary in scientific and industrial scale.

REFERENCES

[293]. Wills, B. A, –Mineral Processing Tecnology", Sixth edition, pp. 214-235. 2001.
[294]. Kokkılıc, O., Langlois,R., Waters, K.E, –A design of experiments investigation into dry separation using a Knelson Concentrator", Minerals Engineering, Vol.72, pp.73-86. 2015.

[295]. Xia,W., Xie, G., Peng,Y, –Recent advances in beneficiation for low rank coals", Powder Technology, Vol.277, pp.206–221. 2015.

[296]. Yang,X., Zhao, Y., Zhou, E., Luo, Z., Fu,Z., Dong, L, Jiang, H, –Kinematic properties and beneficiation performance of fine coal in a continuous vibrated gas-fluidized bed separator", Fuel, Vol.162, pp. 281–287. 2015.

[297]. Huang, L. –Upgrading of Gold Gravity Concentrates: A Study of the Knelson Concentrator", PhD thesis, Department of Mining and Metallurgical Engineering, McGill University, Montreal. 1996.

[298]. Laplante A.R., Shu, Y., and Marois, J, –Experimental Characterization of a Laboratory Centrifugal Separator", Canadian Metallurgical Quarterly, Vol.35 No.1. pp.23- 29. 1996.
[299]. Magumbe, L, –Process Desing for Gold Recovery from The Chester Deposit", Master Thesis, Laurentian Üniversitesi. 2002.

[300]. Sabah, E. and Koltka, S, "Separation Development Studies on the Beneficiation of Fine Lignite Coal Tailings by the Knelson Concentrator", Energy&Fuels, Vol.28.No.7, pp. 4819-4827. 2014.
[301]. Greenwood,M., Langlois,R., Waters, K.E, –The potential for dry processing using a Knelson Concentrator", Minerals Engineering, Vol.45, pp.44–46.2013.

[302]. Kıyak, T., Karaguzel., Knelson konsantratörü çalışma parametrelerinin kromit zenginleştirme tesisi artıklarından kromit kazanımına etkisi, IMCET 2015 Bildiriler Kitabı, Antalya, TURKEY. 2015.

[303]. Majumder, A.K., Barnwal J.P.ve Ramakrishnan, –A. Modelling of enhanced gravity", Mineral Processing& Extractive Metalurgy, Vol.27, pp.61-86. 2006.
[304]. Öney, O., –Inevestigation of the enrichment of Zonguldak fine coal", Dokuz Eylül University of Science Institute, Izmir-TURKEY. 2012.

[305]. (2016) The website. [Online]. Available:https://www.911metallurgist.com.

[306]. Falconer, A, –Gravity separation old techniques /new methods", Physical Separation in Science and Engineering, Vol. 12, No. 1, pp. 31–48. 2003.

[307]. Lu, D.,Wang,Y., Jiang,T.,Sun,W.,Hu,Y, –Study On Pre Concentration efficiency of wolframite from tungsten ore using gravity and magnetic separations", Physicochem. Probl. Miner. Process. Vol.52, No.2. pp.718−728 . 2015.

[308]. Liu,Q.,Cui,Z.,Etsell,T.H, –Pre-concentration and residual bitumen removal from Athabasca oilsands froth treatment tailings by a Falcon centrifugal concentrator", International Journal of Mineral Processing, Vol.78, pp. 220–230. 2006.

[309]. Oruç, F.,Özgen,S, Sabah,E, –An enhanced-gravity method to recover ultra-fine coal from tailings: Falcon concentrator", Fuel, Vol.89, pp. 2433–2437. 2010.

[310]. Bastürkcü,H, –Removal of sulphur from coal with falcon concentrator", Istanbul Technical University of Science Institute, Istanbul-TURKEY. 2011.

[311]. Ozgen,S, –Modelling and optimization of clean chromite production from fine chromite tailings by a combination of multigravity separator and hydrocyclone", The Journal of The Southern African Institute of Mining and Metallurgy, Vol.112, pp. 387-393, 2012.

[312]. Göktepe,F, –Treatment of lead mine waste by a Mozley multi-gravity separator (MGS)", Journal of Environmental Management Vol.76, pp.277–281. 2005.

[313]. Özgen,S., Can,F.M., Sabah,E, –Studies of a Multi Gravity Separator (MGS) to Produce Clean Coal from Turkish Lignite and Hard Coal Fine Tailings", Conference Paper, OCT. 2010.

[314]. Singh, R.K., Das,A, –Analysis of separation response of Kelsey centrifugal jig in processing fine coal", Fuel Processing Technology, Vol.115, pp. 71–78.2013.
[315]. Honaker,R.Q, –Development of an advenced deshaling technology to improve the energy efficiency of coal handling processing and utilization operations", Technical Repor t,p.34.2007.

[316]. Ghosh, R.Q. Honaker, D. Patil, B.K. Parekh, –Upgrading low-rank coal using a dry, density-based separator technology", Int. J. Coal Prep. Util. Vol.34, pp.198–209. 2014.

[317]. Das, A., Sarkar, B., Mehrotra,S.P, –Prediction of separation performance of Floatex Density Separator for processing of fine coal particles", Int. J. Miner. Process. Vol. 91, pp. 41–49. 2009.

[318]. Raghukumar,C., Tripathy, S.K.,Mohanan,S, ―Beneficiation of Indian High Alumina Iron Ore Fines a Case Study", International Journal of Mining Engineering and Mineral Processing Vol.1, No.2, pp. 94-100, 2012.

[319]. Rowe P.N., Nienow A.W, ―Particle mixing and segregation in gas fluidised beds. A review". Powder Technol,Vol.15.No.141.1976.

ISBN: 978-605-83575-0-1

2016 BOOK OF PROCEEDINGS

ICENS
International Conference on Engineering and Natural Sciences
www.icens.eu

ICOEST
International Conference on Environmental Science and Technology
www.icoest.eu

ICSD
International Conference on Sustainable Development
www.icsd.eu